



Universitat Autònoma de Barcelona

**Nanostructured micromaterials and devices
for sensing and removing of chemical
contaminants**

Adaris María López Marzo

Directors

**Prof. Dr. Arben Merkoçi
Dr. Josefina Pons Picart**

Chemistry Doctorate

**Chemistry Department
Science Faculty
PhD Thesis, 2013**

Document presented to obtain the PhD degree by Adaris María López Marzo

Adaris María López Marzo

Prof. Dr. Arben Merkoçi

ICREA and Nanobioelectronics
and Biosensors Group,
Catalan Institute of Nanoscience
and Nanotechnology, ICN2

Dr. Josefina Pons Picart

Department of Chemistry,
Faculty of Science,
Universitat Autònoma de Barcelona,
UAB

Bellaterra, 3 of May of 2013

To my mother, my aunts and uncles

Agradecimientos

Hace alrededor de tres años y medio esto era apenas un sueño, sólo una ilusión. Mi primer paso en llegar hasta aquí fue a través de un correo de contacto realizado a la Dra Josefina Pons donde le solicitaba un proyecto para optar a una beca de doctorado en España. Sin conocerme su respuesta fue totalmente positiva. A partir de ahí se desencadenaron una serie de correos que desembocaron en la solicitud y posterior aceptación de la beca de la Generalitat de Catalunya que me permitió viajar a Barcelona. Este era el inicio de lo que se convertiría en una estrecha relación alumno director. Aún recuerdo mi primer día en la planta de química inorgánica y mi primera reunión con Fina como si fuera ahora mismo. Gracias Fina por darme siempre apoyo, confianza y seguridad en el trabajo, gracias por el soporte científico y emocional. Quiero expresarle también mi agradecimiento al Dr. Arben Merkoçi por haberme recibido en su grupo, por su paciencia conmigo en las reuniones de trabajo, por sus novedosas ideas, sugerencias, sus constantes correcciones a mi inglés y gracias porque siempre que abrí la puerta de tu oficina tuviste una sonrisa para mí.

Mi agradecimiento para la Dra Diane A. Blake quien también sin conocerme respondió a mi primer correo de contacto con mucha disposición, para lo que se convertiría después en una colaboración, proporcionándonos el anticuerpo monoclonal 2A81G5 con el cual fue posible la realización de dos artículos científicos.

Gracias al Dr. Jordi García Antón por su ayuda y amistad incondicional siempre que lo he necesitado. Gracias al Dr. J. C. Bayón por su especial susceptibilidad, generosidad y preocupación por los problemas de los doctorandos extranjeros; gracias al Dr. J. Ros Badosa por su colaboración y al Dr Ramón Yañez por su ayuda con la informática y la recuperación de ficheros dañados en momentos límites.

Ar Dr. Alfredo de la Escosura porque siempre que acudí con duda supo solucionarlas.

A todas las personas que me han ofrecido soporte técnico con equipos y mediciones tanto en la UAB, ICMAB, como en el ICN, Ignasi, Isidre, los cristalógrafos Anna Crespi and Pablo, Belén Ballesteros (me fueron muy útiles tus explicaciones de SAED y HTEM), Cristina Granaderos y muy en especial Marco Rosado Iglesias con quien compartí muchísimas sesiones de SEM, a todos ellos muchas gracias.

A mis compañeros de la planta de inorgánica con quien he compartido agradables e inolvidables momentos. Muy en especial a mis ya amigos Dani Peral (gracias por siempre estar ahí para todo cuánto necesité), Joan Aguiló (gracias por ser como eres), Joan Lecina (gracias por tu ayuda con la tecnología), Miguel Guerrero (gracias por tan magnífica acogida desde mi llegada, has sido tú el primero en asesorarme aquí en el laboratorio. Igual a ti Gemma, por tus conocimientos y ejemplo. En general a todo el resto de chicos en la planta de inorgánica y a algunos que ya han marchado: Edu, Alba, Lourdes, Miquel, Fernando, Leo, Mireia, Katia, Catalina, Mercè, Hai Jie, Laia, Sílvia, Adu, Karen, Frank, M^a Angeles y otros.

A mis compañeros del Laboratorio de Nanobioelectrónica y Biosensores, a Anna Puig una excelente "group manager" siempre dispuesta a colaborar conmigo, a M^a Guix, la bella catalana, siempre ofreciendo buenos consejos. A Cláudio por pasarme sus habilidades con la técnica del lateral flow, a Carmen por su disposición en utilizar mi material para su trabajo, a tí Alex por recordarme siempre a Cuba. Lenka gracias por tu comprensión y tu rápida respuesta con las cartas. En general a todo el resto del grupo Merkoçi por los momentos de recreación compartidos: a Briza, Marisol, Mariza, Luis, Sandrine, Mariana, Helena, Eden, Flavio y otros.

Al club de amigos latinos: a Caty, Lena Ana Iris, Ana, Caro, Mauricio, y otros, por el soporte emocional y de despeje tan necesario cuando se hace un trabajo intelectual intenso, los buenos momentos, fiestas, comidas, etc. A mis compañeros de piso, por hacerme la vida mas entretenida cuando llegaba de la uni, sobre todo a ti Victor.

A mi familia por haber dado siempre tanto de sí para educarme, muy en especial a mi madre, e incluso a aquellos que ya no están con nosotros, por la educación que me dieron y los valores humanos que me supieron inculcar como el amor al trabajo y el respeto y consideración hacia los otros.

Finalmente quisiera agradecer el estar en esta bella, fantástica y cosmopolita ciudad que es Barcelona. Barcelona tiene el encanto de ciudad de la que no te puedes desprender nunca, sus calles, sus bares, su arquitectura y el catalán, esa lengua encantadora como música para los oídos.

También es importante destacar el soporte financiero recibido de: La Generalitat de Catalunya por la beca concedida, el proyectos del Ministerio de Ciencia e Innovación MAT 2011-25870 y el proyecto internacional bilateral España-Japón PIB2010JP-00278.



GLOSSARY OF MOST USED TERMS AND ABBREVIATIONS

AAS: atomic absorption spectroscopy

AuNPs: gold nanoparticles

BET: Brunauer–Emmett–Teller

BJH: Barret–Joyner–Halenda

CGM: crystal growth modifier

EDTA: ethylenediaminetetraacetic acid

FTIR: Fourier transform infrared spectroscopy

GFAAS: graphite furnace atomic absorption spectroscopy

HRTEM: high resolution transmission electron microscope

ICPES: inductively coupled plasma emission spectrometry

ICPMS: inductively coupled plasma mass spectrometry

IR: infrared spectroscopy

LFA: lateral flow assay

LFIA: lateral flow immunoassay

LFD: lateral flow device

LFID: lateral flow immunodevice

LoD: limit of detection

LoQ: limit of quantification

mAb: monoclonal antibody

NPs: nanoparticles:

NRs: nanorods

NTs: nanotubes

pAb: polyclonal antibody

PEI: poly(ethyleneimine)

Q_{max}: maximum adsorption capacity

SAED: selected-area electron diffraction

SEM: scanning electron microscopes

TEM: transmission electron microscope

TGA: thermogravimetry analysis

XRD: X-ray diffraction

PREFACE

This PhD thesis has been developed during the period from June 2010 to April 2013 in the frame of the *Generalitat de Catalunya* scholarship (2010FI-B 00791) awarded to the author. It corresponds to the doctorate program RD 1393/2007: Studies of Chemistry Doctorate.

According to the decision of PhD commission of the UAB taken on March, 2013, this PhD thesis is presented as compendia of publications. Considering the works presented to the UAB PhD commission the following publications have been considered for this thesis presentation as ‘compendia of publications’:

- 1- Adaris López-Marzo, Josefina Pons and Arben Merkoçi. *Controlled formation of nanostructured CaCO₃-PEI microparticles with high biofunctionalizing capacity*. Journal of Material Chemistry, 2012, 22, 15326.
- 2- Adaris López-Marzo, Josefina Pons, Diane A. Blake and Arben Merkoçi. *High sensitive gold-nanoparticle based lateral flow immunodevice for Cd²⁺ detection in drinking waters*. Biosensing and Bioelectronics, 2013, DOI: 10.1021/ac3034536.
- 3- Adaris López-Marzo, Josefina Pons, Diane A. Blake and Arben Merkoçi. *Analytical Chemistry. All-integrated and highly sensitive paper-based device with sample treatment platform for cadmium immunodetection in drinking/tap waters*. Analytical Chemistry, Just Accepted Manuscript DOI: 10.1021/ac3034536.

In addition the following manuscripts are used as annexes or non-fundamental part although commented in the part of results and discussion as determined by the UAB PhD commission:

- 4- Adaris López-Marzo, Josefina Pons and Arben Merkoçi. *Multifunctional system based on hybrid nanostructured calcite-PEI microrods formation, for lead ‘sensoremoval’ applications* (manuscript that will be submitted).
- 5- Adaris López-Marzo, Josefina Pons and Arben Merkoçi. *Extremely fast and high Pb²⁺ adsorption capacity via use of a hybrid nanostructured vaterite-PEI* (manuscript that will be submitted).
- 6- Carmen C. Mayorga-Martinez, Lenka Hlavata, Sandrine Miserere, Adaris López-Marzo, Jan Labuda, Josefina Pons and Arben Merkoçi. *A simple phenol sensing and removing system using a nanostructured platform*. (2013, submitted to publish).

- 7- Carmen C. Mayorga-Martinez, Lenka Hlavata, Sandrine Miserere, Adaris López-Marzo, Jan Labuda, Josefina Pons and Arben Merkoçi. *Nanostructured CaCO₃-PEI microparticles for phenol sensing in fluidic system*. (2013, submitted to publish).

In addition to the mentioned publications, part of this PhD thesis was presented in the following scientific events:

- 1- Adaris M. López Marzo, Claudio Parolo, Josefina Pons, Diane A. Blake and Arben Merkoçi. “High sensitive and integrated LFD for Cd²⁺ determination in drinking water”, *Jornades doctorals UAB*, June 2012, Barcelona, Spain.
- 2- Adaris M. López Marzo, Claudio Parolo, Josefina Pons, Diane A. Blake and Arben Merkoçi. “High sensitive lateral flow device for cadmium determination”. *Wam-Nano2012 Workshop*, June 2012, Barcelona, Spain.
- 3- Adaris M. López Marzo, Gemma Aragay, Claudio Parolo, Alfredo de la Escosura, Josefina Pons and Arben Merkoçi. “Synthesis of CaCO₃ micro and nanoparticles for future biosensing applications. *XVI^{èmes} Rencontres Transfrontalières “Capteurs at Biocapteurs”*”, September 2011, Toulouse, Francia.

This PhD thesis contains seven chapters. Chapter one is the introduction where some topics of interest for the thesis fields (chemical contaminants and their reported sensing and removing strategies) are described. In chapter two the objectives of the whole thesis work are highlighted. The results and discussions are displayed through the chapters three, four, five and six while chapter seven discloses the general and specific conclusions. In the annexes are attached as published papers or as manuscripts the results from this work. Annex I contains articles accepted by the PhD commission. Annex II the submitted manuscripts and annex III additional articles as support for electrochemical applications of the CaCO₃ material developed in this PhD thesis work.

SUMMARY OF THE THESIS

The control and elimination of the environmental levels of chemical contaminants is an actual problem that science is trying to solve. The development of new, fast, cheap and effective materials, devices and systems for sensing and removing chemical contaminants continues to be of interest for preserve the environment and human health. This PhD thesis is related to the study and development of innovative nanostructured materials, devices and strategies with interest for pollutants detection and removal being in line with the nowadays challenging of environmental technologies. Of special interest is the integration of sensing and removing processes achieving a dual “sensoremoval” actuation for contaminants within the same platform/system. While chapter I and II give a general introduction of the topic and objectives of the thesis work, large part of the results and discussions (included in the chapters III to V) is related to the development of novel nanostructured materials based on a CaCO_3 -polymer composite with different morphologies and polymorphs that were synthesized, characterized and applied to sensing and removing of chemical contaminants such as heavy metals. The design and evaluation of highly sensitive LFIDs for heavy metal sensing has also been an important focus of this work included in chapter VI. Other works (collaborative works) as support of the electrochemical applications of the CaCO_3 -polymer material for sensing and removing low phenol concentrations are attached at annex III.

Chapter III, is related to the article titled “*Controlled formation of nanostructured CaCO_3 -PEI microparticles with high biofunctionalizing capacity*”, published in Journal of Material Chemistry, 2012, 22, 15326. It deals with the development of a novel route of synthesis of vaterite structures with the obtaining of the final nanostructured CaCO_3 (vaterite)-PEI microparticles (spheres/ellipsoids-like shape) hybrid material. This new synthesis was shown to be able to provide a complete polymorphic discrimination along with a controlled and homogeneous particle size distribution of a nanosctructured CaCO_3 (vaterite)-PEI formed through the reaction between CaCl_2 and NaCO_3 under 45 min sonication, using 8 mg/mL PEI as CGM in mixed water–organic solvent ($\text{H}_2\text{O}/\text{EtOH}$). The CaCO_3 (vaterite)-PEI material presented a high functionalizing capacity for biomolecules and an increase of the superficial charge, properties that make it suitable for electrochemical application as demonstrated in the supporting articles at annex III.

Chapter IV, corresponds to the manuscript titled “*Extremely fast and high Pb²⁺ removal capacity via use of a hybrid nanostructured vaterite-PEI*”, that studies the performance of the hybrid/nanostructured vaterite-PEI as heavy metals removal. The developed material shows an extremely high and fast Pb²⁺ removal capacity without precedents. Just 3 min are enough to remove between 97-100% of this metal contaminant from a large concentration range from 0 to 1000 ppm with a dosage of 0.5 g/L at pH 6 the most common water pH. The maximum adsorption capacity was 2762 mg of Pb²⁺/g adsorbent material obtained at 1500 ppm Pb²⁺ initial concentration and removing in 6 min around 92% of this initial Pb²⁺ contamination. This surprising result of removing capacity is ascribed to the excellent nucleophilic character of PEI by metal centers besides the re-crystallization process via ionic exchange where Ca²⁺ are substituted by Pb²⁺ behaving the vaterite-PEI material like a wide ionic interchanger. The results showed that it could be a promising material for practical water treatment applications, facile to be synthesized, cheap, biodegradable and innocuous.

In chapter V a multifunctional system based on hybrid nanostructured calcite-PEI microrods formation, for lead ‘sensoremoval’ applications is described. The hybrid and nanostructured calcite-PEI particles in suspension permit the Pb²⁺ detection through a simple turbidimetric measurement, and at the same time act as heavy metal remover. This sensing and removing system is able to detect up to 1 ppm lead (being between 1 and 1000 ppm the lineal range) and reaches an adsorption capacity of 240 mg Pb²⁺/g calcite as evaluated at pH 4 after 30 min incubation time. The Pb²⁺ detection range found for this system is suitable to evaluate levels of metal contamination from industrial waste waters that use to be around 1-100 ppm. In addition the maximum Pb²⁺ removal capacity reported here is higher than other ones reported before using materials not as cheap and biodegradable as calcite. This chapter corresponds to the manuscript “*Multifunctional system based on hybrid nanostructured calcite-PEI microrods formation, for lead ‘sensoremoval’ applications*”.

Finally the results shown in chapter VI belong to publications “*High sensitive gold-nanoparticle based lateral flow immunodevice for Cd²⁺ detection in drinking waters*, Biosensing and Bioelectronics, 2013, 47, 190” and “*All-integrated and highly sensitive paper-based device with sample treatment platform for cadmium immunodetection in drinking/tap waters*, Analytical Chemistry, 2013, 85, 3532”. These parts of the thesis are related to a novel LFID for Cd²⁺ determination in drinking and tap waters using the Cd-EDTA-BSA-AuNP conjugate as signal producer tool. The working principle is

based on competitive reaction between the Cd-EDTA-BSA-AuNP conjugate deposited on the conjugation pad strip and the Cd-EDTA complex formed in the analysis sample for the same binding sites of the 2A81G5 mAb, specific to Cd-EDTA but not to free Cd²⁺, which is immobilized onto the test line. The device has a large response range within 0.4-2000 ppb, being the linear response between 0.4 and 10 ppb. The LoQ and LoD of 0.4 and 0.1 ppb, respectively, represent the lowest ones reported so far for paper based metal sensors. During the specificity assay the optimum and adequate EDTA and ovalbumin (OVA) (0.005mM and 10%) concentrations for masking the metals interferences and allow Cd²⁺ detection were found. In addition a second integrated device was designed and fabricated. This new platform operates without any sample pretreatment step thanks to an extra conjugation pad that ensures Cd²⁺ complexation with EDTA and interference masking through OVA. The recoveries of the device were between 95-105% with coefficient of variation of the intermediate precision assay inferior to 10%. This integrated platform is easy to be built, cheap, portable and simple to manage even by non skilled persons, which makes it very useful for cadmium analysis in point of care diagnostics or where a rapid contamination monitoring is very necessary or in field analysis in remote locations with limited facilities.

The research carried out in the framework of this PhD thesis aims to develop materials, systems and devices to be used as sensing or removal strategies or even with the simultaneous dual sensing-removal function of chemical contaminants. These results are very important for industrial applications where practical, cheap and fast control and remediation technologies are needed. Moreover the materials and devices here proposed and the corresponding technologies are with interest for mass production at industrial level, are cost/effective and related to green technologies. In addition this PhD thesis will open the way to new research lines for various other applications with interest not only for environment science but also for health, safety and security as well as other industries.

TABLE OF CONTENTS

INTRODUCTION

Chapter I. General Introduction	1
I.1 Chemical contaminants	1
I.2 Heavy metals: dangerous chemical contaminants	1
I.2.1 Nanomaterials based approaches for removing	2
I.2.2 Brief summary of analytical detection methods	3
I.3 Analytical detection methods using paper based platforms	4
I.3.1 General overview	4
I.3.1- a) State-of-the-art of paper-based assays	4
I.3.1- b) First types of paper based assays. LFAs	5
I.3.1- c) Competitive and sandwich formats: the two classical LFA approaches	8
I.3.1- d) LFA advantages and limitations.....	10
I.3.2 Strategies to overcome the drawbacks in paper-based devices	11
I.3.2- a) Signal producers particles used in paper-based devices.....	11
i) Particles used in connection to AuNPs for signal amplification	12
ii) Microparticles used as carriers of dyes	13
iii) Other (nano)materials	13
I.3.2- b) Paper based architectures.....	15
I.3.2- c) Integrated hybrids approaches	18
i) Integration with electrochemical methods	18
ii) Integration with microfluidic and Lab-on-Chip technologies	19
I.3.3 Applications in heavy metal detection	23
i) Use of enzymes as analyte recognizer molecules	23
ii) Use of other proteins as analyte capturing molecules	24
iii) Use of mAbs as analyte capturing molecules	24
iv) Use of specific-DNAzymes as analyte capturing molecules	25
v) Use of small chemical structures as analyte recognizer molecules	25

I.3.4 Conclusions and future prospects -----	28
I.4 References -----	30
Chapter II. Objectives -----	41
RESULTS AND DISCUSSION	
Chapter III. Controlled formation of nanostructured CaCO₃-PEI microparticles with high biofunctionalizing capacity -----	51
III.1 Introduction -----	51
III.2 Experimental part-----	53
III.2.1 Chemicals -----	53
III.2.2 Characterization techniques -----	53
III.2.3 Synthesis -----	54
III.2.4 Conjugation -----	55
III.3 Results and Discussion-----	55
III.3.1 Synthesis and characterization -----	55
III.3.2 Possible mechanism of formation of the vaterite microparticles-----	62
III.3.3 Z-Potential studies -----	65
III.3.4 Conjugation studies-----	66
III.3.5 Electrochemical applications of vaterite-PEI material-----	69
III.4 Conclusions -----	69
III.5 Supporting Information-----	71
III.6 References -----	75
Chapter IV. Extremely fast and high Pb²⁺ removal capacity via use of a hybrid nanostructured vaterite -----	83
IV.1 Introduction-----	83
IV.2 Experimental part-----	84
IV.2.1 Chemicals and synthesis of the adsorbent material -----	84
IV.2.2 Characterization techniques -----	84
IV.2.3 Removal kinetic experiments-----	84
IV.3 Results and Discussion-----	85

IV.3.1 Competitive assay of removal -----	85
IV.3.2 Adsorption isotherm of Pb ²⁺ onto NV-PEI material -----	88
IV.3.3 The N ₂ adsorption-desorption isotherms-----	89
IV.3.4 Interaction of the metal ions with the NV-PEI hybrid materials. Mechanisms of adsorption. -----	90
IV.4 Conclusions-----	94
IV.5 Supporting Information -----	96
IV.6 References -----	102
Chapter V. Multifunctional system based on hybrid calcite-PEI nanostructured- rods formation, for Pb²⁺ ‘sensoremoval’ applications-----	109
V.1 Introduction-----	109
V.2 Experimental part -----	111
V.2.1 Chemicals-----	111
V.2.2 Characterization techniques-----	111
V.2.3 Calcite formation and Pb ²⁺ sensing -----	112
V.2.4 Pb ²⁺ removal -----	113
V.3 Results and Discussion -----	113
V.3.1 Multifunctional integrated <i>sensoremoval</i> system-----	113
V.3.2 Characterization of the CaCO ₃ crystallization product in the proposed system-----	114
V.3.3 Pb²⁺ sensing by changes of turbidity during the calcite precipitation 118	
V.3.4 Pb ²⁺ removal via CaCO ₃ -PEI NRs -----	120
V.4 Conclusions-----	123
V.5 Supporting Information -----	125
V.6 References -----	130
Chapter VI. All-integrated and highly sensitive paper based device with sample treatment platform for Cd²⁺ immunodetection in drinking/tap waters-----	137
VI.1 Introduction-----	137
VI.2.1 Experimental part I: Conventional design -----	139

VI.2.1-1 Chemicals -----	139
VI.2.1-2 Characterization techniques -----	139
VI.2.1-3 Conjugation of Cd-EDTA-BSA with AuNPs. Gold aggregation test---	139
VI.2.1-4 Optimization of the LFID operational conditions-----	140
VI.2.1-5 Preparation of the conventional LFID -----	141
VI.2.1-6 Linearity and limits of detection and quantification-----	141
VI.2.1-7 Specificity assay -----	142
VI.3.1 Results and Discussion part I: Conventional design -----	143
VI.3.1-1 Conjugation of Cd-EDTA-BSA with AuNPs. Gold aggregation test---	143
VI.3.1-2 Design and operation principle of the convectional LFID-----	145
VI.3.1-3 Optimization of the LFID operational conditions-----	146
VI.3.1-4 Linearity and limits of detection and quantification-----	147
VI.3.1-5 Specificity assay -----	149
VI.2.2 Experimental part II: Integrated design -----	153
VI.2.2-1 Chemicals -----	153
VI.2.2-2 Characterization techniques -----	153
VI.2.2-3 Preparation of the integrated LFID -----	153
VI.2.2-4 Linearity and limits of detection and quantification -----	153
VI.2.1-5 Accuracy and precision assays -----	153
VI.3.2 Results and Discussion part II: Integrated design -----	154
VI.3.2-1 Design and operation principle of the integrated LFID -----	154
VI.3.2-3 Linearity and limits of detection and quantification -----	156
VI.3.2-4 Accuracy and precision assays -----	157
VI.4 Conclusions-----	160
VI.5 Supporting Information -----	162
VI.6 References -----	169
Chapter VII. General conclusions -----	175

Annex I. Articles accepted by the PhD commission

Annex II. Submitted manuscripts

Annex III. Additional support articles

CHAPTER I. GENERAL INTRODUCTION

I. GENERAL INTRODUCTION

I.1 Chemical contaminants.

Chemical contaminants are elements or compounds that can potentially harm the environment, living organisms and even the health of humans. Toxic chemicals are constantly entering the environment as consequence of industrialization or the natural process. They persist in water, soil, air and plants as source of intoxication. They generally are cytotoxic, carcinogenic, mutagenic or immunosuppressive, so that their monitoring is necessary to help protection of the environment and the human health. The regulatory agencies have addressed the problem by adopting regulatory limits and regulations that are now being strictly enforced in almost all countries. Chemical contaminants can be classified as organic or inorganic materials, natural or synthetic and by its physical state as solid, dust, fiber, smoke, metal fume, liquid, mist, brumes, aerosol and gas.¹

Typical water chemical contaminants are pesticides that come from agricultural activity (atrazine, carbaryl, diazinon, oryzalin and other), phenols, carboxylic acids, chloroform, benzene, toluene, sodic esterato, heavy metals, residues drugs (clenbuterol, fluoroquinolone, chloramphenicol) and other that come from industrial activity. Many of these chemical contaminants are still widely used.²

Others chemical contaminants as toxins are products of natural processes. Toxins are any poisonous substance to an organism; often restricted to poisons produced by living organisms as bacterias (endotoxin), fungus (micotoxins such as aflatoxin (AFT), ochratoxin A (OTA) and deoxynivalenol (DON)), higher plants (phytotoxins e.g., pyrethrins, nicotine and rotenone) and animals (zootoxins or venoms).³

I.2. Heavy metals: dangerous chemical contaminants.

Heavy metals at significant intake concentrations in living organisms can produce detrimental effects even hazard health in the case of human beings (e.g., lead, silver, mercury, copper, nickel, chromium, iron, manganese, zinc, cadmium and tin). In small quantities, certain heavy metals are nutritionally essential for life (e.g. iron, manganese, copper, etc). However, heavy metals show a great trend to form complexes, especially with ligands of biological matter containing nitrogen, sulfur and oxygen. As a result, changes in the molecular structure of proteins, breaking of hydrogen bonds or inhibition of enzymes can occur. These interactions, among others, may explain the toxicological

and carcinogenic effects of heavy metals such as those affecting the central nervous system (Hg^{2+} , Pb^{2+} , As^{3+}), the kidneys or liver (Cu^{2+} , Cd^{2+} , Hg^{2+} , Pb^{2+}), or skin, bones, or teeth (Ni^{2+} , Cu^{2+} , Cd^{2+} , Cr^{3+}).⁴⁻⁶ Heavy metals are not biodegradable and therefore they remain indefinitely in the ecological systems and in the food chain exposing top-level predators to very high levels of pollution.^{7,8}

Pollution by heavy metal ions is one of the worldwide environmental problems. Heavy metals have been isolated from soil and drinking water in residential areas. Efficient strategies to remove heavy metals from wastewater as well as analytical methods to monitoring their environmental levels continue to be of interest for ongoing researches.^{7,9-12}

I.2.1 Nanomaterials based approaches for removing.

Wastewaters from several industrial activities are an important source of environmental pollution, because of their high content of heavy-metal ions. The wastewater industrial residues that contain heavy metals must be removed to certain levels until meeting of discharge requirements. Currently, water treatment technologies for the removal of heavy-metal ions include chemical precipitation, membrane filtration, adsorption, ion exchange and electrochemical processes. In fact, metals removal from industrial wastewaters can be performed through the use of several unit operations, such as chemical precipitation, sedimentation, filtration and sludge treatment.¹³⁻¹⁵

Increasing efforts are showing last year to use nanotechnology as an environmental technology to protect the environment through pollution prevention, treatment, and clean-up of long-term problems such as hazardous waste sites. Advances in nanoscale science and engineering are providing new opportunities to develop more cost-effective and environmentally acceptable water purification processes through the use of nanomaterials. The development of nanomaterials and nanotechnology suggests that many of the current water treatment challenges could be resolved or greatly ameliorated by using nanostructured materials.¹⁶

Nanomaterials have several physicochemical properties, such as high surface area per unit volume and the ability to be functionalized with a number of surfactants to enhance their affinity toward target molecules, which make them particularly attractive for water purification. The special properties of nanomaterials are originated from the rich valence states and variable electronic structures. Nanomaterials have highly desired properties for *in situ* applications because of their minute size and innovative surface

coatings that may be able to pervade very small spaces in the subsurface and remain suspended in groundwater allowing the particles to travel farther than larger, macro-sized particles and achieve wider distribution. Because of the small size of nanoscale particles Brownian movement or random motion, rather than wall effects, dominates their physical movement or transport in water. Nanosized particles can be easily suspended in water during the design and manufacturing stages, thus providing a versatile remediation tool that allows direct injection as a liquid into the subsurface where contaminants are present.¹⁷⁻²¹

Many different nanoscale materials such as nanoscale zeolites, metal oxides and hydroxides, carbon nanotubes and fibers, enzymes, various noble metals (even bimetallic nanoparticles (BNPs)) and titanium dioxides have been explored for water remediation. Nanomaterials from transition metal hydroxides or oxides, especially iron, are extensively studied to remove toxic heavy metal ion in view of their low cost, natural abundance, and environment-friendly properties. In some applications typically, a noble metal (e.g., palladium, silver, copper) can be added as a catalyst. In the last ten years biominerals as CaCO_3 have been added to the list of potential water treatment nanomaterials.¹⁶

I.2.2 Brief summary of analytical detection methods.

As it is well-known GFAAES²² and ICPES²³ are the standard techniques for trace heavy metal analysis. However, these labor-intensive and time-consuming techniques require complex and expensive instruments and specialized personnel to carry out the operational procedures.^{23,24} For this reason, other analytical techniques as colorimetric,^{25, 26} fluorimetric,²⁷ and immunoassays more cheaper and faster than the two above mentioned and in addition highly sensitive and selective have been developed for heavy metal sensing.^{28, 29} Other methods that have been adapted to allow the miniaturization and in-field applications are the electrochemical methods, specially voltammetric^{30, 31} and potentiometric^{32, 33} techniques which also offer high sensitivity, low cost and simplicity, besides the possibility for in-field applications.

The development of colorimetric, flourimetric and electrochemical analytical methods (ex. ion-selective electrodes) for metal detection, is strongly related to the development of several kinds of molecules used as synthetic or natural receptors called ionophores. Many ionophores including small organic molecules³⁴⁻³⁹, macromolecules or caged molecules (crown ethers, calixarenes, ciclodextrins and other) have been described so

far,⁴⁰⁻⁴³ which can operate by two different ways of recognition: chemical affinity, cavity entrapment or both ways at the same time. Not only the binding affinity is important for the chemical sensing, but also the chemical response of the ionophore after the analyte binding. The biomolecules like nucleic acids,^{44,45} antibodies,⁴⁶⁻⁴⁸ proteins^{49,50} where enzymes play a highlight role have also been tested. Especially for electrochemical methods such as electrochemical stripping analysis metal alloys have been useful for films electrodes as Hg, Ag, Au, Ir, Bi and Sb.⁵¹⁻⁵³

However, for the mentioned heavy metals sensing techniques relatively cost equipment and even trained personnel are still necessary to carry out the analysis preventing their extended application in the routine detections of heavy metals. In this context analytical methods based on paper play an important role as tool of point of care assay to monitor heavy metals in different samples.

I.3 Analytical detection methods using paper based platforms

I.3.1 General overview

I.3.1-a) State-of-the-art of paper-based assays.

The first paper-based bioassay was introduced in 1957 for the identification of glucose in urine.⁵⁴ A strip of paper was impregnated with glucose oxidase, peroxidase, and 3,3'-dimethylbenzidine, dried, and then dipped in urine. Abnormal glucose levels were indicated on the strip by the development of a blue color. By the mid-1960s, this assay had been developed into a commercial product to diagnose and manage diabetes. In the same year a triple-test dipstick comprising three spatially-distinct chemically-coated areas ("patches") that developed distinct colors in response to urinary glucose, albumin, and pH was introduced.⁵⁵ After that other dipsticks tests for analytes like leukocytes, nitrite, ketones, urobilinogen, bilirubin, and blood, were developed and commercialized.⁵⁶ These dipsticks are packaged with a color-coded chart that allows the user to read out the detected quantity of a given analyte at a defined location along the length of the strip similar to paper-pH reader. In 1982, immunorecognition was first introduced to dipsticks by immobilizing antibodies on nitrocellulose, thereby increasing both the specificity and range of detectable analytes.⁵⁷ Urine-based home-use immunoassay test kits for various bioanalytes, including human chorionic gonadotropin (hCG, pregnancy hormone) and 9-tetrahydrocannabinol (pharmacological agent of marijuana) are now commercially available. Blood-based home-use dipsticks include

those for cholesterol, diabetes, hepatitis C, and human immunodeficiency virus type 1 (HIV-1).⁵⁸

Capillary-driven lateral flow was introduced to conventional dipstick technology in 1989.^{59,60} Lateral flow eliminated the incubation and wash steps of the standard protocol of dipstick-based assays. It also increased the total number of captured and detected analyte molecules in a given time improving the lower limits of detection. When wetted with an analyte-containing liquid at one end of the strip, the porous material provides a motive force for the movement of liquid from wet to dry areas of the strip, with the main motive force being capillary action within the pores.⁶¹

I.3.1-b) First types of paper based assays. LFAs

The technological advances in the last decades have driven to a new era in the analysis of biological agents and chemical contaminants. Analytical tools that are highly accurate, rapid, cheap and that can be used in the field have emerged allowing the development of point-of-care tests, such as dipstick, flow through, and LFA.⁶² These technologies offer advantages when compared to the conventional detection methods overall in terms of rapidity of response, simplicity and cost-effectiveness. In all of them paper is the main material used for developing these sensing devices. Paper is a low cost material, environment friendly material that can be easily printed, coated and impregnated with chemical reagents or (bio)molecules.⁶³ Furthermore paper based platform can be developed by using inkjet,^{64,65} wax printing⁶⁶ or screen printing⁶⁷ technology, making them amenable to in-situ fabrication⁶⁸ with interest to be delivered or even produced in areas with limited resources.

Dip sticks: Dipstick assays are based on the immunoblotting principle and do not rely on lateral fluid flow through a membrane. Dipstick usually follows the standard ELISA procedure, but uses a membrane (pre-stored with reagents) as immobilized antibody-coating support instead of microtiter plates (**figure 1-A**). But similar to ELISA, the performance of the four necessary working steps such as washing, blocking, sample incubation and staining requires a total time of 30 min to 3 h to obtain the test results, which cannot compete with 15–20 min LFA. The typical format used is the competitive immunoassay. A dipstick example is the pH strip.^{69,70}

Flow-through: In the flow-through device, the filter paper acts as an absorbent actively drawing liquid reagent quickly through the membrane without lateral spreading. Flow-through membrane based immunoassays are comparable with lateral-flow test strips in

rapidity and ease of use, but differently with this doesn't have all the reagents pre-stored in the strip. These are qualitative or semi-quantitative tests and interpretation of results may be difficult when the test result is close to the cut-off level (figure 1-B).⁷¹

LFAs: LFAs are currently the most versatile (several formats can be designed), fastest (the assay can be done in 20 min and in one-step) and therefore the more popular membrane-based assay, especially for applications outside the laboratory as “point of care”. The LFA can be considered as a well-established diagnostic tool. The best-known application is the pregnancy test. Similar to dipstick it has all the reagents pre-stored in the strip, but essential in the current LFA formats is the movement of a liquid sample containing the analyte of interest, along a strip of polymeric material passing various zones. A simple LFA device consists of four sections or zones (sample pad, conjugate pad, nitrocellulose membrane and absorbent pad) which are laminated into a sheet of plastic (backed accordingly) mostly formed of 5 mm wide and 50 mm long strip (figure 1C-1). The sample pad made of cellulose, contains the assay buffer and BSA in dried forms, which assures the optimal conditions for the analyte during all the flux. The conjugation pad, made of glass fibers, is used as dry-reagent storage for the labels (ex. dyes, gold nanoparticles etc.). In this pad the first binding reaction between the labels and the analyte starts. In the detection lines, made onto nitrocellulose membrane, the capture reagents are fixed and the signal is developed (figure 1C-2). Finally, cellulose filters are used as absorbent pad. The function of the absorbent pad is to wick the fluid through the membrane.^{70,72}

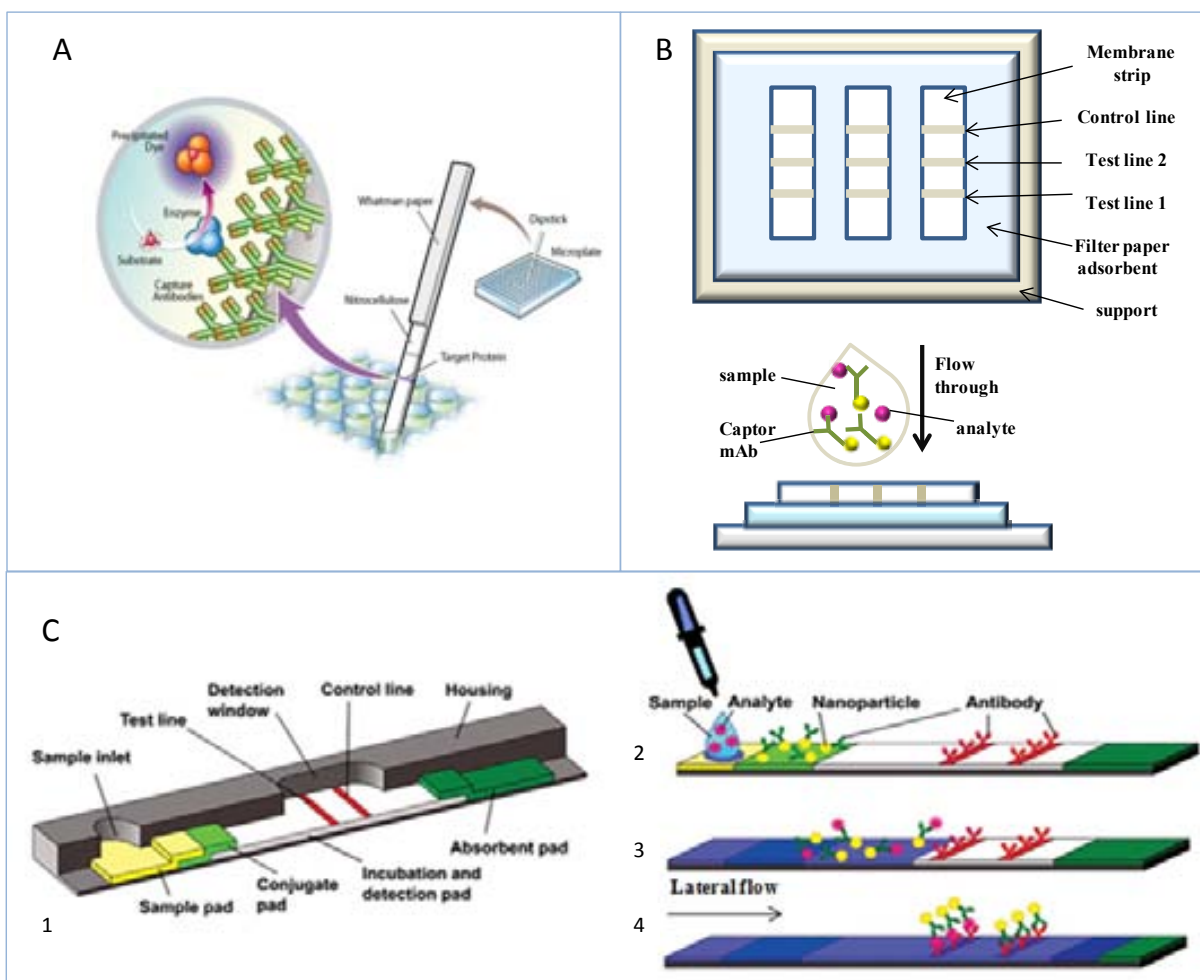


Figure 1. Schemes of the most classical formats of paper-based assays. A) Dipsticks, B) Flow through, C) Lateral flow, 1: parts that compound a lateral flow strip, 2: reagents deposition onto each part, 3: movement of the reagents along with the flow pass and 4: reagents capture onto their corresponding parts.

The sample with the analyte is transported by capillary action with the passing liquid flow from an application zone to other along the membrane. When sample containing analyte deposited in the sample pad reaches the conjugation pad the colour labeled mAb binds the analyte and in an analyte-mAb-colored particle complex (figure 1C-3). When the analyte-mAb-labeled complex reaches the test line an immobilized secondary mAb traps the previous complex in a combined capture and detection zone. While other mAb immobilized in the control line traps the excess of mAb-labeled for control purpose. The non-bound particles are washed away with the passing liquid flow (figure 1C-4). The visual detection of colour developed using a negative control joint to the comparison with reference color of known concentration allows semi-quantitative analyses. For more accurate analyses the quantitative evaluation of the produced color

can be achieved by using a portable colour reader such as a reflectometer or a common scanner.

I.3.1 -c) Competitive and sandwich formats: the two classical LFA approaches.

Various LFA formats that depend on the type of target analyte can be used. The two kinds of format frequently used are competitive and sandwich assay. Competitive format is most often employed when the analytes present a single antigenic determinant as generally occurs with target molecules of low molecular weight due to difficulty to generate large immunologic response.^{73,74} In a competitive format (**figure 2A**) when there is not analyte in the sample, an anti-analyte mAb complex labeled with the signal colour producer particles (e.g. colloidal gold) captures an analyte-protein conjugate deposited on the test zone of the nitrocellulose membrane, allowing colour development in a visible formation line on the test zone. Another specific antibody deposited on the control line allows the capture of the excess of the labeled antibody and therefore other band colour will be visible in the control zone regardless of the presence of target analytes, confirming correct test development. Consequently, a negative sample without analyte will result to the formation of two colored visible bands (test line and control line) (figure 2A-1). Conversely, when there is analyte in the sample the labeled-mAb binds with analyte in the complex analyte-mAb-label and the formed complex pass through the test line without being bound and consequently no producing signal color in this region (figure 2A-2).⁷⁵

On the other hand, the assay with sandwich format (figure 2B) is employed to test analytes presenting several epitopes such as viral proteins. The system in sandwich assay can employ two different antibodies (polyclonal and monoclonal) that bound distinct epitopes of the analyte: a labeled pAb used to be placed in a dehydrated state onto the conjugate pad and a mAb specific to the analyte is deposited at the test line onto the nitrocellulose membrane to serve as capture reagent. The response in the capture zone (test line) is directly proportional to the amount of analyte in the sample.⁶²

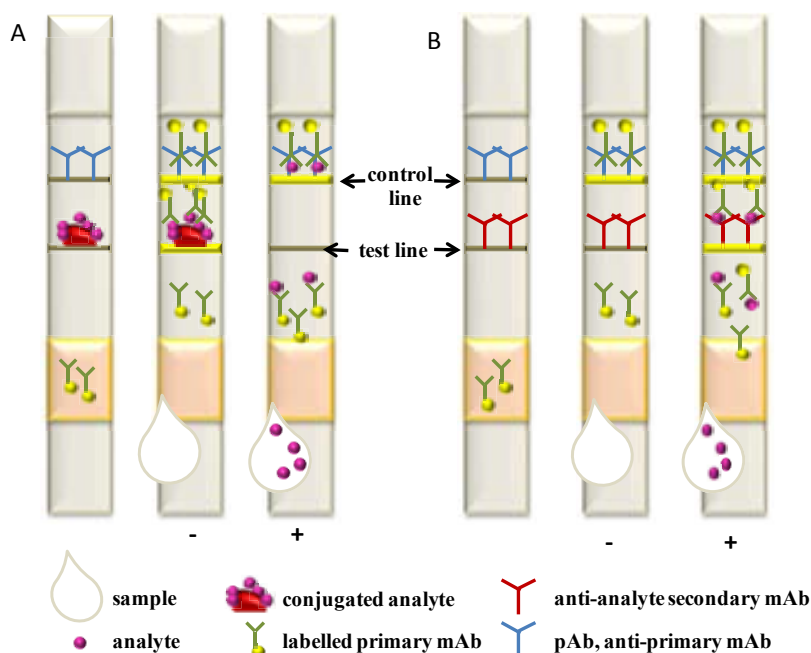


Figure 2. Schematic representation of LFA with competitive format (A) and sandwich format (B). In competitive format the signal response on the test line is inversely proportional to the analyte concentration. In contrast, with sandwich format the response on the test line is proportional to the analyte concentration. (+) means positive sample; (-) means negative sample. The lower line is the “test” line and the upper line is the “control” line.

Another kind of format or classification takes into consideration the type of used recognition molecules. When exclusively antibodies are used as recognition elements in LFAs, the tests are called “LFIA”. Recently, new advances have been made to develop cost effective and rapid nucleic acid testing based on lateral flow platform.⁷⁶⁻⁷⁸ Nucleic acids can be captured on lateral flow test strips either in an antibody-dependent or antibody independent manner. Antibody-dependent format also called “nucleic acid lateral flow immunoassay (NALFIA)” employs an antibody capture line and a labelled amplicon or oligonucleotide probe of complementary sequence to the amplicon. Alternatively, antibody-independent format “nucleic acid lateral flow assay (NALFA)” is based on the use of two binding units such as biotinylated probe or amplicon, and a streptavidin, which present high affinity and irreversible linkage. Two convenient approaches are possible: the immobilization of the oligonucleotide capture probe to the nitrocellulose membrane through passive adsorption or via passive absorption using BSA oligonucleotide conjugate capture probe. The responses are directly proportional to the amount of analytes.⁷⁹

I.1.3-d) LFA advantages and limitations

LFA is a simple detection tool, facile to be used (the user just needs to deposit a sample drop onto the sample pad), that doesn't require specialized users or previously laboratory treatment of the sample and the result, a colorimetric change generally in one-step assay, can be carried out by a naked-eye constituting its principal advantage. The low cost, fast answer (in qualitative or semi-quantitative analysis where time-to-result never exceeds 20 minutes), versatile format and the possibility of point of care applications make this technique an attractive alternative to conventional analysers. The sample volume used never exceeds the 500 μL , which is another advantage considering that in many occasions larger sample volumes aren't always available. In addition, prolonged shelf life without the need to refrigerate and the possibility to prepare large batches in advance, because of prepared strips can be stored for a long time without refrigeration, gives to this method a fair chance for in off-laboratory or resource-poor settings uses. Other advantages like the elimination of transporting and storage of large numbers of samples and the possibility to determine unstable analytes or short-term variations in analyte concentration can be adjudicated. However some limitations are necessities to overcome.⁷⁰

LFA is usually designed for individual tests, not for high-throughput screening.⁷⁰ Future researches can be therefore dedicated to the development of novel formats with more capture test lines to detect several analytes in complex samples (multi-analysis systems). Just one assay is possible by each strip, no reusable strip are designed so far. The sample has to be in the liquid state, and sample pretreatment is obligatory when solid samples, or dust particles in the atmosphere are analyzed. Even sometimes when the sample is liquid, sample clean-up may be necessary. Analysis of complex samples like milk, blood/urine, soil or groundwater requires rigorous pretreatments (centrifugation, serial dilution or filtration, pH adjustment, etc) to prevent any problem during analysis. For applications using blood/plasma/serum or extracts, special sample pad materials that filter cells and/or debris from obstructing the immunostrip are available. Also, when the analyte has a very low concentration, a preliminary concentration step is obligatory too due to the fact that LoD of the device sometimes are not low enough.^{62,70} Precisely other challenge in the current LFA and paper based assays in general, is to increase the sensibility in the quantitative determinations. In this context a critical parameter is the correct choice of the signal producer particles because

of the fact that big majority of the LFA are developed using nanoparticles (mostly AuNPs) as colour label.

I.3.2 Strategies to overcome the drawbacks in paper based devices.

The need to perform an individual test for each paper strip (no reusable strip), the use of sample treatment step to concentrate, separate or prepare the sample for the analysis and the relatively low sensibility in the quantitative determinations are some of the drawbacks of paper based devices. Innovative designs and paper architectures and hybrid platforms integrated with electrochemical and microfluidic tools are some of the strategies used to overcome these limitations. The fabrication of hybrid platforms brings advantages over the simple LFAs like the increasing of sensibility, the reduction of steps of processes in a single-step or the automatization of sequential multistep procedures and the possibility of the multicomponent analyses.

In the following parts some aspects related to the use of other kinds of signal producer particles with the aim to improve the LoD, as well as several designs and hybrid platforms used to integrate analytical steps, to reduce the analysis time and achieve the multidetection in paper based assays are discussed.

I. 3.2-a) Signal producer particles used in paper-based devices.

The most used labels in paper-based devices are AuNPs.⁶² AuNPs have excellent properties to be used as labels: easy synthesis, easy functionalization, easy manipulation, a strong red color with a characteristic surface plasmon resonance (SPR) and electrochemical activity that can be used in optical or electrical detection of several analytes.⁸⁰ The AuNPs are not the only nanoparticles used in paper based devices. Several signal producer alternatives have been tested to increase the signal response and consequently improve the sensitivity of the devices.

In order to address better the types of signal producer particles their classification in three groups, as indicated below can be considered.

The first group is related to particles that are used joint to AuNPs to enhance the response. The enhancement of the signal is done combining the use of enzymes (such as horse radish peroxidase, HRP⁸¹⁻⁸⁴) or silver solutions,⁸⁵⁻⁹¹ with AuNPs, or using directly composites of AuNPs with other materials;^{69,92,93} or combing two different size AuNPs.⁹⁴ The second group considers microparticles used as carriers of dyes. The particles for this purpose are liposomes⁹⁵⁻⁹⁹ or latex beads^{100,101} with colored dyes such as sulforhodamine B (SRB),¹⁰² hexacyanoferrate(II),¹⁰³ blue carboxylate,¹⁰⁴ blue

microspheres,¹⁰⁵ and blue polystyrene.¹⁰⁶ In the third group other (nano)materials are considered. Magnetic nanoparticles,¹⁰⁷⁻¹⁰⁹ quantum dots (QDs),¹¹⁰⁻¹¹⁵ carbon materials^{116,117} (particles,^{118,119} nanoparticles,^{120,121} multi-walled carbon nanotubes-polyvinylpyrrolidone (MWCNTs-PPy)¹²²), selenium,¹²³ Eu³⁺ onto porous silica nanoparticles (SiNPs)¹²⁴ or ceria nanoparticles¹²⁵ have been used for such purpose.

i. Particles used in connection to AuNPs for signal amplification

Considering the first approach several works can be addressed here. Choi *et al.*⁹⁴ combined two different sizes of AuNPs using sandwich format to detect the Troponin I with a LoD of 10 pg/mL in serum samples of patients with myocardial infarction. In other report an ultrasensitive lateral flow strip biosensor based on thiolated DNA-HRP-AuNPs conjugated to determine nucleic acid was developed. HRP attached onto the AuNPs surface played very important roles to improve the sensitivity of the assay. The LoD of current approach was 1000 times lower than that using just AuNPs. Combining the HRP enzyme catalytic amplification with unique optical properties of AuNPs, this platform was capable of detecting 0.01 pM of target molecule.⁸¹ Parolo *et al.* used in a LFA sandwich format AuNPs as carriers of HRP as labels and achieved to increase the signal from 6 ng/mL to 200 pg/mL LoD for the HIgG analysis.⁸² Apart from losing the “one-step” concept when using an enzyme, a biological element with limited stability is introduced; shelf life may decrease and handling becomes more complicated. Silver enhancement of the AuNPs has also been mentioned to increase the sensitivity, although this enhancement process also requires a second step.⁸⁷⁻⁹¹ In this way botulism neurotoxin A, botulism neurotoxin B and staphylococcus aureus enterotoxin B using LFA sandwich format with AuNPs coupled with silver enhancements achieving LoD of 1 ng/mL, 50 pg/mL, and 10 pg/mL, respectively, have been analyzed.⁸⁷⁻⁸⁹ Shyu *et al.* (2002) reported, for example, that silver enhancement enabled the detection of 100 pg/mL ricin while it was 50 ng/mL by the typical AuNP-based LFA.⁹⁰ Other approaches using other physical properties of the AuNPs, such as the localized SPR of the AuNPs¹²⁶ and surface enhanced Raman scattering (SERS) of gold or silver nanoparticles,^{127, 128} to increase the LFA signal have been used too. While probing AuNPs mixed with other particles a novel LFA for the fast screening of aflatoxin B2 (AFT B2) in food samples was developed by Tang *et al.*⁹² In this study, the signal color reagent consisted of magnetic nanogold microspheres (MnGMs) made of nano- Fe₂O₃ particles as core and

AuNPs as shell that were bio-functionalized with anti-AFT B2 mAbs. Using a competitive format and colorimetric detection a 0.9 ng/mL of LoD was achieved.

ii. Microparticles used as carriers of dyes.

Colored or fluorescent nanoparticles are encapsulated inside other bigger particles (for examples latex and liposomes) with sizes of 200-800 nm, that allow an unobstructed flow through the membrane, being used as labels to quantify the response. Thus particles of sulforhodamine B (SRB) inside liposome's cavities were conjugated to Ara h1 toxin (a peanut allergen toxin) to detect Ara h1. A colorimetric detection using a LFA of competitive format was carried out obtaining a LoD of 45 ppm.¹⁰¹ In other work SRB also encapsulated in liposomes but conjugated to aflatoxin B1 (AFB1) was used to detect until 18 ng/mL of this micotoxin by a competitive LFA too.¹⁰² An interesting study using fluorescent immunoliposome as label for the detection of staphylococcus aureus enterotoxin B (SEB) has been described by Khreich et al.⁹⁵ Nicarbazin pesticide residues have been examined using blue latex microspheres labeled primary antibody.¹⁰⁵

iii. Other (nano)materials.

The third type of signal tracers' particles (which just uses only one type of particle) has also been applied for several analyses. Using independently AuNPs and HRP as tracers in flow-through and lateral-flow formats for multianalysis of carbaryl and endosulfan (two broad-spectrum insecticides) was found that the visual LoD for carbaryl and endosulfan were 100 and 10 $\mu\text{g/L}$ in gold-based assays, respectively, while for immunoassay using HRP as tracer, the visual detection limits were 10 $\mu\text{g/L}$ for carbaryl and 1 $\mu\text{g/L}$ for endosulfan. In the developed assays used HRP as labels 10 times enhancement in the visual detection limit was obtained comparing with AuNPs.⁷¹

Florescent tracers like QDs¹¹⁰⁻¹¹⁵ and up converting phosphor technology (UPT)¹²⁹⁻¹³¹ have attracted the attention of the researchers due to the better sensibility of the fluorescent methods in comparison with colorimetric ones. A multiple toxins analysis using CdSe-ZnS core-shell QDs as measured fluorescence was performed in sandwich format. Cholera toxin (CT), Ricin, Shiga-like toxin and SEB were detected with 10, 30, 300 and 3 ng/mL of LoD.¹¹⁰ In other study organophosphorus pesticide metabolites were detected by competitive LFA using QDs too. The principle of this sensor is based on analytes competition with QD-conjugated analogs to bind to antibodies on a test zone. Captured QDs serve as signal vehicles for fluorescent readout. In this work, 3,5,6-trichloropyridinol (TCP) is used as a model analyte to demonstrate the performance of

the immunosensor. QD-TCP conjugates are capable of detecting up to 1.0 ng/mL TCP standard analyte in 15 min.¹¹³ Other simple fluorescent strip sensor based on aptamer–quantum dots as recognizer conjugate for monitoring ochratoxin A (OTA) as a model toxin was reported. The design was based on the competition reaction between the QDs-labeled aptamer setting in the conjugation pad and DNA probe 1 immobilized in the test zone. If OTA target in the sample solution bound the aptamer-QDs conjugated, the aptamer would not hybridize with the DNA probe 1 in the test zone. Regardless the presence of OTA in the sample solution, as the buffer migrated on the strip, the corresponding part sequence in the aptamer strand would hybridize with the DNA probe 2 in the control zone. This QDs–aptamer-based fluorescent strips exhibited slightly higher sensitivity than AuNPs label achieving a LoD of 1.9 ng/mL (**figure 3A**).¹¹⁵

UPT used as label may be 10-100 fold more sensitive than colloidal gold or colored latex beads.^{130,131} In 2001 P. Corstjens *et al*¹³⁰ used the reporter UPT for the detection of specific nucleic acid sequences in LFD. It was applied to screen the presence of human papillomavirus type 16 (HPV16) in a defined series of cervical carcinomas. This LFD was used to capture haptenized DNA molecules and hybrids, which were immunolabeled with 400-nm UPT particles. These particles emit visible light after excitation with infrared in a process called up-conversion, characteristic of phosphor lattice. The use of the UPT reporter in LF-DNA tests, as compared with colloidal gold, improved the detection limit at least 100-fold. Europium chelate-loaded silica nanoparticles have also proven great potential to improve sensitivity in LFAs. A commercial LFID for hepatitis B surface antigen (HBsAg) was designed using anti-HBsAg mAb labeled with Eu^{3+} nanoparticles to replace colloidal gold achieving a LoD of 0.03 $\mu\text{g/L}$ which was 100 times lower than the colloidal gold-based (**figure 3B**).¹²⁴

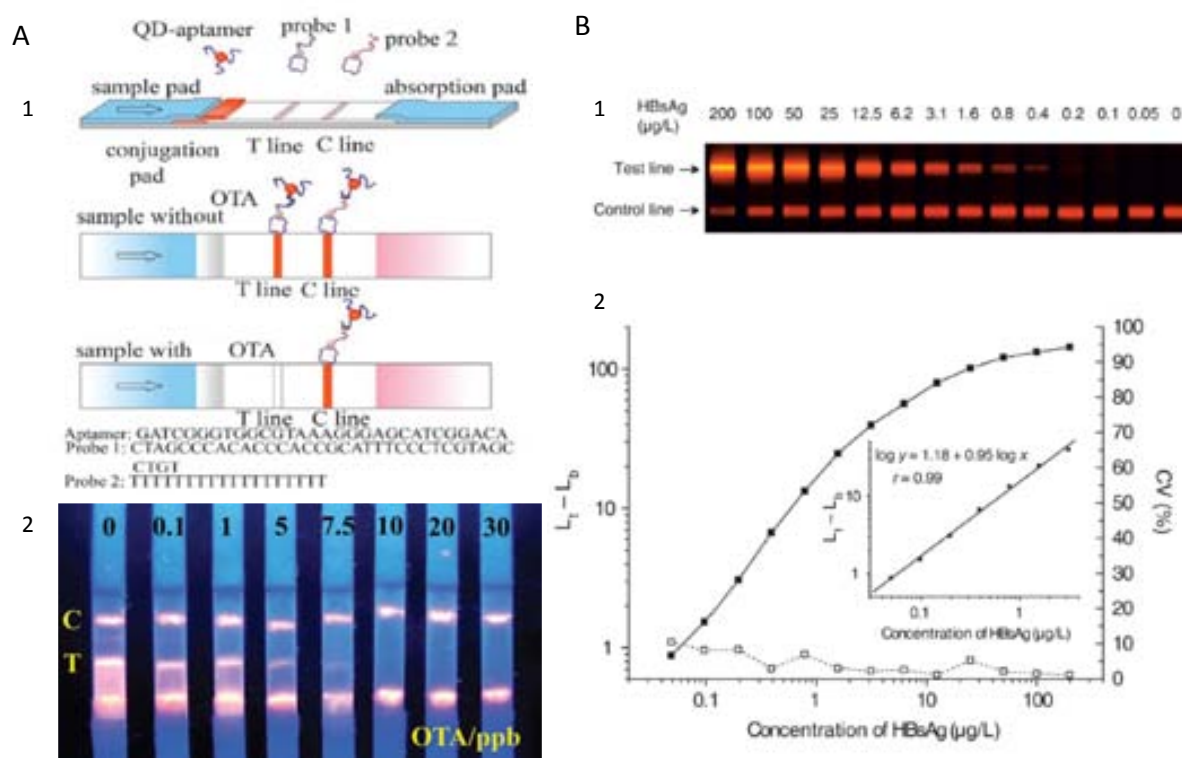


Figure 3. Schematic representation of working principles and the obtained results in LFAs where different labels are used. A) Use of QD-aptamer to analyze OTA -1- configuration and the principle of the detection., 2- Image of typical detection results by the fluorescent strip under the ultraviolet irradiation. B) Eu^{3+} nanoparticle-based LFIA of HBsAg. 1) Digital image of test strips carried out with 2-fold serially diluted HBsAg calibrator and a negative control in assay buffer. 2), Calibration curves (■) and imprecision profiles (□) of panel B1. The inset illustrates the linear range region of the plot. L_t and L_b indicate the mean value of luminosity of the test line and the background, respectively. A and B reprint adapted from reference 115 and 124, respectively.

I. 3.2-b) Paper architectures

A lot of works are focused on the change of the conventional geometry of the paper strips to introduce larger volumes of sample or to concentrate the sample analyte. In this direction some alternative have been described. C. Parolo et al.¹³² reported a strategy that yielded up to an 8-fold in sensibility improvement in AuNPs-based LFIA, increasing 3 times the width of the pads. The increasing of the size of both the conjugation and the sample pads in 1X, 2X and 3X, improved the sensitivity of the HIgG assay to 5.89, 1.83 and 0.70 ng/mL, respectively. Their flow speed simulations also corroborated its experimental results (figure 4-A).

The changes in the traditional geometry of the LFAs besides to enhance the sensibility of the platforms provide other advantages like the multiple analytes analysis and the reduction of the steps in the reagents incorporation and consequently the time of the

analysis. For example a two-dimensional shaping of porous media, that allows the spotting of multiple bioassay reagents to produce multiplex LFAs, was introduced by E. M. Fenton *et al.*¹³³ The paper- and nitrocellulose-based LFDs were cut in two dimensions by a computer controlled knife as star, candelabra, and other structures like shapes (figure 4-B). E. Fu *et al.*¹³⁴⁻¹³⁷ carried out several studies with two-dimensional paper network (2DPN) format. They first demonstrated the multi-analyte detection capability of paper networks with multiple outlets per inlet. In other works the same authors focused on the capabilities of 2DPN with multiple inlets per outlet demonstrating methods for controlling the transport of reagents fluids using the 2D geometry of the network and dissolvable barriers within paper devices (figure 4-C). From the investigation on the processing capabilities provided by convergence of reagents from multiple inlets to a common detection region they concluded that this capability of 2DPN can be used to autonomously drive multi-step sequences such as chemical amplification, which require multiple reagent delivery in washing steps.¹³⁴⁻¹³⁶ The same research team demonstrated the real possibility of 2DPN format to enhanced sensibility, allowing signal amplification by incorporation of multistep processes of the adding of the rinse and signal amplification solutions in one process step, for hCG analyses. In the signal amplification method used here (gold enhancement of AuNPs), catalytic deposition of gold onto the surface of the original particle labels increased their size and resulted in a change in color of the labels from pink to dark purple (figure 4-D).¹³⁷

The insertion of an extra pad between the sample pad and the conjugation pad has been used to eliminate steps of analysis. Choi *et al.*⁹⁴ in 2010 deposited, for signal amplification without an additional operation step in LFA using AuNPs, an anti-BSA antibody labeled AuNPs in a second conjugation pad as carrier particles of AuNPs-BSA-anti-troponin I immobilized in the first conjugation pad to enhance the signal colour. Three years later A. López_Marzo *et al.*¹³⁸ designed other LFA device using AuNPs with an extra inserted pad with the adequate reagents concentration to avoid the sample treatment step in water Cd²⁺ analysis.

A plasmonic AuNRs paper-based analytical platform with functional versatility and subattomolar ($<10^{-18}$ M) LoD using SERS as a transduction method was reported by A. Abbas *et al.* The microfluidic paper-based analytical device (μ PAD) is made with a lithography-free process by a simple cut of the paper like star shape and drop method. Complex samples are separated by a surface chemical gradient created by differential

mixture of polyelectrolytes (PAH and PSS) coating of paper star like shape. This design generates a rapid capillary-driven flow capable of dragging liquid samples as well as AuNPs into a single cellulose microfiber, thereby providing separation and an extremely pre-concentrated and optically active detection spot (figure 4-E). The shape-enhanced capillary forces, i.e., the small size of the paper like-star tips (the radius of the tips is 10–20 μm), result in a much faster drying of the solvent at the tips compared to the rest of the paper substrate, in turn causing a rapid flow from the wetted surface to the dry area, separating and concentrating the analytes and even the AuNRs to the tiny test regions. This seems to be an excellent work that demonstrates the versatility of an adequate choice of the paper shape.¹³⁹

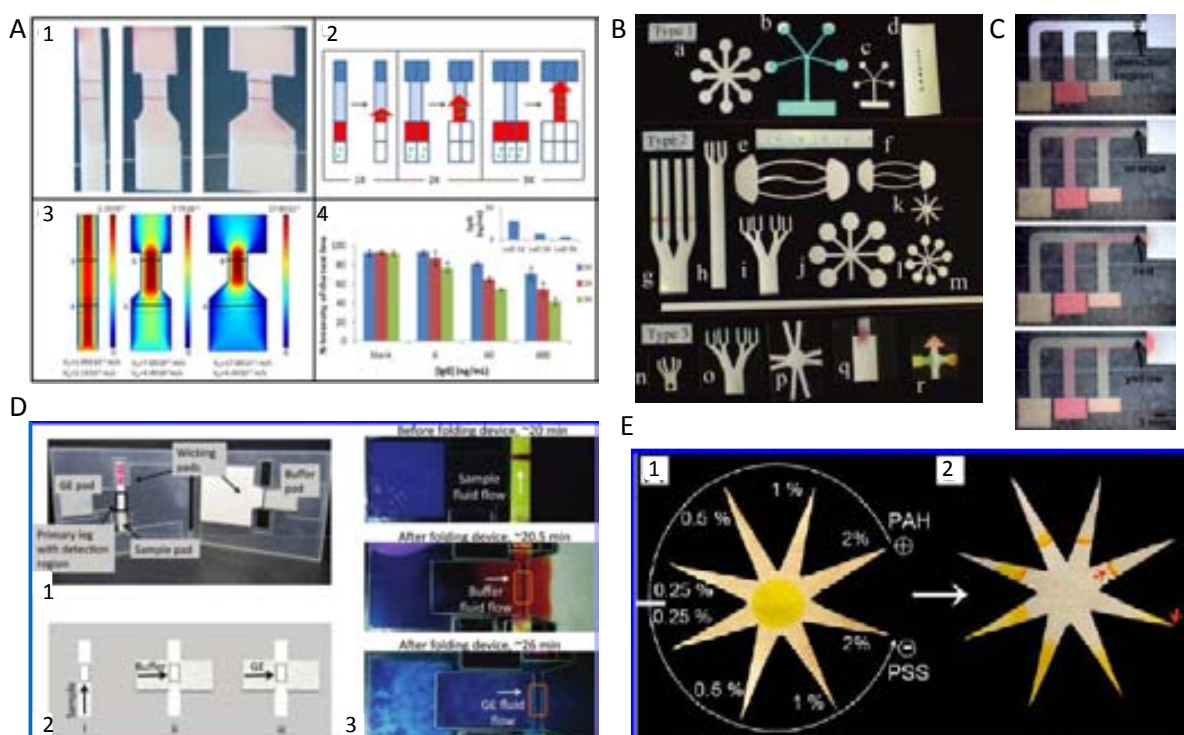


Figure 4. Reported alternatives that change the traditional shape of the paper strips with the aim to increase their sensibility and versatility. **A)** The use of bigger sample and conjugation pads (A-1) Photos of LFIA with different sample and conjugation pads architectures for 60 ng/mL HIgG analyses. (A-2) Scheme of the amount of analyte and the flow speed for LFIA using bigger sample and conjugation pads. The red arrows represent the speed of the AuNPs in the flow and the green point stated for the analyte. (A-3) Results of the flow speed simulations for sample and conjugation pads with different sizes. (A-4) Effect of the sample and conjugation pads relative sizes on the quantitative measurement for different HIgG concentrations and the corresponding LoDs obtained (inset). **B)** Device types fabricated by two-dimensional shaping. Top row: Type 1 devices formed by shaping uncapped sheets of nitrocellulose. Type 2 devices formed by shaping laminar composites comprised of vinyl-backed nitrocellulose, capped by sheets of cover tape. Type 3 devices formed by shaping laminar composites in a two-step process. **C)**

Demonstration of programmed fluid delivery using a simple 2DPN. The arrival time of multiple reagents at the “detection region” of the paper strip is staggered by placing 3 inlets along the common segment of the device. The geometry of the inlets results in the sequential arrival of fluid from each of the three inlets; orange, red, and yellow colored fluid. **D)** 2DPN card allows for the automation of additional processing steps. (D-1) Image of a 2DPN card that performs rinse and signal amplification steps. (D-2) Schematic of the flow sequence in the 2DPN card. The user first loads gold enhancement solution (GE), rinse buffer, and sample onto appropriate pads of the card. Sample flows in the primary leg of the card to the detection region (see “i” in panel 2). The user folds the card at 20 min, in a mode that fluids can flow through the secondary leg to the detection region of the card; buffer (see “ii” in panel B) and then GE solution (see “iii” in panel 2). Additional steps could be implemented in a straightforward manner through extension of the network. (D-3) Image series showing the sequential delivery of fluids in the 2DPN card: (top) yellow fluid represents the sample, (middle) red fluid represents the rinse buffer, and (bottom) blue fluid represents the gold enhancement solution. **E)** Star like-shape separation by surface charge gradient. (1) Charge gradient obtained by different concentrations of PAH and PSS polyelectrolytes. The yellow spot at the center is caused by a fluorescein droplet as deposited. (2) Migration of fluorescein into different star fingers. The red arrows indicate the concentration at which fluorescein forms either a band or concentrates at the tip. A, B, C, D and E figures adapted from references 132, 133, 134, 138 and 139, respectively.

I. 3.2-c) Integrated hybrid approaches.

As discussed before the latest trends in paper based assays are focused in the integration of methodologies. The electrochemistry and microfluidics tools used in Lab-on Chip are the most attractive hybridization options. The large variety of interesting reported works in the last 10 years reveals a new upcoming era: the engineering paper-sensors. Here we show some performances of these devices.

i. Integration with electrochemical methods

S. Ngin *et al*¹⁴⁰ presented a device for electrochemical detection of Pb^{2+} traces in $10 \mu\text{L}$ solutions using a paper disk previously impregnated with necessary reagents, including an internal standard of Zn^{2+} and buffer. The paper with pre-storage of reagents was left on the screen printed electrode surface; then a fixed volume of sample ($10 \mu\text{L}$) was dropped on the paper for the square wave anodic stripping voltammetry (SWASV) (**figure 5-A**) relying on in situ plating of bismuth film. This hybrid platform leads to accurate results giving advantages as the one step detection without addition of external reagent due to previous reagents storage onto the paper, and self-calibration integrated on the portable device via the Zn^{2+} internal standard.

A lab-on-paper device combining electrochemical and colorimetric detection for the rapid screening of Au^{3+} in the presence of a common interference, Fe^{3+} , was described

by A. Apilux *et al*¹⁴¹. They simultaneously detected Au³⁺ by electrochemical method while Fe³⁺ determination was carried out by a colorimetric method based on the reaction of Fe²⁺ (previously reduced with ascorbic acid) with 1,10-phenanthroline. Both the necessary reagents for the assay as the electrodes were printed onto paper. The method gives linear response in the concentration range of 1-200 ppm of Au³⁺ presenting a LoD of 1 ppm. The merit of this paper is that combines the advantages of colorimetric detection based on paper and the electrochemical detection for quantitative simultaneous determination of Au³⁺ and Fe³⁺.

Other assay that combines conventional LFA with an electrochemical readout technique reaching highly sensitive QDs labels for determination of nicotine (a metabolite of nicotine) in serum was proposed by H. Nian *et al.*¹⁴² In this assay, QD-cotinine conjugates placed at the conjugation pad competes with the cotinine in sample to bind to anti-cotinine antibody in the test strip. The QDs serve as colorimetric or fluorescent signal vehicles in the test line and once these are delivered by use of acid solution they serve as electrochemical signal producers for readout (figure 5-B). The sensor showed a wide linear range from 1 ng/mL to 100 ng/mL cotinine with a LoD of 1.0 ng/mL.

ii. Integration with microfluids and Lab on Chip technologies

μ PADs have recently attracted great interest since Whitesides and co/workers first introduced this concept in 2007.¹⁴³ Compared to the conventional microfluidic devices fabricated with silicon, glass, and polymer materials, μ PADs possess attractive features such as inexpensive, biocompatible, easy-to-use, (especially without need of external fluid-driving pump), and easy-to-dispose. As a result, varieties of μ PADs for medical diagnosis, food analysis, and environmental monitoring have been developed in the recent 5 years.¹⁴⁴ The μ PADs are devices which integrate the paper advantages with those of microfluidics. They require a very low amount of sample and can be used in multiplex and quantitative analyses.¹⁴⁵ They are made by forming hydrophilic channels in hydrophobic paper. Many techniques such as photolithography, polydimethylsiloxane (PDMS) plotting, inkjet etching, plasma etching, cutting, and wax printing have been used to produce μ PADs.¹⁴⁶ μ PADs besides the use of optical detection,¹⁴³ can employ more sophisticated devices and techniques, like microplate readers,^{147,148} chemiluminescence,^{149,150} electrochemistry,¹⁵¹ transmission of light through paper,¹⁵² piezoresistive MEMS sensors¹⁵³ or electromagnetic resistor.⁶³

Zakir *et al.*¹⁵⁴ reported the detection of acetylcholinesterase (AChE) inhibitors such as neurotoxins and organophosphates through a novel paper-based solid-phase biosensor that utilizes piezoelectric inkjet printing of biocompatible, enzyme-doped, sol-gel based inks to create colorimetric sensor strips. For this purpose, polyvinylamine (PVAm), which captures anionic agents was first printed and then AChE was overprinted by sandwiching the enzyme within two layers of biocompatible sol-gel derived silica on paper. AChE inhibitors, including paraoxon and aflatoxin B1, were detected successfully using this sensor by measuring the residual activity of AChE on paper, using Ellman's colorimetric assay, with capture of the 5-thio-2-nitrobenzoate (TNB⁻) product on the PVAm layer. The assay provided good detection limits (paraoxon, ~100 nM; aflatoxin B1, ~30 nM) and rapid response times (<5 min) (figure 5-C).

Hossain *et al.*¹⁵⁵ used acetylcholinesterase (AChE) to analyze organophosphate pesticides AChE inhibitors, in a reagentless bioactive paper-based solid-phase biosensor. The assay strip is composed of a paper support (1 × 10 cm), onto which AChE and a chromogenic substrate, indophenyl acetate (IPA), were entrapped using biocompatible sol-gel derived silica inks in two different zones (e.g., sensing and substrate zones). The acetylcholinesterase (AChE) hydrolyzes the red-yellow colored substrate, IPA, to the blue-purple indophenoxide anion (IDO⁻) which is then trapped over a finite region by the cationic polymer, polyvinyl amine (PVAm). The absence or decrease in blue-purple color, over this region, is indicative of the presence of AChE inhibitors. The modified sensor is able to detect pesticides without the use of any external reagents with excellent LoDs (bendiocarb ~1 nM; carbaryl ~10 nM; paraoxon ~1 nM; malathion ~10 nM) and rapid response times (~5 min). The sensor strip showed negligible matrix effects in detection of pesticides in spiked milk and apple juice samples.

A paper-based colorimetric detection with immobilized tyrosinase as analyte dependent concentration for the phenolic compounds including phenol, bisphenol A, catechol and cresols was reported by Alkasir *et al.*¹⁵⁶ The sensor is based on a layer-by-layer (LbL) assembly approach by alternatively inkjet printing layers of chitosan and alginate polyelectrolytes onto filter paper disk (diameter of 0.6 cm) and physically entrapping the tyrosinase enzyme between these layers. The sensor response is quantified as a color change resulting from the specific binding of the enzymatically generated quinone to the multilayers of immobilized chitosan on the paper. The color change can be quantified

with the naked eye but a digitalized picture can also be used to provide more sensitive comparison to a calibrated color scheme. They found a LoD of 0.86 ppb for each of the phenolic compounds tested.

An interesting paper-based microfluidic device is presented by Q. He *et al*¹⁴⁴ for colorimetric assays of nitrite ions in food samples. They created a novel and easy approach for the fabrication of μ PADs via the hydrophobization of the original filter paper by coupling octadecyltrichlorosilane (OTS) to paper fibers, followed by UV-lithography of the OTS coating. The hydrophilic and hydrophobic channels had a width of 233 ± 30 and 137 ± 21 μm , respectively (figure 5-D).

M. Ornatska *et al*¹²⁴ (2011) reported the detection of H_2O_2 and Glucose with ceria-modified paper. Ceria nanoparticles and glucose oxidase were coimmobilized onto Whatman filter paper 0.6 cm round -shaped using a silanization procedure. In the presence of glucose, the enzymatically generated hydrogen peroxide induces a visual color change of the ceria nanoparticles immobilized onto the bioactive sensing paper, from white-yellowish to dark orange, in a concentration-dependent manner. A detection limit of 0.5 mM glucose with a linear range up to 100 mM and a reproducibility of 4.3% for $n=11$ ceria paper strips were obtained. . The assay is fully reversible and can be reused for at least 10 consecutive measurement cycles, without significant loss of activity. Another unique feature is that it does not require external reagents, as all the sensing components are fixed onto the paper platform.

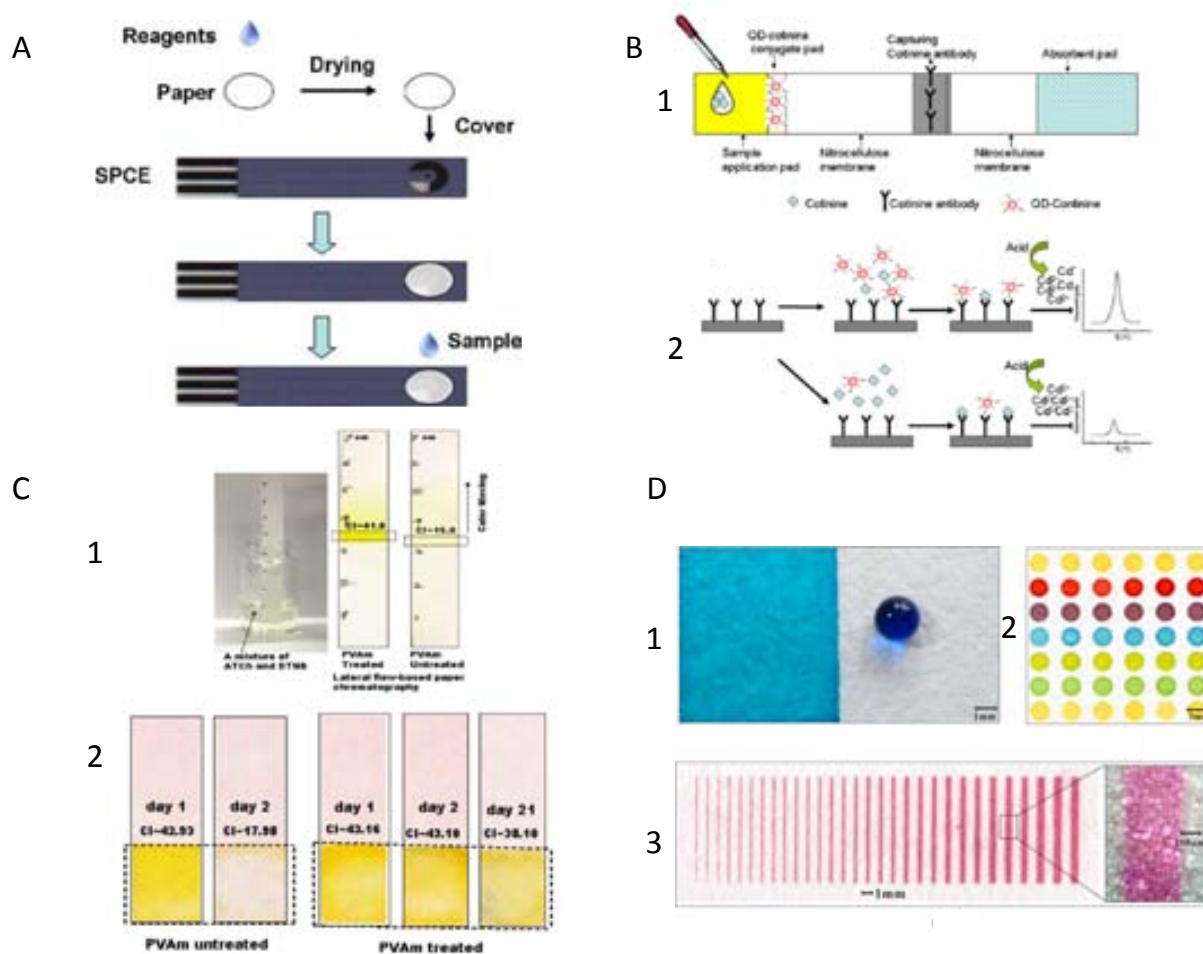


Figure 5. Typical alternatives that combine paper based assays with other analytical tool. A and B combine paper-based assays with electrochemical methods, while C and D with microfluidic tools. **A)** Preparation and application of the paper disk integrated with SPCE. Typically 10 μ L of buffer with an internal standard were dropped on the filter surface and dried in the air; the paper with prestorage of reagents was left on the electrode surface; then a fixed volume of sample (10 μ L) was dropped on the paper for electrochemical detection. **B)** B-1 Schematic design of the QD-based electrochemical LFID. B-2 Principle of QD-based electrochemical competitive LFA on the strip. With lower cotinine concentration in samples, more QD–cotinine will be captured by antibodies, leading to a larger electrochemical signal; while the inverse, the signal will be smaller. **C)** A paper based biosensor for AChE inhibitors was over printed by sandwiching the enzyme within two PVAm layers. C-1) Color intensity (CI) due to elution of ATCh (300 μ M, final concentration) in the LFD. The areas within the dashed boxes were printed without (control) and with PVAm (0.5 wt %), followed by the printing of AChE (50 U/mL). PVAm concentrates the reaction product (the yellow TNB anion), while in the control experiment, the yellow TNB anion is dispersed over a large area. C-2) Cardboard dipstick with inkjet-printed PVAm or control (no PVAm) and silica/AChE/DTNB/silica layers after being immersed in a ATCh solution. Both materials show an initial color response, but only the PVAm (0.5 wt %)-treated paper retains the reaction product (a yellow TNB-) for a period of 3 weeks. **D)** Hydrophilic–hydrophobic contrast on the UV/O₃-patterned OTS-paper: D-1) drop of dye solution (5 μ L) was applied on unmasked region (left side) and masked region (right side), respectively; D-2) after aliquots of 0.5 μ L differently colored solutions being pipetted into hydrophilic

reservoirs (3 mm in diameter); D-3) after a pattern of hydrophilic lines with varied widths being immersed in a Rodamine B solution and drying. A, B, C, D and E figures adapted reprints from references 140, 142, 154 and 144, respectively.

I.3.3 Applications in heavy metals detection.

The heavy metals are particular cases of analyte because are small molecules unable to generate a large immune response when are introduced in experimental animals to obtain antibodies. Taking into account that generally mAbs use to be the most classical analyte captor molecules when high specificity to recognize an analyte is required, the development of highly specify mAb against heavy metal is a difficult task. Up to date few reports on heavy metal detection using paper based assays have appeared in the literature. Enzymes although have been widely used generally recognize several similar molecules with close properties. For this reason searching for new and specific analyte recognizer molecules and introduce them in paper-based sensors to determine heavy metals is a challenge in this field.

Specifically for paper based metals sensors, enzymes,¹⁵⁷ metal-specific mAbs,¹⁵⁸⁻¹⁶⁰ DNA molecule,¹⁶¹ metal-specific DNazymes,^{162,163} others proteins,¹⁶⁴ small organic molecules¹⁶⁵⁻¹⁶⁷ and even inorganic structures¹⁶⁸ are the recognition molecules used up to date.

i. Use of enzymes as analyte recognizer molecules.

Paper-based sensors with immobilized enzymes as analyte recognizer have been reported in recent years as simple and rapid tools for chemical contaminants analysis. In their vast majority, these devices utilize join to the biorecognition elements, that are physically adsorbed onto the paper surface, conventional colorimetric or fluorimetric reagents (e.g., soluble redox dyes, quantum dots,¹¹⁰ AuNPs,^{159,160} and redox active cerium oxide nanoparticles¹²⁵). In these assays, detection is based on the monitoring of optical changes in the dye, the redox state, or the physicochemical properties (e.g., aggregation or dispersion) of nanoparticles, induced by the presence of an analyte.

Hossain *et al.*¹⁵⁷ fabricated a bioactive lab-on paper sensor that is inkjet printed with sol-gel entrapped reagents to allow colorimetric visualization of the enzymatic activity of β -galactosidase (β -GAL) in heavy metals presence. The bioactive paper assay is able to detect a range of heavy metals, either alone or as mixtures, in as little as 10 min, with detection limits as follows: $\text{Hg}^{2+} = 0.001 \text{ ppm}$; $\text{Ag}^{2+} = 0.002 \text{ ppm}$, $\text{Cu}^{2+} = 0.020 \text{ ppm}$;

$\text{Cd}^{2+} = 0.020$ ppm; $\text{Pb}^{2+} = 0.140$ ppm; $\text{Cr}^{6+} = 0.150$ ppm; $\text{Ni}^{2+} = 0.230$ ppm (**figure 6-A**).

- ii. Use of other proteins as analyte capturing molecules.

An infrared fluorescent protein (IFP) and its chromophore biliverdin (BV) were tested as an infrared fluorescence probe for Hg^{2+} detection. Hg^{2+} has specific binding affinity to a cysteine residue (C24) of IFP, thereby inhibiting the conjugation of IFP chromophore BV to C24 and “turning off” the infrared emission of IFP. The Hg^{2+} IFP/BV sensor had a LoD of 10 ppb.¹⁶⁴

- iii. Use of mAbs as analyte capturing molecules.

Some metals detection with sensors based on paper have been patented but the first reported use in the scientific literature was in 2011 with the work of K. Abe *et al.*¹⁵⁸ They determined Cd^{2+} in food samples that were previously treated by an analyte extraction and concentration process. Here, EDTA is added to the treated food samples to form the complex Cd-EDTA and after a MAb specific against Cd-EDTA complex labeled with AuNPs is added. The sample is spotted in the paper and flows to the test line where is immobilized the Cd-EDTA conjugate used as reaction probe. Samples negative give the maximum of color in the test line because all the specific MAb-AuNPs against Cd-EDTA binds with the Cd-EDTA conjugate that is immobilized in the test line. The achieved LoD was of 10, 5 and 2.5 ppb for rice, wheat grain and egg plant, respectively.¹⁵³ Following in 2012 a LFA to quantify Cr^{3+} in water and serum samples with a LoD of 5 ppb was developed by Xi Liu *et al.* The principle of this method was based on the competition between the anti- Cr^{3+} - EDTA specific MAb-AuNPs conjugate, that was deposited onto the conjugation pad glass fibers, with the analyte in the sample by the sites of the conjugated Cr^{3+} -EDTA that is immobilized onto the test line (figure 6-C). Recently A. Lopez_Marzo *et al.*^{138,160} reported all integrated sample treatment LFIA platform for Cd^{2+} detection in drinking and tap waters. The working principle was based on competitive reaction between the Cd-EDTA-BSA-AuNP conjugate (used as signal producer tool) deposited on the conjugation pad strip and the Cd-EDTA complex formed in the analysis sample for the same binding sites of the 2A81G5 mAb, specific to Cd-EDTA but not Cd^{2+} free, which is immobilized onto the test line. The lowest LoD and LoQ, 0.1 and 0.4 ppb, respectively, reported so far for metal paper based sensors was reported with this device.

iv. Use of specific-DNAzymes as analyte capturing molecules.

Metal-specific DNAzymes, functional DNA molecules that can catalyze a reaction in the presence of a particular metal ion, have emerged as a new class of metal-ion sensors because DNAzymes with desired metal specificity and affinity can be obtained by a combinatorial biology technique called *in vitro* selection. When combined with AuNPs, the DNAzymes have been transformed into highly sensitive and selective colorimetric biosensors, producing color changes between red (dispersed AuNPs) to blue (aggregated AuNPs) in response to a target recognized by DNA. Very recently applications of NALFA by use of metal-dependent DNA-cleaving labeled AuNPs have been developed for the visual detection of Pb^{2+} , Cu^{2+} and Hg^{2+} in works reported by D. Manzumbar *et al.*,¹⁶² 2010; Z. Fang *et al.*,¹⁶³ 2010 and Z. Gu *et al.*,¹⁶⁴ 2011 achieving LoD of 10, 0.63 and 10 ppb, respectively. The principle of detection is based on the metal specific cleavage onto DNAzyme-AuNPs producing two cleaved DNA strands while in the test and control line are deposited recognizer DNA probe for the two cleavage strands obtained. In the absence of M^{2+} (negative control), AuNP-uncleaved substrate is captured at the control zone via streptavidin–biotin interaction, producing a single red line. In presence of M^{2+} (positive test) the substrate is cleaved and the AuNPs cleaved product is captured at the test zone by hybridization to complementary DNA probe. The color intensity produced by AuNPs is directly proportional to metal concentration in the sample (figure 6-C).

v. Use of small chemical structures as analyte recognizer molecules.

Two specific metal ion sensitive chitosan films cross-linker with hexamethylene 1,6-di-(aminocarboxysulfonate) (HDACS) and poly(allylamine) PAH-HDACS, respectively, were presented in 2004 by SCHAUER *et al.* Chitosan- HDACS colored thin films from colorless starting materials were selective to Cr^{6+} (chitosan-HDACS) and $\text{Cu}^{2+}/\text{Cu}^{1+}$ (chitosan PAH-HDACS) through a change of its optical properties and thickness. The films are measured using reflectance and ellipsometry before and after dipping into a 50 ppm aqueous metal salt solution. The chitosan-HDACS films used in the metal ion study were blue in color with a thickness of 124 ± 1 nm and a reflectance maximum wavelength at 454 ± 3 nm.¹⁶⁵

Au_{15} quantum clusters (QCs) were encapsulated in cyclodextrin (CD) cavities and embedded after in a chitosan film. The sensitivity of the red emission fluorescence of the cluster in the composite to Cu^{2+} was used to make a freestanding Cu^{2+} sensor,

similar to pH paper, in the published work by George et al. The Au₁₅-QCs composite chitosan film exhibited visual sensitivity to Cu²⁺ up to 1 ppm.¹⁶⁸

Aragay *et al* (2012)¹⁶⁶ reported a fluorescence based paper test strip to quantify Hg²⁺ in aqueous media using an N-alkylaminopyrazole ligand as Hg²⁺ receptor molecule. The N-alkylaminopyrazole fluorescence was sensible to Hg²⁺ concentration. A linear range from 10 to 100 ppb Hg²⁺ was obtained with this paper-based system (figure 6-E).

Most recent report can be ascribed to Kaoutit *et al*¹⁶⁷(2013), who presented colorimetric sensor polymer membranes for detecting Hg²⁺ in aqueous media. Nanomolar concentrations of Hg²⁺ are detected by the naked eye due to colour changes of membranes, while quantifications were made by means of analyzing the digital information of pictures taken, with the digital camera of conventional mobile phone, to the membranes after dipping them in Hg²⁺ water containing. These dense polymer membranes, with gel behaviour in aqueous media, were prepared as colorimetric and fluorogenic Hg²⁺ sensory materials by incorporation of a water insoluble co-monomer rhodamine derivative. Rhodamine derivatives have been widely studied as fluorogenic and chromogenic chemosensors for the detection and quantification of mercury species. In neutral and basic media, the presence of Hg²⁺ causes the development of a pink colour and fluorescence due to the opening of the lactam to give the amide (figure 6-D).

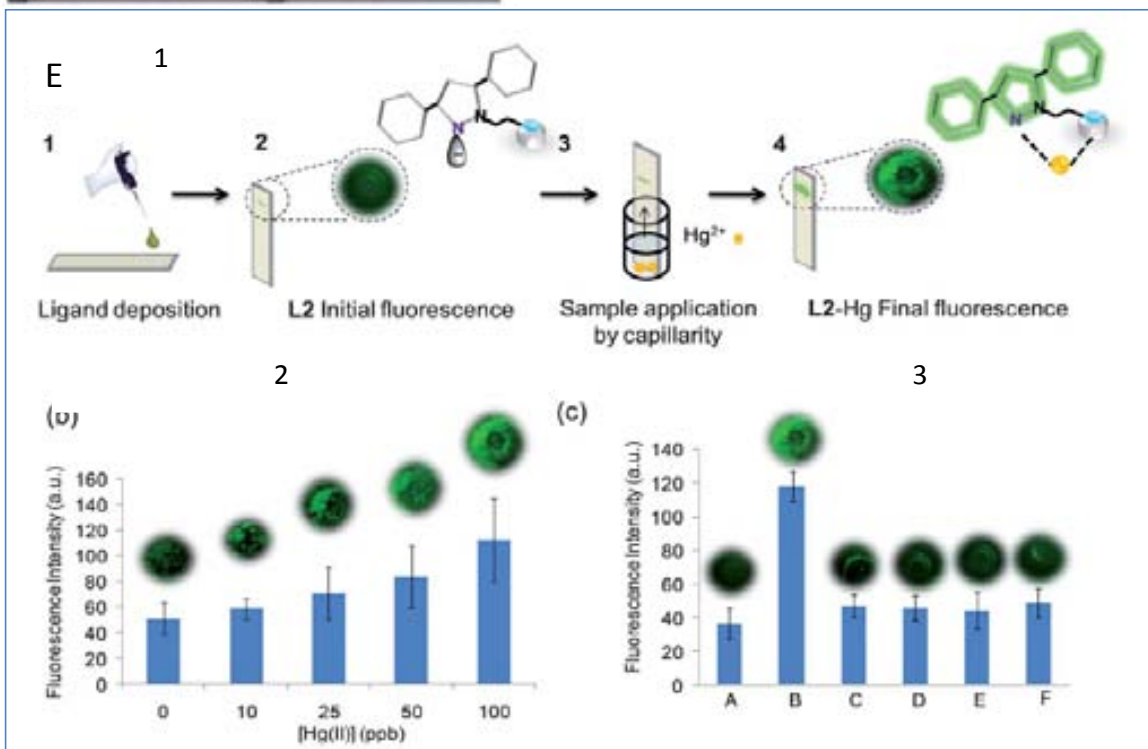
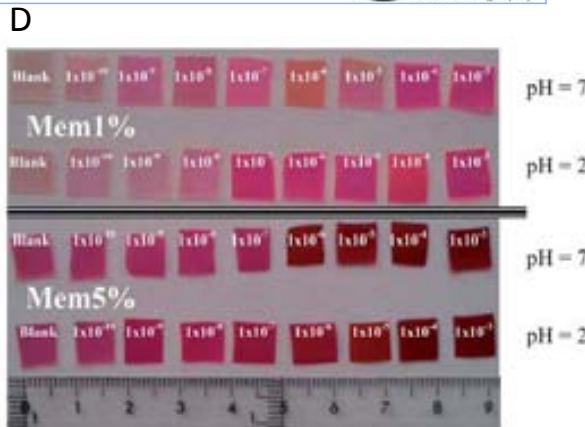
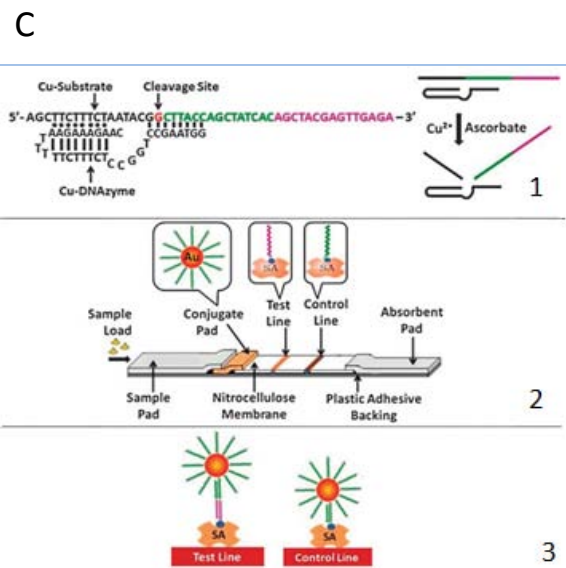
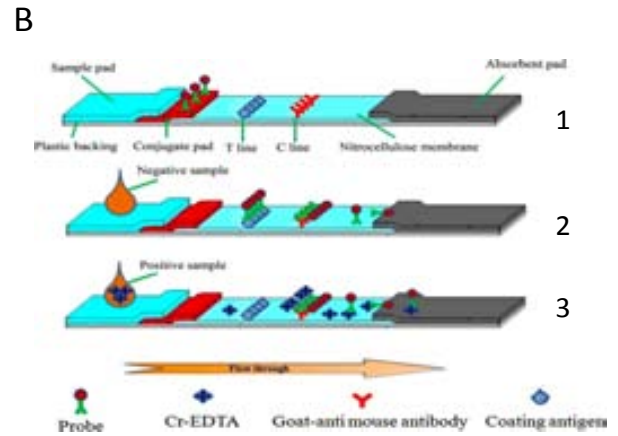
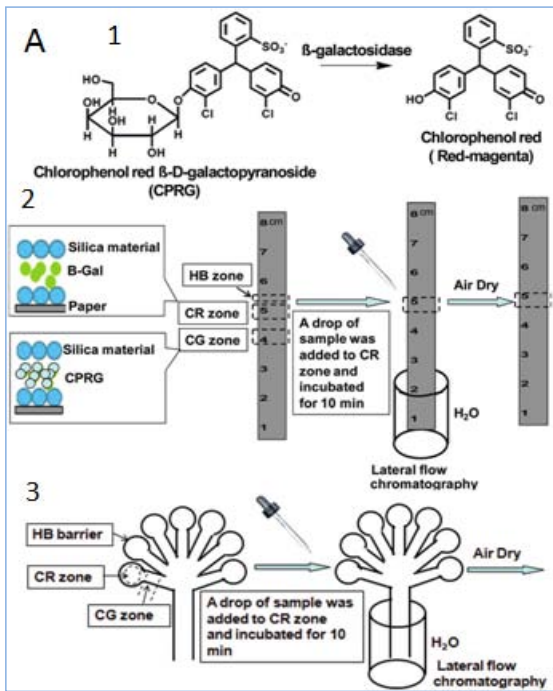


Figure 6. Typical representative designs of paper-based sensors and their working principles using different analytes receptor molecules for heavy metals sensing (A and B: using enzymes, C: using mAbs, D: using DNAzymes and E: using small organic molecule). **A)** A-1. The chromogenic substrate, chlorophenol red β -galactopyranoside (CPRG), is hydrolyzed by β -galactosidase (β -GAL) to form a red-magenta colored product and the heavy metals presence in the sample causes a color change in a concentration-dependent manner; A-2 B-GAL (color reaction, CR zone) and CPRG (CG zone) were entrapped within sol-gel derived silica materials in the two dashed regions on a Whatman paper via inkjet printing. A hydrophobic barrier (HB zone) composed was introduced at the top of the sensing zone to prevent leaching of color; A-3 Multiplexed sensor with a hydrophobic barrier (HB zone) in which B-GAL and CPRG were entrapped within silica materials in the circular region (CR zone) and arm (CG zone), respectively. The sensing zones (CR zones) were incubated with a drop of sample to be analysed. **B)** B-1 Competitive LFIA used in Cr^{3+} detection, B-2 the principle of negative detection and, B-3 the principle of positive detection. **C)** C-1 Structure of the Cu^{2+} -specific-DNAzyme (left) and cleavage of the substrate in the presence of Cu^{2+} and ascorbate (right). C-2 Schematic illustration of lateral flow nucleic acid biosensor for detecting the cleaved DNA strands. C-3 Visual detection of Cu^{2+} by capturing AuNPs on the test and control zones of the lateral flow nucleic acid biosensor. SA: streptavidin. **D)** Digital pictures of strips of Mem1% and Mem5% after dipping for 25 min into water containing different concentrations of Hg^{2+} . The digital pictures were taken with a mobile phone (Samsung Galaxy) **E)** E-1 Assay procedure for the paper based fluorescent assay for Hg^{2+} ions. E-2 Calibration curve from 0 to 100 ppb of Hg^{2+} using this paper assay and its corresponding fluorescence images used for signal reading. E-3 Fluorescence responses for various heavy metals: blank (MilliQ water), (A) 100 ppb of Hg^{2+} (B), Zn^{2+} (C), Cd^{2+} (D), Pb^{2+} (E) and Cu^{2+} (F). A, B, C, D and E figures adapted from reference 157, 159, 163, 167 and 166, respectively

1.3.4 Conclusions and future prospects.

Although various paper based formats such as dipsticks, flow through and LFAs have been developed, LFA is the most disseminated and versatile. Advances in microfluidics and lab/on/a/ chip platforms are providing new opportunities for their tools to be applied in paper sensor designs. Interesting simple designs by using microfluidics and Lab on Chip technologies have brought advantages over the old paper formats. The reuse of paper sheets, the multi-analyte determination, the reduction of analysis steps beside other are some of the inputs coming to these engineering paper sensors technologies. Recent trends in this technology are directed to (bio)functionalizing and patterning of paper platforms by using photolithography, ink jet etching, wax printing and dipping, plotter printing, flexography printing, and hand plotting. The obtained paper designs known also as μ PADs contain patterned hydrophobic materials physically deposited on the surface of paper fibers. The patterned hydrophobic materials might be attacked by organic solvents, which would be used during assay for elution of analyte or cleaning of

channels, etc. The silanization to obtain hydrophobic paper sheets and the entrapment of biomolecules within sol-gel-derived materials have generally shown good results.

Several materials as labels to generate the measuring signal have been tested. The development and application of more sensitive labels is highly recommended. Localized SPR of metal nanostructures is sensitive to local changes in dielectric environment. It renders an attractive transduction platform for chemical and biological sensing. Localized SPR and the measurement of other highly sensitive physical properties provide extremely low LoDs and for this reason a great interest for its application in paper sensor is being showed.

I.4 References

- [1] http://www.chesapeakebay.net/issues/issue/chemical_contaminants
- [2] <http://fsrio.nal.usda.gov/pathogens-and-contaminants/chemical-and-physical-contaminants>
- [3] <http://www.opcw.org/about-chemical-weapons/types-of-chemical-agent/toxins/>
- [4] J. W. Hamilton, R.C. Kaltreider, O.V. Bajenova, M. A. Ihnat, J. McCaffrey, B. W. Turpie, E. E. Rowell, J. Oh, M. J. Nemeth, C. A. Pesce, J. P. Lariviere, *J. Environ. Health*, **1998**, 106, 1005.
- [5] B. L. Vallee, D.D. Ulmer, *Annu. Rev. Biochem.* **1972**, 41, 91.
- [6] T. Partanen, P. Heikkila, S. Hernberg, T. Kauppinen, G. Moneta, A. Ojajarvi, *Scand. J. Work. Environ. Health*, **1991**, 17, 231.
- [7] M. Khosraviani, R. A. Pavlov, C. G. Flowers, D. A. Blake, *Environ. Sci. Technol.* **1998**, 32, 137.
- [8] I. A. Darwish, D. A. Blake, *Anal. Chem.* **2001**, 73, 1889.
- [9] C. L. Schauer, P. R. R. Mu-Sanchen, P. Schoen, F. S. Ligler, *Environ. Sci. Technol.* **2004**, 38, 4409.
- [10] R. G. Bhagure, S. R. Mirgane, *Environ. Monit. Assess.* **2011**, 173, 643.
- [11] J. Pandey, K. Shubhashish, R. Pandey, *Tropical Ecol.* **2010**, 51, 365.
- [12] R. Reza, G. Singh, *Int. J. Environ. Sci. Tech.* **2010**, 7, 785.
- [13] B. Volesky, *Hydrometallurgy*, **2001**, 59, 203.
- [14] A. Guijarro-Aldaco, V. Hernández-Montoya, A. Bonilla-Petriciolet, M. A. Montes-Morán, D. I. Mendoza-Castillo, *Ind. Eng. Chem. Res.* **2011**, 50, 9354.
- [15] <http://www.hoffland.net/hydroxide-precipitation.html>
- [16] B. Karn, T. Kuiken, M. Otto, *Environ. Health Perspectives*, **2009**, 117, 1823.
- [17] W. Yantasee, C. L. Warner, T. Sangvanich, R. S. Addleman, T. G. Carter, R. J. Wiacek, G. E. Fryxell, C. Timchalk, M. G. Warner, *Environ. Sci. Technol.* **2007**, 41, 5114.
- [18] I. Ojea-Jiménez, X. López, J. Arbiol, V. Puentes, *ACS Nano*, **2012**, 6, 2253.
- [19] M. Arkas, D. Tsiourvas, C. M. Paleos, *Chem. Mater.* **2003**, 15, 2844.
- [20] L. C. A. Oliveira, D. I. Petkowicz, A. Smaniotto, S. B. C. Pergher, *Water Res.* **2004**, 38, 3699.
- [21] H. M. Chen, P. K. Chu, J. H. He, T. Hu, M. Q. Yang, *J. Colloid. Interf. Sci.* **2011**, 359, 68.
- [22] J. Gasparik, D. Vladarova, M. Capcarova, P. Smehyl, J. Slamecka, P. Garaj, R.

- Stawarz, P. Massanyi, *J. Environ. Sci. Health A* **2010**, 45, 818.
- [23] T.-Y. Hoa, Ch.-T. Chiena, B.-N. Wanga, A. Siriraks, *Talanta*, **2010**, 82, 1478.
- [24] B. F. Senkal, M. Ince, E. Yavuz, M. Yaman, *Talanta*, **2007**, 72, 962.
- [25] M. R. Knecht, M. Sethi, *Anal. Bioanal. Chem.* **2009**, 394, 33.
- [26] J. Du, Y. Sun, L. Jiang, X. Cao, D. Qi, S. Yin, J. Ma, C. F. Y. Boey, X. Chen, *Small*, **2011**, 7, 1407.
- [27] Ch. Zong, K. Ai, G. Zhang, H. Li, L. Lu, *Anal. Chem.* **2011**, 83, 3126.
- [28] H.-W. Zhao, Ch.-G. Xue, Tie-Gui Nan, G.-Y. Tan, Z. Li, Q.-X. Li, Q.-Ch. Zhang, B.-M. Wang, *Anal. Chim. Acta*, **2010**, 676, 81.
- [29] D. A. Blake, R. C. II Blake, M. Khosraviani, A. R. Pavlov, *Anal. Chim. Acta*, **1998**, 376, 13.
- [30] A. Afkhami, T. Madrakian, S. J. Sabounchei, M. Rezaei, S. Samiee, M. Pourshahbaz, *Sensor Actuat. B*, **2012**, 161, 542.
- [31] G. Aragay, A. Puig-Font, M. Cadevall, A. Merkoci, *J. Phys. Chem. C* **2010**, 114, 9049.
- [32] G. Aragay, J. Pons, A. Merkoci, *J. Mater. Chem.* **2011**, 21, 4326.
- [33] M. Adami, S. Marco, C. Nicolini, *Electroanal.* **2007**, 19, 1288.
- [34] J. K. Schneider, *Helv. Chim. Acta*, **1980**, 63, 217.
- [35] L. Marbella, B. Serli-Mitasev, P. Basu, *Angew. Chem., Int. Ed.* **2009**, 48, 3996.
- [36] G. Aragay, J. Pons, J. García-Antón, X. Solans, M. Font-Bardía, J. Ros, *J. Organomet. Chem.* **2008**, 693, 3396.
- [37] G. Aragay, J. Pons, V. Branchadell, J. García-Antón, X. Solans, M. Font-Bardía, J. Ros, *Aust. J. Chem.* **2010**, 63, 257.
- [38] M. C. Castellano, J. Pons, J. García-Antón, X. Solans, M. Font-Bardía, J. Ros, *Inorg. Chim. Acta*, **2008**, 361, 2923.
- [39] J. Pons, J. García-Antón, M. Font-Bardía, T. Calvet, J. Ros, *Inorg. Chim. Acta*, **2008**, 362, 2698.
- [40] O. S. Kwon, H. S. Kim, *Supramol. Chem.* **2007**, 19, 277.
- [41] V. Bhalla, R. Tejpal, M. Kumar, A. Sethi, *Inorg. Chem.* **2009**, 48, 11677.
- [42] A.B. Othman, J.W. Lee, J. Wu, J.S. Kim, R. Abidi, P. Thuéry, J.M. Strub, A. V. Dorsseleer, J. Vicens, *J. Org. Chem.* **2007**, 72, 7634.
- [43] E. Norkus, *J. Incl. Phenom. Macrocycl. Chem.* **2009**, 65, 237.
- [44] T. Dudev, C. Lim. *Annu. Rev. Biophys.* **2008**, 37, 97.

- [45] I. Bontidean, C. Berggren, G. Johansson, E. Csoregi, B. Mattiasson, J. R. Lloyd, K. J. Jakeman, N. L. Brown, *Anal. Chem.* **1998**, *70*, 4162.
- [46] D. E. Wylie, D. Lu, L. D. Carlson, R. Carlson, K. F. Babacan, S. M. Schuster, F. W. Wagner, *Anal. Biochem.* **1991**, *194*, 381.
- [47] D. A. Blake, P. Chakrabarti, M. Khosraviani, F. M. Hatcher, C. M. Westhoff, P. Goebel, D. E. Wylie, R. C. Blake, *J. Biol. Chem.* **1996**, *271*, 27677.
- [48] D. E. Wylie, D. Lu, R. Carlson, K. F. Babacan, S. M. Schuster, F. E. Wagner, *Proc. Natl. Acad. Sci.* **1992**, *89*, 4104.
- [49] S. Wegner, A. Okesli, P. Chen, C. He, *J. Am. Chem. Soc.* **2007**, *129*, 3473.
- [50] K. Hamaguchi, H. Kawasaki, R. Arakawa, *Colloids Surfaces A: Physicochem. Eng. Aspects*, **2010**, *367*, 167.
- [51] B. Yosypchuk, L. Novotný, *Electroanal.* **2002**, *14*, 1733.
- [52] B. Yosypchuk, J. Barek, *Crit. Rev. Anal. Chem.* **2009**, *39*, 189.
- [53] J. Wang, J. Lu, S.B. Hocevar, P.A.M. Farias, *Anal. Chem.* **2000**, *72*, 3218.
- [54] A. H. Free, E. C. Adams, M. L. Kercher, H. M. Free, M. H. Cook, *Clin. Chem.* **1957**, *3*, 63.
- [55] H. M. Free, G. F. Collins, A. H. Free, *Clin. Chem.* **1960**, *6*, 352.
- [56] N. A. Brunzel, *Fundamentals of Urine and Body Fluid Analysis*, 2nd ed.; Saunders: New York, **2004**; pp 123-163.
- [57] R. Hawkes, E. Niday, J. Gordon, *Anal. Biochem.* **1982**, *119*, 142.
- [58] S. R. Binder, *Lupus* **2006**, *15*, 412.
- [59] R. W. Rosenstein, T. G. Bloomster, *U.S. Patent*, **1989**, 4, 855, 240.
- [60] J. Gordon, M. E. McMahon, S. Ching, *U.S. Patent*, **1990**, 4, 960, 691.
- [61] S. Haerberle, R. Zengerle, *Lab Chip*, **2007**, *7*, 1094.
- [62] B. B. Ngom, Y. Guo, X. Wang, D. Bi, *Anal. Bioanal. Chem.* **2010**, *397*, 1113.
- [63] H. Tao, L. R. Chieffo, M. A. Brenckle, S. M. Siebert, M. Liu, A. C. Strikwerda, K. Fan, D. L. Kaplan, X. Zhang, R. D. Averitt, F. G. Omenetto, *Adv. Mater.* **2011**, *23*, 3197.
- [64] M. H. Tsai, W. S. Hwang, H. H. Chou, P. H. Hsieh, *Nanotechnology* **2008**, *19*, 335304.
- [65] S. M. Zakir Hossain, R. E. Luckham, A. M. Smith, J. M. Lebert, L. M. Davies, R. H. Pelton, C. D. M. Filipe, J. D. Brennan, *Anal. Chem.* **2009**, *81*, 5474.
- [66] E. Carrilho, A. W. Martinez and G. M. Whitesides, *Anal. Chem.*, **2009**, *81*, 7091.

- [67] A. Savolainen, Y. Zhang, D. Rochefort, U. Holopainen, T. Erho, J. Virtanen, M. Smolander, *Biomacromolecules*, **2011**, 12, 2008.
- [68] A. W. Martinez, S. T. Phillips, G. M. Whitesides and E. Carrilho, *Anal. Chem.* **2010**, 82, 3.
- [69] J.-H. Kim, J.-H. Cho, G. S. Cha, Ch.-W. Lee, H.-B. Kim, S.-H. Paek, *Biosens. Bioelectron.* **2000**, 14, 907.
- [70] G. A. Posthuma-Trumpie, J. Korf, A. van Amerongen, *Anal. Bioanal. Chem.* **2009**, 393, 569.
- [71] C. Zhang, Y. Zhang, S. Wang, *J. Agric. Food Chem.* **2006**, 54, 2502.
- [72] C. Parolo, A. Merkoçi, *Chem. Soc. Rev.* **2013**, 42, 450.
- [73] S.-H. Peak, S.-H. Lee, J.-H. Cho, Y.-S. Kim, *Method* **2000**, 22, 53.
- [74] S. Qian, H.-H. Bau, *Anal Biochem.* **2004**, 326, 211.
- [75] X. Wang, K. Li, D. Shi, N. Xiong, X. Jin, D. Yi, D. Bi, *J. Agric. Food Chem.* **2007**, 55, 2072.
- [76] R. Barnard, C. George, K. Jacobs, A. C. K. Wu, T. K. Nagasaki, J. Shan, K. Greenwood, E. Kachab, *Point-of Care*, **2005**, 4,108.
- [77] M. Blaskoza, M. Koet, P Rauch, A. V. Amerogen, *Eur Food Res Technol.* **2009**, 229, 867.
- [78] K. A. Edwards, E. J. Baeumner, *Method Mol Bio.* **2008**, 504,185.
- [79] P. L. A. M. Corstjens, M Zuiderwijk, M Nilson, H Feindt, R. S. Niedbala, H. J. Tanke, *Anal Biochem.* **2003**, 312,191.
- [80] K. Saha, S. S. Agasti, Ch. Kim, X. Li, V. M. Rotello, *Chem. Rev.* **2012**, 112, 2739.
- [81] Y. He, S. Zhang, X. Zhang, M. Baloda, A. S. Gurung, H. Xu, X. Zhang, G. Liu, *Biosens. Bioelectron.*, **2011**, 26, 2018.
- [82] C. Parolo, A. de la Escosura-Muñiz, A. Merkoçi, *Biosens. Bioelectron.* **2013**, 40, 412.
- [83] X. Mao, Y. Ma, A. Zhang, L. Zhang, L. Zeng, G. Liu, *Anal. Chem.* **2009**, 81, 1660.
- [84] J. H. Cho, S.-M. Han, E.-H. Paek, H. Cho, S.-H. Paek, *Anal. Chem.* **2006**, 78, 793.
- [85] J. K. Horton, S. Swinburne, M. J. O'Sullivan, *J. Immunol. Methods* **1991**, 140, 131.
- [86] I.-H. Cho, S.-M. Seo, E.-H. Paek, S.-H. Paek, *J. Chromatogr. B*, **2010**, 878, 271.
- [87] D.-J. Chiao, J.-J. Wey, R.-H. Shyu, S.-S. Tang, *Hybridoma*, **2008**, 27, 31.

- [88] D-J. Chiao, R-H. Shyu, C-S. Hu, H-Y. Chiang, S-S. Tang. *J. Chromatogr B*, **2004**, 809, 37.
- [89] R-H. Shyu, S-S. Tang, D-J. Chiao, Y-W. Hung, *Food Chem*, **2010**, 118, 462.
- [90] R-H. Shyu, H-F. Shyu, H-W. Liu, S-S. Tang, *Toxicon*, **2002**, 40, 255.
- [91] P. Zhou, Y. Lu, J. Zhu, J. Hong, B. Li, J. Zhou, D. Gong, A. Montoya, *J. Agric. Food Chem.* **2004**, 52, 4355
- [92] A. J. Baeumner, J. Pretz, S. Fang, *Anal. Chem.* **2004**, 76, 888.
- [93] A. J. Baeumner, C. Jones, C. Y. Wong, A. Price, *Anal. Bioanal. Chem.* **2004**, 378, 1587.
- [94] D. H. Choi, S. K. Lee, Y. K. Oh, B. W. Bae, S. D. Lee, S. Kim, Y.-B. Shin, M.-G. Kim, *Biosens. Bioelectron.* **2010**, 25, 1999.
- [95] N. Khreich, P. Lamourette, H. Boutal, K. Deveilliers, C. Creminon, H. Volland *Anal Biochem.* **2008**, 377, 182.
- [96] S. Shukla, H. Leem and M. Kim, *Anal. Bioanal. Chem.*, **2011**, 401, 2581.
- [97] A. J. Baeumner, *Food Technol.* **2004**, 58, 51.
- [98] J-A. Ho, S-C. Zeng, W-H Tseng, Y-J Lin, C-H Chen. *Anal. Bioanal. Chem.* **2008**, 391, 479.
- [99] J-A. Ho, M. R. Huang, *Anal. Chem.* **2005**, 77, 3431.
- [100] G. C. Gussenhoven, M. A. van der Hoorn, M. G. Goris, W. J. Terpstra, R. A. Hartskeerl, B. W. Mol, C. W. van Ingen, H. L. Smits, *J. Clin. Microbiol*, **1997**, 35, 92.
- [101] H.-W. Wen, W. Borejsza-Wysocki, T. R. DeCory, R. A. Durst, *Anal. Bioanal. Chem.* **2005**, 382, 1217.
- [102] J.-A. A. Ho, R. D. Wauchope, *Anal. Chem.* **2002**, 74, 1493.
- [103] K. S Lee, T-H Kim, M-C Shin, W-Y Lee, J-K Park, *Anal Chim Acta*, **1999** 380, 17.
- [104] R. Greenwald, J. Esfandiari, S. Lesellier, R. Houghton, J. Pollock, C. Aagaard, P. Andersen, R. G. Hewinson, M. Chambers, K. Lyashchenko, *Diagn. Microbiol. Infect. Dis.* **2003**, 46, 197.
- [105] K Campbell, T Fodey, J Flint, C Danks, M Danaher, M O’Keeffe, D. G. Kennedy, C. Elliott, *J Agric Food Chem*, **2007**, 55, 2497.
- [106] K. Nielsena, W. L. Yua, M. Lina, S. A. Nadin Davisa, C. Elmgrena, R. MacKenzieb, J. Tanhab, S. Lib, G. Dubuch, E. G. Brownc, L. Keletac; J. Pasickd, *J. Immuno. Immunochem.* **2007**, 28, 307

- [107] S. Puertas, M. Moros, R. Fernández-Pacheco, M. R. Ibarra, V. Grazú, J. M. de la Fuente, *J. Phys. D: Appl. Phys.*, **2010**, 43, 474012.
- [108] D. Tang, J. C. Saucedo, Z. Lin, B. Soe, I. Goryacheva, S. Biselli, J. Lin, R. Niessner, D. Knopp, *Biosens Bioelectron.* **2009**, 25, 514.
- [109] M. Fisher, Y. Atiya-Nasagi, I. Simon, M. Gordin, A. Mechaly, S. Yitzhaki, *Lett Appl Microbiol.* **2009**, 48, 413.
- [110] E. R. Goldman, A. R. Clapp, G. P. Anderson, H. T. Uyeda, J. M. Mauro, I. L. Medintz, H. Mattoussi, *Anal Chem.* **2004**, 76, 684.
- [111] X.-D. Wang, H.-X. Chen, T.-Y. Zhou, Z.-J. Lin, J.-B. Zeng, Z.-X. Xie, X. Chen, K.-Y. Wong, G.-N. Chen, X.-R. Wang, *Biosens. Bioelectron.* **2009**, 24, 3702.
- [112] Z. Li, Y. Wang, J. Wang, Z. Tang, J. G. Pounds and Y. Lin, *Anal. Chem.*, **2010**, 82, 7008.
- [113] Z. Zou, D. Du, J. Wang, J. N. Smith, Ch. Timchalk, Y. Li, Y. Lin *Anal. Chem.*, **2010**, 82, 5125
- [114] X. Zhu, L. Chen, P. Shen, J. Jia, D. Zhang, L. Yang, *J. Agric. Food Chem.*, **2011**, 59, 2184.
- [115] L. Wang, W. Chen, W. Ma, L. Liu, W. Ma, Y. Zhao, Y. Zhu, L. Xu, H. Kuang, Ch. Xu, *Chem. Commun.* **2011**, 47, 1574.
- [116] M. Lonnberg, J. Carlsson, *Anal. Biochem*, **2001**, 293, 224.
- [117] A. van Amerongen, J. H. Wichers, L. B. J. M Berendsen, A. J. M. Timmermans, G. D. Keizer, A. W. J. van Doorn, A. Bantjes, W. M. J. van Gelder, *J. Biotechnol.* **1993**, 30, 185.
- [118] M. Blaskova, B. Mickova-Holubova, P. Rauch, L. Fukal, *Biosens. Bioelectron.* **2009**, 25, 753.
- [119] Z. Smidova, M. Blazkova, L. Fukal, P. Rauch, *Czech J Food Sci*, **2009**, 27, S414.
- [120] M. Blazková, B. Javurková, L. Fukal, P. Rauch, *Biosens. Bioelectron.*, **2011**, 26, 2828.
- [121] D. P. Kalogianni, L. M. Boutsika, P. G. Kouremenou, T. K. Christopoulos, P. C. Ioannou, *Anal. Bioanal. Chem.* **2011**, 400, 1145.
- [122] P. Noguera, G. A. Posthuma-Trumpie, M. van Tuil, F. J. van der Wal, A. de Boer, A. P. H. A. Moers, A. van Amerongen, *Anal. Bioanal. Chem.* **2011**, 399, 831.
- [123] S. Lou, C. Patel, S. Ching, J. Gordon, *Clin Chem.* **1993**, 39, 619.

- [124] X. Xia, Y. Xu, X. Zhao, Q. Li, *Clin. Chem.* **2009**, 55, 179.
- [125] M. Ornatska, E. Sharpe, D. Andreescu, S. Andreescu, *Anal. Chem.* **2011**, 83, 4273.
- [126] R. Tanaka, T. Yuhi, N. Nagatani, T. Endo, K. Kerman, Y. Takamura, E. Tamiya, *Anal. Bioanal. Chem.* **2006**, 385, 1414.
- [127] W. E. Doering, M. E. Piotti, M. J. Natan, R. G. Freeman, *Adv. Mater.* **2007**, 19, 3100.
- [128] L. Tian, J. J. Morrissey, *Anal Chem.* **2012**, 84, 9928.
- [129] M. Zuiderwijk, H. J. Tanke, R. S. Niedbala, PLAM Corstjens, *Clin. Biochem.* **2003**, 36, 401.
- [130] P. Corstjens, M. Zuiderwijk, A. Brink, S. Li, H. Feindt, R. S. Niedbala, H. Tanke, *Clin. Chem.* **2001**, 47, 1885.
- [131] J. Hampl, M. Hall, N. A. Mufti, Y. M. D. Yao, D. MacQueen, W. H. Wright, D. E. Cooper, *Anal. Biochem.* **2001**, 288, 176.
- [132] C. Parolo, M. Medina-Sánchez, A. de la Escosura-Muñiz, A. Merkoçi, *Lab Chip*, **2013**, 13, 386.
- [133] E. M. Fenton, M. R. Mascarenas, G. P. López, S. S. Sibbett, *ACS Applied Mater Interfaces* **2009**, 1, 124.
- [134] E. Fu, B. Lutz, P. Kauffman, P. Yager, *Lab Chip*, **2010**, 10, 918.
- [135] E. Fu, P. Kauffman, B. Lutz, P. Yager, *Sensors Actuat. B Chem.* **2010**, 149, 325.
- [136] E. Fu, S. A. Ramseyb, P. Kauffman, B. Lutz, P. Yager, *Microfluidics Nanofluidics*, **2011**, 10, 29.
- [137] E. Fu, T. Liang, J. Houghtaling, S. Ramachandran, S. A. Ramsey, B. Lutz, P. Yager, *Anal. Chem.* **2011**, 83, 7941
- [138] A. M. López_Marzo, J. Pons, D. A. Blake, A. Merkoçi, *Anal. Chem.* **2013**, 85, 3532.
- [139] A. Abbas, A. Brimer, J. M. Slocik, L. Tian, R. R. Naik, S. Singamaneni, *Anal. Chem.* **2013** doi:10.1021/ac303567g
- [140] S. N. Tan, L. Ge, W. Wang, *Anal. Chem.* **2010**, 82, 8844.
- [141] A. Apilux, W. Dungchai, W. Siangproh, N. Praphairaksit, Ch. S. Henry, O. Chailapakul, *Anal. Chem.* **2010**, 82, 1727.
- [142] H. Nian, J. Wang, H. Wu, J.-G. Lo, K.-H. Chiu, J. G. Pounds, Y. Lin, *Anal. Chim. Acta*, **2012**, 713, 50.

- [143] A. W. Martinez, S. T. Phillips, M. J. Butte, G. M. Whitesides, *Angew. Chem. Int., Ed.* **2007**, 46, 1318.
- [144] Q. He, C. Ma, X. Hu, H. Chen, *Anal. Chem.* **2013**, 85, 1327
- [145] A. R. Rezk, A. Qi, J. R. Friend, W. H. Li, L. Y. Yeo, *Lab Chip*, **2012**, 12, 773
- [146] W. Dungchai, O. Chailapakul, C. S. Henry, *Analyst*, **2011**, 136, 77.
- [147] E. Carrilho, S. T. Phillips, S. J. Vella, A. W. Martinez, G. M. Whitesides, *Anal. Chem.*, **2009**, 81, 5990.
- [148] C.-M. Cheng, A. W. Martinez, J. Gong, C. R. Mace, S. T. Phillips, E. Carrilho, K. a. Mirica, G. M. Whitesides, *Angew. Chem. Int., Ed.* **2010**, 49, 4771.
- [149] S. Wang, L. Ge, X. Song, J. Yu, S. Ge, J. Huang, F. Zeng, *Biosens. Bioelectron.* **2012**, 31, 212.
- [150] C.-G. Shi, X. Shan, Z.-Q. Pan, J.-J. Xu, C. Lu, N. Bao, H.-Y. Gu, *Anal. Chem.*, **2012**, 84, 3033.
- [151] Z. Nie, C. A. Nijhuis, J. Gong, X. Chen, A. Kumachev, A. W. Martinez, M. Narovlyansky, G. M. Whitesides, *Lab Chip*, **2010**, 10, 477.
- [152] A. K. Ellerbee, S. T. Phillips, A. C. Siegel, K. a. Mirica, A. W. Martinez, P. Striehl, N. Jain, M. Prentiss, G. M. Whitesides, *Anal. Chem.* **2009**, 81, 8447.
- [153] X. Liu, M. Mwangi, X. Li, M. O'Brien, G. M. Whitesides, *Lab Chip*, **2011**, 11, 2189.
- [154] S. M. Z. Hossain, R. E. Luckham, A. M. Smith, J. M. Lebert, L. M. Davies, R. H. Pelton, C. D. M. Filipe, J. D. Brennan, *Anal. Chem.* **2009**, 81, 5474
- [155] R. S. J. Alkasir, M. Ornatska, S. Andreescu, *Anal. Chem.* **2012**, 84, 9729.
- [156] S. M. Zakir Hossain, R. E. Luckham, M. J. McFadden, J. D. Brennan, *Anal. Chem.* **2009**, 81, 9055.
- [157] H. S. M. Zakir, J. D. Brennan, *Anal. Chem.* **2011**, 83, 8772.
- [158] K. Abe, K. Nakamura, T. Arao, Y. Sakurai, A. Nakano, Ch. Suginuma, K. Tawaradae, K. Sasaki, *J. Sci. Food Agric.* **2011**, 91, 1392.
- [159] X. Liu, J.-J. Xiang, Y. Tang, X.-L. Zhang, Q.-Q. Fu, J.-H. Zou, Y.-H. Lin, *Anal. Chim. Acta*, **2012**, 45, 99.
- [160] A. M. López-Marzo, J. Pons, D. A. Blake, A. Merkoçi, *Biosens. Bioelectron.* **2013**, 85, 3532.
- [161] S.-F. Torabia, Y. Lu, *Faraday Discuss.* **2011**, 149, 125.
- [162] Z. Fang, J. Huang, P. Lie, Z. Xiao, Ch. Ouyang, Q. Wu, Y. Wu, G. Liu, L. Zeng, *Chem. Commun.* **2010**, 46, 9043

- [163] D. Mazumdar, J. Liu, G. Lu, J. Zhou, Y. Lu, *Chem. Commun.* **2010**, 46, 1416.
- [164] Z. Gu, M. Zhao, Y. Sheng, L. A. Bentolila, Y. Tang, *Anal. Chem.* **2011**, 83, 2324.
- [165] C. L. Schauer, P. R. R. Mu-Sanchen, P. Schoen, F. S. Ligler, *Environ. Sci. Technol.* **2004**, 38, 4409.
- [166] G. Aragay, H. Monton, J. Pons, M. Font-Bardia, A. Merkoçi, *J. Mater. Chem.* **2012**, 22, 5978.
- [167] H. El Kaoutit, P. Estévez, F. C. García, F. Serna, J. M. García, *Anal. Methods*, **2013**, 5, 54.
- [168] A. George, E. S. Shibu, Sh. M. Maliyekkal, M. S. Bootharaju, T. Pradeep, *Appl. Mater. Interfaces* **2012**, 4, 639.

CHAPTER II. OBJECTIVES OF THE THESIS

II. Objectives

Controlling and removing of chemical contaminants in the environment are important focuses for the nowadays science and technology. The development of new, fast, cheap and effective materials, devices and systems for sensing and removing chemical contaminants continues to be of interest to preserve the environment and human health. This doctoral thesis has as main objective to contribute to this end, developing and evaluating novel nanostructured micromaterials and devices for sensing and removing of chemical contaminants with a main focus to heavy metals although successful application to phenol is also demonstrated through other works (included as annexes).

General and specific objectives can be disclosed as follows:

General Objective

- 1- Develop nanostructured micromaterials and devices for sensing and/or removing of chemical contaminants.

Specific Objectives

- 1- Develop a nanostructured, biodegradable, cheap and easy to synthesize material based on vaterite-polymer with potential for multiples applications.
 - 1.1- Study the syntheses of CaCO_3 and the effect of reaction conditions such as type of mixing, reagents volume, use and type of CGM and type of reaction medium (solvents) upon the CaCO_3 product. Characterize the polymorphic composition and the morphology of the CaCO_3 crystallization products obtained in the syntheses by use of XRD, IR, SEM and TEM techniques.
 - 1.2- Study the bio-functionalizing capacity of the most promising CaCO_3 product, for a large variety of (bio)molecules by using CLMS and UV-Vis characterization techniques, and evaluate its Z-potential directly related to future applications.
- 2- Evaluate the heavy metals removal capacity of the nanostructured vaterite modified with PEI (NV-PEI) material for wastewaters treatment applications.
 - 2.1- Evaluate the preferential adsorption onto the NV-PEI material of various metal ions through competitive adsorption assay.
 - 2.2- Determine for the metal with preferential adsorption the values of Q_{max} and its corresponding concentration and time of contact. Determine the equilibrium adsorption isotherm that describes the removal process for this metal.

- 2.3- Determinate the physical adsorption parameters of the NV-PEI material such as the BET, BJH and characteristic porous volume.
- 2.4- Analyse by SEM and XRD the adsorbent material after the removal process.
Propose the removal mechanism that takes place during the treatment process.
- 3- Design and develop a new integrated system based on the nanostructured CaCO_3 -polymer material, able to sense and remove simultaneously heavy metals (introduction of a new *sensoremoval* concept for environmental applications).
 - 3.1- Design the system, that allows the simultaneous Pb^{2+} (as model metal) sensing and removal purpose, through the formation of CaCO_3 by using an initial Pb^{2+} contaminated solution.
 - 3.2- Study the reaction system varying reaction conditions such as the effect of the use or not of CGM, type of CGM, reagents volume, order of reagents addition, reaction medium, reagents concentration, etc. Characterize the polymorphic composition and the morphology of the precipitation products obtained in these syntheses by use of XRD, IR, SEM and TGA characterization techniques.
 - 3.3- Study with the most appropriate CaCO_3 material the Pb^{2+} detection using the measurement of turbidity produced during the formation of the CaCO_3 precipitate.
 - 3.4- Evaluate the Pb^{2+} removal capacity of the formed CaCO_3 precipitate.
- 4- Develop a new highly sensitive LFID for Cd^{2+} detection in waters with integrated sample treatment platform.
 - 4.1- Design first the format of the conventional LFID. Evaluate the performance of the corresponding recognition reactions (antigen-antibody) of each reagent deposited onto device when the fluid crosses through membrane.
 - 4.2- Optimize parameters in the LFID such as mAbs and conjugate concentrations in order to enhance the LoD and the LoQ reported so far in metal sensors based on paper.
 - 4.3- Evaluate the LoD, LoQ and linearity in the proposed conventional device through the analysis of Cd^{2+} pattern dissolutions.
 - 4.4- Perform a specificity assay by evaluating fundamentally the interference effect produced by other metallic ions. Design and apply an effective strategy to avoid interferences.
 - 4.5- Design a highly sensitive and integrated LFID with an extra conjugation pad that permits the direct sample analysis eliminating the sample pre-treatment step.

This extra pad could contains the adequate concentration reagents to 'in-situ' prepare the analyte for the analysis and mask the possible metal interferences.

4.6- Evaluate the performance of the integrated LFID: the LoD, LoQ and linearity through the analysis of pattern dissolutions and the accuracy, precision, range of response, etc through the analysis of real drinking and tap waters samples.

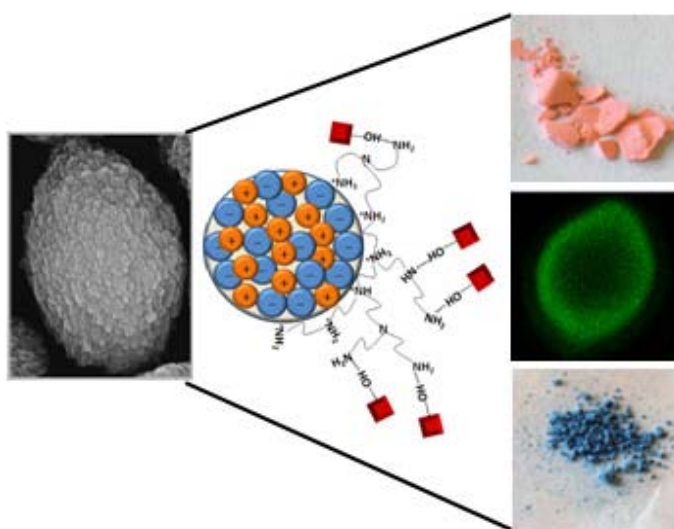
CHAPTERS III-VI: RESULTS AND DISCUSSION

Chapter III. Controlled formation of nanostructured CaCO₃-PEI microparticles with high biofunctionalizing capacity.

These results are related in the publication “Controlled formation of nanostructured CaCO₃-PEI microparticles with high biofunctionalizing capacity”, A. López_Marzo, J. Pons, A. Merkoçi, *Journal Materials Chemistry*, **2012**, 22, 15326.

Chapter III. Controlled formation of nanostructured CaCO_3 -PEI microparticles with high biofunctionalizing capacity.

Graphical abstract and content



Controlled formation of nanostructured CaCO_3 -PEI microparticles was achieved by a new route via water/organic solvent+PEI. These microparticles due to the formation of hydrogen bonds between PEI's nitrogen and acid's hydrogen in (bio)molecules possess high functionalizing capacities for (bio)molecules. Such obtained CaCO_3 -PEI structures allow any (bio)molecule independently of its type, charge and size to be conjugated onto their surface. These properties make this composite useful as protein carrier in drug delivery, signal increasing tool in biosensor area and even as carrier of fluorescence probes for imaging applications between others fields.

III.1 Introduction

Calcium carbonate is one of the most abundant minerals in nature.¹ Its biocompatibility, biodegradability and industrial application as filler in paints, plastics, ceramics, rubbers, and papers has converted it to one of the most investigated materials.² It has three anhydrous crystalline polymorphs known as calcite, aragonite and vaterite. Thermodynamically, the least stable phase of calcium carbonate is vaterite followed by aragonite and calcite. Calcite is the thermodynamically most stable phase at room temperature and normal atmospheric pressure. Aragonite is a metastable phase stabilized either at temperatures higher than 60 °C or in the presence of ions such as Mg²⁺. Aragonite has been obtained by the transformation of calcite to aragonite at a high-pressure of 6.16 GPa and a temperature of 345 °C. Vaterite is formed in aqueous media under conditions of spontaneous precipitation and high supersaturation. The vaterite phase transforms to the stable calcite phase in the presence of water via a solvent-mediated process. Other forms of the CaCO₃ are its hydrated phases: monohydrocalcite (CaCO₃·H₂O), ikaite (CaCO₃·6H₂O), hydrated amorphous calcium carbonate (HACC) and amorphous calcium carbonate (ACC). ACC is formed as a solid phase which then undergoes rearrangement to one of the crystalline phases of calcium carbonate (calcite, aragonite and vaterite).^{1,2}

Vaterite is rarely found in either biological or non biological systems, but it exists in some biological tissues (e.g., the shell or nacre of mussels, abalones and eggs or the exoskeleton of algae and sea urchin spines) and some sediments. In laboratories, vaterite (or aragonite) is frequently prepared in the presence of specific additives. Its stabilization in water still remains a challenging issue in biomineralization studies,³ not only because of its rareness, but also because it is expected to have a potential role in biomedical and industrial applications. Vaterite exhibits unique properties such as high surface area, high solubility, high dispersion, and a smaller specific gravity compared with the other two crystalline phases.⁴ In addition, the high loading capacity, low price, easy preparation, and mild decomposition conditions stimulate the utilization of the CaCO₃ cores for template-assisted synthesis to produce biologically active polymeric capsules.⁵ The porous CaCO₃ microspheres can be an effective host for the fabrication of biocompatible composite materials for drug delivery and protein encapsulation.^{4, 6} Moreover CaCO₃ composite has been already shown to be with interest in biosensing area.⁷

The difficulty to use CaCO_3 lies in the difficulty to control its polymorphic character.⁸ Many approaches such as the use of double hydrophilic block copolymers,^{8,9} natural and synthetic hard templates,^{2,10} Langmuir monolayers,¹¹ peptoids¹² and synthetic and natural polymers^{7d,13} have been widely chosen to control the polymorphs and morphology of CaCO_3 . Although all these crystallizations have been carried out in aqueous media, crystallization in a mixed solvent system using organic additives is emerging and has been found to be a new way toward hierarchical superstructures.^{1,14}

Herein a novel route for synthesis of vaterite structures has been described. The new procedure integrates sonication process, PEI as CGM and the mixed water/organic solvent in a unique system able to provide a complete polymorphic discrimination along with a controlled and homogeneous particle size distribution. In order to arrive to the final system three blocks of experiments have been firstly studied. In the first block of assays simple mixing reactions between water dissolutions of CaCl_2 and Na_2CO_3 under sonication using different volumes and reaction times have been studied. These syntheses performed under long sonication time yielded vaterite microspheres and calcite rhombohedra. In a second series of assays the effect of different PEI concentrations onto the CaCO_3 product was evaluated. Reduction in the reagents volumes and increasing of PEI concentration decreased and homogenized the microsphere size. PEI present in the system increased the vaterite fraction in the product composition and provided a high vaterite stabilizing effect up to 8 months. To the best of our knowledge there are few reports in CaCO_3 crystallization using PEI as CGM.¹⁵ However some works report the use of PEI in CaCO_3 mineralization medium only as capturing protons because it is a basic polymer that has branched structure with a distribution of primary, secondary and tertiary amine groups in the ratio 1:2:1.¹⁶

Generally the role of CGM remains related to acid molecules and ionic surfactants such as polyacrylic acid (PAA),^{10a,17} polystyrene sulfonate (PSS),¹⁸ dihexadecyl phosphate (DHP),¹⁹ sodium dodecyl sulfate (SDS),²⁰ polystyrene-alt-maleic acid (PSMA)²¹ and cetyltrimethylammomium bromide (CTAB),^{20b,21,22} that are the most common CGMs used in the CaCO_3 crystallization. In addition, there are only few reports on ultrasonic agitation used in the CaCO_3 crystallization.²³ Here for the first time the reported ability of ultrasonic process to sequester CO_2 is related with the apparition of $\text{HCO}_3^-/\text{CO}_3^{2-}$ nucleation center to enhance vaterite ratio.

In the third group of syntheses the use of equal volumes of water/organic solvent mixture under ultrasonic conditions with or without PEI as CGM has permitted an

effective phase control of CaCO_3 mineralization process. The synergistic effect between mixed solvents and PEI permits a completely vaterite phase discrimination with homogeneous and controlled microparticles size.

Many routes of biofunctionalizing for CaCO_3 vaterite microparticles have been described. For example physical adsorption- adsorption of molecules from the solutions onto preformed CaCO_3 microparticles; coprecipitation- molecules capture by CaCO_3 microparticles in the process of precipitation;^{3b, 6c} decomposable template for loading polyelectrolytes for microcapsule fabrication;^{6b,24} phase transition²⁵ and others. Herein we use a chemical adsorption of molecules onto the CaCO_3 particles using for first time PEI as chemical mediator for molecular immobilization. The PEI's use has the advantage that allows a high capacity of immobilizing for a large variety of molecules onto CaCO_3 microparticles surface with good stability. The microparticles synthesized using PEI that have presented a high efficient loading capacity for dyes and biomolecules, independently of their charges and sizes, could be useful for multiples applications such as signal amplification in biosensing. The high functionalizing capacity of CaCO_3 microparticles and the versatility of molecules that can be immobilized onto its surface are associated with the formation of hydrogen bonds between the acids hydrogens of the conjugated molecule and the PEI's nitrogens.

III.2 Experimental part

III.2.1 Chemicals

All chemical reagents (analytical grade) were purchased from Sigma Aldrich and used as received. A PEI solution 50 % (w/v) in H_2O ($M_w=750000$, $M_n=60000$) was used. Milli-Q water (resistivity 18.2 $\Omega\cdot\text{cm}$ at 25 °C) was obtained from Advantage Milli-Q apparatus (Millipore). All glass material were soaked with aqua regia for 3h, rinsed with distilled water and dried before use.

III.2.2 Characterization techniques

The syntheses were carried out using an Ultrasons J. P. Selecta ultrasonic bath. SEM images were taken with a ZEISS Merlin scanning electron microscope. A water dispersion of samples was coated on glass support and dried at room temperature. Colloidal silver solution was deposited on the edges of the glass for the sample examination. SEM images with high resolution were recorded depositing the samples on silica support and sputtering gold during 1min.

XRD patterns of CaCO_3 were recorded using a Siemens D-5000 X-ray diffractometer with Cu $K\alpha$ radiation, 2θ range from 10 to 70° at 40 kV and 40 mA. The phase identification was done by comparing the XRD patterns of the crystals with the standard data available from Joint Committee on Powder Diffraction Standards. Calculus of vaterite fraction from XRD pattern was carried out using two methods: the Kawaguchi equation³³ and the Chung equation.³⁴ Scherrer equation based on the broadening diffraction peaks and the diffraction angle by crystallographic planes of the vaterite XRD pattern was used to calculate the size of nanostructures in vaterite microparticles. FTIR measurements were performed on an IR-200 spectrometer (ThermoNicolet) using KBr pellets. KBr was previously dried overnight at 110°C . KBr (40 mg) were mixed with the sample (3 mg) for quantitative infrared measurements. Quantitative analysis of CaCO_3 phase using IR spectra was carried out based on vaterite absorptivity previously reported.³⁵

Zeta potential of aqueous dispersion of CaCO_3 was measured using a Malvern Zetasizer Nanoseries at room temperature. The pH of the used Milli-Q water was between 6 and 7.

Confocal laser scanning microscopy (CLSM) images were captured with a LEICA SP5 confocal scanning system equipped with a 63x/1.4 oil immersion objective. (Bio)molecules immobilized onto the CaCO_3 surface were observed by using fluorescein isothiocyanate (FITC) label. Absorption measurements were made on a SpectraMax M2 spectrophotometer.

III.2.3 Synthesis

CaCO_3 crystallization was studied for three blocks of experiments. In a general procedure of synthesis (first block of experiments) equal volumes ratio of aqueous dissolutions of CaCl_2 (0.33 M) and Na_2CO_3 (0.33 M) were quickly mixed under sonication at room temperature. After this, the reaction vessel was covered with parafilm. CaCO_3 precipitates were washed three times, air dried and collected. The type of agitation (magnetic or ultrasonic), the reagent volume (from 5 to 0.5 mL) and the sonication time (from 15 to 60 min) were modified. Typical reactions of the second block of experiments were assayed with PEI in the system, using 45 min of sonication time and 5 mL of each reagent volume. Aqueous dissolutions of PEI (0.1, 0.4, 2 and 4 mg/mL in 5 mL) with CaCl_2 (0.33 M) were mixed with Na_2CO_3 (0.33 M). Finally in the third block of experiments, CaCl_2 (0.33 M) in equal volumes of mixed solvents (5 mL)

without or using PEI (4 or 8 mg/mL) were mixed with Na_2CO_3 (0.33 M, 5 mL). The mixtures in equal volumes of tested solvents were water/EtOH(ethanol), water/EtOAc (ethylacetate), water/DMSO (dimethylsulfoxide) and water/DMF (N,N-dimethylformamide).

III.2.4 Conjugation

CaCO_3 (10 mg) obtained with and without PEI were incubated with a known quantity of biomolecules or dyes under shaking conditions during 45 min. Bovine serum albumin isothiocyanate (BSA-FITC), human IgG isothiocyanate (HIgG-FITC), anti-Human IgG-peroxidase (HIgG-Per) produced in goat, tyrosinase from mushroom (Tyr), methylene blue (MB), bromocresol green (BG), methyl orange (MO), methyl red (MR), rhodamine B (R) and fluorescein (F) were tested. The estimation of the quantity of (bio)molecules immobilized onto the CaCO_3 surface was made by difference between the concentration of the initial molecule solution and the concentration of the appropriate supernatants obtained after centrifugation of the suspension for each washed sample. The concentration in each washed sample was calculated by interpolation of absorbance intensity in the calibration curve for the (bio)molecule solution.

III.3 Results and Discussion

III.3.1 Synthesis and characterization

When the CaCO_3 synthesis was carried out using 5mL of reagents (CaCl_2 and Na_2CO_3) volume during 15 to 45 min of magnetic agitation almost only calcite rhombohedra appeared in the crystallization product. However when this reaction was taken place under ultrasonic mixing during the same times a mixture of typical rhombohedra calcite crystals and vaterite microspheres was obtained. The calcite precipitate was found in three different morphologies: the standard rhombohedra, intergrown rhombohedra and layered rhombohedra (see Figure _S1 in Supporting Information section). **Figure 1** shows the effect of reagents volume and sonication time upon the microspheres size. The reduction in the reagent volume from 5 to 1 mL produces a decreasing in the microspheres average size for the studied reaction times. For example, when 5 mL of CaCl_2 and Na_2CO_3 solutions are mixed during the syntheses for 45 min the particle size was 2.1 ± 0.3 mm and this value decreased to 1.1 ± 0.15 mm when the used reagent volumes were decreased to 1 mL, with the relative errors of around 14%. In addition, variations in the sonication times from 15-60 min did not significantly affect the

microspheres size. The reason why there is no significant effect on size under different reaction times is due to the fact that the system has a fast precipitation reaction rate and the nucleation and growth occur completely within 15 min.

On the other hand, while microspheres morphology is affected by the reduction of the reagents volume no morphological change was found by increasing the reaction times using the same reagents volume (results not shown). The reduction of the reagents volume from 5 to 1 mL produces a microspheres surface with more density of nanostructures. The increasing of the density of nanostructures on microspheres surface is correlated with the diminution of microparticles and nanostructures size when the reagents volume is reduced from 5 to 1 mL.

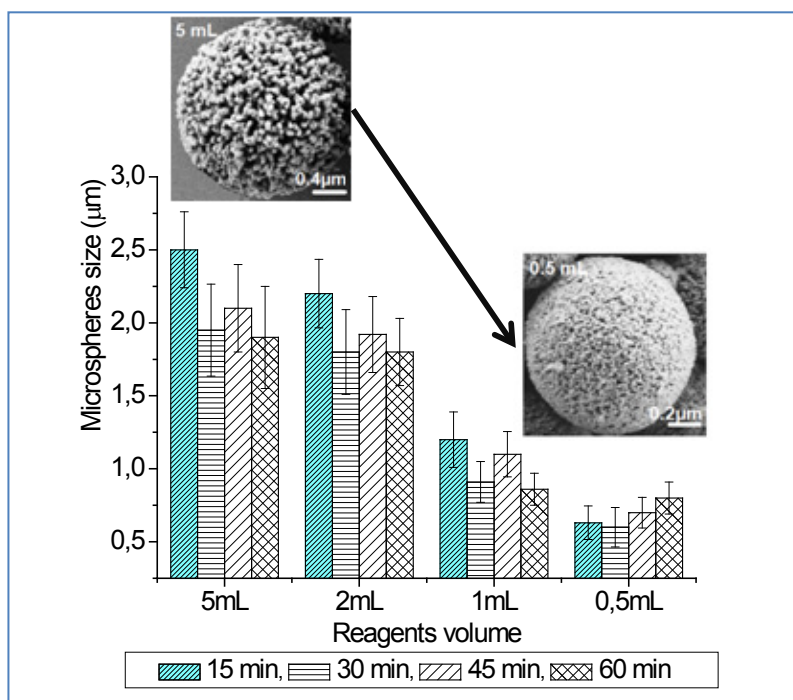


Figure 1. Effect of the reagents (CaCl_2 and Na_2CO_3) volume and the sonication time upon the vaterite microspheres size without PEI in the system. The inserted SEM images belong to 5 and 0.5 mL of reagents volumes under 45 min of ultrasonic stirring. Other experimental conditions as described in the text.

In this way, the vaterite microspheres synthesized with 5 mL of reagents volume are made of nanoparticles with a ranging size of 28-32 nm and a highly porous surface can be observed. However microspheres synthesized by using reagents volumes equal or smaller than 1 mL are made of nanoparticles with size of around 17-20 nm and show a surface with a higher density of nanostructures ('tentacle' like structures, see inset zooms a1, b1, of **figure 2**) that ensure a major superficial area.

It is important to highlight that the reduction of the volume from 5 to 2 mL is accompanied by doubling of vaterite fraction (from 35 to 70% approximately) and that the obtained nanostructured microparticles were stable enough even up to 6 months since their preparation (see SEM image of figure 2c).

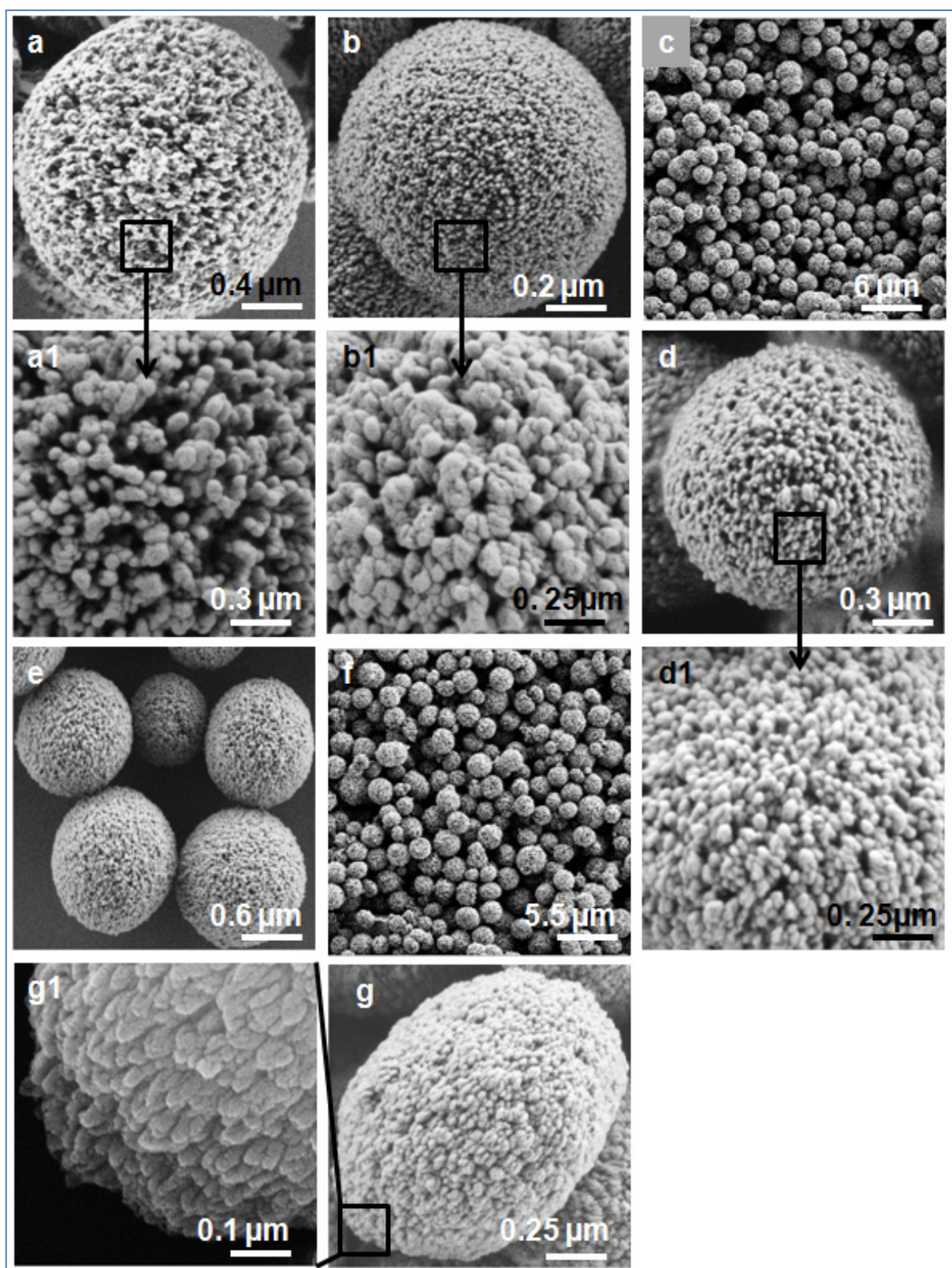


Figure 2. (a-c) SEM images of vaterite microspheres synthesized without PEI. (a) 5 mL of the reagents (CaCl_2 and Na_2CO_3) volume and 45min of the reaction time, (b) 1 mL of the reagents volume and 45 min of the reaction time and (c) 5 mL of the reagents volume and 45min of the reaction time with the image obtained 6 months after the synthesis. (d-f) SEM images of vaterite microspheres synthesized with PEI using 5 mL of the reagents volume and 45 min of the reaction time. (d) 2 mg/mL of PEI, (e) 2 mg/mL of

PEI and (f) 0.44 mg/mL of PEI with the image obtained 8 months after the synthesis. (g) SEM images of the vaterite ellipsoid synthesized via water/EtOH+8mg/mL PEI. a1, b1 d1 and g1 are amplifications of their corresponding SEM images in the selected zones, which confirmed that the microspheres are made of nanoparticles. Other experimental conditions as described in the text.

Several experiments were carried out with different CGMs such as, Tween-20, TritonX-100, CTAB and PEI using 5 mL of the reagent volume and 45 min of sonication time (results not shown). Better results in relation to the obtaining of nanostructured vaterite particles were found working with PEI. Figure 3, a and b shows respectively the XRD patterns and IR spectra of CaCO₃ synthesized in presence of different PEI concentrations. In a rapid view we can see that, the intensity of vaterite XRD peaks (see **figure 3a**) at 21.0, 24.9, 27.1, 32.8, 44.0, 49.1, 50.1 and 55.8° increase on increasing the PEI concentration in the reaction medium. Accordingly the vaterite IR band (see Figure 3b) at 745 cm⁻¹ increases while calcite band at 712 cm⁻¹ decreases with the increase of PEI concentration. The vaterite fraction in the product increases from 36 to 72 % while the PEI concentration increases from 0 to 4 mg/mL. Moreover the vaterite microspheres size decreases from 2.0 ± 0.3 to 1.32 ± 0.16 μm with the increasing of the PEI concentration from 0 to 4 mg/mL. The effect of the distribution of the equal quantity of PEI between CaCl₂ and Na₂CO₃ dissolutions and the reduction of the reagent volume brings additional increase in the vaterite fraction and the microspheres size. In consequence an 86% in vaterite composition and 0.83 ± 0.16 μm in spheres size with nanoparticles of around 17-22 nm were reached. Table_S1 in SI shows a summary of these results related to the effect of PEI upon microsphere size and vaterite fraction.

The surface of vaterite microspheres synthesized in presence of PEI is smoother than vaterite surface obtained without PEI (see figure 2 d1). In the figure 2d the polymer layer recovering the CaCO₃ structure is displayed. In the IR spectrum realized on CaCO₃ produced via PEI (figure_S2), the bands at 3480-3440 cm⁻¹ corresponding to the vibration frequency N-H of the primary and secondary amino groups and the bands at 2970, 2930 and 2850 cm⁻¹ belong to the vibration frequency C-H of the CH₂ and CH₃ groups in PEI polymer, which indicate the PEI presence onto microspheres surface. These microspheres presented higher stability, which is attributed to the polymer layer that recovered it. The SEM image in figure 2f shows vaterite microspheres after 8 months of their synthesis in presence of 0.44 mg/mL of the PEI. It is necessary to highlight that the increasing in the PEI content has the same effect on the microspheres size and vaterite fraction as the reduction of the volume in the assays without PEI.

However by using PEI more quantity of CaCO_3 in comparison to the volume reduction can be achieved.

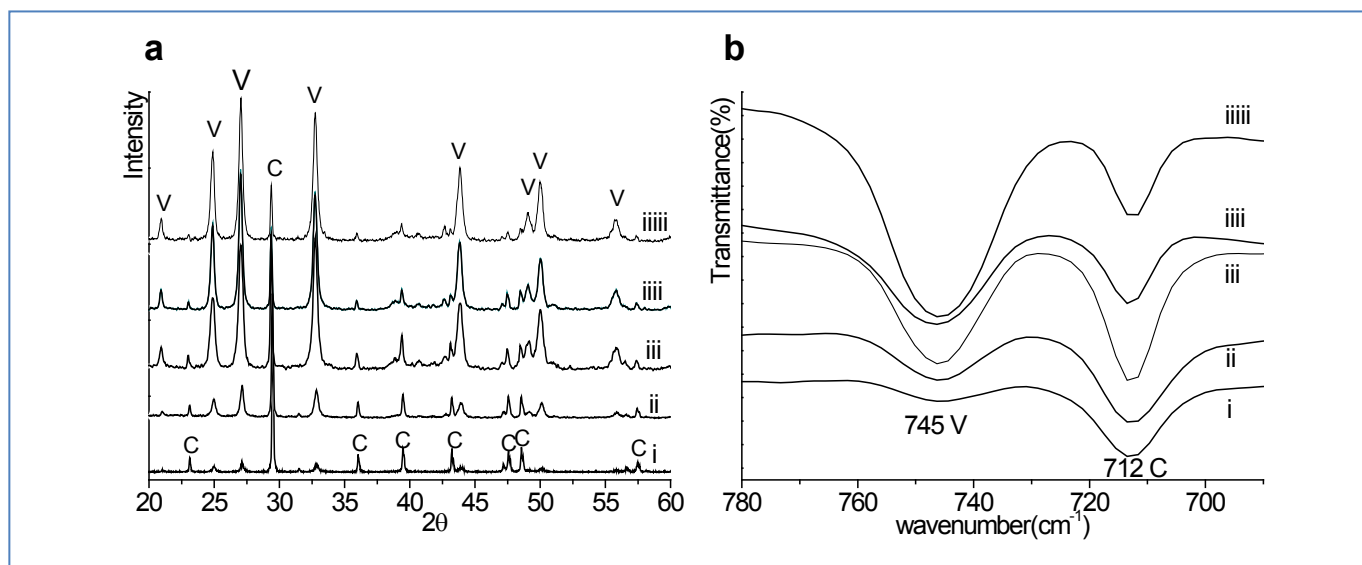


Figure 3. a and b. (Figure 3a, i-iiii) XRD patterns corresponding to the CaCO_3 obtained with different PEI concentrations and using 5 mL of the reagents volume and 45 min of the sonication time: (i) 0 mg/mL of PEI, (ii) 0.44 mg/mL of PEI in the initial CaCl_2 dissolution, (iii) 2 mg/mL of PEI in the initial CaCl_2 dissolution, (iiii) 4 mg/mL of PEI divided in 2mg/mL for each initial CaCl_2 and Na_2CO_3 dissolutions; (Figure 3a, iiiii) XRD patterns corresponding to the CaCO_3 product obtained with 4 mg/mL of PEI divided in 2 mg/mL for each initial CaCl_2 and Na_2CO_3 dissolutions and including the reduction of volume to 2 mL. (Figure 3b, i-iiiiii) IR spectra correspond to samples described before in the same nomenclature order. V denotes vaterite and C calcite phase. Other experimental conditions as described in the text.

Figure 4a illustrates SEM images of CaCO_3 obtained using various water/organic solvent mixtures with or without PEI, 5 mL reagents volume and 45 min sonication time. When only mixed water/organic solvents are used during the reaction, the crystallization product is completely calcite rhombohedra (Figure 4a-i) independently of the organic solvent used in the mixture (EtOH, EtOAc, DMSO and DMF). When 4 mg/mL of PEI is added to the CaCl_2 solution, microspheres and/or ellipsoids appear in the product together with rhombohedra crystals (Figure 4a-ii). A second addition of 4 mg/mL of PEI in the Na_2CO_3 solution yielded completely vaterite microspheres or/and microellipsoids in the precipitation product (Figure 4a-iii). These results suggested by SEM analysis were also confirmed by XRD and FTIR measurements.

The XRD patterns observed in figure 4b correspond to CaCO_3 that has been synthesized via water/ EtOH system with or without PEI using 5 mL of reagents volume and 45 min of sonication time. A complete polymorphic discrimination from calcite (Figure 4b-i) to calcite-vaterite (Figure 4b-ii) and vaterite (Figure 4b-iii) can be seen from water/EtOH to

water/EtOH+4mg/mL of PEI and water/EtOH+8mg/mL of PEI. Figure 4c corresponds to infrared spectra of CaCO₃ formed using water/DMSO with or without PEI. When PEI is not present in solution, just the band at 712 cm⁻¹ corresponding to calcite is observed (Figure 4c-i). By using 4 mg/mL of PEI the bands at 712 and 745 cm⁻¹ that belong to calcite and vaterite are respectively observed (Figure 4c-ii). However with 8mg/mL of PEI only the band at 745 cm⁻¹ corresponding to vaterite can be observed (Figure 4c-iii).

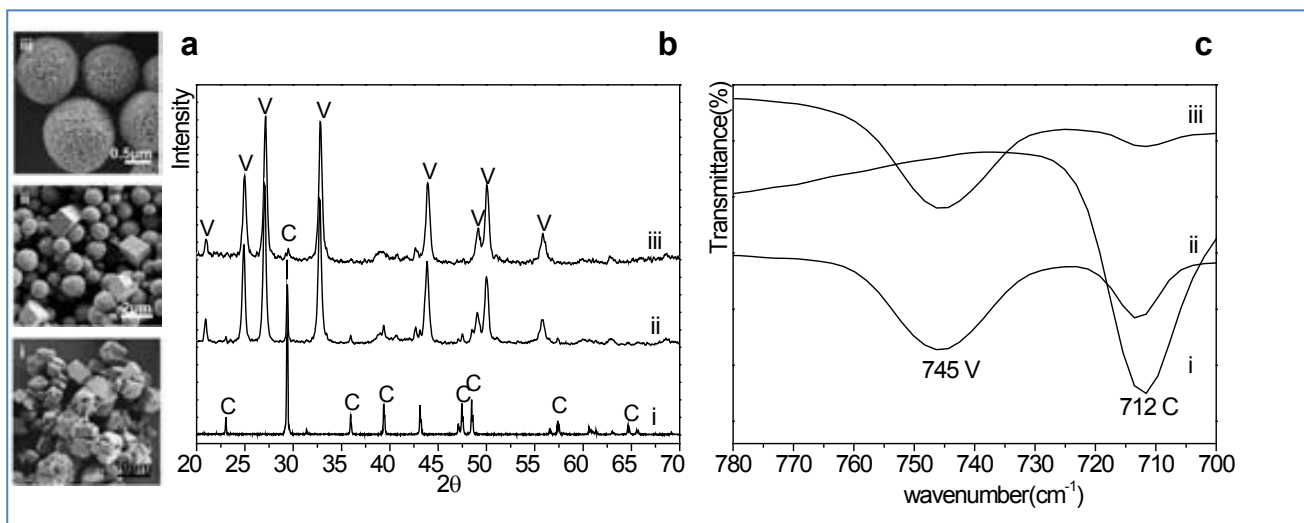


Figure 4. (Figure 4a, i-iii) SEM images of the CaCO₃ obtained from water/organic solvent system with or without PEI under 45 min of sonication and using 5 mL of reagents volume. (i) Calcite rhombohedra obtained from water/DMSO, (ii) Calcite rhombohedra and vaterite spheres obtained by water/EtOH+4mg/mL of PEI, (iii) vaterite spheres obtained by water/Ethylacetate+8mg/mL of PEI. (Figure 4b, i-iii) XRD patterns of CaCO₃ crystals obtained in water/EtOH system without or with PEI: (i) only water/EtOH, (ii) water/EtOH +4mg/mL of PEI, (iii) water/EtOH+8mg/mL of PEI. (Figure 4c, i-iii) IR spectra of the CaCO₃ obtained via water/DMSO system with or without PEI: (i) water/DMSO, (ii) water/DMSO+4mg/mL of PEI, (iii) water/DMSO+8mg/mL of PEI. V denotes vaterite and C calcite phase. Other experimental conditions as described in the text.

The introduction of organic solvent inside the reaction medium for crystallizing vaterite microparticles was determinant to achieve the polymorphic discrimination. In previous experiments discussed here, just using water dissolution of CaCl₂ and Na₂CO₃ with and without PEI a mixture of calcite and vaterite was obtained. However, under the same conditions the introduction of the water/organic solvent mixture without PEI yielded 100 % of calcite phase while the synergetic effect between the mixture of water/organic solvent with 8 mg/mL of PEI yielded almost 100% of vaterite phase. This polymorphic

discrimination doesn't depend on the used organic solvent (i.e. DMSO, EtOH, EtOAc or DMF).

The appearance of spherical or elliptical shapes for vaterite crystals depends on the polarity of the solvent mixture (Figure _S3). When pure water and PEI constituted the reaction medium, the vaterite shapes were spheres. However, when half of the volume of water is substituted by equal volume of DMSO, DMF or EtOH (the polarity of the mixture decreases with respect to pure water) the vaterite particles with spherical shapes almost disappear and ellipsoidal ones get increased. Spherical shapes are observed much more in the case of the reaction with EtOAc due to the fact that the polarity of water remains almost the same due to the immiscibility of these two solvents. Figure 2g displays the SEM image of an ellipsoid shape particle synthesized by using water/EtOH+8mg/mL of PEI (see also the amplified image 2g1) and used later for functionalization purposes. Compact unions of 'tentacle' like nanostructures composed of nanoparticles seem to be part of the microellipsoid particles. More details in relation to water/organic solvent+PEI synthesis can be seen in table _S2 at SI section.

The effect of the reduction of the reagent volume on microparticle synthesis via mixing solvents with PEI was also studied and in disagreement with the previous results presented here, no diminution effect was observed on the average size or the homogeneity of the microparticles. Far from what was expected a mixture of spheres, ellipsoids, bicone, shuttle and few rhombohedra like shapes (see Fig _S4 in SI) as reported before ^{14b} were observed. In all the above mentioned experiments the calcite precipitate was always observed in the morphologies displayed at figure 1 supporting information section.

III.3.2 Possible mechanism of formation of the vaterite microparticles

The transformation from vaterite or aragonite to calcite is thermodynamically favored. The prevalence of kinetic rather than thermodynamic factors permits to see vaterite at sustained supersaturation conditions. The degree of supersaturation that provokes local nucleation centers, and the growth of the crystals are dominant factors in CaCO₃ crystallization. Both are closely related with the Gibb's free energy. ^{8, 13b, 17c, 26} These two factors can convert from ionic growth attributable to thermodynamically stable calcite rhombohedra, to assembly of nanoparticles under a kinetic control of nucleation attributable to usually vaterite spheres. ^{1, 13b, 14a}

The initial experiments for crystallization of CaCO_3 without PEI and using magnetic agitation yielded almost completely calcite phase. When the same experiments were repeated using ultrasonic agitation the amount of vaterite was increased. Y. Mori et al. also found that ultrasonic homogenizer is better than magnetic homogenizer to obtain higher yield in vaterite.²³ The possible explanation could be related to the fact that ultrasonic homogenization is more effective than magnetic homogenization considering that a good homogenization is essential to achieve the growth of vaterite crystals. The effective homogenization with fast convective currents increases the number of impacts between the aggregate particles in the supersaturated nucleation centers favouring their growth to yield vaterite.^{26a} We propose here that ultrasonic process can also increase the nucleation centers of local supersaturation by inducing the CO_2 sequestering from the air-solution interface into the suspension; in addition it can improve the growth of the aggregate particles in the supersaturated nucleation centers. The facility to sequester CO_2 from the gas to the liquid phase by using ultrasonic waves has been previously reported.²⁷ Moreover, in our experimental conditions to stimulate the transference of CO_2 from the gas to liquid phase we use two procedures. In first case Milli-Q water with high electrical resistance ($10^8 \Omega\cdot\text{cm}$, CO_2 free) was used while in second one a closed reaction vessel with atmospheric air inside was employed.²⁸ Therefore, if the solution is in CO_2 free water the transference of CO_2 from the gas to the liquid phase to reestablish the CO_2 equilibrium is necessary to occur. The sonication might induce the CO_2 sequestering at the air-solution interface through the creation of a pressure difference between the layer closer to the interface and the layers immediately in the upper part. The superficial energy near to the surface is decreased and to reestablish the original equilibrium the superior layer of the air descends very close to the surface until making possible the CO_2 dissolution. The dissolved CO_2 is hydrated to produce H_2CO_3 which yields HCO_3^- and CO_3^{2-} (the pH decreasing by H_2CO_3 formation via CO_2 sequestering is illustrated in figure_S5). In this way a superficial supersaturation of $\text{HCO}_3^-/\text{CO}_3^{2-}$ allows the creation of additional supersaturated nucleation centers by kinetic control and the apparition of the vaterite phase.

Y. Mori et al.²³ found that the reduction in the reagents volume increases the vaterite fraction and they related it with a better homogenizing and consequently with the growth of the aggregated particles in the supersaturated nucleation centers. The decreasing in the reagent volume presented in this work yields the diminution of microspheres size and the increasing in vaterite fraction too. This result is more

consistent with the increasing nucleation by CO₂ sequestering rather than to the increasing growth of the aggregated particles in the supersaturated nucleation centers. The diminution of the reagent volume enhances the homogenizer effect due to the acceleration in convection currents provoked by the sonication process inside the suspension. In consequence the supersaturated HCO₃⁻/CO₃²⁻ nucleation centers at the surface of the suspension can migrate faster to the interior of the bulk. This allows new CO₂ molecules to be captured by the suspension during the sonication process and consequently a faster and homogeneous nucleation process by local supersaturation takes place (see scheme of the mechanism in **figure 5a**).

The addition of PEI to the system facilitates the formation of two different supersaturated nucleation centers, one of HCO₃⁻/CO₃²⁻ (provided by Na₂CO₃ reagent) due to its binding with the cationic protonated amino groups in the PEI,¹⁵ and the other one of Ca²⁺ (provided by CaCl₂ reagent) by its binding with nucleophilic nitrogens of the amino group in the PEI polymer. This creates HCO₃⁻/CO₃²⁻ and Ca²⁺ supersaturated centers onto the PEI structure able to initiate nucleation with the subsequent controlled growth by self-assembling of small primary nanoparticles into highly organized vaterite crystals. Moreover, PEI can bind the H⁺ of the HCO₃⁻/H₂CO₃ species formed during the hydration of the sequestered CO₂ favouring the CO₃²⁻ migration from the liquid surface into the bulk suspension and the creation of CO₃²⁻ supersaturated centers onto the polymer's chain. In this way, the increasing of PEI concentration provokes more Ca²⁺ and CO₃²⁻ supersaturated nucleation centers on coils of the PEI, therefore large vaterite formation (see scheme of the mechanism in figure 5b). All this is consistent with the increasing in vaterite fraction and diminution in microspheres size when the PEI concentration is increased (see table_S1). The solvent mixture changes the polymer's solution properties. The addition of EtOH, DMF or DMSO to the system decreases the polarity of water and in consequence decreases the hydrogen bonds interaction between dissolved PEI and mixed solvent in comparison with previous hydrogen bonds interaction between dissolved PEI and water. This effect of weakening of the interaction between the solvent and PEI favours the bond between Ca²⁺ or HCO₃⁻/CO₃²⁻ ions and PEI, which increases the nucleation centers and the tendency of supersaturation and the kinetic precipitation of vaterite phase.

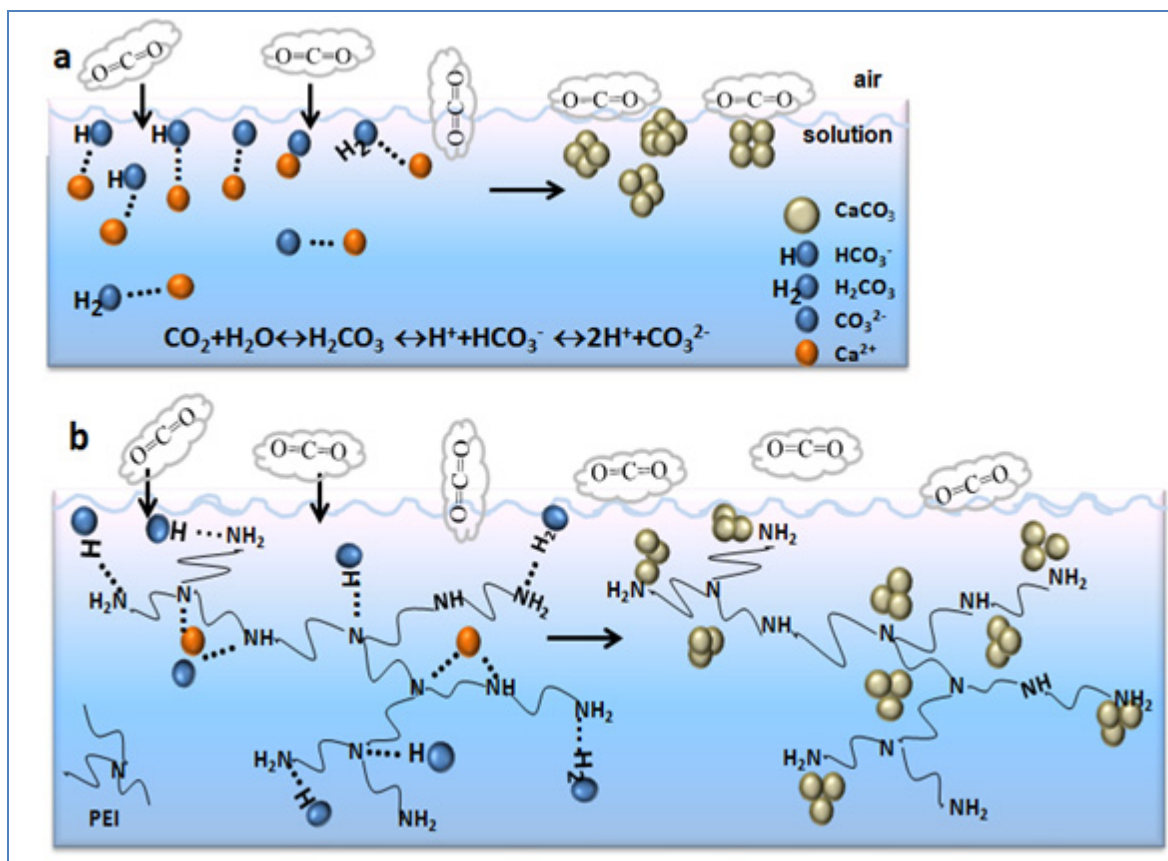


Figure 5. Schematic representation not in scale of the possible crystallization mechanisms. (a) HCO₃²⁻/CO₃²⁻ supersaturated nucleation centers by CO₂ sequester. (b) HCO₃²⁻/CO₃²⁻ and Ca²⁺ supersaturated nucleation centers by interaction with the PEI polymer.

III.3.3 Z-potential studies

Z-potential measurements indicate that microparticles obtained without PEI have negative z-potential values; however microparticles synthesized with PEI in the reaction medium yield positive values of z-potentials and positive superficial charges. These positive z-potential values augment by increasing PEI concentration in the reaction medium (see **figure 6**). The positive superficial charge is provoked by basic character of PEI able to bind the nitrogen of its amino groups with the protons present in the water and consequently to create a positive density charge. In the same way, the conductivity of microparticles increases from 0.04 to 0.08 mS/cm once PEI is present onto their surface. Such an enhancement in the z-potential and the conductivity of the vaterite microparticles obtained via PEI, could be with interest for electrochemical biosensor application where an improvement of the charge transference through the CaCO₃-PEI composite may be expected.

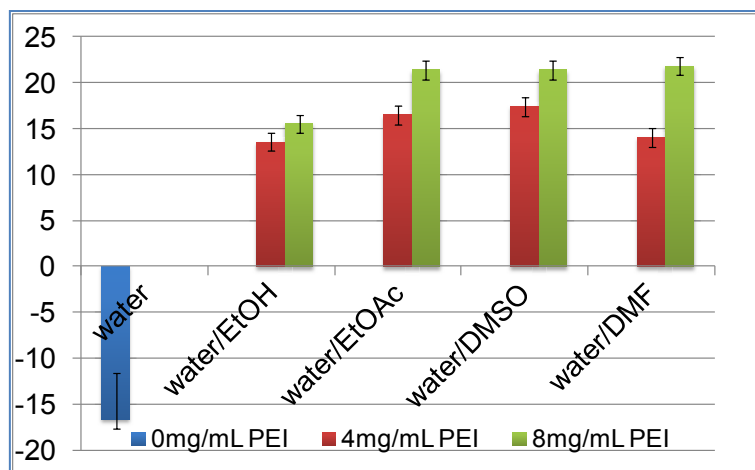


Figure 6. Z-potential values (mV) of vaterite microparticles obtained via water/organic solvent + PEI reactions. Other experimental conditions as described in the text.

III.3.4 Conjugation studies

Several (bio)molecules were tested for their possible conjugation with vaterite microparticles synthesized with and without the PEI presence. A good loading capability was found for functionalization process using biomolecules (see table_S3 in supporting information). These results are similar to those obtained during immobilization of similar biomolecules onto polymer microcapsules obtained by CaCO_3 template assisted method.^{6c, 24, 29} CLSM images of vaterite microparticles conjugated with FITC as a fluorescence label demonstrated that a good functionalization was performed and the original shape of the microparticles remains stable after immobilization process (**figure 7 a and b**). It is important to note that microspheres synthesized without PEI presence can not be conjugated with these (bio)molecules.

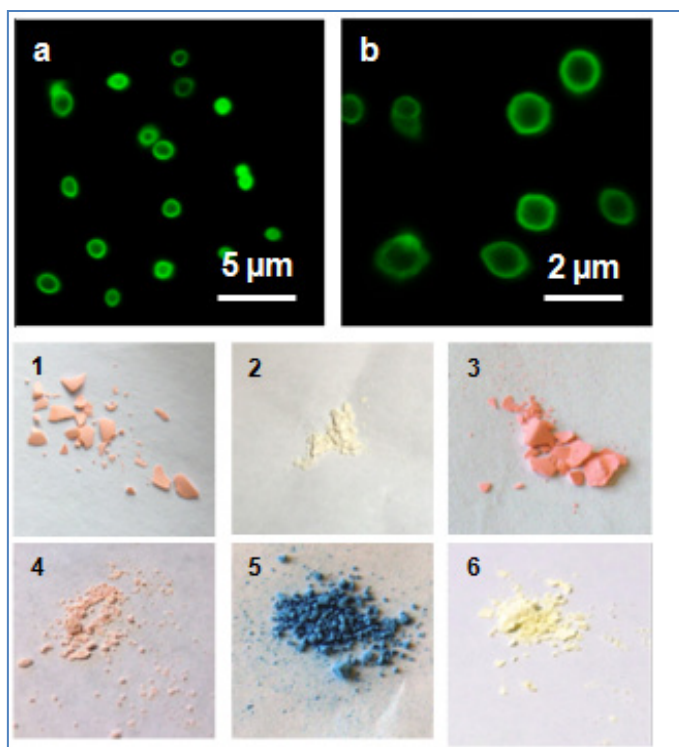


Figure 7. CLSM images corresponding to CaCO_3 -BSA-FITC (a) and CaCO_3 -HIgG-FITC (b). (1-6) Photos of the CaCO_3 precipitated by using water/EtOH+8mg/mL PEI and conjugated with (1) HIgG-FITC, (2) anti-HIgG-Per, (3) BSA-FITC, (4) Fluorescein, (5) Bromocresol Green and (6) Methyl Orange. Other experimental conditions as described in the text.

It suggests that the presence of PEI on the microspheres surface makes possible the conjugation due to its high affinity toward the H^+ proton of the OH groups in the (bio)molecules resulting in hydrogen bonds between the nitrogen of the PEI amino groups and hydrogen of the OH group in the conjugated (bio)molecule (see figure 8). For the same reason, molecules without OH groups as methylene blue and methyl red can not be conjugated with CaCO_3 /PEI microparticles. Based on these results we can conclude that any protein could be conjugated onto CaCO_3 /PEI composite surface because of the presence of OH in the carboxylic groups of their amino acids. Even some amino acids could be more favoured in the CaCO_3 /PEI conjugation due to the presence of two carboxylic groups or SH group. In a similar way any carbohydrates, any nucleotic sequence through the OH groups in their sugars units (ribose or deoxyribose), any type of molecule with acid hydrogens (OH, SH, NH) or any type of molecule with electrophilic atoms like the transition metals could be easily conjugated with CaCO_3 /PEI.

Table_S3 in SI shows the estimated values of the immobilized biomolecules onto the microspheres. A significantly high level of proteins onto the CaCO_3/PEI surface even when both species possess the same sign of charge can be observed. The conjugation is visible also when uncharged molecules as bromocresol, methyl orange and fluorescein are exposed to CaCO_3/PEI . In fact, the conjugation results indicate that (bio)molecules immobilizing is dominated by hydrogen bonds rather than electrostatic interaction. This is because at pH of the particle suspension (pH between 6 and 7) although an IgG-FITC³⁰ and anti-human IgG-Per^{29b} are positively charged the conjugation took place. In the case of negatively charged BSA-FITC^{24, 31} and tyrosinase³² the immobilization is also favored by the electrostatic forces in addition to the hydrogen bonds. In agreement with this, the highest value of molecule conjugated onto CaCO_3/PEI surface corresponded to tyrosinase enzyme.

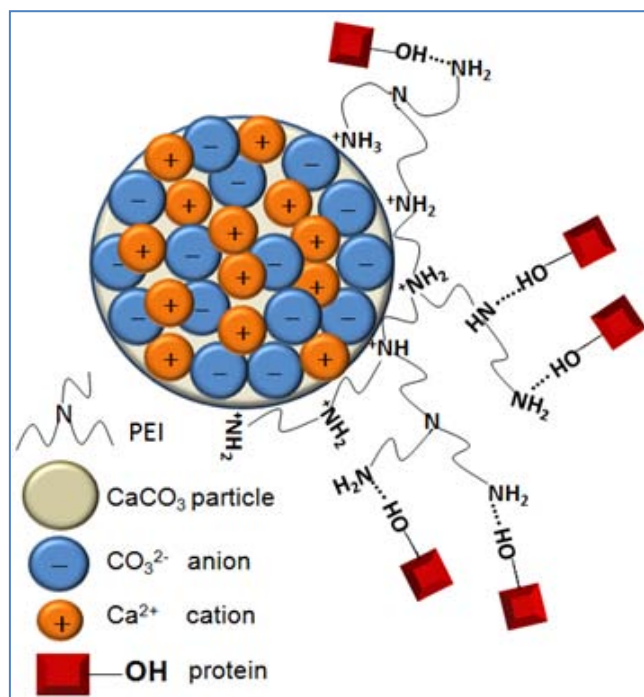


Figure 8. Schematic representation not in scale of the interactions between PEI polymer with the CaCO_3 microparticle surface and the conjugated protein.

These results demonstrated that vaterite microparticles synthesized via water/organic solvent with PEI can be loaded with a large variety of (bio)molecules. This conjugation capacity may provide them with a high capability for multiple applications. These nanostructured CaCO_3 microparticles can be loaded with signal tagging molecules (i. e. enzymes, dyes, etc.) or analyte receptor molecules (i.e. antibodies, DNA, etc.) as

interesting platform to enhance the sensitivity of the enzymatic biosensors, immunosensors or DNA sensors. In addition these microparticles can be used in drug delivery or as carrier fluorescent probes for bioimaging applications between others.

III.3.5 Electrochemical applications of CaCO₃-PEI microparticles

The results of conjugation studies and the z-potential measurements presented here suggest that the CaCO₃-PEI microparticles synthesized via water/EtOH+8mg/mL PEI can be useful in the biosensing fields to increase the sensibility of the device as carrier of the analyte recognition molecule or signal producer molecule or to enhance the charge transference in electrochemical sensors. Considering this issue two electrochemical biosensors were developed and the results presented in the submitted manuscripts titled “A simple phenol sensing and removing system using a nanostructured platform” and “Nanostructured CaCO₃-PEI microparticles for phenol sensing in fluidic microsystem” (see annex III).

The first biosensor detects very low phenol concentrations (LoD of 4.64 nM) by using chrono-impedimetric measurements in a microfluidic chip platform made of polydimethylsiloxane-glass. Integrated screen printing carbon electrodes modified with nanostructured CaCO₃-PEI microparticles and tyrosinase through cross linking with glutaraldehyde was integrated to the micro fluidic platform. In addition the same system includes a phenol removing piece that contains 5 mg of CaCO₃-PEI nanostructured particles. This integrated microfluidic chip is shown to be effective in “on line” phenol sensing and removal actuation. While in the second work the phenol biosensing is also achieved through the PDMS/glass fluidic platform with integrated screen-printed-electrodes (SPE) modified with CaCO₃-PEI MPs and tyrosinase but using amperometric measurements in batch monitoring.

III.4 Conclusions

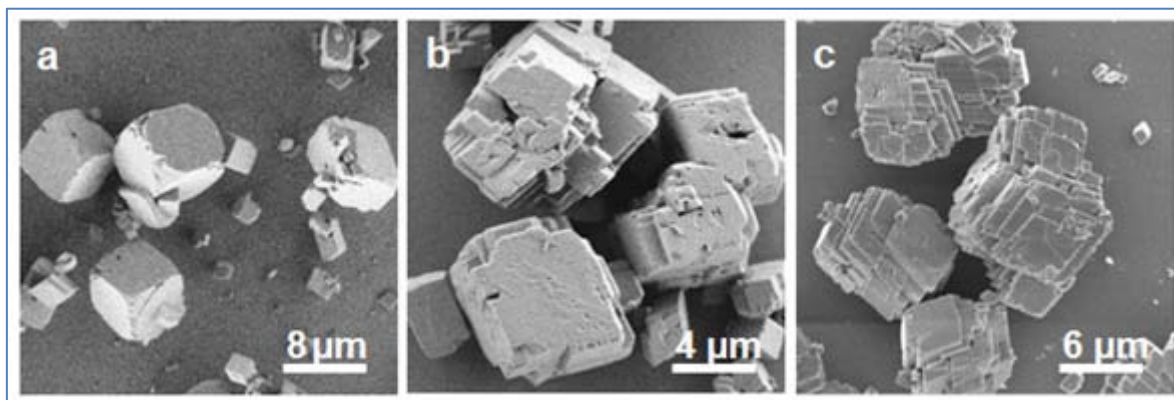
A new route of synthesis for nanostructured vaterite microparticles with high biofunctionalizing capacity using a water/organic solvent mixture with PEI under sonication mixing conditions has been achieved. In order to optimize the final process, syntheses based on simple sonication mixing of CaCl₂ and Na₂CO₃ in water with or without PEI as CGM have been studied. Independently from the presence of PEI in the system a mixture of calcite rhombohedra and vaterite microspheres has been achieved in water as reaction medium and sonication mixing. As observed the reduction of the

reagents volumes decreases and homogenizes the microsphere mean sizes for water systems. The addition of increasing PEI contents in the reaction system also reduces the microsphere size and its dispersion, permitting microparticles with controlled size. Moreover increasing PEI concentration improves the vaterite fraction in the reaction product. In the final synthesis via water/organic solvents mixing with or without PEI (water/EtOH, water/EtOAc, water/DMF or water/DMSO) a completely polymorphic discrimination between calcite and vaterite was also achieved. The synergistic effect between 8 mg/mL of PEI and water/organic solvents yielded around 100% of vaterite polymorph. On the other side 100% of calcite was obtained with only water/organic solvents system.

The presence of PEI layer covering the vaterite microparticle surface has been verified by SEM and infrared spectroscopy. This PEI layer plays multiple roles. First, it gives to vaterite a stabilizing effect already checked up to 8 months. Second, it provides to the microparticles surface more smoothness. Third, it offers additional chemical activity for further modifications with functional molecules. Fourth, it provides high superficial charge to use these nanostructured microparticles in electrochemical sensors.

The vaterite microellipsoids, synthesized via an environmental friendly route (water/EtOH+PEI), were conjugated with various (bio)molecules (i.e. enzymes, antibodies and small organic molecules) independently of their charges and sizes. The wide range of molecules that can be conjugated and the high amount and stability of immobilized molecules are associated with the formation of hydrogen bonds between the PEI's nitrogens and the acid hydrogens in the conjugated molecule. This functionalized CaCO_3 -PEI material is suitable for several applications such as the design and fabrication of biosensing devices due to its use as signal increasing tool or as receptor and biorecognition element for the rapid detection of analytes in a variety of matrixes. Other applications such as bioencapsulation useful for drug delivery, imaging purposes (as carrier of fluorescent label) or as an alternative for water treatment beside other applications can also be previewed.

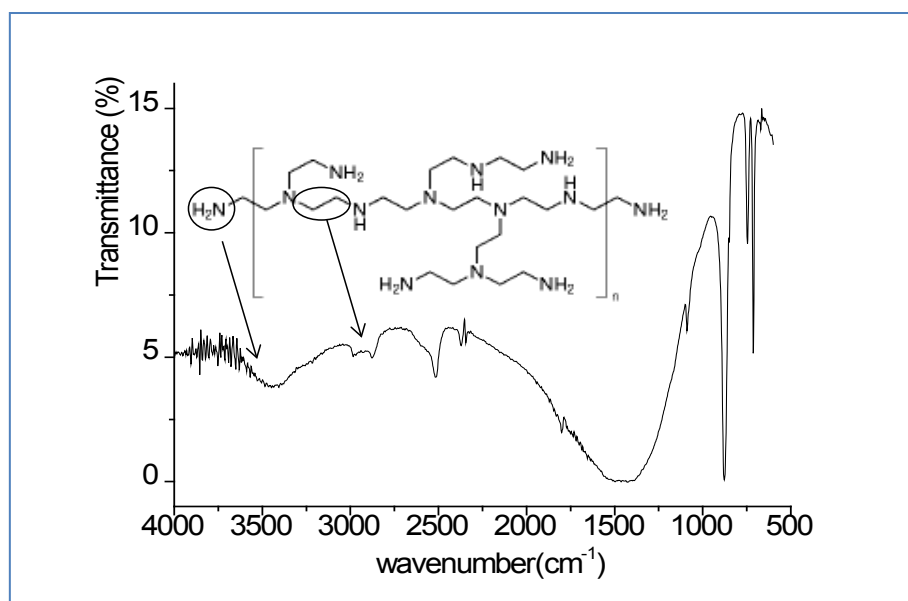
III.5 Supporting Information



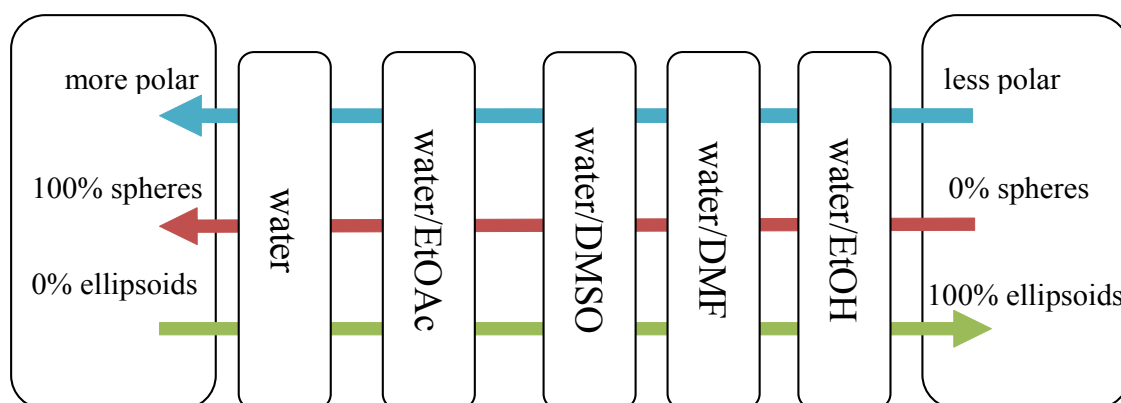
Figure_S1. SEM images of three different shape CaCO_3 in rhombohedra crystal phase recorded in all groups of assays: (a) standard rhombohedra, (b) intergrown rhombohedra and (c) layered rhombohedra. Other experimental conditions as described in the main text.

Table_S1. Variation of microspheres size and vaterite fraction by changing the PEI concentration in the initial CaCl_2 dissolution while using 5 mL of the reagents (CaCl_2 and Na_2CO_3) volume and 45 min of the sonication time. [a] Reaction with 4 mg/mL of PEI divided in 2 mg/mL in each CaCl_2 and Na_2CO_3 initial dissolutions. [b] 4 mg/mL of PEI divided in 2 mg/mL for each initial CaCl_2 and Na_2CO_3 dissolutions and including the reduction of volume to 2 mL.

PEI [mg/mL]	0	0.44	2	4	4 [a]	4[b]
microspheres size [μm]	2.0 ± 0.30	1.8 ± 0.25	1.3 ± 0.13	1.32 ± 0.16	1.13 ± 0.11	0.83 ± 0.16
vaterite fraction [%]	36	55	64	72	75	86



Figure_S2. IR-FTIR spectrum of CaCO_3 product using 4mg/mL of PEI, 5mL of reagents volume and 45min of ultrasonic agitation. Other experimental conditions as described in the main text.

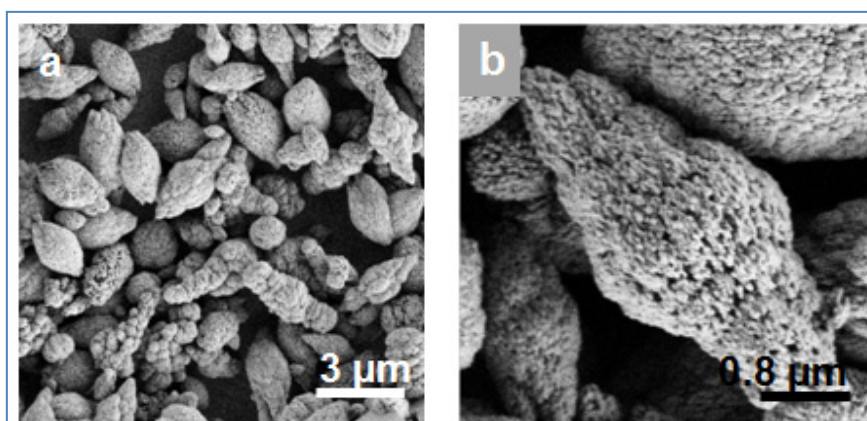


Figure_S3. Effect of the polarity of the mixture water/organic solvent on the particle shape when 8mg/mL of PEI is used.

Table_S2. Summary of the results achieved using water/organic solvents with or without PEI, 5mL of reagents volume and 45min sonication.

	particle shape	vaterite fraction [%]	calcite fraction [%]	microparticles size [μm]
water/EtOAc	r	0	100	-
water/DMSO	r	0	100	-
water/DMF	r	0	100	-
water/EtOH	r	0	100	-
water/EtOAc+4PEI	s >> e and few r	84	16	1.08 ± 0.22
water/DMSO+4PEI	e > s and few r	85	15	1.57 ± 0.21
water/DMF+4PEI	e > s and few r	85	15	1.98 ± 0.28
water/EtOH+4PEI	e >> s and few r	88	12	1.28 ± 0.18
water/EtOAc+8PEI	s >>> e	100	0	1.10 ± 0.13
water/DMSO+8PEI	s > e	96	4	0.75 ± 0.12
water/DMF+8PEI	e > s	99	1	1.18 ± 0.13
water/EtOH+8PEI	e >> s	96	4	1.31 ± 0.12

r: rhombohedra; e: microellipsoids; s: microspheres.



Figure_S4. CaCO_3 of different shapes obtained with the reduction of the reagent volume in the water/organic solvent +PEI system. Other experimental conditions as described in the main text.

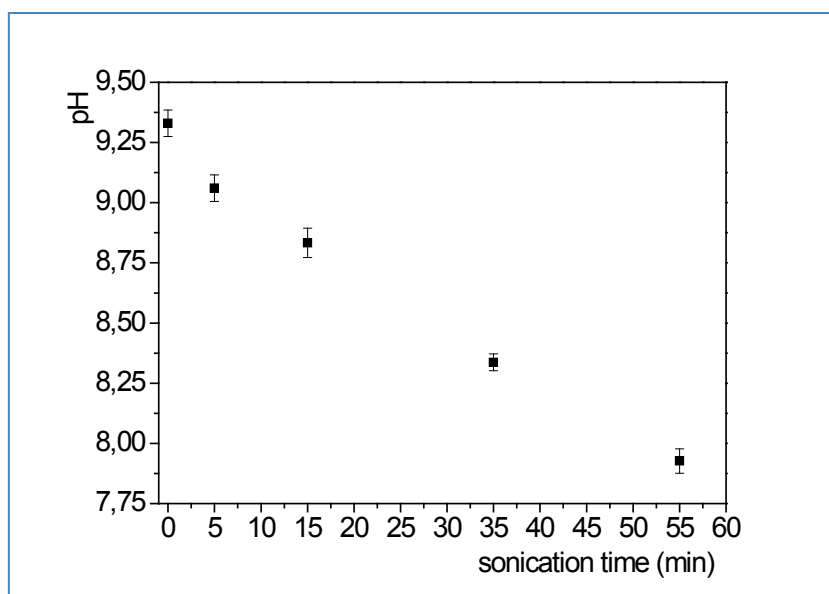


Figure _S5. pH decrease of water dissolutions of CaCl_2 (0.33 M, 15 mL) during the ultrasonic process. Other experimental conditions as described in the main text.

Table _S3. Estimation of the quantity of (bio)molecules (μg of immobilized biomolecule per mg of CaCO_3) deposited onto microparticles surface.

bio(molecule)	BSA-FITC	HIgG-FITC	HIgG-Per	Tyr	BG	MO	F	R	MR	MB
$\mu\text{g}/\text{mg}$	24	13	9	252	12.2	45	8.7	0.31	-	-
Charge at pH 6-7	-	+	+	-	0	0	0	+	+	+

Tyr (tyrosinase), BG (bromocresol green), MO (methyl orange), F (fluorescein), R (rhodamine B), MR (methyl red), MB (methylene blue).

III.6 References

- [1] X. Geng, L. Liu, J. Jiang, S-H. Yu, *Cryst. Growth Des.* **2010**, 10, 3448.
- [2] L. Liu, D. He, G.-S. Wang, S.-H. Yu, *Langmuir*, **2011**, 27, 7199.
- [3] a) S. Kim, C. B. Park, *Langmuir*, **2010**, 26, 14730. b) H. Yang, W. Yao, L. Yang, X. Ma, H. Wang, F. Ye, K. Wong, *J. Cryst. Growth*, **2009**, 311, 2682.
- [4] D. V. Volodkin, R. V. Klitzing, H. Möhwald, *Angew. Chem. Int. Ed.* **2010**, 122, 9444.
- [5] a) Y. Jiang, D. Yang, L. Zhang, Q. Sun, X. Sun, J. Li, Z. Jiang, *Adv. Funct. Mater.* **2009**, 19, 150. b) T. Levy, Ch. Déjugnat, G. B. Sukhorukov, *Adv. Funct. Mater.* **2008**, 18, 1586. c) D. B. Shenoy, G. B. Sukhorukov, *Macromol. Biosci.* **2005**, 5, 451.
- [6] a) W. Wei, G.-H. Ma, G. Hu, D. Yu, T. Mcleish, Z.-G. Su, Z.-Y. Shen, *J. Am. Chem. Soc.* **2008**, 130, 15808. b) B. G. De Geest, S. De Koker, K. Immesoete, J. Demeester, S. C. De Smedt, W. E. Hennink, *Adv. Mater.* **2008**, 20, 3687. c) A. I. Petrov, D. V. Volodkin, G. B. Sukhorukov, *Biotechnol. Prog.* **2005**, 21, 918. d) D. V. Volodkin, A. I. Petrov, M. Prevot, G. B. Sukhorukov, *Langmuir*, **2004**, 20, 3398.
- [7] a) D. Shan, M. Zhu, E. Han, H. Xue, S. Cosnier, *Biosens. Bioelectron.* **2007**, 23, 648. b) F. Li, Y. Feng, Z. Wang, L. Yang, L. Zhuo, B. Tang, *Biosens. Bioelectron.* **2010**, 25, 2244. c) W.-Y. Cai, Q. Xu, X.-N. Zhao, J.-J. Zhu, H.-Y. Chen, *Chem. Mater.* **2006**, 18, 279. d) Y.-H. Won, H. S. Jang, D.-W. Chung, L. A. Stanciu, *J. Mater. Chem.* **2010**, 20, 7728.
- [8] A.-W. Xu, W.-F. Dong, M. Antonietti, H. Cölfen, *Adv. Funct. Mater.* **2008**, 18, 1307.
- [9] a) L. Qi, J. Li, J. Ma, *Adv. Mater.* **2002**, 14, 300. b) B. P. Bastakoti, S. Guragain, Y. Yokoyama, S.-i. Yusa, K. Nakashima, *Langmuir*, **2011**, 27, 379. c) Y.-X. Gao, S.-H. Yu, X.-H. Guo, *Langmuir*, **2006**, 22, 6125.
- [10] a) T. Sakamoto, A. Oichi, Y. Oaki, T. Nishimura, A. Sugawara, T. Kato, *Cryst. Growth Des.* **2009**, 9, 622. b) B. Yeom, K. Char, *Chem. Mater.* **2010**, 22, 101.
- [11] a) E. Loste, E. Díaz-Martí, A. Zarbakhsh, F. C. Meldrum, *Langmuir*, **2003**, 19, 2830. b) E. M. Pouget, P. H. H. Bomans, J. A. C. M. Goos, P. M. Frederik, G. de With, N. A. J. M. Sommerdijk, *Sci.* **2009**, 323, 1455.

- [12] a) Ch-L. Chen, J. Qi, R. N. Zuckermann, J. J. DeYoreo, *J. Am. Chem. Soc.* **2011**, 133, 5214.
- [13] a) S. Sindhu, S. Jegadesan, L. Hairong, P. K. Ajikumar, M. Vetrichelvan, S. Valiyaveetil, *Adv. Funct. Mater.* **2007**, 17, 1698. b) A-W. Xu, M. Antonietti, H. Cölfen, Y.-P. Fang, *Adv. Funct. Mater.* **2006**, 16, 903 c) A. Neira-Carrillo, D. F. Acevedo, M. C. Miras, C. A. Barbero, D. Gebauer, H. Cölfen, J. L. Arias, *Langmuir*, **2008**, 24, 12496.
- [14] a) X.-H. Guo, S.-H. Yu, G.-B. Cai, *Angew. Chem.* **2006**, 118, 4081. b) R.-J. Qi, Y.-J. Zhu, *J. Phys. Chem. B.* **2006**, 110, 8302.
- [15] H. K. Park, I. Lee, K. Kim, *Chem. Commun.* **2004**, 1, 24.
- [16] Sh. Lee, S. G. Lee, D. Kwak, J.-H. Park, K. Cho, *J. Phys. Chem. C.* **2011**, 115, 2026. b) S. Lee, J.-H. Park, D. Kwak, K. Cho, *Cryst. Growth Des.* **2010**, 10, 851.
- [17] a) F. Jiang, Y. Yang, L. Huang, X. Chen, Z. Shao, *J. Appl. Polym. Sci.* **2009**, 114, 3686. b) J. Yu, M. Lei, B. Cheng, X. Zhao, *J. Solid State Chem.* **2004**, 177, 681. c) D. Gebauer, H. Cölfen, A. Verch, M. Antonietti, *Adv. Mater.* **2009**, 21, 435.
- [18] a) J. Yu, H. Guo, S. A. Davis, S. Mann, *Adv. Funct. Mater.* **2006**, 16, 2035. b) Y. Jin, W. Liu, J. Wang, J. Fang, H. Gao, *Colloids Surf. A: Physicochem. Eng. Asp.* **2009**, 342, 40.
- [19] X. Liu, H. Bai, Y. Sha, *Adv. Mater. Res.* **2011**, 194-196, 777.
- [20] a) Z.-G. Cui, Y.-Z. Cui, C.-F Cui, Z. Chen, B. P. Binks, *Langmuir*, **2010**, 26, 12567. b) G. Gao, P. Huang, K. Wang, R. He, D. Cui, *Powder Technol.* **2011**, 205, 270.
- [21] J. Yu, X. Zhao, B. Cheng, Q. Zhang, *J. Solid State Chem.* **2005**, 178, 861.
- [22] E. Altay, T. Shahwan, M. Tanoğlu, *Powder Technol.* **2007**, 178, 194.
- [23] Y. Mori, T. Enomae, A. Isogai, *Mater. Sci. Eng. C.* **2009**, 29, 1409.
- [24] G. B. Sukhorukov, D. V. Volodkin, A. M. Günther, A. I. Petrov, D. B. Shenoy, H. Möhwald, *J. Mater. Chem.* **2004**, 14, 2073.
- [25] M. Fujiwara, K. Shiokawa, M. Araki, N. Ashitaka, K. Morigaki, T. Kubota, Y. Nakahara, *Cryst. Growth Des.* **2010**, 10, 4030.
- [26] a) B. Aziz, D. Gebauer, N. Hedin, *Cryst. Eng. Comm.* **2011**, 13, 4641. b) D. Gebauer, P. N. Gunawidjaja, J. Y. P. Ko, Z. Bacsik, B. Aziz, L. Liu, Y. Hu, L. Bergström, C.-W. Tai, T.-K. Sham, M. Edén, N. Hedin, *Angew. Chem. Int. Ed.* **2010**, 49, 8889. c) A. G. Xyla, P. G. Koutsoukos, *J. Chem. Soc. Faraday Trans. 1*, **1989**, 85, 3165.

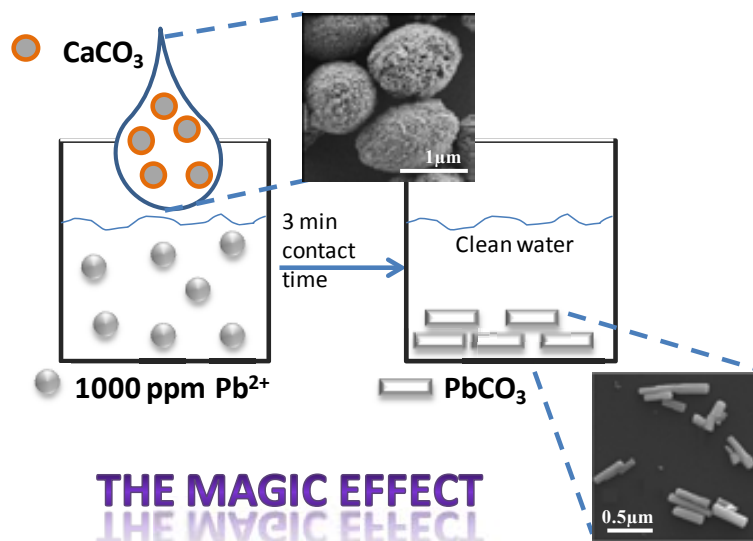
- [27] a) M. T. Timko, J. M. Diffendal, J. W. Tester, K. A. Smith, W. A. Peters, R. L. Danheiser, J. I. Steinfeld, *J. Phys. Chem. A*, **2003**, 107, 5503. b) L. Rong, Y. Kojima, Sh. Koda, H. Nomura, *Ultrason. Sonochem.* **2001**, 8, 11.
- [28] P. Moulin, H. Roques, *J. Colloid Interface Sci.* **2003**, 261, 115.
- [29] a) Y. Yang, X.i Wei, P. Sun, J. Wan, *Molecules*, **2010**, 15, 2872. b) D. V. Volodkin, N. I. Larionova, G. B. Sukhorukov, *Biomolecules*, **2004**, 5, 1962.
- [30] H. Ai, M. Fang, S. A. Jones, Y. M. Lvov, *Biomolecules*, **2002**, 3, 560.
- [31] O. S. Kulakovich, N. D. Strekal, M. V. Artemev, A. P. Stupak, S. A. Maskevich, S. V. Gaponenko, *J. Appl. Spectrosc.* **2006**, 73, 892.
- [32] X. Wan, B. Chai, Y. Liao, Y. Su, T. Ye, P. Shen, X. Chen, *Appl. Microbiol. Biotechnol*, **2009**, 82, 261.
- [33] H. Kawaguchi, H. Hirail, K. Sakai, S. Sera, T. Nakajima, Y. Ebisawa, K. Koyama, *Colloid Polym. Sci.* **1992**, 270, 1176.
- [34] F. H. Chung, *J. Appl. Cryst.* **1974**, 7, 519.
- [35] N. V. Vagenas, A. Gatsouli, C. G. Kontoyannis, *Talanta*, **2003**, 59, 831.

Chapter IV. Extremely fast and high Pb²⁺ removal capacity via use of a hybrid nanostructured vaterite.

These results are related in the submitted manuscript “Extremely fast and high Pb²⁺ removal capacity via use of a hybrid nanostructured vaterite”, A. López_Marzo, J. Pons, A. Merkoçi.

Chapter IV. Extremely fast and high Pb^{2+} removal capacity via use of a hybrid nanostructured vaterite.

Graphical abstract and content



Ultra-fast heavy metals removal using hybrid and nanostructured vaterite- PEI (NV-PEI) is reported here. Especially for Pb^{2+} an extremely high and fast adsorption capacity without precedents is observed. Within a 3 min interval time 97-100% of Pb^{2+} contaminant in water samples at pH 6 (the most common water pH) with a large concentrations range (from 0 to 1000 ppm) and using a dosage of 0.5 g NV-PEI/L have been removed. The maximum adsorption capacity calculated for a 1500 ppm Pb^{2+} initial concentration was 2762 mg of Pb^{2+} /g NV-PEI achieving a 92 % removing of this initial Pb^{2+} contamination in 6 min. This surprising removing capacity is ascribed to a recrystallization process via ionic exchange, where Ca^{2+} is substituted by Pb^{2+} (functioning the vaterite-PEI material behaves like a wide ionic exchanger) and to the excellent nucleophilic character of PEI to attract electrophilic metal centers and the large space inner of the slit macropores of the vaterite material.

IV.1 Introduction

Wastewaters from several industrial activities are an important source of environmental pollution, because of their high content of heavy metals ions. Currently, water treatment technologies for the removal of heavy metals ions occurs through the use of several unit operations, such as chemical precipitation, sedimentation, filtration and sludge treatment.^{1,2} During the process of filtration other procedures such as membrane filtration, ion exchange, electrochemical and adsorption processes are introduced to affine and to improve the heavy metals removal fundamentally at low concentrations. In a wastewater treatment plant in the basin of filtration are placed several ionic interchanger membranes or adsorption membranes, or mixture of both types, to eliminate the residual heavy metal that can't completely be removed during the previous process (sedimentation) and are at low concentrations when water enters the filtration unit.¹⁻³ Nanotechnology has been a useful tool in the fabrication of materials to remove low heavy metals concentration during the water treatment process.⁴ In this way many different nanoscale materials such as oxides, hydroxides or salts of metals (such as iron,⁵⁻⁹ titanium¹⁰), carbon nanotubes,^{11,12} various noble metals (mainly as nanoparticles)^{13,14,15}, inorganic-organic hybrid materials,¹⁶ biomaterial as nanoporous silica,¹⁷ calcium carbonates¹⁸⁻²¹ and calcium phosphates,²²⁻²⁴ nanoscale networks (such as zeolites, MOF)²⁵ and others^{26,27} have been explored for remediation.

Here a hybrid material composed of nanostructured vaterite-PEI (NV-PEI) microparticles has been evaluated for heavy metal removal from water. Ultra fast removal capacity achieved within 6 min, never reached before, has been found for several metals at 100 ppm of initial concentration. 3 min is completely sufficient to remove almost the 100% of Pb^{2+} contamination in a wide concentrations range from 2-1000 ppm using a dosage of 0.5 g NV-PEI /L at pH 6, the usual water pH. Although there is a large number of studies using multiples nanostructure materials this extremely rapid and high adsorption capacity to remove Pb^{2+} has never been achieved so far.^{5,10,11,15,17-19} Generally the heavy metal removal processes using the nanostructured microparticles (like fibres, sheet, tubes, rods, spheres, etc) are generally described by Langmuir isotherms^{9,10,17,18} but in this case only Freundlich isotherm is the ascribed model. In addition to the excellent Pb^{2+} removal, the material here evaluated is cheap, easy to be synthesized, biocompatible, biodegradable, which makes it superior to others reported so far and an attractive alternative for industrial applications.

IV.2 Experimental part

IV.2.1 Chemical and synthesis of the absorbent material.

The $\text{Pb}(\text{NO}_3)_2$, $\text{CuCl}_2 \cdot 2\text{H}_2\text{O}$, HgCl_2 , ZnCl_2 , CdCl_2 , $\text{NiCl}_2 \cdot 6\text{H}_2\text{O}$, CaCl_2 and Na_2CO_3 reagents were purchased from sigma Aldrich. The NV-PEI adsorbent material was synthesized mixing under 45 min sonication equal volumes (5 mL) and concentrations (0.33 M) of CaCl_2 and Na_2CO_3 dissolutions each PEI containing (4 mg/mL). In the case of CaCl_2 dissolution a mixed solvent of water/ethanol 1:1 (v/v) was used.²⁸ The final product is 100% of vaterite polymorph compound of nanostructured microelipsoides and microspheres of about 1 μm size covered with PEI polymer.

IV.2.2 Characterization techniques.

XRD measurements were performed on a Siemens D-5000 X-ray diffractometer with graphite monochromatized Cu-K α radiation ($\lambda = 0.15406$ nm). A scanning rate of 0.02 $^\circ/\text{s}$ was applied to record the pattern in the 2θ range of 10-80 $^\circ$ using 40 kV and 40 mA. The phase identification was done by comparing the XRD patterns of the powders with the standard data available from Joint Committee on Powder Diffraction Standards. The morphology of NV-PEI was observed by means of ZEISS Merlin, Quanta 650FEG SEM and TECNAI-F20 HRTEM microscopes. N_2 adsorption-desorption isotherms were recorded on a Micromeritics Instrument Corporation ASAP 2000 sorption analyzer at liquid nitrogen temperature (77 K). The samples were degassed at 120 $^\circ\text{C}$ overnight (22 h) prior to the measurement. The surface area was obtained by the BET method, and the pore size distribution was calculated from the adsorption branch of the isotherms by the BJH model. TGA was conducted on a TGA7 Perkin-Elmer with argon flow rate of 20 mL/min and a heating rate of 10 $^\circ\text{C}/\text{min}$.

IV.2.3 Removal kinetic experiments

In a typical kinetic experiment the used Pb^{2+} , Cu^{2+} , Hg^{2+} , Zn^{2+} , Cd^{2+} and Ni^{2+} dissolutions at different concentrations were prepared by dissolving a weighed quantity of $\text{Pb}(\text{NO}_3)_2$, $\text{CuCl}_2 \cdot 2\text{H}_2\text{O}$, HgCl_2 , ZnCl_2 , CdCl_2 and $\text{NiCl}_2 \cdot 6\text{H}_2\text{O}$, respectively, in Milli-Q water (resistivity 18.2 $\Omega \cdot \text{cm}$ at 25 $^\circ\text{C}$) and pH adjusted to 6. As-prepared hybrid NV-PEI microparticles (25 mg) were added to 50 mL of the metal solutions under stirring until 6 h of contact time. Aqueous samples (500 μL) were taken using improvised homemade filter-collector sample at several fixed time intervals and the metal ions concentrations were analyzed by using an ICPMS Agilent 7500ce model system. The

amount q_t (mg/g) of metal adsorption onto microparticles surface at time interval t was calculated by:

$$q_t = \frac{(C_0 - C_t)}{W} V$$

where C_0 and C_t (mg/L) are the liquid phase concentrations of Pb^{2+} ions at initial and any time interval t , respectively, V is the volume of the solution (L) and W is the mass of NV-PEI used as adsorbent (g).

IV.3 Results and Discussion

IV. 3.1 Competitive assay of removal

Figure S_1 in the SI shows SEM and TEM images of the NV-PEI particles, as prepared in experimental conditions described before and used as adsorbent material in the removing related experiments. The first removing probes were carried out in multi-metal competitive assays, using the most important heavy metal contaminants. The NV-PEI adsorbent material exhibited the highest selectivity and adsorption capacity for Pb^{2+} and Cu^{2+} , followed for Hg^{2+} , Zn^{2+} and Cd^{2+} with a similar removal preference between them. NV-PEI showed the lowest selectivity and removal for Ni^{2+} between all the assayed metals (**figure 1A**). At 6 min of contact time the maximum adsorption capacity for the six assayed metals using both 20 and 100 ppm as initial concentration (lower times were not assayed) is reached indicating that the whole adsorption process is very fast. The maximum adsorption capacity for the total metals contamination was around 430 mg/g which corresponds to 31% of removal of the total initial metal concentration of 600 ppm. The change of color from white to blue in the adsorbent material after 6 min of contact time is related to the adsorption of Cu^{2+} and Ni^{2+} onto this material (**figure 1B**).

When 20 ppm of each metal is used as initial concentration, almost 100% of Pb^{2+} and Cu^{2+} are removed followed by around 50-60% of removal for Hg^{2+} , Zn^{2+} and Cd^{2+} and 20% for Ni^{2+} . While using 100 ppm of each metal as initial concentration, around 60% of Pb^{2+} and Cu^{2+} , 20% of Hg^{2+} , Zn^{2+} , Cd^{2+} and 10% of Ni^{2+} are removed. This decreasing in the removal percentage when the initial metal concentration increases from 20 to 100 ppm could be related with the fact that at high concentrations the different removing mechanisms for these metals start blocking/interfering each other, allowing major removal for each metal in comparison to the case when only one metal should be present. Moreover some mechanisms start to saturate at high concentrations

onto the NV-PEI surface, which is reflected in the increasing of the adsorption capacity and the decreasing in the removal capacity when metal concentration increases from 20 to 100 ppm.

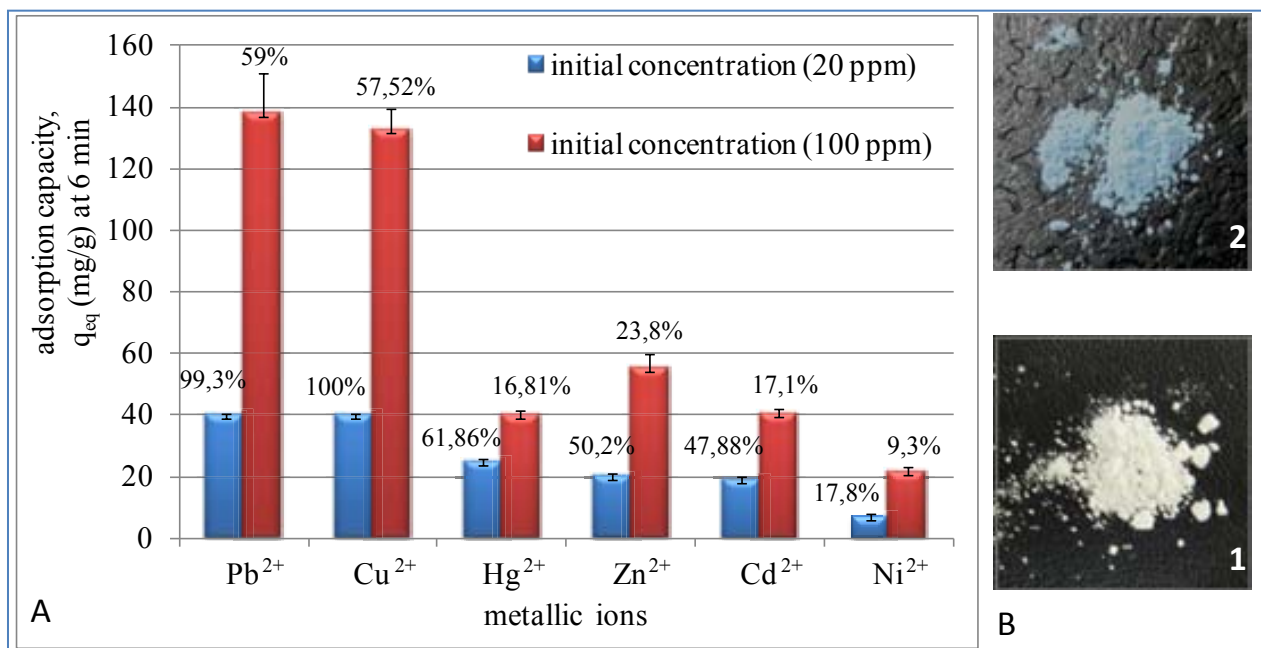


Figure 1. (A) Adsorption capacities of NV-PEI (0.5 g/L dosage) obtained during 6 min of contact time for different metallic ions in a competitive assay using 20 and 100 ppm of initial concentration for each metal. The number over the bar is the percentage of removal. (B) Photos of the adsorbent powder of the NV-PEI before (1) and after (2) the removal process.

As this material in the multi-metal competitive removal assay showed the highest adsorption capacity for Pb^{2+} , the following adsorption kinetic studies for the Pb^{2+} removal as shown below were performed.

The equilibrium adsorption capacity increases dramatically by increasing of Pb^{2+} initial concentration, until it reaches the maximum adsorption capacity of 2762 mg Pb^{2+} /g NV-PEI at 1500 ppm of Pb^{2+} initial concentration (**figure 2-i**). For concentrations from 0 to 1000 ppm 3 min of contact time is enough to remove around 97-100% of the total Pb^{2+} initial mass using a dose of 0.5 g NV-PEI/L (**figure 2-ii**). Contact times longer than 3 min don't change significantly the adsorption capacity, because all the contaminant that can be removed from 0 to 1000 ppm is adsorbed in the first 3 min of reaction. This fast and high Pb^{2+} removal capacity has not been reported so far as shown in **table 1**.

Table 1. Summary of the most significant and latest (last five years) works related with the use of nanostructured microparticles for heavy metals removal for wastewater treatment potential applications.

These reported materials were proposed as better than the previous one.

Material	Metal- q_{\max} (mg/g)	Dose g/L	pH	CT (min)	BET (m^2/g)	BJH (nm) V (cm^3/g)	Reference
CaCO ₃ -PEI	Pb ²⁺ - 2762	0.5	6	3	20	2-190 0.7	This work
α -FeOOH microspheres	Pb ²⁺ - 80 As ⁵⁺ - 58	0.5;	6	180 180	96.9	3-20 0.36	<i>Adv. Mater.</i> 2012 , 24, 1111.
γ -Fe ₂ O ₃ CHNs Fe ₃ O ₄ CHNs Fe ₂ O ₃ CAHNs	As ⁵⁺ - 101.4 As ⁵⁺ - 6.07 As ⁵⁺ - 137.5	0.4	4	30 180 30	96.4 14.90 143.1	2-100 —	<i>ACS Appl. Mater. Interfaces</i> 2012 , 4, 3987.
CNTs-in- α Fe ₂ O ₃ Core-in-shell microcapsules	Pb ²⁺ - 46.6 Cr ³⁺ - 29.16	0.36	5	20 20	200	—	<i>Adv. Funct. Mater.</i> 2010 , 20, 820.
MWCNTs- cysteine	Cd ²⁺ - 60.3	1	5.5	60	—	—	<i>Adv. Funct. Mater.</i> 2008 , 18, 1536.
CaCO ₃ -maltose vaterite hexagonal plates	Pb ²⁺ - 3242 Ni ²⁺ - 769 Cu ²⁺ - 629 Mn ²⁺ - 558.7 Cd ²⁺ - 487.8 Co ²⁺ - 393.7	0.57	7	45 45 45 45 45	63.2	— 2-12	<i>J. Hazardous Mater.</i> 2012 , 209-21, 467.
CaCO ₃ -pepsin tetrahedral microaggregates	Pb ²⁺ - 1167 Cu ²⁺ - 611	0.43	—	60 60	—	—	<i>J. Crystal Growth</i> 2012 , 338, 272.
AuNPs (8.9±1.6 nm)	Hg ²⁺ - 102	0.028	—	50	—	—	<i>ACS NANO</i> 2012 , 6, 2253.
polyaniline nano wires/tubes	Cr ⁶⁺ - 147.3	0.6	5	60	—	—	<i>J. Phys. Chem. C</i> 2010 , 115, 1608.
Nanosheets Na-TNSs Na ₂ Ti ₃ O ₇ ·nH ₂ O	Pb ²⁺ - 10.88 Cu ²⁺ - 12.84 Eu ³⁺ - 10.42 Ag ²⁺ - 10.12	1.25	—	120 30 60 60	203	—	<i>Adv. Funct. Mater.</i> 2012 , 22, 835.
Ni@SiO ₂ core/shell particles modified with BODIPY	Pb ²⁺ - 100	10	7	—	—	—	<i>Angew. Chem. Int. Ed.</i> 2009 , 48, 1239.

Nomenclature: CT: contact time during which the maximum adsorption capacity is reached, V: volume of porous, C(A)HNs: chestnutlike (amorphous) hierarchical nanostructures; CNTs: carbon nanotubes; MWCNTs: multi-walled carbon nanotubes, TNSs: titanates nanosheets, BODIPY: 4,4-difluoro-4-bora-3a,4-diazas-indacene.

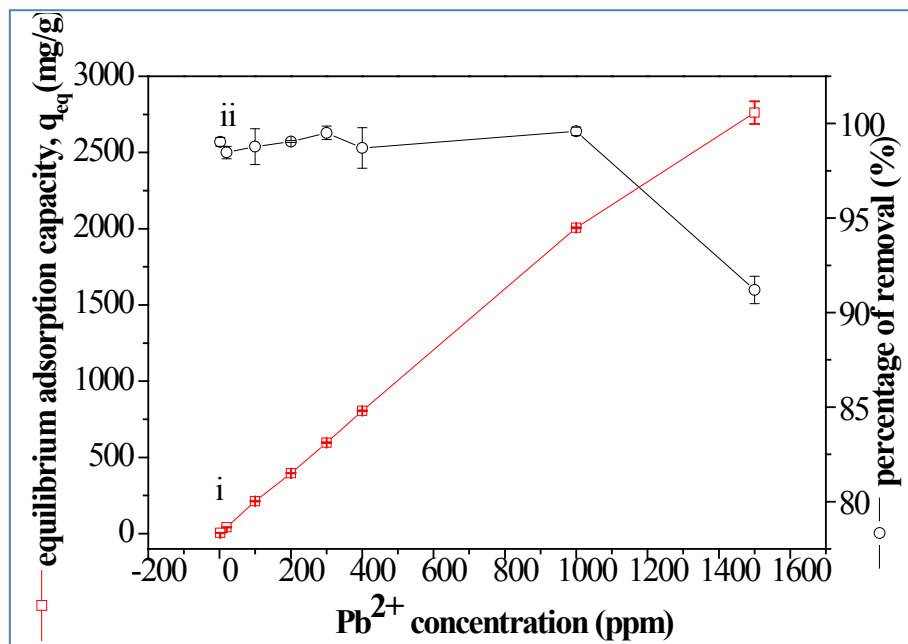


Figure 2. Adsorption rate for Pb^{2+} cations onto NV-PEI. (—□—) Curve of adsorption capacity reached at 3 min of contact time when initial metal concentration is increased. (—○—) Metal removal percentage when the equilibrium adsorption capacity is reached at different metal initial concentrations using 0.5 g NV-PEI/L dosage and 3 min of contact time.

IV.3.2 Adsorption isotherm of Pb^{2+} onto NV-PEI material

Although sometimes Freundlich^{11,18} and other models are found out as the best fit isotherm models to the experimental equilibrium data obtained during the removal processes. Generally the adsorption isotherms that describe the removal processes for the majority of the adsorbent materials of heavy metals reported correspond to the Langmuir model.^{9,10,17,18}

Our experimental data can't be adjusted with the Langmuir isotherm adsorption, which indicates that this model is not suitable for describing this process. This is because the adsorption not only occurs at the monolayer surface as is necessary assumed by Langmuir isotherm model, according to which the homogeneous surfaces have sites energetically equivalent and the adsorbates adsorb only in a monolayer way and there is no interaction between the adsorbed molecules. The adjusting of our experimental points is close to Freundlich model (figure_S2 at SI). This suggests that the Pb^{2+} adsorption behaviour onto the NV-PEI can be considered as a multilayer adsorption process that follows more the Freundlich isotherm model, an empirical equation based on the multilayer adsorption on heterogeneous surfaces.²⁹ In figure S2 are calculated the experimental parameters for Freundlich isotherm. Values of n relatively close to 1

indicate that the sorption intensity is good over the entire range of concentrations studied, while n values between 0.2 and 0.8 indicate that sorption intensity fits better at high concentrations but much less at lower concentrations.²⁹ In our case the n value obtained is 0.96 (close to 1) which is in agreement with the excellent removal capacity found over the entire range of concentrations from 2 to 1500 ppm. Other models such as Dubinin–Redushkevich (D-R) and Temkin models don't describe our experimental points (results not shown).

IV.3.3 The N₂ adsorption-desorption isotherms

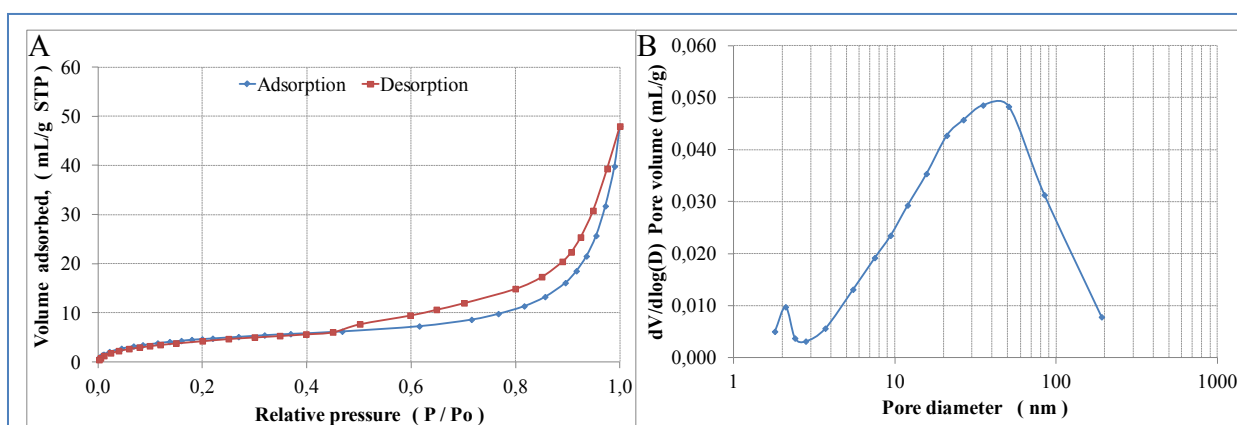


Figure 3. N₂ adsorption and desorption isotherms (A) and the corresponding BJH pore size distribution curve for the synthesized product (B).

The nitrogen adsorption and desorption isotherms of the NV-PEI adsorbent material exhibit type II isotherm with a type III hysteresis loop in the relative pressure range of 0.45–1 (**figure 3A**), suggesting that the adsorbing material structure is composed in majority by macropores with good pore connectivity associated with slit-like pores.^{30,31} In addition as shown in figure 3 A and B some mesoporous part in the size range of 2–50 nm for low relative pressures (P/P_0 0.4) is also present. The nitrogen amount adsorbed rises very steeply at high relative pressure ($P/P_0 > 0.85$), which also suggests the presence of an appreciable amount of very large pores in the material.^{30, 31} The BJH pore size distribution curve derived from the adsorption branch of the isotherm shows one very narrow distribution centered at 2.1 nm indicating that few microporous parts make up the material structure and one broad peak in the range of 2.8–191 nm centered at 40 nm that indicates that high percentage of the structure porosity are mesoporous and macroporous morphologies (see Fig. 3B). It is interesting to highlight that the final

part of the adsorption branch reaches large macropores diameter (50-190 nm). Moreover the material has a BET surface area of 20 m²/g and a pore volume of around 0.07 mL/g.

IV.3.4 Interaction of the metal ions with the NV-PEI hybrid materials. Removing mechanisms.

It is evident from the results that this hybrid material has powerful capability for fast and high removal of toxic ions of heavy metals. This is related with the large pore size in the NV-PEI structure, the PEI in the material surface that traps metallic cations by adsorption through the electrophilic-nucleophilic interactions and the recrystallization process mediated by the ionic exchange in the entire structure. **Figure 4** displays a representative scheme of the principle of the Pb²⁺ removing mechanism.

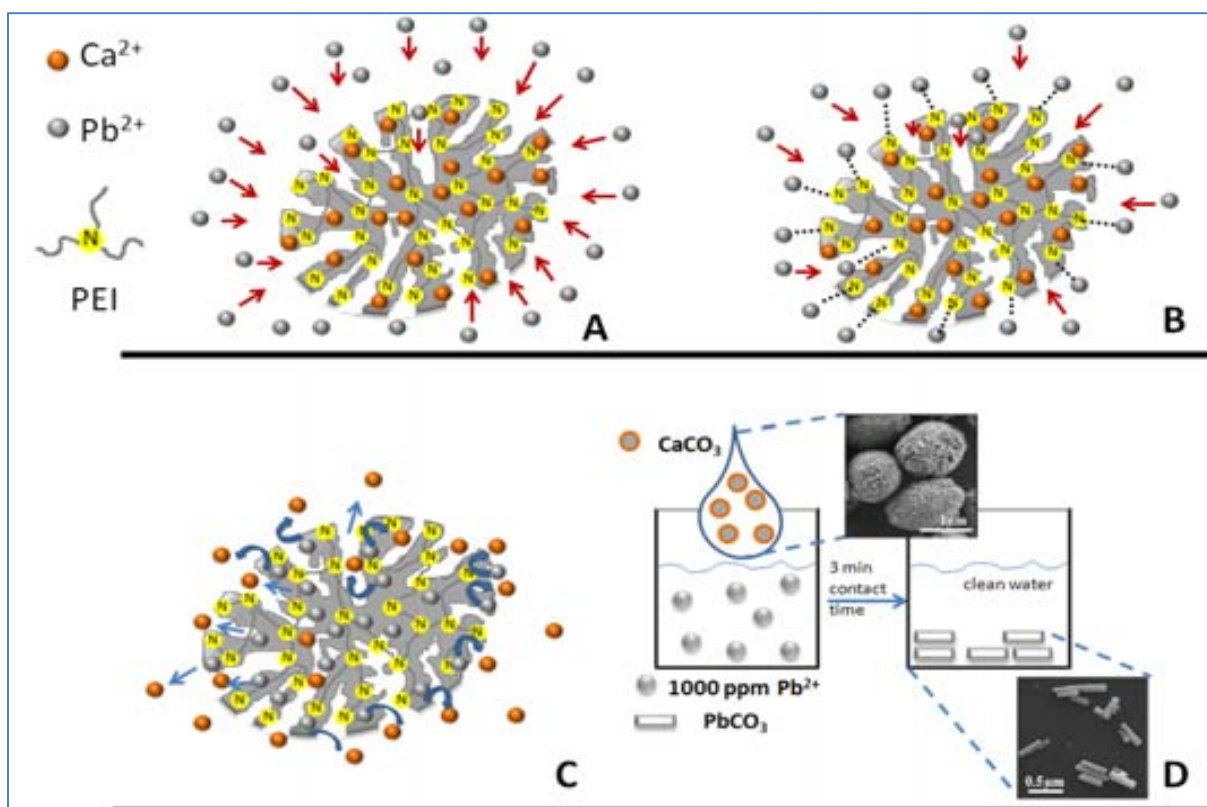


Figure 4. Schematic representation of the Pb²⁺ removing mechanism by use of NV-PEI material. A) Pb²⁺ cations diffusion toward the NV-PEI structure occurs. B) The PEI layer onto the surface material traps cations via electrophilic-nucleophilic interactions between PEI's nitrogen and Pb²⁺. The slit macroporous structure permits a rapid accessibility to the inner parts in the NV-PEI structure. The red arrows indicate the movement of the Pb²⁺ cations into the adsorbent structure. C) Ionic exchange of Ca²⁺ by Pb²⁺ cations leading to the recrystallization process. The blue arrows indicate the movement of released Ca²⁺ ions after exchanging with Pb²⁺ ions. D) Attractive scheme of the whole removing process.

The large size of the macropores that dominate in the structure (typical SEM images are displayed in figure_S1B where large pore sizes of this material can be observed) as

found by BJH method, and the high affinity power of the PEI with metallic cations as part of this hybrid material can explain the ultra rapid metal adsorption process that takes place in our system. The large size porous in this material permits big accessibility, as well as, a fast and simultaneous penetration of large quantity of ions to the inner parts of the NV-PEI microparticles together with the high affinity of PEI for metal cations acting as ionic trap network of chemical adsorption mechanism (figure 4A and B) are the two most important and determinant factors in the fast Pb^{2+} removal process.

The PEI presence in this material was observed using TGA (figure_S3 at SI). The loss in weight of about 6% that appears in the range of 250-350 °C corresponds to PEI delivery from CaCO_3 structure. This result indicates that a NV-PEI hybrid material was synthesized. The PEI structure is a branched polymer that contains a large number of amines functional groups with strong nucleophilic character which result electrophilic-nucleophilic interactions between nitrogen's PEI and the metal cation. It was observed that the removing equilibrium can be established in an extremely short time (about 6 min) during which a complete removal of heavy metal ions and especially of Pb^{2+} ions (nearly 100% removal after 3 min) occurred. The fast uptake of heavy metal ions indicates a high affinity rate between the metal ions and the amino groups at PEI that covers the adsorbent as well as a rapid mass transference to the inner parts of the structure propitiated by the large pore size.

The value of BET surface area as obtained from N_2 adsorption and desorption isotherms is discrete in comparison with the reported ones for other materials (see table 1) and doesn't justify the high Pb^{2+} removal capacity. This reasonably suggests that the high BET is not the only criterion for the high Pb^{2+} adsorption capacity. The adsorption capacity sometimes is intensively affected by the surface quality/property. In this case the Pb^{2+} adsorption mechanism is far a way of a simple superficial adsorption. This possibly results in a multilayer adsorption behavior and consequently a superior adsorption capacity. The Pb^{2+} adsorption process onto the as-obtained NV-PEI microparticles, as also explained before, obeys well the Freundlich isotherm model rather than the Langmuir one, suggesting that a multilayered adsorption occurs onto particles surface, which is in agreement with the ionic exchange mechanism that is also taking place and is demonstrated in **figure 5**.

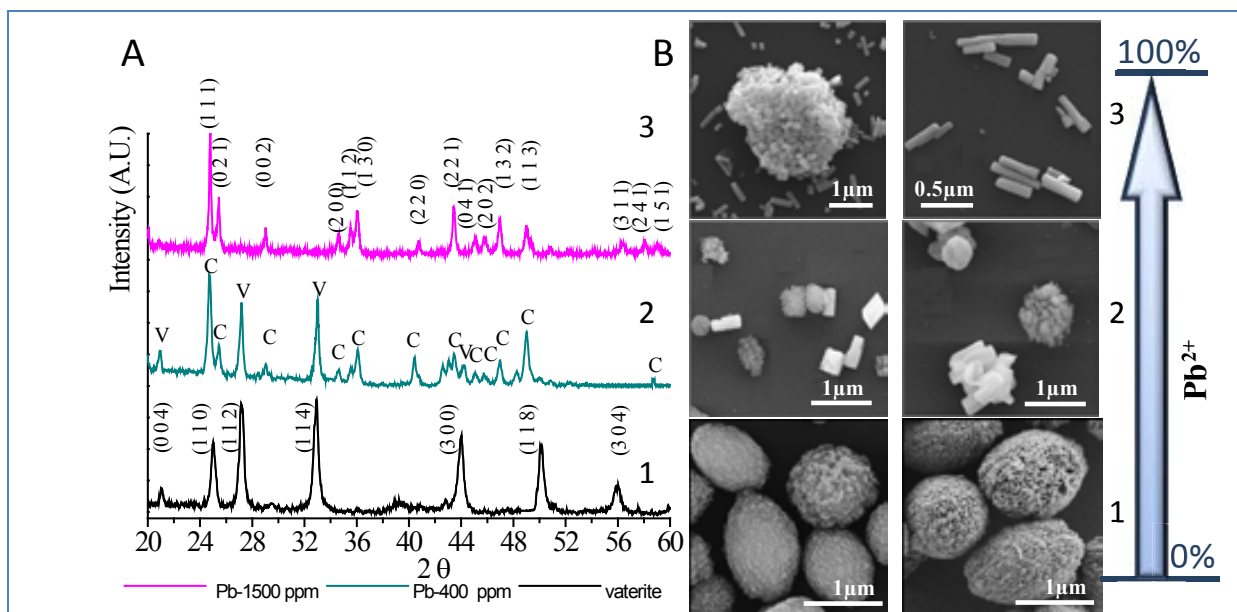


Figure 5. (A) XRD patterns correspond to the NV-PEI product at different contact times and Pb^{2+} initial concentrations (1) before treatment at initial time when there is not contact with Pb^{2+} solution, (2) after 6 min of treatment in contact with 400 ppm of Pb^{2+} solution, (3) after 6 min of treatment in contact with 1500 ppm of Pb^{2+} solution. V means vaterite and C cerussite. (B) SEM images of the corresponding products.

XRD patterns and SEM images in figure 5 A and B, respectively, indicate that a new precipitation process is taking place during the water treatment process. Figure 5 A-1 shows the pattern of vaterite before its contact with Pb^{2+} dissolutions while its corresponding SEM images of spherical/ellipsoidal microparticles are shown in figure 5 B-1. After the contact of the NV-PEI material with Pb^{2+} dissolutions of increasing initial concentration a transformation of part of vaterite in cerussite (orthorhombic PbCO_3) (figure 5 A-2 and B-2) occurs until that using 1500 ppm of Pb^{2+} dissolution a complete vaterite transformation into cerussite takes place (figure 5 A-3 and B-3). The NV-PEI behaves like an ionic exchanger network of Ca^{2+} by Pb^{2+} cations. The exchanging process takes place both at superficial level as well as at the interior of NV-PEI material. The structure of NV-PEI collapses during the ion exchange, resulting in a recrystallization process by an irreversible ion exchange. The SEM images in figure 5B-3 displays the orthorhombic PbCO_3 precipitate appeared from the starting NV-PEI microspheres/ellipsoids. Figure 4-D is a schematic illustration of the whole ionic exchange process explained previously.

The CaCO_3 precipitate transformation into PbCO_3 precipitate is favoured because the K_{ps} of the PbCO_3 (7.3×10^{-14}) is much lower than CaCO_3 K_{ps} (3.3×10^{-9}) in addition to

their close ionic radius (table_S1) that facilitates the substitution inside the CaCO_3 structure. An analysis of these and other properties for each metal that could favour the metal removing process by a recrystallization via ionic exchange is presented in table_S2. Following the analysis of the table_S2 Pb^{2+} has all the conditions to be removed preferentially in a multi-metal competitive assay, as occurs in the experimental results at figure 1A (previously discussed).

As shown in the XRD patterns of the figure_S4 the metals are removed from their solutions following the recrystallization mechanism that transforms CaCO_3 into the corresponding metal carbonates (figure_S4 A) or by precipitation induced by the adsorption of the original metal species onto the CaCO_3 surface via electrophilic-nucleophilic interactions with PEI's nitrogen (figure_S4 B). The selectivity order and the chemical form in which these metal are removed depend on several factors related with their different affinities for the surface of the NV-PEI hybrid material such as: (a) Ionic radius of the M^{2+} cations; metals of ionic radius close to Ca^{2+} exchange easier than other metals; (b) electronegativity of the metals; metals of higher electronegativity should be attracted more easily because the increasing in electronegativity reinforces the electrophilic-nucleophilic interactions with the PEI's nitrogen; (c) Solubility of the hydrate complexes; metals of less soluble complexes with hydrate have increased adsorptive capacity because the trend of the ion to crystallize will be higher than the tendency to remain dissolved as hydrate complexes; (d) Solubility of the carbonates; the metal ions that form less soluble carbonates should be exchanged stronger than metal ions which form more soluble carbonates; (e) Amino affinity; metals of big affinity with amino groups have more interaction with the surface and in consequence more possibility to be removed. Table_S1 at SI shows the values of the mentioned properties for each metal that are related with the removing mechanisms in this process. In this way metal ions such as Pb^{2+} , Cd^{2+} and Hg^{2+} with the closest Ca^{2+} ionic radius and with highly insoluble carbonates and hydroxides (table_S1) should be preferably removed by ionic exchange than the other. While Cu^{2+} , Zn^{2+} and Ni^{2+} that present less insoluble carbonates and hydroxides and ionic radius values far a way of Ca^{2+} tend to be removed by adsorption of their metal species through electrophilic-nucleophilic interactions with PEI's nitrogen. According with this analysis in figure_S4-A i and ii in addition to CaCO_3 peaks other peaks corresponding to Cd^{2+} and Hg^{2+} carbonates, respectively, can be observed. While in figure_S4-B iii, iv and v in addition to CaCO_3 peaks, other peaks can be associated to Cu^{2+} chloride, hydroxide, hydroxide chloride and their hydrated

species, Zn^{2+} chloride and hydroxide chloride and Ni^{2+} hydroxide, respectively. These metals are removed through their stable species that form in our system by precipitation induced by absorption onto the $CaCO_3$ surface via interactions with PEI.

As can be seen in the XRD patterns of figure_S4 during the treatment part of the original vaterite phase recrystallizes to calcite as a consequence of the metal removing process in its structure.

It is also important to point out that many adsorption results reported in the literature are obtained at an optimized pH value (usually pH 3-4) with longer adsorption duration that end up to 2 h. Therefore, we believe that the exceptionally fast and high removal capacities obtained by using the NV-PEI using pH 6 are more indicative for a promising use of this material in real water treatment applications. Although the obtained results are in the laboratory scale, we expect satisfactory removal efficiencies in industrial scale especially for Pb^{2+} . Moreover this material can be easily produced at industrial amounts because it is facile to be synthesized, cheap, biodegradable and innocuous. In addition this material has a high loading capacity for organic molecules (dyes such as methylene blue, bromocresol green and methyl orange) through the hydrogen bond interaction of acid hydrogens in the contaminants molecules and the nitrogen's PEI onto the vaterite microparticles surface as reported previously.²⁸ This would increase the NV-PEI interest as a potential adsorbent for simultaneous removing of many co-existing pollutants that usually appear in industrial effluents. The development of such multipurpose adsorbents which can remove both organic and heavy metal pollution would improve the cost / efficiency of water treatment process and might have impact on both the waste water treatment technology as well as the science behind the phenomena occurring during the operation of such integrated and hybrid nanostructured materials.

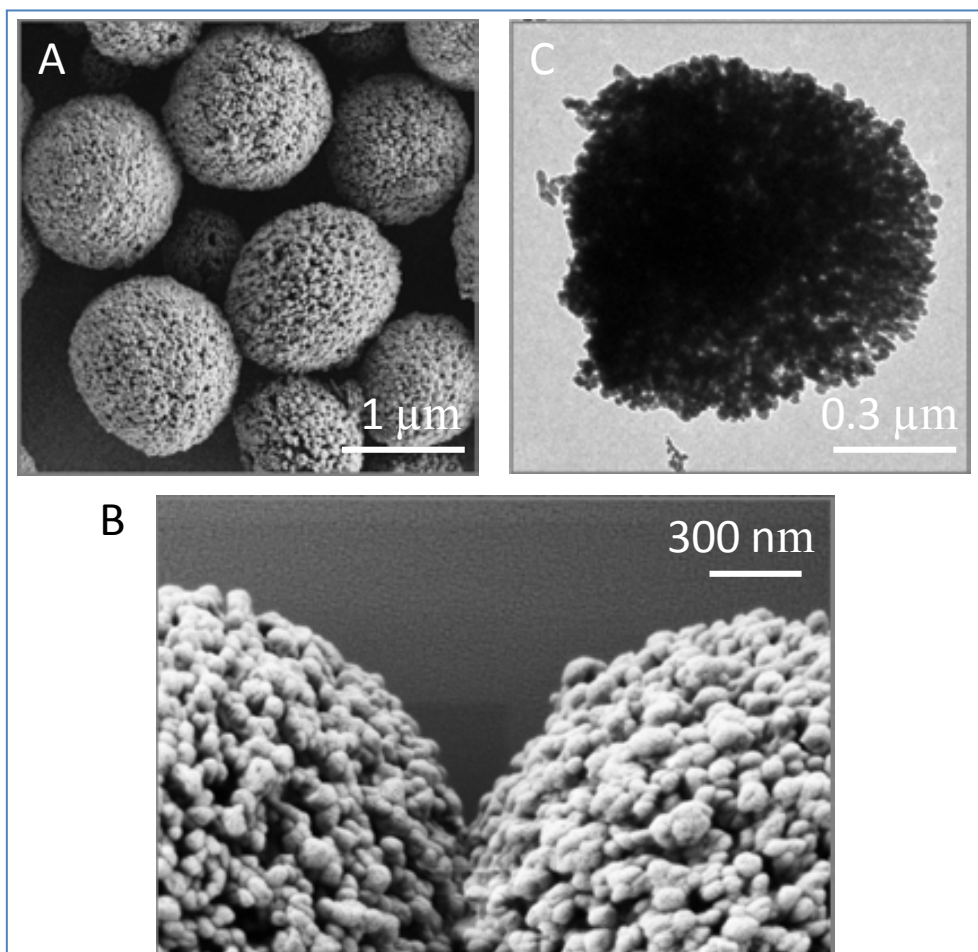
IV.4 Conclusions

A very fast heavy metals removal by using the hybrid NV-PEI, (composed of mixed nanostructured microspheres and microellipsoids of about $1\mu m$ size) is here reported. Especially ultra fast and high adsorption capacity for Pb^{2+} never reported before was achieved. Just a 3 min contact time, under stirring conditions, is enough to remove between 97 and 100% of this metal contaminant over an entire range of initial concentrations from 0 to 1000 ppm using a dosage of 0.5 g NV-PEI/L at the usual pH 6 water samples. The maximum adsorption capacity was 2762 mg of Pb^{2+} /g adsorbent material. These results show a powerful capability for fast and effective removal of

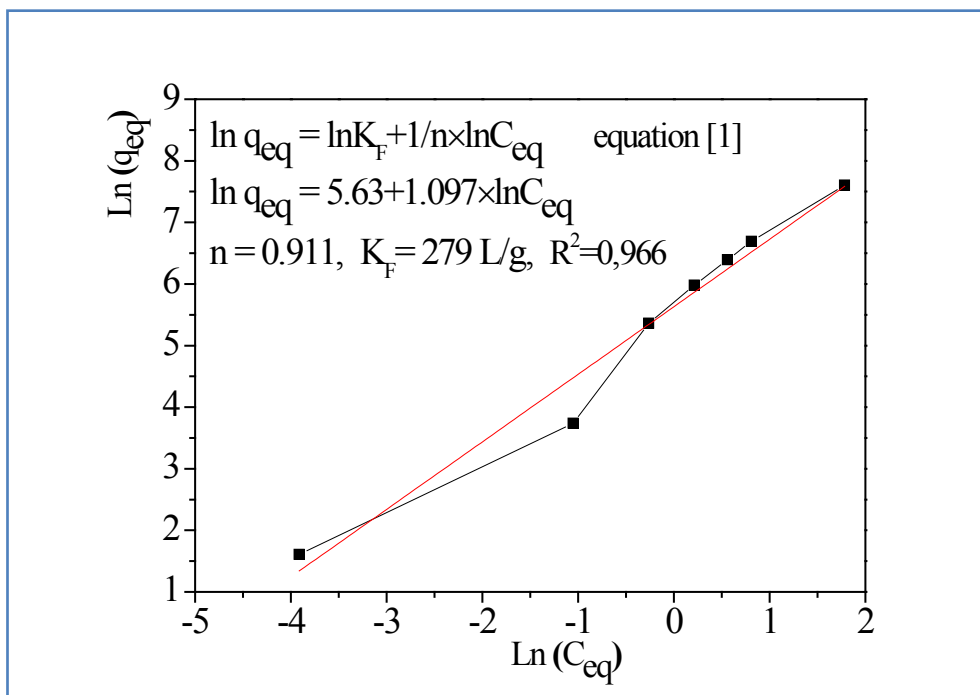
toxic Pb^{2+} , doing this material an efficient absorbent alternative for the complete removing of Pb^{2+} from high to trace concentrations during water treatment process. It is important to highlight that most of the materials used so far for heavy metal removing are not efficient at low metal concentrations.

The metal removal mechanisms are based on recrystallization process via ion exchange with Ca^{2+} in the NV-PEI material and the precipitation mediated by the adsorption via electrophilic-nucleophilic interactions between PEI's nitrogens and the metallic centres.

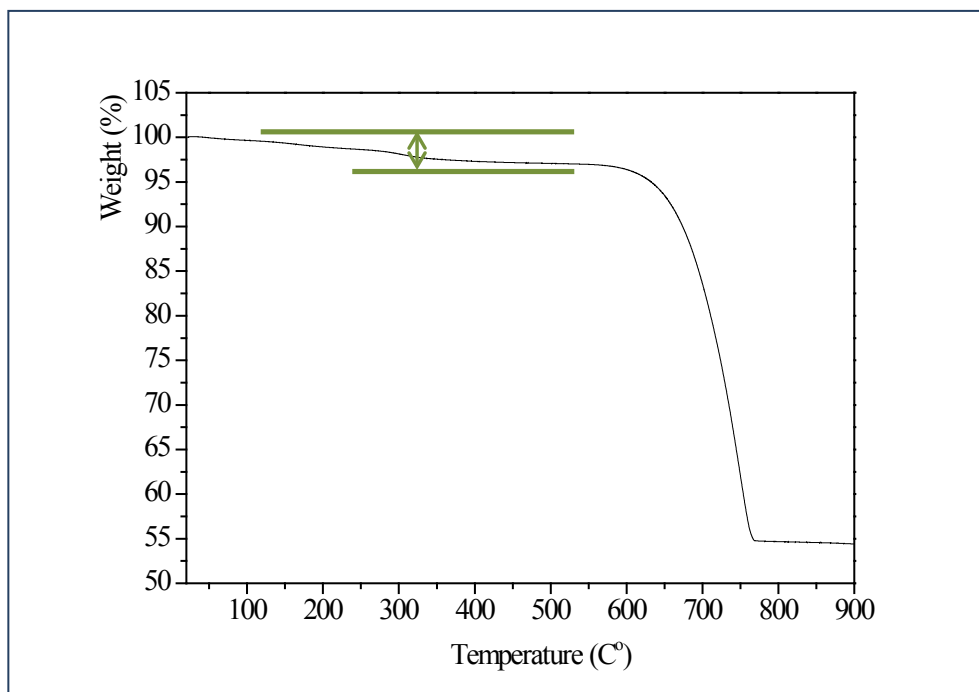
I.V. 5 Supporting Information



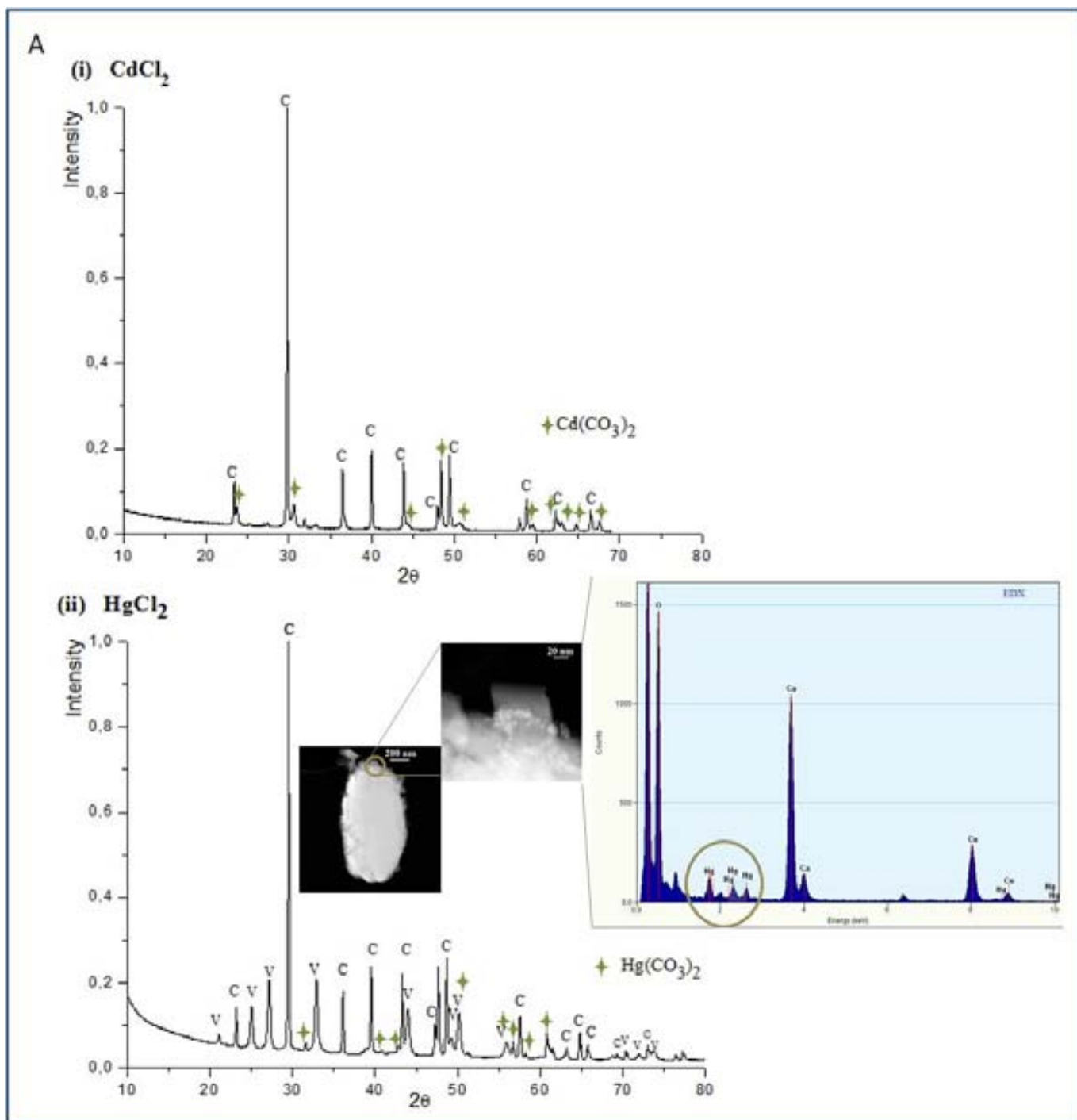
Figure_S1. Images of the synthesized NV-PEI microparticles. A and B SEM images and C TEM image. (B) Close up to the NV-PEI surface that displays the large macroporous caverns like structure that makes this material.

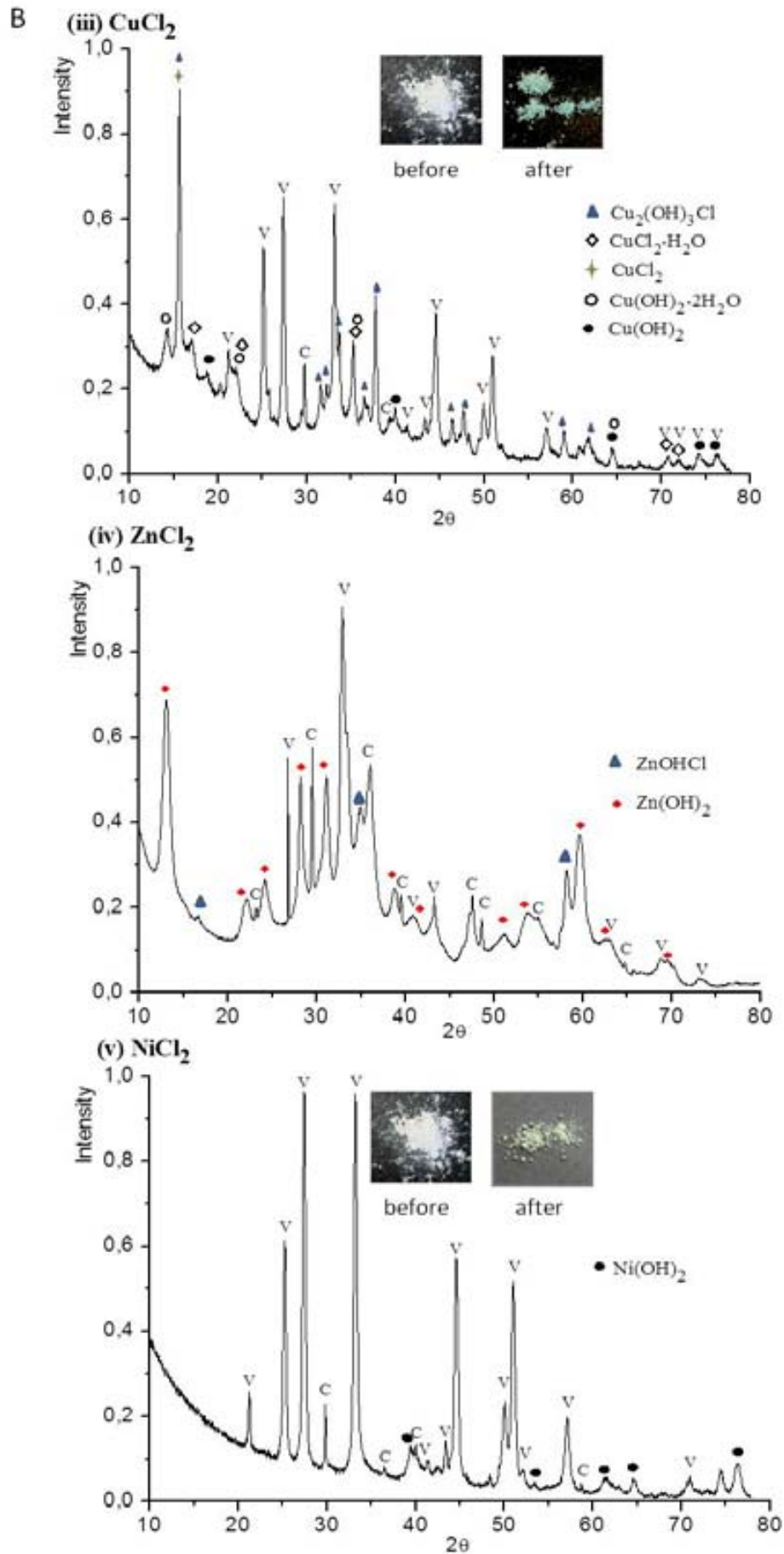


Figure_S2. Adjusting of the experimental points obtained during the Pb^{2+} adsorption onto NV-PEI surface at 25°C by the use of the Freundlich isotherm model. The equation 1 is the linear form of the Freundlich equation where K_F is the Freundlich constant (L/g) and $1/n$ the heterogeneity factor.



Figure_S3. TGA curve obtained for NV-PEI powder.





Figure_S4. XRD patterns of the solids obtained after 30 min of the treatment of the NV-PEI material with 400 ppm of initial metal dissolutions: (i) CdCl₂, (ii) HgCl₂, (iii) CuCl₂, (iv) ZnCl₂ and (v) NiCl₂ dissolutions. (A) Metal removing by ion exchange of Ca²⁺ in the CaCO₃ structure, and (B) metal removing by adsorption through interactions between the metallic species with the PEI's nitrogens. (A) The new peaks that arising in addition to corresponding CaCO₃ phases can be associated to the formation of Cd²⁺ (i) and Hg²⁺ (ii) carbonates. The inserts in A-ii correspond to scanning transmission electron microscope (STEM) images recorded to the power after the treatment and its energy dispersive X-ray (EDX). (B) The new peaks that arising in addition to those corresponding to CaCO₃ phases can be associated to the formation of Cu²⁺ chlorides, hydroxides and their hydrated species (iii), Zn²⁺ hydroxide and hydroxide chloride (iv), and Ni²⁺ hydroxide (v). The inserts in B-iii and B-v correspond to photos recorded before and after the treatment. Note: V means vaterite and C calcite.

Table_S1. Some of the properties of the studied heavy metal ions.

Metallic ions (M ²⁺)	K _{ps} MCO ₃	K _{ps} M(OH) ₂	Ionic Radius (Å)	Electronegativity (Pauling)
Pb ²⁺	7.30 x 10 ⁻¹⁴	1.43 x 10 ⁻¹⁵	1.19	2.33
Cu ²⁺	1.40 x 10 ⁻¹⁰	2.20 x 10 ⁻²⁰	0.73	1.90
Zn ²⁺	1.46 x 10 ⁻¹⁰	3.00 x 10 ⁻¹⁷	0.88	1.65
Hg ²⁺	3.60 x 10 ⁻¹⁷	2.00 x 10 ⁻²⁴	1.02	2.00
Cd ²⁺	1.00 x 10 ⁻¹²	7.20 x 10 ⁻¹⁵	0.99	1.69
Ni ²⁺	1.40 x 10 ⁻¹⁷	5.46 x 10 ⁻¹⁶	0.69	1.91
Ca ²⁺	3.40 x 10 ⁻⁹	5.50 x 10 ⁻⁶	1.10	1.00

Table_S2. Analysis of the properties that favour the removal mechanism by the recrystallization process mediated by ionic exchange. Note: +1 means that the property value favours this process, 0 means that property value is intermediate in relation to the other ones and don't determine an inclination, and -1 means that property value disfavour the ionic exchange process.

Metallic ions (M^{2+})	Kps MCO_3	Kps $M(OH)_2$	Ionic Radius (\AA)	Electronegativity (Pauling)	Total of favoured properties
Pb^{2+}	+1	+1	+1	+1	+4
Cu^{2+}	0	+1	-1	+1	+1
Zn^{2+}	0	+1	0	0	+1
Hg^{2+}	+1	+1	+1	+1	+4
Cd^{2+}	+1	+1	+1	0	+3
Ni^{2+}	+1	+1	-1	+1	+2
Ca^{2+}	reference of comparison				

IV.6 References

- [1] R. Ludwig, *Angew. Chem. Int. Ed.* **2002**, *41*, 2611.
- [2] A. Guijarro-Aldaco, V. Hernández-Montoya, A. Bonilla-Petriciolet, M. A. Montes-Morán, D. I. Mendoza-Castillo, *Ind. Eng. Chem. Res.* **2011**, *50*, 9354.
- [3] Y. Han, Zh. Xu, C. Gao, *Adv. Funct. Mater.* **2013**, DOI: 10.1002/adfm.201202601.
- [4] B. Karn, T. Kuiken, M. Otto, *Environ. Health Perspectives* **2009**, *117*, 1823.
- [5] B. Wang, H. Wu, L. Yu, R. Xu, T.-T. Lim, X. W. Lou, *Adv. Mater.* **2012**, *24*, 1111.
- [6] S.-W. Cao, Y.-J. Zhu, *J. Phys. Chem. C* **2008**, *112*, 6253.
- [7] F. Mou, J. Guan, H. Ma, L. Xu, W. Shi, *ACS Appl. Mater. Interfaces* **2012**, *4*, 3987.
- [8] W. Yantasee, C. Warner, T. Sangvanich, R. Sh. Addleman, T. Carter, R. J. Wiacek, G. Fryxell, Ch. Timchalk, M. Warner, *Environ. Sci. Technol.* **2007**, *41*, 5114.
- [9] Z. Wei, R. Xing, X. Zhang, S. Liu, H. Yu, P. Li, *ACS Appl. Mater. Interfaces* **2013**, *5*, 598.
- [10] N. Li, L. Zhang, Y. Chen, M. Fang, J. Zhang, H. Wang, *Adv. Funct. Mater.* **2012**, *22*, 835.
- [11] W. S. Choi, H. M. Yang, H. Y. Koo, H.-J. Lee, Y. B. Lee, T. S. Bae, Ch. Jeon, *Adv. Funct. Mater.* **2010**, *20*, 820.
- [12] Y. Liu, Y. Li, X.-P. Yan, *Adv. Funct. Mater.* **2008**, *18*, 1536.
- [13] I. Ojea-Jiménez, X. López, J. Arbiol, V. Puentes, *ACS Nano*, **2012**, *6*, 2253.
- [14] L. Lu, R. Capek, A. Kornowski, N. Gaponik, A. Eychmüller, *Angew. Chem.* **2005**, *117*, 6151.
- [15] H. Y. Lee, D. R. Bae, J. Ch. Park, H. Song, W. S. Han, J. H. Jung, *Angew. Chem. Int. Ed.* **2009**, *48*, 1239.
- [16] B. Saha, S. Chakraborty, G. Das, *J. Phys. Chem. C* **2010**, *114*, 9817.
- [17] W. Yantasee, R. D. Rutledge, W. Chouyyok, V. Sukwarotwat, G. Orr, C. L. Warner, M. G. Warner, G. E. Fryxell, R. J. Wiacek, Ch. Timchalk, R. Sh. Addleman, *ACS Appl. Mater. Interfaces*, **2010**, *2*, 2749.
- [18] X. Ma, L. Li, L. Yang, C. Su, K. Wang, Sh. Yuan, J. Zhou, *J. Hazard. Mater.* **2012**, *209-210*, 467.
- [19] X. Man, L. Li, L. Yang, C. Su, K. Wang, K. Jiang, *J. Cryst. Growth* **2012**, *338*, 272.
- [20] Y. Ma, Ch. Lin, Y. Jiang, W. Lu, Ch. Si, Y. Liu, *J. Hazard. Mater.* **2009**, *172*, 1288.

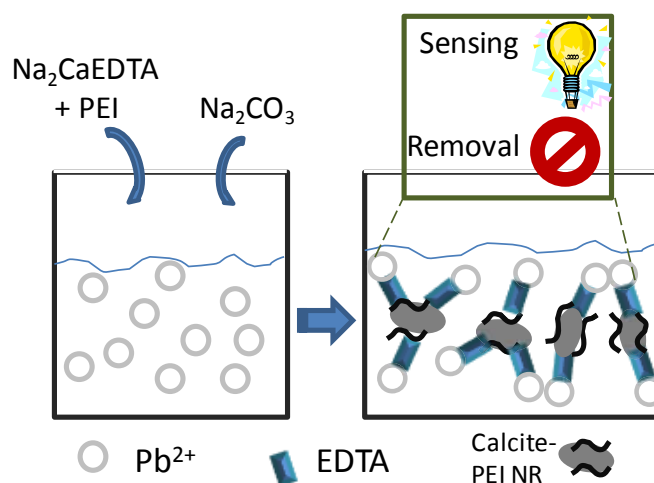
- [21] G. B. Cai, G. X. Zhao, X. K. Wang, S. H. Yu, *J. Phys. Chem. C*, **2010**, *114*, 12948.
- [22] R. Tovar-Gómez, D. A. Rivera-Ramírez, V. Hernández-Montoya, A. Bonilla-Petriciolet, C. J. Durán-Valle, M. A. Montes-Morán, *J. Hazardous Mater.* **2012**, *199-200*, 290.
- [23] Sh. Sugiyama, T. Ichii, M. Fujisawa, K. Kawashiro, T. Tomida, N. Shigemoto, H. Hayashi *J. Colloid Interface Sci.* **2003**, *259*, 408.
- [24] X. Chen, J. V. Wright, J. L. Conca, L. M. Peurrung, *Environ. Sci. Technol.* **1997**, *31*, 624.
- [25] B. C. Tappan, S. A. Steiner, E. P. Luther, *Angew. Chem. Int. Ed.* **2010**, *49*, 4544.
- [26] X. Guo, G. Ta. Fei, H. Su, L. D. Zhang, *J. Phys. Chem. C* **2011**, *115*, 1608.
- [27] M. J. Manos, V. G. Petkov, M. G. Kanatzidis, *Adv. Funct. Mater.* **2009**, *19*, 1087.
- [28] A. López_Marzo, J. Pons, A. Merkoçi, *J. Mater. Chem.* **2012**, *22*, 15326.
- [29] J. U. Kennedy-Oubagaranadina, N. Sathyamurthy, Z.V.P. Murthy, *J. Hazardous Mater.* **2007**, *142*, 165.
- [30] M. Khalfaoui, S. Knani, M. A. Hachicha, A. Ben Lamine. *J. Colloid Interface Sci.* **2003**, *263*, 350.
- [31] K. S. W. Sing, D. H. Everett, R. A. W. Haul, L. Moscou, R. A. Pierotti, J. Rouquerol, T. Siemieniewska, *Pure Appl. Chem.* **1985**, *57*, 603.

Chapter V. Multifunctional system based on hybrid calcite- PEI nanostructured-rods formation, for Pb^{2+} 'sensoremoval' applications

These results are related in the submitted manuscript “Multifunctional system based on hybrid calcite-PEI nanostructured-rods formation, for Pb^{2+} ‘sensoremoval’ applications”, A. López_Marzo, J. Pons, A. Merkoçi.

Chapter V. Multifunctional system based on hybrid calcite-PEI nanostructured-rods formation, for Pb^{2+} ‘sensoremoval’ applications

Graphical abstract and content



Multifunctional system based on hybrid calcite-PEI nanostructured rods (NRs) formation, that senses and removes Pb^{2+} (sensoremoval concept) for environmental applications was developed. The addition of $CaNa_2EDTA$ and CO_3^{2-} solutions to a Pb^{2+} contaminated water to guide to the crystallization of calcite-PEI NRs, composed of self-assembly hexagonal plate-like shapes of around 450 nm. The just formed calcite-PEI NRs in suspension permit the Pb^{2+} detection through a simple turbidimetric measurement, and at the same time act as heavy metal remover. This sensing and removing system is able to detect up to 1 ppm Pb^{2+} (1-1000 ppm lineal range) and reaches an adsorption capacity of 240 mg Pb^{2+} /g in 30 min at pH 4. This maximum Pb^{2+} removal capacity reported here is higher than other ones reported before using materials that are not as cheap and biodegradable as calcite. This system based on an advanced biomaterial constitutes a useful tool as proof-of-concept in the design of future multifunctional platforms for the development of integrated environmental technologies with sensing and remediation functions.

V.1. Introduction

Presence of heavy metals in industrial or municipal waste waters requires a previous monitoring and afterward an effective treatment strategy according to the contamination levels for the further use of these waters or their confinable delivery to rivers, lakes, etc, following the permissible limits of contamination statements by the regulatory agencies.^{1,2}

Although colorimetric,³ fluorimetric⁴ and electrochemical^{5,6} techniques have been developed for heavy metal detection, ICPEES⁷ and AAS⁸ continue to be the main techniques used for metal determination, in spite of these methods are expensive and require a trained personnel.^{9,10} On the other hand, the most known methods used to remove heavy metal ions, are the chemical precipitation of metal hydroxides at high pH, ion-exchange with zeolites, adsorption, membrane filtration, and electro-chemical treatment technology. Especially adsorption is an effective and economic method for heavy metal wastewater treatment. Although activated carbon is the most used adsorbent, it is relatively expensive. Many researchers have tried to find low-cost and easily available adsorbents to remove heavy metal ions, for examples, agricultural wastes composed mainly of cellulose fibers, plant wastes, zeolites, and clays.^{1,2,11,12}

Advances in nanoscale science and engineering are providing new opportunities to develop more cost-effective and environmentally acceptable water purification processes through the use of nanomaterials. Nanomaterials have several physicochemical properties that make them particularly attractive for water purification such as higher surface area per unit volume and the ability to be functionalized with a number of surfactants to enhance their affinity toward target molecules. Many different nanoscale materials such as nanoscale zeolites, metal oxides, carbon nanotubes and fibers, enzymes, various noble metals (mainly as bimetallic nanoparticles) and titanium dioxide have been explored for water remediation. Nanomaterials from transition metal hydroxides or oxides, especially iron, are extensively studied for monitoring, remediation and water pollution prevention. In the last ten years biominerals as CaCO₃ have been added to the list of potential water treatment nanomaterials.¹³⁻¹⁷

Calcium carbonate is one of the most important and cheapest biomineral in nature. Many organisms produce calcium carbonate with unique hierarchical structures and fascinating characters in their tissues for a variety of functions. Calcium carbonate has ideal biocompatibility and biodegradability properties. Several studies have

demonstrated continuous interest to CaCO_3 crystallization.¹⁸⁻²⁶ Although calcium carbonate has been studied for removal of heavy metal ions, the low efficiency and further treatment necessity, significantly limit the practical applications in water treatment. Considerable research has been focused on using hierarchical structures of hybrid CaCO_3 -organic materials as adsorbent for removal of heavy metal ions.^{11,18, 27-30} The development of materials, systems, devices or methods that integrate several process steps in one multifunctional step for clinical, environmental or industrial proposal constitutes a challenge for many ongoing researches. Multifunctional integrated materials and systems permit to manage with more rapidity and efficiency the whole process saving resources and time in obtaining of the desired results. Advanced multifunctional materials and systems with medical interest have been matter of several works, but with respect to environmental applications these are more reduced.³¹⁻³⁷ Here an original and complete multifunctional system for sensing and removing ('*sensoremoval*') of Pb^{2+} as proof-of-concept strategy with interest for environment is shown. This sensing and removing system is based on hybrid calcite-PEI NRs formation in Pb^{2+} contaminated waters followed by the subsequent detection and removal of the heavy metal contaminant thanks to the in situ NRs formation. Three components, Pb^{2+} ions or other contaminant metal ions to be removed, Na_2CaEDTA complex and carbonate ions are mixed and subsequently the metal-EDTA complexation and the CaCO_3 precipitation take place. A study of this CaCO_3 crystallization through changes in the reaction conditions such as the use or not of CGMs as PEI, glycerol and diethanolamine (DEA), the reagent order, the solvents reaction, the reagent volume, etc., is presented. Decreasing dramatically the reagents concentration for first time perfect hexagonal plates were found for calcite polymorph. A simple Pb^{2+} sensing based on the turbidity caused during the CaCO_3 precipitation, reaching 1 ppm of detection limit and a lineal response range between 1 and 1000 ppm is obtained when PEI is used as CGM. This detection range is suitable to evaluate levels of metals contamination in industrial waste waters that use to be around 1-100 ppm. Once CaCO_3 NRs are formed the heavy metal removal takes place by adsorption of the EDTA-metal onto their surface. The maximum adsorption capacity for an initial metal contamination of 342 ppm is 240 mg Pb/g NRs for 30 min of treatment time using CaCO_3 -PEI NRs at pH 4. This Pb^{2+} removal capacity reported here is higher than other ones reported before using materials which are not so cheap and environmental friendly as calcite.^{1,15, 38, 39} The introduced calcite NRs formation system can be easily applicated for fast control and

remediation of heavy metals in case of accidents where urgent in-field measurements and remediation are necessary. It represents a low cost alternative for heavy metals detection and removing. In addition, the developed system, that constitutes a novel approach to integrate the detection and removal of chemical contaminants in one step process (*sensoremoval concept*), may open the way to several other simple and efficient systems, materials or methods for environment applications.

V.2 Experimental part

V.2.1 Chemicals

All chemical reagents (analytical grade) were purchased from Sigma Aldrich and used as received. PEI solution in H₂O (50% w/v) (M_w=750000, M_n=60000), diethanolamine (DEA, NH(CH₂CH₂OH)₂) (98%), glycerol (99%) and anhydrous ethylenediaminetetraacetic acid (H₄EDTA) (99%) were used. Milli-Q water (resistivity 18.2 Ω·cm at 25 °C) was obtained from Advantage Milli-Q apparatus (Millipore). All glass material were soaked with aqua regia for 3 h, rinsed with distilled water and dried before use.

V.2.2 Characterization techniques

The syntheses were carried out using an Ultrasons J. P. Selecta 45 ultrasonic bath. SEM images were taken with ZEISS Merlin and Quanta 650FEG scanning electron microscopes. A water dispersion of samples (150 μL) was deposited on glass support and dried at room temperature. Colloidal silver solution was deposited on the edges of the glass for the sample examination. High resolution SEM images were recorded depositing samples on silica support and gold sputtering during 1 min. HRTEM images and the SAED patterns were obtained on TECNAI-F20 microscope with an accelerating voltage of 200 kV. Sample grids were prepared by sonicating powdered samples in milli-Q water for 20 s and evaporating one drop of the suspension onto a carbon-coated holey film supported on a copper grid for TEM measurements. For resolve the SAED patterns Gatan Digital Micrograph and CaRine crystallography programs were used.

XRD studies of CaCO₃ were recorded using a Siemens D-5000 X-ray diffractometer with Cu Kα radiation, scanning rate of 0.02°/s and 2θ range from 10 to 70° at 40 kV and 40 mA. The phase identification was done by comparing the XRD patterns of the crystals with the standard data available from Joint Committee on Powder Diffraction Standards (JCPDS) and Cambridge Structural Database (CSD). The CaCO₃ turbidity

measurements were performed on 2100N turbidimeter. The concentration of Pb^{2+} ions in the aqueous solution was analyzed by using an ICPMS Agilent 7500ce model system. TGA was conducted by a TGA7 Perkin-Elmer with argon flow rate of 20 mL/min and a heating rate of 10 °C/min.

V.2.3 Calcite formation and Pb^{2+} sensing

In a general procedure to obtain CaCO_3 NRs, 5 mL of CaNa_2EDTA (3.3×10^{-1} M) were quickly poured into equal volume of $\text{Pb}(\text{NO}_3)_2$ dissolution (3.3×10^{-1} M) under sonication, before to end this addition was added the Na_2CO_3 dissolution (3.3×10^{-1} M). The reaction vessel was capped and the reaction left for 15 min. The solid obtained was washed three times with milli-Q water through a centrifugation process, air dried and collected for further analysis. The supernatant after the first solid centrifugation was collected, dried, following washed quickly with cool water and dried again. This product that contains the Pb-EDTA synthesized complex was used for further XRD analysis.

In other assays to obtain the CaCO_3 NRs dissolutions of CaNa_2EDTA (3.3×10^{-1} M) prepared with PEI, glycerol or DEA (4 mg/mL) as CGMs were used. The CaNa_2EDTA was prepared by reaction of Na_3HEDTA (4×10^{-1} M) with CaCl_2 (3.3×10^{-1} M). The Na_3HEDTA was previously obtained mixing 1.3 M NaOH with 0.4 M H_4EDTA anhydride. The identification of the Na_3HEDTA and CaNa_2EDTA complexes was realized comparing its XRD patterns obtained experimentally with those corresponding in the CSD.

For obtaining the calibration curve used for Pb^{2+} sensing by turbidity measurement, different suspensions of calcite precipitation were prepared for each point of the curve. Dissolutions of the three reagent components $\text{Pb}(\text{NO}_3)_2$, CaNa_2EDTA and Na_2CO_3 in a range of 1 to 1300 ppm were mixed at the equal volume and concentration for each calcite precipitation suspension. To evaluate the accuracy of this Pb^{2+} sensing method a spike-and-recovery experiment was performed. A known amount of Pb^{2+} is added to the $\text{Pb}(\text{NO}_3)_2$ dissolution that is used to produce CaCO_3 turbidity as described before. The chosen spike concentration range was between 2 and 150 ppm (the low concentrations of the calibration curve). The recovery percent are determinate using the Pb^{2+} concentration obtained through the turbidity calibration curve (calculated) and the prepared known concentration (spike) by the equation:

$$\frac{\text{calculated concentration}}{\text{spike concentration}} \times 100\% = \text{recovery (\%)}$$

V.2.4 Pb²⁺ removal

Adsorption kinetic experiments were carried out to evaluate the Pb²⁺ removal. The CaCO₃ NRs (25 mg) obtained under different conditions were suspended in Na₂PbEDTA solutions (50 mL) with different concentrations (1, 27, 54, 137, 342 ppm) at pH 4 or 6 and stirred during 48 h. Aqueous samples (500 μL) were taken at several time intervals and the concentrations of Pb²⁺ ions were measured by ICP-MS. The amount of Pb²⁺ adsorption onto NRs surface at time interval t, q_t (mg/g), was calculated by:

$$q_t = \frac{(C_o - C_t)}{W} V$$

where C₀ and C_t (mg/L) are the concentrations of Pb-EDTA in liquid phase at initial and any time interval t, respectively, V is the volume of the solution (L) and W is the mass of calcite used as adsorbent (g).

V.3 Results and Discussion

V.3.1 Multifunctional integrated *sensoremoval* system

The synthesis of CaCO₃ NRs using as reagents equal volumes and concentrations of an initial contaminated solution of Pb²⁺, Na₂CaEDTA and Na₂CO₃ permitted to create a multifunctional system that integrates the formation of CaCO₃ NRs for its afterwards use in the detection and removal of the Pb²⁺ in the initial contaminated solution. The reaction of the CaCO₃ formation and a schematic representation of this system operation are displayed in **figure 1**. When into a Pb²⁺ dissolution are poured the Na₂CaEDTA and Na₂CO₃ dissolutions, the Pb²⁺ cations preferentially bind to EDTA ligand releasing Ca²⁺ cations able to react with CO₃²⁻ anions starting in this way the CaCO₃ precipitation. The possible collateral reaction in this system could be the formation of PbCO₃ precipitate, because the PbCO₃ K_{ps} (3.3x10⁻¹⁴) is smaller than CaCO₃ K_{ps} (3.3x10⁻⁹), but given that the Pb-EDTA complex formation constant (1x10¹⁸) is higher than Ca-EDTA constant (5x10¹⁰) all the Pb²⁺ ions form the complex with the EDTA, being the CaCO₃ the only precipitation product. The XRD patterns corresponding to all crystallization products obtained with different reaction conditions demonstrate that calcite is the unique precipitation product. Figure S_1A at SI shows an

example of calcite XRD patterns that were obtained in all cases. While in figure S_1B the XRD pattern obtained from the aqueous medium of the reaction is presented. The peaks in this powder pattern corresponding with those indexed for $\text{Na}_2\text{PbEDTA} \cdot 2\text{H}_2\text{O}$ complex that has been reported in the CSD.⁴⁰

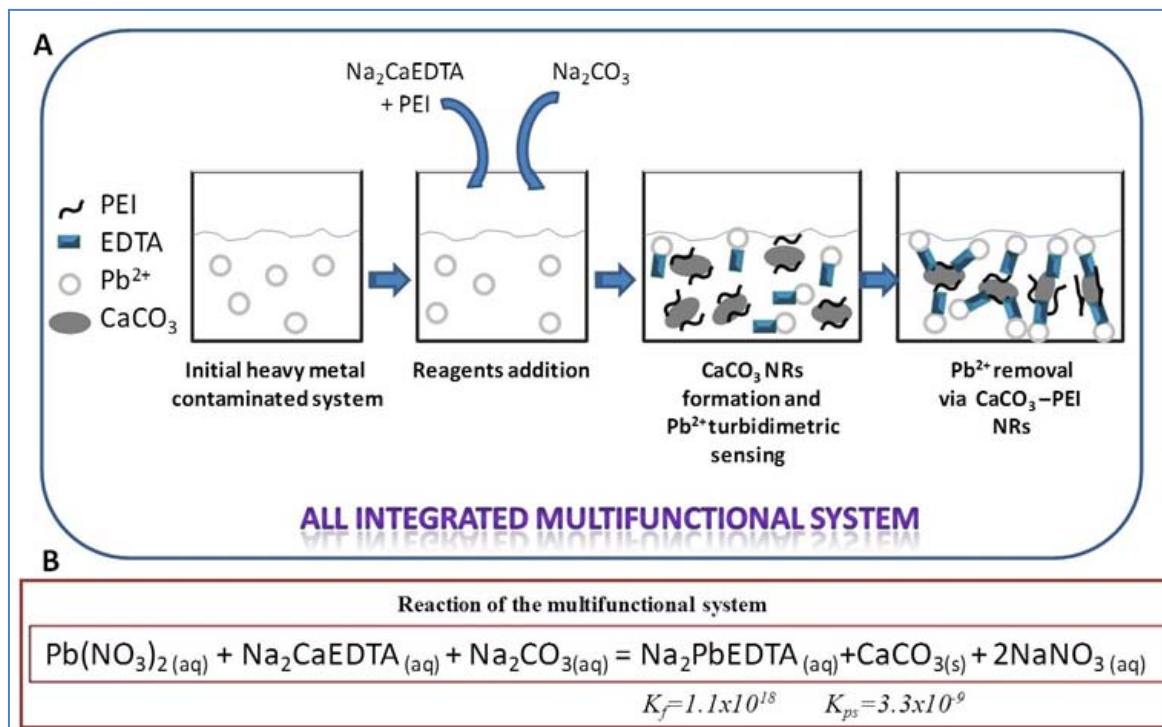


Figure 1. (A) Pb^{2+} sensor-removal (sensing and removing) principle based on the formation of the CaCO_3 -PEI NRs absorbent material. (B) Reaction of the proposed CaCO_3 crystallization process.

V.3.2 Characterization of the CaCO_3 crystallization product in the proposed system.

Morphologic analysis demonstrated that NRs-like structures form the crystallization product (**figure 2 A and B**). Although NRs-like shape has been synthesized before,^[20, 21] it still represents an unusual morphology in the CaCO_3 crystallization product. Usually the calcite polymorph can crystallize in rhombohedral shape, while vaterite polymorph usually aggregate into spherical particles. Other polymorphic shapes use to be difficult to be obtained, offering few repeatability and high susceptibility to changes in the reaction conditions. However, these calcite NRs with sizes of around 2, 1 or 0.6 μm , depending on the type of reaction, were permanently synthesized changing the reagents order, using or not CGMs as PEI, DEA or glycerol, modifying the solvent used as reaction medium (ethanol, ethylacetate, etc), the use of $\text{Ca}(\text{NO}_3)_2$ instead of CaCl_2 or decreasing the reaction volumes. All these large variety of changes in the reaction

conditions only affect the size or the surface texture of the NRs or as much the shape at the ends of the NRs, but the main rod shape continually persists in the crystallization product (figure_S2 at SI). The persistent formation of structures with rods-like shape in spite of the changes applied in the reaction conditions is ascribed to the fact that, Na₂CaEDTA in addition to be the reagent that supplies the Ca²⁺ cations is also the CGM that determines the crystallization process due to its high concentration in the system.

Nevertheless, a dramatic decreasing in the concentration of the reagents used in this reaction system produces large morphological changes with reduction of the size and variation of shape in the structures. A large decreasing in the reagents concentration guides to the small elemental structures that are making of the rods, which is related with the fact that at low concentrations there is not enough mass to favour their extensive growth. In this way, the formed precipitate can pass from rods-like structures, of around 2, 1 or 0.6 μm length and 350-450 nm width using 3.3x10⁻¹ M of reagents concentration, (figure 2, A-D) to perfect size and homogeneous calcite hexagonal nanoplates of around 450-550 nm length and 50-70 nm width (figure 2 E and G) or heterogeneous calcite nanoplates of around 150-250 nm length and 20-40 nm width (figure 2 F and H) using 3.3x10⁻⁴ M of reagents concentration. These results suggest that the initial NRs synthesized using 3.3x10⁻¹ M of reagents are obtained as consequence of a self assembly process of hexagonal or irregular plate-like nanoparticles.

More detailed information of the hexagonal plates is provided by figure 2 I-K with the SAED, TEM and HRTEM analyses. The figure 2I displays the SAED corresponding to the selected area taken from the single hexagonal plate that is shown in figure 2J. Reflections A, B, C, D and E correspond to Miller indices and measured d spacing of (1 -2 0), (2.54 Å), (-1 -1 0) (2.51 Å), (-2 1 0) (2.49 Å), (-1 2 0) (2.53 Å) and (0 -3 0) (1.45 Å) respectively; measured interplanar angles: A[^]B=60.0°, A[^]C=119.35°, A[^]D=179.35°. This ED pattern can be indexed as calcite single crystal (R-3c space group) viewed from the [001] zone axis. The corresponding HRTEM image (figure 2-K) is mainly composed of (1 1 0) plane of calcite with d spacing of about 0.25 nm indicating that the nanoparticles are formed along the (1 1 0) direction. The arrows in figure 2K show the formation of amorphous CaCO₃ nanoparticles indicating that our calcite hexagonal plates are in fact mesocrystal. These hexagonal plates-like structures have been reported before for vaterite polymorph [18, 22, 24, 25] but for first time perfect hexagonal plates are observed in calcite phase.

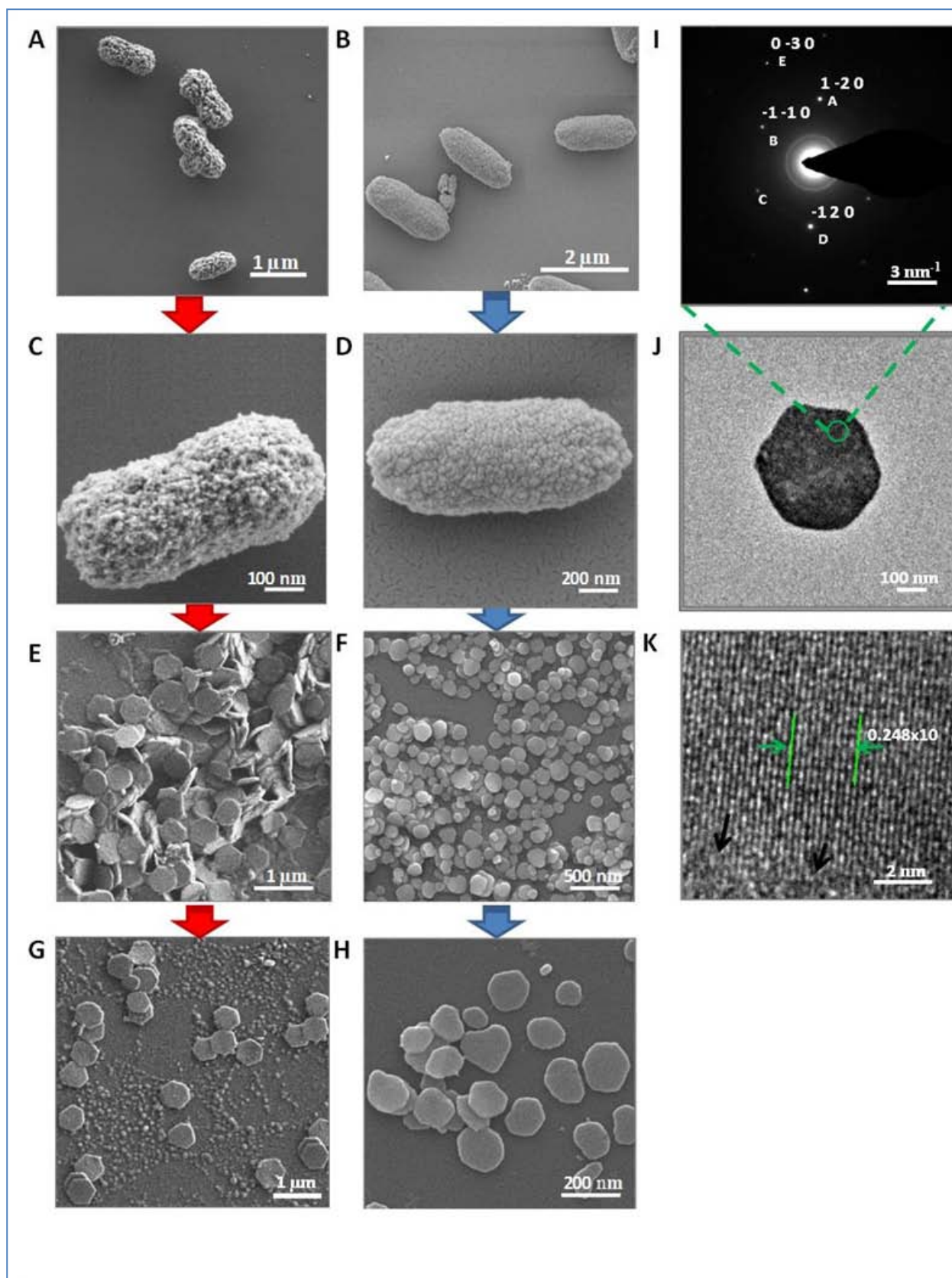


Figure 2. (A-H) SEM images of the CaCO₃ crystallization product synthesized under different reaction conditions. (A and B) Mixing 3.3×10^{-1} M of Pb(NO₃)₂, CaNa₂EDTA and NaNO₃ solutions with 4mg/mL

PEI as CGM (A) and without the use of CGM (B). (C and D) Close up each one of the structures obtained before. (E and F) Structures obtained mixing 3.3×10^{-4} M of $\text{Pb}(\text{NO}_3)_2$, CaNa_2EDTA and NaNO_3 solutions, (E) using 4mg/mL PEI as CGM homogeneous hexagonal plates like structures are obtained, (F) without the use of CGM heterogeneous plates are obtained. (G and H) Close up each one of the structures obtained before. (I-L) SAED, TEM and HRTEM images of the hexagonal plates obtained mixing 3.3×10^{-4} M of $\text{Pb}(\text{NO}_3)_2$, CaNa_2EDTA /4mg/mL PEI and NaNO_3 solutions. (I and K) ED data corresponding to the superposition of several single crystals and just single crystal, respectively. (J) TEM image of single hexagonal plate. (K) HRTEM image taken from a part of calcite hexagonal plate with resolved (1 1 0) planes ($d=0.25$ nm).

A possible explanation for the entire crystallization process that happens here is to consider that the proposed reactions constitute a self-reagent-delivery system, because while Ca^{2+} cations are being displaced by Pb^{2+} cations in the Na_2CaEDTA complex, the CO_3^{2-} anions are being added forming the first CaCO_3 nucleation centers. In the initial stages of crystallization when Ca^{2+} ions are being delivered by Pb^{2+} ions in the Na_2CaEDTA complex, a $\text{Ca-Na}_2\text{EDTA-Pb}$ unstable intermediate complex, which keeps associated Ca^{2+} to Na_2PbEDTA as a first nucleation center for further addition of CO_3^{2-} anions, could appear (figure_S3-A). Once the Na_2PbEDTA complex is formed the Ca^{2+} can interact with the nucleophilic carboxylic acid groups of Na_2PbEDTA creating several local CaCO_3 nucleation centers by Ca^{2+} local supersaturation (figure_S3-B1). Several CaCO_3 nucleation clusters lead to the formation of the primary CaCO_3 nanoparticles. At this moment the primary plate-like crystals start growing by aggregation of the nearly CaCO_3 nanoparticles in a preferential y -axis (figure_S3-C1). These primary plates-like crystals are temporally stabilized by metal-organic coating layer (Na_2PbEDTA). This stabilizer acts as building blocks in a spontaneous self-assembling process into preferential x -axis. Several plate-like crystals grow in a self-assembly process of multiple plates propitiated by the interaction with the carboxyl acid groups of Na_2PbEDTA that could be preferentially adsorbed onto the growing crystal surfaces parallel to y -axis and grow along x -axis crystallographic direction during the crystallographic process, resulting in a rod-like primary crystal (figure_S3-D1). The figure_S3-E1 shows a close up of the NRs surface obtained without PEI that suggests, that microrods are composed by assemble of thin nanostructures (20-40 nm) like-plate along the x axis.

J. Yu et al.²⁰ explained microrods formation shape taking into account the rate of nucleation and growth through certain direction. They explained that when the rate of

nucleation and growth if preferentially directed along the rod axes at the side-surfaces the rod-like shape is formed.

If PEI is added to initial Na_2CaEDTA reagent solution, the effect of formation of the local nucleation centers by Ca^{2+} supersaturation is increased. Under PEI presence when Ca^{2+} is delivered by Pb^{2+} from the Na_2CaEDTA complex, it is bound by the nucleophilic nitrogen (or cations captor nitrogen) of the amino group of PEI polymer, which creates additional nucleation centers of those created by Na_2PbEDTA (figure_S3-B2). Consequently, more CaCO_3 nanoparticles appear with the subsequence directional aggregation in primary hexagonal plate crystals (figure_S3-C2). Differently with the Na_2PbEDTA stabilizer, the PEI coating layer persists onto the surface of the primary hexagonal plate crystals, allowing better organization during the self-assemble of these small primary nanocrystals through a more oriented-attachment mechanism, in which the adjacent nanocrystals are self-assembled sharing a common crystallographic orientation process (figure_S3-D2). The final result is a more ordered structure with high porous surface than without PEI (figure-2 C). The figure_S3-E2 shows a close up of the NRs surface obtained with PEI that suggests, that microrods are composed by assemble of thin nanostructures (50-70 nm) like- hexagonal plate along the x axis. The presence of PEI in the CaCO_3 structure was demonstrated in the thermogravimetric analysis plotted in figure_S4 at SI. The weight loss of about 3% that appears in the temperature range of 250-350 °C corresponds to PEI delivery from CaCO_3 structure and therefore that the CaCO_3 -PEI hybrid material has been synthesized.

In general, it seems that the use of Na_2CaEDTA and the delivering of Ca^{2+} ions through Pb^{2+} ions are determining the shape of the calcite product in the majority of the reactions. While few works have already reported the use of EDTA in the CaCO_3 crystallization process and in these cases the EDTA is used only as CGM,⁴¹ it is the first time that EDTA is also used as Ca^{2+} reagent-delivery through Pb^{2+} and Na_2CaEDTA solutions.

V.3.3 Pb^{2+} sensing by changes of turbidity during the calcite precipitation.

The Pb^{2+} concentration can be detected through the turbidity produced during calcite precipitation. In the described system Pb^{2+} cations present in the dissolution displace the Ca^{2+} cations from its Na_2CaEDTA complex and in consequence these Ca^{2+} cations remain free to bind with the CO_3^{2-} anions. A quantitative relation $1\text{Pb}^{2+}:1\text{Ca}^{2+}$, between each Ca^{2+} cation that form CaCO_3 precipitate and each Pb^{2+} cation that remains bound

with EDTA, can be established. In this way, the CaCO_3 turbidity can be related with the Pb^{2+} concentration when there is not other metal present in the system.

Between the assayed systems only adding PEI to the previous Na_2CaEDTA solution to obtain calcite NRs, a visible turbidity produced by calcite precipitation, is reached up to around 34 ppm of Pb^{2+} mixing 1.6×10^{-4} M of reagents concentration. While without or with the use of other CGMs a visible turbidity is reached until around 68 ppm of Pb^{2+} mixing 3.3×10^{-4} M of reagents concentration. It suggests that the use of PEI notably increases the CaCO_3 precipitation which gives more sensibility for Pb^{2+} detection.

Figure 3A shows photos of the suspensions formed by CaCO_3 precipitation obtained for different Pb^{2+} concentrations using PEI as modifier agent. An estimation of Pb^{2+} concentration even at naked eye can be made by turbidity observation until 34 ppm.

Photos of the turbidity produced by CaCO_3 precipitation, when the reagents concentration decreases, are shown in Figure_S5. The turbidity produced by decreasing the reagent concentration was evaluated making comparison tests with the traditional CaCO_3 precipitation reaction and the proposed CaCO_3 precipitation system with and without PEI use. The turbidity was observed by naked eye until 3.3×10^{-3} M of the reagents concentrations (that correspond to 684 ppm of Pb^{2+}) when simple CaCl_2 and NaCO_3 solutions are mixed (figure_S5-A). When PEI is present in the initial CaCl_2 solution the observed turbidity at 3.3×10^{-3} M is more significant than in the previous case (without PEI in the initial CaCl_2 solution) and can be observed by naked eye until around 342 ppm of Pb^{2+} (figure_S5-B). When the reaction to obtain CaCO_3 precipitate is the system based in the mixture of $\text{Pb}(\text{NO}_3)_2$, Na_2CaEDTA and Na_2CO_3 , then the visual CaCO_3 turbidity reaches 3.3×10^{-4} M in reagents concentration (that correspond to around 68 ppm of Pb^{2+}) (figure_S5-C). Using this same system when PEI is present in the Na_2CaEDTA solution the observed turbidity is more marked at 3.3×10^{-4} M than in the previous case, reaching visibility by naked eye until 1.6×10^{-4} M in reagents concentration (that corresponds to 34 ppm of Pb^{2+}) (figure_S5-D).

The CaCO_3 -PEI NRs formation in presence of Pb^{2+} concentration inferior to 34 ppm can be detected by use of a turbidimeter. In the figure 3B the calibration curve between the Pb^{2+} concentration and the CaCO_3 turbidity is presented. The lineal range from 1 to 1000 ppm is obtained, being 1 ppm the lowest Pb^{2+} concentration detected by CaCO_3 formation over the measured signal blank. A mixture of the Na_2CaEDTA and $\text{Pb}(\text{NO}_3)_2$ disolutions (1 ppm) whose turbidity response was similar to the Milli-Q water was used as blank. The lowest Pb^{2+} concentration detected by CaCO_3 turbidity formation depend

on the characteristic turbidimeter and the concentrations of Ca^{2+} and CO_3^{2-} in the aqueous phase of the studied system. The insert in the figure 3B shows the graphic obtained during the accuracy assay plotting the spiked vs. calculated concentrations. The slope and the intercept values of the fitting curve are not significantly different from theoretical values of 1 and 0, respectively. It means that the spiked and calculated concentrations are very close to each other and the recovery is almost 100% in the concentration interval from 2 to 150 ppm.

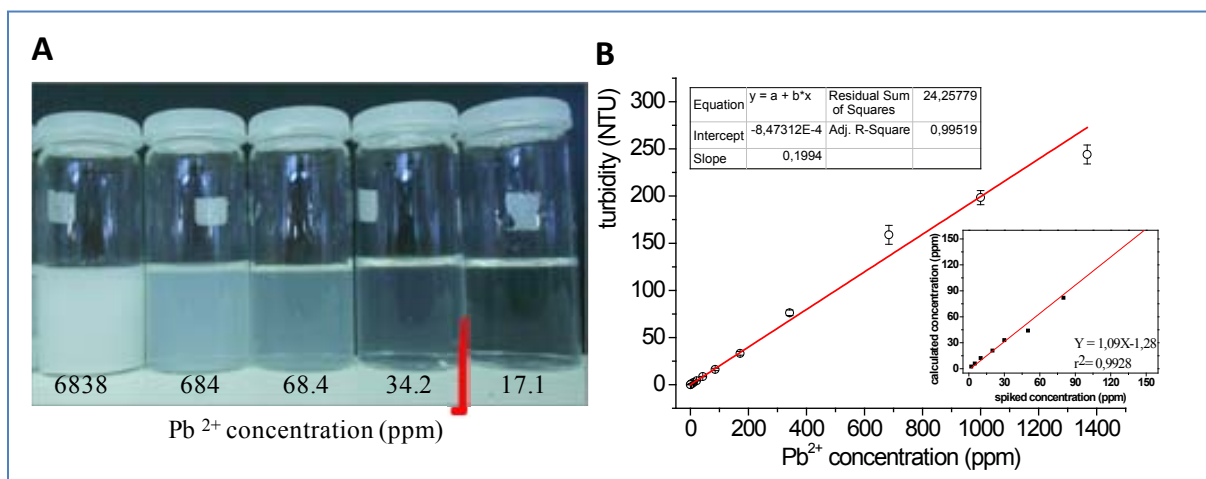


Figure 3. Pb^{2+} sensing by changes in the turbidity during calcite precipitation. (A) Pb^{2+} detection by naked eye through the turbidity produced in the CaCO_3 precipitation. (B) Correlation between the turbidity produced in the CaCO_3 precipitation and Pb^{2+} concentration. The insert graph corresponds to the plotting of the accuracy assay results.

V.3.4 Pb^{2+} removal via CaCO_3 -PEI NRs.

After the CaCO_3 -PEI NRs formation, the initial Pb^{2+} cations in the contaminated solution remain as Na_2PbEDTA complex. This transformation of Pb^{2+} cations into Na_2PbEDTA complex, although becomes harmless the Pb^{2+} contaminant, makes difficult the Pb^{2+} removal due to the high stability constant between the Pb^{2+} and EDTA ligand, so that, the contaminant would have to be removed as Na_2PbEDTA complex. In this situation, the type of CGM used in the crystallization process, which covers the NRs surface, plays an important role in the removal process. The adsorption rate experiments carried out demonstrate that the best Pb^{2+} removal capacity was obtained using CaCO_3 -PEI NRs in comparison to those obtained under the same conditions but using NRs synthesized without CGM or using CGMs as glycerol or DEA (**figure 4A**). Figure 4A shows that the maximum adsorption capacity of an initial Na_2PbEDTA dissolution of 342 ppm at pH 4 for CaCO_3 -PEI, CaCO_3 -glycerol, CaCO_3 -DEA and CaCO_3 NRs is respectively of 240, 126, 120 and 70 mg/g and that 30 min are enough to

reach the maximum removal capacity in all the cases. The maximum adsorption capacity of 240 mg Pb/g CaCO₃-PEI NRs is higher than other ones previously reported.^[1, 15, 38, 39] The experiments demonstrate that when the removal process is carried out at pH 6, the adsorption capacity decreases in relation to that achieved at pH 4, as is shown in figure 4A with the curves labelled with the blue circle. Experiments (not shown here) demonstrated that initial concentrations of 2, 27, 54 and 137 ppm are almost declined to 0 in 30 min at pH 4 under the experimental condition used here. The Pb²⁺ removal process takes place just at superficial level due to the fact that the EDTA binds to Pb²⁺ keeping it trapped in a complex. The complex formation between Pb²⁺ and EDTA avoids substitutions of Ca²⁺ in the calcite structure by Pb²⁺ cations in a new recrystallization process as occurs in other reported works where Pb²⁺ is directly removed using other CaCO₃ materials.^[11,18] In figure _S6 images SEM recorded after 48 h of the Pb²⁺ removal process indicate that the morphology of calcite NRs remain stable.

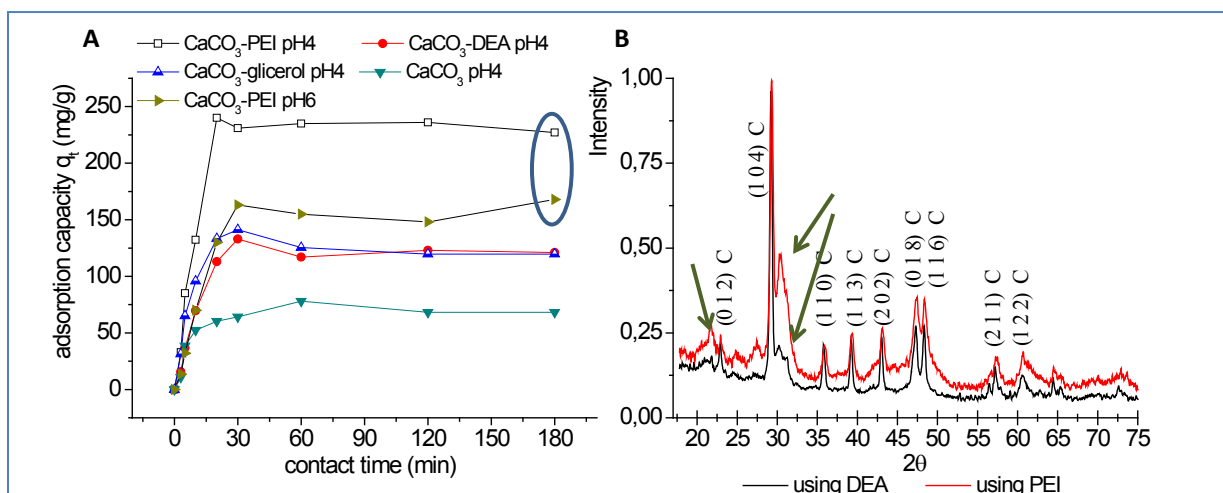


Figure 4. PbNa₂EDTA removal. (A) Adsorption kinetic curves for PbNa₂EDTA solutions (342 ppm) at pH 4 using the NRs obtained without or with different CGMs. The cases labelled with the circle correspond to the same experiment at different pH. (B) XRD patterns of the powder obtained after the removal process corresponding to 48 h of contact time (the C label denotes calcite phase and the green arrows denote the new phase corresponding to Pb²⁺ removal from dissolution as EDTA complex).

The better removal of Na₂PbEDTA complex using calcite NRs modified with PEI with respect to the other NRs synthesized here is related with two factors. First, the NR surface obtained using PEI is more porous in relation to NR surface obtained without PEI presence (as seen in figure 2_C y D), which increases the contact surface for the adsorption/removal process. Second, PEI is a branched polymer that contains large

numbers of amino groups that present basic nitrogens atoms that act as hydrogens captors which are expected to undertake interactions with the hydroxylic groups of the Na_2PbEDTA complex through hydrogen bonds formation. When the medium is more acidic these hydrogen bond interactions are intensified by the protonation of some PEI nitrogens or the carbonylic oxygens in the Na_2PbEDTA arising new hydrogen bonds.

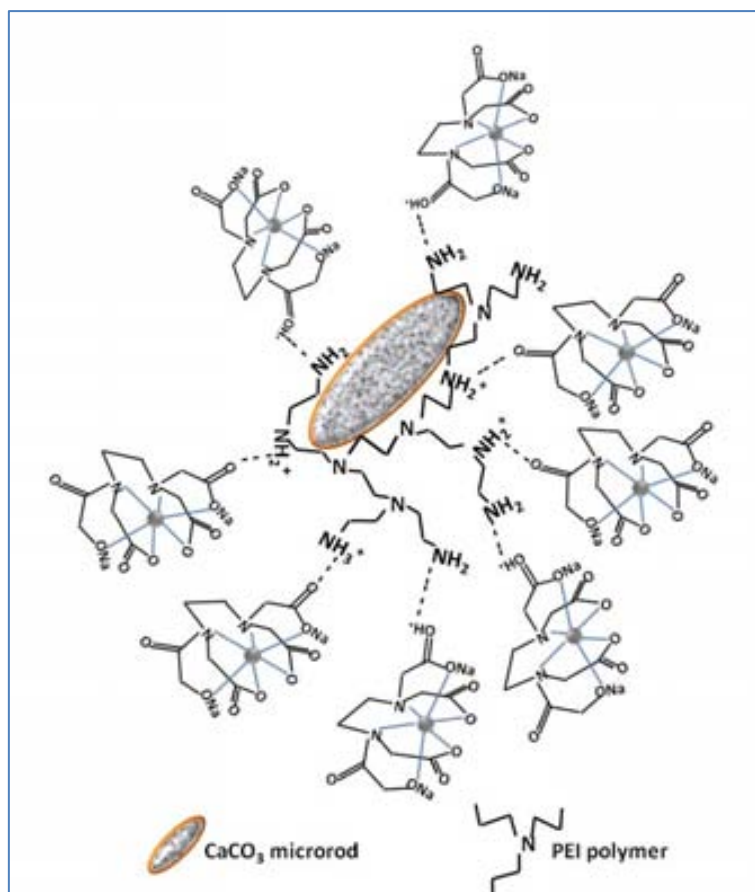


Figure 5. Schematic representation of the hydrogen bonds interactions between PbNa_2EDTA and PEI polymer onto NRs surface. The possibility of protonation of the amino and carboxylic groups increases at more acid pH which allows new hydrogen bond interactions, intensifying the adsorption of the Pb^{2+} complex onto NRs surface.

These new hydrogen bonds are produced by the interaction between the protonated carbonylic oxygen ($=\text{OH}^+$) with the nitrogen amino in PEI or by the interaction between the protonated nitrogen in amino PEI ($-\text{NH}_3^+$) with the carbonylic oxygens in Na_2PbEDTA (**figure 5**). This explains the better removal that occurs at pH 4 than pH 6, because at acid pH the hydrogen bond interactions between Na_2PbEDTA and PEI are increased. In figure 4B, the XRD pattern of the calcite powder after being used in the Pb^{2+} removal process can be seen. The raised peaks at 21.7 , 25.0 , 27.4 and 30.2° can be

associated with peaks in the Na₂PbEDTA powder XRD pattern, which suggests that Na₂PbEDTA complex is adsorbed onto calcite-PEI NRs surface.

The multifunctional integrated system described here could be easily extended to other contaminated solutions with heavy metals (that have EDTA complex formation constant higher than Ca²⁺ such as Cd²⁺, Hg²⁺, Ni²⁺, Zn²⁺ and Cu²⁺) having only one metal contaminant, by synthesizing new advanced CaCO₃ materials with more complex crystalline structure and their further use as sensoremoval platforms. As this sensoremoval system is not specific, in the case of a multi-metal contamination the turbidity by CaCO₃ precipitation could be correlated with the total metal concentration. The sensing and removal capability of this novel nanostructured platform could lead to the next generation of environment ‘sensoremoval’ systems in the same way as in health applications, theranostic joins in the same platform diagnostic and therapy offering new opportunities in patient treatment. The introduction of this low cost and efficient alternative as ‘sensoremoval’ system may be useful for fast control and remediation of pollution where urgent in-field monitoring and immediate remediations are necessary.

V.4 Conclusions

A new and simple strategy based on calcite NRs formation for *sensoremoval* (sensing and removing) of Pb²⁺ from wastewater is presented. We propose a novel multifunctional system that integrates three process, the *in situ* formation of the CaCO₃ NRs from Pb²⁺ contaminated initial solution, Na₂CaEDTA complex and CO₃²⁻ anions, followed by the utilization of the as-synthesized particles as sensing and adsorbing material of Pb²⁺. To the best of our knowledge, for the first time the detection and removing of chemical contaminant are integrated in the same system.

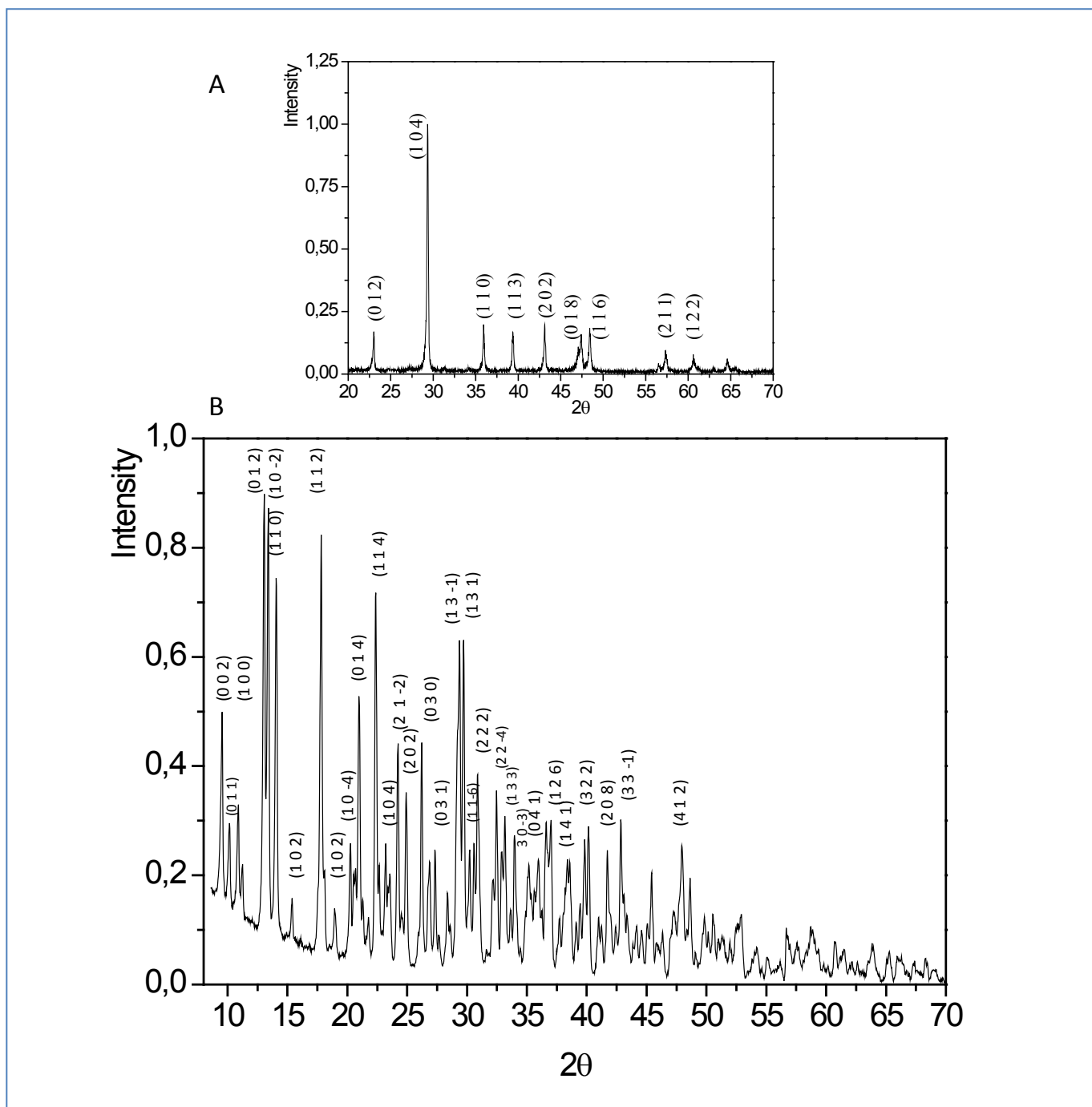
By decreasing the reagents concentration homogeneous and perfect hexagonal plates for calcite, never reported so far, were obtained for this polymorphic phase.

With the simple Pb²⁺ sensing strategy introduced here, via changes in turbidity during the CaCO₃ precipitation, until 34 ppm of Pb²⁺ can be estimated by naked eye and a concentration range from 1 to 1000 ppm can be quantified using a turbidimeter. This quantification range is suitable to evaluate levels of metals contamination in industrial waste waters that use to be around 1-100 ppm. On the other hand, in adsorption kinetic studies for calcite-PEI NRs, also without precedents, the maximum adsorption capacity reached in 30 min at pH 4 was 240 mg Pb²⁺/g of NRs obtained using PEI. The

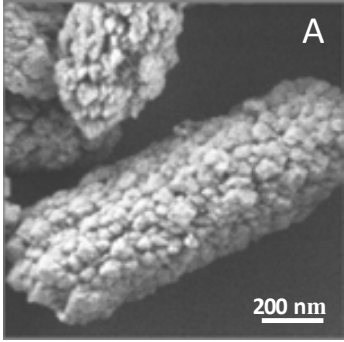
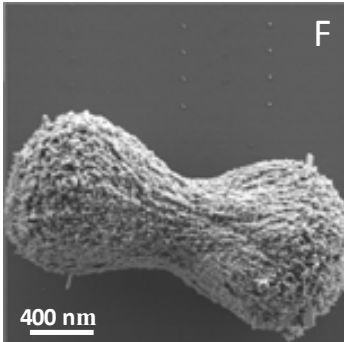
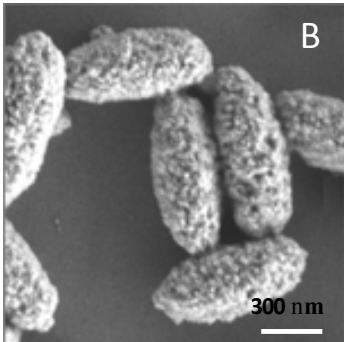
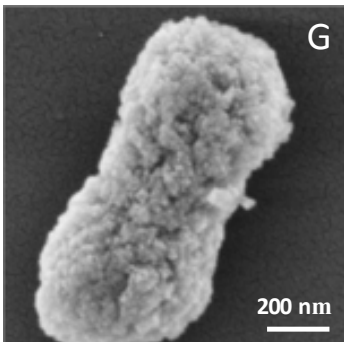
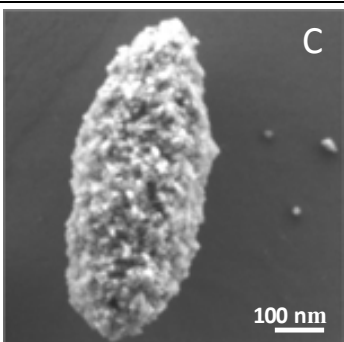
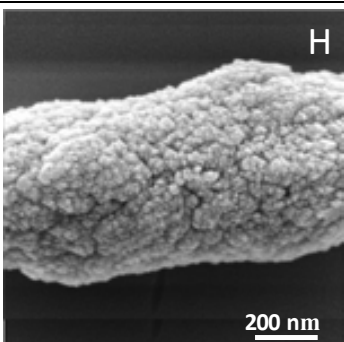
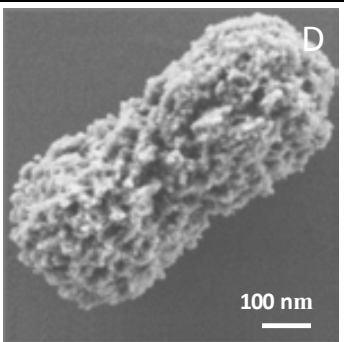
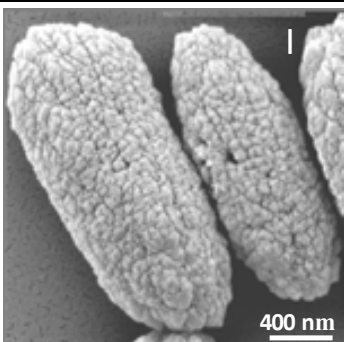
maximum removal capacity reported here for Pb^{2+} is higher than other reported before using materials which are not so cheap and environmental friendly as calcite.

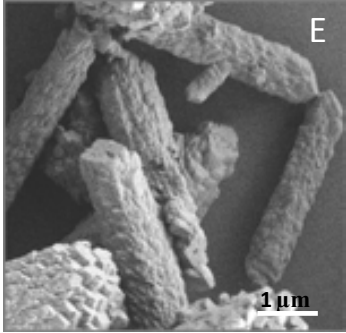
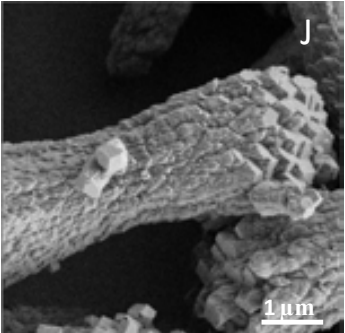
It is important to highlight that the PEI used as CGM allowed to improve the Pb^{2+} LoD by increasing of the CaCO_3 precipitation and the turbidity produced during this precipitation, as well as, permitted to achieve better Na_2PbEDTA adsorption and removal through the obtaining of more porous NRs surface. In addition PEI enhances the removal process offering the appropriate chemical modification onto the NR surface to favour the interaction of this with the Na_2PbEDTA complex by via of hydrogen bond formation.

V.5 Supporting Information



Figure_S1. XRD patterns of calcite polymorph phase (A) and the $\text{Na}_2\text{PbEDTA}\cdot 2\text{H}_2\text{O}$ complex (B). The XRD pattern shown in (A) exhibits sharp reflections corresponding to the (0 1 2), (1 0 4), (1 1 0), (1 1 3), (2 0 2), (0 1 8), (1 1 6), (2 1 1) and (1 2 2) crystallographic planes of calcite, the most stable polymorph of CaCO_3 . The XRD pattern displayed in (B) exhibits the peaks corresponding with $\text{Na}_2\text{PbEDTA}\cdot 2\text{H}_2\text{O}$ (P21/c) indexed in CSD.⁴⁰

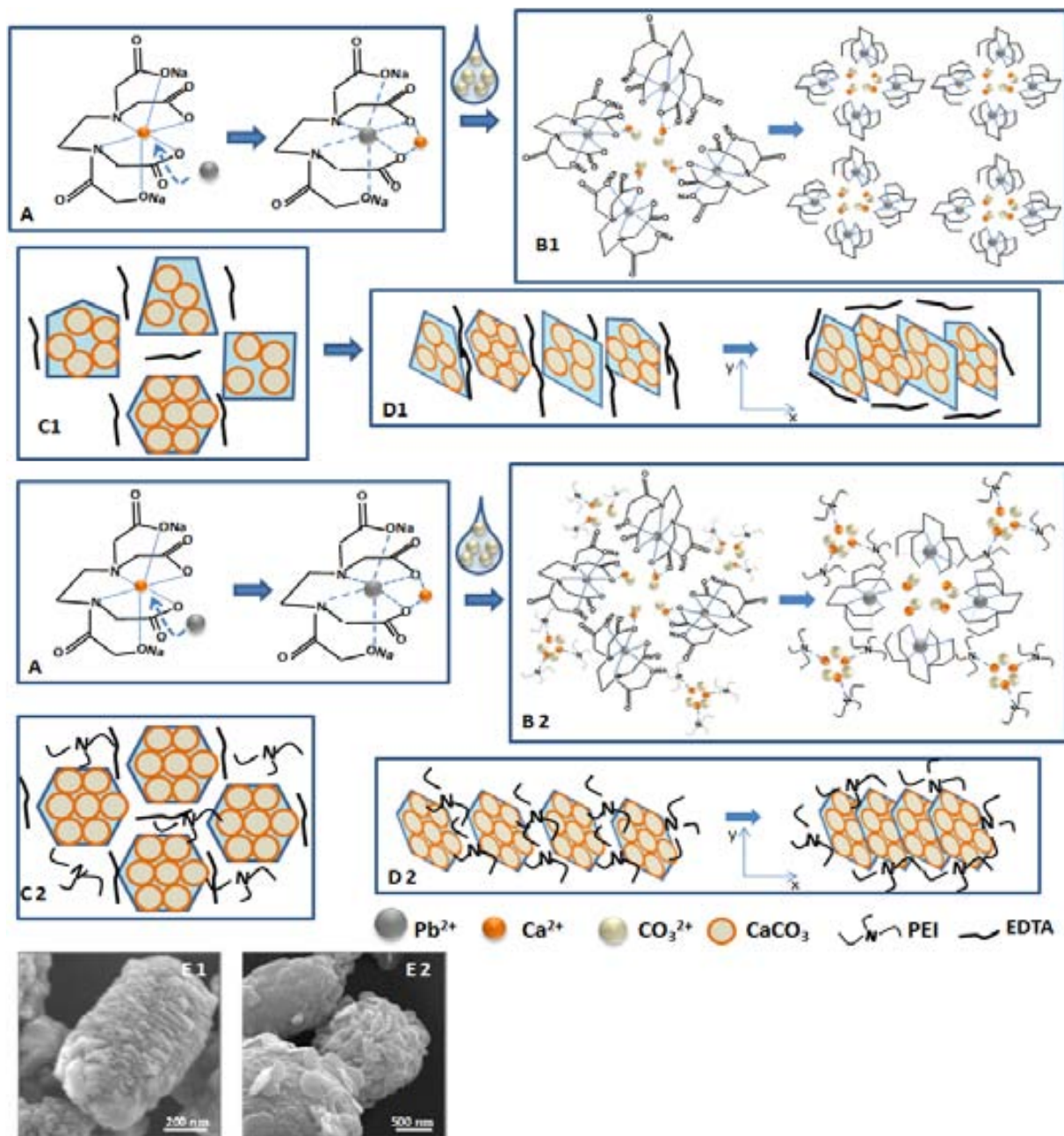
Reaction conditions and type of assay	SEM view and structure average size [μm]	Reaction conditions and type of assay	SEM view and structure average size [μm]
$\left[\frac{0.33\text{M CaCl}_2 + 0.4\text{M Na}_3\text{EDTA}}{5\text{mL H}_2\text{O}} \right]$ $+ \left[\frac{0.33\text{M Pb(NO}_3)_2}{5\text{mL H}_2\text{O}} \right]$ $+ \left[\frac{0.33\text{M Na}_2\text{CO}_3}{5\text{mL H}_2\text{O}} \right]$ <p>Assay 1-A</p>	 <p>1.16 \pm 0.41</p>	$\left[\frac{0.33\text{M CaCl}_2 + 0.4\text{M Na}_3\text{EDTA}}{2\text{mL H}_2\text{O}} \right]$ $+ \left[\frac{0.33\text{M Pb(NO}_3)_2}{2\text{mL H}_2\text{O}} \right]$ $+ \left[\frac{0.33\text{M Na}_2\text{CO}_3}{2\text{mL H}_2\text{O}} \right]$ <p>Assay 1-E</p>	 <p>1.19 \pm 0.42</p>
$\left[\frac{0.33\text{M CaCl}_2/\text{PEI} + 0.4\text{M Na}_3\text{EDTA}}{5\text{mL H}_2\text{O}} \right]$ $+ \left[\frac{0.33\text{M Pb(NO}_3)_2}{5\text{mL H}_2\text{O}} \right]$ $+ \left[\frac{0.33\text{M Na}_2\text{CO}_3}{5\text{mL H}_2\text{O}} \right]$ <p>Assay 1-B</p>	 <p>0.62 \pm 0.06</p>	$\left[\frac{0.3\text{M CaCl}_2/\text{PEI} + 0.4\text{M Na}_3\text{EDTA}}{2\text{mL H}_2\text{O}} \right]$ $+ \left[\frac{0.33\text{M Pb(NO}_3)_2}{2\text{mL H}_2\text{O}} \right]$ $+ \left[\frac{0.33\text{M Na}_2\text{CO}_3}{2\text{mL H}_2\text{O}} \right]$ <p>Assay 1-B-E</p>	 <p>1.11 \pm 0.25</p>
$\left[\frac{0.33\text{M CaCl}_2 + 0.4\text{M Na}_3\text{EDTA}}{5\text{mL H}_2\text{O} + 2\text{mL ethylacetate}} \right]$ $+ \left[\frac{0.33\text{M Pb(NO}_3)_2}{5\text{mL H}_2\text{O}} \right]$ $+ \left[\frac{0.33\text{M Na}_2\text{CO}_3}{5\text{mL H}_2\text{O}} \right]$ <p>Assay 1-C</p>	 <p>0.65 \pm 0.18</p>	$\left[\frac{0.33\text{M CaCl}_2 + 0.4\text{M Na}_3\text{EDTA}}{2.5\text{mL H}_2\text{O} + 2.5\text{mL ethanol}} \right]$ $+ \left[\frac{0.33\text{M Pb(NO}_3)_2}{5\text{mL H}_2\text{O}} \right]$ $+ \left[\frac{0.33\text{M Na}_2\text{CO}_3}{5\text{mL H}_2\text{O}} \right]$ <p>Assay 1-C</p>	 <p>1.02 \pm 0.31</p>
$\left[\frac{0.33\text{M CaCl}_2/\text{PEI} + 0.4\text{M Na}_3\text{EDTA}}{5\text{mL H}_2\text{O} + 2\text{mL ethylacetate}} \right]$ $+ \left[\frac{0.33\text{M Pb(NO}_3)_2}{5\text{mL H}_2\text{O}} \right]$ $+ \left[\frac{0.33\text{M Na}_2\text{CO}_3}{5\text{mL H}_2\text{O}} \right]$ <p>Assay 1-B-C</p>	 <p>0.63 \pm 0.11</p>	$\left[\frac{0.33\text{M Pb(NO}_3)_2}{5\text{mL H}_2\text{O}} \right] +$ $\left[\frac{0.3\text{M CaCl}_2/\text{gly} + 0.4\text{M Na}_3\text{EDTA}}{5\text{mL H}_2\text{O}} \right]$ $+ \left[\frac{0.33\text{M Na}_2\text{CO}_3}{5\text{mL H}_2\text{O}} \right]$ <p>Assay 2-B</p>	 <p>1.80 \pm 0.30</p>

Reaction conditions and type of assay	SEM view and structure average size [μm]	Reaction conditions and type of assay	SEM view and structure average size [μm]
$\left[\frac{0.33\text{M Ca(NO}_3)_2 + 0.4\text{M Na}_3\text{EDTA}}{5\text{mL H}_2\text{O}} \right]$ $+ \left[\frac{0.33\text{M Pb(NO}_3)_2}{5\text{mL H}_2\text{O}} \right]$ $+ \left[\frac{0.33\text{M Na}_2\text{CO}_3}{5\text{mL H}_2\text{O}} \right]$ <p>Assay 1-D</p>	 <p>3.43 ± 0.51</p>	$\left[\frac{0.33\text{M Ca(NO}_3)_2 + 0.4\text{M Na}_3\text{EDTA}}{2\text{mL H}_2\text{O}} \right]$ $+ \left[\frac{0.33\text{M Pb(NO}_3)_2}{2\text{mL H}_2\text{O}} \right]$ $+ \left[\frac{0.33\text{M Na}_2\text{CO}_3}{2\text{mL H}_2\text{O}} \right]$ <p>Assay 1-D-E</p>	 <p>5.42 ± 0.52</p>

Figure_S2. Effect of different reaction conditions on the calcite morphology. [1], pouring Pb^{2+} and CO_3^{2-} solutions over CaNa_2EDTA solution; [2], pouring CaNa_2EDTA and CO_3^{2-} solutions over Pb^{2+} solution; [A], without use of CGM; [B], with the use of CGM; [C], using mixed solvents; [D], using $\text{Ca(NO}_3)_2$ as source of Ca^{2+} cations, [E], decreasing the reagents volume.

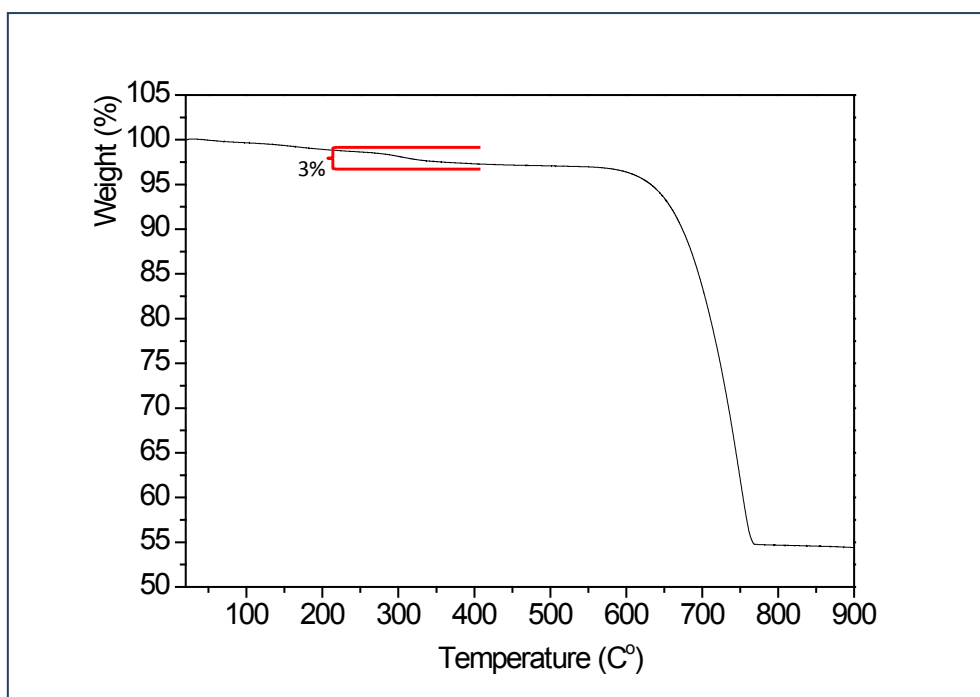
The analysis of the morphology of the product obtained under different changes in the reaction conditions guides to some regularity of behavior for the shape and the surface of the calcite product produced and the applied reaction condition. In first place, rod-like shapes are always obtained using 3.3×10^{-1} M of the basis mixture of CaNa_2EDTA , $\text{Pb(NO}_3)_2$ and NaNO_3 . In second place, the reagents addition order ($\text{CaNa}_2\text{EDTA} + \text{Pb(NO}_3)_2 + \text{NaNO}_3$ or $\text{Pb(NO}_3)_2 + \text{CaNa}_2\text{EDTA} + \text{NaNO}_3$) don't affect the product as view in SEM images of the figure 2B and figure_S2-A or figure 2A and figure_S2-B. The addition of PEI in the original Ca^{2+} solution conduces to microrods with high porous surface and rounded to the ends as shown in figure_S2-B, D and G. While those obtained without CGM (figure_S2-A) or with other CGM as ethanol (figure_S2-H) or glycerol (figure_S2-I) don't present a high porous surface. In the same way, the use of water/ethylacetate as mixed solvents produces high porous surface microrods but with sharp ends (figure_S2-C) and when PEI is introduced in this system the ends of this microrods became in rounded ends (figure_S2-D). The substitution of CaCl_2 by $\text{Ca(NO}_3)_2$ to produce CaNa_2EDTA leads to microrods compound of perfect nanocubes typical of calcite phase. Finally the diminution of the reaction volume from 15 to 7 mL produces the dumbbell-like shape structures (figure_S2-F, G and J). The dumbbell-like shape structure has been reported before by J. Yu *et al.*²⁰ They explain the dumbbell shape in terms of nucleation and growth stimulated at the both ends of the rod-like

primary crystals along electric field lines further than the nucleation and growth on the side-surfaces of rod-like primary crystals.

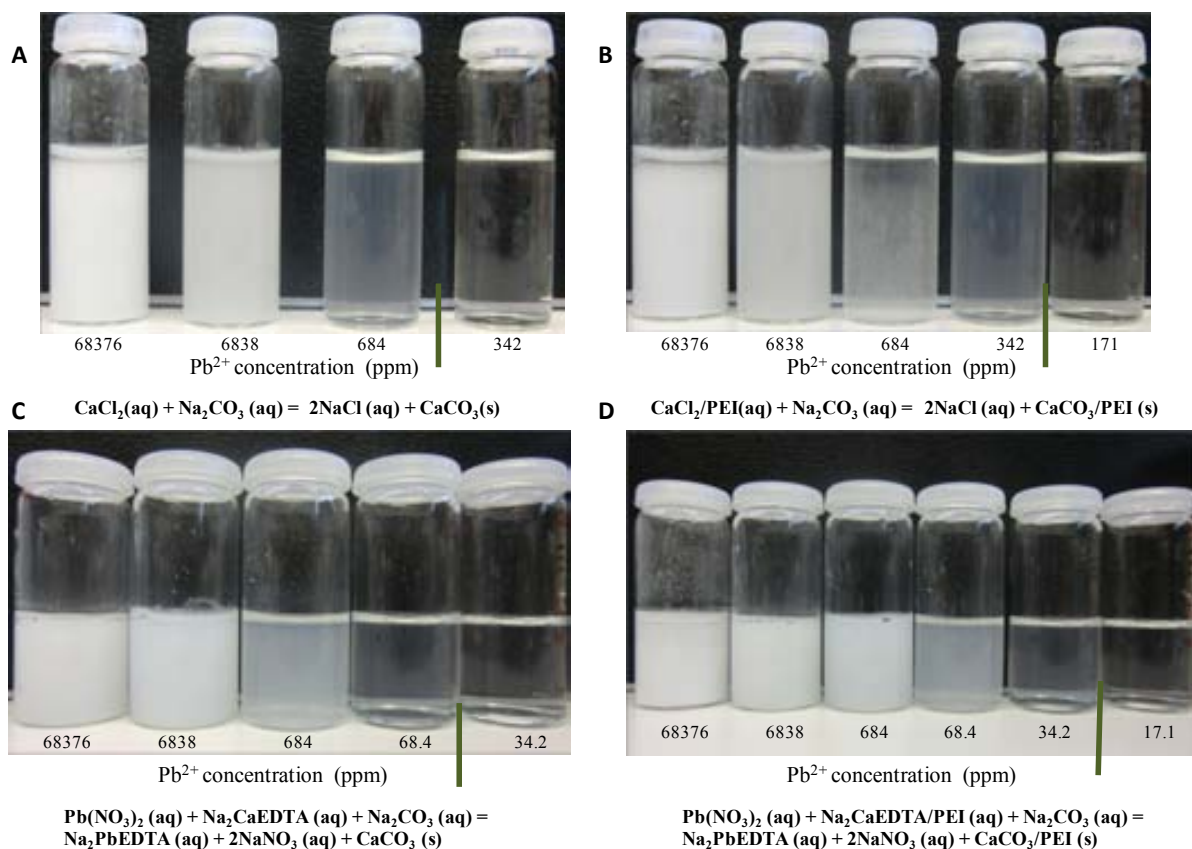


Figure_S3. Schematic representation of the NRs formation mechanism without use of CGM (1) and using PEI as CGM (2). (A) Formation of the possible intermediate complex $\text{Ca-Na}_2\text{EDTA-Pb}$ as Ca^{2+} self-reagent-delivery. (B1) Arising of the first local CaCO_3 nucleation centers by calcium supersaturation and nearly CaCO_3 nanoparticles stabilized by Na_2PbEDTA ; (B2) Formation of additional primary CaCO_3 nanoparticles by calcium supersaturation due to its interaction with nitrogen amino in PEI polymer. (C1) Growth of heterogeneous plate-like crystals by aggregation of the nearly CaCO_3 nanoparticles in preferential y -axis and its temporal Na_2PbEDTA stabilization. (C2) Growth of homogeneous hexagonal plate-like crystals by aggregation of the nearly CaCO_3 nanoparticles in preferential y -axis and its PEI stabilization by polymer retention onto particle surface. (D) Spontaneous self-assembly of the

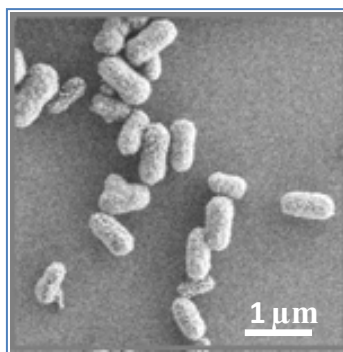
heterogeneous (D1) or hexagonal (D2) plate crystals mediated by organic stabilizer that acts as link of the plate building block into preferential x -axis. E1 and E2 SEM images that suggest the microrods composition by self assemble of heterogeneous and hexagonal nanoplates, respectively.



Figure_S4. TGA curve obtained for CaCO₃-PEI powder.



Figure_S5. Photos corresponding to the turbidity assays produced by CaCO_3 precipitation when decrease the reagents concentration. (A) Turbidity produced by CaCO_3 precipitation using CaCl_2 and Na_2CO_3 to synthesize the CaCO_3 . (B) Turbidity produced by CaCO_3 precipitation using CaCl_2/PEI and Na_2CO_3 to synthesize the CaCO_3 . (C) Turbidity produced by CaCO_3 precipitation using $\text{Pb}(\text{NO}_3)_2$, Na_2CaEDTA and Na_2CO_3 to synthesize the CaCO_3 . (D) Turbidity produced by CaCO_3 precipitation using $\text{Pb}(\text{NO}_3)_2$, $\text{Na}_2\text{CaEDTA}/\text{PEI}$ and Na_2CO_3 to synthesize the CaCO_3 .



Figure_S6. SEM image taken to calcite powder after 48 h of removal treatment to initial Na_2PbEDTA solution (342 ppm) at pH 4.

V.6 References

- [1] W. Yantasee, R. D. Rutledge, W. Chouyyok, V. Sukwarotwat, G. Orr, C. L. Warner, M. G. Warner, G. E. Fryxell, R. J. Wiacek, Ch. Timchalk, R. Sh. Addleman, *ACS Appl. Mater. Interfaces*, **2010**, 2, 2749.
- [2] A. Guijarro-Aldaco, V. Hernández-Montoya, A. Bonilla-Petriciolet, M. A. Montes-Morán, D. I. Mendoza-Castillo, *Ind. Eng. Chem. Res.* **2011**, 50, 9354.
- [3] J. Du, Y. Sun, L. Jiang, X. Cao, D. Qi, S. Yin, J. Ma, C. F. Y Boey, X. Chen, *Small* **2011**, 7, 1407.
- [4] Ch. Zong, K. Ai, G. Zhang, H. Li, L. Lu, *Anal. Chem.* **2011**, 83, 3126.
- [5] G. Aragay, A. Puig-Font, M. Cadevall, A. Merkoçi, *J. Phys. Chem. C* **2010**, 114, 9049.
- [6] G. Aragay, J. Pons, A. Merkoçi, *J. Mater. Chem.* **2011**, 21, 4326.
- [7] T.-Y. Hoa, Ch.-T. Chiena, B.-N. Wanga, A. Siriraks, *Talanta* **2010**, 82, 1478.
- [8] J. Gasparik, D. Vladarova, M. Capcarova, P. Smehyl, J. Slamecka, P. Garaj, R. Stawarz, P. Massanyi, *J. Environ. Sci. Health A* **2010**, 45, 818.
- [9] G. Aragay, J. Pons, A. Merkoçi, *Chem. Rev.* **2011**, 111, 3433.
- [10] G. Aragay, A. Merkoçi, *Electrochim. Acta* **2012**, 84, 49.
- [11] K.-S. Hong, H. M. Lee, J. S. Bae, M. G. Ha, J. S. Jin, T. E. Hong, J. P. Kim, E. D.

- Jeong, *J. Anal. Sci. Technol.* **2011**, *2*, 75.
- [12] F. Mou, J. Guan, H. Ma, L. Xu, W. Shi, *ACS Appl. Mater. Interfaces*, **2012**, *4*, 3987.
- [13] B. Karn, T. Kuiken, M. Otto, *Environ. Health Perspectives* **2009**, *117*, 1823.
- [14] I. Ojea-Jiménez, X. López, J. Arbiol, V. Puntès, *ACS Nano*, **2012**, *6*, 2253.
- [15] B. Wang, H. Wu, L. Yu, R. Xu, T.-T. Lim, X. W. Lou, *Adv. Mater.* **2012**, *24*, 1111.
- [16] S.-W. Cao, Y.-J. Zhu, *J. Phys. Chem. C* **2008**, *112*, 6253.
- [17] Z. Wei, R. Xing, X. Zhang, S. Liu, H. Yu, P. Li, *ACS Appl. Mater. Interfaces* **2013**, *5*, 598.
- [18] X. Ma, L. Li, L. Yang, C. Su, K. Wang, Sh. Yuan, J. Zhou, *J. Hazard. Mater.* **2012**, *209-210*, 467.
- [19] Ch. Li, L. Qi, *Angew. Chem., Int. Ed.* **2008**, *47*, 2388.
- [20] J. Yu, X. Zhao, B. Cheng, Q. Zhang, *J. Solid State* **2005**, *178*, 861.
- [21] J. Yu, M. Lei, B. Cheng, X. Zhao, *J. Solid State* **2004**, *177*, 681.
- [22] A.-W. Xu, M. Antonietti, H. Cölfen, Y.-P. Fang, *Adv. Funct. Mater.* **2006**, *16*, 903.
- [23] A. López_Marzo, J. Pons, A. Merkoçi, *J. Mater Chem.* **2012**, *22*, 15326.
- [24] J. Xiao, Y. Zhu, Y. Liu, H. Liu, Y. Zeng, F. Xu, L. Wang, *Cryst. Growth Des.* **2008**, *8*, 2887.
- [25] J. Ahmed, M. A. Ganguli, K. Ganguli, *CrystEngComm*, **2009**, *11*, 927.
- [26] S. Kim, Ch. B. Park, *Adv. Funct. Mater.* **2013**, *23*, 10.
- [27] M. Lee, I. S. Paik, I. Kima, H. Kang, S. Lee, *J. Hazard. Mater.* **2007**, *144*, 2084.
- [28] Y. Ma, Ch. Lin, Y. Jiang, W. Lu, Ch. Si, Y. Liu, *J. Hazard. Mater.* **2009**, *172*, 1288.
- [29] X. Man, L. Li, L. Yang, C. Su, K. Wang, K. Jiang, *J. Cryst. Growth*, **2012**, *338*, 272.
- [30] G. B. Cai, G.X. Zhao, X. K. Wang, S. H. Yu, *J. Phys. Chem. C*, **2010**, *114*, 12948.
- [31] O. Yavuz, R. Guzel, F. Aydin, I. Tegin, R. Ziyadanogullari, *Pol. J. Environ. Stud.* **2007**, *16*, 467.
- [32] J. Zhang, F. Laiwalla, J. A. Kim, H. Urabe, R. V. Wagenen, Y.-K. Song, B. W. Connors, F. Zhang, K. Deisseroth, A. V. Nurmikko, *J. Neural Eng.* **2009**, *6*, 055007.

- [33] A. Adami, C. S. Pedrotti, L. Lorenzelli, *Biosens. Bioelectron.* **2013**, *40*, 315.
- [34] M. Zhou, N. Zhou, F. Kuralay, J. R. Windmiller, S. Parkhomovsky, G. Valdés-Ramírez, E. Katz, J. Wang, *Angew. Chem., Int. Ed.* **2012**, *51*, 2686.
- [35] F. Khan, J. O. Smith, J. M. Kanczler, R. S. Tare, R. O. C. Oreffo, M Bradley, *Adv. Funct. Mater.* **2013**, DOI: 10.1002/adfm.201202710ark.
- [36] S. Wang, G. Kim, Y. E. K. Lee, H. J. Hah, M. Ethirajan, R. K. Pandey, R. Kopelman, *ACS Nano*, **2012**, *6*, 6843.
- [37] S. Wang, G. Kim, Y. E. Lee, H. J. Hah, M. Ethirajan, R. K. Pandey, R. Kopelman, *Nanomedicine*, **2012**, *6*, 941.
- [38] N. Li, L. Zhang, Y. Chen, Mi. Fang, J. Zhang, H. Wang, *Adv. Funct. Mater.* **2012**, *22*, 835.
- [39] W. S. Choi, H. M. Yang, H. Y. Koo, H.-J. Lee, Y. B. Lee, T. S. Bae, Ch. Jeon, *Adv. Funct. Mater.* **2010**, *20*, 820.
- [40] a) Cambridge Structural Database version 5.33. Cambridge Crystal Data Centre, Cambridge UK, 2012. b) P. G. Harrison, A. T. Steel, *J. Organomet. Chem.* **1982**, *239*, 105.
- [41] E. Altay, T. Shahwan, M. Tanoğlu, *Powder Technol.* **2007**, *178*, 194.

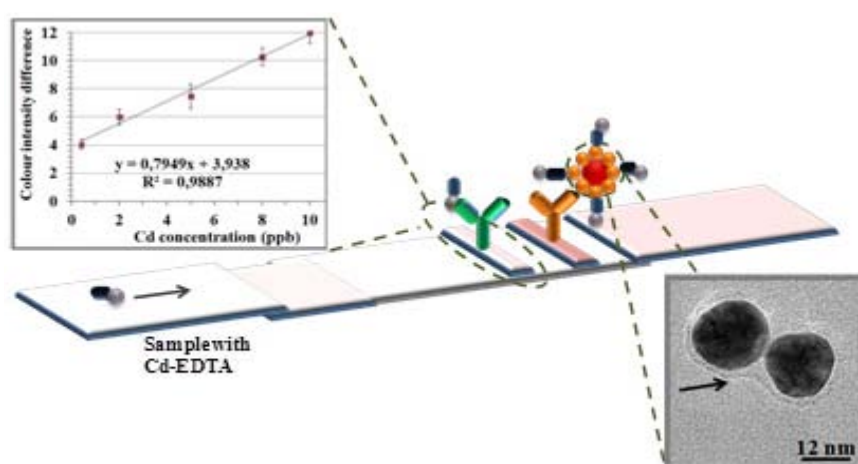
Chapter VI. All-integrated and highly sensitive paper-based device with sample treatment platform for Cd²⁺ immunodetection in drinking/tap waters.

These results are related in the publications:

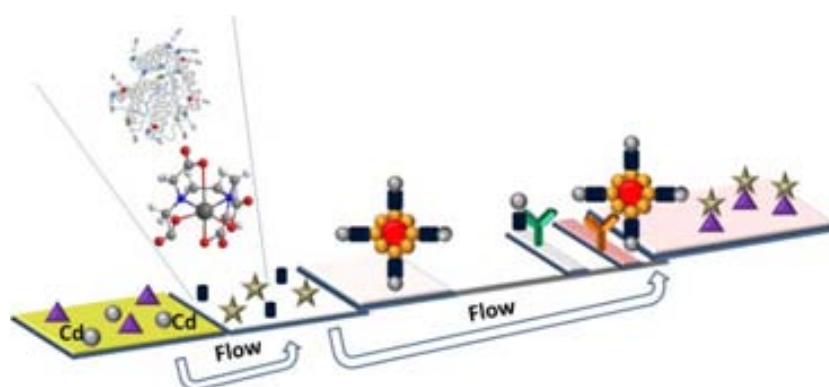
- High sensitive gold-nanoparticle based lateral flow immunodevice for Cd²⁺ detection in drinking waters, A. M. López_Marzo, J. Pons, D. A. Blake, A. Merkoci, *Biosensors and Bioelectronic*, **2013**, 47, 190.
 - All-integrated and highly sensitive paper-based device with sample treatment platform for Cd²⁺ immunodetection in drinking/tap waters, A. M. López_Marzo, J. Pons, D. A. Blake, A. Merkoci, *Analytical Chemistry*, **2013**, 85, 3532.
-

Chapter VI. All-integrated and highly sensitive paper-based device with sample treatment platform for Cd^{2+} immunodetection in drinking/tap waters.

Graphical abstracts and contents



A high sensitive Cd-EDTA-BSA-AuNP conjugate based lateral flow immunosensor device for Cd^{2+} determination in drinking waters has been introduced.



All-integrated and highly sensitive paper-based device with an extra inserted pad for sample treatment has been evaluated for Cd^{2+} immunodetection in drinking/tap waters.

VI.1 Introduction

The release of Cd^{2+} into environment has noticeably increased as a result of industrialization. Cd^{2+} continues being an analyte that requires a careful environmental monitoring. It can be accumulated in the human body mainly in the liver and kidneys and shows a biological half-life of greater than 10 years. Cd^{2+} exposure can affect kidney (Cd^{2+} appears to accumulate with age, especially in the kidney leading to kidney failure), lung function, or produce cardiovascular diseases. Many studies provide evidence that low-level chronic Cd^{2+} exposure, can contribute to an increased risk of cancer.¹⁻⁹ Thus, the permissible limits for Cd^{2+} intake required by the regulatory authorities are becoming lower. For drinking water an enforceable regulation for Cd^{2+} in terms of a maximum contaminant level of 5 and 3 ppb is permitted by the US Environmental Protection Agency (EPA) and the World Health Organization (WHO), respectively.¹⁰

As it is well-known, GFAAS¹¹ and ICPEs¹² are the standard techniques for trace heavy metal analysis. However, these labor-intensive and time-consuming techniques require complex and expensive instruments and specialized personnel to carry out the operational procedures.^{1,2} In order to overcome all these limitations other rapid, low-cost, simple, sensible and friendly-use techniques for heavy metals detection, such as colorimetric,^{13,14} fluorimetric,¹⁵ immunoassay, voltammetric¹⁶⁻¹⁸ and potentiometric^{19,20} techniques have been proposed. In addition the mentioned electrochemical methods have been adapted to allow the miniaturization and in-field applications.

Although all these proposed techniques for heavy metals detection are cheaper and faster than the two traditional above mentioned, and in addition are highly sensitive and selective;^{6-8,21,22} relatively cost equipments and even trained personnel are still necessary to carry out the analyses preventing their extended application in the routine detection of Cd^{2+} or other heavy metals. In these context analytical methods based on paper play an important role as tool of point of care assay to monitor heavy metals in different samples.^{3,23-25,29} Paper based sensors represent cheap, portable and simple detection tool. These are facile to be used, portable, low cost, use low sample volume and do not require specialized users. The analysis using paper based platforms can be carried out even by a naked-eye colorimetric change.^{26,27} Enzymes,³ DNA molecule,²⁸ metal-specific DNazymes,^{25,29} metal-specific mAbs,^{23,24} others proteins³⁰ and even small organic molecules^{31,32} are the recognition molecules used to date in paper based

metals biosensing both in simple format as LFDs.

In the first part of this work a novel and highly sensitive LFID for Cd^{2+} detection in aqueous samples using the Cd-EDTA-BSA conjugate labeled with AuNPs as signal producer tool is implemented. The developed LFID is based on the recognition of Cd-EDTA complex (formed after Cd^{2+} analyte complexation) by using the specific 2A81G5 mAb. In the device the Cd-EDTA-BSA-AuNP conjugate placed onto the conjugation pad strip competes with the Cd-EDTA by the same binding sites in the 2A81G5 mAb deposited onto the test line. The decrease of the conjugate and mAbs concentrations at its corresponding zones, used as tool to increase the sensibility of the device in the competitive format allows the obtaining of a large operation range (from 0.4 to 2000 ppb) and very low LoD and LoQ. This is an interesting approach considering the fact that a lot of efforts to enhance the LoD and LoQ in the LFDs field are put by the nowadays research in this field. These approaches are either based on the change of the geometry of the sample pad (so as to introduce larger volumes of sample or concentrate the sample) or in finding of new signal color producer particles or even loading of a second particle with a color producer that improves the signal.³³⁻³⁷ The LoD and LoQ achieved with this LFID (of 0.1 and 0.4 ppb, respectively) are the lowest limits reached with a metal sensing paper^{3,23-25,28-32} and even considering large part of metal electrochemical methods.¹⁷⁻²⁰ Moreover other symbiotic platforms like lab-on-a-chip voltammetric sensor^{38,39} and paper based voltammetry^{40,41} have not yet reported such low LoD for metal sensing. In addition, during the specificity assay with interest for real sample analysis, all metal interferences were masked by sample treatment using appropriate EDTA and ovalbumin (OVA) concentrations achieving interference levels lower than 5% when eleven metallic ions are present in higher concentrations than those expected in drinking waters samples.

On the other hand the development of analytical systems, devices or methods that integrate several process steps in one multifunctional step (called also multifunctional integrated systems) for clinical, environmental or industrial proposal constitutes a challenge for many ongoing researches. The multifunctional integrated systems or devices permit to manage with more rapidity and efficiency a whole process, which saves resources while achieving the desired result.⁴²⁻⁴⁵ In the second part of this work taking into account the first results (conventional device) a new integrated and sensitive paper immunodevice for Cd^{2+} sensor that integrates the sample treatment process with the analyte detection process is presented. This LFID has an extra dual-function

conjugation pad inserted in the same platform that allows interferences masking with albumin and Cd^{2+} complex formation with EDTA to obtain the Cd^{2+} complex (Cd-EDTA). As far as we know such a LFD that integrates the sample treatment with the samples analysis in a whole platform has not yet been reported. The accuracy of the device was determined by evaluation of spiked drinking and tap water real samples. The performance of the device was also validated through the analysis of a certified reference sample (effluent wastewater) and by using ICPEs method.

VI.2.1 Experimental part I - Conventional LFID

VI.2.1-1 Chemicals

The 2A81G5 mAb and the Cd-EDTA-BSA conjugate were prepared and characterized as described in a previous work.⁴⁶ The albumin from bovine serum (BSA), monoclonal anti-bovine serum albumin -antibody produced in mouse- (anti-BSA), ethylenediaminetetraacetic acid disodium salt dihydrate ($\text{Na}_2\text{EDTA}\cdot 2\text{H}_2\text{O}$), albumin from chicken egg white -ovalbumin- (OVA), Tween 20, gold(III) chloride trihydrate ($\text{HAuCl}_4\cdot 3\text{H}_2\text{O}$, 99.9% metals basis), 4-(2-hydroxyethyl)piperazine-1-ethanesulfonic acid ($\text{C}_8\text{H}_{18}\text{N}_2\text{O}_4\text{S}$, HEPES) and effluent wastewater (trace elements) certified reference material were purchased from sigma Aldrich. Cd^{2+} , Zn^{2+} , Ni^{2+} , Fe^{3+} , Pb^{2+} , Al^{3+} , Cu^{2+} , Co^{2+} , Ca^{2+} , Mg^{2+} , Mn^{2+} and Hg^{2+} metallic ion solutions were prepared by diluting AAS grade standard solutions (1000 ppm in 2% HNO_3) (Panreac) using Milli-Q water. The Hi-Flow Plus nitrocellulose membrane (HF240), the cellulose fiber sample pad and the glass fiber conjugate pad were acquired from Millipore.

VI.2.1-2 Characterization techniques

The antibodies dissolutions on lateral flow membranes were dispensed in automatic mode using an IsoFlowTM Dispenser. The color intensity of the lines in the strips was measured by using a COZARTTM RapidScan colour intensity reader.

Absorption measurements were carried out on SpectraMax M2 spectrophotometer. TEM images were recorded on Tecnai F20 HRTEM/STEM.

VI.2.1-3 Conjugation of Cd-EDTA-BSA with AuNPs. Gold aggregation test.

Preparation of AuNPs. Approximately 20 nm diameter AuNPs dissolution were synthesized according to the citrate reduction of HAuCl_4 disolution.⁴⁷ All glassware used in this preparation was thoroughly cleaned in aqua regia overnight and rinsed with

double distilled H₂O and the reflux was used for all the procedure. A 50 mL aqueous solution of 0.01% HAuCl₄ was heated to boiling and vigorously stirred in a 250 mL round-bottom flask; 5 mL sodium citrate 40 mM were added quickly to this solution. Boiling was continued for an additional 10 min. The solution was cooled to room temperature with a continuous stirring for another 15 min. The colloids were stored in dark bottles at 4 °C.

Preparation of the Cd-EDTA-BSA-AuNPs conjugate. The pH of AuNPs-citrate dissolution was adjusted to 7.4 with 0.01 M NaOH. 15 µL of different concentrations of BSA solutions (from 0 to 300 µg/mL) were added to 135 µL of AuNPs pH 7.4 and incubated during 30 min at 650 rpm and 25°C. An absorbance measurement at 520 nm was performed first, followed by a second one after adding 20 µL of 10% NaCl and a third one after adding 160 µL of 10% NaCl both measured again at the same wavelength.

In a typical labeling of the Cd-EDTA-BSA conjugate with AuNPs, 900 µL of AuNPs-citrate pH 7.4 were incubated with 100 µL (0.8 mg/mL) of the Cd-EDTA-BSA conjugate in HEPES buffered saline (HBS: 137 mM NaCl, 3 mM KCl, and 10 mM HEPES, pH 7.4) during 30 min.

VI.2.1-4 Optimization of the LFID operational conditions.

The first parameter to study was the efficiency of the recognition reactions between antigen/antibody that occurs at the test and control zones in terms of the AuNPs visibility. The quantities of mAbs deposited onto the membrane (the 2A81G5 mAb at the test zone and anti-BSA mAb at the control zone) and the quantity of Cd-EDTA-BSA-AuNPs conjugate deposited onto the conjugation pad were the most important parameters to optimize.

Initial assays used for optimizations were carried out by drop coating of 0.5 and 1 µL (0.5, 1 and 2 mg/mL) of 2A81G5 and anti-BSA mAbs working with conjugation strips with lengths of 7.5, 9 and 11 cm. For preparing the conjugation pad solution 900 µL of AuNP-citrate pH 7.4 was incubated with 100 µL (0.8 mg/mL) of the Cd-EDTA-BSA conjugate in HBS pH 7.4 during 30 min, centrifuged and resuspended in 300 µL HBS buffer pH 7.4, 10% sucrose and 0.1% Tween 20.

Using the last optimized conditions and following the same approach new assays were carried out by automatic dispensing of the mAb solutions onto the membrane. Thus, 0.5 and 0.375 µg/mm of the 2A81G5 mAb were tested on the test line and 0.32 and 0.4

$\mu\text{g}/\text{mm}$ of the anti-BSA mAb were tested on the control line. Conjugation strips of 10, 12, 14, 16 and 18 cm length were respectively soaked into 300, 350, 400, 500 and 600 μL of the conjugation pad solution and evaluated afterwards as previously described.

VI.2.1-5 Preparation of the conventional LFID.

For a typical LFID preparation, a conjugation strip with a length of 18 cm was cut and soaked in 600 μL of the conjugation pad solution. The strip was dried at vacuum during 50 min and stored at 4 °C. For preparing the conjugation pad solution 900 μL of AuNP-citrate pH 7.4 were incubated with 100 μL (0.8 mg/mL) of the Cd-EDTA-BSA conjugate in HBS pH 7.4 during 30 min, centrifuged at 14000 g and resuspended in 600 μL of the conjugation strip solution (HBS pH 7.4, 10% sucrose and 0.1% Tween 20). The sample pad was treated with 10 mM HBS pH 7.4, containing 5% BSA and 0.1% Tween-20, then dried at 60 °C for 1 h.

The nitrocellulose membrane, the prepared conjugation pad strip as well as the sample and absorption pads were assembled in the same order onto a plastic backing card. At a distance of 0.5 cm from the top of the membrane, a band of anti-BSA mAb was dispensed as control line at 0.4 $\mu\text{g}/\text{mm}$ and analogously 2A81G5 mAb was applied as detection line at 0.375 $\mu\text{g}/\text{mm}$ to a distance of 1.0 cm from membrane top. The lateral flow strips were cut at 0.7 cm of width. For the analysis 150 μL of sample was deposited on the sample pad and washed with 150 μL of 10 mM of HBS pH 7.4 with 0.1% Tween 20 (running buffer).

VI.2.1-6 Linearity and limits of detection and quantification.

For evaluating the linearity of the conventional device, Cd^{2+} standard dissolutions were prepared in HBS pH 7.4 and Na_2EDTA (14 mM) in the concentration range of 0.02 to 2000 ppb by diluting an AAS grade Cd^{2+} ion standard dissolution (1000 ppm in 2% nitric acid). 150 μL of each Cd^{2+} dissolution was deposited onto the sample pad, and the analysis was left to run until the mobile phase migrated toward the absorption pad. The test and control zones were visually evaluated within 10 min. For quantitative measurement the dry strip was inserted into the *RapidScan* color intensity portable reader. The measured value of the color intensity on the test and control lines of the strip remains stable for more of two months giving statistically the same measured value. Samples with high Cd^{2+} contents give high response values in the test line of the *RapidScan* reader, which corresponds by visual inspection to the lower color intensity while samples with low Cd^{2+} contents give low responds values in the test line of the

RapidScan reader, which corresponds by visual inspection to the higher color intensity. The calibration curve was obtained by plotting the difference of the color intensity between the Cd^{2+} standard dissolutions and the blank. The values of the experimental points for the calibration curve correspond to the mean of values obtained during a five days period making each day three independence replies by each concentration.

The LoQ was assumed as the lowest amount of Cd^{2+} which can be quantitatively determined with suitable precision and accuracy, while the LoD was calculated as three times the standard deviation of the sevenfold analysis of a blank. A more accurate determination of the LoD was carried out with the calibration curve and using the equation [1]:

$$LOD = \frac{3 \times Sbl}{b} \times \frac{1}{\sqrt{n}}$$

where *Sbl* is the standard deviation of the blank, *n* is the number of measurements and *b* is the slope of the calibration curve.⁴⁸

VI.2.1-7 Specificity assay.

For the specificity assay the obtained response for different 10 ppb Cd^{2+} dissolutions that contain an excess of the possible interfering metal (total metallic response) and 14 mM Na_2EDTA in HBS was compared with the response obtained for 10 ppb Cd^{2+} dissolution with 14 mM Na_2EDTA in HBS. The difference in the response between them expressed in percentage was assumed as the estimated interference for each metal (equation 2). For those metals with not significant expected interference (for example Ca^{2+} , Mg^{2+} , Al^{3+} , Fe^{3+} and Pb^{2+}) solution mixtures of 10 ppb Cd^{2+} and 25 ppm of the metal were tested, while for metals with a moderate or notable expected interference (for example Ni^{2+} , Cu^{2+} , Zn^{2+} , Co^{2+} , Mn^{2+} and Hg^{2+}) solution mixtures of 10 ppb Cd^{2+} and 5 ppm of the metal were tested. Similar specificity assays were also carried out in presence of 1% OVA or BSA and 14 mM Na_2EDTA .

5, 10 or 100 ppb Cd^{2+} spiked water samples containing the mentioned 11 most frequent possible interfering metals in amounts of 15 ppm Ca^{2+} , 15 ppm Mg^{2+} , 400 ppb Al^{3+} , 400 ppb Fe^{3+} , 10 ppb Pb^{2+} , 20 ppb Ni^{2+} , 2.5 ppm Cu^{2+} , 5 ppm Zn^{2+} , 1ppm Co^{2+} , 300 ppb Mn^{2+} and 5 ppb Hg^{2+} (these concentrations are even higher than its permitted limits in drinking water; see table_S1 at SI) with different EDTA (0.005, 0.05, 0.5 and 0.9 mM) and OVA (5, 10 and 15%) concentrations were evaluated. In a similar way the difference in the response between samples with Cd^{2+} and others metals with samples

containing only Cd^{2+} expressed in a percentage was assumed as the interference level caused by the studied metals.

$$\frac{(\text{total metallic response} - \text{Cd response})}{\text{Cd response}} \times 100\% = \text{estimated interference} \quad [2]$$

VI.3.1 Results and Discussion part I – Conventional LFID

VI.3.1-1 Conjugation of Cd-EDTA-BSA with AuNPs. Gold aggregation test.

Figure 1A shows the results of the gold aggregation test used to evaluate the loading of AuNPs with Cd-EDTA-BSA conjugate. When increasing concentrations of Cd-EDTA-BSA solutions are added to the same quantity of AuNPs, the absorption of AuNPs decreases until reaching a constant value (see figure1A-1). When to equals AuNPs solutions with increasing concentrations of Cd-EDTA-BSA solutions are added 1.2 or 5.5% NaCl, the absorption initially decreases due to the aggregation of AuNPs caused by salt effect. Afterwards the absorption begins to increase by increasing the Cd-EDTA-BSA concentration until reaching a constant value of absorbance above 50 $\mu\text{g/mL}$ of Cd-EDTA-BSA (see figure1A-2 and 1A-3). This concentration from which a constant absorbance value is reached means that, for Cd-EDTA-BSA concentrations higher than 50 $\mu\text{g/mL}$ enough protein is coating the surface of the AuNPs allowing the stabilization of AuNPs, which prevents their aggregation in presence of salts. Although in the 50-200 $\mu\text{g/mL}$ Cd-EDTA-BSA concentration range the AuNPs aggregation by salts effect is already blocked, we decide to perform the following assays at 80 $\mu\text{g/mL}$ of the conjugate, because by using a large excess of the conjugate could occur its delivery from the AuNPs surface and this would affect the well operation of the LFD. Taking into account that the Cd-EDTA-BSA-AuNP conjugate ensures the signaling colour in this device, a good stabilization of the AuNPs is very important to have appreciable and stable signal intensities onto the control and test lines, which in turn would directly improve the precision of the results.

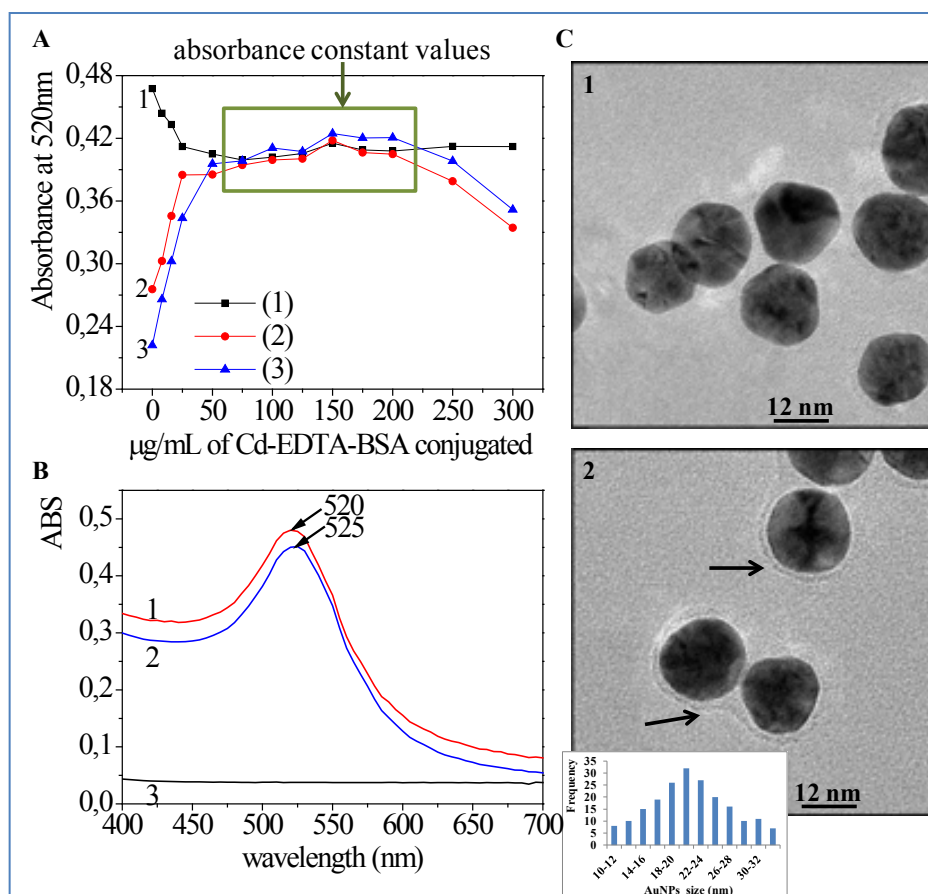


Figure 1. Results related with the labeling of the Cd-EDTA-BSA conjugate with AuNPs. (A) Gold aggregation test for the Cd-EDTA-BSA conjugate. Absorption behavior at 520 nm of the AuNPs solution in presence of increasing concentrations of the Cd-EDTA-BSA with and without the addition of NaCl: (1) AuNPs+Cd-EDTA-BSA, (2) AuNPs+Cd-EDTA-BSA+1.2% NaCl, (3) AuNPs+Cd-EDTA-BSA+5.5% NaCl. (B) Absorption spectra of some components of the Cd-EDTA-BSA-AuNPs conjugated: (1) 135 μL AuNPs+15 μL HBS, (2) 135 μL AuNPs+15 μL Cd-EDTA-BSA (80 mg/mL) and (3) 135 μL HBS+15 μL Cd-EDTA-BSA (80 mg/mL). (C) TEM images of the AuNPs (1) and the Cd-EDTA-BSA-AuNP (2) with the inset graph that shows the nanoparticles distribution size.

Figure 1B shows evidences of the conjugation between Cd-EDTA-BSA and AuNPs. In the figure 1B-2 it can be observed that the Cd-EDTA-BSA-AuNP absorption spectrum has a bathochromic shift of 5 nm and the absorption intensity decreases in comparison with the AuNPs solution at the same concentration (figure 1B-1). This shift is also reported by other authors for the AuNPs-BSA conjugate.⁴⁹ Figure 1C presents two TEM views, one with as prepared AuNPs and the other one with the Cd-EDTA-BSA-AuNPs conjugate formed as explained in the experimental section. In figure 1C-2 the shadow around AuNPs (indicated by arrows) corresponds to BSA-EDTA organic phase while this shadow doesn't appear in figure 1C-1.

VI.3.1-2 Design and operation principle of the conventional LFID.

The detection principle of the developed LFID is based on the use of a purified 2A81G5 mAb that recognizes with high specificity Cd-EDTA complexes but not the free Cd²⁺ ions. The affinity of 2A81G5 mAb for the Cd-EDTA complex is associated with the histidine-H96 (His-96) and tryptophan (Trp-H52) residues in the heavy chain variable regions of this mAb being these important as antigen recognition sites. The analysis of 3D structure model of the mAb made in previous works demonstrated that, there was closest distance of 2.72 Å between Cd²⁺ and N of His-96 in the CDR3 region of the heavy chain of 2A81G5 mAb, which suggests a possible interaction antigen-antibody. The model also revealed a possible hydrogen bonding interaction with the nitrogen of the antigen and the Trp-H52 residue.⁴⁶ The differences in the dimensional structures and conformational changes between the metal-EDTA complexes as they shift to accommodate various metal ions appear to be an important factor in the antibody recognition.⁴⁶

The Cd²⁺ detection principle is based on the competition between the Cd-EDTA complex (previously formed by reaction of Cd²⁺ with EDTA at 1:1 stoichiometric relation and deposited onto the sample pad during the sample analysis) with the Cd-EDTA-BSA-AuNP conjugate (deposited onto the conjugation pad) for the same binding sites of the immobilized 2A81G5 mAb in the test line. For controlling purposes in the control line an anti-BSA mAb is immobilized to capture the excess of Cd-EDTA-BSA-AuNP conjugate (**figure 2A**), giving always a color red as control when there is fluid crossing the membrane. The Cd²⁺ concentration in a sample is quantified by the ability of Cd-EDTA complex to substitute the binding sites of the Cd-EDTA-BSA-AuNP with the 2A81G5 mAb producing a decrease of the color intensity (provided by AuNPs in the Cd-EDTA-BSA-AuNP conjugate) in the test line. In this way, when there isn't Cd²⁺ in the sample and just running buffer flows through the membrane the maximal color intensity is developed in the test line (**figure 2B**). On the other hand, when increasing concentrations of Cd²⁺ are present in the samples the color intensity in the test line gets decreasing (**figure 2C**). The color development is inversely proportional to the increasing concentration of Cd²⁺ in the original sample.

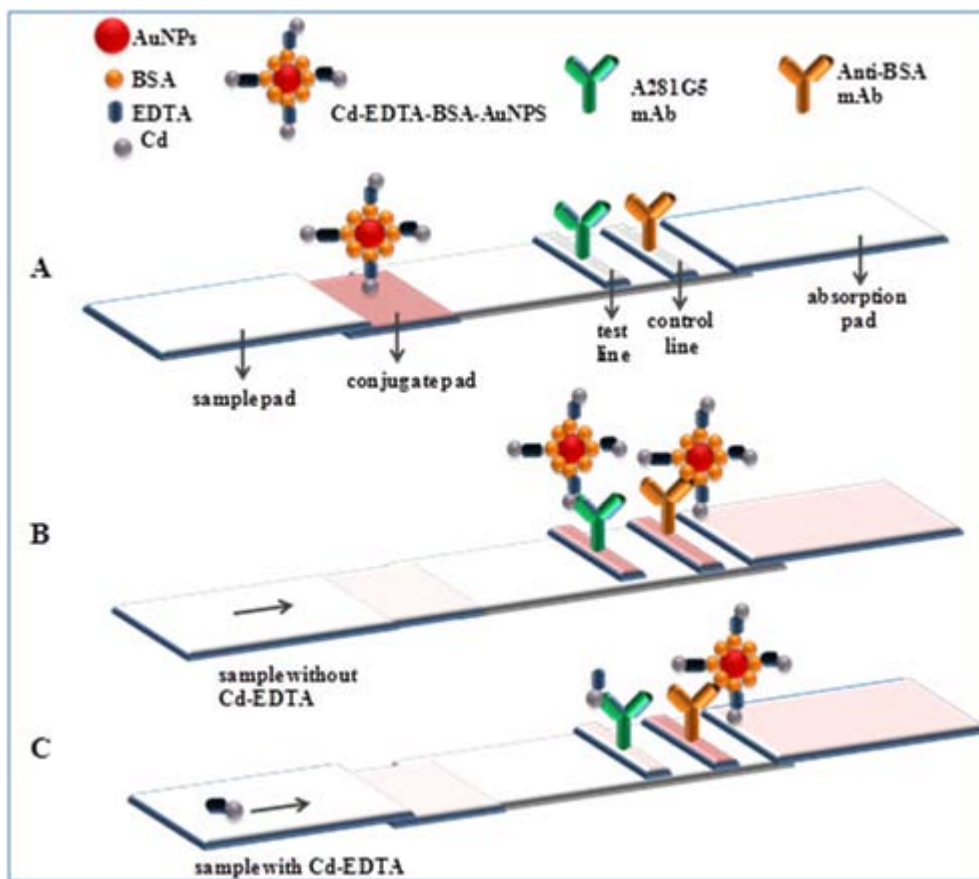


Figure 2. Schematic representation of the configuration and measurement principle of the Cd-EDTA biosensor device. (A) Configuration of the biosensor: components deposited in each part, (B) the principle of visual detection analyzing samples without Cd-EDTA and (C) the principle of visual detection analyzing samples with Cd-EDTA.

VI.3.1-3 Optimization of the LFID operational conditions.

Optimization of the conjugate and antibodies concentrations in the device.

In order to obtain a high sensibility and better performance of the device for Cd^{2+} analysis, the optimization of the antibodies onto the test and control zones and the conjugate onto the conjugation strip was strictly necessary. The first optimizations of the LFID were carried out by drop coating of different mAbs concentrations onto the membrane for the same conjugation strip preparation. Other optimizations were made by decreasing the concentration of the conjugate onto the conjugation strip and keeping the same immobilized amount of the mAbs previously determined. Finally the last optimizations assays were made using the automatic dispensing. A detailed explanation of the optimization process appears in the SI (figure_S1, S2 and S3). In general the sensibility of the device increases when decreases the mAbs and the Cd-EDTA-BSA-AuNP conjugate concentrations.

The decrease of the 2A81G5 mAb and the conjugate concentrations onto the test zone and the conjugation strip, respectively, improves the resolution of the device, due to the fact that the Cd-EDTA detection takes place by a competitive format between the Cd-EDTA-BSA-AuNP conjugate and Cd-EDTA by the same sites of the 2A81G5 mAb immobilized onto the membrane. The key for a successful detection is to set the device operation parameters that favor the competition to the Cd-EDTA contained in the sample by the mAb binding sites. In samples with Cd-EDTA between 0-10 ppb, the quantity of Cd²⁺ that competes with the conjugate is very low and unable to produce a notable discoloration in the test line by displacing the large quantity of the conjugate at the 2A81G5 mAb sites. By contrary a high quantity of mAb onto the test line doesn't allow to the Cd-EDTA to produce notable discoloration due to the fact that large quantity of the colored conjugate will also bind to the mAb sites. Consequently the reduction of the concentrations of the conjugate onto the conjugation strip and the 2A81G5 mAb onto the test line favors the Cd-EDTA competition by the mAb binding sites in order to obtain a notable discoloration at low analyte concentration increasing in this way the sensibility of the device.

VI.3.1-4 Linearity and limits of detection and quantification

The image in **figure 3A** represents a typical Cd²⁺ analysis with the LFID. The violet color onto the test and control line appears once the strips are dried and this color measured by RapidScan equipment remains stable for two months. The developed LFID has a response range between 0.4 and 2000 ppb, being the linearity of the calibration curve from 0.4 to 10 ppb. Although the difference in color intensities between 0, 0.4, 2 and 5 ppb were not detectable at naked eye they can perfectly be discriminated by using the color reader equipment. Figure 3 B and C show the lineal and exponential mathematic fit obtained by using the plotted experimental points of the calibration curve. The plotted values in the vertical axis correspond to the difference between the measured values of the samples and the blank in the test line.

The LoD of the device was 0.1 ppb being 0.4 ppb the LoQ corresponding to the lowest Cd²⁺ quantity that can be quantified with acceptable accuracy and precision. To the best of our knowledge both the LoD of 0.1 ppb and the LoQ of 0.4 ppb are the lowest values obtained using metal sensing papers^{3,23-25,29-30} or even by most of Cd²⁺ electrochemical analysis methods^{16-18,20,41} reported so far as is displayed in **table_1**.

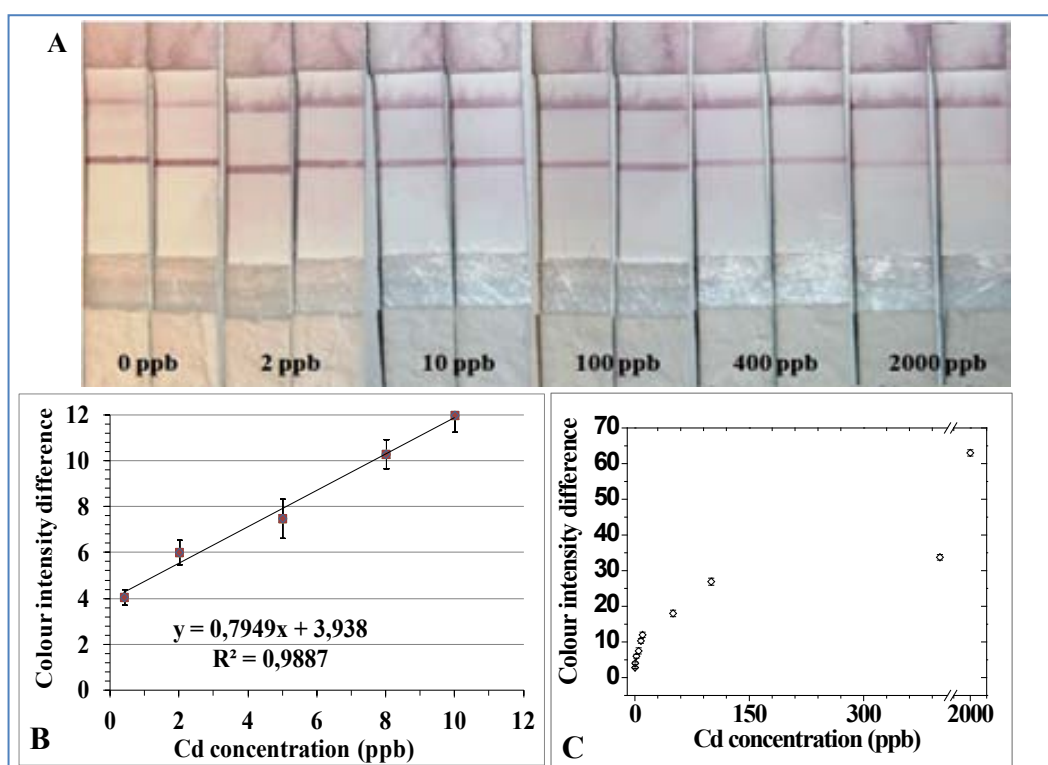


Figure 3. Results related with the linearity assays. (A) Typical image of the Cd^{2+} detection by the LFID. A series of dilutions (0.4-2000 ppb) of Cd^{2+} standard atomic absorption grade were made in HBS with 14mM EDTA. (B) Lineal range of the device for Cd-EDTA analysis. (C) Sensitivity over the entire range of the device for Cd-EDTA analysis.

Table 1. Summary of the related works with metal sensing based on paper reported up to date.

Analytical performance data of reported paper based sensors						
Metal	RSD (%)	Linear range (ppb)	LOD (ppb)	LOQ (ppb)	samples	Reference
Cd ²⁺	<5	0.4-10	0.1	0.4	spiked water	This work
Cr ³⁺ , Cr ⁶⁺	<9	5-80	5	5	serum, waters	Liu et al., 2012
Cu ²⁺	-	50-500	50	> 50	spiked water	George et al., 2012
Cd ²⁺	14	10-100	10	> 10	rice	Abe et al., 2011
	15	5-50	5	> 5	wheat grain	
	9	2.5-25	2.5	> 2.5	eggplant	
Hg ²⁺	-	10-60	10	> 10	spiked solutions	Gu et al., 2011
		120-480				
Hg ²⁺ ; Ag ¹⁺ Cu ²⁺ ; Cd ²⁺ Pb ²⁺ ; Cr ⁶⁺ Ni ²⁺	-	-	1; 2 20; 20 140; 150 230	>1; >2 >20; >20 >140; >150 >230	spiked solutions and environmental waters	Zakir and Brennan, 2011
Cu ²⁺	-	-	0.63	-	spiked solutions	Fang et al., 2010
Pb ²⁺	-	-	10	-	paints	Mazumbar et al., 2010

VI.3.1-5 Specificity assay

Results of the specificity assays are shown in **figure 4**. The interfering metals for Cd²⁺ determination can be classified in three groups. The first group is composed by the metallic ions with a non-significant interference such as Ca²⁺, Mg²⁺, Fe³⁺, Al³⁺ and Pb²⁺. 25 ppm of these metals almost do not interfere in the 10 ppb Cd²⁺ analysis using a 14 mM Na₂EDTA solution (figure 4A). This result is important because Ca²⁺, Mg²⁺, Al³⁺ and Fe³⁺ are the ions commonly found in drinking water samples at relatively high concentrations (for example the permissible limits of Al³⁺ and Fe³⁺ in drinking water are 0.2 and 0.3 ppm respectively while WHO guidelines doesn't make recommendations for Ca²⁺ and Mg²⁺, table_S1)¹⁰ and it can be expected that the developed LFID shouldn't face any significant interference during the Cd²⁺ analysis. The second group is made up by metals with moderate interference such as Co²⁺, Ni²⁺, Cu²⁺ and Zn²⁺. As observed (figure 4B) 5 ppm of these metals interfere between 5-10% in the 10 ppb Cd²⁺ analysis using 14 mM Na₂EDTA. The third group is composed of notable interfering metals

such as Mn^{2+} and Hg^{2+} . The presence of 5 ppm of Mn^{2+} or Hg^{2+} shows a 15-18% interference to the 10 ppb Cd^{2+} analysis using 14 mM Na_2EDTA (figure 4C). The ability of these metal-EDTA complexes to interfere in the Cd-EDTA analysis is in agreement with the reported equilibrium dissociation constant of the mAb to bind metal-EDTA complexes. The equilibrium dissociation constant of the 2A81G5 mAb with Cd^{2+} complexes are in the order of 7.4×10^{-11} and 2.1×10^{-8} for Cd-EDTA-BSA and Cd-EDTA, respectively.^{6,46} Thus, metal-EDTA complexes with the highest equilibrium dissociation constants for 2A81G5 mAb (Al^{3+} 8.2×10^{-4} , Mg^{2+} 2.2×10^{-4} , Fe^{3+} 5.4×10^{-5} and Pb^{2+} 7.4×10^{-5}) do not show significant interference in the Cd^{2+} analysis. Metal-EDTA complexes with intermediate equilibrium dissociation constants for 2A81G5 mAb have moderate interference in the Cd^{2+} analysis (Co^{2+} 2.3×10^{-6} , Ni^{2+} 2.1×10^{-6} , Cu^{2+} 4.9×10^{-6} and Zn^{2+} 2.5×10^{-6}) and metal-EDTA complexes with the lowest equilibrium dissociation constants for 2A81G5 mAb (Mn^{2+} 4.1×10^{-7} and Hg^{2+} 10^{-8}) present the most notable interference.

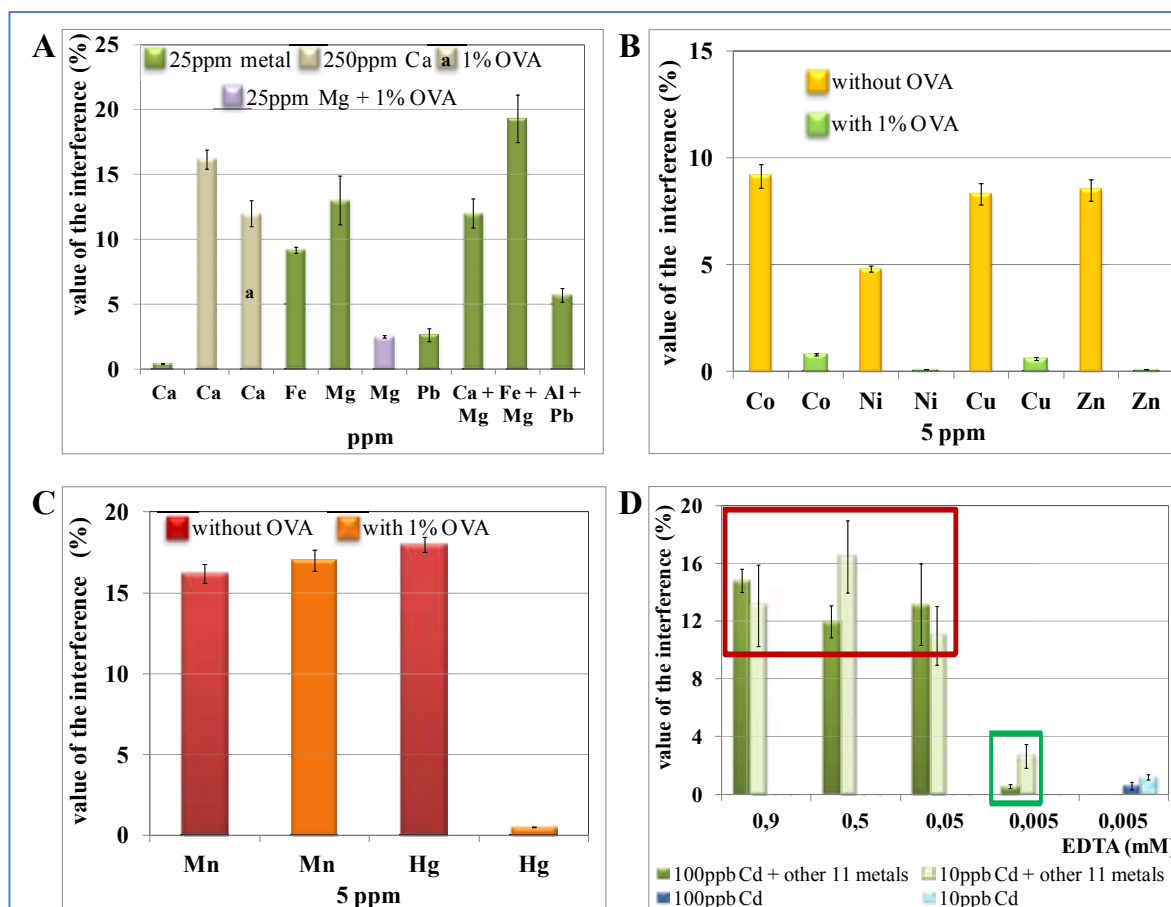


Figure 4. Analysis of the interfering effect for the most important metals present in drinking water with and without OVA. (A) Interference of the Ca^{2+} , Mg^{2+} , Fe^{3+} and Al^{3+} ions in presence of 10 ppb Cd^{2+} and 14 mM Na_2EDTA prepared in spiked samples. The (+) symbol is used to indicate that the interference of

two metals were simultaneously evaluated. (B) Interference of the Co^{2+} , Ni^{2+} , Zn^{2+} and Cu^{2+} ions in presence of 10 ppb Cd^{2+} and 14 mM Na_2EDTA prepared in spiked samples. (C) Interference of the Mn^{2+} and Hg^{2+} ions in presence of 10 ppb Cd^{2+} and 14 mM Na_2EDTA prepared in spiked samples. (D) Effect of the interference provoked by others 11 metals in spiked samples prepared with the most important metals present in drinking water in presence of 100 and 10 ppb Cd^{2+} , using 10% OVA and varying Na_2EDTA concentration. Effect of the interference produced by 10% OVA when 100 and 10 ppb Cd^{2+} are analyzed.

Often, a "masking reagent" that specifically binds an interfering metal and removes it from the antibody binding reaction can be added to reduce interference from a cross-reactive metal.²² The formation of complexes between different types of albumins and multiples metals (Mg^{2+} , Co^{2+} , Ni^{2+} , Cu^{2+} , Zn^{2+} , Cd^{2+} , Mn^{2+} and Hg^{2+}) is already demonstrated.⁵⁰⁻⁵⁴ In this work BSA or OVA were used as 'masking agents'. These albumins have multiples metal binding sites through their functional groups of the amino acid sequence as schemed at figure_S4-B and C at SI.

In the figure 4 (A-C) are represented the obtained results in Cd^{2+} analysis with the addition of 1% BSA or OVA and using 14mM EDTA in presence of the interfering metal. The addition of BSA or OVA (1%) to the spiked samples can significantly reduce the interfering effect for metals such as Mg^{2+} (25 ppm), Co^{2+} , Ni^{2+} , Cu^{2+} , Zn^{2+} (5 ppm each) and Hg^{2+} (5 ppm) where the 1% OVA addition can decrease the interference from 13 to 2.5% (figure 4A), from 9 to less than 0.8% (figure 4B) and from 17 to 0.5% (figure 4C), respectively. Although the Metal-EDTA complexes formation constants are higher (between 13 and 21) than the metal-albumin complexes formation constants of the principal interfering metals (between 5 and 12) (table_S2) the metallic interference can be masked using albumin as demonstrated here. We can explain the masking effect of the BSA/OVA addition considering that, the Cd-EDTA complex formation constant (figure_S4-A) is much higher than the Cd-BSA/OVA complex formation constant and that, the affinities of Cu^{2+} , Zn^{2+} , Hg^{2+} , Ni^{2+} , Co^{2+} and Mn^{2+} toward BSA or OVA functional groups are higher than the Cd^{2+} affinity toward BSA or OVA functional groups being the affinity decreased in the same order (figure_S4-D).^{50,52,53} Taking into account that each metal has multiples, similar and different, binding sites with a unique albumin molecule (figure_S4-C), while with EDTA the ratio Metal: EDTA in the M-EDTA complex is 1:1 (figure_S4-A), it is clear that the interfering metal will bind with preference to albumin rather than EDTA. In the case of Mn^{2+} under the applied experimental conditions the addition of 1% BSA or OVA doesn't reduce the manganese interference (figure 4C), because Mn^{2+} don't has a good affinity by the albumins and

moreover the Mn-EDTA complex has a 2A81G5 mAb equilibrium dissociation constant near to Cd-EDTA complex. The interfering effect coming from manganese can be reduced only by decreasing the EDTA concentration due to its small complex formation constant with EDTA in comparison to Cd²⁺.⁵⁵

Figure 4D displays the interference values obtained analyzing spiked water samples with 10 and 100 ppb Cd²⁺ and others 11 metals usually present in drinking water using 10% OVA and different EDTA concentrations (the metallic concentrations are over its permitted limits in drinking water; see table_S1 at SI). EDTA variations from 0.9 to 0.05 mM don't show significant changes in the response allowing similar metallic interference levels. By using the same EDTA concentrations and 5, 10 and 15% BSA or OVA no significant changes in the Cd²⁺ analysis (being the estimated interference between 12 and 18%) was observed (results not shown). An optimum ratio between EDTA and BSA/OVA for which the interference coming from other metals can be reduced from around 15 up to a minimum value of around 4% was found using 0.005 mM EDTA and 10% OVA.

Several parameters involved in the reduction of the interference coming from other metals can be considered: the affinity constants of the complexes metal-EDTA, metal-albumin, metal/EDTA-mAb, the expected metallic ionic concentrations in the sample (table S_2 at the SI), the optimized EDTA and OVA concentrations used in the assays and the stoichiometry in the complexes metal-mAb, metal-EDTA and metal-albumin. The masking of the interferences was possible by using 5×10^{-6} and 2×10^{-3} M of EDTA and albumin optimized concentrations, respectively. Under this condition interfering metals with albumin affinity constant higher than 5 can bind the albumin protein with preference to EDTA (such as Hg²⁺, Cu²⁺, Zn²⁺, Ni²⁺, Co²⁺, Mg²⁺) leaving free the EDTA to bind metallic ions such as Cd²⁺, Al³⁺, Fe³⁺, Ca²⁺, Mn²⁺ that have very low albumin affinity. As albumin concentration is 10^3 times higher than EDTA concentration and the stoichiometry metal-EDTA is 1:1 while the stoichiometry metal-albumin is $n:1$, these factors permit that the majority of metal ions with albumin affinity remain preferably bound to the albumin. In the case of Al³⁺, Fe³⁺ and Ca²⁺ that preferably bind with EDTA because of its poor albumin affinity, the interference produced by these metal-EDTA complexes could be low due to the fact that their affinity constants with the 2A81G5 mAb are very low in comparison to the affinity constant of the Cd-EDTA-2A81G5 mAb. In the case of Mn²⁺ for which the affinity constant Mn-EDTA-2A81G5 mAb is close to that of Cd²⁺, some quantity of Mn-EDTA

complex interferes in the Cd^{2+} determination, maximum if Mn^{2+} concentration is 40 times higher than Cd^{2+} concentration where an interference value of about 3% was found (see figure 4D using 0.005 mM EDTA and 10 ppb Cd^{2+} + 11 other metals).

VI.2.2 Experimental part II – Integrated LFID

VI.2.2-1 Chemicals

The chemical reagents and materials were the same that in the experimental part I.

VI.2.2-2 Characterization techniques

In addition to the techniques used in experimental part I, the Cd^{2+} determination by ICPMS was performed by using an Agilent 7500ce model device.

VI.2.2-3 Preparation of the integrated LFID.

For a typical integrated LFID preparation an extra conjugation pad was inserted between the sample pad and the conjugation pad. The rest of the manufacturing of the sensor was kept equal that the previous conventional sensor.

For preparing the extra conjugation pad strip, exactly 11 cm of the conjugation strip were embedded in 375 μL of 0.05 mM EDTA and 10% OVA and dried at vacuum during 50 min.

VI.2.2-4 Linearity and limits of detection and quantification.

For evaluating the linearity, LoD and LoQ in the integrated LFID was followed the same procedure that in conventional LFID.

VI.2.2-5 Accuracy and precision assays.

For the accuracy and precision studies different water samples (two different bottled drinking and two different tap waters) from the Barcelona area were spiked with 0.4, 2, 5, 10 and 50 ppb of Cd^{2+} . For Cd^{2+} analysis the samples were directly deposited, without any preliminary treatment, onto the sample pad of the device with the final design that contains another conjugation pad strip with the adequate concentration of EDTA and OVA previously optimized (results not shown here). Each sample was subsequently analyzed in quadruplicate for Cd^{2+} content. The analytical recovery was calculated as the ratio, expressed as percentage, between the Cd^{2+} concentration found with the device and the one added before (equation 3).

For comparison purposes ICPES was also carried out for one of the spiked bottled

drinking and tap water samples. In addition the analysis of a wastewater certificate reference material was also carried out to complete the validation of the new Cd²⁺ sensing device. The corresponding variance analysis (ANOVA) and student tests were used in the statistical comparisons.⁵⁶

For the precision of the device the repeatability and the intermediate precision were evaluated. The repeatability of the device at different concentrations was estimated as the standard deviation or the coefficient of variation obtained in the analysis (six repeated measurements of the same sample) using the same piece device by the same operator. The intermediate precision of the device at different concentrations was calculated as the standard deviation or the coefficient of variation obtained in the analysis of different samples (for drinking and tap waters) using different devices by the same operator.⁴⁸

$$\frac{\text{found concentration}}{\text{added concentration}} \times 100\% = \text{recovery (\%)} \quad [3]$$

VI.3.2 Results and Discussion part II - Integrated LFID

VI.3.2-1 Design and operation principle of the integrated LFID.

With the aim to analyze real water samples without previous treatment a novel integrated LFID platform was fabricated. **Figure 5A** presents a scheme of the developed integrated platform. The sample treatment pad inserted between the sample and the Cd-EDTA-BSA-Au conjugate pads contains an adequate concentration of EDTA and OVA (previously optimized results not shown here) that ensures, that when the sample containing Cd²⁺ and other metallic ions is deposited in the sample pad and reaches this zone, complexation reactions forming Cd-EDTA and interfering metal-OVA take place. Equal to the conventional device the Cd²⁺ detection principle is based on the competition between the Cd-EDTA complex (formed before by reaction of Cd²⁺ with EDTA in the first conjugation pad or sample treatment pad) with Cd-EDTA-BSA-AuNP conjugate, deposited onto the second conjugation pad, for the same binding sites of the immobilized 2A81G5 mAb in the test line. For controlling purposes in the control line an anti-BSA mAb is immobilized to capture the excess of Cd-EDTA-BSA-AuNP conjugate in consequence a red band always appears at the control line (which color is provided by AuNPs in the Cd-EDTA-BSA-AuNP conjugate) when the fluid crosses the membrane (see figure 5 B and D). The concentration of Cd²⁺ in a sample is quantified by the ability of Cd-EDTA complex to compete with the Cd-EDTA-BSA-AuNPs

conjugate by the same binding sites in the 2A81G5 mAb immobilized onto the membrane, producing a decreasing of the color intensity in the test line with respect to the maximum color intensity that is developed when all the labeled conjugate is bound onto this zone (figure 5-D). In this way, when there isn't Cd^{2+} in the sample and just running buffer flows through the membrane the maximal red color intensity is developed in the test line (figure 5-B). On the other hand, when increasing concentrations of Cd^{2+} are present in the samples the color intensity in the test line gets decreasing (figure 5C-D). The color development is inversely proportional to the increasing concentration of Cd^{2+} in the original sample.

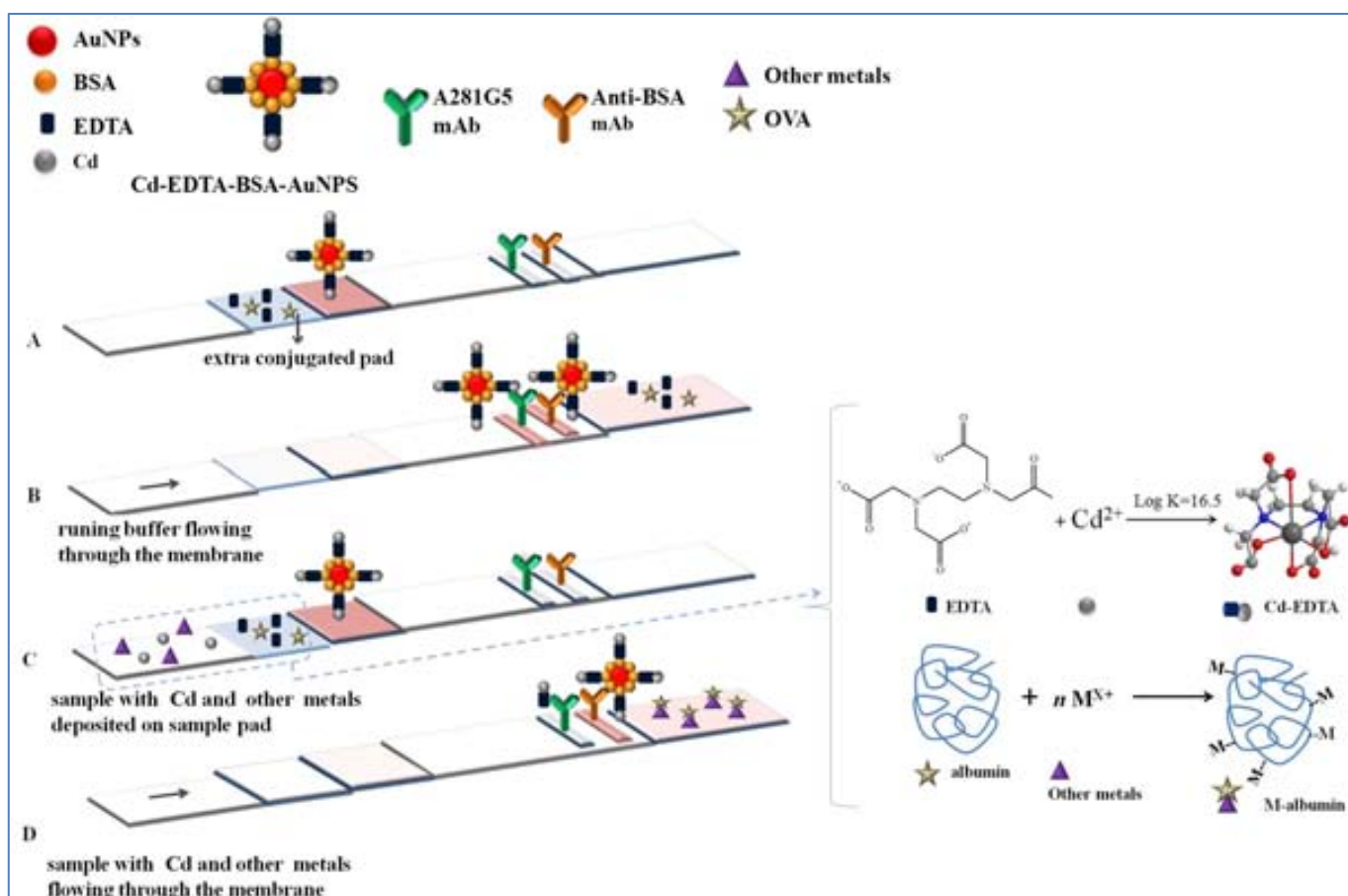


Figure 5. Scheme of the configuration and measurement principle of the integrated Cd^{2+} biosensor device used in the accuracy and precision assays. (A) Components deposited in each part, (B) the principle of visual detection analyzing samples without Cd^{2+} , (C) deposition on sample pad of real water samples with Cd^{2+} and other metallic ions, and (D) the principle of visual detection analyzing samples with Cd^{2+} and other metallic ions.

Several optimizations were necessary to carry out the development of the integrated device (results shown in part I). Thus the Cd-EDTA-BSA-Au conjugate and the mAbs concentrations onto the corresponding zones in the nitrocellulose membrane were

previously optimized in a conventional LFD. Moreover specificity studies to evaluate potential metals interferences as well as the masking and reduction of these interferences were realized using the conventional LFD version with previous treatment sample.

VI.3.2-2 Linearity and limits of detection and quantification.

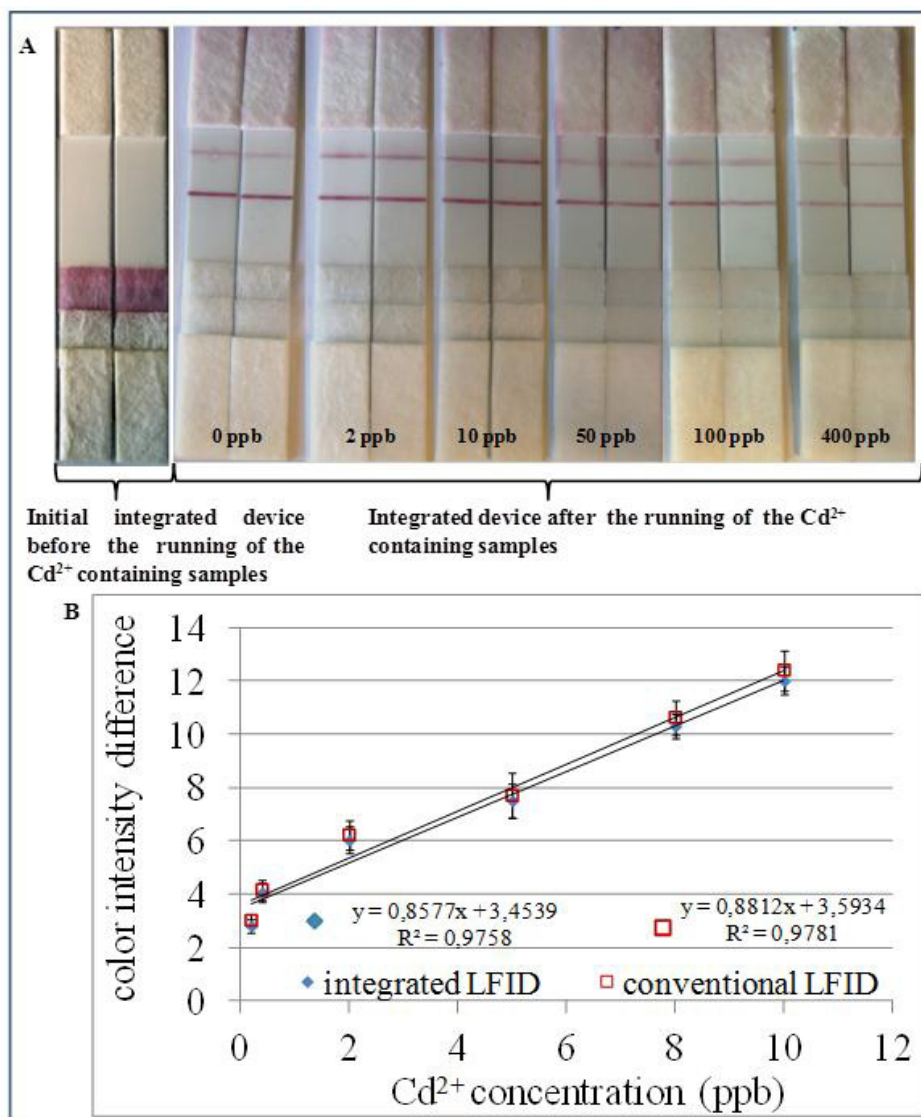


Figure 6. (A) Typical image before and after Cd²⁺ detection in tap or drinking waters by using the integrated LFID. A series of dilutions (0.4-400 ppb) of Cd²⁺ standard atomic absorption grade were made in HBS with 14 mM EDTA. (B) Lineal range of the calibration curves obtained for conventional and integrated LFIDs during Cd-EDTA analysis.

The image in **figure 6A** represents a typical Cd²⁺ analysis with the integrated LFID. The color intensity in the test line is related to Cd²⁺ concentration in the sample. Figure 6B shows the calibration curves obtained using both the conventional and the integrated LFIDs by measuring of the intensity color at test line with the RapidScan reader and

correcting these values with the signal of the blank for different Cd^{2+} concentrations. Similar to conventional LFID the integrated one has a linearity range from 0.4 to 10 ppb and a whole response range from 0.4 to 400 ppb describing an exponential decay. The LoD and LoQ were 0.1 and 0.4 ppb, respectively, equal to obtained values for the conventional design.

VI.3.2-3 Accuracy and precision assays

Table 2 shows the Cd^{2+} recoveries means when Cd^{2+} spiked samples of drinking and tap waters were directly deposited on the sample pad. Around 95 and 105% of Cd^{2+} recovery were obtained without showing the total recoveries mean significant differences with 100% as evaluated by Student test. The obtained results indicate that the device is able to determine with almost 100% of accuracy Cd^{2+} in drinking and tap waters samples at concentration levels between 0.4 and 50 ppb. These results show that when Cd^{2+} containing samples are deposited onto the sample pad and afterwards flow through the first conjugation pad, that contains EDTA and OVA, all Cd^{2+} (from 0.4 to 50 ppb) can be rapidly complexed with the EDTA forming Cd-EDTA complex, able to be immunodetected in the LFD and that the potential metal interferences present in these waters can be removed with OVA. In tap and drinking waters Ca^{2+} and Mg^{2+} followed by Cu^{2+} , Zn^{2+} , Al^{3+} and Fe^{3+} are the potential majority metallic ions. Table_S3 at SI displays that the Ca^{2+} and Mg^{2+} containings reported for these analyzed water samples are from 30 to 80 and from 8 to 15 ppm, respectively, while that considering the permissible metal limits in drinking water (table_S1), a total metal containing of around 3 ppm for Cu^{2+} , Zn^{2+} , Fe^{3+} and Al^{3+} can be estimated for these analyzed samples. Specificity results (in the conventional device) demonstrate that the interference in the analysis of 10 ppb Cd^{2+} that comes from 25 ppm of Ca^{2+} or Al^{3+} is low and inferior to 1 and 3%, respectively. In the same way the interference found for 25 ppm of the Fe^{3+} and Mg^{2+} ions in the analysis of 10 ppb Cd^{2+} reaches about of 9 and 13%, respectively, due to the fact that, EDTA complexes with Ca^{2+} , Mg^{2+} , Al^{3+} and Fe^{3+} show a very low affinity with the 2A81G5 mAb (see table_S2). In the case of Mg^{2+} , that is a majority metal in drinking and tap waters, although it represents a potential interference (25 ppm of Mg^{2+} shows a 13% interference in Cd^{2+} analysis), the interference can be reduced up to a 3% with OVA addition (figure 4A). Other important potential interferences are Cu^{2+} and Zn^{2+} . 5 ppm of Cu^{2+} and Zn^{2+} interfere in about of 8% in the 10 ppb Cd^{2+} analysis. This interference value was also almost completely removed using OVA

(figure 4B). Other possible metal interferences like Hg^{2+} , Mn^{2+} and Ni^{2+} whose permissible concentration limits in drinking waters are similar with Cd^{2+} (table_S1) don't affect the response due to the fact that at this concentration the 2A81G5 mAb will preferably bind with Cd^{2+} . The result labeled with a green box in figure 4D displays the reduction of the interferences below 5% in the 10 ppb Cd^{2+} analysis when 11 metals ions are present in concentrations over expected in drinking water by using the optimized EDTA and OVA concentrations. In summary, the total value of Cd^{2+} recoveries of around 100% suggests that the possible metal interferences above explained remain blocked due to bounding with the albumin while the Cd^{2+} analyte is complexed with EDTA followed by its determination in the integrated biosensor device. In addition during the analysis of a certified effluent wastewater sample, which metallic composition is shown at table_S4 in SI, the evaluation of both effects, EDTA for complexing preferably Cd^{2+} ions and OVA for masking preferably the other metallic ions interferences once the sample crosses the first conjugation strip was again demonstrated. The obtaining of 105% of recovery for the 5 ppb Cd^{2+} containing sample in presence of others possible metal interferences indicates the device efficiency with EDTA and OVA deposited in the first conjugation pad to detect with high accuracy Cd^{2+} .

The comparison of the slope and the intercept of the line of adjust (see **figure 7**), calculated by plotting of the found concentrations via the new integrated LFID and ICP-MS method, with 1 and 0 values, respectively, demonstrated that there isn't a significant difference with theses theoretical values over the studied concentration range. Therefore, the Cd^{2+} determination by using the LFIA device is statistically equal to the one using ICP-MS, and the device can be used for Cd^{2+} analysis instead of the traditional and expensive ICP-MS or AAS equipments that in addition require high qualified users.

The standard deviation and coefficient of variation values for the studied concentrations were lower than 2 and 5%, respectively. The intermediate precision of the device was found between 10 and 5.8% in the range of 5 to 50 ppb Cd^{2+} (table S_5 in SI).

Table 2. Cd²⁺ recoveries (%) at different concentrations for each water samples analyzed. The number of analyzed replicate is 4 (n=4).

Waters samples	Cd ²⁺ recoveries (%)				
	0.4 ppb Cd ²⁺	2 ppb Cd ²⁺	5 ppb Cd ²⁺	10 ppb Cd ²⁺	50 ppb Cd ²⁺
drinking water 1	103.35±3.12	104.83±3.11	101.25±0.56	102.98±0.11	101.11±0.32
drinking water 2	104.53±1.23	95.63±2.36	98.54±0.73	101.33±1.75	98.82±2.50
tap water 1	105.23±2.03	99.83±2.05	103.50±2.15	102.47±0.71	95.63±2.75
tap water 2	104.80±1.95	105.03±1.28	96.83±2.67	98.94±1.89	95.79±1.25
waste water reference pattern	–	–	105.02±0.85	–	–
variance analysis	$F_{calculated} = 0.73 < F_{0.95}^{4,15} = 3.06$				
recoveries total mean	$\bar{X} = 101.02$				
t student	$t_{calculated} = 1.36 < t_{(0.05;19)} = 1.73$				

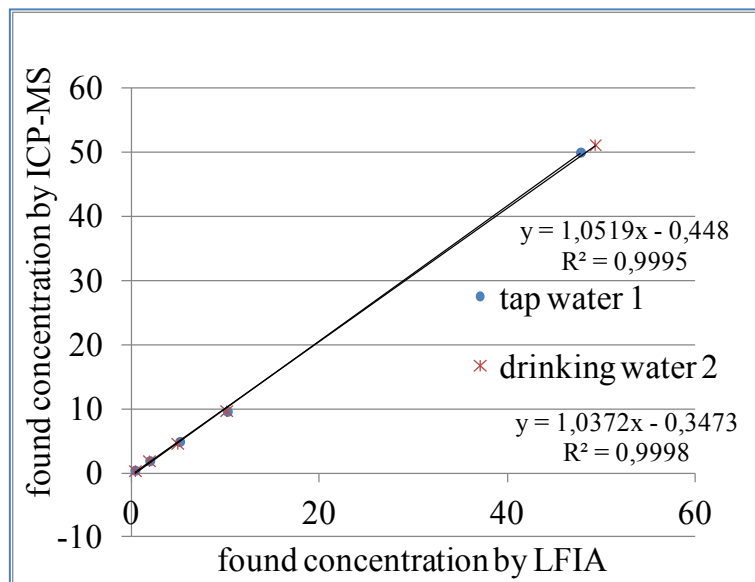


Figure 7. Graph of the found concentrations by the integrated LFID and the ICP-MS methods. Lines and equations obtained by adjusting of the plot of the experimental points are shown.

VI.4 Conclusions

A novel and highly sensitive lateral flow immunodevice with integrated sample treatment platform for Cd^{2+} detection in drinking and tap water samples using the Cd-EDTA-BSA conjugate labeled with AuNPs as signal producer tool has been successfully developed.

In the first part of this work a conventional LFD based on competitive reaction between the Cd-EDTA-BSA-AuNP conjugate (deposited on the conjugation pad strip) and the Cd-EDTA complex (formed in the analysis sample) for the same binding sites of the 2A81G5 mAb (specific to Cd-EDTA, which is immobilized onto the test line at the optimized concentrations) was performed. A strategy to increase the sensibility of the LFDs in a competitive format by decreasing the mAbs and conjugate concentrations is introduced. The Cd-EDTA-BSA-AuNP conjugate concentration onto the conjugate strip was decreased by increasing the length of the conjugate strip and soaking it either in the same or in a bigger volume of the conjugate strip solution. This optimization process permits to reach, in first place, a great large operation range from 0.4 to 2000 ppb being the lineal working range from 0.4 to 10 ppb, and in second place, very low LoD and LoQ of 0.1 and 0.4 ppb, respectively. These metal detection and quantification levels are much lower than the previously reported for metal biosensors based on paper and even for many metal electrochemical methods.

The specificity assay carried out with this conventional device demonstrated that Ca^{2+} , Mg^{2+} , Fe^{3+} , Al^{3+} and Pb^{2+} ions show a slight or almost no interference in the Cd^{2+} analysis. Co^{2+} , Ni^{2+} , Zn^{2+} and Cu^{2+} ions have a moderate interference (5 ppm of these metallic ions causes an interference between 5-10% in the determination of 10 ppb Cd^{2+} using 14 mM Na_2EDTA) while Hg^{2+} and Mn^{2+} ions have a notable interference (the presence of 5 ppm Mn^{2+} or Hg^{2+} interferes between 15-18% in the 10 ppb Cd^{2+} analysis using 14 mM Na_2EDTA). The interferences can be reduced below 5% by lowering the EDTA concentration to 0.005 mM and by adding 10% OVA or BSA.

The second part of this work describes the fabrication and evaluation of a high sensitive and integrated LFID. This integrated device has an extra dual function pad strip inserted between the sample and the conjugated pad. It has the double function, to mask interferences using OVA and to prepare the sample for Cd^{2+} analysis using EDTA. This novel integrated device allowed the direct analysis of real water samples without any pretreatment.

The results of the accuracy assays show that the device is able to determine Cd^{2+} in drinking and tap waters with almost 100% accuracy. The repeatability and inter-assay precision variation coefficient for these determinations are around 5 and 10% even for the lowest concentration (0.4 ppb).

This work represents a suitable and available alternative for Cd^{2+} quantification in drinking and tap waters, able to detect heavy metals 50 times below the maximum allowable limit. This integrated platform is easy to be built, cheap, portable and simple to manage even by non skilled persons, which makes it very useful for Cd^{2+} analysis in point of care diagnostics or where a rapid contamination monitoring is very necessary or in field analysis in remote locations with limited facilities. The extended application of the device developed here for analyzing Cd^{2+} in a large variety of samples like seawater, serum, etc, could be easily implemented. In addition it constitutes an accurate and precise tool that can substitute even traditional and expensive methods such as AAS and ICP-MS well known for their high analytical performance in Cd^{2+} analysis. We expect that such sensors could be particularly useful in large scale routine screening of drinking water samples or industrial process streams in developing countries, where the heavy metal concentrations are usually relatively high.

VI.5 Supporting Information

Table_S1. Permissible limits of heavy metal (in ppm) in drinking water. * No specification is set at this moment.

	Ca ²⁺	Mg ²⁺	Co ²⁺	Al ³⁺	Fe ³⁺	Zn ²⁺	Mn ²⁺	Cu ²⁺	Ni ²⁺	Pb ²⁺	Hg ²⁺	Cd ²⁺
WHO		*		0.2	0.3	3	0.10	2	0.07	0.01	0.001	0.003
EPA		*		0.2	0.2	5	0.05	1.3	0.04	0.015	0.002	0.005
U.S.		*		0.05	0.3	5	0.05	1.3	0.10	0.01	0.001	0.005

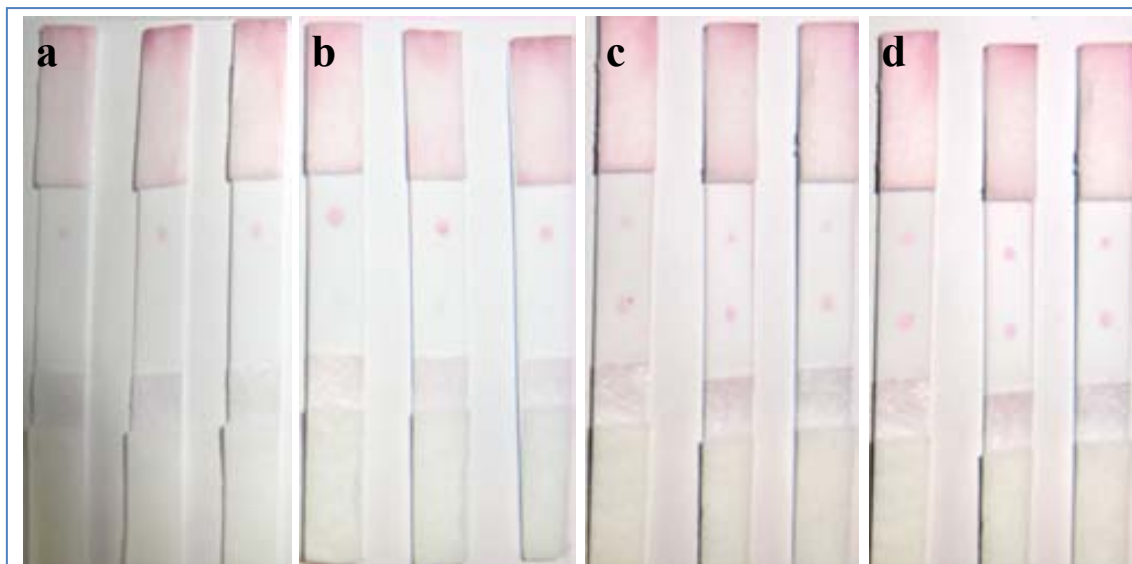
Optimization of the conventional LFID operational conditions.

Optimization of the conjugate and antibodies concentrations in the device.

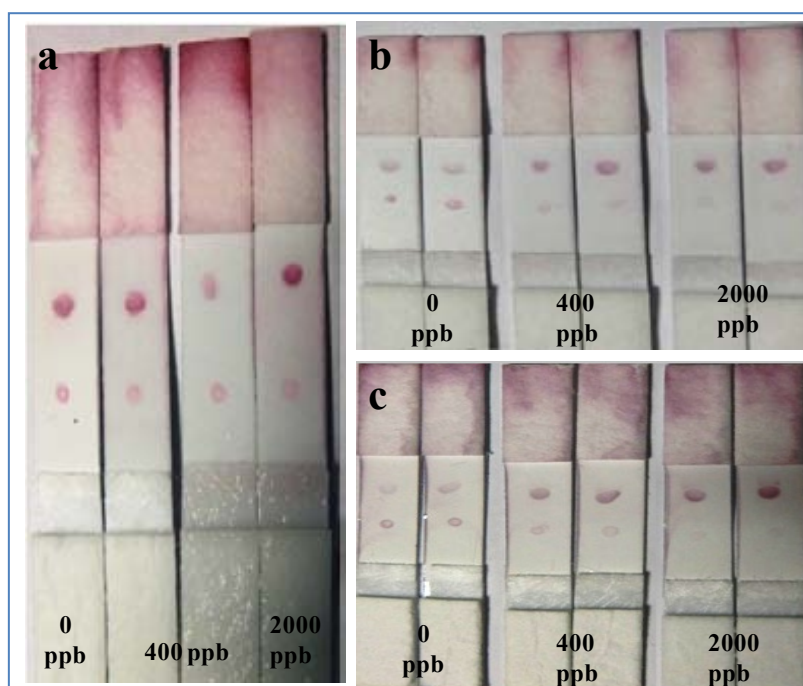
The first optimizations of the LFID were carried out by drop coating of different mAbs concentrations onto the membrane for the same conjugation strip preparation (7.5 cm conjugation strip length soaked into 300 μ L of the conjugation trip solution). By depositing 0.5 or 0.8 μ L of 0.5 mg/mL of the 2A81G5 mAb and 1 mg/mL of the anti-BSA mAb no visible (naked eye) response was observed at test line while a pink color was observed in control zone (figure_S1-a). By increasing the 2A81G5 mAb concentration on the test zone up to 1 mg/mL and keeping the use of 1 mg/mL of the anti-BSA at control zone a pale pink color is observed in the test zone while the pink color at control zone remains constant (figure_S1-b). By increasing the 2A81G5 mAb concentration up to 2 mg/mL at the test zone and continuing with the use of 1 mg/mL of the anti-BSA mAb at control zone a strong pink color is observed on the test zone but a pale pink color appeared in the control zone (figure_S1-c). Good color intensity in the test and control zone using 2 mg/mL of the both mAbs (figure_S1-d) is observed. This assay demonstrated that the recognition reaction between the 2A81G5 mAb and the Cd-EDTA contained in the Cd-EDTA-BSA-Au conjugate, and the recognition reaction between anti-BSA mAb and the BSA contained in the Cd-EDTA-BSA-Au conjugate, took place satisfactorily. In addition to that, around 2 mg/mL of the mAbs is necessary to immobilize onto the membrane by drop coating deposition to obtain good color intensity.

Standard dissolutions of Cd-EDTA (0, 400 and 2000 ppb) were analyzed immobilizing 2 mg/mL of the mAbs onto the membrane and decreasing the concentration of the conjugate onto the conjugation strip. The conjugate concentration onto the conjugation strip can be decreased by increasing the length of the conjugation strip and soaking it either in the same or in a bigger volume of the conjugation strip solution. By using a 7.5

cm conjugation strip length soaked into 300 μL of the conjugation trip solution no color difference between the samples in the test zone was observed (see figure_S2-a). However using 9 and 11 cm conjugation strip lengths soaked into 300 μL of the conjugation pad solution a color difference between 0, 400 and 2000 ppb of Cd-EDTA can be detected (see figure_S2-b,c).

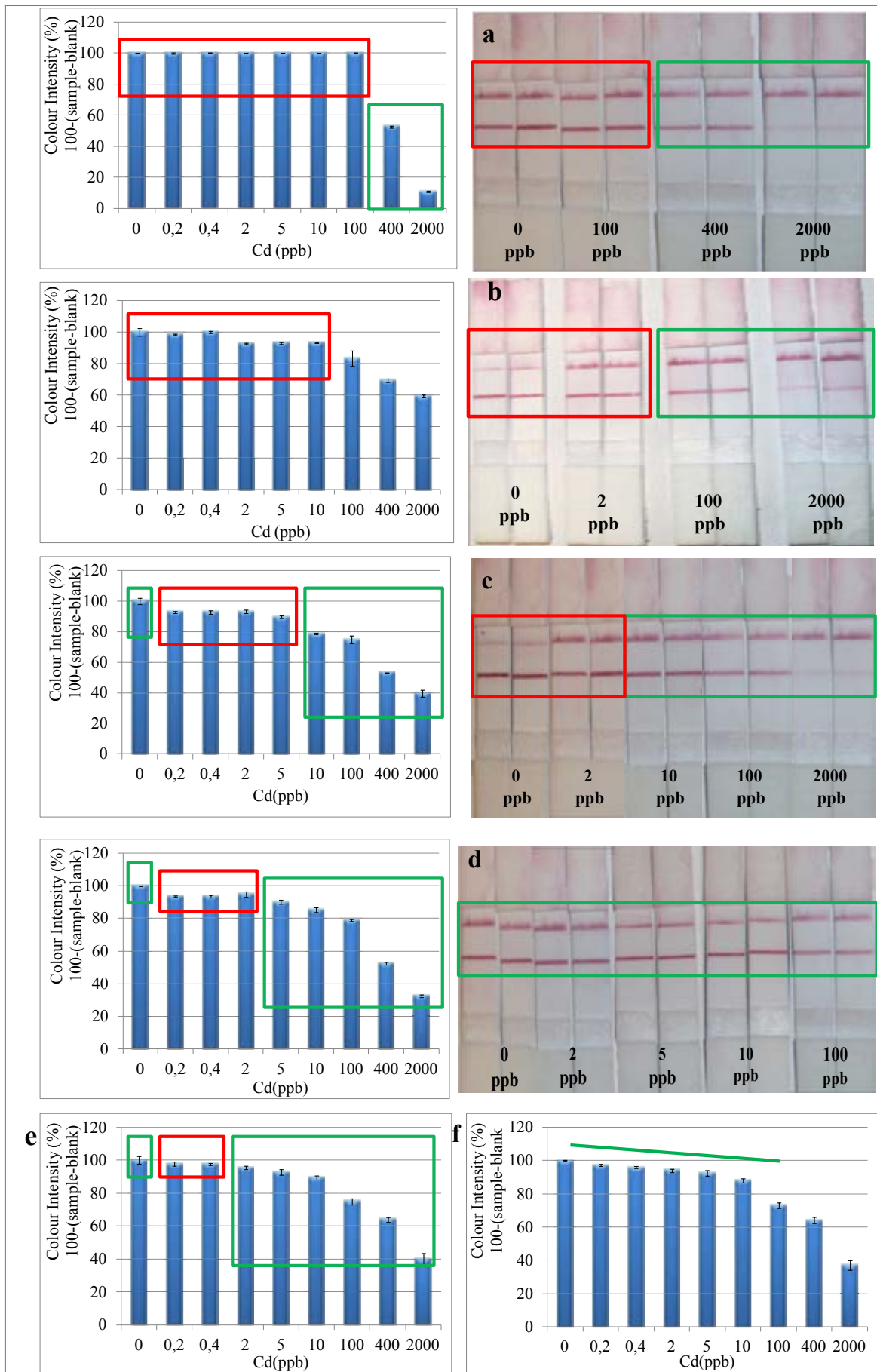


Figure_S1. Images of the initial probes of LF performed with different mAbs concentrations deposited by drop coating (0.5 μL) in the test and control zones: (a) using 0.5 mg/mL of 2A81G5 and 1 mg/mL of anti-BSA mAbs, (b) using 1 mg/mL of 2A81G5 and 1 mg/mL of anti-BSA mAbs, (c) using 2 mg/mL of 2A81G5 and 1 mg/mL of anti-BSA mAbs and (d) using 2 mg/mL of 2A81G5 and 2 mg/mL of anti-BSA mAbs.



Figure_S2. Images of the LF used for analysis of Cd-EDTA standard dissolutions using 0.1 μL (2 mg/mL) of the mAbs deposited by drop coating onto the membrane: (a) using a conjugation strip length of 7.5 cm, (b) using a conjugation strip length of 10 cm and (c) using a conjugation strip length of 11 cm.

In general the sensibility of the device increases when decreases the mAbs and the Cd-EDTA-BSA-AuNP conjugate concentrations. Optimizations with higher precisions were made dispensing automatically the mAbs dissolutions with the dispensing equipment. Using the automatic dispensing 0.5 $\mu\text{g/mL}$ of 2A81G5 mAb are deposited in the test line and 300 μL of the Cd-EDTA-BSA-AuNP conjugate are deposited onto 10 cm long of the conjugation strip and the device is able to discriminate between 0, 400 and 2000 ppb of Cd-EDTA. This large quantity of 2A81G5 mAb collocated onto the test line provokes the development of a strong color intensity when the Cd-EDTA-BSA conjugate labeled with AuNP is bound in this site, and in consequence it doesn't allow any discoloration that Cd-EDTA concentrations below 400 ppb could provoke (figure_S3-a). Decreasing to 0.375 $\mu\text{g/mm}$ the 2A81G5 mAb concentration onto the test line and using the same concentration of the Cd-EDTA-BSA-AuNP, the color differences between 0, 100, 400 and 2000 ppb can be observed with the device (figure_S3-b). Keeping 0.375 $\mu\text{g/mm}$ of the 2A81G5 mAb onto the test line and using a 12 cm long conjugation strip soaked inside of more diluted conjugation pad solution (350 μL), better results were obtained due to the fact that the discoloration caused by 0, 10, 100, 400 and 2000 ppb of Cd-EDTA could be observed (figure_S3-c). By keeping the same quantity of mAbs immobilized onto the membrane and increasing to 14 cm the length of the conjugation strip soaked inside of a more diluted conjugation pad solution (400 μL) a color difference between 0, 5, 10, 100, 400 and 2000 ppb of Cd-EDTA can be seen (figure_S3-d). With a 16 cm long conjugation strip soaked inside of a more diluted conjugation pad solution (500 μL) the distinguishing of the color difference between 0, 2, 5, 100, 400 and 2000 ppb by using the rapid scan equipment was possible (figure_S3-e). Finally by increasing the length of the conjugation strip up to 18 cm and soaking it inside of a more diluted conjugation pad solution (600 μL) a better resolution and color differences between 0, 0.4 and 2 ppb of Cd-EDTA via rapid scan equipment were possible to be observed (figure_S3-f).



Figure_S3. Graphs and lateral flow photos of the color intensity variation in relation to cadmium concentration during the optimization of the mAbs and the Cd-EDTA-BSA-AuNPs conjugate concentrations onto the device. (a) 0.5 $\mu\text{g}/\text{mm}$ 2A81G5 mAb, 0.32 $\mu\text{g}/\text{mm}$ anti-BSA mAb and 10 cm length of the conjugation strip soaked in 300 μL of the conjugation pad solution, (b) 0.375 $\mu\text{g}/\text{mm}$ 2A81G5 mAb, 0.32 $\mu\text{g}/\text{mm}$ anti-BSA mAb and 10 cm length of the conjugation strip soaked in 300 μL of the conjugation pad solution, (c) 0.375 $\mu\text{g}/\text{mm}$ 2A81G5 mAb, 0.32 $\mu\text{g}/\text{mm}$ anti-BSA mAb and 12 cm length of the conjugation strip soaked in 350 μL of the conjugation pad solution, (d) 0.375 $\mu\text{g}/\text{mm}$ 2A81G5 mAb, 0.4 $\mu\text{g}/\text{mm}$ anti-BSA mAb and 14 cm length of the conjugation strip soaked in 400 μL of the conjugation pad solution, (e) 0.375 $\mu\text{g}/\text{mm}$ 2A81G5 mAb, 0.4 $\mu\text{g}/\text{mm}$ anti-BSA mAb and 16 cm length of the conjugation strip soaked in 500 μL of the conjugation pad solution and (f) 0.375 $\mu\text{g}/\text{mm}$ 2A81G5 mAb, 0.4 $\mu\text{g}/\text{mm}$ anti-BSA mAb and 18 cm length of the conjugation strip soaked in 600 μL of the conjugation pad solution. The square in green indicates the change of color difference for each cadmium concentration and the red square indicates the constant color independently of cadmium concentration.

Specificity assay

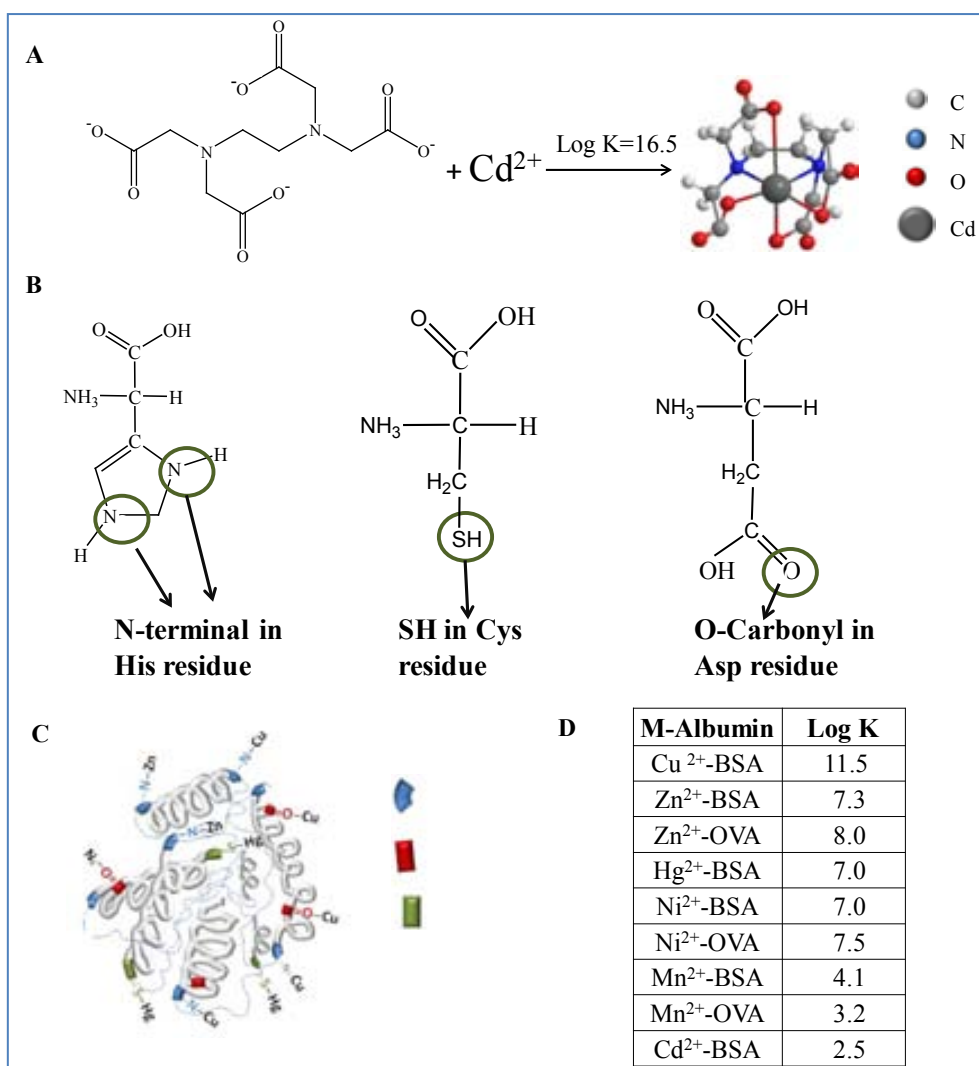
Table_S2. Values of the complexes formation constants (log Kf) of the Metal-EDTA, Metal-albumin and Metal/EDTA-2A81G5 mAb at 25°C and pH ~7. The over expected metal concentrations in real samples is also given.

Formation Constants			Metal concentrations in spiked samples (ppm)
Metal-EDTA	Metal-albumin	Metal/EDTA-2A81G5 mAb	
Fe ³⁺ 25.1; Hg ²⁺ 21.5;	Cu ²⁺ 11.5; Zn ²⁺ 8.0;	Cd ²⁺ 8.3; Hg ²⁺ 7.5; Mn ²⁺ 6.4	Ca ²⁺ = Mg ²⁺ 15; Zn ²⁺ 5;
Ni ²⁺ 18.6; Cu ²⁺ 18.8;	Ni ²⁺ 7.5; Hg ²⁺ 7.0;	Ni ²⁺ 5.7; Zn ²⁺ 5.6; Co ²⁺ 5.5	Cu ²⁺ 2.5; Al ³⁺ = Fe ³⁺ 0.4;
Pb ²⁺ 18.0; Cd ²⁺ 16.5;	Pb ²⁺ 4.2; Mn ²⁺ 4.1;	Cu ²⁺ 5.3; Fe ³⁺ 4.3; Pb ²⁺ 4.1	Mn ²⁺ 0.3; Ni ²⁺ 0.02
Co ²⁺ 16.3; Zn ²⁺ 16.5;	Cd ²⁺ ~ 2.5	Mg ²⁺ 3.7; Al ³⁺ 3.1	Pb ²⁺ 0.01; Hg ²⁺ 0.05
Al ³⁺ 16.4; Mn ²⁺ 14.0;			
Ca ²⁺ 10.7; Mg ²⁺ 8.7			

The most common metal binding site in albumins.

Metals have multiples, similar and different, binding sites through the large amino acidic sequence in albumins. The N-terminal nitrogen of the imidazole ring of histidine (His) residue is the first most common binding site in BSA and OVA for the majority of these metals.⁵⁰⁻⁵⁴ Other binding sites are the carbonyl oxygen of aspartic acid (Asp) and sulfhydryl group of cysteine (Cys) residue (figure_S4-B).^{50,53} For example in the case of BSA structure, it has 15 His residues, 17 sulfhydryl bridges between Cys residues and 35 Asp residues as possible metal binding sites. The figure_S4-C shows a schematic representation of the reaction metal-albumin where is shown the multiples

binding sites with metals through the functional groups of the amino acid sequence in albumin.




Figure_S4. Schematic representation of the reactions, binding sites and formation complex constant involved between metal, EDTA and albumin during cadmium analysis. (A) Equation of the reaction between cadmium and EDTA. (B) Preferential metal binding sites in amino acid residues. (C) Schematic representation of metal immobilizing onto albumin. (S4-D) Metal-BSA/OVA complexes formation constant (values at table are applied at 25 °C and pH 7.4).

Table_S3. Metals contents of the studied water samples. The values of Ca^{2+} and Mg^{2+} ions with the asterisk tag (*) were determined in the lab by EDTA titration.

Waters	Metals contents (ppm)			
	Ca^{2+}	Mg^{2+}	Na^+	K^+
Drinking water 1	35.5	8.6	11.9	-
Drinking water 2	82.3	14.9	0.7	1.29
Tap water 1	70*	130*	-	-
Tap water 2	28*	115*	-	-

Table_S4. Metals content in the wastewater certificate reference material (N° 713).

Certificated Reference Material BCR [®] -713	Metal	Certificated value (ppb)
	As	9.7 ± 1.1
	Cd	5.1 ± 0.6
	Cr	21.9 ± 2.4
	Cu	69.0 ± 4.0
	Fe	400.0 ± 40.0
	Mn	43.4 ± 3.0
	Ni	30.0 ± 5.0
	Pb	47.0 ± 4.0
	Se	5.6 ± 1.0

Table_S5. Obtained results in the precision assay.

		Cd^{2+} added concentration (ppb)			
		10 ppb Cd^{2+}		50 ppb Cd^{2+}	
		S	CV(%)	S	CV(%)
repeatability n=6	UAB tap water	0.35	3.56	0.21	0.41
	Font Vella drinking water	0.24	2.40	0.28	0.56
Intermediate precision n=12	UAB tap and Font Vella drinking water	0.73	7.30	2.91	5.83

VI. 6 References

- [1] G. Aragay, J. Pons, A. Merkoçi, *Chem. Rev.* **2011**, 111, 3433.
- [2] G. Aragay, A. Merkoçi, *Electrochim. Acta* **2012**, 84, 49.
- [3] H. S. M Zakir, J. D. Brennan, *Anal. Chem.* **2011**, 83, 8772.
- [4] C. L. Schauer, P. R. R. Mu-Sanchen, P. Schoen, F. S. Ligler, *Environ. Sci. Technol.* **2004**, 38, 4409.
- [5] R. G. Bhagure, S. R. Mirgane, *Environ. Monit. Assess.* **2011**, 173, 643.
- [6] M. Khosraviani, R. A. Pavlov, C. G. Flowers, D. A. Blake, *Environ. Sci. Technol.* **1998**, 32, 137.
- [7] I. A. Darwish, D. A. Blake, *Anal. Chem.* **2001**, 73, 1889.
- [8] I. A. Darwish, D. A. Blake, *Anal. Chem.* **2002**, 74, 52.
- [9] R. Guell, G. Aragay, C. Fontas, E. Antico, A. Merkoçi, *Anal. Chim. Acta* **2008**, 627, 219.
- [10] WHO Guidelines for Drinking Water Quality; in: Chemical aspects. 3rd Ed. Geneva **2008**, Vol. 1, p.145.
- [11] J. Gasparik, D. Vladarova, M. Capcarova, P. Smehyl, J. Slamecka, P. Garaj, R. Stawarz, P. Massanyi, *J. Environ. Sci. Health A* **2010**, 45, 818.
- [12] T.-Y. Hoa, Ch.-T. Chiena, B.-N. Wang, A. Siriraks, *Talanta* **2010**, 82, 1478.
- [13] M. R. Knecht, M. Sethi, *Anal. Bioanal. Chem.* **2009**, 394, 33.
- [14] J. Du, Y. Sun, L. Jiang, X. Cao, D. Qi, S. Yin, J. Ma, C. F. Y. Boey, X. Chen, *Small* **2011**, 7, 1407.
- [15] Ch. Zong, K. Ai, G. Zhang, H. Li, L. Lu, *Anal. Chem.* **2011**, 83, 3126.
- [16] A. Afkhami, T. Madrakian, S. J. Sabounchei, M. Rezaei, S. Samiee, M. Pourshahbaz, *Sensor Actuat. B*, **2012**, 161, 542.
- [17] G. Aragay, A. Puig-Font, M. Cadevall, A. Merkoçi, *J. Phys. Chem. C* **2010**, 114, 9049.
- [18] T. Shtoyko, S. Conklin, A. T. Maghasi, J. N. Richardson, A. Piruska, C. J. Seliskar, W. R. Heineman, *Anal. Chem.* **2004**, 76, 1466.
- [19] G. Aragay, J. Pons, A. Merkoçi, *J. Mater. Chem.* **2011**, 21, 4326.
- [20] M. Adami, S. Marco, C. Nicolini, *Electroanal.* **2007**, 19, 128816.
- [21] H.-W. Zhao, Ch.-G. Xue, T.-G. Nan, G.-Y. Tan, Z. Li, Q.-X. Li, Q.-Ch. Zhang, B.-M. Wang, *Anal. Chim. Acta*, **2010**, 676, 81.
- [22] D. A. Blake, R. C. II Blake, M. Khosraviani, A. R. Pavlov, *Anal. Chim. Acta*, **1998**,

- 376, 13.
- [23] K. Abe, K. Nakamura, T. Arao, Y. Sakurai, A. Nakano, Ch. Suginuma, K. Tawaradae, K. Sasakif, *J. Sci. Food Agric.* **2011**, 91, 1392.
- [24] X. Liu, J.-J. Xiang, Y. Tang, X.-L. Zhang, Q.-Q. Fu, J.-H. Zou, Y.-H. Lin, *Anal. Chim. Acta*, **2012**, 745, 99.
- [25] D. Mazumdar, J. Liu, G. Lu, J. Zhou, Y. Lu, *Chem. Commun.* **2010**, 46, 1416.
- [26] C. Parolo, A. Merkoçi, *Chem. Soc. Rev.* **2013**, 42, 450.
- [27] B. Ngom, Y. Guo, X. Wang, D. Bi, *Anal. Bioanal. Chem.* **2010**, 397, 1113.
- [28] S.-F. Torabia, Y. Lu, *Faraday Discuss.* **2011**, 149, 125.
- [29] Z. Fang, J. Huang, P. Lie, Z. Xiao, Ch. Ouyang, Q. Wu, Y. Wu, G. Liu, L. Zeng, *Chem. Commun.* **2010**, 46, 9043.
- [30] Z. Gu, M. Zhao, Y. Sheng, L. A. Bentolila, Y. Tang, *Anal. Chem.* **2011**, 83, 2324.
- [31] G. Aragay, H. Monton, J. Pons, M. Font-Bardia, A. Merkoci, *J. Mater. Chem.* **2012**, 22, 5978.
- [32] A. George, E. S. Shibu, Sh. M. Maliyekkal, M. S. Bootharaju, T. Pradeep, *Appl. Mater. Interfaces* **2012**, 4, 639.
- [33] Ch. Chen, J. Wu, *Sensors*, **2012**, 12, 11684.
- [34] D. H. Choi, S. K. Lee, Y. K. Oh, B. W. Bae, S. D. Lee, S. Kim, Y.-B. Shin, M.-G. Kim, *Biosens. Bioelectron.* **2010**, 25, 1999.
- [35] C. Parolo, M. Medina-Sánchez, A. de la Escosura-Muñiz, A. Merkoçi, *Lab Chip* **2013**, 13, 386.
- [36] C. Parolo, A. de la Escosura-Muñiz, A. Merkoçi, *Biosens. Bioelectron.* **2013**, 40, 412.
- [37] R.-H. Shyu, S.-S. Tang, D.-J. Chiao, Y.-W. Hung, *Food Chem.* **2010**, 118, 462.
- [38] A. Jang, Zh. Zou, K. K. Lee, Ch. H. Ahn, P. L. Bishop, *Talanta*, **2010**, 83, 1.
- [39] W. Jung, A. Jang, P. L. Bishop, Ch. H. Ahn, *Sensors Actuat. B* **2011**, 155, 145.
- [40] A. Apilux, W. Dungchai, W. Siangproh, N. Praphairaksit, Ch. S. Henry, O. Chailapakul, *Anal. Chem.* **2010**, 82, 1727.
- [41] S. N. Tan, L. Ge, W. Wang, *Anal. Chem.* **2010**, 82, 8844.
- [42] J. Zhang, F. Laiwalla, J. A. Kim, H. Urabe, R. V. Wagenen, Y.-K. Song, B. W. Connors, F. Zhang, K. Deisseroth, A. V. Nurmikko, *J. Neural Eng.* **2009**, 6, 055007.
- [43] A. Adami, C. Röss, C. Collini, S. Pedrotti, L. Lorenzelli, *Biosens. Bioelectron.* **2013**, 40, 315.

- [44] M. Zhou, N. Zhou, F. Kuralay, J. R. Windmiller, S. Parkhomovsky, G. Valdés-Ramírez, E. Katz, J. Wang, *Angew. Chem. Int. Ed.* **2012**, 51, 2686.
- [45] D. H. Choi, S. K. Lee, Y. K. Oh, B. W. Bae, S. D. Lee, S. Kim, Y.-B. Shin, M.-G Kim, *Biosens. Bioelectron.* **2010**, 25, 1999.
- [46] D. A. Blake, P. Chakrabarti, M. Khosraviani, F. M. Hatcher, C. M. Westhoff, P. Goebel, D. E. Wylie, R. C. II Blake, *J. Biol.Chem.* **1996**, 271, 27677.
- [47] K. Saha, S. S. Agasti, Ch. Kim, X. Li, V. M. Rotello, *Chem. Rev.* **2012**,112, 2739.
- [48] *United States Pharmacopeia 30, National Formulary 25*. Validation of Compendia methods; Rockville, Md., USA, **2007**, General Chapter 1225.
- [49] N. T. H. Lien, L. T. Huyen, V. X. Hoa, C. V. Ha, N. T. Hai, L. Q. Huan, E. Fort, D. Q. Hoa, T. H. Nhung, *Adv. Nat. Sci.: Nanosci. Nanotechnol.* **2010**. 1, 025009, DOI:10.1088/2043-6254/1/2/025009.
- [50] W. Bal, J. Christodoulou, P. J. Sadler, A. Tucker, *J. Inorg. Biochem.* **1998**, 70, 33.
- [51] W. J. Goux, P. N. Venkatasubramanian, *Biochem.* **1986**, 25, 84.
- [52] J. Masuoka, J. Hegenauer, B. R. Van Dyke, P. Saltman, *J. Biol. Chem.* **1993**, 268, 21533.
- [53] J. Masuoka, P. Saltman, *J. Biol. Chem.* **1994**, 269, 25557.
- [54] S. R. Verma, J. P. S. Arora, J. S. Shankar, D. Dutt, C. Pal, *Water Air Soil Pollut.* **1989**, 43, 53.
- [55] K. Sasaki, S. H. Oguma, T. Glass, Y. Namiki, H. Sugiyama, N. Ohmura, D. A. Blake, *J. Agric. Food Chem.* **2008**. 56, 7613.
- [56] R. Delgado de la Torre, *Iniciación a la Probabilidad y la Estadística*. Universitat Autònoma de Barcelona, Eds.; Barcelona, Spain, **2004**; pp.115.

VII. CONCLUSIONS OF THE THESIS

VII. Conclusions

Considering the objectives of this PhD thesis (as proposed in Chapter II) and the obtained experimental results the following conclusions can be remarked:

General conclusion

Cheap and easy to synthesize nanostructured materials based on CaCO₃-PEI (as calcite microrods and vaterite microspheres/ellipsoids) for both sensing and removing of heavy metals including a simple cost-effective paper biosensor for Cd²⁺ based on Cd-EDTA-BSA-AuNPs conjugate as color producer tool have been developed.

Specific conclusions

1. A novel and easy route of synthesis of nanostructured vaterite microparticles as hybrid composite (CaCO₃-polymer) based on sonication mixing, the use of PEI as CGM and the mixed water/organic solvent has been developed. The new method is able to provide a complete polymorphic discrimination in addition to a controlled and homogeneous particle size distribution. The CaCO₃-PEI microparticles possess a high functionalizing capacity for large variety of (bio)molecules.

1.1. Different reactions of vaterite synthesis have been studied:

1.1-1 The simple mixture of equal volumes and concentrations (5 mL and 0.33 M) of the CaCl₂ and Na₂CO₃ dissolutions using magnetic stirring just yielded calcite product. The same reaction under ultrasonic mixing yielded a mixture of calcite and vaterite, being vaterite yield at around 35%. The reduction of the reaction volume from 5 to 1 mL (under ultrasonic mixing) produces a decreasing in the microparticle size from $2.1 \pm 0.3 \mu\text{m}$ to $1.1 \pm 0.15 \mu\text{m}$, an increasing in the vaterite fraction from 35 to 70 % and the production of nanostructures with high density of porosity as corroborated by XRD, IR and SEM studies. The changes in the reaction times from 15 to 60 min do not affect neither the size nor the morphology of vaterite product.

1.1-2 The reaction carried out with ultrasonic mixing and the PEI use as CGM yield calcite and vaterite mixture too. The increase of PEI concentration in the system from 0 to 4 mg/mL increased the vaterite fraction from 36 to 76% and decreases the microparticle size from 2.0 ± 0.3 to $1.36 \pm 0.16 \mu\text{m}$. The distribution of equal quantity of PEI between the CaCl₂ and Na₂CO₃ dissolutions brought

additional increasing in vaterite fraction up to 86% and reduction of the microspheres size to $0.83 \pm 0.16 \mu\text{m}$.

1.1-3 In the reactions carried out using various water-organic solvent mixtures with or without PEI a complete polymorph discrimination was achieved. When only mixed water/organic solvents are used during the reaction, the crystallization product is completely calcite rhombohedra independently of the organic solvent used in the mixture (EtOH, EtOAc, DMSO and DMF). When 4 mg/mL of PEI is added to the CaCl_2 solution, microspheres and/or ellipsoids together with rhombohedra crystals appear in the product. Further increase of PEI (a second addition of 4 mg/mL of PEI in the Na_2CO_3 solution) yielded completely vaterite microspheres or/and microellipsoids in the precipitation product. The fraction of spheres and ellipsoids is related with the polarity of the solvents mixture. The increasing of the polarity of the solvents mixture produces more sphere like-shapes in relation to ellipsoids like-shapes.

- 1.2 The vaterite-PEI microparticles synthesized via water/EtOH+8mg/mL PEI system presented a high efficient loading capacity for large variety of dyes and biomolecules with hydrogen acids, independently of their charges and sizes. This high loading capacity was associated with the formation of hydrogen bonds between the acids hydrogens of the conjugated molecule and the PEI's nitrogens. The developed material is useful for multiple applications such as signal amplification in biosensors and enhancing of the electro transfer in electrochemical sensors as shown in the works presented at annex III and done in collaboration with other projects.
 - 1.3 The presence of PEI layer covering the vaterite microparticle surface was verified by SEM and IR spectroscopy. This PEI layer that covers the vaterite microparticle surface conferred to the material multiple properties with interest for several applications. First, it gives to vaterite a stabilizing effect checked up to 8 months. Second, it offered additional chemical properties for further modifications with functional molecules. Third, it provided high superficial charge as shown by z-potential measurements.
- 2- A very fast and efficient heavy metals removing by using a hybrid nanostructured vaterite-PEI material (NV-PEI) composed of mixed nanostructured microspheres and microellipsoids of about $1 \mu\text{m}$ size has been achieved.

- 2.1- According to the multicomponent competitive assays studies it was found that Pb^{2+} and Cu^{2+} were the metals with preferential adsorption by NV-PEI.
 - 2.2- Especially ultra-fast and high adsorption capacity for Pb^{2+} never reported before was achieved. Just a 3 min contact time, under stirring conditions, is enough to remove between 97 and 100% of this metal contaminant over an entire range of initial concentrations from 0 to 1000 ppm using a dosage of 0.5 g NV-PEI/L at the usual pH 6 water samples. The maximum adsorption capacity was 2762 mg of Pb^{2+} /g adsorbent material.
 - 2.3- The value of adsorption parameters in the NV-PEI material such as BET, BJH, and porous volume were 20 m^2/g , 2.1, 2.8-191 nm and 0.07 mL/g, respectively.
 - 2.4- The metal removal mechanisms are based on the recrystallization process via ion exchange with Ca^{2+} in the NV-PEI material and the adsorption of metal species by nucleophilic-electrophilic interactions between PEI's nitrogens and the metallic center.
 - 2.5- The NV-PEI material displayed a powerful capability for fast and effectively removal of toxic heavy metal especially Pb^{2+} , doing this material an efficient adsorbent alternative for the water treatment processes. In addition, this material is facile to be synthesise, available, biodegradable and multipurpose adsorbents that can remove both organic and heavy metal pollution (many co-existing pollutants usually appear in industrial effluents), which provide important characteristics for industrial water treatment.
- 3-** An original, simple and complete multifunctional system for sensing and removing ('*sensoremoval*') of Pb^{2+} from waste water as proof-of-concept strategy with interest for environment is presented. To the best of our knowledge, for the first time the detection and removing of chemical contaminant are integrated in the same system.
- 3.1 This sensing and removing system is based on hybrid calcite-PEI NRs formation from initial Pb^{2+} contaminated waters to which Na_2CaEDTA and Na_2CO_3 reagents are added followed by Na_2PbEDTA complex formation and CaCO_3 precipitation. The calcite-PEI NRs precipitate is the unique crystallization product in this system as determined by XRD and SEM characterizations techniques. The as-synthesized particles were used as sensing and removing material of Pb^{2+} .
 - 3.2-1 Calcite NRs with sizes of around 2, 1 or 0.6 μm , depending on the type of reaction, were permanently synthesized changing the reagents order, using or not CGMs as PEI, DEA or glycerol, modifying the solvent used as reaction medium

(ethanol, ethylacetate, etc), the use of $\text{Ca}(\text{NO}_3)_2$ instead of CaCl_2 or decreasing the reaction volumes. All these large variety of changes in the reaction conditions only affect the size or the surface texture of the NRs or as much the shape at the ends of the NRs, but the main rod shape persists in the crystallization product.

- 3.2-2 The dramatic decreasing of the reagents concentration guides to calcite nanoplates that compose the NRs. In the absence of PEI in the system the diminution of the reagents concentration (from 3.3×10^{-1} to 3.3×10^{-4} M) guides to heterogeneous calcite nanoplates, while in the presence of PEI this reagent diminution leads to perfect hexagonal calcite plates.
- 3.3- The simple Pb^{2+} sensing strategy introduced here, via changes in turbidity during the CaCO_3 precipitation, allows estimating up to 34 ppm of Pb^{2+} by naked eye while lower concentrations can be quantified using a turbidimeter. A lineal range of response between 1 and 1000 ppm was found.
- 3.4- According to adsorption kinetic studies for calcite-PEI NRs, also without precedents, the maximum adsorption capacity at pH 4 was 240 mg Pb^{2+} /g of NRs/PEI obtained in 30 min. This maximum Pb^{2+} removal capacity reported here is higher than other reported before using materials which are not so cheap and environmental friendly as calcite.
- 3.5- The PEI used as CGM allowed to improve the Pb^{2+} LoD by increasing of the CaCO_3 precipitation and the turbidity produced during this precipitation, as well as, permitted to achieve better Na_2PbEDTA adsorption and subsequently removal through the obtaining of more porous NRs surface. In addition to that, PEI offers the appropriate chemical modification onto the NR surface to favor the interaction of this with the Na_2PbEDTA complex by hydrogen bond formation and increase the Pb^{2+} removal.
- 4.- A novel and highly sensitive lateral flow immunodevice with integrated sample treatment platform for Cd^{2+} detection in drinking and tap water samples using the Cd-EDTA-BSA conjugate labeled with AuNPs as signal producer tool has been successfully developed.
- 4.1- LFID is based on competitive reaction between the Cd-EDTA-BSA-AuNPs conjugate (deposited on the conjugation pad strip) and the Cd-EDTA complex (formed in the analysis sample) for the same binding site of the 2A81G5 mAb (specific to Cd-EDTA, which is immobilized onto the test line at the optimized concentrations) was performed.

- 4.2- The concentrations of the conjugate and the mAbs at the conjugation pad and the test and control lines, respectively, are optimized. The decreasing of the conjugate and the mAbs concentrations onto their corresponding zones brought to increase of the sensibility of the device. A strategy to decrease the Cd-EDTA-BSA-AuNPs conjugate concentration by increasing the length of the conjugate pad and soaking it either in the same or in a bigger volume of the conjugate strip solution was introduced. A large response range (0.2-2000 ppb) and low LoD and LoQ (0.1 and 0.4 ppb, respectively) were reached with this procedure.
- 4.3- The specificity in the conventional device demonstrated that Ca^{2+} , Mg^{2+} , Fe^{3+} , Al^{3+} and Pb^{2+} ions almost do not interfere in the Cd^{2+} analysis. Co^{2+} , Ni^{2+} , Zn^{2+} and Cu^{2+} ions have a moderate interference (5 ppm of these metallic ions causes an interference between 5-10% in the determination of 10 ppb Cd^{2+} using 14 mM Na_2EDTA) while Hg^{2+} and Mn^{2+} ions have a notable interference (the presence of 5 ppm Mn^{2+} or Hg^{2+} interferes between 15-18% in the 10 ppb Cd^{2+} analysis using 14 mM Na_2EDTA). All these metallic interferences can be reduced below 5% by lowering the EDTA concentration to 0.005 mM and by adding 10% OVA or BSA.
- 4.4- The integrated LFID with the inserted sample treatment pad was able to detect Cd^{2+} with almost 100% of accuracy and good precision. The repeatability and inter-assay precision variation coefficient were around 5 and 10% even for low Cd^{2+} concentration (0.4 ppb).

**ANNEX I. ARTICLES ACCEPTED BY THE
PHD COMMISSION**

Controlled formation of nanostructured CaCO₃–PEI microparticles with high biofunctionalizing capacity†Adaris López-Marzo,^{ab} Josefina Pons^b and Arben Merkoçi^{*ac}

Received 10th April 2012, Accepted 15th May 2012

DOI: 10.1039/c2jm32240d

Nanostructured vaterite microparticle formation with high biofunctionalizing capacity for biosensing platforms using a water–organic solvent mixture with poly(ethyleneimine) (PEI) under sonication mixing conditions has been studied. A novel and effective polymorph discrimination is found with this system. A pure rhombohedral calcite phase has been observed using just water–organic mixed solvent systems. By increasing the PEI concentration (from 4 to 8 mg mL⁻¹) a transformation from calcite and vaterite polymorphic mixture to only vaterite phase has been observed. The introduction of PEI as a crystal growth modifier (CGM) in the reaction systems increases the vaterite fraction in the mineralization product and offers to vaterite microspheres a stability of up to 8 months. The PEI layer on the microparticle surface provides additional chemical activity to microparticles for further immobilization of (bio)molecules *via* hydrogen bond formation between acid hydrogen in the biomolecule and PEI's nitrogen. The CaCO₃–PEI microparticles synthesized here represent an interesting platform for the immobilization of a large range of biomolecules, from enzymes, antibodies, nucleic acids such as aptamers and DNA enzymes including other molecules with labile hydrogens. The obtained nanostructured material could be useful as a biosensing platform beside drug delivery, imaging and other applications.

1. Introduction

Calcium carbonate is one of the most abundant minerals in nature.¹ Its biocompatibility, biodegradability and industrial application as a filler in paints, plastics, rubber, and paper has led to it being one of the most investigated systems.² It has three anhydrous crystalline polymorphs known as calcite, aragonite and vaterite. Thermodynamically, the least stable phase of calcium carbonate is vaterite followed by aragonite and calcite. Vaterite is rarely found in either biological or non-biological systems. In laboratories, vaterite (or aragonite) is frequently prepared in the presence of specific additives. Its stabilization in water still remains a challenging issue in biomineralization studies,³ not only because of its rareness, but also because it is expected to have a potential role in biomedical and industrial applications. Vaterite exhibits unique properties such as high surface area, high solubility, high dispersion, and a smaller specific gravity compared with the other two crystalline phases.⁴ In addition, the high loading capacity, low price, easy

preparation, and mild decomposition conditions stimulate the utilization of the CaCO₃ cores for template-assisted synthesis to produce biologically active polymeric capsules.⁵ The porous CaCO₃ microspheres can be an effective host for the fabrication of biocompatible composite materials for drug delivery and protein encapsulation.^{4,6} Moreover CaCO₃ composites have already been shown to be of interest in the biosensing area.⁷

The difficulty in using CaCO₃ lies in the difficulty of controlling its polymorphic character.⁸ Many approaches such as the use of double hydrophilic block copolymers,^{8,9} natural and synthetic hard templates,^{2,10} Langmuir monolayers,¹¹ peptoids¹² and synthetic and natural polymers^{7d,13} have been widely chosen to control the polymorphs and morphology of CaCO₃. Although all these crystallizations have been carried out in aqueous media, crystallization in a mixed solvent system using organic additives is emerging and has been found to be a new way toward hierarchical superstructures.^{1,14}

Herein a novel route for synthesis of vaterite structures has been described. The new procedure integrates the sonication process, poly(ethyleneimine) (PEI) as a crystal growth modifier (CGM) and the mixed water–organic solvent in a unique system able to provide a complete polymorphic discrimination along with a controlled and homogeneous particle size distribution. In order to arrive at the final system three blocks of experiments have been firstly studied. In the first block of assays simple mixing reactions between water dissolutions of CaCl₂ and Na₂CO₃ under sonication using different volumes and reaction

^aNanobioelectronics & Biosensors Group, Institut Català de Nanotecnologia, 08193 Bellaterra, Spain. E-mail: arben.merkoci@icn.cat; Fax: +34 935813797

^bDepartment of Chemistry, Universitat Autònoma de Barcelona, 08193 Bellaterra, Spain. Fax: +34 935813101

^cICREA, Barcelona, Spain

† Electronic supplementary information (ESI) available. See DOI: 10.1039/c2jm32240d

times have been studied. These syntheses performed under long sonication time yielded vaterite microspheres and calcite rhombohedra. In a second series of assays the effect of different PEI concentrations on the CaCO_3 product was evaluated. Reduction in the reagent volumes and increase of the PEI concentration decreased and homogenized the microsphere size. PEI present in the system increased the vaterite fraction in the product composition and provided a high vaterite stabilizing effect up to 8 months. To the best of our knowledge there are few reports on CaCO_3 crystallization using PEI as CGM.¹⁵ However some works report the role of PEI in a CaCO_3 mineralization medium only as capturing protons because it is a basic polymer that has a branched structure with a distribution of primary, secondary and tertiary amine groups in the ratio 1 : 2 : 1.¹⁶

Generally the role of a CGM remains related to acid molecules and ionic surfactants such as polyacrylic acid (PAA),^{10a,17} polystyrene sulfonate (PSS),¹⁸ dihexadecyl phosphate (DHP),¹⁹ sodium dodecyl sulfate (SDS),²⁰ polystyrene-*alt*-maleic acid (PSMA)²¹ and cetyltrimethylammonium bromide (CTAB)^{20b,21,22} that are the most common CGMs used in the CaCO_3 crystallization. In addition, there are only a few reports on ultrasonic agitation used in the CaCO_3 crystallization.²³ Here for the first time the reported ability of the ultrasonic process to sequester CO_2 is related to the apparition of the $\text{HCO}_3^-/\text{CO}_3^{2-}$ nucleation center to enhance the vaterite ratio.

In the third group of syntheses the use of equal volumes of a water–organic solvent mixture under ultrasonic conditions with or without PEI as a CGM has permitted an effective phase control of the CaCO_3 mineralization process. The synergistic effect between mixed solvents and PEI permits a completely vaterite phase discrimination with homogeneous and controlled microparticles size.

Many routes of biofunctionalization for CaCO_3 vaterite microparticles have been described, for example, physical adsorption – adsorption of molecules from the solutions onto the preformed CaCO_3 microparticles; coprecipitation – molecule capture by CaCO_3 microparticles in the process of precipitation;^{3b,6c} decomposable template for loading polyelectrolytes for microcapsule fabrication;^{6b,24} phase transition²⁵ and others. Herein we use a chemical adsorption of molecules onto the CaCO_3 particles using for the first time PEI as a chemical mediator for molecular immobilization. PEI's use has the advantage that it allows a high capacity for immobilization of a large variety of molecules on the CaCO_3 microparticle surface with good stability. The microparticles synthesized using PEI that have presented a highly efficient loading capacity for dyes and biomolecules, independently of their charges and sizes, could be useful for multiple applications such as signal amplification in biosensing. The high functionalizing capacity of CaCO_3 microparticles and the versatility of molecules that can be immobilized on its surface are associated with the formation of hydrogen bonds between the acidic hydrogens of the conjugated molecule and the PEI's nitrogens.

2. Experimental part

2.1 Chemicals

All chemical reagents (analytical grade) were purchased from Sigma Aldrich and used as received. A poly(ethyleneimine) (PEI)

solution 50% (w/v) in H_2O ($M_w = 750\,000$, $M_n = 60\,000$) was used. Milli-Q water ($18.2\ \Omega\ \text{cm}^{-1}$) was obtained from an Advantage Milli-Q apparatus (Millipore). All glass materials were soaked in aqua regia for 3 h, rinsed with distilled water and dried before use.

2.2 Characterization techniques

The syntheses were carried out using an Ultrasons J. P. Selecta ultrasonic bath. Scanning electron microscope (SEM) images were taken with a ZEISS Merlin scanning electron microscope. A water dispersion of samples was coated on a glass support and dried at room temperature. A colloidal silver solution was deposited on the edges of the glass for the sample examination. SEM images with high resolution were recorded depositing the samples on a silica support and sputtering gold during 1 min.

X-ray diffraction patterns of CaCO_3 were recorded using a Siemens D-5000 X-ray diffractometer with $\text{Cu K}\alpha$ radiation, 2θ ranging from 10° to 70° at 40 kV and 40 mA. The phase identification was done by comparing the X-ray diffraction patterns of the crystals with the standard data available from Joint Committee on Powder Diffraction Standards. Calculation of the vaterite fraction from the XRD pattern was carried out using two methods: the Kawaguchi equation³³ and the Chung equation.³⁴ The Scherrer equation based on the broadening of diffraction peaks and the diffraction angle by crystallographic planes of the vaterite XRD pattern was used to calculate the size of nanostructures in vaterite microparticles.

Fourier transform infrared (FT-IR) measurements were performed on an IR-200 spectrometer (ThermoNicolet) using KBr pellets. KBr was previously dried overnight at $110\ ^\circ\text{C}$. KBr (40 mg) was mixed with the sample (3 mg) for quantitative infrared measurements. Quantitative analysis of the CaCO_3 phase using IR spectra was carried out based on vaterite absorptivity previously reported.³⁵

The zeta potential of an aqueous dispersion of CaCO_3 was measured using a Malvern Zetasizer Nanoseries at room temperature. The pH of the used Milli-Q water was between 6 and 7.3. Confocal laser scanning microscopy (CLSM) images were captured with a LEICA SP5 confocal scanning system equipped with a $63\times/1.4$ oil immersion objective. (Bio)molecules immobilized on the CaCO_3 surface were observed by using a fluorescein isothiocyanate (FITC) label. Absorption measurements were made on a SpectraMax M2 spectrophotometer.

2.3 Synthesis

CaCO_3 crystallization was studied for three blocks of experiments. In a general procedure of synthesis (first block of experiments) an equal volume ratio of aqueous dissolutions of CaCl_2 (0.33 M) and Na_2CO_3 (0.33 M) was quickly mixed under sonication at room temperature. After this, the reaction vessel was covered with parafilm. CaCO_3 precipitates were washed three times, air dried and collected. The type of agitation (magnetic or ultrasonic), the reagent volume (from 5 to 0.5 mL) and the sonication time (from 15 to 60 min) were modified. Typical reactions of the second block of experiments were assayed with PEI in the system, using 45 min of sonication time and 5 mL of each reagent volume. Aqueous dissolutions of PEI (0.1, 0.4, 2

and 4 mg mL⁻¹ in 5 mL) with CaCl₂ (0.33 M) were mixed with Na₂CO₃ (0.33 M). Finally in the third block of experiments, CaCl₂ (0.33 M) in equal volumes of mixed solvents (5 mL) without or with PEI (4 or 8 mg mL⁻¹) was mixed with Na₂CO₃ (0.33 M, 5 mL). The mixtures in equal volumes of tested solvents were water–EtOH (ethanol), water–EtOAc (ethylacetate), water–DMSO (dimethylsulfoxide) and water–DMF (*N,N*-dimethylformamide).

2.4 Conjugation

CaCO₃ (10 mg) obtained with and without PEI was incubated with a known quantity of biomolecules or dyes under shaking conditions for 45 min. Bovine serum albumin isothiocyanate (BSA–FITC), human IgG isothiocyanate (HIgG–FITC), anti-Human IgG–peroxidase (anti-HIgG–Per) produced in goat, tyrosinase from mushroom (Tyr), methylene blue (MB), bromocresol green (BG), methyl orange (MO), methyl red (MR), rhodamine B (R) and fluorescein (F) were tested. The estimation of the quantity of (bio)molecules immobilized on the CaCO₃ surface was made from the difference between the concentration of the initial molecule solution and the concentration of the appropriate supernatants obtained after centrifugation of the suspension for each washed sample. The concentration in each washed sample was calculated by interpolation of absorbance intensity in the calibration curve for the (bio)molecule solution.

3. Results and discussion

3.1 Synthesis and characterization

When the CaCO₃ synthesis was carried out using 5 mL of reagent (CaCl₂ and Na₂CO₃) volume for 15 to 45 min of magnetic agitation almost only calcite rhombohedra appeared in the crystallization product. However when this reaction was carried out under ultrasonic mixing for the same time intervals a mixture of typical rhombohedral calcite crystals and vaterite microspheres was obtained. The calcite precipitate was found in three different morphologies: the standard rhombohedra, intergrown rhombohedra and layered rhombohedra (see Fig. S1† in the ESI). Fig. 1 shows the effect of reagent volume and sonication time on the microsphere size. The reduction in the reagent volume from 5 to 1 mL produces a decrease in the microsphere average size for the studied reaction times. For example, when 5 mL of CaCl₂ and Na₂CO₃ solutions are mixed during the syntheses for 45 min the particle size was 2.1 ± 0.3 μm and this value decreased to 1.1 ± 0.15 μm when the used reagent volumes were decreased to 1 mL, with the relative errors of around 14%. In addition, variations in the sonication times from 15 to 60 min did not significantly affect the microsphere size. The reason why there is no significant effect on size under different reaction times is the fact that the system has a fast precipitation reaction rate and the nucleation and growth occur completely within 15 min.

On the other hand, while microsphere morphology is affected by the reduction of the reagent volume no morphological change was found by increasing the reaction times using the same reagent volume (results not shown). The reduction of the reagent volume from 5 to 1 mL produces a microsphere surface with high density of nanostructures. The increase of the density of nanostructures on the microsphere surface is correlated with the

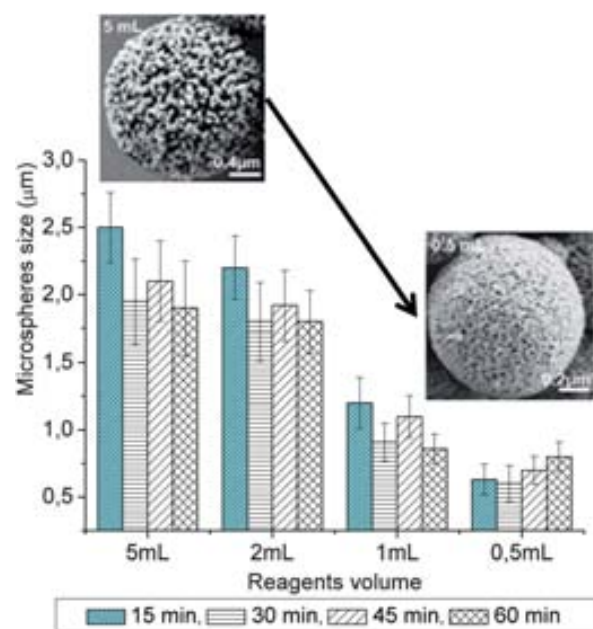


Fig. 1 Effect of the reagent (CaCl₂ and Na₂CO₃) volume and the sonication time on the vaterite microsphere size without PEI in the system. The inserted SEM images belong to 5 and 0.5 mL of reagent volumes under 45 min of ultrasonic stirring. Other experimental conditions are described in the text.

diminution of the microparticle and nanostructure size when the reagent volume is reduced from 5 to 1 mL.

In this way, the vaterite microspheres synthesized with 5 mL of reagent volume are made of nanoparticles with the size range of 28–32 nm and a highly porous surface can be observed. However microspheres synthesized by using reagent volumes equal to or smaller than 1 mL are made of nanoparticles with the size of around 17–20 nm and show a surface with a higher density of nanostructures (‘tentacle’ like structures, see inset zooms a1 and b1 of Fig. 2) that ensure a major superficial area.

It is important to highlight that the reduction of the volume from 5 to 2 mL is accompanied by doubling of the vaterite fraction (from 35 to 70% approximately) and that the obtained nanostructured microparticles were stable enough even up to 6 months since their preparation (see the SEM image of Fig. 2c).

Several experiments were carried out with different CGMs such as, Tween-20, Triton-X-100, CTAB and PEI using 5 mL of the reagent volume and 45 min of sonication time (results not shown). Better results in relation to the obtaining of nanostructured vaterite particles were found on working with PEI. Fig. 3a and b show respectively the XRD patterns and IR spectra of CaCO₃ synthesized in the presence of different PEI concentrations. In a rapid view we can see that the intensities of vaterite XRD peaks (see Fig. 3a) at 21.0, 24.9, 27.1, 32.8, 44.0, 49.1, 50.1 and 55.8° increase on increasing the PEI concentration in the reaction medium. Accordingly the vaterite IR band (see Fig. 3b) at 745 cm⁻¹ increases while the calcite band at 712 cm⁻¹ decreases with the increase of PEI concentration. The vaterite fraction in the product increases from 36 to 72% while the PEI concentration increases from 0 to 4 mg mL⁻¹. Moreover the vaterite microsphere size decreases from 2.0 ± 0.3 to 1.32 ± 0.16 μm with the increase of the PEI concentration from 0 to 4 mg mL⁻¹. The

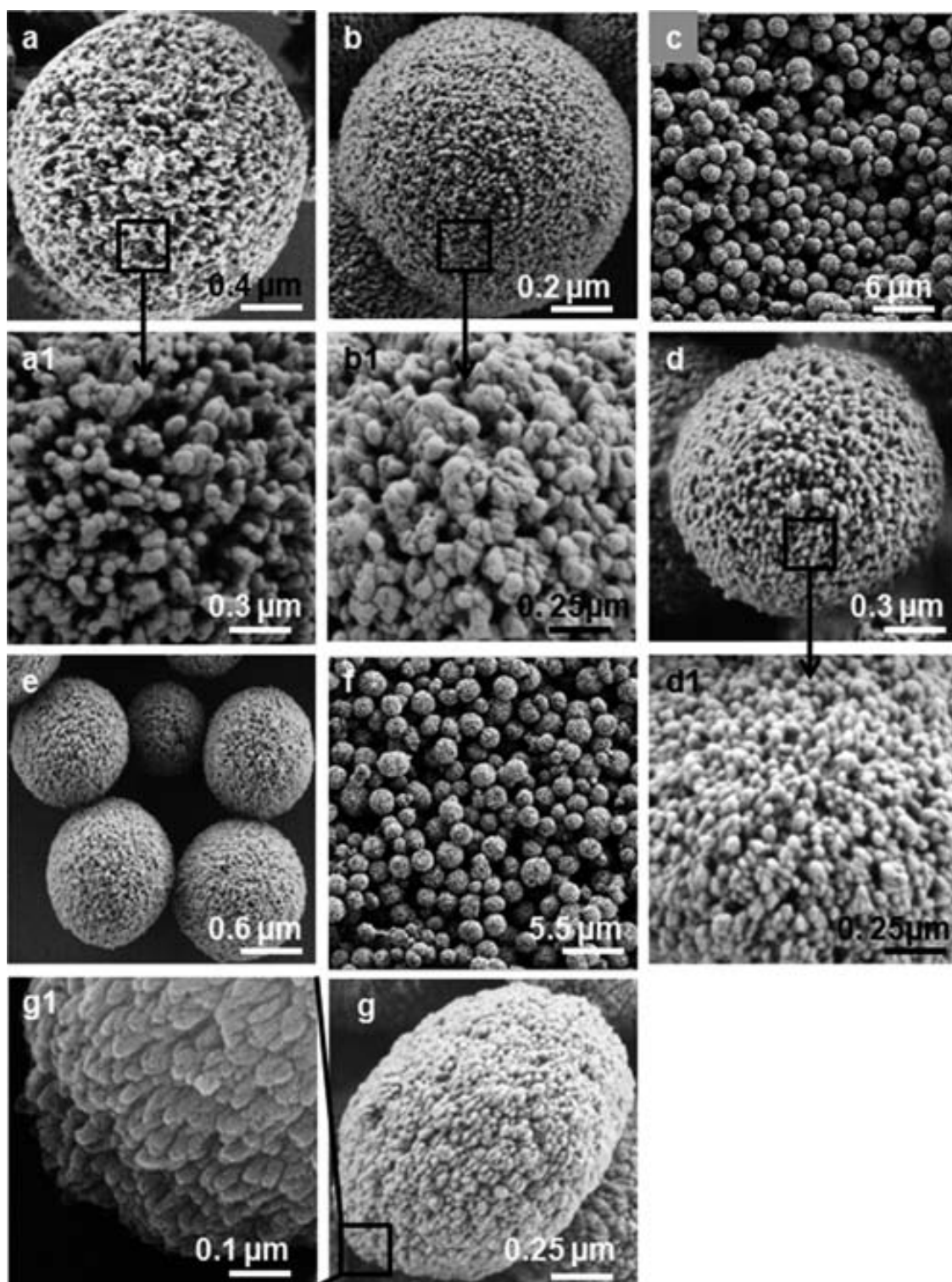


Fig. 2 (a–c) SEM images of vaterite microspheres synthesized without PEI. (a) 5 mL reagent (CaCl_2 and Na_2CO_3) volume and 45 min reaction time, (b) 1 mL reagent volume and 45 min reaction time and (c) 5 mL reagent volume and 45 min reaction time with the image obtained 6 months after the synthesis. (d–f) SEM images of vaterite microspheres synthesized with PEI using 5 mL reagent volume and 45 min reaction time. (d) 2 mg mL^{-1} of PEI, (e) 2 mg mL^{-1} of PEI and (f) 0.44 mg mL^{-1} of PEI with the image obtained 8 months after the synthesis. (g) SEM images of the vaterite ellipsoid synthesized *via* water–EtOH + 8 mg mL^{-1} PEI. a1, b1, d1 and g1 are amplifications of their corresponding SEM images in the selected zones, which confirmed that the microspheres are made of nanoparticles. Other experimental conditions are described in the text.

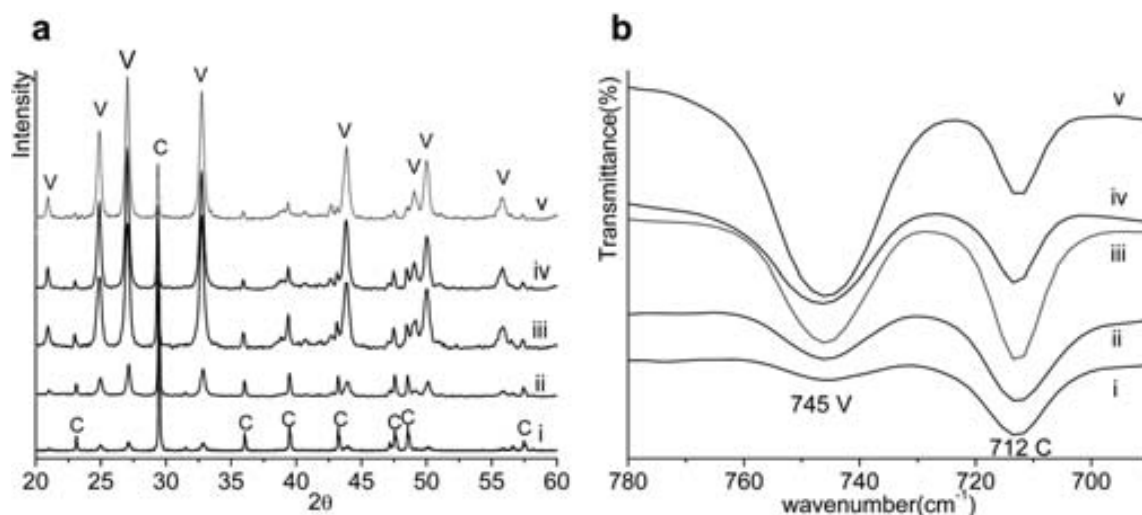


Fig. 3 (a, i–v) XRD patterns corresponding to the CaCO_3 obtained with different PEI concentrations and using 5 mL reagent volume and 45 min sonication time: (i) 0 mg mL^{-1} of PEI, (ii) 0.44 mg mL^{-1} of PEI in the initial CaCl_2 dissolution, (iii) 2 mg mL^{-1} of PEI in the initial CaCl_2 dissolution, (iv) 4 mg mL^{-1} of PEI divided into 2 mg mL^{-1} for each initial CaCl_2 and Na_2CO_3 dissolution; (v) XRD patterns corresponding to the CaCO_3 product obtained with 4 mg mL^{-1} of PEI divided into 2 mg mL^{-1} for each initial CaCl_2 and Na_2CO_3 dissolution and including the reduction of volume to 2 mL. (b, i–v) IR spectra correspond to samples described before in the same nomenclature order. V denotes vaterite and C calcite phase. Other experimental conditions are described in the text.

effect of the distribution of the equal quantity of PEI between CaCl_2 and Na_2CO_3 dissolutions and the reduction of the reagent volume brings additional reduction in the vaterite fraction and the microsphere size. In consequence an 86% vaterite composition and $0.83 \pm 0.16 \mu\text{m}$ sphere size with nanoparticles of around 17–22 nm were reached. Table S1† in the ESI shows a summary of these results related to the effect of PEI on the microsphere size and vaterite fraction.

The surface of vaterite microspheres synthesized in the presence of PEI is smoother than the vaterite surface obtained without PEI (see Fig. 2d1). In Fig. 2d the polymer layer recovering the CaCO_3 structure is displayed. In the IR spectrum obtained on CaCO_3 produced *via* PEI (Fig. S2†), the bands at 3480–3440 cm^{-1} correspond to the vibration frequency N–H of the primary and secondary amino groups and the bands at 2970, 2930 and 2850 cm^{-1} belong to the vibration frequency C–H of the CH_2 and CH_3 groups in the PEI polymer, which indicate the PEI presence on the microsphere surface. These microspheres presented higher stability, which is attributed to the polymer layer that recovered it. The SEM image in Fig. 2f shows vaterite microspheres after 8 months of their synthesis in the presence of 0.44 mg mL^{-1} of the PEI. It is necessary to highlight that the increase in the PEI content has the same effect on the microsphere size and vaterite fraction as the reduction of the volume in the assays without PEI. However by using PEI a greater quantity of CaCO_3 in comparison to the volume reduction can be achieved.

Fig. 4a illustrates SEM images of CaCO_3 obtained using various water–organic solvent mixtures with or without PEI, 5 mL reagent volume and 45 min sonication time. When only mixed water–organic solvents are used during the reaction, the crystallization product is completely calcite rhombohedra (Fig. 4a-i) independent of the organic solvent used in the mixture (EtOH, EtOAc, DMSO and DMF). When 4 mg mL^{-1} of PEI is added to the CaCl_2 solution, microspheres and/or ellipsoids

appear in the product together with rhombohedral crystals (Fig. 4a-ii). A second addition of 4 mg mL^{-1} of PEI in the Na_2CO_3 solution yielded completely vaterite microspheres or/and microellipsoids in the precipitation product (Fig. 4a-iii). These results suggested by SEM analysis were also confirmed by XRD and FTIR measurements.

The XRD patterns observed in Fig. 4b correspond to CaCO_3 that has been synthesized *via* a water–EtOH system with or without PEI using 5 mL of reagent volume and 45 min of sonication time. A complete polymorphic discrimination from calcite (Fig. 4b-i) to calcite–vaterite (Fig. 4b-ii) and vaterite (Fig. 4b-iii) can be seen from water–EtOH to water–EtOH + 4 mg mL^{-1} of PEI and water–EtOH + 8 mg mL^{-1} of PEI. Fig. 4c corresponds to infrared spectra of CaCO_3 formed using water–DMSO with or without PEI. When PEI is not present in the solution, only the band at 712 cm^{-1} corresponding to calcite is observed (Fig. 4c-i). By using 4 mg mL^{-1} of PEI the bands at 712 and 745 cm^{-1} that belong to calcite and vaterite are respectively observed (Fig. 4c-ii). However with 8 mg mL^{-1} of PEI only the band at 745 cm^{-1} corresponding to vaterite can be observed (Fig. 4c-iii).

The introduction of an organic solvent inside the reaction medium for crystallizing vaterite microparticles was the determinant to achieve the polymorphic discrimination. In previous experiments discussed here, just using water dissolutions of CaCl_2 and Na_2CO_3 with and without PEI a mixture of calcite and vaterite was obtained. However, under the same conditions the introduction of the water–organic solvent mixture without PEI yielded 100% of calcite phase while the synergetic effect between the mixture of water–organic solvent and 8 mg mL^{-1} of PEI yielded almost 100% of the vaterite phase. This polymorphic discrimination does not depend on the used organic solvent (*i.e.* DMSO, EtOH, EtOAc or DMF).

The appearance of spherical or elliptical shapes of vaterite crystals depends on the polarity of the solvent mixture (Fig. S3†). When pure water and PEI constituted the reaction medium, the

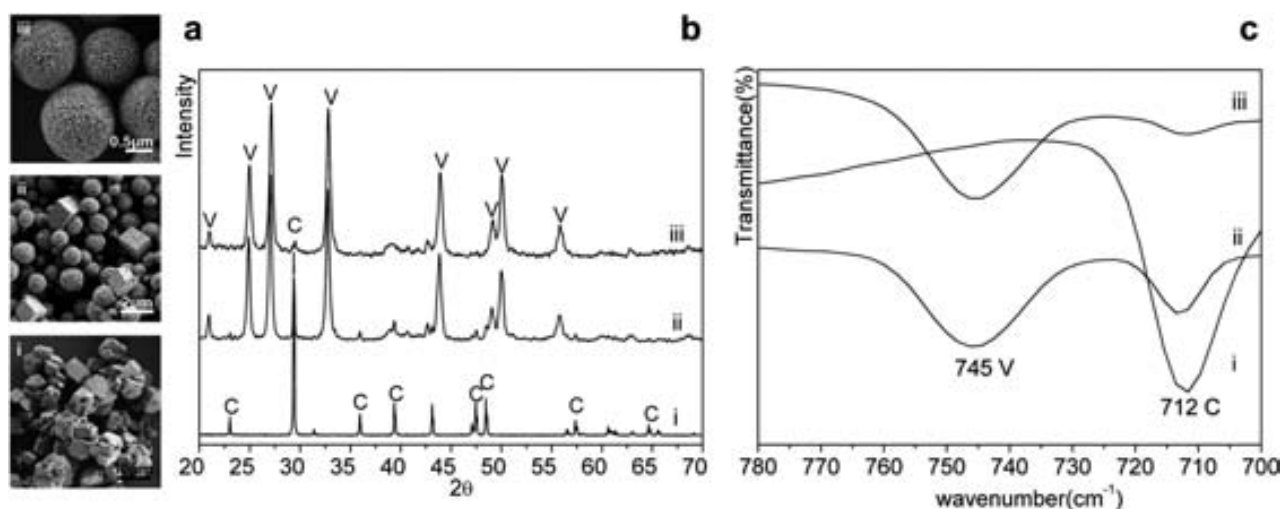


Fig. 4 (a, i–iii) SEM images of the CaCO_3 obtained from a water–organic solvent system with or without PEI under 45 min of sonication and using 5 mL of reagent volume. (i) Calcite rhombohedra obtained from water–DMSO, (ii) calcite rhombohedra and vaterite spheres obtained from water–EtOH + 4 mg mL^{-1} of PEI, and (iii) vaterite spheres obtained from water–ethylacetate + 8 mg mL^{-1} of PEI. (b, i–iii) XRD patterns of CaCO_3 crystals obtained in a water–EtOH system without or with PEI: (i) only water–EtOH, (ii) water–EtOH + 4 mg mL^{-1} of PEI, and (iii) water–EtOH + 8 mg mL^{-1} of PEI. (c, i–iii) IR spectra of the CaCO_3 obtained *via* a water–DMSO system with or without PEI: (i) water–DMSO, (ii) water–DMSO + 4 mg mL^{-1} of PEI, and (iii) water–DMSO + 8 mg mL^{-1} of PEI. V denotes vaterite and C calcite phase. Other experimental conditions are described in the text.

vaterite shapes were spheres. However, when half of the volume of water is substituted by an equal volume of DMSO, DMF or EtOH (the polarity of the mixture decreases with respect to pure water) the vaterite particles with spherical shapes almost disappear and the amount of ellipsoidal ones increases. Spherical shapes are observed to a greater extent in the case of the reaction with EtOAc due to the fact that the polarity of water remains almost the same due to the immiscibility of these two solvents. Fig. 2g displays the SEM image of an ellipsoid shaped particle synthesized by using water–EtOH + 8 mg mL^{-1} of PEI (see also the amplified image in Fig. 2g1) and used later for functionalization purposes. Compact unions of ‘tentacle’ like nanostructures composed of nanoparticles seem to be part of the microellipsoid particles. More details in relation to water–organic solvent + PEI synthesis can be seen in Table S2† in the ESI.

The effect of the reduction of the reagent volume on micro-particle synthesis *via* mixing solvents with PEI was also studied and in disagreement with the previous results presented here, no diminution effect was observed on the average size or the homogeneity of the microparticles. Far from what was expected a mixture of spheres, ellipsoids, bicones, shuttles and few rhombohedra like shapes (see Fig. S4† in the ESI) as reported before^{14b} were observed. In all the above-mentioned experiments the calcite precipitate was always observed with the morphologies displayed in Fig. S1† of ESI.

3.2 Possible mechanism of formation of the vaterite microparticles

The transformation from vaterite or aragonite to calcite is thermodynamically favored. The prevalence of kinetic rather than thermodynamic factors permits to see vaterite at sustained supersaturation conditions. The degree of supersaturation that provokes local nucleation centers and the growth of the crystals are dominant factors in CaCO_3 crystallization. Both are closely

related to the Gibb’s free energy.^{8,13b,17c,26} These two factors can convert from ionic growth attributable to thermodynamically stable calcite rhombohedra to assembly of nanoparticles under a kinetic control of nucleation attributable to usually vaterite spheres.^{1,13b,14a}

The initial experiments for crystallization of CaCO_3 without PEI and using magnetic agitation yielded almost completely calcite. When the same experiments were repeated using ultrasonic agitation the amount of vaterite was increased. Y. Mori *et al.* also found that an ultrasonic homogenizer is better than a magnetic homogenizer to obtain a higher yield of vaterite.²³ The possible explanation could be related to the fact that ultrasonic homogenization is more effective than magnetic homogenization considering that a good homogenization is essential to achieve the growth of vaterite crystals. The effective homogenization with fast convective currents increases the number of impacts between the aggregate particles in the supersaturated nucleation centers favouring their growth to yield vaterite.^{26a} We propose here that an ultrasonic process can also increase the nucleation centers of local supersaturation by inducing the CO_2 sequestering from the air–solution interface into the suspension; in addition it can improve the growth of the aggregate particles in the supersaturated nucleation centers. The facility to sequester CO_2 from the gas to the liquid phase by using ultrasonic waves has been previously reported.²⁷ Moreover, in our experimental conditions to stimulate the transference of CO_2 from the gas to the liquid phase we use two procedures. In the first case Milli-Q water with high electrical resistance ($10^8 \Omega \text{ cm}$, CO_2 free) was used while in the second one a closed reaction vessel with atmospheric air inside was employed.²⁸ Therefore, if the solution is in CO_2 free water the transference of CO_2 from the gas to the liquid phase to reestablish the CO_2 equilibrium is necessary. The sonication might induce the CO_2 sequestering at the air–solution interface through the creation of a pressure difference between the layer closer to the interface and the layers immediately in the upper

part. The superficial energy near the surface is decreased and to reestablish the original equilibrium the superior layer of the air descends very close to the surface until making possible the CO_2 dissolution. The dissolved CO_2 is hydrated to produce H_2CO_3 which yields HCO_3^- and CO_3^{2-} (the pH decreasing by H_2CO_3 formation *via* CO_2 sequestering is illustrated in Fig. S5†). In this way a superficial supersaturation of $\text{HCO}_3^-/\text{CO}_3^{2-}$ allows the creation of additional supersaturated nucleation centers by kinetic control and the apparition of the vaterite phase.

Y. Mori *et al.*²³ found that the reduction in the reagent volume increases the vaterite fraction and they related it to a better homogenization and consequently to the growth of the aggregated particles in the supersaturated nucleation centers. The decrease in the reagent volume presented in this work yields the diminution of the microsphere size and the increase in the vaterite fraction too. This result is more consistent with the increasing nucleation by CO_2 sequestering rather than with the increasing growth of the aggregated particles in the supersaturated nucleation centers. The diminution of the reagent volume enhances the homogenizer effect due to the acceleration in convection currents provoked by the sonication process inside the suspension. In consequence the supersaturated $\text{HCO}_3^-/\text{CO}_3^{2-}$ nucleation centers at the surface of the suspension can migrate faster to the interior of the bulk. This allows new CO_2 molecules to be captured by the suspension during the sonication process and consequently a faster and homogeneous nucleation process by local supersaturation takes place (see the scheme of the mechanism in Fig. 5a).

The addition of PEI to the system facilitates the formation of two different supersaturated nucleation centers, one of $\text{HCO}_3^-/\text{CO}_3^{2-}$ (provided by Na_2CO_3 reagent) due to its binding with the cationic protonated amino groups in the PEI,¹⁵ and the other one of Ca^{2+} (provided by CaCl_2 reagent) by its binding with nucleophilic nitrogens of the amino group in the PEI polymer. This creates $\text{HCO}_3^-/\text{CO}_3^{2-}$ and Ca^{2+} supersaturated centers on the PEI structure able to initiate nucleation with the subsequent controlled growth by self-assembling of small primary nanoparticles into highly organized vaterite crystals.

Moreover, PEI can bind the H^+ of the $\text{HCO}_3^-/\text{H}_2\text{CO}_3$ species formed during the hydration of the sequestered CO_2 favouring the CO_3^{2-} migration from the liquid surface into the bulk suspension and the creation of CO_3^{2-} supersaturated centers on the polymer's chain. In this way, the increase of PEI concentration provokes more Ca^{2+} and CO_3^{2-} supersaturated nucleation centers on coils of the PEI, therefore leading to large vaterite formation (see the scheme of the mechanism in Fig. 5b). All this is consistent with the increase in the vaterite fraction and diminution in the microsphere size when the PEI concentration is increased (see Table S1†).

The solvent mixture changes the polymer's solution properties. The addition of EtOH, DMF or DMSO to the system decreases the polarity of water and in consequence decreases the hydrogen bond interaction between the dissolved PEI and the mixed solvent in comparison with previous hydrogen bond interaction between dissolved PEI and water. This effect of weakening of the interaction between the solvent and PEI favours the bond

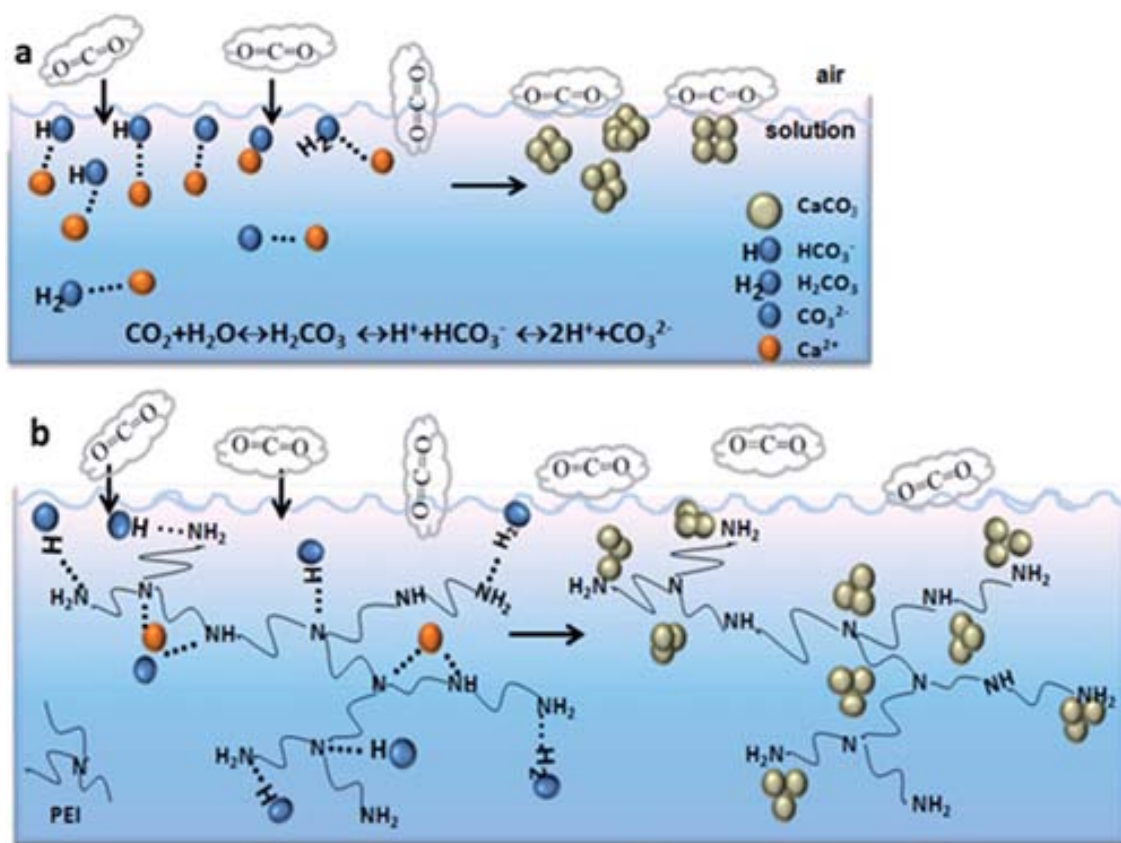


Fig. 5 Schematic representation not in scale of the possible crystallization mechanisms. (a) $\text{HCO}_3^-/\text{CO}_3^{2-}$ supersaturated nucleation centers by CO_2 sequestering. (b) $\text{HCO}_3^-/\text{CO}_3^{2-}$ and Ca^{2+} supersaturated nucleation centers by interaction with the PEI polymer.

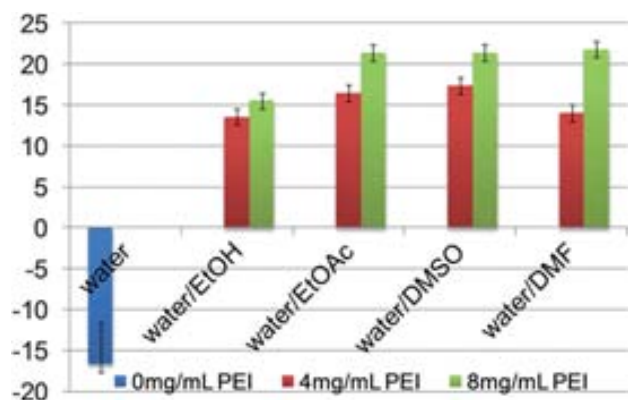


Fig. 6 Z-Potential values (mV) of vaterite microparticles obtained *via* water–organic solvent + PEI reactions. Other experimental conditions are described in the text.

formation between Ca^{2+} or $\text{HCO}_3^-/\text{CO}_3^{2-}$ ions and PEI, which increases the nucleation centers and the tendency of supersaturation and the kinetic precipitation of the vaterite phase.

3.3 Z-Potential studies

Z-Potential measurements indicate that microparticles obtained without PEI have negative z -potential values; however microparticles synthesized with PEI in the reaction medium yield positive values of z -potentials and positive superficial charges. These positive z -potential values are augmented by increasing PEI concentration in the reaction medium (see Fig. 6). The positive superficial charge is provoked by the basic character of PEI being able to bind the nitrogen of its amino groups with the protons present in the water and consequently to create a positive density charge. In the same way, the conductivity of microparticles increases from 0.04 to 0.08 mS cm^{-1} once PEI is present on their surface. Such an enhancement in the z -potential and the conductivity of the vaterite microparticles obtained *via* PEI could be of interest for electrochemical biosensor application where an improvement of the electron transference through the CaCO_3 –PEI composite may be expected.

3.4 Conjugation studies

Several (bio)molecules were tested for their possible conjugation with vaterite microparticles synthesized with and without PEI. A good loading capability was found for the functionalization process using biomolecules (see Table S3† in the ESI). These results are similar to those obtained during immobilization of similar biomolecules on polymer microcapsules obtained by a CaCO_3 template assisted method.^{6c,24,29} CLSM images of vaterite microparticles conjugated with FITC as a fluorescence label demonstrated that a good functionalization was performed and the original shape of the microparticles remained stable after the immobilization process (Fig. 7a and b). It is important to note that microspheres synthesized without PEI cannot be conjugated with these (bio)molecules.

It suggests that the presence of PEI on the microsphere surface makes possible the conjugation due to its high affinity toward the H^+ proton of the OH groups in the (bio)molecules resulting in hydrogen bonds between the nitrogen of the PEI amino groups

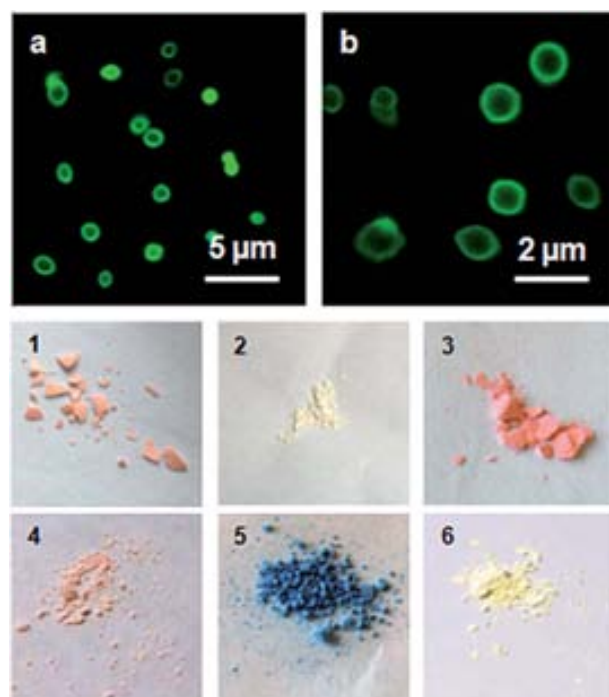


Fig. 7 CLSM images corresponding to CaCO_3 –BSA–FITC (a) and CaCO_3 –HiG–FITC (b). (1–6) Photos of the CaCO_3 precipitated by using water–EtOH + 8 mg mL^{-1} PEI and conjugated with (1) HiG–FITC, (2) anti-HiG–Per, (3) BSA–FITC, (4) fluorescein, (5) bromocresol green and (6) methyl orange. Other experimental conditions are described in the text.

and the hydrogen of the OH group in the conjugated (bio) molecule (see Fig. 8). For the same reason, molecules without OH groups such as methylene blue and methyl red cannot be

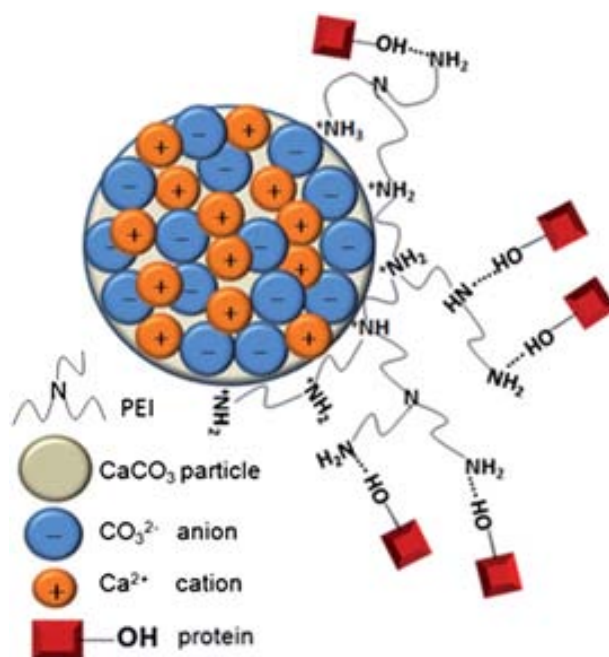


Fig. 8 Schematic representation not in scale of the interactions between the PEI polymer with the CaCO_3 microparticle surface and the conjugated protein.

conjugated with CaCO₃-PEI microparticles. Based on these results we can conclude that any protein could be conjugated on the CaCO₃-PEI composite surface because of the presence of OH in the carboxylic groups of their amino acids. Even some amino acids could be more favoured in the CaCO₃-PEI conjugation due to the presence of two carboxylic groups or an SH group. In a similar way any carbohydrates, with any nucleotidic sequence through the OH groups in their sugar units (ribose or deoxyribose), any type of molecule with acidic hydrogens (OH, SH, NH) or any type of molecule with electrophilic atoms like the transition metals could be easily conjugated with CaCO₃-PEI. Table S3† in the ESI shows the estimated values of the immobilized biomolecules on the microspheres. A significantly high level of proteins on the CaCO₃-PEI surface even when both species possess the same sign of charge can be observed. The conjugation is visible also when uncharged molecules such as bromocresol, methyl orange and fluorescein are exposed to CaCO₃-PEI. In fact, the conjugation results indicate that (bio) molecule immobilization is dominated by hydrogen bonds rather than electrostatic interaction. This is because at the pH of the particle suspension (pH between 6 and 7) although IgG-FITC³⁰ and anti-human IgG-Per^{29b} are positively charged the conjugation took place. In the case of negatively charged BSA-FITC^{24,31} and tyr³² the immobilization is also favored by the electrostatic forces in addition to the hydrogen bonds. In agreement with this, the highest value of molecules conjugated on the CaCO₃-PEI surface corresponded to tyrosinase enzyme.

These results demonstrated that vaterite microparticles synthesized *via* a water-organic solvent with PEI can be loaded with a large variety of (bio)molecules. This conjugation capacity may provide them with a high capability for multiple applications. These nanostructured CaCO₃ microparticles can be loaded with signal tagging molecules (*i.e.* enzymes, dyes, *etc.*) or analyte receptor molecules (*i.e.* antibodies, DNA, *etc.*) as an interesting platform to enhance the sensitivity of the enzymatic biosensors, immunosensors or DNA sensors. In addition these microparticles can be used in drug delivery or as carrier fluorescent probes for bioimaging applications among others.

4. Conclusions

A new route of synthesis of nanostructured vaterite microparticles with high biofunctionalizing capacity using a water-organic solvent mixture with PEI under sonication mixing conditions has been achieved. In order to optimize the final process, syntheses based on simple sonication mixing of CaCl₂ and Na₂CO₃ in water with or without PEI as a CGM have been studied. Independent of the presence of PEI in the system a mixture of calcite rhombohedra and vaterite microspheres has been achieved with water as the reaction medium and sonication mixing. As observed the reduction of the reagent volumes decreases and homogenizes the microsphere mean sizes for water systems. The addition of increasing PEI contents in the reaction system also reduces the microsphere size and its dispersion, permitting microparticles with controlled size. Moreover increasing PEI concentration improves the vaterite fraction in the reaction product. In the final synthesis *via* water-organic solvent mixing with or without PEI (water-EtOH, water-EtOAc, water-DMF or water-DMSO) a completely polymorphic discrimination between calcite and

vaterite was also achieved. The synergistic effect between 8 mg mL⁻¹ of PEI and water-organic solvents yielded around 100% of a vaterite polymorph. On the other side 100% of calcite was obtained only with a water-organic solvent system.

The presence of a PEI layer covering the vaterite microparticle surface has been verified by SEM and infrared spectroscopy. This PEI layer plays multiple roles. First, it gives to vaterite a stabilizing effect already checked for up to 8 months. Second, it provides to the microparticle surface more smoothness. Third, it offers additional chemical activity for further modifications with functional molecules. Fourth, it provides high superficial charge to use these nanostructured microparticles in electrochemical sensors.

The vaterite microellipsoids, synthesized *via* an environmentally friendly route (water-EtOH + PEI), were conjugated with various (bio)molecules (*i.e.* enzymes, antibodies and small organic molecules) independent of their charges and sizes. The wide range of molecules that can be conjugated and the high amount and stability of immobilized molecules are associated with the formation of hydrogen bonds between the PEI's nitrogens and the acidic hydrogens in the conjugated molecule. This functionalized CaCO₃-PEI material is suitable for several applications such as the design and fabrication of biosensing devices due to its use as a signal increasing tool or as a receptor and biorecognition element for the rapid detection of analytes in a variety of matrices. Other applications such as bioencapsulation useful for drug delivery, imaging purposes (as a carrier of fluorescent labels) or as an alternative for water treatment beside other applications can also be foreseen.

Acknowledgements

MICINN (Spain) for MAT2011-25870 project is acknowledged. Adaris López Marzo thanks Generalitat of Catalunya for the FI-2010 scholarship given.

Notes and references

- X. Geng, L. Liu, J. Jiang and S.-H. Yu, *Cryst. Growth Des.*, 2010, **10**, 3448.
- L. Liu, D. He, G.-S. Wang and S.-H. Yu, *Langmuir*, 2011, **27**, 7199.
- (a) S. Kim and C. B. Park, *Langmuir*, 2010, **26**, 14730; (b) H. Yang, W. Yao, L. Yang, X. Ma, H. Wang, F. Ye and K. Wong, *J. Cryst. Growth*, 2009, **311**, 2682.
- D. V. Volodkin, R. V. Klitzing and H. Möhwald, *Angew. Chem.*, 2010, **122**, 9444.
- (a) Y. Jiang, D. Yang, L. Zhang, Q. Sun, X. Sun, J. Li and Z. Jiang, *Adv. Funct. Mater.*, 2009, **19**, 150; (b) T. Levy, Ch. Déjugnat and G. B. Sukhorukov, *Adv. Funct. Mater.*, 2008, **18**, 1586; (c) D. B. Shenoy and G. B. Sukhorukov, *Macromol. Biosci.*, 2005, **5**, 451.
- (a) W. Wei, G.-H. Ma, G. Hu, D. Yu, T. Mcleish, Z.-G. Su and Z.-Y. Shen, *J. Am. Chem. Soc.*, 2008, **130**, 15808; (b) B. G. De Geest, S. De Koker, K. Immesoete, J. Demeester, S. C. De Smedt and W. E. Hennink, *Adv. Mater.*, 2008, **20**, 3687; (c) A. I. Petrov, D. V. Volodkin and G. B. Sukhorukov, *Biotechnol. Prog.*, 2005, **21**, 918; (d) D. V. Volodkin, A. I. Petrov, M. Prevot and G. B. Sukhorukov, *Langmuir*, 2004, **20**, 3398.
- (a) D. Shan, M. Zhu, E. Han, H. Xue and S. Cosnier, *Biosens. Bioelectron.*, 2007, **23**, 648; (b) F. Li, Y. Feng, Z. Wang, L. Yang, L. Zhuo and B. Tang, *Biosens. Bioelectron.*, 2010, **25**, 2244; (c) W.-Y. Cai, Q. Xu, X.-N. Zhao, J.-J. Zhu and H.-Y. Chen, *Chem. Mater.*, 2006, **18**, 279; (d) Y.-H. Won, H. S. Jang, D.-W. Chung and L. A. Stanciu, *J. Mater. Chem.*, 2010, **20**, 7728.
- A.-W. Xu, W.-F. Dong, M. Antonietti and H. Cölfen, *Adv. Funct. Mater.*, 2008, **18**, 1307.

- 9 (a) L. Qi, J. Li and J. Ma, *Adv. Mater.*, 2002, **14**, 300; (b) B. P. Bastakoti, S. Guragain, Y. Yokoyama, S.-i. Yusa and K. Nakashima, *Langmuir*, 2011, **27**, 379; (c) Y.-X. Gao, S.-H. Yu and X.-H. Guo, *Langmuir*, 2006, **22**, 6125.
- 10 (a) T. Sakamoto, A. Oichi, Y. Oaki, T. Nishimura, A. Sugawara and T. Kato, *Cryst. Growth Des.*, 2009, **9**, 622; (b) B. Yeom and K. Char, *Chem. Mater.*, 2010, **22**, 101.
- 11 (a) E. Loste, E. Díaz-Martí, A. Zarbakhsh and F. C. Meldrum, *Langmuir*, 2003, **19**, 2830; (b) E. M. Pouget, P. H. H. Bomans, J. A. C. M. Goos, P. M. Frederik, G. de With and N. A. J. M. Sommerdijk, *Science*, 2009, **323**, 1455.
- 12 (a) Ch.-L. Chen, J. Qi, R. N. Zuckermann and J. J. DeYoreo, *J. Am. Chem. Soc.*, 2011, **133**, 5214.
- 13 (a) S. Sindhu, S. Jegadesan, L. Hairong, P. K. Ajikumar, M. Vetrichelvan and S. Valiyaveetil, *Adv. Funct. Mater.*, 2007, **17**, 1698; (b) A.-W. Xu, M. Antonietti, H. Cölfen and Y.-P. Fang, *Adv. Funct. Mater.*, 2006, **16**, 903; (c) A. Neira-Carrillo, D. F. Acevedo, M. C. Miras, C. A. Barbero, D. Gebauer, H. Cölfen and J. L. Arias, *Langmuir*, 2008, **24**, 12496.
- 14 (a) X.-H. Guo, S.-H. Yu and G.-B. Cai, *Angew. Chem.*, 2006, **118**, 4081; (b) R.-J. Qi and Y.-J. Zhu, *J. Phys. Chem. B*, 2006, **110**, 8302.
- 15 H. K. Park, I. Lee and K. Kim, *Chem. Commun.*, 2004, **1**, 24.
- 16 (a) Sh. Lee, S. G. Lee, D. Kwak, J.-H. Park and K. Cho, *J. Phys. Chem. C*, 2011, **115**, 2026; (b) S. Lee, J.-H. Park, D. Kwak and K. Cho, *Cryst. Growth Des.*, 2010, **10**, 851.
- 17 (a) F. Jiang, Y. Yang, L. Huang, X. Chen and Z. Shao, *J. Appl. Polym. Sci.*, 2009, **114**, 3686; (b) J. Yu, M. Lei, B. Cheng and X. Zhao, *J. Solid State Chem.*, 2004, **177**, 681; (c) D. Gebauer, H. Cölfen, A. Verch and M. Antonietti, *Adv. Mater.*, 2009, **21**, 435.
- 18 (a) J. Yu, H. Guo, S. A. Davis and S. Mann, *Adv. Funct. Mater.*, 2006, **16**, 2035; (b) Y. Jin, W. Liu, J. Wang, J. Fang and H. Gao, *Colloids Surf., A*, 2009, **342**, 40.
- 19 X. Liu, H. Bai and Y. Sha, *Adv. Mater. Res.*, 2011, **194–196**, 777.
- 20 (a) Z.-G. Cui, Y.-Z. Cui, C.-F. Cui, Z. Chen and B. P. Binks, *Langmuir*, 2010, **26**, 12567; (b) G. Gao, P. Huang, K. Wang, R. He and D. Cui, *Powder Technol.*, 2011, **205**, 270.
- 21 J. Yu, X. Zhao, B. Cheng and Q. Zhang, *J. Solid State Chem.*, 2005, **178**, 861.
- 22 E. Altay, T. Shahwan and M. Tanoglu, *Powder Technol.*, 2007, **178**, 194.
- 23 Y. Mori, T. Enomae and A. Isogai, *Mater. Sci. Eng., C*, 2009, **29**, 1409.
- 24 G. B. Sukhorukov, D. V. Volodkin, A. M. Günther, A. I. Petrov, D. B. Shenoy and H. Möhwald, *J. Mater. Chem.*, 2004, **14**, 2073.
- 25 M. Fujiwara, K. Shiokawa, M. Araki, N. Ashitaka, K. Morigaki, T. Kubota and Y. Nakahara, *Cryst. Growth Des.*, 2010, **10**, 4030.
- 26 (a) B. Aziz, D. Gebauer and N. Hedin, *CrystEngComm*, 2011, **13**, 4641; (b) D. Gebauer, P. N. Gunawidjaja, J. Y. P. Ko, Z. Bacsik, B. Aziz, L. Liu, Y. Hu, L. Bergström, C.-W. Tai, T.-K. Sham, M. Edén and N. Hedin, *Angew. Chem., Int. Ed.*, 2010, **49**, 8889; (c) A. G. Xyla and P. G. Koutsoukos, *J. Chem. Soc., Faraday Trans. 1*, 1989, **85**, 3165.
- 27 (a) M. T. Timko, J. M. Diffendal, J. W. Tester, K. A. Smith, W. A. Peters, R. L. Danheiser and J. I. Steinfeld, *J. Phys. Chem. A*, 2003, **107**, 5503; (b) L. Rong, Y. Kojima, Sh. Koda and H. Nomura, *Ultrason. Sonochem.*, 2001, **8**, 11.
- 28 P. Moulin and H. Roques, *J. Colloid Interface Sci.*, 2003, **261**, 115.
- 29 (a) Y. Yang, X. Wei, P. Sun and J. Wan, *Molecules*, 2010, **15**, 2872; (b) D. V. Volodkin, N. I. Larionova and G. B. Sukhorukov, *Biomolecules*, 2004, **5**, 1962.
- 30 H. Ai, M. Fang, S. A. Jones and Y. M. Lvov, *Biomolecules*, 2002, **3**, 560.
- 31 O. S. Kulakovich, N. D. Strekal, M. V. Artem'ev, A. P. Stupak, S. A. Maskevich and S. V. Gaponenko, *J. Appl. Spectrosc.*, 2006, **73**, 892.
- 32 X. Wan, B. Chai, Y. Liao, Y. Su, T. Ye, P. Shen and X. Chen, *Appl. Microbiol. Biotechnol.*, 2009, **82**, 261.
- 33 H. Kawaguchi, H. Hirail, K. Sakai, S. Sera, T. Nakajima, Y. Ebisawa and K. Koyama, *Colloid Polym. Sci.*, 1992, **270**, 1176.
- 34 F. H. Chung, *J. Appl. Crystallogr.*, 1974, **7**, 519.
- 35 N. V. Vagenas, A. Gatsouli and C. G. Kontoyannis, *Talanta*, 2003, **59**, 831.

Supporting Information for Journal of Materials Chemistry

Controlled formation of nanostructured CaCO₃-PEI microparticles with high biofunctionalizing capacity

*Adaris López_Marzo,^{a,b} Josefina Pons,^b and Arben Merkoçi^{*a,c}*

^a Nanobioelectronics and Biosensors Group,

Catalan Institute of Nanotechnology,

Campus de la UAB, 08193 Bellaterra, Barcelona, Spain

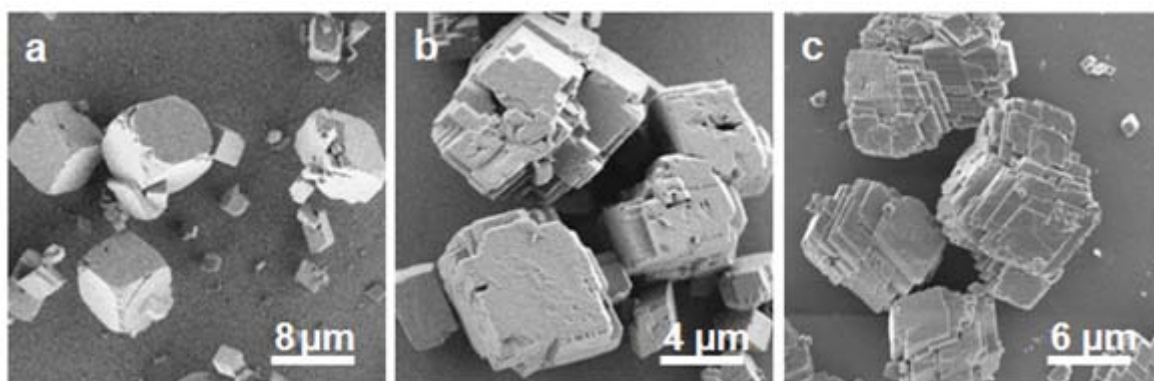
^b Department of Chemistry,

Universitat Autònoma de Barcelona,

Bellaterra 08193, Barcelona, Spain.

^c ICREA, Barcelona, Spain

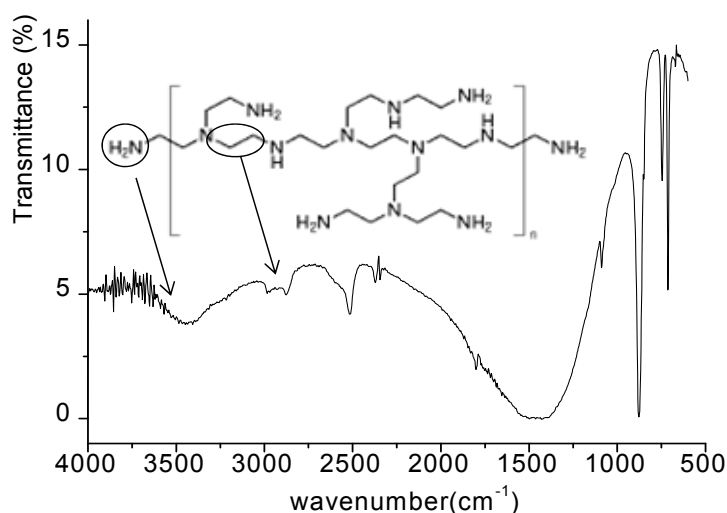
*Corresponding author: E-mail: arben.merkoci@icn.cat



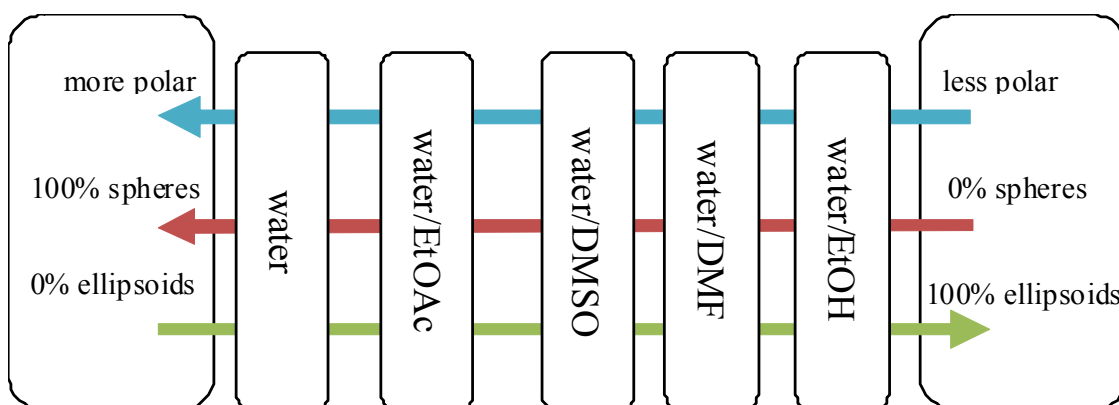
Figure_S1. SEM images of three different shape CaCO₃ in rhombohedra crystal phase recorded in all groups of assays: (a) standard rhombohedra, (b) intergrown rhombohedra and (c) layered rhombohedra. Other experimental conditions as described in the main text.

Tabla_S1. Variation of microspheres size and vaterite fraction by changing the PEI concentration in the initial CaCl₂ dissolution while using 5 mL of the reagents (CaCl₂ and Na₂CO₃) volume and 45 min of the sonication time. [a] Reaction with 4 mg/mL of PEI divided in 2 mg/mL in each CaCl₂ and Na₂CO₃ initial dissolutions. [b] 4 mg/mL of PEI divided in 2 mg/mL for each initial CaCl₂ and Na₂CO₃ dissolutions and including the reduction of volume to 2 mL.

PEI [mg/mL]	0	0.44	2	4	4 [a]	4[b]
microspheres size [μm]	2.0±0.3	1.8±0.25	1.3±0.13	1.32±0.16	1.13±0.11	0.83±0.16
vaterite fraction [%]	36	55	64	72	75	86



Figure_S2. IR-FTIR spectrum of CaCO₃ product using 4mg/mL of PEI, 5mL of reagents volume and 45min of ultrasonic agitation. Other experimental conditions as described in the main text.

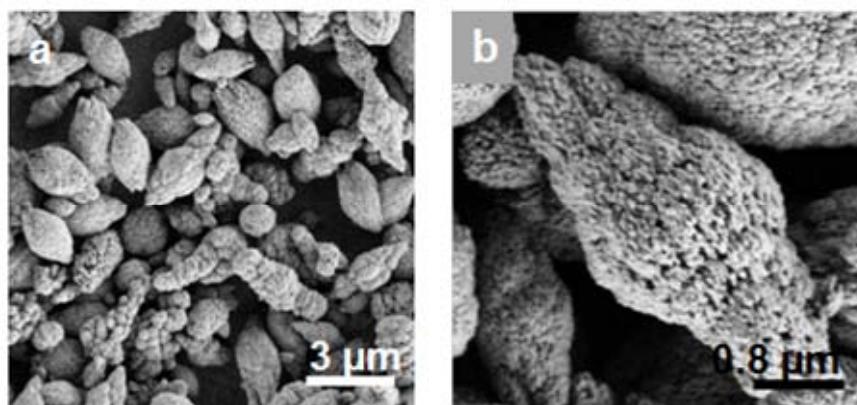


Figure_S3. Effect of the polarity of the mixture water/organic solvent on the particle shape when 8mg/mL of PEI is used.

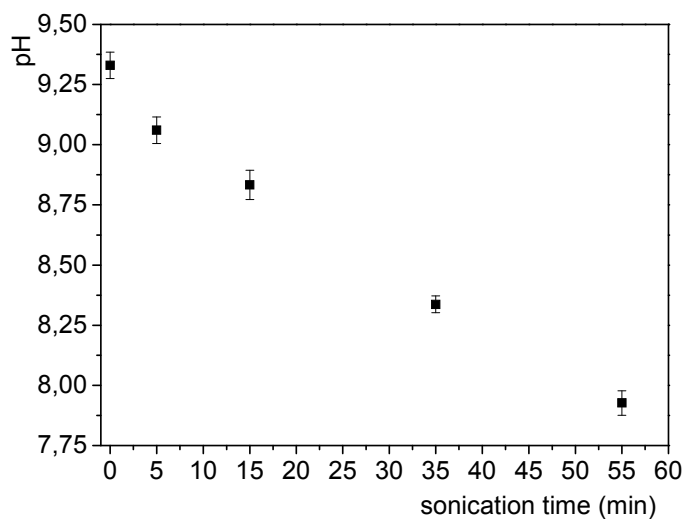
Table_S2. Summary of the results achieved using water/organic solvents with or without PEI, 5mL of reagents volume and 45min sonication.

	Shape of particle	vaterite fraction [%]	calcite fraction [%]	microparticles size [μm]
water/EtOAc	r	0	100	-
water/DMSO	r	0	100	-
water/DMF	r	0	100	-
water/EtOH	r	0	100	-
water/EtOAc+4PEI	s >> e and few r	84	16	1.08±0.22
water/DMSO+4PEI	e > s and few r	85	15	1.57±0.21
water/DMF+4PEI	e > s and few r	85	15	1.98±0.28
water/EtOH+4PEI	e >> s and few r	88	12	1.28±0.18
water/EtOAc+8PEI	s >>> e	100	0	1.10±0.13
water/DMSO+8PEI	s > e	96	4	0.75±0.12
water/DMF+8PEI	e > s	99	1	1.18±0.13
water/EtOH+8PEI	e >> s	96	4	1.31±0.12

r: rhombohedra; e: microellipsoids; s: microspheres.



Figure_S4. CaCO₃ of different shapes obtained with the reduction of the reagent volume in the water/organic solvent +PEI system. Other experimental conditions as described in the main text.



Figure_S5. pH decrease of water dissolutions of CaCl₂ (0.33M, 15 mL) during the ultrasonic process. Other experimental conditions as described in the main text.

Table _S3. Estimation of the quantity of (bio)molecules (μg of immobilized biomolecule per mg of CaCO_3) deposited onto microparticles surface.

bio(molecule)	BSA-FITC	HIgG-FITC	HIgG-Per	Tyr	BG	MO	F	R	MR	MB
$\mu\text{g}/\text{mg}$	24	13	9	252	12.2	45	8.7	0.31	-	-
Charge at pH 6-7	-	+	+	-	0	0	0	+	+	+

Tyr (tyrosinase), BG (bromocresol green), MO (methyl orange), F (fluorescein), R (rhodamine B), MR (methyl red), MB (methylene blue).



High sensitive gold-nanoparticle based lateral flow Immunodevice for Cd²⁺ detection in drinking waters



Adaris M. López-Marzo^{a,b}, Josefina Pons^b, Diane A. Blake^c, Arben Merkoçi^{a,d,*}

^a Nanobioelectronics & Biosensors Group, Catalan Institute of Nanoscience and Nanotechnology, Campus de la UAB, 08193 Bellaterra, Barcelona, Spain

^b Department of Chemistry, Universitat Autònoma de Barcelona, 08193, Bellaterra, Barcelona, Spain

^c Department of Biochemistry and Molecular Biology, Tulane University School of Medicine, New Orleans, LA 70112, USA

^d ICREA, Barcelona, Spain

ARTICLE INFO

Article history:

Received 21 January 2013

Received in revised form

19 February 2013

Accepted 19 February 2013

Available online 22 March 2013

Keywords:

Gold nanoparticle

Immunodevice

Cadmium

Detection

Water

ABSTRACT

In this work for first time a lateral flow immunosensor device (LFID) for Cd²⁺ determination in drinking and tap waters using the Cd-EDTA-BSA-AuNP conjugate as signal producer tool is introduced. The principle of working is based on competitive reaction between the Cd-EDTA-BSA-AuNP conjugate deposited on the conjugation pad strip and the Cd-EDTA complex formed in the analysis sample for the same binding sites of the 2A81G5 monoclonal antibody, specific to Cd-EDTA but not Cd²⁺ free, which is immobilized onto the test line. The device has a large response range within 0.4–2000 ppb, being the linear response between 0.4 and 10 ppb. The quantification and detection limits of 0.4 and 0.1 ppb, respectively, represent the lowest ones reported so far for paper based metal sensors. The obtained detection limit is 50 times lower than the maximum contamination level required for drinking water. Here we also show a new option for increasing the sensibility in the LFDs with competitive format, through the decreasing in concentrations of the Cd-EDTA-BSA-AuNP conjugate deposited in the conjugation strip and the mAbs deposited in the test and control zones until to reach optimized concentrations. It is an important result take into account that the increase in sensibility is one of the challenges in the field of LFD sensors, where are focused many of the ongoing researches. In addition, a specificity study of the device for several metal interferences, where potential metal interferences are masked with the use of the EDTA and OVA optimized concentrations, is presented too.

© 2013 Elsevier B.V. All rights reserved.

1. Introduction

Heavy metals are not biodegradable and therefore they remain indefinitely in the ecological systems and in the food chain exposing top-level of pollution. They have been isolated from soil, drinking water and surface and ground waters in residential areas (Aragay et al., 2011a; Aragay et al., 2011b; Bhagure and Mirgane, 2011; Schauer et al., 2004; Zakir and Brennan, 2011). Especially Cd²⁺ is one of the most harmful heavy metal. It can be accumulated in the human body mainly in the liver and kidneys and shows a biological half-life of greater than 10 years. Depending upon the ingestion route, Cd²⁺ exposure can affect kidney (Cd²⁺ appears to accumulate with age, especially in the kidney leading to kidney failure), lung function, or produce cardiovascular diseases. Experimental and epidemiologic studies provide evidence that

* Corresponding autor at: Nanobioelectronics & Biosensors Group, Catalan Institute of Nanoscience and Nanotechnology, Campus de la UAB, 08193 Bellaterra, Barcelona, Spain. Tel.: +34 935811976; fax: +34 935812379.

E-mail addresses: arben.merkoci@icn.cat, merkoci.biosensorseditor@icn.cat (A. Merkoçi).

low-level chronic Cd²⁺ exposure, in combination with other environmental factors, can contribute to an increased risk of cancer (Darwish and Blake, 2001; Darwish and Blake, 2002; Khosraviani et al., 1998).

The release of Cd²⁺ into environment has noticeably increased as a result of industrialization (Guell et al., 2008). Thus, different world organizations such as the World Health Organization (WHO), the US Environmental Protection Agency (EPA) and the Food and Agriculture Organization (FAO) have regulated the maximum level of this metal in the environment. In seawater the acute and chronic Cd²⁺ exposure criteria are 9.3 and 4 ppb (Khosraviani et al., 1998), respectively, and in groundwater 3 ppb (Bhagure and Mirgane, 2011). For drinking water has set an enforceable regulation for Cd²⁺ in terms of a maximum contaminant level of 5 and 3 ppb permitted by EPA and WHO, respectively The WHO (2008). The maximum levels for Cd²⁺ in foodstuff are between 0.05 and 3 µg/kg The Commission of the European Communities (2008). In 2010 the Joint FAO/WHO Expert Committee on Food Additives (JECFA) reassessed the tolerable provisional Cd²⁺ human intake levels in a Provisional Tolerable Weekly Intake (PTMI) of 6 µg per kg of body weight The JECFA (2011). The European Food Safety Authority

(EFSA) adopted an opinion in January 2009 establishing a new tolerable weekly intake level for Cd^{2+} (TWI) of 2.5 $\mu\text{g}/\text{kg}$ body weight The EFSA (2009).

Due to the mentioned reasons Cd^{2+} continue to be an important analyte that requires a careful environment monitoring. The ability for rapid, sensitive and low cost Cd^{2+} monitoring in environment is a requisite for controlling human and animal exposure.

As it is well-known graphite furnace atomic absorption spectroscopy (GFAAES) (Gasparik et al., 2010) and inductively coupled plasma emission spectroscopy (ICPES) (Hoa et al., 2010) are the standard techniques for trace heavy metal analysis. However, these labor-intensive and time-consuming techniques require complex and expensive instruments and specialized personnel to carry out the operational procedures (Aragay et al., 2011a; Aragay and Merkoçi 2012b). In addition, sample preparation usually requires acid digestion or some complex samples like seawater present some difficulties due to the high salt content, causing matrix interference and insufficient precision (Knecht and Sethi, 2009; Senkal et al., 2007). For this reason, there are ongoing researches on the development of rapid, low-cost and friendly-use techniques for trace heavy metals detection suitable for in situ monitoring assays. Colorimetric (Du et al., 2011; Knecht and Sethi, 2009), fluorimetric (Zong et al., 2011), X-Ray Fluorescence Spectroscopy (X-RFS) (McNeill and O'Meara, 1999) and immunoassays techniques for heavy metal sensing are cheaper and faster than the two above mentioned and in addition are highly sensitive and selective (Blake et al., 1998; Darwish and Blake, 2001, 2002; Khosraviani et al., 1998; Zhao et al., 2010). Other methods that have been adapted to allow the miniaturization and in-field applications are the electrochemical methods, specially voltammetric (Afkhami et al., 2012; Aragay et al., 2010; Shtoyko et al., 2004; Tan et al., 2010) and potentiometric (Adami et al., 2007; Aragay et al., 2011a) techniques which offer high sensitivity, low cost, simplicity and the possibility for in-field applications. Although often during the analysis of real samples (i.e. by using electrochemical stripping analysis), the Pb^{2+} due to its close oxidation potential with the Cd^{2+} uses to interfere to Cd^{2+} analysis (Adami et al., 2007).

However, for the mentioned heavy metals sensing techniques relatively cost equipments and even trained personnel are still necessary to carry out the analysis preventing their extended application in the routine detection of Cd^{2+} or other heavy metals. In this context analytical methods based on paper play an important role as tool of point of care assay to monitor the heavy metals in different samples. Paper based sensors represent cheap, portable and simple detection tool. These are facile to be used, portable, low cost, use low sample volume and do not require specialized users. The analysis using paper based platforms can be carried out even by a naked-eye colorimetric change (Ngom et al., 2010; Parolo and Merkoçi, 2013a). Enzymes (Zakir and Brennan, 2011), DNA molecule Torabia and Lu (2011), metal-specific DNAs (Fang et al., 2010; Mazumdar et al., 2010), metal-specific monoclonal antibodies (mAbs) (Abe et al., 2011; Liu et al., 2012), others proteins (Gu et al., 2011) and even small organic molecules (Aragay et al., 2012a; George et al., 2012) are the recognition molecules used up to date in paper based metals biosensing both in simple format or as lateral flow devices (LFDs).

Here a novel and high sensitivity lateral flow immunoassay device (LFID) for Cd^{2+} detection in aqueous samples using the Cd-EDTA-BSA conjugate labeled with gold nanoparticles as signal producer tool is implemented. The developed LFID is based on the recognition of Cd-EDTA complex (formed after Cd^{2+} analyte complexation) by using the specific 2A81G5 monoclonal antibody (mAb). In the device the Cd-EDTA-BSA-AuNP conjugate placed onto the conjugation pad strip competes with the Cd-EDTA by the

same binding sites in the 2A81G5 mAb deposited onto the test line. The decrease of the conjugate and mAbs concentrations at its corresponding zones, used as tool to increase the sensibility of the device in the competitive format allows the obtaining of a large operation range (from 0.4 to 2000 ppb) and very low limits of detection (LOD) and quantification (LOQ). This is an interesting approach considering the fact that a lot of efforts to enhance the LOD and LOQ in the LFDs field are put by the nowadays research in this field. These approaches are either based on the change of the geometry of the sample pad (so as to introduce larger volumes of sample or concentrate the sample) or in finding of new signal color producer particles or even loading of a second particle with a color producer that improves the signal (Chen and Wu, 2012; Choi et al., 2010; Parolo et al., 2013b, 2013c; Xia et al., 2009). The LOD and LOQ achieved with our LFID (of 0.1 and 0.4 ppb respectively) are the lowest limits reached with a metal sensing paper (Abe et al., 2011; Fang et al., 2010; George et al., 2012; Gu et al., 2011; Liu et al., 2012; Mazumdar et al., 2010; Torabia and Lu, 2011) and even considering Cd^{2+} detection in large part of electrochemical methods (Adami et al., 2007; Aragay et al., 2010; Aragay et al., 2011a; Shtoyko et al., 2004). Moreover other integrated platforms like lab-on-a-chip voltammetric sensor (Jang et al., 2010; Jung et al., 2011) and paper based voltammetry (Apilux et al., 2010; Tan et al., 2010) have not yet reported such low LOD for metal sensing. In addition, during the specificity assay with interest for real sample analysis, all metal interferences were masked by sample treatment using appropriate EDTA and OVA concentrations achieving interference levels lower than 5% when eleven metallic ions are present in higher concentrations than those expected in drinking waters samples.

2. Experimental section

The 2A81G5 mAb and the Cd-EDTA-BSA conjugate were prepared and characterized as described in a previous work (Blake et al., 1996). The albumin from bovine serum (BSA), monoclonal anti-bovine serum albumin-antibody produced in mouse (anti-BSA), ethylenediaminetetraacetic acid disodium salt dihydrate ($\text{Na}_2\text{EDTA}\cdot 2\text{H}_2\text{O}$), albumin from chicken egg white - ovalbumin - (OVA), Tween 20, gold(III) chloride trihydrate ($\text{HAuCl}_4\cdot 3\text{H}_2\text{O}$, 99.9% metals basis), 4-(2-hydroxyethyl)piperazine-1-ethanesulfonic acid ($\text{C}_8\text{H}_{18}\text{N}_2\text{O}_4\text{S}$, HEPES) and effluent wastewater (trace elements) certified reference material were purchased from Sigma Aldrich. Cd^{2+} , Zn^{2+} , Ni^{2+} , Fe^{3+} , Pb^{2+} , Al^{3+} , Cu^{2+} , Co^{2+} , Ca^{2+} , Mg^{2+} , Mn^{2+} and Hg^{2+} metallic ion solutions were prepared by diluting atomic absorption spectroscopy (AAS) grade standard solutions (1000 ppm in 2% HNO_3) (Panreac) using Milli-Q water. The Hi-Flow Plus nitrocellulose membrane (HF240), the cellulose fiber sample pad and the glass fiber conjugate pad were acquired from Millipore. The antibodies dissolutions on lateral flow membranes were dispensed in automatic mode using an IsoFlow™ Dispenser. The color intensity of the lines in the strips was measured by using a COZART™ RapidScan color intensity reader.

Absorption measurements were carried out on SpectraMax M2 spectrophotometer.

2.1. Conjugation of Cd-EDTA-BSA with gold nanoparticles. Gold aggregation test.

2.1.1. Preparation of gold nanoparticles (AuNPs)

Approximately 20 nm diameter AuNPs dissolution were synthesized according to the citrate reduction of HAuCl_4 dissolution (Saha et al., 2012). All glassware used in this preparation was thoroughly cleaned in aqua regia overnight and rinsed with double

distilled H₂O and the reflux was used for all the procedure. A 50 mL aqueous solution of 0.01% HAuCl₄ was heated to boiling and vigorously stirred in a 250 mL round-bottom flask; 5 mL sodium citrate 40 mM were added quickly to this solution. Boiling was continued for an additional 10 min. The solution was cooled to room temperature with a continuous stirring for another 15 min. The colloids were stored in dark bottles at 4 °C.

2.1.2. Preparation of the Cd-EDTA-BSA-Au conjugate

The pH of AuNPs-citrate dissolution was adjusted to 7.4 with 0.01 M NaOH. 15 µL of different concentrations of BSA solutions (from 0 to 300 µg/mL) were added to 135 µL of AuNPs pH 7.4 and incubated during 30 min at 650 rpm and 25 °C. An absorbance measurement at 520 nm was performed first, followed by a second one after adding 20 µL of 10% NaCl and a third one after adding 160 µL of 10% NaCl both measured again at the same wavelength.

In a typical labeling of the Cd-EDTA-BSA conjugate with AuNPs, 900 µL of AuNPs-citrate pH 7.4 were incubated with 100 µL (0.8 mg/mL) of the Cd-EDTA-BSA conjugate in HEPES buffered saline (HBS: 137 mM NaCl, 3 mM KCl, and 10 mM HEPES, pH 7.4) during 30 min.

2.2. Optimization of the LFID operational conditions

The first parameter to study was the efficiency of the recognition reactions between antigen/antibody that occurs at the test and control zones in terms of the AuNP visibility. The quantities of mAbs deposited onto the membrane (the 2A81G5 mAb at the test zone and anti-BSA mAb at the control zone) and the quantity of Cd-EDTA-BSA-AuNPs conjugate deposited onto the conjugation pad were the most important parameters to optimize.

Initial assays used for optimizations were carried out by drop coating of 0.5 and 1 µL (0.5, 1 and 2 mg/mL) of 2A81G5 and anti-BSA mAbs working with conjugation strips with lengths of 7.5, 9 and 11 cm. For preparing the conjugation pad solution 900 µL of AuNP-citrate pH 7.4 were incubated with 100 µL (0.8 mg/mL) of the Cd-EDTA-BSA conjugate in HBS pH 7.4 during 30 min, centrifuged and resuspended in 300 µL HBS buffer pH 7.4, 10% sucrose and 0.1% Tween 20.

Using the last optimized conditions and following the same approach new assays were carried out by automatic dispensing of the mAb solutions onto the membrane. Thus, 0.5 and 0.375 µg/mm of the 2A81G5 mAb were tested on the test line and 0.32 and 0.4 µg/mm of the anti-BSA mAb were tested on the control line. Conjugation strips of 10, 12, 14, 16 and 18 cm length were respectively soaked into 300, 350, 400, 500 and 600 µL of the conjugation pad solution and evaluated afterwards as previously described.

2.3. Preparation of the LFID.

For a typical LFI preparation, a conjugation strip with a length of 18 cm was cut and soaked in 600 µL of the conjugation pad solution. The strip was dried at vacuum during 50 min and stored at 4 °C. For preparing the conjugation pad solution 900 µL of AuNP-citrate pH 7.4 were incubated with 100 µL (0.8 mg/mL) of the Cd-EDTA-BSA conjugate in HBS pH 7.4 during 30 min, centrifuged at 14,000 g and resuspended in 600 µL of the conjugation strip solution (HBS pH 7.4, 10% sucrose and 0.1% Tween 20). The sample pad was treated with 10 mM HBS pH 7.4, containing 5% BSA and 0.1% Tween-20, then dried at 60 °C for 1 h.

The nitrocellulose membrane, the prepared conjugation pad strip as well as the sample and absorption pads were assembled in the same order onto a plastic backing card. At a distance of 0.5 cm from the top of the membrane, a band of anti-BSA mAb was

dispensed as control line at 0.4 µg/mm and analogously 2A81G5 mAb was applied as detection line at 0.375 µg/mm to a distance of 1.0 cm from membrane top. The lateral flow strips were cut at 0.7 cm of width. For the analysis 150 µL of sample were deposited on the sample pad and were washed with 150 µL of 10 mM of HBS pH 7.4 with 0.1% Tween 20 (running buffer).

2.4. Linearity and limits of detection and quantification

For evaluating the linearity of the device Cd²⁺ standard dissolutions were prepared in HBS pH 7.4 and Na₂EDTA (14 mM) in the concentration range of 0.02 to 2000 ppb by diluting an AAS grade Cd²⁺ ion standard dissolution (1000 ppm in 2% nitric acid). 150 µL of each Cd²⁺ dissolutions were deposited onto the sample pad, and the analysis was left to run until the mobile phase migrated toward the absorption pad. The test and control zones were visually evaluated within 10 min. For quantitative measurement the dry strip was inserted into the *RapidScan* color intensity portable reader. The measured value of the color intensity on the test and control lines of the strip remains stable for more of two months giving statistically the same measured value. Samples with high Cd²⁺ contents give high response values in the test line of the *RapidScan* reader, which corresponds by visual inspection to the lower color intensity while samples with low Cd²⁺ contents give low responds values in the test line of the *RapidScan* reader, which corresponds by visual inspection to the higher color intensity. The calibration curve was obtained by plotting the difference of the color intensity between the Cd²⁺ standard dissolutions and the blank. The values of the experimental points for the calibration curve correspond to the mean of values obtained during a five days period making each day three independence replies by each concentration.

The LOQ was assumed as the lowest amount of Cd²⁺ which can be quantitatively determined with suitable precision and accuracy, while the LOD was calculated as three times the standard deviation of the sevenfold analysis of a blank. A more accurate determination of the LOD was carried out with the calibration curve and using the Eq. (1):

$$LOD = \frac{3 \times Sbl}{b} \times \frac{1}{\sqrt{n}}, \quad (1)$$

where *Sbl* is the standard deviation of the blank, *n* is the number of measurements and *b* is the slope of the calibration curve (The United States Pharmacopeia, 2007).

2.5. Specificity assay

For the specificity assay the obtained response for different 10 ppb Cd²⁺ dissolutions that contain an excess of the possible interfering metal (total metallic response) and 14 mM Na₂EDTA in HBS was compared with the response obtained for 10 ppb Cd²⁺ dissolution with 14 mM Na₂EDTA in HBS. The difference in the response between them expressed in percentage was assumed as the estimated interference for each metal (Eq. (2)). For those metals with not significant expected interference (for example Ca²⁺, Mg²⁺, Al³⁺, Fe³⁺ and Pb²⁺) solution mixtures of 10 ppb Cd²⁺ and 25 ppm of the metal were tested, while for metals with a moderate or notable expected interference (for example Ni²⁺, Cu²⁺, Zn²⁺, Co²⁺, Mn²⁺ and Hg²⁺) solution mixtures of 10 ppb Cd²⁺ and 5 ppm of the metal were tested. Similar specificity assays were also carried out in presence of 1% OVA or BSA and 14 mM Na₂EDTA.

5, 10 or 100 ppb Cd²⁺ spiked water samples containing the mentioned 11 most frequent possible interfering metals in amounts of 15 ppm Ca²⁺, 15 ppm Mg²⁺, 400 ppb Al³⁺, 400 ppb Fe³⁺, 10 ppb Pb²⁺, 20 ppb Ni²⁺, 2.5 ppm Cu²⁺, 5 ppm Zn²⁺,

1 ppm Co^{2+} , 300 ppb Mn^{2+} and 5 ppb Hg^{2+} (these concentrations are even higher than its permitted limits in drinking water; see Table S1 at SI) with different EDTA (0.005, 0.05, 0.5 and 0.9 mM) and OVA (5%, 10% and 15%) concentrations were evaluated. In a similar way the difference in the response between samples with Cd^{2+} and others metals with samples containing only Cd^{2+} expressed in a percentage was assumed as the interference level caused by the studied metals.

estimated interference

$$= \frac{(\text{total metallic response} - \text{Cd}^{2+} \text{ response})}{\text{Cd}^{2+} \text{ response}} \times 100\% \quad (2)$$

3. Results and discussion

3.1. Conjugation of Cd-EDTA-BSA with gold nanoparticles. Gold aggregation test

Fig. 1A shows the results of the gold aggregation test used to evaluate the loading of AuNPs with Cd-EDTA-BSA conjugate. When increasing concentrations of Cd-EDTA-BSA solutions are added to the same quantity of AuNPs, the absorption of AuNPs decreases until it reaches a constant value (see Fig. 1A-1). When to equals AuNPs solutions with increasing concentrations of Cd-EDTA-BSA solutions are added 1.2% or 5.5% NaCl, the absorption

initially decreases due to the aggregation of AuNPs caused by salt effect. Afterwards the absorption begins to increase by increasing the Cd-EDTA-BSA concentration until reaching a constant value of absorbance above 50 $\mu\text{g}/\text{mL}$ of Cd-EDTA-BSA (see Fig. 1A-2 and A-3). This concentration from which a constant absorbance value is reached means that, for Cd-EDTA-BSA concentrations higher than 50 $\mu\text{g}/\text{mL}$ enough protein is coating the surface of the AuNPs allowing the stabilization of AuNPs, which prevents their aggregation in presence of salts. Although in the 50–200 $\mu\text{g}/\text{mL}$ Cd-EDTA-BSA concentration range the AuNPs aggregation by salts effect is already blocked, we decide to perform the following assays at 80 $\mu\text{g}/\text{mL}$ of the conjugate, because by using a large excess of the conjugate could occur its delivery from the AuNPs surface and this would affect the well operation of the LFD. Taking into account that the Cd-EDTA-BSA-AuNP conjugate ensures the signaling color in this device, a good stabilization of the AuNPs is very important to have appreciable and stable signal intensities onto the control and test lines, which in turn would directly improve the precision of the results.

Fig. 1B shows evidences of the conjugation between Cd-EDTA-BSA and AuNPs. In the Fig. 1B-2 it can be observed that the Cd-EDTA-BSA-AuNP absorption spectrum has a bathochromic shift of 5 nm and the absorption intensity decreases in comparison with the AuNPs solution at the same concentration (Fig. 1B-1). This shift is also reported by other authors for the AuNPs-BSA conjugate (Lien et al., 2010). Fig. 1C presents two TEM views, one with as prepared AuNPs and the other one with the

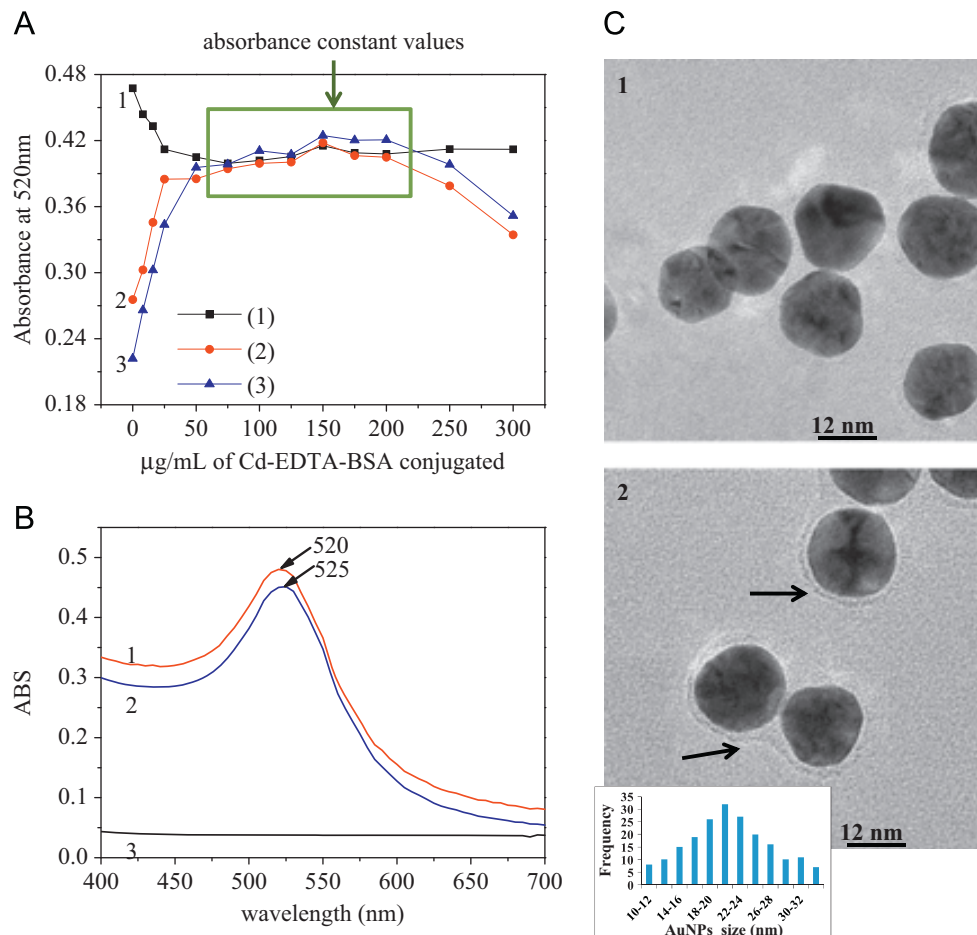


Fig. 1. Results related with the labeling of the Cd-EDTA-BSA conjugate with AuNPs. (A) Gold aggregation test for the Cd-EDTA-BSA conjugate. Absorption behavior at 520 nm of the AuNPs solution in presence of increasing concentrations of the Cd-EDTA-BSA with and without the addition of NaCl: (1) AuNPs + Cd-EDTA-BSA, (2) AuNPs + Cd-EDTA-BSA + 1.2% NaCl, (3) AuNPs + Cd-EDTA-BSA + 5.5% NaCl. (B) Absorption spectra of some components of the Cd-EDTA-BSA-AuNPs conjugated: (1) 135 μL AuNPs + 15 μL HBS, (2) 135 μL AuNPs + 15 μL Cd-EDTA-BSA (80 mg/mL) and (3) 135 μL HBS + 15 μL Cd-EDTA-BSA (80 mg/mL). (C) TEM images of the AuNPs (1) and the Cd-EDTA-BSA-AuNP (2) with the inset graph that shows the nanoparticles distribution size.

Cd-EDTA-BSA-AuNPs conjugate formed as explained in the experimental section. In Fig. 1C-2 the shadow around AuNPs (indicated by arrows) corresponds to BSA-EDTA organic phase while this shadow does not appear in Fig. 1C-1.

3.2. Design and operation principle of the LFID

The detection principle of the developed LFID is based on the use of a purified 2A81G5 mAb that recognizes with high specificity Cd-EDTA complexes but not the free Cd^{2+} ions. The affinity of 2A81G5 mAb for the Cd-EDTA complex is associated with the histidine-H96 (His-96) and tryptophan (Trp-H52) residues in the heavy chain variable regions of this mAb being these important as antigen recognition sites. The analysis of 3D structure model of the mAb made in previous works demonstrated that, there was closest distance of 2.72 Å between Cd^{2+} and N of His-96 in the CDR3 region of the heavy chain of 2A81G5 mAb, which suggests a possible interaction antigen-antibody. The model also revealed a possible hydrogen bonding interaction with the nitrogen of the antigen and the Trp-H52 residue (Blake et al., 1996). The differences in the dimensional structures and conformational changes between the metal-EDTA complexes as they shift to accommodate

various metal ions appear to be an important factor in the antibody recognition (Blake et al., 1996).

The Cd^{2+} detection principle is based on the competition between the Cd-EDTA complex (previously formed by reaction of Cd^{2+} with EDTA at 1:1 stoichiometric relation and deposited onto the sample pad during the sample analysis) with the Cd-EDTA-BSA-AuNP conjugate (deposited onto the conjugation pad) for the same binding sites of the immobilized 2A81G5 mAb in the test line. For controlling purposes in the control line an anti-BSA mAb is immobilized to capture the excess of Cd-EDTA-BSA-AuNP conjugate (Fig. 2A), giving always a color red as control when there is fluid crossing the membrane. The Cd^{2+} concentration in a sample is quantified by the ability of Cd-EDTA complex to substitute the binding sites of the Cd-EDTA-BSA-AuNP with the 2A81G5 mAb producing a decrease of the color intensity (provided by AuNPs in the Cd-EDTA-BSA-AuNP conjugate) in the test line. In this way, when there is not Cd^{2+} in the sample and just running buffer flows through the membrane the maximal color intensity is developed in the test line (Fig. 2B). On the other hand, when increasing concentrations of Cd^{2+} are present in the samples the color intensity in the test line gets decreasing (Fig. 2C). The color development is inversely proportional to the increasing concentration of Cd^{2+} in the original sample.

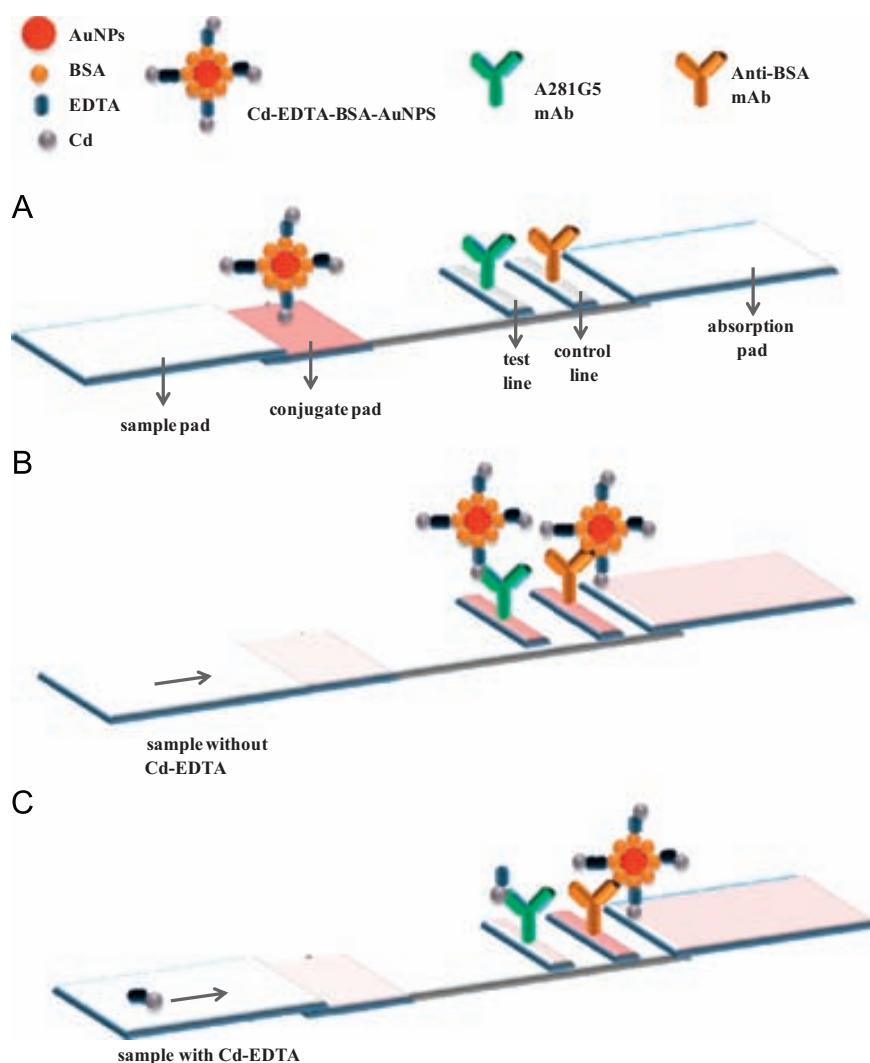


Fig. 2. Schematic representation of the configuration and measurement principle of the Cd-EDTA biosensor device. (A) Configuration of the biosensor: components deposited in each part, (B) the principle of visual detection analyzing samples without Cd-EDTA and (C) the principle of visual detection analyzing samples with Cd-EDTA. (For interpretation of the references to color in this figure, the reader is referred to the web version of this article.)

3.3. Optimization of the LFID operational conditions

3.3.1. Optimization of the conjugate and antibodies concentrations in the device

In order to obtain a high sensibility and better performance of the device for Cd^{2+} analysis, the optimization of the antibodies onto the test and control zones and the conjugate onto the conjugation strip was strictly necessary. The first optimizations of the LFID were carried out by drop coating of different mAbs concentrations onto the membrane for the same conjugation strip preparation. Other optimizations were made by decreasing the concentration of the conjugate onto the conjugation strip and keeping the same immobilized amount of the mAbs previously determined. Finally the last optimizations assays were made using the automatic dispensing. A detailed explanation of the optimization process appears in the SI (Fig. S1–S3). In general the sensibility of the device increases when decreases the mAbs and the Cd–EDTA–BSA–AuNP conjugate concentrations.

The decrease of the 2A81G5 mAb and the conjugate concentrations onto the test zone and the conjugation strip, respectively, improves the resolution of the device, due to the fact that the Cd–EDTA detection takes place by a competitive format between the Cd–EDTA–BSA–AuNP conjugate and Cd–EDTA by the same sites of the 2A81G5 mAb immobilized onto the membrane. The key for a successful detection is to set the device operation parameters that favor the competition to the Cd–EDTA contained in the sample by the mAb binding sites. In samples with Cd–EDTA between 0 and 10 ppb, the quantity of Cd^{2+} that competes with the conjugate is very low and unable to produce a notable discoloration in the test line by displacing the large quantity of the conjugate at the 2A81G5 mAb sites. By contrary a high quantity of mAb onto the test line does not allow to the Cd–EDTA to produce notable

discoloration due to the fact that large quantity of the colored conjugate will also bind to the mAb sites. Consequently the reduction of the concentrations of the conjugate onto the conjugation strip and the 2A81G5 mAb onto the test line favors the Cd–EDTA competition by the mAb binding sites in order to obtain a notable discoloration at low analyte concentration increasing in this way the sensibility of the device.

3.4. Linearity and limits of detection and quantification

The image in Fig. 3A represents a typical Cd^{2+} analysis with the LFID. The violet color onto the test and control line appears once the strips are dried and this color measured by RapidScan equipment remains stable for two months. The developed LFID has a response range between 0.4 and 2000 ppb, being the linearity of the calibration curve from 0.4 to 10 ppb. Although the difference in color intensities between 0, 0.4, 2 and 5 ppb were not detectable at naked eye they can perfectly be discriminated by using the color reader equipment. Fig. 3 B and C show the lineal and exponential mathematic fit obtained by using the plotted experimental points of the calibration curve. The plotted values in the vertical axis correspond to the difference between the measured values of the samples and the blank in the test line.

The LOD of the device was 0.1 ppb being 0.4 ppb the LOQ corresponding to the lowest Cd^{2+} quantity that can be quantified with acceptable accuracy and precision. To the best of our knowledge both the LOD of 0.1 ppb and the LOQ of 0.4 ppb are the lowest values obtained using metal sensing papers (Abe et al., 2011; Fang et al., 2010; Gu et al., 2011; Liu et al., 2012; Mazumdar et al., 2010; Torabia and Lu, 2011; Zakir and Brennan, 2011) or even by most of Cd^{2+} electrochemical analysis methods (Adami et al., 2007; Afkhami et al., 2012;

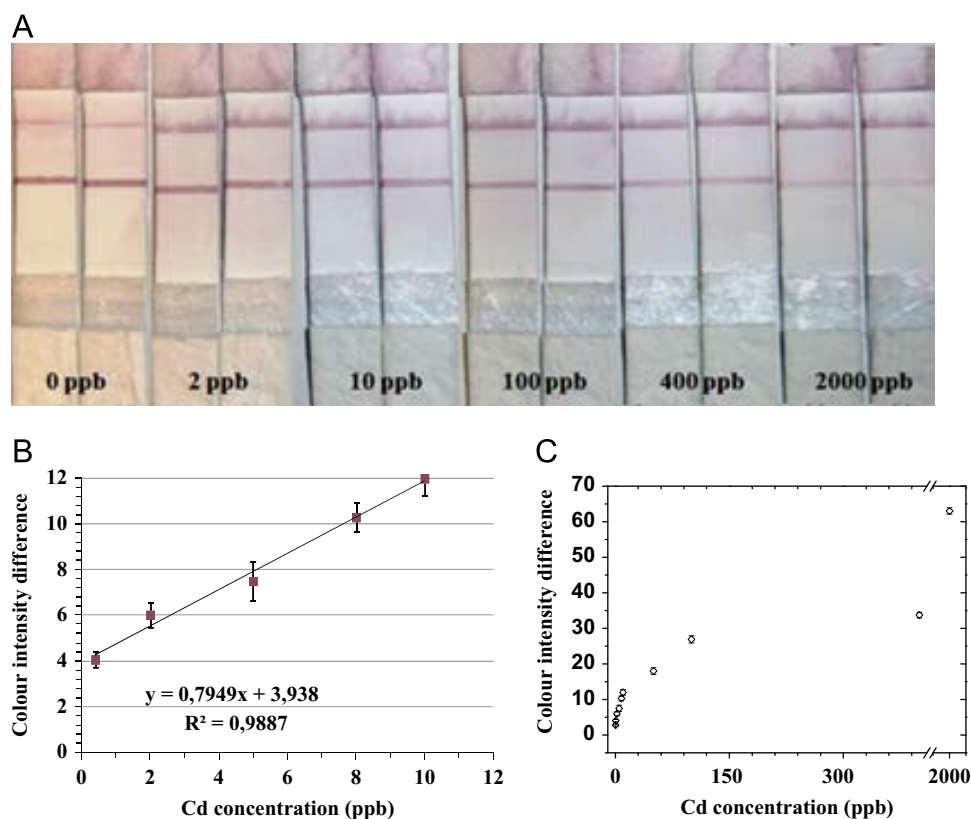


Fig. 3. Results related with the linearity assays. (A) Typical image of the Cd^{2+} detection by the LFID. A series of dilutions (0.4–2000 ppb) of Cd^{2+} standard atomic absorption grade were made in HBS with 14 mM EDTA. (B) Lineal range of the device for Cd–EDTA analysis. (C) Sensitivity over the entire range of the device for Cd–EDTA analysis. (For interpretation of the references to color in this figure, the reader is referred to the web version of this article.)

Table 1
Analytical performance data of reported paper based sensors.

Metal	RSD (%)	Linear range (ppb)	LOD (ppb)	LOQ (ppb)	samples	Reference
Cd ²⁺	< 5	0.4–10	0.1	0.4	spiked water	This work
Cr ³⁺ , Cr ⁶⁺	< 9	5–80	5	5	serum, waters	Liu et al. (2012)
Cu ²⁺	–	50–500	50	> 50	spiked water	George et al. (2012)
Cd ²⁺	14	10–100	10	> 10		
	15	5–50	5	> 5	rice wheat grain eggplant	Abe et al. (2011)
	9	2.5–25	2.5	> 2.5		
Hg ²⁺	–	10–60 120–480	10	> 10	spiked solutions	Gu et al. (2011)
Hg ²⁺ ; Ag ¹⁺	–	–	1; 2	> 1; > 2		
Cu ²⁺ ; Cd ²⁺	–	–	20; 20	> 20; > 20		
Pb ²⁺ ; Cr ⁶⁺	–	–	140; 150	> 140; > 150	spiked solutions and environmental waters	Zakir and Brennan (2011)
Ni ²⁺	–	–	230	> 230		
Cu ²⁺	–	–	0.63	–	spiked solutions	Fang et al. (2010)
Pb ²⁺	–	–	10	–	paints	Mazumdar et al. (2010)

Aragay et al., 2010; Shtoyko et al., 2004; Tan et al., 2010) reported so far as is displayed in Table 1.

3.5. Specificity assay

Results of the specificity assays are shown in Fig. 4. The interfering metals for Cd²⁺ determination can be classified in three groups. The first group is composed by the metallic ions with a non-significant interference such as Ca²⁺, Mg²⁺, Fe³⁺, Al³⁺ and Pb²⁺. 25 ppm of these metals almost do not interfere in the 10 ppb Cd²⁺ analysis using a 14 mM Na₂EDTA solution (Fig. 4A). This result is important because Ca²⁺, Mg²⁺, Al³⁺ and Fe³⁺ are the ions commonly found in drinking water samples at relatively high concentrations (for example the permissible limits of Al³⁺ and Fe³⁺ in drinking water are 0.2 and 0.3 ppm respectively, Table S1 The WHO (2008), while WHO guidelines does not make recommendations for Ca²⁺ and Mg²⁺) and it can be expected that the developed LFI should not face any significant interference during the Cd²⁺ analysis. The second group is made up by metals with moderate interference such as Co²⁺, Ni²⁺, Cu²⁺ and Zn²⁺. As observed (Fig. 4B) 5 ppm of these metals interferes between 5–10% in the 10 ppb Cd²⁺ analysis using 14 mM Na₂EDTA. The third group is composed of notable interfering metals such as Mn²⁺ and Hg²⁺. The presence of 5 ppm of Mn²⁺ or Hg²⁺ shows a 15–18% interference to the 10 ppb Cd²⁺ analysis using 14 mM Na₂EDTA (Fig. 4C). The ability of these metal–EDTA complexes to interfere in the Cd–EDTA analysis is in agreement with the reported equilibrium dissociation constant of the mAb to bind metal–EDTA complexes. The equilibrium dissociation constant of the 2A81G5 mAb with Cd²⁺ complexes are in the order of 7.4×10^{-11} and 2.1×10^{-8} for Cd–EDTA–BSA and Cd–EDTA respectively (Blake et al., 1996; Khosraviani et al., 1998), thus, metal–EDTA complexes with the highest equilibrium dissociation constants for 2A81G5 mAb (Al³⁺ 8.2×10^{-4} , Mg²⁺ 2.2×10^{-4} , Fe³⁺ 5.4×10^{-5} and Pb²⁺ 7.4×10^{-5}) do not show significant interference in the Cd²⁺ analysis. Metal–EDTA complexes with intermediate equilibrium dissociation constants for 2A81G5 mAb have moderate interference in the Cd²⁺ analysis (Co²⁺ 2.3×10^{-6} , Ni²⁺ 2.1×10^{-6} , Cu²⁺ 4.9×10^{-6} and Zn²⁺ 2.5×10^{-6}) and metal–EDTA complexes with the lowest equilibrium dissociation constants for 2A81G5 mAb (Mn²⁺ 4.1×10^{-7} and Hg²⁺ 10^{-8}) present the most notable interference.

Often, a “masking reagent” that specifically binds an interfering metal and removes it from the antibody binding reaction can be added to reduce interference from a cross-reactive metal (Blake et al., 1998). The formation of complexes between different types of albumins and multiples metals (Mg²⁺, Co²⁺, Ni²⁺, Cu²⁺, Zn²⁺,

Cd²⁺, Mn²⁺ and Hg²⁺) is already demonstrated (Bal et al., 1998; Goux and Venkatasubramanian, 1986; Masuoka et al., 1993; Masuoka and Saltman, 1994; Verma et al., 1989). In this work BSA or OVA were used as “masking agents”. These albumins have multiples metal binding sites through their functional groups of the amino acid sequence as schemed at Fig. S4–B and C at SI.

In the Fig. 4(A–C) are represented the obtained results in Cd²⁺ analysis with the addition of 1% BSA or OVA and using 14 mM EDTA in presence of the interfering metal. The addition of BSA or OVA (1%) to the spiked samples can significantly reduce the interfering effect for metals such as Mg²⁺ (25 ppm), Co²⁺, Ni²⁺, Cu²⁺, Zn²⁺ (5 ppm each) and Hg²⁺ (5 ppm) where the 1% OVA addition can decrease the interference from 13% to 2.5% (Fig. 4A), from 9% to less than 0.8% (Fig. 4B) and from 17% to 0.5% (Fig. 4C), respectively. Although the Metal–EDTA complexes formation constants are higher (between 13 and 21) than the metal–albumin complexes formation constants of the principal interfering metals (between 5 and 12) (Table S2) the metallic interference can be masked using albumin as demonstrated here. We can explain the masking effect of the BSA/OVA addition considering that, the Cd–EDTA complex formation constant (Fig. S4–A) is much higher than the Cd–BSA/OVA complex formation constant and that, the affinities of Cu²⁺, Zn²⁺, Hg²⁺, Ni²⁺, Co²⁺ and Mn²⁺ toward BSA or OVA functional groups are higher than the Cd²⁺ affinity toward BSA or OVA functional groups being the affinity decreased in the same order (Fig. S4–D) (Bal et al., 1998; Masuoka et al., 1993; Masuoka and Saltman, 1994). Taking into account that each metal has multiples, similar and different, binding sites with a unique albumin molecule (Fig. S4–C), while with EDTA the ratio Metal: EDTA in the M–EDTA complex is 1:1 (Fig. S4–A), it is clear that the interfering metal will bind with preference to albumin rather than EDTA. In the case of Mn²⁺ under the applied experimental conditions the addition of 1% BSA or OVA doesn't reduce the manganese interference (Fig. 4C), because Mn²⁺ do not has a good affinity by the albumins and moreover the Mn–EDTA complex has a 2A81G5 mAb equilibrium dissociation constant near to Cd–EDTA complex. The interfering effect coming from manganese can be reduced only by decreasing the EDTA concentration due to its small complex formation constant with EDTA in comparison to Cd²⁺ (Sasaki et al., 2008).

Fig. 4D displays the interference values obtained analyzing spiked water samples with 10 and 100 ppb Cd²⁺ and others 11 metals usually present in drinking water using 10% OVA and different EDTA concentrations (the metallic concentrations are over its permitted limits in drinking water; see Table S1 at SI). EDTA variations from 0.9 to 0.05 mM do not show significant changes in the response allowing similar metallic interference

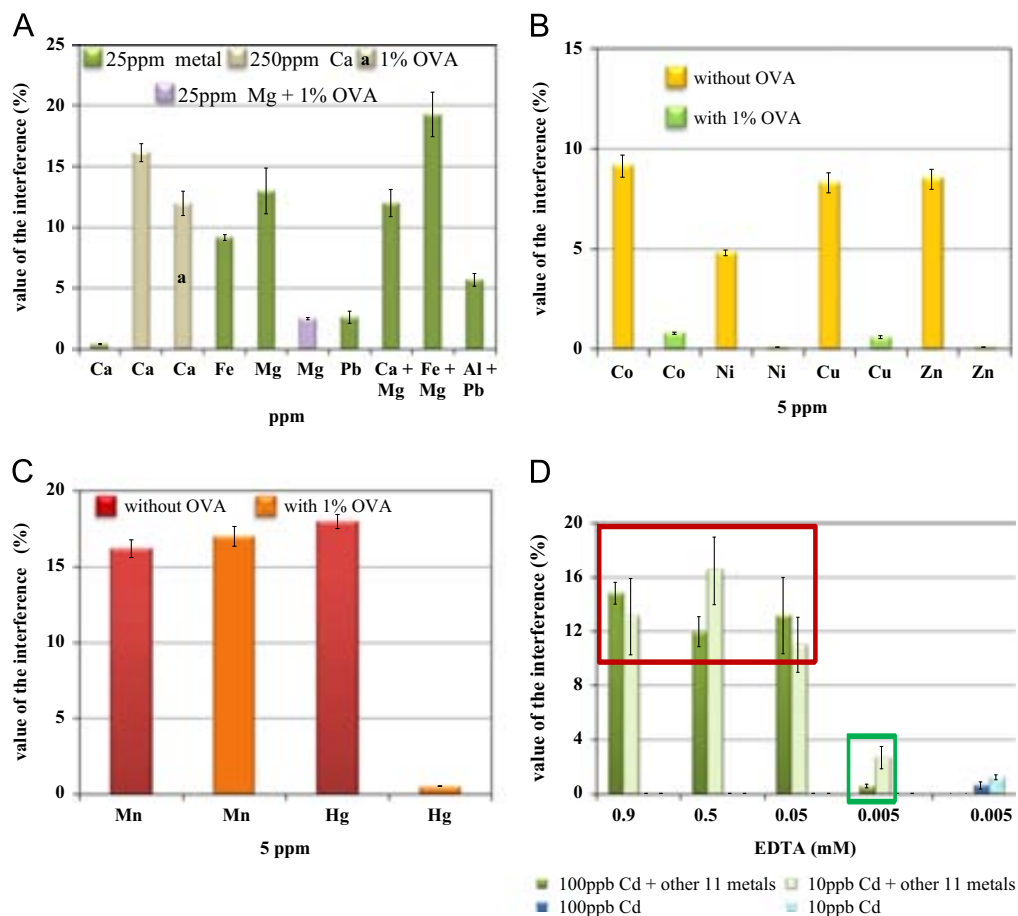


Fig. 4. Analysis of the interfering effect for the most important metals present in drinking water with and without OVA. (A) Interference of the Ca²⁺, Mg²⁺, Fe³⁺ and Al³⁺ ions in presence of 10 ppb Cd²⁺ and 14 mM Na₂EDTA prepared in spiked samples. The (+) symbol is used to indicate that the interference of two metals were simultaneously evaluated. (B) Interference of the Co²⁺, Ni²⁺, Zn²⁺ and Cu²⁺ ions in presence of 10 ppb Cd²⁺ and 14 mM Na₂EDTA prepared in spiked samples. (C) Interference of the Mn²⁺ and Hg²⁺ ions in presence of 10 ppb Cd²⁺ and 14 mM Na₂EDTA prepared in spiked samples. (D) Effect of the interference provoked by others 11 metals in presence of 100 and 10 ppb Cd²⁺, using 10% OVA and varying Na₂EDTA concentration. Effect of the interference produced by 10% OVA when 100 and 10 ppb Cd²⁺ are analyzed.

levels. By using the same EDTA concentrations and 5%, 10% and 15% BSA or OVA no significant changes in the Cd²⁺ analysis (being the estimated interference between 12% and 18%) was observed (results not shown). An optimum ratio between EDTA and BSA/OVA for which the interference coming from other metals can be reduced from around 15 up to a minimum value of around 4% was found using 0.005 mM EDTA and 10% OVA.

Several parameters involved in the reduction of the interference coming from other metals can be considered: the affinity constants of the complexes metal–EDTA, metal–albumin, metal/EDTA–mAb, the expected metallic ionic concentrations in the sample (Table S-2 at the SI), the optimized EDTA and OVA concentrations used in the assays and the stoichiometry in the complexes metal–mAb, metal–EDTA and metal–albumin. The masking of the interferences was possible by using 5×10^{-6} and 2×10^{-3} M of EDTA and albumin optimized concentrations, respectively. Under this condition interfering metals with albumin affinity constant higher than 5 can bind the albumin protein with preference to EDTA (such as Hg²⁺, Cu²⁺, Zn²⁺, Ni²⁺, Co²⁺, Mg²⁺) leaving free the EDTA to bind metallic ions such as Cd²⁺, Al³⁺, Fe³⁺, Ca²⁺, Mn²⁺ that have very low albumin affinity. As albumin concentration is 10³ times higher than EDTA concentration and the stoichiometry metal–EDTA is 1:1 while the stoichiometry metal–albumin is *n*:1, these factors permit that the majority of metal ions with albumin affinity remain preferably bound to the albumin. In the case of Al³⁺, Fe³⁺ and Ca²⁺ that preferably bind with EDTA

because of its poor albumin affinity, the interference produced by these metal–EDTA complexes could be low due to the fact that their affinity constants with the 2A81G5 mAb are very low in comparison to the affinity constant of the Cd–EDTA–2A81G5 mAb. In the case of Mn²⁺ for which the affinity constant Mn–EDTA–2A81G5 mAb is close to that of Cd²⁺, some quantity of Mn–EDTA complex interferes in the Cd²⁺ determination, maximum if Mn²⁺ concentration is 40 times higher than Cd²⁺ concentration where an interference value of about 3% was found (see Fig. 4D using 0.005 mM EDTA and 10 ppb Cd²⁺ + 11 other metals).

4. Conclusion

A novel and highly sensitive lateral flow device for Cd²⁺ detection in drinking water samples using the Cd–EDTA–BSA conjugate labeled with gold nanoparticles as signal producer tool has been successfully developed. The device presented here is based on a competitive format by setting Cd–EDTA–BSA–AuNP on the conjugation pad strip and the 2A81G5 mAb specific to Cd–EDTA onto the test line at the optimized concentrations. A strategy to increase the sensibility of the LFDs in a competitive format by decreasing the mAbs and conjugate concentrations is introduced. The Cd–EDTA–BSA–AuNP conjugate concentration onto the conjugate strip was decreased by increasing the length of the conjugate strip and soaking it either in the same or in a bigger

volume of the conjugate strip solution. This optimization process permits to reach, in first place, a great large operation range from 0.4 to 2000 ppb being the lineal working range from 0.4 to 10 ppb, and in second place, very low detection and quantification limits of 0.1 and 0.4 ppb, respectively. These metal detection and quantification levels are much lower than the previously reported for metal biosensors based on paper and even for many metal electrochemical methods.

The specificity assay demonstrated that Ca^{2+} , Mg^{2+} , Fe^{3+} , Al^{3+} and Pb^{2+} ions show a slight or almost no interference in the Cd^{2+} analysis. Co^{2+} , Ni^{2+} , Zn^{2+} and Cu^{2+} ions have a moderate interference (5 ppm of these metallic ions causes an interference between 5–10% in the determination of 10 ppb Cd^{2+} using 14 mM Na_2EDTA) while Hg^{2+} and Mn^{2+} ions have a notable interference (the presence of 5 ppm Mn^{2+} or Hg^{2+} interferes between 15–18% in the 10 ppb Cd^{2+} analysis using 14 mM Na_2EDTA). The interferences can be reduced below 5% by lowering the EDTA concentration to 0.005 mM and by adding 10% OVA or BSA. This last result demonstrates that the developed device could be useful for a simple, low cost and point-of-care Cd^{2+} determination in drinking water samples in substitution of the ICP technique which is more expensive and needs trained personnel. The present device could be extended to many other fields such as diagnostics, safety and security. There are only few methods that fulfill all these requisites and for this reason aspects related to further applications of the developed system in real samples analysis including the integration of the interference removal process within an integrated LFD will be object of a future publication.

Acknowledgments

MICINN (Spain) for MAT2011-25870 and PIB2010JP-00278 projects are acknowledged. A. Lopez-Marzo thanks to Generalitat of Catalunya for the FI-2010 scholarship given. D.A.B. thanks the U. S. National Science Foundation (OISE-1253272) for partial support of this work.

Appendix A. Supporting information

Supplementary data associated with this article can be found in the online version at <http://dx.doi.org/10.1016/j.bios.2013.02.031>.

References

Abe, K., Nakamura, K., Arao, T., Sakurai, Y., Nakano, A., Suginuma, Ch., Tawaradae, K., Sasakif, K., 2011. *Journal of the Science of Food and Agriculture* 91, 1392–1397.

Adami, M., Marco, S., Nicolini, C., 2007. *Electroanalysis* 19, 1288–1294.

Afkhami, A., Madrakian, T., Sabounchei, S.J., Rezaei, M., Samiee, S., Pourshahbaz, M., 2012. *Sensors and Actuators B* 161, 542–548.

Apilux, A., Dungchai, W., Siangproh, W., Praphairaksit, N., Henry, S., Chailapakul, O., 2010. *Analytical Chemistry* 82, 1727–1732.

Aragay, G., Puig-Font, A., Cadevall, M., Merkoçi, A., 2010. *Journal of Physical Chemistry C* 114, 9049–9055.

Aragay, G., Pons, J., Merkoçi, A., 2011a. *Journal of Materials Chemistry* 21, 4326–4331.

Aragay, G., Pons, J., Merkoçi, A., 2011b. *Chemical Reviews* 111, 3433–3458.

Aragay, G., Monton, H., Pons, J., Font-Bardia, M., Merkoçi, A., 2012a. *Journal of Materials Chemistry* 22, 5978–5983.

Aragay, G., Merkoçi, A., 2012b. *Electrochimica Acta* 84, 49–61.

Bal, W., Christodoulou, J., Sadler, P.J., Tucker, A., 1998. *J. Inorg. Biochem.* 70, 33–39.

Bhagure, R.G., Mirgane, S.R., 2011. *Environmental Monitoring and Assessment* 173, 643–652.

Blake, D.A., Chakrabarti, P., Khosraviani, M., Hatcher, F.M., Westhoff, C.M., Goebel, P., Wylie, D.E., Blake, R.C., 1996. *Journal of Biological Chemistry* 271, 27677–27685.

Blake, D.A., Blake, R.C., Khosraviani, M., Pavlov, A.R., 1998. *Analytica Chimica Acta* 376, 13–19.

Chen, C.H., Wu, J., 2012. *Sensors* 12, 11684–11696.

Choi, D.H., Lee, S.K., Oh, Y.K., Bae, B.W., Lee, S.D., Kim, S., Shin, Y.B., Kim, M.G., 2010. *Biosensors & Bioelectronics* 25, 1999–2002.

Darwish, I.A., Blake, D.A., 2001. *Analytical Chemistry* 73, 1889–1895.

Darwish, I.A., Blake, D.A., 2002. *Analytical Chemistry* 74, 52–58.

Du, J., Sun, Y., Jiang, L., Cao, X., Qi, D., Yin, S., Ma, J., Boey, C.F.Y., Chen, X., 2011. *Small* 7, 1407–1411.

Fang, Z., Huang, J., Lie, P., Xiao, Z., Ouyang, C.H., Wu, Q., Wu, Y., Liu, G., Zeng, L., 2010. *Chemical Communications* 46, 9043–9045.

Gasparik, J., Vladarova, D., Capcarova, M., Smechl, P., Slamecka, J., Garaj, P., Stawarz, R., Massanyi, P., 2010. *Journal of Environmental Science and Health, Part A* 45, 818–823.

George, A., Shibu, E.S., Maliyekkal, M., Bootharaju, M.S., Pradeep, T., 2012. *Applied Materials & Interfaces* 4, 639–644.

Goux, W.J., Venkatasubramanian, P.N., 1986. *Biochemistry* 25, 84–94.

Gu, Z., Zhao, M., Sheng, Y., Bentolila, L.A., Tang, Y., 2011. *Analytical Chemistry* 83, 2324–2329.

Guelli, R., Aragay, G., Fontas, C., Antico, E., Merkoçi, A., 2008. *Analytica Chimica Acta* 627, 219–224.

Hoa, T.Y., Chiena, C.H.T., Wang, B.N., Siriraks, A., 2010. *Talanta* 82, 1478–1484.

Jang, A., Zou, Zh., Lee, K.K., Ahn, H., Bishop, P.L., 2010. *Talanta* 83, 1–8.

Jung, W., Jang, A., Bishop, P.L., Ahn, H., 2011. *Sensors and Actuators B* 155, 145–153.

Khosraviani, M., Pavlov, R.A., Flowers, C.G., Blake, D.A., 1998. *Environmental Science & Technology* 32, 137–142.

Knecht, M.R., Sethi, M., 2009. *Analytical and Bioanalytical Chemistry* 394, 33–46.

Lien, N.T.H., Huyen, L.T., Hoa, V.X., Ha, C.V., Hai, N.T., Huan, L.Q., Fort, E., Hoa, D.Q., Nhung, T.H., 2010. *Advances in Natural Sciences: Nanoscience and Nanotechnology* 1, 025009, <http://dx.doi.org/10.1088/2043-6254/1/2/025009>.

Liu, X., Xiang, J.J., Tang, Y., Zhang, X.L., Fu, Q.Q., Zou, J.H., Lin, Y.H., 2012. *Analytica Chimica Acta* 745, 99–105.

Masuoka, J., Hegenauer, J., Van Dyke, B.R., Saltman, P., 1993. *Journal of Biological Chemistry* 268, 21533–21537.

Masuoka, J., Saltman, P., 1994. *Journal of Biological Chemistry* 269, 25557–25561.

Mazumdar, D., Liu, J., Lu, G., Zhou, J., Lu, Y., 2010. *Chemical Communications* 46, 1416–1418.

McNeill, F.E., O'Meara, J.M., 1999. *Advances in X-Ray Analysis* 41, 910–916.

Ngom, B., Guo, Y., Wang, X., Bi, D., 2010. *Analytical and Bioanalytical Chemistry* 397, 1113–1135.

Parolo, C., Merkoçi, A., 2013a. *Chemical Society Reviews* 42, 450–457.

Parolo, C., Medina-Sánchez, M., de la Escosura-Muñiz, A., Merkoçi, A., 2013b. *Lab-on-Chip* 13, 386–390.

Parolo, C., de la Escosura-Muñiz, A., Merkoçi, A., 2013c. *Biosensors and Bioelectronics* 40, 412–416.

Saha, K., Agasti, S.S., Kim, C.H., Li, X., Rotello, V.M., 2012. *Chemical Review* 112, 2739–2779.

Sasaki, K., Oguma, S.H., Glass, T., Namiki, Y., Sugiyama, H., Ohmura, N., Blake, D.A., 2008. *Journal of Agriculture and Food Chemistry* 56, 7613–7616.

Schauer, C.L., Mu-Sanchen, P.R.R., Schoen, P., Ligler, F.S., 2004. *Environmental Science & Technology* 38, 4409–4413.

Senkal, B.F., Ince, M., Yavuz, E., Yaman, M., 2007. *Talanta* 72, 962–967.

Shtoyko, T., Conklin, S., Maghasi, A.T., Richardson, J.N., Piruska, A., Seliskar, C.J., Heineman, W.R., 2004. *Analytical Chemistry* 76, 1466–1473.

Tan, S.N., Ge, L., Wang, W., 2010. *Analytical Chemistry* 82, 8844–8847.

The Commission of the European Communities, 2008. *Official Journal of the European Union* 3.7 173/6–9.

The EFSA, 2009. *The EFSA Journal* 980, 1–139.

The JECFA, 2011. *Safety evaluation of certain food additives and contaminants, seventy-third report*, Geneva, pp 307–334.

The United States Pharmacopeia 30 and National Formulary 25, 2007. In: *Validation of Compendial Methods*, Rockville, Md., USA, pp 1225–1226.

The WHO, 2008. *Guidelines for drinking water quality. In: Chemical Aspects*, third ed., Geneva, pp. 145–196.

Torabia, S.F., Lu, Y., 2011. *Faraday Discussions* 149, 125–135.

Verma, S.R., Arora, J.P.S., Shankar, J.S., Dutt, D., Pal, C., 1989. *Water, Air and Soil Pollution* 4353–59.

Xia, X., Xu, Y., Zhao, X., Li, Q., 2009. *Clinical Chemistry* 55, 179–182.

Zakir, H.S.M., Brennan, J.D., 2011. *Analytical Chemistry* 83, 8772–8778.

Zhao, H.W., Xue, C.H.G., Tie-Gui, Nan, Tan, G.Y., Li, Z., Li, Q.X., Zhang, Q.C.H., Wang, B.-M., 2010. *Analytica Chimica Acta* 676, 81–86.

Zong, K., Zhang, G., Li, H., Lu, L., 2011. *Analytical Chemistry* 83, 3126–3132.

Supporting Information

High sensitive gold-nanoparticle based lateral flow immunodevice for Cd²⁺
detection in drinking waters

Adaris M. López_Marzo^{a,b}, Josefina Pons^b, Diane A. Blake^c and Arben Merkoci^{a,d}*

^aNanobioelectronics & Biosensors Group, Catalan Institute of Nanotechnology, Campus de la UAB, 08193, Bellaterra, Barcelona, Spain

^b Department of Chemistry, Universitat Autònoma de Barcelona, 08193, Bellaterra, Barcelona, Spain.

^c Department of Biochemistry and Molecular Biology, Tulane University School of Medicine, New Orleans, LA 70112 USA

^d ICREA, Barcelona, Spain.

*E-mail: arben.merkoci@icn.cat; Phone number: +34935811976; Fax number: +34935812379

Table_S1. Permissible limits of heavy metal (in ppm) in drinking water. * No specification is set at this moment.

	Ca ²⁺	Mg ²⁺	Co ²⁺	Al ³⁺	Fe ³⁺	Zn ²⁺	Mn ²⁺	Cu ²⁺	Ni ²⁺	Pb ²⁺	Hg ²⁺	Cd ²⁺
WHO		*		0.2	0.3	3	0.10	2	0.07	0.01	0.001	0.003
EPA		*		0.2	0.2	5	0.05	1.3	0.04	0.015	0.002	0.005
U.S.		*		0.05	0.3	5	0.05	1.3	0.10	0.01	0.001	0.005

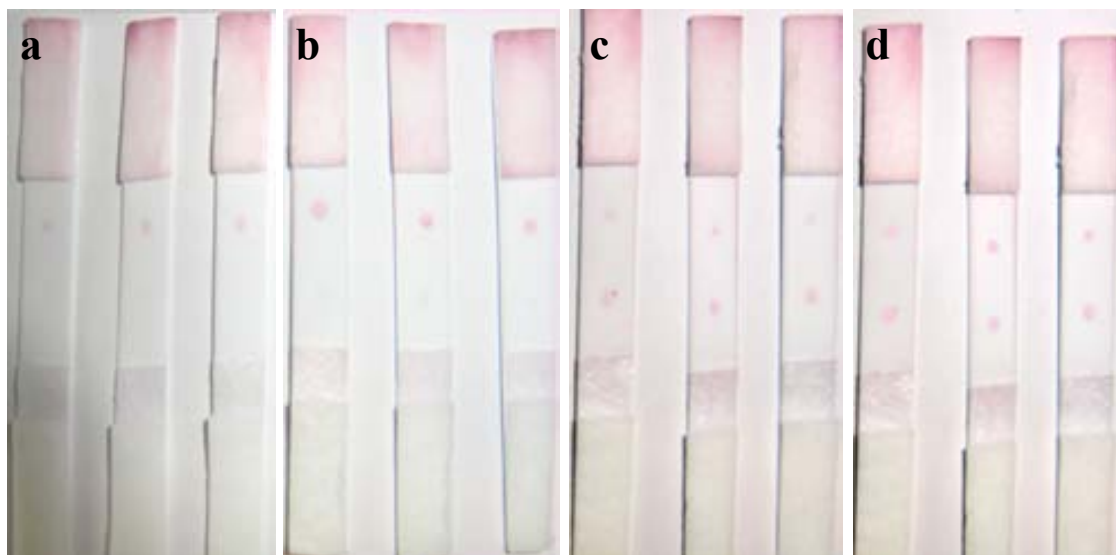
3.3 Optimization of the LFID operational conditions.

Optimization of the conjugate and antibodies concentrations in the device.

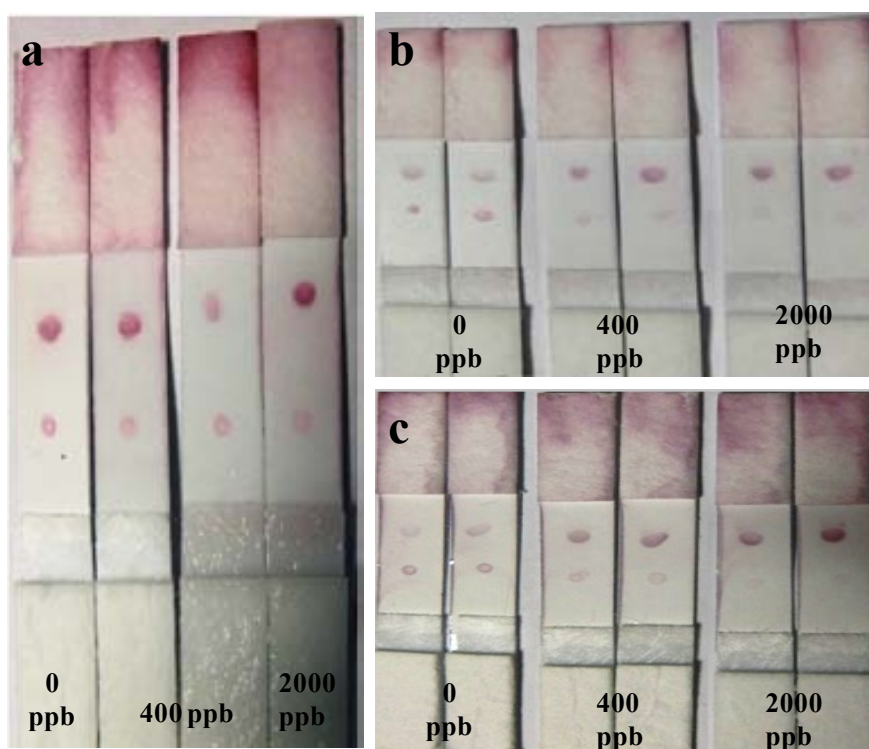
The first optimizations of the LFID were carried out by drop coating of different mAbs concentrations onto the membrane for the same conjugation strip preparation (7.5 cm conjugation strip length soaked into 300 μ L of the conjugation trip solution). By depositing 0.5 or 0.8 μ L of 0.5 mg/mL of the 2A81G5 mAb and 1 mg/mL of the anti-BSA mAb no visible (naked eye) response was observed at test line while a pink color was observed in control zone (figure_S1-a). By increasing the 2A81G5 mAb concentration on the test zone up to 1 mg/mL and keeping the use of 1 mg/mL of the anti-BSA at control zone a pale pink color is observed in the test zone while the pink color at control zone remains constant (figure_S1-b). By increasing the 2A81G5 mAb concentration up to 2 mg/mL at the test zone and continuing with the use of 1 mg/mL of the anti-BSA mAb at control zone a strong pink color is observed on the test zone but a pale pink color appeared in the control zone (figure_S1-c). Good color intensity in the test and control zone using 2 mg/mL of the both mAbs (figure_S1-d) is observed. This assay demonstrated that the recognition reaction between the 2A81G5 mAb and the Cd-EDTA contained in the Cd-EDTA-BSA-Au conjugate, and the recognition reaction between anti-BSA mAb and the BSA contained in the Cd-EDTA-BSA-Au conjugate, took place satisfactorily. In addition to that, around 2 mg/mL of the mAbs is necessary to immobilize onto the membrane by drop coating deposition to obtain good color intensity.

Standard dissolutions of Cd-EDTA (0, 400 and 2000 ppb) were analyzed immobilizing 2 mg/mL of the mAbs onto the membrane and decreasing the concentration of the conjugate onto the conjugation strip. The conjugate concentration onto the conjugation strip can be decreased by increasing the length of the conjugation strip and soaking it either in the same or in a bigger volume of the conjugation strip solution. By using a 7.5 cm conjugation strip length soaked into 300 μ L of the conjugation trip solution no color difference between the samples in the test zone

was observed (see figure_S2-a). However using 9 and 11 cm conjugation strip lengths soaked into 300 μ L of the conjugation pad solution a color difference between 0, 400 and 2000 ppb of Cd-EDTA can be detected (see figure_S2-b,c).



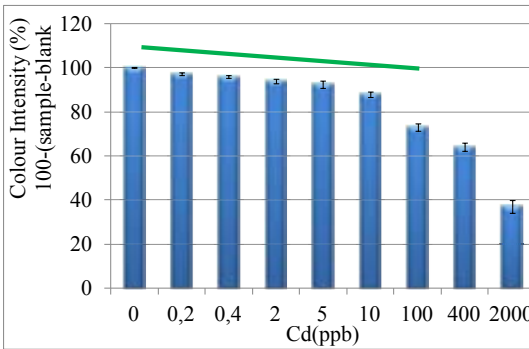
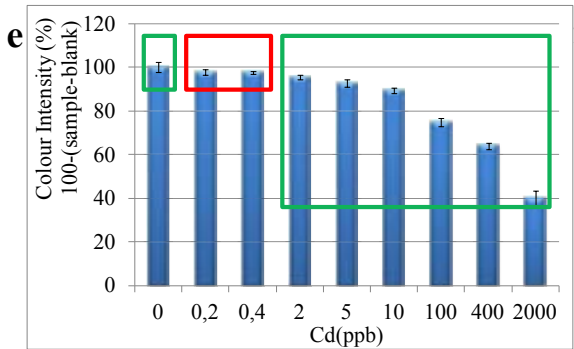
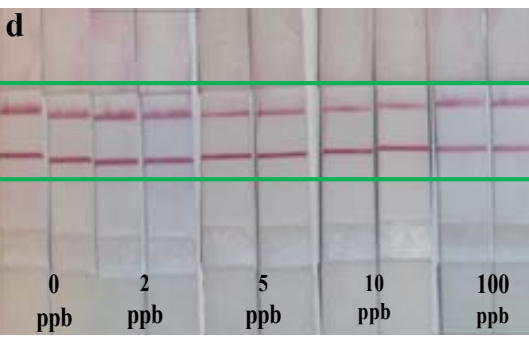
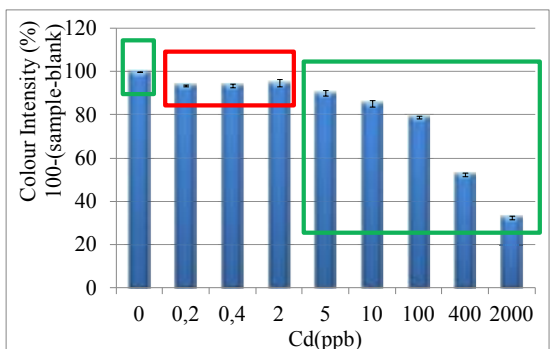
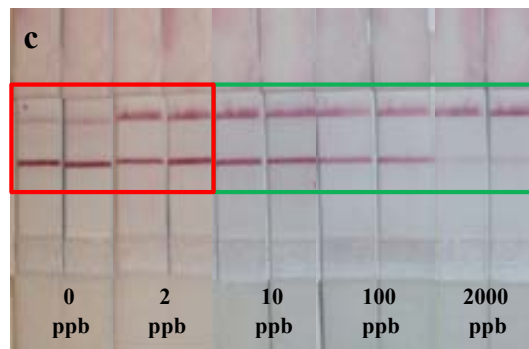
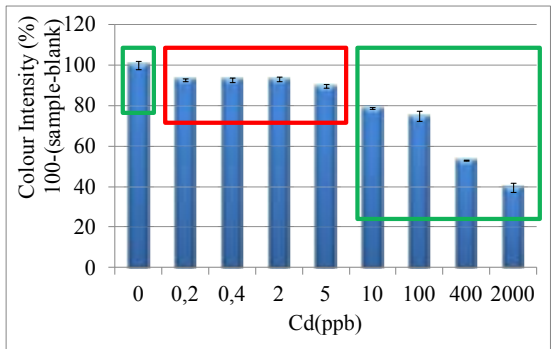
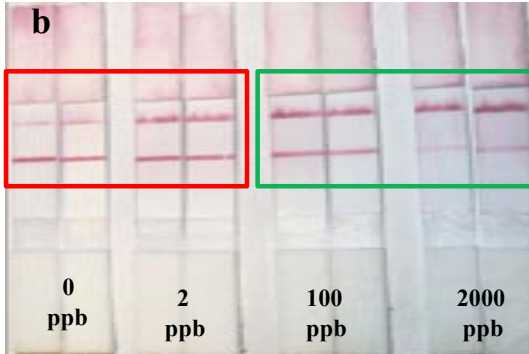
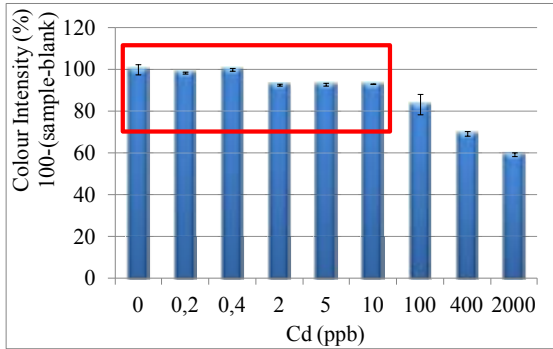
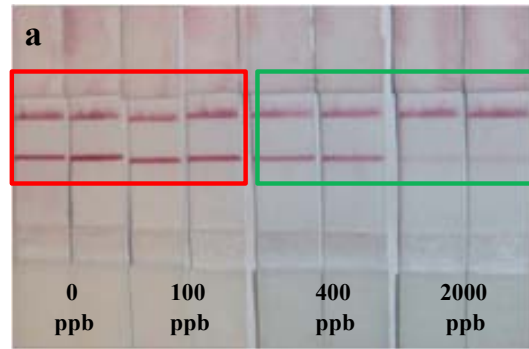
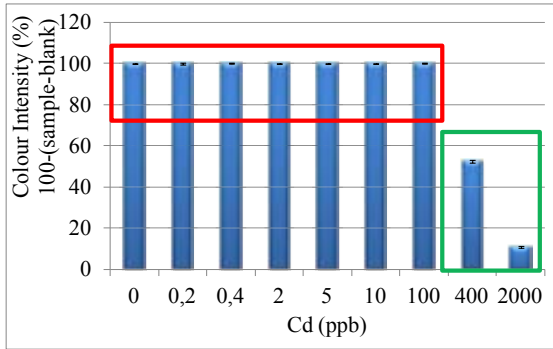
Figure_S1. Images of the initial probes of LF performed with different mAbs concentrations deposited by drop coating (0.5 μ L) in the test and control zones: (a) using 0.5 mg/mL of 2A81G5 and 1 mg/mL of anti-BSA mAbs, (b) using 1 mg/mL of 2A81G5 and 1 mg/mL of anti-BSA mAbs, (c) using 2 mg/mL of 2A81G5 and 1 mg/mL of anti-BSA mAbs and (d) using 2 mg/mL of 2A81G5 and 2 mg/mL of anti-BSA mAbs.



Figure_S2. Images of the LF used for analysis of Cd-EDTA standard dissolutions using 0.1 μL (2 mg/mL) of the mAbs deposited by drop coating onto the membrane: (a) using a conjugation strip length of 7.5 cm, (b) using a conjugation strip length of 10 cm and (c) using a conjugation strip length of 11 cm.

In general the sensibility of the device increases when decreases the mAbs and the Cd-EDTA-BSA-AuNP conjugate concentrations. Optimizations with higher precisions were made dispensing automatically the mAbs dissolutions with the dispensing equipment. Using the automatic dispensing 0.5 $\mu\text{g/mL}$ of 2A81G5 mAb are deposited in the test line and 300 μL of the Cd-EDTA-BSA-AuNP conjugate are deposited onto 10 cm long of the conjugation strip and the device is able to discriminate between 0, 400 and 2000 ppb of Cd-EDTA. This large quantity of 2A81G5 mAb collocated onto the test line provokes the development of a strong color intensity when the Cd-EDTA-BSA conjugate labeled with AuNP is bound in this site, and in consequence it doesn't allow any discoloration that Cd-EDTA concentrations below 400 ppb could provoke (figure_S3-a). Decreasing to 0.375 $\mu\text{g/mm}$ the 2A81G5 mAb concentration onto the test line and using the same concentration of the Cd-EDTA-BSA-AuNP, the color

differences between 0, 100, 400 and 2000 ppb can be observed with the device (figure_S3-b). Keeping 0.375 $\mu\text{g}/\text{mm}$ of the 2A81G5 mAb onto the test line and using a 12 cm long conjugation strip soaked inside of more diluted conjugation pad solution (350 μL), better results were obtained due to the fact that the discoloration caused by 0, 10, 100, 400 and 2000 ppb of Cd-EDTA could be observed (figure_S3-c). By keeping the same quantity of mAbs immobilized onto the membrane and increasing to 14 cm the length of the conjugation strip soaked inside of a more diluted conjugation pad solution (400 μL) a color difference between 0, 5, 10, 100, 400 and 2000 ppb of Cd-EDTA can be seen (figure_S3-d). With a 16 cm long conjugation strip soaked inside of a more diluted conjugation pad solution (500 μL) the distinguishing of the color difference between 0, 2, 5, 100, 400 and 2000 ppb by using the rapid scan equipment was possible (figure_S3-e). Finally by increasing the length of the conjugation strip up to 18 cm and soaking it inside of a more diluted conjugation pad solution (600 μL) a better resolution and color differences between 0, 0.4 and 2 ppb of Cd-EDTA via rapid scan equipment were possible to be observed (figure_S3-f).



Figure_S3. Graphs and lateral flow photos of the color intensity variation in relation to cadmium concentration during the optimization of the mAbs and the Cd-EDTA-BSA-AuNPs conjugate concentrations onto the device. (a) 0.5 $\mu\text{g}/\text{mm}$ 2A81G5 mAb, 0.32 $\mu\text{g}/\text{mm}$ anti-BSA mAb and 10 cm length of the conjugation strip soaked in 300 μL of the conjugation pad solution, (b) 0.375 $\mu\text{g}/\text{mm}$ 2A81G5 mAb, 0.32 $\mu\text{g}/\text{mm}$ anti-BSA mAb and 10 cm length of the conjugation strip soaked in 300 μL of the conjugation pad solution, (c) 0.375 $\mu\text{g}/\text{mm}$ 2A81G5 mAb, 0.32 $\mu\text{g}/\text{mm}$ anti-BSA mAb and 12 cm length of the conjugation strip soaked in 350 μL of the conjugation pad solution, (d) 0.375 $\mu\text{g}/\text{mm}$ 2A81G5 mAb, 0.4 $\mu\text{g}/\text{mm}$ anti-BSA mAb and 14 cm length of the conjugation strip soaked in 400 μL of the conjugation pad solution, (e) 0.375 $\mu\text{g}/\text{mm}$ 2A81G5 mAb, 0.4 $\mu\text{g}/\text{mm}$ anti-BSA mAb and 16 cm length of the conjugation strip soaked in 500 μL of the conjugation pad solution and (f) 0.375 $\mu\text{g}/\text{mm}$ 2A81G5 mAb, 0.4 $\mu\text{g}/\text{mm}$ anti-BSA mAb and 18 cm length of the conjugation strip soaked in 600 μL of the conjugation pad solution. The square in green indicates the change of color difference for each cadmium concentration and the red square indicates the constant color independently of cadmium concentration.

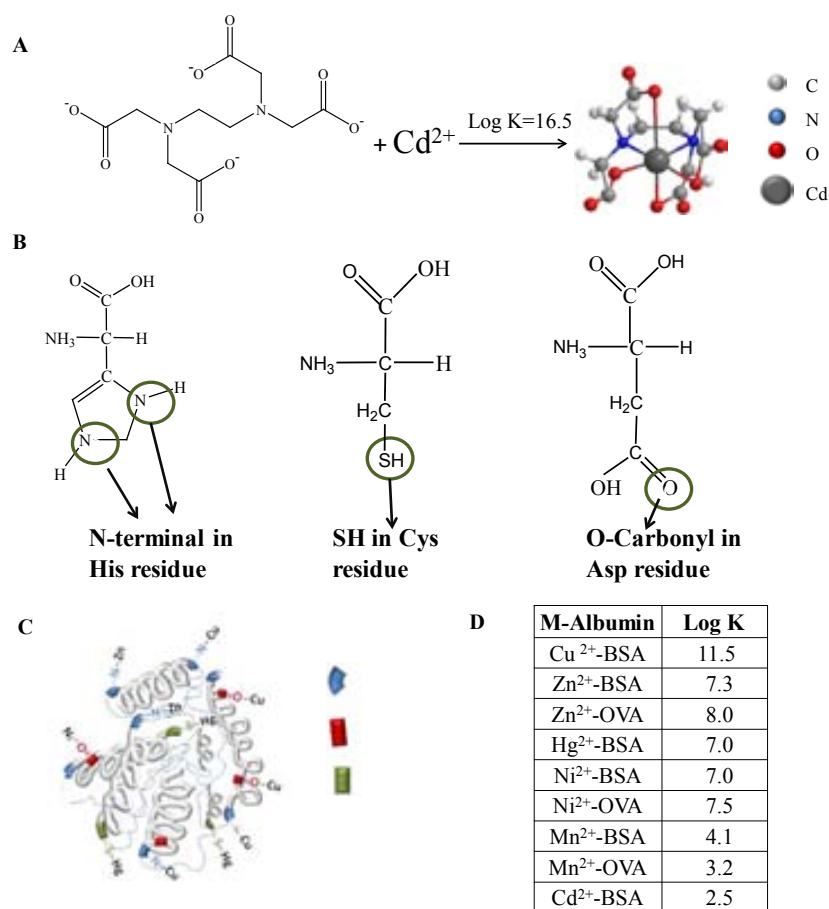
3.5 Specificity assay

Table_S2. Values of the complexes formation constants (log Kf) of the Metal-EDTA, Metal-albumin and Metal/EDTA-2A81G5 mAb at 25°C and pH ~7. The over expected metal concentrations in real samples is also given.

Formation Constants			Metal concentrations in spiked samples (ppm)
Metal-EDTA	Metal-albumin	Metal/EDTA-2A81G5 mAb	
Fe ³⁺ 25.1; Hg ²⁺ 21.5;	Cu ²⁺ 11.5; Zn ²⁺ 8.0;	Cd ²⁺ 8.3; Hg ²⁺ 7.5; Mn ²⁺ 6.4	Ca ²⁺ = Mg ²⁺ 15; Zn ²⁺ 5;
Ni ²⁺ 18.6; Cu ²⁺ 18.8;	Ni ²⁺ 7.5; Hg ²⁺ 7.0;	Ni ²⁺ 5.7; Zn ²⁺ 5.6; Co ²⁺ 5.5	Cu ²⁺ 2.5; Al ³⁺ = Fe ³⁺ 0.4;
Pb ²⁺ 18.0; Cd ²⁺ 16.5;	Pb ²⁺ 4.2; Mn ²⁺ 4.1;	Cu ²⁺ 5.3; Fe ³⁺ 4.3; Pb ²⁺ 4.1	Mn ²⁺ 0.3; Ni ²⁺ 0.02
Co ²⁺ 16.3; Zn ²⁺ 16.5;	Cd ²⁺ ~ 2.5	Mg ²⁺ 3.7; Al ³⁺ 3.1	Pb ²⁺ 0.01; Hg ²⁺ 0.05
Al ³⁺ 16.4; Mn ²⁺ 14.0;			
Ca ²⁺ 10.7; Mg ²⁺ 8.7			

The most common metal binding site in albumins.

Metals have multiples, similar and different, binding sites through the large amino acidic sequence in albumins. The N-terminal nitrogen of the imidazole ring of histidine (His) residue is the first most common binding site in BSA and OVA for the majority of these metals (Bal et al., 1998; Goux and Venkatasubramanian, 1986; Masuoka et al., 1993; Masuoka et al., 1994; Verma et al., 1989). Other binding sites are the carbonyl oxygen of aspartic acid (Asp) and sulfhydryl group of cysteine (Cys) residue (figure_S4-B) (Bal et al., 1998; Masuoka et al., 1994). For example in the case of BSA structure, it has 15 His residues, 17 sulfhydryl bridges between Cys residues and 35 Asp residues as possible metal binding sites. The figure_S4-C shows a schematic representation of the reaction metal-albumin where is shown the multiples binding sites with metals through the functional groups of the amino acid sequence in albumin.



Figure_S4. Schematic representation of the reactions, binding sites and formation complex constant involved between metal, EDTA and albumin during cadmium analysis. (A) Equation of the reaction between cadmium and EDTA. (B) Preferential metal binding sites in amino acid residues. (C) Schematic representation of metal immobilizing onto albumin. (S4-D) Metal-BSA/OVA complexes formation constant (values at table are applied at 25 °C and pH 7.4).

All-Integrated and Highly Sensitive Paper Based Device with Sample Treatment Platform for Cd²⁺ Immunodetection in Drinking/Tap Waters

Adaris M. López Marzo,^{†,‡} Josefina Pons,[‡] Diane A. Blake,[§] and Arben Merkoçi^{*,†,⊥}

[†]Nanobioelectronics and Biosensors Group, Catalan Institute of Nanotechnology, Campus de la UAB, 08193, Bellaterra, Barcelona, Spain

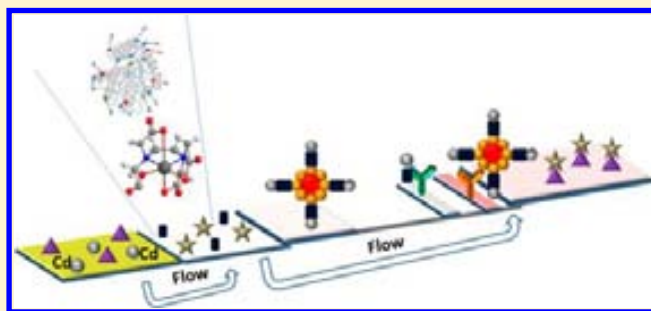
[‡]Department of Chemistry, Universitat Autònoma de Barcelona, 08193, Bellaterra, Barcelona, Spain

[§]Department of Biochemistry and Molecular Biology, Tulane University School of Medicine, New Orleans, Louisiana 70112, United States

[⊥]ICREA, Barcelona, Spain

Supporting Information

ABSTRACT: Nowadays, the development of systems, devices, or methods that integrate several process steps into one multifunctional step for clinical, environmental, or industrial purposes constitutes a challenge for many ongoing research projects. Here, we present a new integrated paper based cadmium (Cd²⁺) immunosensing system in lateral flow format, which integrates the sample treatment process with the analyte detection process. The principle of Cd²⁺ detection is based on competitive reaction between the cadmium–ethylenediaminetetraacetic acid–bovine serum albumin–gold nanoparticles (Cd–EDTA–BSA–AuNP) conjugate deposited on the conjugation pad strip and the Cd–EDTA complex formed in the analysis sample for the same binding sites of the 2A81G5 monoclonal antibody (mAb), specific to Cd–EDTA but not Cd²⁺ free, which is immobilized onto the test line. This platform operates without any sample pretreatment step for Cd²⁺ detection thanks to an extra conjugation pad that ensures Cd²⁺ complexation with EDTA and interference masking through ovalbumin (OVA). The detection and quantification limits found for the device were 0.1 and 0.4 ppb, respectively, these being the lowest limits reported up to now for metal sensors based on paper. The accuracy of the device was evaluated by addition of known quantities of Cd²⁺ to different drinking water samples and subsequent Cd²⁺ content analysis. Sample recoveries ranged from 95 to 105% and the coefficient of variation for the intermediate precision assay was less than 10%. In addition, the results obtained here were compared with those obtained with the well-established inductively coupled plasma emission spectroscopy (ICPES) and the analysis of certificate standard samples.



The release of Cd²⁺ into the environment has noticeably increased as a result of industrialization. Cd²⁺ continues to be an analyte that requires careful environmental monitoring. It can be accumulated in the human body mainly in the liver and kidneys and shows a biological half-life of greater than 10 years. Cd²⁺ exposure can affect the kidney (Cd²⁺ appears to accumulate with age, especially in the kidney leading to kidney failure) or lung function or lead to cardiovascular disease. Many studies provide evidence that low-level chronic Cd²⁺ exposure can contribute to an increased risk of cancer.^{1–9} Thus, the permissible limits for Cd²⁺ intake required by the regulatory authorities are becoming lower. For drinking water, an enforceable regulation for Cd²⁺ in terms of a maximum contaminant level of 5 and 3 ppb is permitted by EPA and WHO, respectively.¹⁰

As it is well-known, graphite furnace atomic absorption spectroscopy (GFAAES)¹¹ and inductively coupled plasma emission spectroscopy (ICPES)¹² are the standard techniques

for trace heavy metal analysis. However, these labor-intensive and time-consuming techniques require complex and expensive instruments and specialized personnel to carry out the operational procedures.^{1,2} In order to overcome all these limitations, other rapid, low-cost, simple, sensible, and friendly use techniques for heavy metals detection, such as colorimetric,^{13,14} fluorimetric,¹⁵ immunoassay,^{16–18} and potentiometric^{19,20} techniques, have been proposed. In addition, the mentioned electrochemical methods have been adapted to allow miniaturization and in-field applications.

Although all these proposed techniques for heavy metals detection are cheaper and faster than the two traditional methods above-mentioned and, in addition, are highly sensitive and selective,^{6–8,21,22} relatively costly equipment and even

Received: November 28, 2012

Accepted: February 27, 2013

Published: February 27, 2013

trained personnel are still necessary to carry out the analyses, preventing their extended application in the routine detection of Cd^{2+} or other heavy metals. In this context, analytical methods based on paper play an important role as a tool of point of care assays to monitor heavy metals in different samples.^{23–25} Paper based sensors represent cheap, portable, and simple detection tools. These are facile to be used and portable, have low cost, use low sample volume, and do not require specialized users. The analysis using paper based platforms can be carried out even by a naked-eye colorimetric change.^{26,27} Enzymes,³ DNA molecule,²⁸ metal-specific DNAzymes,^{25,29} metal-specific mAbs,^{23,24} other proteins,³⁰ and even small organic molecules^{31,32} are the recognition molecules used to date in paper based metals biosensing both in simple format as lateral flow devices (LFDs).

The development of analytical systems, devices, or methods that integrate several process steps in one multifunctional step (called also multifunctional integrated systems) for clinical, environmental, or industrial purposes constitutes a challenge for many ongoing research projects. Multifunctional integrated systems or devices permit one to manage with more rapidity and efficiency a whole process. Moreover, the use of these systems saves resources while achieving the desired result.^{32–36} Here, we present a new integrated and sensitive paper based immunosensing system for Cd^{2+} sensor that works in lateral flow format and integrates the sample treatment process with the analyte detection process. This lateral flow immunodevice (LFID) has an extra dual function conjugation pad inserted in the same platform that allows interferences masking with albumin and Cd^{2+} complex formation with ethylenediaminetetraacetic acid to obtain the Cd^{2+} complex (Cd-EDTA). As far as we know, such a LFD that integrates the sample treatment with the samples analysis in a whole platform has not yet been reported. The proposed LFID is based on the recognition of Cd-EDTA complex by the specific 2A81G5 mAb and uses the Cd-EDTA –bovine serum albumin (BSA) conjugate labeled with gold nanoparticles (AuNPs) as signal producer tool. The design of the competitive format setting Cd-EDTA-BSA-AuNP on the conjugation pad strip and the 2A81G5 mAb specific to Cd-EDTA onto the test line at the optimized concentrations permits one to reach a linear range from 0.4 to 10 ppb. The detection and quantification limits (LOD and LOQ) achieved with this LFID (of 0.1 and 0.4 ppb, respectively) are the lowest limits reached with a metal sensing paper^{23–25,28–32} and even considering a large part of the metal electrochemical methods.^{17–20} Moreover, other symbiotic platforms like lab-on-a-chip voltammetric sensor^{37,38} and paper based voltammetry^{39,40} have not yet reported such low LOD for metal sensing. The accuracy of the device was determined by evaluation of real-world samples of spiked drinking and tap water. The performance of the device was also validated through the analysis of a certified reference sample (effluent wastewater) and by using the ICPES method.

EXPERIMENTAL SECTION

The 2A81G5 mAb and the Cd-EDTA-BSA conjugate were prepared and characterized as described in a previous work.⁴¹ The albumin from bovine serum (BSA), monoclonal anti-bovine serum albumin-antibody produced in mouse (anti-BSA mAb), ethylenediaminetetraacetic acid disodium salt dihydrate ($\text{Na}_2\text{EDTA}\cdot 2\text{H}_2\text{O}$), albumin from chicken egg white (ovalbumin, OVA), Tween 20, gold(III) chloride trihydrate ($\text{HAuCl}_4\cdot 3\text{H}_2\text{O}$, 99.9% metals basis), 4-(2-hydroxyethyl)-

piperazine-1-ethanesulfonic acid ($\text{C}_8\text{H}_{18}\text{N}_2\text{O}_4\text{S}$, HEPES), and effluent wastewater (trace elements) certified reference material were purchased from Sigma Aldrich.

Cd^{2+} metallic ion solutions were prepared by diluting atomic absorption spectroscopy (AAS) grade standard solutions (1000 ppm in 2% HNO_3) (Panreac) using Milli-Q water. The Hi-Flow Plus nitrocellulose membrane (HF240), the cellulose fiber sample pad, and the glass fiber conjugate pad were acquired from Millipore. The antibodies dissolutions on lateral flow membranes were dispensed in automatic mode using an IsoFlow Dispenser. The color intensity of the lines in the strips was measured by using a COZART *RapidScan* color intensity reader. The Cd^{2+} determination by inductively coupled plasma mass spectrometry (ICPMS) was performed by using an Agilent 7500ce model device.

Preparation of Gold Nanoparticles (AuNPs). Approximately 20 nm diameter AuNPs dissolutions were synthesized according to the citrate reduction of HAuCl_4 dissolution.⁴² All glassware used in this preparation was thoroughly cleaned in aqua regia overnight and rinsed with double distilled H_2O , and the reflux was used for all the procedures. A 50 mL aqueous solution of 0.01% HAuCl_4 was heated to boiling and vigorously stirred in a 250 mL round-bottom flask; 5 mL of sodium citrate (40 mM) was added quickly to this solution. Boiling was continued for an additional 10 min. The solution was cooled to room temperature with a continuous stirring for another 15 min. The colloids were stored in dark bottles at 4 °C.

Preparation of the Integrated LFID. For a typical integrated LFID preparation, three pad preparations were necessary: the sample pad, an extra pad with reagents for sample pretreatment, and the conjugate pad impregnated with the Cd-EDTA-BSA-AuNPs . The sample pad was treated with 10 mM HEPES buffered saline (HBS): 137 mM NaCl, 3 mM KCl, and 10 mM HEPES, pH 7.4, containing 5% BSA and 0.1% Tween-20, and then dried at 60 °C for 1 h. For preparing the extra conjugation pad strip, exactly 11 cm of the conjugation strip was embedded in 375 μL of 0.05 mM EDTA and 10% OVA and dried at vacuum during 50 min. For obtaining the Cd-EDTA-BSA-Au conjugate, 900 μL of AuNPs–citrate, pH 7.4, was incubated with 100 μL (0.8 mg/mL) of the Cd-EDTA-BSA conjugate in HBS pH 7.4) during 30 min, centrifuged at 14 000g and resuspended in 600 μL of the conjugation pad solution (HBS, pH 7.4, 10% sucrose and 0.1% Tween 20). A conjugation strip with a length of 18 cm was cut and soaked in this last resuspended solution. The strip was dried at vacuum during 50 min and stored at 4 °C.

The nitrocellulose membrane and the as prepared two conjugation strips as well as the sample and absorption pads were assembled in the same order onto a plastic backing card. At a distance of 0.5 cm from the top of the membrane, a band of anti-BSA mAb was dispensed as control line at 0.4 $\mu\text{g}/\text{mm}$, and analogously 2A81G5 mAb, that recognizes the Cd-EDTA complex, was applied as detection line at 0.375 $\mu\text{g}/\text{mm}$ at a distance of 1.0 cm from membrane top. The lateral flow strips were cut at 0.7 cm of width. For the analysis, 150 μL of sample was deposited on the sample pad and were washed with 150 μL of 10 mM of HBS, pH 7.4, with 0.1% Tween 20 (running buffer).

Linearity and Limits of Detection and Quantification. For evaluating the linearity of the device, Cd^{2+} standard dissolutions were prepared in HBS, pH 7.4, and Na_2EDTA (14 mM) in the concentration range of 0.02 to 2000 ppb by diluting an AAS grade Cd^{2+} ion standard dissolution (1000

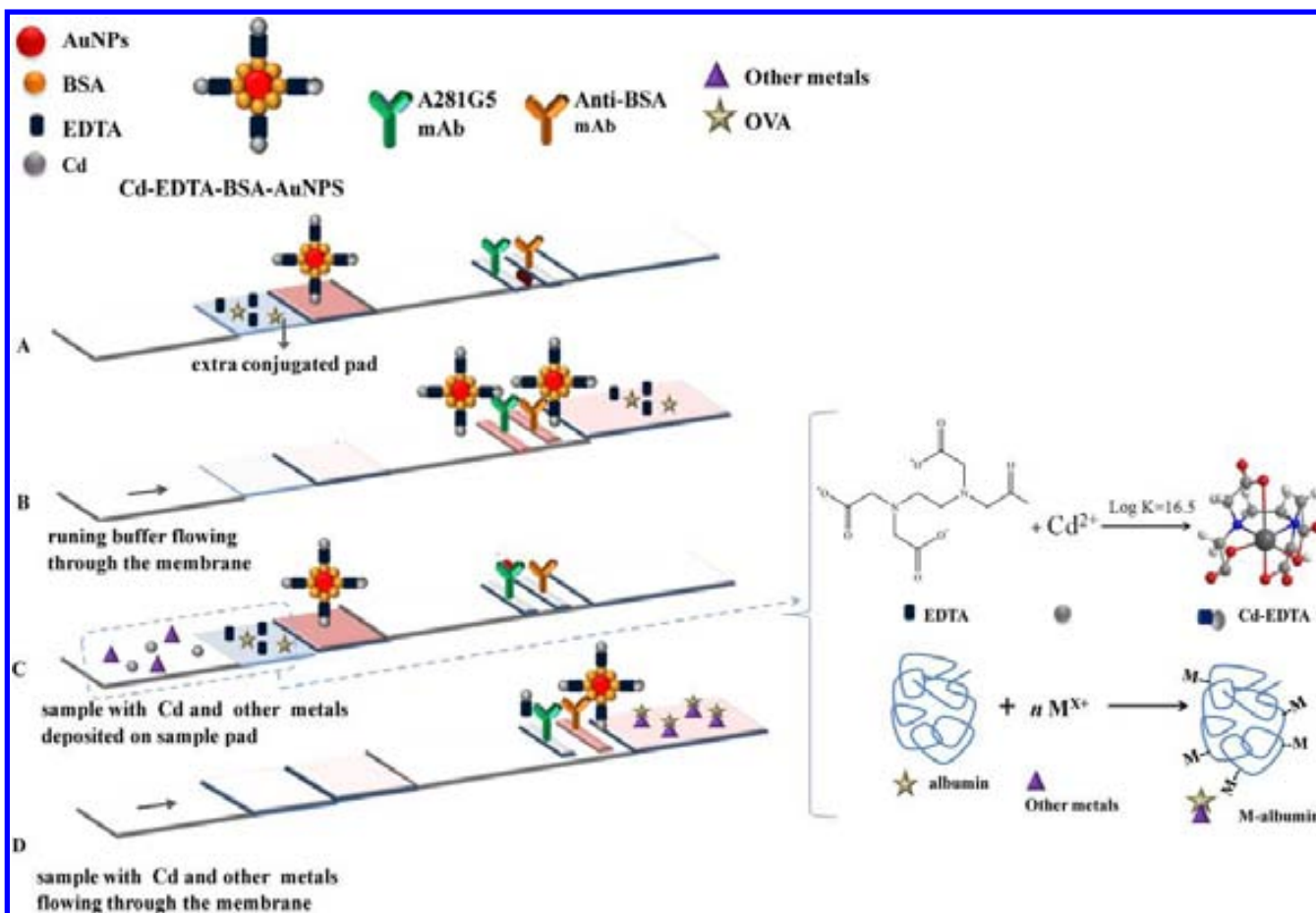


Figure 1. Scheme of the configuration and measurement principle of the integrated Cd²⁺ biosensor device used in the accuracy and precision assays. (A) Components deposited in each part, (B) the principle of visual detection analyzing samples without Cd²⁺, (C) deposition on sample pad of real water samples with Cd²⁺ and other metallic ions, and (D) the principle of visual detection analyzing samples with Cd²⁺ and other metallic ions.

ppm in 2% nitric acid). 150 μ L of each Cd²⁺ dissolution was deposited onto the sample pad, and the analysis was left to run until the mobile phase migrated toward the absorption pad. The test and control zones were visually evaluated within 10 min. For quantitative measurement, the dry strip was inserted into the *RapidScan* color intensity portable reader. The measured value of the color intensity on the test and control lines of the strip remains stable for more than two months, giving statistically the same measured value. Samples with high Cd²⁺ contents give high response values in the test line of the *RapidScan* reader, which corresponds by visual inspection to the lower color intensity while samples with low Cd²⁺ contents give low response values in the test line of the *RapidScan* reader, which corresponds by visual inspection to the higher color intensity. The calibration curve was obtained by plotting the difference of the color intensity between the Cd²⁺ standard dissolutions and the blank. The values of the experimental points for the calibration curve correspond to the mean of values obtained during a five day period, making each day three independent replies by each concentration.

The LOQ was assumed as the lowest amount of Cd²⁺ which can be quantitatively determined with suitable precision and accuracy, while the LOD was calculated as three times the standard deviation of the 7-fold analysis of a blank. A more accurate determination of the LOD was carried out with the calibration curve and using the eq 1:

$$\text{LOD} = \frac{3 \times \text{Sbl}}{b} \times \frac{1}{\sqrt{n}} \quad (1)$$

where Sbl is the standard deviation of the blank, n is the number of measurements, and b is the slope of the calibration curve.⁴³

Accuracy and Precision Assays. For the accuracy and precision studies, different water samples (two different bottled drinking waters and two different tap waters) from the Barcelona area were spiked with 0.4, 2, 5, 10, and 50 ppb of Cd²⁺. For Cd²⁺ analysis, the samples were directly deposited, without any preliminary treatment, onto the sample pad of the device that contains another conjugation pad strip with the adequate concentration of EDTA and OVA previously optimized (results not shown here). Each sample was subsequently analyzed in quadruplicate for Cd²⁺ content. The analytical recovery was calculated as the ratio, expressed as percentage, between the Cd²⁺ concentration found with the device and the theoretical value (eq 2).

For comparison purposes, ICPES was also carried out for one of the spiked bottled drinking and tap water samples. In addition, the analysis of a wastewater certified reference material was also carried out to complete the validation of the new Cd²⁺ sensing device. The corresponding variance analysis (ANOVA) and Student's test were used in the statistical comparisons.⁴⁴

For the precision of the device, the repeatability and the intermediate precision were evaluated. The repeatability of the device at different concentrations was estimated as the standard deviation or the coefficient of variation obtained in the analysis (six repeated measurements of the same sample) using the same piece device by the same operator. The intermediate precision of the device at different concentrations was calculated as the standard deviation or the coefficient of variation obtained in the analysis of different samples (for drinking and tap waters) using different devices by the same operator.⁴³

$$\frac{\text{found concentration}}{\text{added concentration}} \times 100\% = \text{recovery (\%)} \quad (2)$$

RESULTS AND DISCUSSION

Design and Operation Principle of the Integrated LFID. With the aim to analyze real water samples without previous treatment, a novel integrated LFID platform was fabricated. Figure 1A presents a scheme of the developed integrated platform. The sample treatment pad inserted between the sample and the Cd–EDTA–BSA–Au conjugate pads contains an adequate concentration of EDTA and OVA (previously optimized results not shown here) that ensures, when the sample containing Cd²⁺ and other metallic ions is deposited in the sample pad and reaches this zone, complexation reactions forming Cd–EDTA and interfering metal–OVA take place. The Cd²⁺ detection principle is based on the competition between the Cd–EDTA complex (formed before by reaction of Cd²⁺ with EDTA in the first conjugation pad or sample treatment pad) with Cd–EDTA–BSA–AuNP conjugate, deposited onto the second conjugation pad, for the same binding sites of the immobilized 2A81G5 mAb in the test line. For controlling purposes in the control line, an anti-BSA mAb is immobilized to capture the excess of Cd–EDTA–BSA–AuNP conjugate; in consequence, a red band always appears at the control line (which color is provided by AuNPs in the Cd–EDTA–BSA–AuNP conjugate) when the fluid crosses the membrane (see Figure 1B,D). The concentration of Cd²⁺ in a sample is quantified by the ability of Cd–EDTA complex to compete with the Cd–EDTA–BSA–AuNPs conjugate by the same binding sites in the 2A81G5 mAb immobilized onto the membrane, producing a decrease of the color intensity in the test line with respect to the maximum color intensity that is developed when all the labeled conjugate is bound onto this zone (Figure 1D). In this way, when there is no Cd²⁺ in the sample and just running buffer flows through the membrane, the maximal red color intensity is developed in the test line (Figure 1B). On the other hand, when increasing concentrations of Cd²⁺ are present in the samples, the color intensity in the test line decreases (Figure 1C,D). The color development is inversely proportional to the increasing concentration of Cd²⁺ in the original sample.

Several optimizations were necessary to carry out the development of the integrated device. Thus, the Cd–EDTA–BSA–Au conjugate and the mAbs concentrations onto the corresponding zones in the nitrocellulose membrane were previously optimized in a conventional LFID (results not shown). Calibration curves with the Cd²⁺ patterns dissolutions were obtained using the conventional and integrated LFIDs. Moreover, specificity studies to evaluate potential metals interferences as well as the masking and reduction of these

interferences were realized using the conventional LFID version with previously determined sample pretreatment.

Linearity and Limits of Detection and Quantification. The image in Figure 2A represents a typical Cd²⁺ analysis with

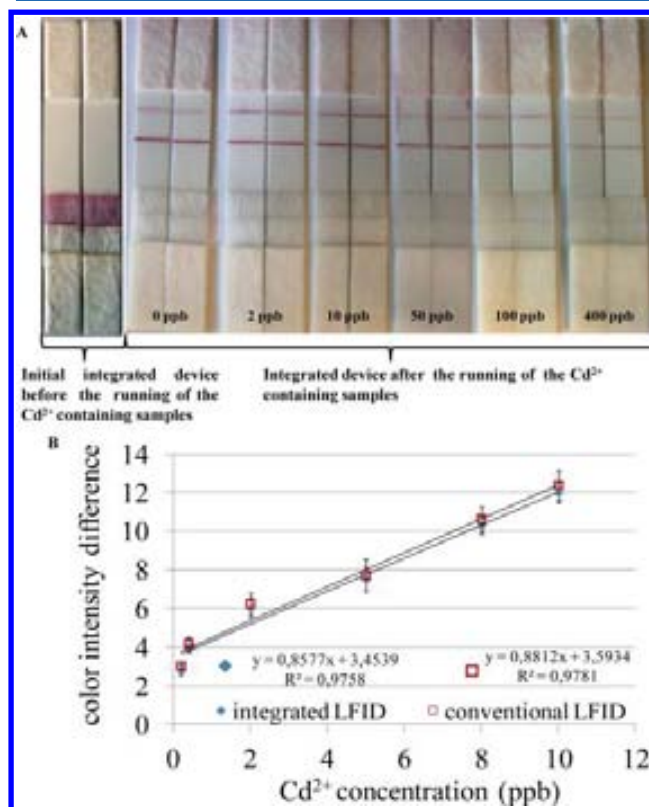


Figure 2. (A) Typical image before and after Cd²⁺ detection in tap or drinking waters by using the integrated LFID. A series of dilutions (0.4–400 ppb) of Cd²⁺ standard atomic absorption grade was made in HBS with 14 mM EDTA. (B) Lineal range of the calibration curves obtained for conventional and integrated LFIDs during Cd–EDTA analysis.

the integrated LFID. The color intensity in the test line is related to Cd²⁺ concentration in the sample. Figure 2B shows the calibration curves obtained using both the conventional and the integrated LFIDs by measuring the intensity color at test line with the *RapidScan* reader and correcting these values with the signal of the blank for different Cd²⁺ concentrations. The developed LFID has a linearity range from 0.4 to 10 ppb and a whole response range from 0.4 to 400 ppb describing an exponential decay. Although the difference in color intensities between 0, 0.4, 2, and 5 ppb were not detectable with the naked eye, they could be perfectly discriminated by using the color reader equipment.

The LOD of the device was 0.1 ppb with 0.4 ppb, the LOQ, corresponding to the lowest Cd²⁺ quantity that can be quantified with acceptable accuracy and precision. To the best of our knowledge, both the LOD of 0.1 ppb and the LOQ of 0.4 ppb are the lowest values obtained using metal sensing papers^{23–25,28–32} or even by most of the Cd²⁺ electrochemical analysis methods^{9,16–21} reported so far (Table_S1, Supporting Information).

Accuracy and Precision Assays. Table 1 shows the mean Cd²⁺ recoveries when Cd²⁺ spiked samples of drinking and tap waters were directly deposited on the sample pad. Around 95% and 105% of Cd²⁺ recovery were obtained without showing the

Table 1. Cd²⁺ Recoveries (%) at Different Concentrations for Each Water Sample Analyzed^a

waters samples	Cd ²⁺ recoveries (%)				
	0.4 ppb Cd ²⁺	2 ppb Cd ²⁺	5 ppb Cd ²⁺	10 ppb Cd ²⁺	50 ppb Cd ²⁺
drinking water 1	103.35 ± 3.12	104.83 ± 3.11	101.25 ± 0.56	102.98 ± 0.11	101.11 ± 0.32
drinking water 2	104.53 ± 1.23	95.63 ± 2.36	98.54 ± 0.73	101.33 ± 1.75	98.82 ± 2.50
tap water 1	105.23 ± 2.03	99.83 ± 2.05	103.50 ± 2.15	102.47 ± 0.71	95.63 ± 2.75
tap water 2	104.80 ± 1.95	105.03 ± 1.28	96.83 ± 2.67	98.94 ± 1.89	95.79 ± 1.25
wastewater reference pattern			105.02 ± 0.85		
variance analysis			$F_{\text{calculated}} = 0.73 < F_{0.95}^{4,15} = 3.06$		
recoveries total mean			$\bar{X} = 101.02$		
t student			$t_{\text{calculated}} = 1.36 < t_{(0.05;19)} = 1.73$		

^aThe number of analyzed replicate is 4 ($n = 4$).

total recoveries mean significant differences with 100% as evaluated by the Student's test. The obtained results indicate that the device is able to determine with almost 100% accuracy Cd²⁺ in drinking and tap waters samples at concentration levels between 0.4 and 50 ppb. These results show that when Cd²⁺ containing samples are deposited onto the sample pad and afterward flow through the first conjugation pad, that contains EDTA and OVA, all Cd²⁺ (from 0.4 to 50 ppb) can be rapidly complexed with the EDTA forming Cd–EDTA complex, able to be immunodetected in the LFD, and that the potential metal interferences present in these waters can be removed with OVA. In tap and drinking waters, Ca²⁺ and Mg²⁺ followed by Cu²⁺, Zn²⁺, Al³⁺, and Fe³⁺ are the potential majority metallic ions. Table_S2, Supporting Information, displays that the Ca²⁺ and Mg²⁺ containing samples reported for these analyzed water samples are from 30 to 80 and from 8 to 15 ppm, respectively. While considering the permissible metal limits in drinking water (Table_S3, Supporting Information), a total metal concentration of around 3 ppm for Cu²⁺, Zn²⁺, Fe³⁺, and Al³⁺ can be estimated for these analyzed samples. Specificity results demonstrate that the interference in the analysis of 10 ppb Cd²⁺ that comes from 25 ppm of Ca²⁺ or Al³⁺ is low and inferior to 1 and 3%, respectively (Figure_S1, Supporting Information). In the same way, the interference found for 25 ppm of the Fe³⁺ and Mg²⁺ ions in the analysis of 10 ppb Cd²⁺ reaches about 9% and 13%, respectively, due to the fact that EDTA complexes with Ca²⁺, Mg²⁺, Al³⁺, and Fe³⁺ show a very low affinity with the 2A81G5 mAb; see Table_S4, Supporting Information. Mg²⁺, a major metal in drinking and tap waters, represents a potential interference (25 ppm of Mg²⁺ shows a 13% interference in Cd²⁺ analysis); however, the interference can be reduced to 3% with OVA addition (Figure_S1, Supporting Information). Other important potential interferences are Cu²⁺ and Zn²⁺. Five ppm of Cu²⁺ and Zn²⁺ interfere in about 8% in the 10 ppb Cd²⁺ analysis. This interference value was also almost completely removed using OVA (Figure_S1, Supporting Information). Other possible metal interferences like Hg²⁺, Mn²⁺, and Ni²⁺ whose permissible concentration limits in drinking waters are similar with Cd²⁺ (Table_S3, Supporting Information) do not affect the response due to the fact that at this concentration the 2A81G5 mAb will preferably bind with Cd²⁺. The result labeled with a green box in Figure_S1, Supporting Information, displays the reduction of the interferences below 5% in the 10 ppb Cd²⁺ analysis when 11 metals ions are present in concentrations over those expected in drinking water by using the optimized EDTA and OVA concentrations. In summary, the total value of Cd²⁺ recoveries of around 100% suggests that the possible metal interferences explained above remain blocked due to binding with the albumin while the Cd²⁺

analyte is complexed with EDTA, followed by its determination in the integrated biosensor device.

During analysis of a certified effluent wastewater sample, whose metallic composition is shown in Table_S5 (Supporting Information), the efficiency of the pretreatment pad, which added EDTA at a concentration that preferentially complexed Cd²⁺ ions and OVA at a concentration that masked other interfering metals, was once again demonstrated. A 105% recovery for the 5 ppb Cd²⁺ containing sample in the presence of other possible metal ion interferences indicates that the final device, with EDTA and OVA deposited in the first conjugation pad, detects Cd²⁺ with high accuracy.

The comparison of the slope and the intercept of the line of adjust (see Figure 3), calculated by plotting the found

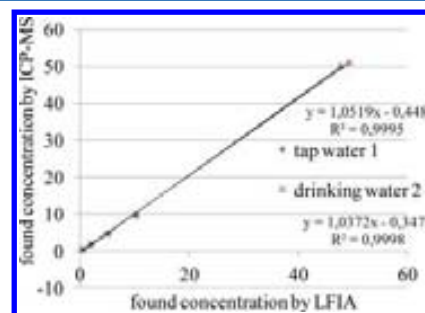


Figure 3. Graph of the found concentrations by the integrated LFID and the ICPMS methods. Lines and equations obtained by adjusting the plot of the experimental points are shown.

concentrations via the new integrated LFID and ICPMS method, with 1 and 0 values, respectively, demonstrated that there is not a significant difference with these theoretical values over the studied concentration range. Therefore, the Cd²⁺ determination by using the LFIA device is statistically equal to the one using ICPMS, and the device can be used for Cd²⁺ analysis instead of the traditional and expensive ICPMS or AAS equipment that in addition requires highly qualified users.

The standard deviation and coefficient of variation values for the studied concentrations were lower than 2% and 5%, respectively. The intermediate precision of the device was found between 10% and 5.8% in the range of 5 to 50 ppb Cd²⁺ (Table_S_6, Supporting Information).

CONCLUSION

A novel and highly sensitive lateral flow device with integrated sample treatment for Cd²⁺ detection in drinking and tap water samples using the Cd–EDTA–BSA conjugate labeled with AuNPs as signal producer tool has been successfully developed.

The insertion of an extra dual function pad strip between the sample and the conjugated pad is performed. It has a double function, to mask interferences using OVA and to prepare the sample for Cd²⁺ analysis using EDTA. This original integrated device allowed the direct analysis of real samples without any pretreatment. The device presented here is based on a competitive format setting Cd–EDTA–BSA–AuNP on the conjugation pad strip and the 2A81G5 mAb specific to Cd–EDTA onto the test line at the optimized concentrations. The device reaches a linear working range from 0.4 to 10 ppb, with 0.1 and 0.4 ppb as the LOD and LOQ, respectively. These metal detection and quantification levels are much lower than those previously reported for metal biosensors based on paper and even for many electrochemical methods in Cd²⁺ detection.

The results of the accuracy assays show that the device is able to determine Cd²⁺ in drinking and tap waters with almost 100% accuracy. The repeatability and interassay precision variation coefficient for these determinations are around 5% and 10% even for the lowest concentration (0.4 ppb).

This work represents a suitable and available alternative for Cd²⁺ quantification in drinking and tap waters, able to detect heavy metals 50 times below the maximum allowable limit. This integrated platform is easily built, cheap, portable, and simple to manage even by nonskilled persons, which makes it very useful for Cd²⁺ analysis in point of care diagnostics or where rapid contamination monitoring is very necessary or in field analysis in remote locations with limited facilities. The extended application of the device developed here for analyzing Cd²⁺ in a large variety of samples like seawater, serum, etc. could be easily implemented. In addition, it constitutes an accurate and precise tool that can substitute even traditional and expensive methods such as AAS and ICPMS well-known for their high analytical performance in Cd²⁺ analysis. We expect that such sensors could be particularly useful in large scale routine screening of drinking water samples or industrial process streams in developing countries, where the heavy metal concentrations are usually relatively high.

■ ASSOCIATED CONTENT

📄 Supporting Information

Informative tables with the quality of the analyzed waters, the composition of the certified reference pattern used, and results of the precision assays and part of the specificity assays. This material is available free of charge via the Internet at <http://pubs.acs.org>.

■ AUTHOR INFORMATION

Corresponding Author

*Tel: +34 935868014. Fax: +34 935868020. E-mail: arben.merkoci@icn.cat. Internet: <http://www.icn.cat>, www.nanobiosensors.org.

Notes

The authors declare no competing financial interest.

■ ACKNOWLEDGMENTS

MICINN (Spain) for MAT2011-25870 and PIB2010JP-00278 projects are acknowledged. A.M.L.M. thanks the Generalitat of Catalunya for the FI-2010 scholarship. D.A.B. thanks the U.S. National Science Foundation (OISE-1253272) for partial support of this work.

■ REFERENCES

- (1) Aragay, G.; Pons, J.; Merkoci, A. *Chem. Rev.* **2011**, *111*, 3433.
- (2) Aragay, G.; Merkoçi, A. *Electrochim. Acta* **2012**, *84*, 49.
- (3) Zakir, H. S. M.; Brennan, J. D. *Anal. Chem.* **2011**, *83*, 8772.
- (4) Schauer, C. L.; Mu-Sanchen, P. R. R.; Schoen, P.; Ligler, F. S. *Environ. Sci. Technol.* **2004**, *38*, 4409.
- (5) Bhagure, R. G.; Mirgane, S. R. *Environ. Monit. Assess.* **2011**, *173*, 643.
- (6) Khosraviani, M.; Pavlov, R. A.; Flowers, C. G.; Blake, D. A. *Environ. Sci. Technol.* **1998**, *32*, 137.
- (7) Darwish, I. A.; Blake, D. A. *Anal. Chem.* **2001**, *73*, 1889.
- (8) Darwish, I. A.; Blake, D. A. *Anal. Chem.* **2002**, *74*, 52.
- (9) Guell, R.; Aragay, G.; Fontas, C.; Antico, E.; Merkoci, A. *Anal. Chim. Acta* **2008**, *627*, 219.
- (10) WHO *Guidelines for Drinking Water Quality*, 3rd ed.; WHO: Geneva, 2004; Vol. 1, p 515.
- (11) Gasparik, J.; Vladarova, D.; Capcarova, M.; Smehyl, P.; Slamecka, J.; Garaj, P.; Stawarz, R.; Massanyi, P. *J. Environ. Sci. Health A* **2010**, *45*, 818.
- (12) Hoa, T.-Y.; Chiena, Ch.-T.; Wang, B.-N.; Siriraks, A. *Talanta* **2010**, *82*, 1478.
- (13) Knecht, M. R.; Sethi, M. *Anal. Bioanal. Chem.* **2009**, *394*, 33.
- (14) Du, J.; Sun, Y.; Jiang, L.; Cao, X.; Qi, D.; Yin, S.; Ma, J.; Boey, C. F. Y.; Chen, X. *Small* **2011**, *7*, 1407.
- (15) Zong, Ch.; Ai, K.; Zhang, G.; Li, H.; Lu, L. *Anal. Chem.* **2011**, *83*, 3126.
- (16) Afkhami, A.; Madrakian, T.; Sabounchei, S. J.; Rezaei, M.; Samiee, S.; Pourshahbaz, M. *Sens. Actuators, B* **2012**, *161*, 542.
- (17) Aragay, G.; Puig-Font, A.; Cadevall, M.; Merkoci, A. *J. Phys. Chem. C* **2010**, *114*, 9049.
- (18) Shtoyko, T.; Conklin, S.; Maghasi, A. T.; Richardson, J. N.; Piruska, A.; Seliskar, C. J.; Heineman, W. R. *Anal. Chem.* **2004**, *76*, 1466.
- (19) Aragay, G.; Pons, J.; Merkoci, A. *J. Mater. Chem.* **2011**, *21*, 4326.
- (20) Adami, M.; Marco, S.; Nicolini, C. *Electroanalysis* **2007**, *19*, 128816.
- (21) Zhao, H.-W.; Xue, C.-G.; Nan, T.-G.; Tan, G.-Y.; Li, Z.; Li, Q.-X.; Zhang, Q.-C.; Wang, B.-M. *Anal. Chim. Acta* **2010**, *676*, 81.
- (22) Blake, D. A.; Blake, R. C., II; Khosraviani, M.; Pavlov, A. R. *Anal. Chim. Acta* **1998**, *376*, 13.
- (23) Abe, K.; Nakamura, K.; Arao, T.; Sakurai, Y.; Nakano, A.; Suginuma, Ch.; Tawaradae, K.; Sasakif, K. *J. Sci. Food Agric.* **2011**, *91*, 1392.
- (24) Liu, X.; Xiang, J.-J.; Tang, Y.; Zhang, X.-L.; Fu, Q.-Q.; Zou, J.-H.; Lin, Y.-H. *Anal. Chim. Acta* **2012**, *745*, 99.
- (25) Mazumdar, D.; Liu, J.; Lu, G.; Zhou, J.; Lu, Y. *Chem. Commun.* **2010**, *46*, 1416.
- (26) Parolo, C.; Merkoçi, A. *Chem. Soc. Rev.* **2013**, *42*, 450.
- (27) Ngom, B.; Guo, Y.; Wang, X.; Bi, D. *Anal. Bioanal. Chem.* **2010**, *397*, 1113.
- (28) Torabia, S.-F.; Lu, Y. *Faraday Discuss.* **2011**, *149*, 125.
- (29) Fang, Z.; Huang, J.; Lie, P.; Xiao, Z.; Ouyang, C.; Wu, Q.; Wu, Y.; Liu, G.; Zeng, L. *Chem. Commun.* **2010**, *46*, 9043.
- (30) Gu, Z.; Zhao, M.; Sheng, Y.; Bentolila, L. A.; Tang, Y. *Anal. Chem.* **2011**, *83*, 2324.
- (31) Aragay, G.; Monton, H.; Pons, J.; Font-Bardia, M.; Merkoci, A. *J. Mater. Chem.* **2012**, *22*, S978.
- (32) George, A.; Shibu, E. S.; Maliyekkal, S. M.; Bootharaju, M. S.; Pradeep, T. *Appl. Mater. Interfaces* **2012**, *4*, 639.
- (33) Zhang, J.; Laiwalla, F.; Kim, J. A.; Urabe, H.; Wagenen, R. V.; Song, Y.-K.; Connors, B. W.; Zhang, F.; Deisseroth, K.; Nurmikko, A. V. *J. Neural Eng.* **2009**, *6*, 055007.
- (34) Adami, A.; Ress, C.; Collini, C.; Pedrotti, S.; Lorenzelli, L. *Biosens. Bioelectron.* **2013**, *40*, 315.
- (35) Zhou, M.; Zhou, N.; Kuralay, F.; Windmiller, J. R.; Parkhomovsky, S.; Valdés-Ramírez, G.; Katz, E.; Wang, J. *Angew. Chem., Int. Ed.* **2012**, *51*, 2686.
- (36) Choi, D. H.; Lee, S. K.; Oh, Y. K.; Bae, B. W.; Lee, S. D.; Kim, S.; Shin, Y.-B.; Kim, M.-G. *Biosens. Bioelectron.* **2010**, *25*, 1999.

- (37) Jang, A.; Zou, Z.; Lee, K. K.; Ahn, C. H.; Bishop, P. L. *Talanta* **2010**, *83*, 1.
- (38) Jung, W.; Jang, A.; Bishop, P. L.; Ahn, C. H. *Sens. Actuators, B* **2011**, *155*, 145.
- (39) Apilux, A.; Dungchai, W.; Siangproh, W.; Praphairaksit, N.; Henry, Ch. S.; Chailapakul, O. *Anal. Chem.* **2010**, *82*, 1727.
- (40) Tan, S. N.; Ge, L.; Wang, W. *Anal. Chem.* **2010**, *82*, 8844.
- (41) Blake, D. A.; Chakrabarti, P.; Khosraviani, M.; Hatcher, F. M.; Westhoff, C. M.; Goebel, P.; Wylie, D. E.; Blake, R. C., II *J. Biol. Chem.* **1996**, *271*, 27677.
- (42) Saha, K.; Agasti, S. S.; Kim, Ch.; Li, X.; Rotello, V. M. *Chem. Rev.* **2012**, *112*, 2739.
- (43) *United States Pharmacopeia 30, National Formulary 25. Validation of Compendial methods*; The United States Pharmacopeial Convention: Rockville, Md., USA, 2007; General Chapter 1225.
- (44) Delgado de la Torre, R., Ed. *Iniciación a la Probabilidad y la Estadística*; Universitat Autònoma de Barcelona: Barcelona, Spain, 2004; p 115.

All-integrated and highly sensitive paper-based device with sample treatment platform for Cd²⁺ immunodetection in drinking/tap waters

Adaris M. López_Marzo^{a,b}, Josefina Pons^b, Diane A. Blake^c and Arben Merkoci^{a,d}*

^aNanobioelectronics & Biosensors Group, Catalan Institute of Nanotechnology, Campus de la UAB, 08193, Bellaterra, Barcelona, Spain

^b Department of Chemistry, Universitat Autònoma de Barcelona, 08193, Bellaterra, Barcelona, Spain.

^c Department of Biochemistry and Molecular Biology, Tulane University School of Medicine,

New Orleans, LA 70112 USA

^d ICREA, Barcelona, Spain.

Analytical performance data of reported paper based sensors					
Metal	Linear range (ppb)	LOD (ppb)	LOQ (ppb)	samples	Reference
Cd ²⁺	0.4-10	0.1	0.4	spiked water	This work
Cr ³⁺ , Cr ⁶⁺	5-80	5	5	serum, waters	24
Cu ²⁺	50-500	50	> 50	spiked water	32
Cd ²⁺	10-100	10	> 10	rice	23
	5-50	5	> 5	wheat grain	
	2.5-25	2.5	> 2.5	eggplant	
Hg ²⁺	10-60	10	> 10	spiked solutions	30
	120-480				
Hg ²⁺ ; Ag ¹⁺ Cu ²⁺ ; Cd ²⁺ Pb ²⁺ ; Cr ⁶⁺ Ni ²⁺	-	1; 2 20; 20 140; 150 230	>1; >2 >20; >20 >140; >150 >230	spiked solutions and environmental waters	3
Hg ²⁺	10-100	1	10	spiked solutions	28
Cu ²⁺	-	0.63	-	spiked solutions	29
Pb ²⁺	-	10	-	paints	25

Table_S1. Summary of the reported performances for metal sensing using paper based platforms.

	Metals contents (ppm)			
	Ca ²⁺	Mg ²⁺	Na ⁺	K ⁺
Waters				
Drinking water 1	35.5	8.6	11.9	-
Drinking water 2	82.3	14.9	0.7	1.29
Tap water 1	70*	130*	-	-
Tap water 2	28*	115*	-	-

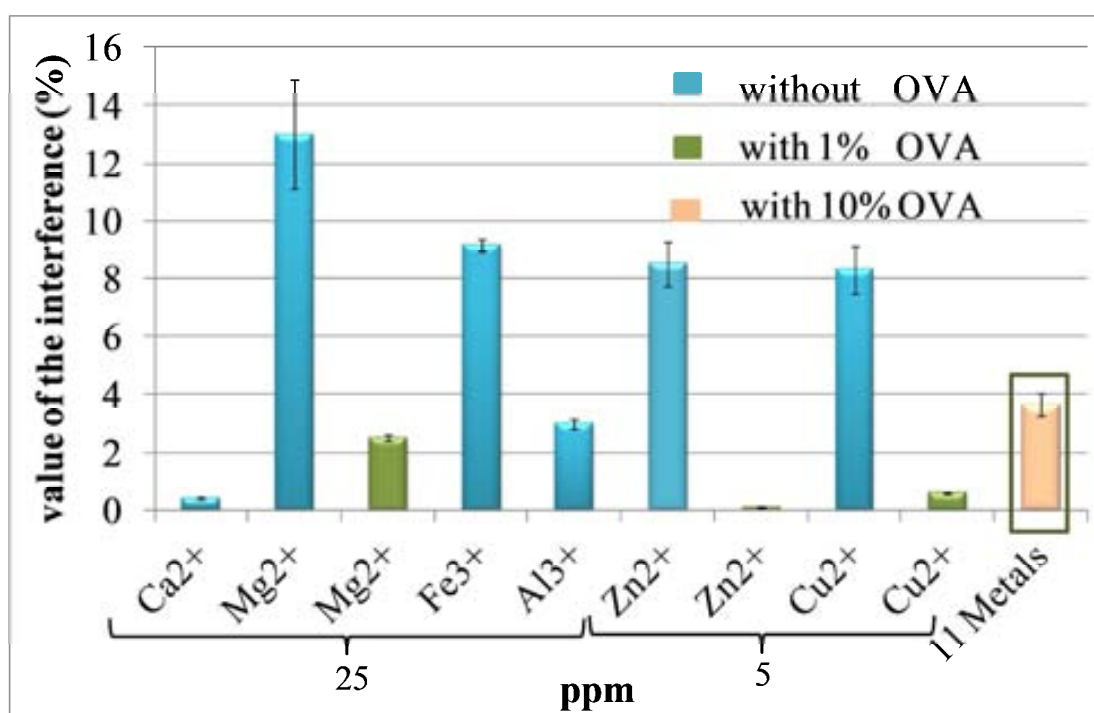
Table_S2. Metals contents of the studied water samples. The values of Ca²⁺ and Mg²⁺ ions with the asterisk tag (*) were determined in the lab by EDTA titration.

	Ca ²⁺	Mg ²⁺	Co ²⁺	Al ³⁺	Fe ³⁺	Zn ²⁺	Mn ²⁺	Cu ²⁺	Ni ²⁺	Pb ²⁺	Hg ²⁺	Cd ²⁺
WHO	*			0.2	0.3	3	0.10	2	0.07	0.01	0.001	0.003
EPA	*			0.2	0.2	5	0.05	1.3	0.04	0.015	0.002	0.005
U.S.	*			0.05	0.3	5	0.05	1.3	0.10	0.01	0.001	0.005


Table_S3. Permissible limits of heavy metals (in ppm) in drinking water. * No specification is set at this moment.

Formation Constants		
Metal-EDTA	Metal-albumin	Metal/EDTA-2A81G5 mAb
Fe ³⁺ 25.1; Hg ²⁺ 21.5; Ni ²⁺ 18.6; Cu ²⁺ 18.8; Pb ²⁺ 18.0; Cd ²⁺ 16.5; Co ²⁺ 16.3; Zn ²⁺ 16.5; Al ³⁺ 16.4; Mn ²⁺ 14.0; Ca ²⁺ 10.7; Mg ²⁺ 8.7	Cu ²⁺ 11.5; Zn ²⁺ 8.0; Ni ²⁺ 7.5; Hg ²⁺ 7.0; Pb ²⁺ 4.2; Mn ²⁺ 4.1; Cd ²⁺ ~ 2.5	Cd ²⁺ 8.3; Hg ²⁺ 7.5; Mn ²⁺ 6.4 Ni ²⁺ 5.7; Zn ²⁺ 5.6; Co ²⁺ 5.5 Cu ²⁺ 5.3; Fe ³⁺ 4.3; Pb ²⁺ 4.1 Mg ²⁺ 3.7; Al ³⁺ 3.1

Table_S4. Values of the complexes formation constants (log Kf) of the Metal-EDTA, Metal-albumin and Metal/EDTA-2A81G5 mAb at 25°C and pH ~7.



Figure_S1. Some results obtained in the specificity assay, for the most important metals present in drinking water, with and without OVA and using the conventional LFID. 25 ppm of the Ca²⁺, Mg²⁺, Fe³⁺ and Al³⁺ ions in presence of 10 ppb Cd²⁺ and 14 mM Na₂EDTA were prepared in spiked samples. 5 ppm of the Zn²⁺ and Cu²⁺ ions in presence of 10 ppb Cd²⁺ and 14 mM Na₂EDTA were prepared in spiked samples. 11 metals at concentrations over expected in drinking water were prepared with the optimized concentrations of 10% OVA and 0.005 mM Na₂EDTA in spiked samples.

Certificated Reference Material BCR [®] -713	Metal	Certificated value (ppb)
	As	9.7 ± 1.1
	Cd	5.1 ± 0.6
	Cr	21.9 ± 2.4
	Cu	69.0 ± 4.0
	Fe	400.0 ± 40.0
	Mn	43.4 ± 3.0
	Ni	30.0 ± 5.0
	Pb	47.0 ± 4.0
Se	5.6 ± 1.0	

Table_S5. Metals content in the wastewater certificate reference material (N° 713).

		Cd ²⁺ added concentration (ppb)			
		10 ppb Cd ²⁺		50 ppb Cd ²⁺	
		S	CV(%)	S	CV(%)
repeatability n=6	UAB tap water	0.35	3.56	0.21	0.41
	Font Vella drinking water	0.24	2.40	0.28	0.56
Intermediate precision n=12	UAB tap and Font Vella drinking water	0.73	7.30	2.91	5.83

Table S_6. Obtained results in the precision assay.

ANNEX II. SUBMITTED MANUSCRIPTS

Extremely fast and high Pb^{2+} adsorption capacity via use of a hybrid nanostructured vaterite

A. López-Marzo^{a,b}, Josefina Pons^b and Arben Merkoçi^{b,c,}*

Nanobioelectronics and Biosensors Group, Catalan Institute of Nanotechnology,^a

Department of Chemistry, Universitat Autònoma de Barcelona,^b

Campus de la UAB, 08193 Bellaterra, Barcelona, Spain

ICREA, Institució Catalana de Recerca i Estudis Avancats, 08010 Barcelona, Spain^c

*E-mail: arben.merkoci@icn.cat

Abstract

Ultra-fast heavy metals removal using hybrid and nanostructured vaterite- poly(ethyleneimine) (NV-PEI) is reported here. Especially for Pb^{2+} an extremely high and fast adsorption capacity without precedents is observed. Within a 3 min interval time 97-100% of Pb^{2+} contaminant in water samples at pH 6 (the most common water pH) with a large concentrations range (from 0 to 1000 ppm) and using a dosage of 0.5 g NV-PEI/L have been removed. The maximum adsorption capacity calculated for a 1500 ppm Pb^{2+} initial concentration was 2762 mg of Pb^{2+} /g NV-PEI achieving a 92 % removing of this initial Pb^{2+} contamination in 6 min. This surprising removing capacity is ascribed to a re-crystallization process via ionic exchange where Ca^{2+} is substituted by Pb^{2+} (functioning the vaterite-PEI material behaves like a wide ionic exchanger) and with the excellent nucleophilic character of PEI (poly-ethyleneimine) to attract transition metals and the large space inner of the slit macropores of the vaterite material. In addition to the excellent Pb^{2+} removal, the developed material is cheap, easy to be synthesised, biocompatible, biodegradable, which make it superior to others reported so far and an attractive alternative for industrial applications.

Keywords: nanostructured vaterite-PEI, high, fast Pb^{2+} removal

1. Introduction

Wastewaters from several industrial activities are an important source of environmental pollution, because of their high content of heavy metals ions. Currently, water treatment technologies for the removal of heavy metals ions occurs through the use of several unit operations, such as chemical precipitation, sedimentation, filtration and sludge treatment.^{1,2} During the process of filtration other procedures such as membrane filtration, ion exchange, electrochemical and adsorption processes are introduced to refine and to improve the heavy

metals removal fundamentally at low concentrations. In a wastewater treatment plant in the basin of filtration are placed several ionic interchanger membranes or adsorption membranes, or mixture of both types, to eliminate the residual heavy metal that can't completely be removed during the previous process (sedimentation) and are at low concentrations when water enters the filtration unit.¹⁻³ Nanotechnology has been a useful tool in the fabrication of materials to remove low heavy metals concentration during the water treatment process.⁴ In this way many different nanoscale materials such as oxides, hydroxides or salts of metals (such as iron,⁵⁻⁹ titanium¹⁰), carbon nanotubes,^{11,12} various noble metals (mainly as nanoparticles)^{13,14,15}, inorganic-organic hybrid materials,¹⁶ biomaterial as nanoporous silica,¹⁷ calcium carbonates¹⁸⁻²¹ and calcium phosphates,²²⁻²⁴ nanoscale networks (such as zeolites, MOF)²⁵ and others^{26,27} have been explored for remediation.

Here a hybrid material composed of nanostructured vaterite-(poly)ethyleneimine (NV-PEI) microparticles has been evaluated for heavy metal removal from water. Ultra fast removal capacity achieved within 6 min, never reached before, has been found for several metals at 100 ppm of initial concentration. 3 min is completely sufficient to remove almost the 100% of Pb²⁺ contamination in a wide concentrations range from 2-1000 ppm using a dosage of 0.5 g NV-PEI /L at pH 6, the usual water pH. Although there is a large number of studies using multiples nanostructure materials this extremely rapid and high adsorption capacity to remove Pb²⁺ has never been achieved so far.^{5,10,11,15,17-19} Generally the heavy metal removal processes using the nanostructured microparticles (like fibres, sheet, tubes, rods, spheres, etc) are generally described by Langmuir isotherms^{9,10,17,18} but in this case only Freundlich isotherm is the ascribed model. In addition to the excellent Pb²⁺ removal, the material here evaluated is cheap, easy to be synthesized, biocompatible, biodegradable, which makes it superior to others reported so far and an attractive alternative for industrial applications.

2 Experimental part

2.1 Chemical and synthesis of the absorbent material.

The Pb(NO₃)₂, CuCl₂·2H₂O, HgCl₂, ZnCl₂, CdCl₂, NiCl₂·6H₂O, CaCl₂ and Na₂CO₃ reagents were purchased from sigma Aldrich. The NV-PEI adsorbent material was synthesized mixing under 45 min sonication equal volumes (5 mL) and concentrations (0.33 M) of CaCl₂ and Na₂CO₃ dissolutions each PEI containing (4 mg/mL). In the case of CaCl₂ dissolution a mixed solvent of water/ethanol 1:1 (v/v) was used.²⁸ The final product is 100% of vaterite polymorph

compound of nanostructured microelipsoides and microspheres of about 1 μm size covered with PEI polymer.

2.2 Characterization techniques.

X-ray diffraction (XRD) measurements were performed on a Siemens D-5000 X-ray diffractometer with graphite monochromatized Cu-K α radiation ($\lambda = 0.15406$ nm). A scanning rate of 0.02 $^\circ/\text{s}$ was applied to record the pattern in the 2θ range of 10-80 $^\circ$ using 40 kV and 40 mA. The phase identification was done by comparing the XRD patterns of the crystals with the standard data available from Joint Committee on Powder Diffraction Standards. The morphology of NV-PEI was observed by means of ZEISS Merlin and Quanta 650FEG (scanning electron microscopes) SEM and TECNAI-F20 high resolution transmission electron microscope (HRTEM). N₂ adsorption–desorption isotherms were recorded on a Micromeritics Instrument Corporation ASAP 2000 sorption analyzer at liquid nitrogen temperature (77 K). The samples were degassed at 120 $^\circ\text{C}$ overnight (22 h) prior to the measurement. The surface area was obtained by the Brunauer–Emmett–Teller (BET) method, and the pore size distribution was calculated from the adsorption branch of the isotherms by the Barret–Joyner–Halenda (BJH) model. The thermogravimetry analysis (TGA) was conducted on a TGA7 Perkin-Elmer with argon flow rate of 20 mL/min and a heating rate of 10 $^\circ\text{C}/\text{min}$.

2.3 Removal kinetic experiments

In a typical kinetic experiment the used Pb²⁺, Cu²⁺, Hg²⁺, Zn²⁺, Cd²⁺ and Ni²⁺ dissolutions at different concentrations were prepared by dissolving a weighed quantity of Pb(NO₃)₂, CuCl₂·2H₂O, HgCl₂, ZnCl₂, CdCl₂ and NiCl₂·6H₂O, respectively, in Milli-Q water (resistivity 18.2 $\Omega\cdot\text{cm}$ at 25 $^\circ\text{C}$) and pH adjusted to 6. As-prepared hybrid NV-PEI microparticles (25 mg) were added to 50 mL of the metal solutions under stirring until 6 h of contact time. Aqueous samples (500 μL) were taken using improvised homemade filter-collector sample at several fixed time intervals and the metal ions concentrations were analyzed by using an ICPMS Agilent 7500ce model system. The amount q_t (mg/g) of metal adsorption onto microparticles surface at time interval t was calculated by:

$$q_t = \frac{(C_o - C_t)}{W} V$$

where C_0 and C_t (mg/L) are the liquid phase concentrations of Pb²⁺ ions at initial and any time interval t , respectively, V is the volume of the solution (L) and W is the mass of NV-PEI used as adsorbent (g).

3 Results and Discussion

3.1 Competitive assay of removal

Figure S_1 in the SI shows SEM and TEM images of the NV-PEI particles, as prepared in experimental conditions described before and used as adsorbent material in the removing related experiments. The first removing probes were carried out in multi-metal competitive assays, using the most important heavy metal contaminants. The NV-PEI adsorbent material exhibited the highest selectivity and adsorption capacity for Pb^{2+} and Cu^{2+} , followed for Hg^{2+} , Zn^{2+} and Cd^{2+} with a similar removal preference between them. NV-PEI showed the lowest selectivity and removal for Ni^{2+} between all the assayed metals (**figure 1A**). At 6 min of contact time the maximum adsorption capacity for the six assayed metals using both 20 and 100 ppm as initial concentration (lower times were not assayed) is reached indicating that the whole adsorption process is very fast. The maximum adsorption capacity for the total metals contamination was around 430 mg/g which corresponds to 31% of removal of the total initial metal concentration of 600 ppm. The change of color from white to blue in the adsorbent material after 6 min of contact time is related to the adsorption of Cu^{2+} and Ni^{2+} onto this material (figure 1B).

When 20 ppm of each metal is used as initial concentration, almost 100% of Pb^{2+} and Cu^{2+} are removed followed by around 50-60% of removal for Hg^{2+} , Zn^{2+} and Cd^{2+} and 20% for Ni^{2+} . While using 100 ppm of each metal as initial concentration, around 60% of Pb^{2+} and Cu^{2+} , 20% of Hg^{2+} , Zn^{2+} , Cd^{2+} and 10% of Ni^{2+} are removed. This decreasing in the removal percentage when the initial metal concentration increases from 20 to 100 ppm could be related with the fact that at high concentrations the different removing mechanisms for these metals start blocking/interfering each other, allowing major removal for each metal in comparison to the case when only one metal should be present. Moreover some mechanisms start to saturate at high concentrations onto the NV-PEI surface, which is reflected in the increasing of the adsorption capacity and the decreasing in the removal capacity when metal concentration increases from 20 to 100 ppm.

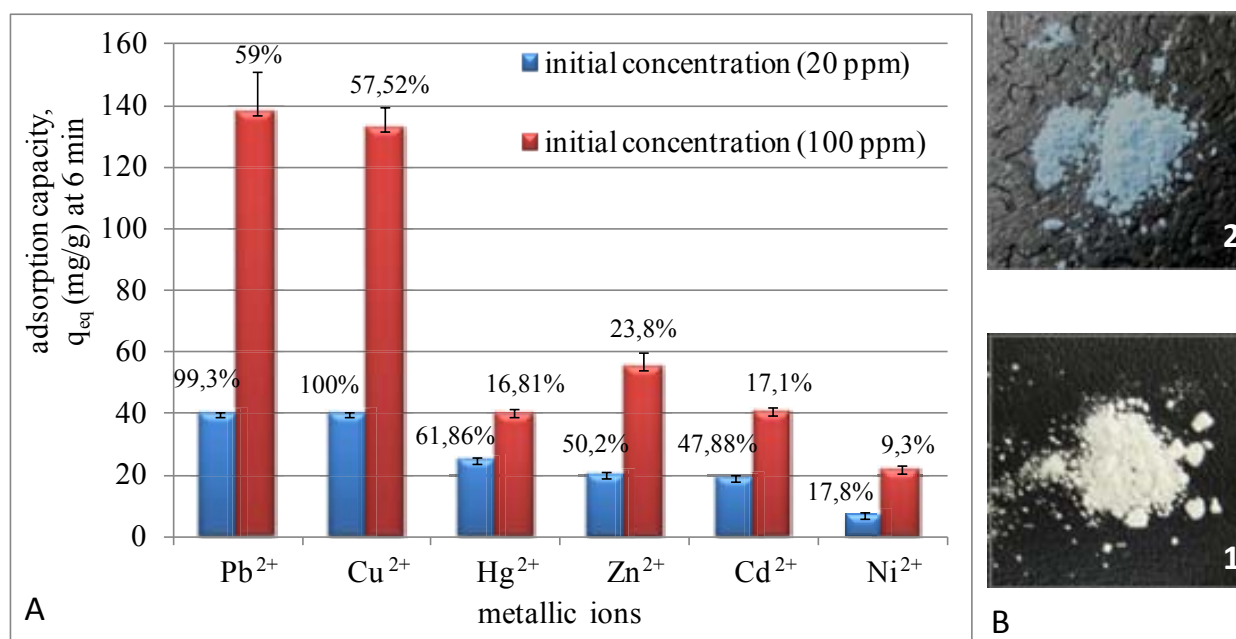


Figure 1. (A) Adsorption capacities of NV-PEI (0.5 g/L dosage) obtained during 6 min of contact time for different metallic ions in a competitive assay using 20 and 100 ppm of initial concentration for each metal. The number over the bar is the percentage of removal. (B) Photos of the adsorbent powder of the NV-PEI before (1) and after (2) the removal process.

As this material in the multi-metal competitive removal assay showed the highest adsorption capacity for Pb^{2+} , the following adsorption kinetic studies for the Pb^{2+} removal as shown below were performed.

The equilibrium adsorption capacity increases dramatically by increasing of Pb^{2+} initial concentration, until it reaches the maximum adsorption capacity of 2762 mg Pb^{2+} /g NV-PEI at 1500 ppm of Pb^{2+} initial concentration (**figure 2-i**). For concentrations from 0 to 1000 ppm 3 min of contact time is enough to remove around 97-100% of the total Pb^{2+} initial mass using a dose of 0.5 g NV-PEI/L (**figure 2-ii**). Contact times longer than 3 min don't change significantly the adsorption capacity, because all the contaminant that can be removed from 0 to 1000 ppm is adsorbed in the first 3 min of reaction. This fast and high Pb^{2+} removal capacity has not been reported so far as shown in **table 1**.

Table 1. Summary of the most significant and latest (last five years) works related with the use of nanostructured microparticles for heavy metals removal for wastewater treatment potential applications. These reported materials

Material	Metal- q_{\max} (mg/g)	Dose g/L	pH	CT (min)	BET (m^2/g)	BJH (nm) V (cm^3/g)	Reference
CaCO ₃ -PEI	Pb ²⁺ - 2762	0.5	6	3	20	2-190 0.7	This work
α -FeOOH microspheres	Pb ²⁺ - 80 As ⁵⁺ - 58	0.5;	6	180 180	96.9	3-20 0.36	<i>Adv. Mater.</i> 2012 , 24, 1111.
γ -Fe ₂ O ₃ CHNs Fe ₃ O ₄ CHNs Fe ₂ O ₃ CAHNS	As ⁵⁺ - 101.4 As ⁵⁺ - 6.07 As ⁵⁺ - 137.5	0.4	4	30 180 30	96.4 14.90 143.1	2-100 —	<i>ACS Appl. Mater. Interfaces</i> 2012 , 4, 3987.
CNTs-in- α -Fe ₂ O ₃ Core-in-shell microcapsules	Pb ²⁺ - 46.6 Cr ³⁺ - 29.16	0.36	5	20 20	200	—	<i>Adv. Funct. Mater.</i> 2010 , 20, 820.
MWCNTs-cysteine	Cd ²⁺ - 60.3	1	5.5	60	—	—	<i>Adv. Funct. Mater.</i> 2008 , 18, 1536.
CaCO ₃ -maltose vaterite hexagonal plates	Pb ²⁺ - 3242 Ni ²⁺ - 769 Cu ²⁺ - 629 Mn ²⁺ - 558.7 Cd ²⁺ - 487.8 Co ²⁺ - 393.7	0.57	7	45 45 45 45 45	63.2	— 2-12	<i>J. Hazardous Mater.</i> 2012 , 209-21, 467.
CaCO ₃ -pepsin tetrahedral microaggregates	Pb ²⁺ - 1167 Cu ²⁺ - 611	0.43	—	60 60	—	—	<i>J. Crystal Growth</i> 2012 , 338, 272.
AuNPs (8.9±1.6 nm)	Hg ²⁺ - 102	0.028	—	50	—	—	<i>ACS NANO</i> 2012 , 6, 2253.
polyaniline nano wires/tubes	Cr ⁶⁺ - 147.3	0.6	5	60	—	—	<i>J. Phys. Chem. C</i> 2010 , 115, 1608.
Nanosheets Na-TNSs Na ₂ Ti ₃ O ₇ ·nH ₂ O	Pb ²⁺ - 10.88 Cu ²⁺ - 12.84 Eu ³⁺ - 10.42 Ag ²⁺ - 10.12	1.25	—	120 30 60 60	203	—	<i>Adv. Funct. Mater.</i> 2012 , 22, 835.
Ni@SiO ₂ core/shell particles modified with BODIPY	Pb ²⁺ - 100	10	7	—	—	—	<i>Angew. Chem. Int. Ed.</i> 2009 , 48, 1239.

were proposed as better than the previous one.

Nomenclature: CT: contact time during which the maximum adsorption capacity is reached, V: volume of porous, C(A)HNs: chestnutlike (amorphous) hierarchical nanostructures; CNTs: carbon nanotubes; MWCNTs: multi-walled carbon nanotubes, TNSs: titanates nanosheets, BODIPY: 4,4-difluoro-4-bora-3a,4adiaza-s-indacene.

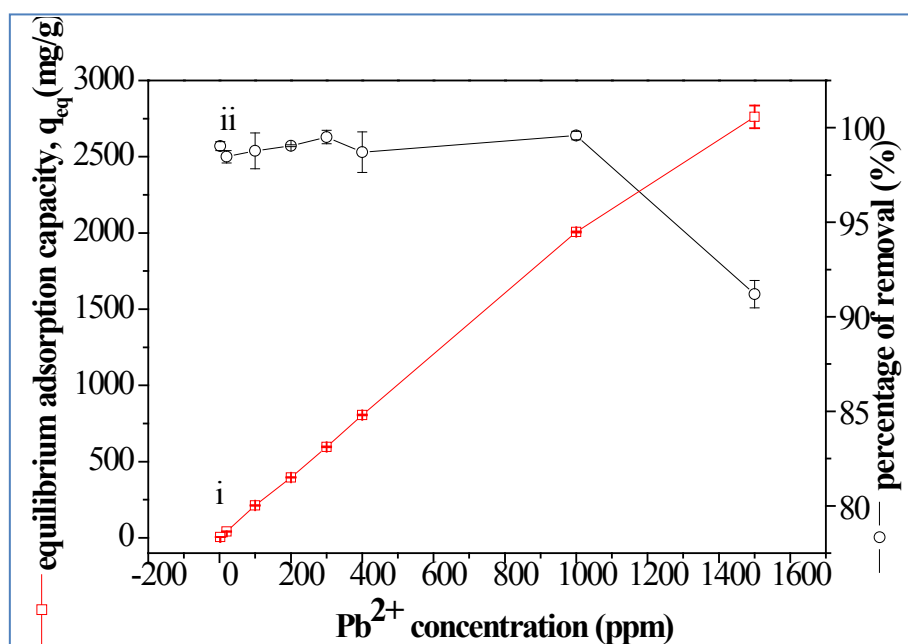


Figure 2. Adsorption rate for Pb^{2+} cations onto NV-PEI. (—□—) Curve of adsorption capacity reached at 3 min of contact time when initial metal concentration is increased. (—○—) Metal removal percentage when the equilibrium adsorption capacity is reached at different metal initial concentrations using 0.5 g NV-PEI/L dosage and 3 min of contact time.

3.2 Adsorption isotherm of Pb^{2+} onto NV-PEI material

Although sometimes Freundlich^{11,18} and other models are found out as the best fit isotherm models to the experimental equilibrium data obtained during the removal processes. Generally the adsorption isotherms that describe the removal processes for the majority of the adsorbent materials of heavy metals reported correspond to the Langmuir model.^{9,10,17,18}

Our experimental data can't be adjusted with the Langmuir isotherm adsorption, which indicates that this model is not suitable for describing this process. This is because the adsorption not only occurs at the monolayer surface as is necessary assumed by Langmuir isotherm model, according to which the homogeneous surfaces have sites energetically equivalent and the adsorbates adsorb only in a monolayer way and there is no interaction between the adsorbed molecules. The adjusting of our experimental points is close to Freundlich model (figure_S2 at SI). This suggests that the Pb^{2+} adsorption behaviour onto the NV-PEI can be considered as a multilayer adsorption process that follows more the Freundlich isotherm model, an empirical equation based on the multilayer adsorption on heterogeneous surfaces.²⁹ In figure S2 are calculated the experimental parameters for Freundlich isotherm. Values of n relatively close to 1

indicate that the sorption intensity is good over the entire range of concentrations studied, while n values between 0.2 and 0.8 indicate that sorption intensity fits better at high concentrations but much less at lower concentrations.²⁹ In our case the n value obtained is 0.96 (close to 1) which is in agreement with the excellent removal capacity found over the entire range of concentrations from 2 to 1500 ppm. Other models such as Dubinin–Redushkevich (D–R) and Temkin models don't describe our experimental points (results not shown).

3.3 The N₂ adsorption-desorption isotherms

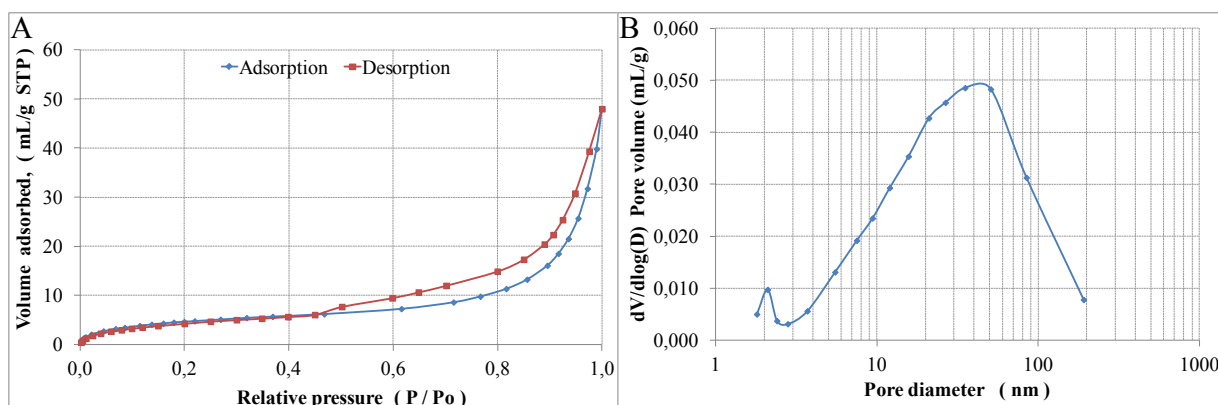


Figure 3. N₂ adsorption and desorption isotherms (A) and the corresponding BJH pore size distribution curve for the synthesized product (B).

The nitrogen adsorption and desorption isotherms of the NV-PEI adsorbent material exhibit type II isotherm with a type III hysteresis loop in the relative pressure range of 0.45–1 (**figure 3A**), suggesting that the adsorbing material structure is composed in majority by macropores with good pore connectivity associated with slit-like pores.^{30,31} In addition as shown in figure 3 A and B some mesoporous part in the size range of 2-50 nm for low relative pressures (P/Po 0.4) is also present. The nitrogen amount adsorbed rises very steeply at high relative pressure (P/P0 > 0.85), which also suggests the presence of an appreciable amount of very large pores in the material.^{30, 31} The BJH pore size distribution curve derived from the adsorption branch of the isotherm shows one very narrow distribution centered at 2.1 nm indicating that few microporous parts make up the material structure and one broad peak in the range of 2.8–191 nm centered at 40 nm that indicates that high percentage of the structure porosity are mesoporous and macroporous morphologies (see Fig. 3B). It is interesting to highlight that the final part of the

adsorption branch reaches large macropores diameter (50-190 nm). Moreover the material has a BET surface area of 20 m²/g and a pore volume of around 0.07 mL/g.

3.4 Interaction of the metal ions with the NV-PEI hybrid materials. Removing mechanisms.

It is evident from the results that this hybrid material has powerful capability for fast and high removal of toxic ions of heavy metals. This is related with the large pore size in the NV-PEI structure, the PEI in the material surface that traps metallic cations by adsorption through the electrophilic-nucleophilic interactions and the recrystallization process mediated by the ionic exchange in the entire structure. **Figure 4** displays a representative scheme of the principle of the Pb²⁺ removing mechanism.

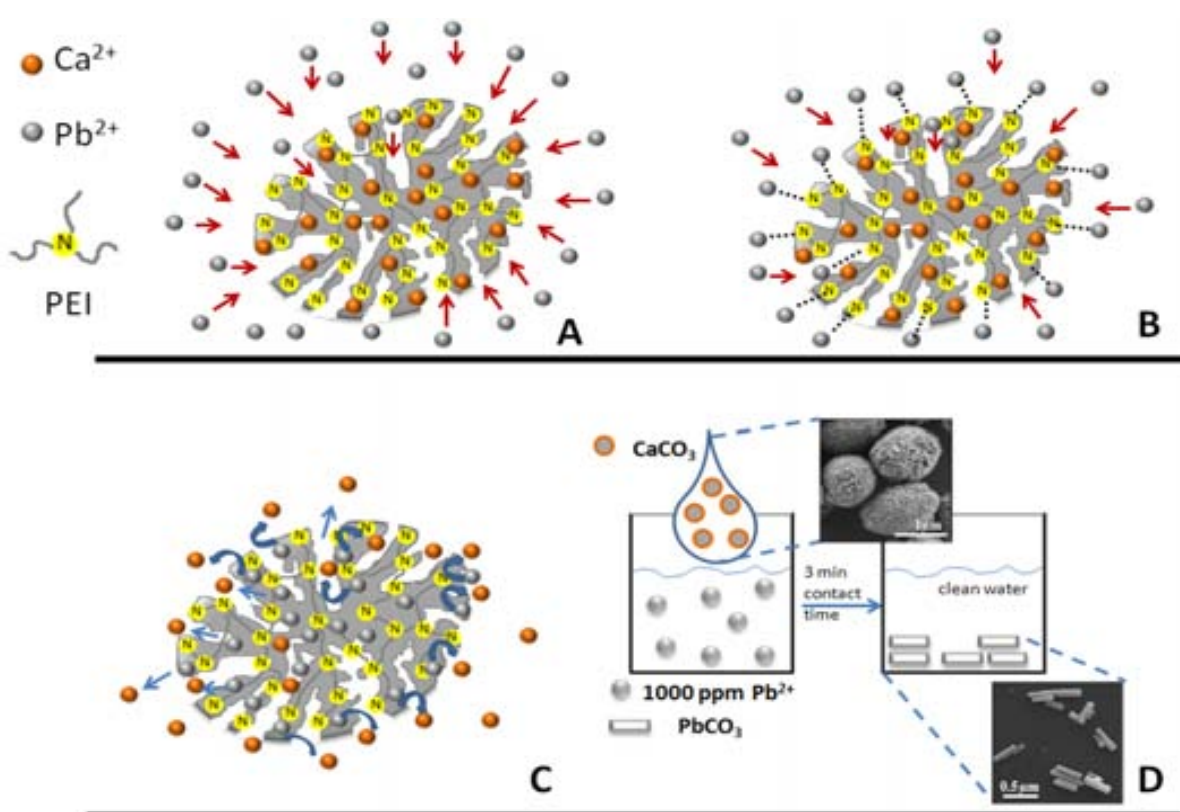


Figure 4. Schematic representation of the Pb²⁺ removing mechanism by use of NV-PEI material. A) Pb²⁺ cations diffusion toward the NV-PEI structure occurs. B) The PEI layer onto the surface material traps cations via electrophilic-nucleophilic interactions between PEI's nitrogen and Pb²⁺. The slit macroporous structure permits a rapid accessibility to the inner parts in the NV-PEI structure. The red arrows indicate the movement of the Pb²⁺ cations into the adsorbent structure. C) Ionic exchange of Ca²⁺ by Pb²⁺ cations leading to the recrystallization

process. The blue arrows indicate the movement of released Ca^{2+} ions after exchanging with Pb^{2+} ions. D) Attractive scheme of the whole removing process.

The large size of the macropores that dominate in the structure (typical SEM images are displayed in figure_S1B where large pore sizes of this material can be observed) as found by BJH method, and the high affinity power of the PEI with metallic cations as part of this hybrid material can explain the ultra rapid metal adsorption process that takes place in our system. The large size porous in this material permits big accessibility, as well as, a fast and simultaneous penetration of large quantity of ions to the inner parts of the NV-PEI microparticles together with the high affinity of PEI for metal cations acting as ionic trap network of chemical adsorption mechanism (figure 4A and B) are the two most important and determinant factors in the fast Pb^{2+} removal process.

The PEI presence in this material was observed using TGA (figure_S3 at SI). The loss in weight of about 6% that appears in the range of 250-350 °C corresponds to PEI delivery from CaCO_3 structure. This result indicates that a NV-PEI hybrid material was synthesized. The PEI structure is a branched polymer that contains a large number of amines functional groups with strong nucleophilic character which result electrophilic-nucleophilic interactions between nitrogen's PEI and the metal cation. It was observed that the removing equilibrium can be established in an extremely short time (about 6 min) during which a complete removal of heavy metal ions and especially of Pb^{2+} ions (nearly 100% removal after 3 min) occurred. The fast uptake of heavy metal ions indicates a high affinity rate between the metal ions and the amino groups at PEI that covers the adsorbent as well as a rapid mass transference to the inner parts of the structure propitiated by the large pore size.

The value of BET surface area as obtained from N_2 adsorption and desorption isotherms is discrete in comparison with the reported ones for other materials (see table 1) and doesn't justify the high Pb^{2+} removal capacity. This reasonably suggests that the high BET is not the only criterion for the high Pb^{2+} adsorption capacity. The adsorption capacity sometimes is intensively affected by the surface quality/property. In this case the Pb^{2+} adsorption mechanism is far a way of a simple superficial adsorption. This possibly results in a multilayer adsorption behavior and consequently a superior adsorption capacity. The Pb^{2+} adsorption process onto the as-obtained NV-PEI microparticles, as also explained before, obeys well the Freundlich isotherm model rather than the Langmuir one, suggesting that a multilayered adsorption occurs onto particles surface, which is in agreement with the ionic exchange mechanism that is also taking place and is demonstrated in **figure 5**.

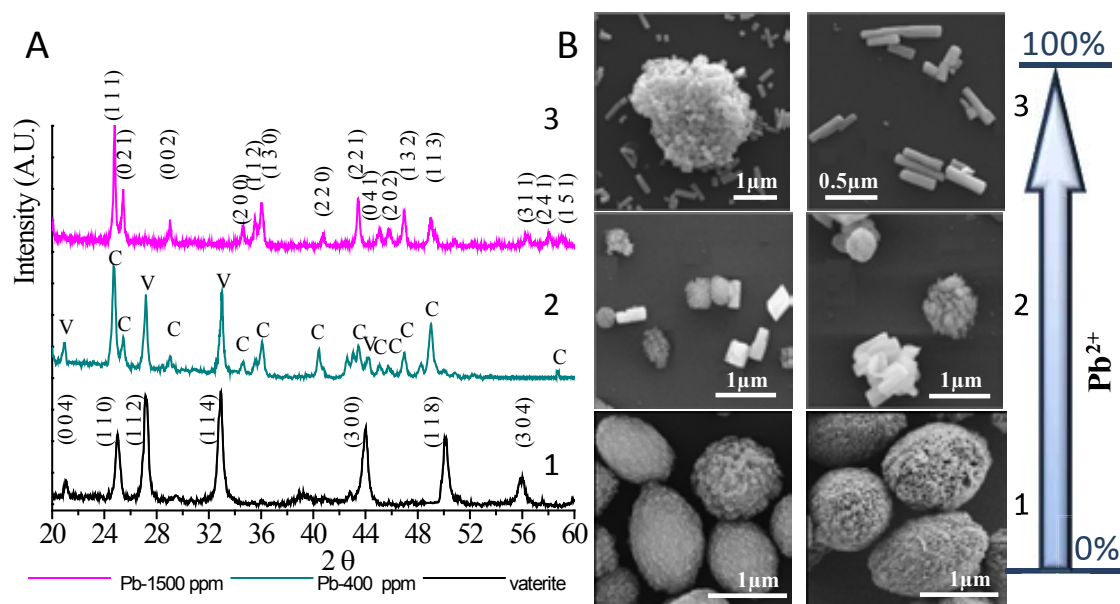


Figure 5. (A) XRD patterns correspond to the NV-PEI product at different contact times and Pb^{2+} initial concentrations (1) before treatment at initial time when there is not contact with Pb^{2+} solution, (2) after 6 min of treatment in contact with 400 ppm of Pb^{2+} solution, (3) after 6 min of treatment in contact with 1500 ppm of Pb^{2+} solution. V means vaterite and C cerussite. (B) SEM images of the corresponding products.

XRD patterns and SEM images in figure 5 A and B, respectively, indicate that a new precipitation process is taking place during the water treatment process. Figure 5 A-1 shows the pattern of vaterite before its contact with Pb^{2+} dissolutions while its corresponding SEM images of spherical/ellipsoidal microparticles are shown in figure 5 B-1. After the contact of the NV-PEI material with Pb^{2+} dissolutions of increasing initial concentration a transformation of part of vaterite in cerussite (orthorhombic PbCO_3) (figure 5 A-2 and B-2) occurs until that using 1500 ppm of Pb^{2+} dissolution a complete vaterite transformation into cerussite takes place (figure 5 A-3 and B-3). The NV-PEI behaves like an ionic exchanger network of Ca^{2+} by Pb^{2+} cations. The exchanging process takes place both at superficial level as well as at the interior of NV-PEI material. The structure of NV-PEI collapses during the ion exchange, resulting in a recrystallization process by an irreversible ion exchange. The SEM images in figure 5B-3 displays the orthorhombic PbCO_3 precipitate appeared from the starting NV-PEI microspheres/ellipsoids. Figure 4-D is a schematic illustration of the whole ionic exchange process explained previously.

The CaCO_3 precipitate transformation into PbCO_3 precipitate is favoured because the K_{ps} of the PbCO_3 (7.3×10^{-14}) is much lower than CaCO_3 K_{ps} (3.3×10^{-9}) in addition to their close ionic radius (table_S1) that facilitates the substitution inside the CaCO_3 structure. An analysis of these and other properties for each metal that could favour the metal removing process by a

recrystallization via ionic exchange is presented in table_S2. Following the analysis of the table_S2 Pb^{2+} has all the conditions to be removed preferentially in a multi-metal competitive assay, as occurs in the experimental results at figure 1A (previously discussed).

As shown in the XRD patterns of the figure_S4 the metals are removed from their solutions following the recrystallization mechanism that transforms $CaCO_3$ into the corresponding metal carbonates (figure_S4 A) or by precipitation induced by the adsorption of the original metal species onto the $CaCO_3$ surface via electrophilic-nucleophilic interactions with PEI's nitrogen (figure_S4 B). The selectivity order and the chemical form in which these metal are removed depend on several factors related with their different affinities for the surface of the NV-PEI hybrid material such as: (a) Ionic radius of the M^{2+} cations; metals of ionic radius close to Ca^{2+} exchange easier than other metals; (b) electronegativity of the metals; metals of higher electronegativity should be attracted more easily because the increasing in electronegativity reinforces the electrophilic-nucleophilic interactions with the PEI's nitrogen; (c) Solubility of the hydrate complexes; metals of less soluble complexes with hydrate have increased adsorptive capacity because the trend of the ion to crystallize will be higher than the tendency to remain dissolved as hydrate complexes; (d) Solubility of the carbonates; the metal ions that form less soluble carbonates should be exchanged stronger than metal ions which form more soluble carbonates; (e) Amino affinity; metals of big affinity with amino groups have more interaction with the surface and in consequence more possibility to be removed. Table_S1 at SI shows the values of the mentioned properties for each metal that are related with the removing mechanisms in this process. In this way metal ions such as Pb^{2+} , Cd^{2+} and Hg^{2+} with the closest Ca^{2+} ionic radius and with highly insoluble carbonates and hydroxides (table_S1) should be preferably removed by ionic exchange than the other. While Cu^{2+} , Zn^{2+} and Ni^{2+} that present less insoluble carbonates and hydroxides and ionic radius values far a way of Ca^{2+} tend to be removed by adsorption of their metal species through electrophilic-nucleophilic interactions with PEI's nitrogen. According with this analysis in figure_S4-A i and ii in addition to $CaCO_3$ peaks other peaks corresponding to Cd^{2+} and Hg^{2+} carbonates, respectively, can be observed. While in figure_S4-B iii, iv and v in addition to $CaCO_3$ peaks, other peaks can be associated to Cu^{2+} chloride, hydroxide, hydroxide chloride and their hydrated species, Zn^{2+} chloride and hydroxide chloride and Ni^{2+} hydroxide, respectively. These metals are removed through their stable species that form in our system by precipitation induced by absorption onto the $CaCO_3$ surface via interactions with PEI.

As can be seen in the XRD patterns of figure_S4 during the treatment part of the original vaterite phase recrystallizes to calcite as a consequence of the metal removing process in its structure.

It is also important to point out that many adsorption results reported in the literature are obtained at an optimized pH value (usually pH 3-4) with longer adsorption duration that end up to 2 h. Therefore, we believe that the exceptionally fast and high removal capacities obtained by using the NV-PEI using pH 6 are more indicative for a promising use of this material in real water treatment applications. Although the obtained results are in the laboratory scale, we expect satisfactory removal efficiencies in industrial scale especially for Pb^{2+} . Moreover, this material can be easily produced at industrial amounts because it is facile to be synthesized, cheap, biodegradable and innocuous. In addition, this material has a high loading capacity for organic molecules (dyes such as methylene blue, bromocresol green and methyl orange) through the hydrogen bond interaction of acid hydrogens in the contaminants molecules and the nitrogen's PEI onto the vaterite microparticles surface as reported previously.²⁸ This would increase the NV-PEI interest as a potential adsorbent for simultaneous removal of many co-existing pollutants that usually appear in industrial effluents. The development of such multipurpose adsorbents which can remove both organic and heavy metal pollution would improve the cost/efficiency of water treatment process and might have an impact on both the wastewater treatment technology as well as the science behind the phenomena occurring during the operation of such integrated and hybrid nanostructured materials.

4 Conclusions

A very fast heavy metals removal by using the hybrid NV-PEI, (composed of mixed nanostructured microspheres and microellipsoids of about 1 μm size) is here reported. Especially ultra fast and high adsorption capacity for Pb^{2+} never reported before was achieved. Just a 3 min contact time, under stirring conditions, is enough to remove between 97 and 100% of this metal contaminant over an entire range of initial concentrations from 0 to 1000 ppm using a dosage of 0.5 g NV-PEI/L at the usual pH 6 water samples. The maximum adsorption capacity was 2762 mg of Pb^{2+} /g adsorbent material. These results show a powerful capability for fast and effective removal of toxic Pb^{2+} , doing this material an efficient adsorbent alternative for the complete removal of Pb^{2+} from high to trace concentrations during water treatment process. It is important to highlight that most of the materials used so far for heavy metal removal are not efficient at low metal concentrations.

The metal removal mechanisms are based on recrystallization process via ion exchange with Ca^{2+} in the NV-PEI material and the precipitation mediated by the adsorption via electrophilic-nucleophilic interactions between PEI's nitrogens and the metallic centres.

References

- [1] R. Ludwig, *Angew. Chem. Int. Ed.*, **2002**, *41*, 2611.
- [2] A. Guijarro-Aldaco, V. Hernández-Montoya, A. Bonilla-Petriciolet, M. A. Montes-Morán, D. I. Mendoza-Castillo, *Ind. Eng. Chem. Res.* **2011**, *50*, 9354.
- [3] Y. Han, Zh. Xu, C. Gao, *Adv. Funct. Mater.* **2013**, DOI: 10.1002/adfm.201202601.
- [4] B. Karn, T. Kuiken, M. Otto, *Environ. Health Perspectives* **2009**, *117*, 1823.
- [5] B. Wang, H. Wu, L. Yu, R. Xu, T.-T. Lim, X. W. Lou, *Adv. Mater.* **2012**, *24*, 1111.
- [6] S.-W. Cao, Y.-J. Zhu, *J. Phys. Chem. C* **2008**, *112*, 6253.
- [7] F. Mou, J. Guan, H. Ma, L. Xu, W. Shi, *ACS Appl. Mater. Interfaces* **2012**, *4*, 3987.
- [8] W. Yantasee, C. Warner, T. Sangvanich, R. Sh. Addleman, T. Carter, R. J. Wiacek, G. Fryxell, Ch. Timchalk, M. Warner, *Environ. Sci. Technol.* **2007**, *41*, 5114.
- [9] Z. Wei, R. Xing, X. Zhang, S. Liu, H. Yu, P. Li, *ACS Appl. Mater. Interfaces* **2013**, *5*, 598.
- [10] N. Li, L. Zhang, Y. Chen, M. Fang, J. Zhang, H. Wang, *Adv. Funct. Mater.* **2012**, *22*, 835.
- [11] W. S. Choi, H. M. Yang, H. Y. Koo, H.-J. Lee, Y.B. Lee, T. S. Bae, Ch. Jeon, *Adv. Funct. Mater.* **2010**, *20*, 820.
- [12] Y. Liu, Y. Li, X.-P. Yan, *Adv. Funct. Mater.* **2008**, *18*, 1536.
- [13] I. Ojea-Jiménez, X. López, J. Arbiol, V. Puntes, *ACS NANO*, **2012**, *6*, 2253.
- [14] L. Lu, R. Capek, A. Kornowski, N. Gaponik, A. Eychmüller, *Angew. Chem.* **2005**, *117*, 6151.
- [15] H. Y. Lee, D. R. Bae, J. Ch. Park, H. Song, W. S. Han, J. H. Jung, *Angew. Chem. Int. Ed.* **2009**, *48*, 1239.
- [16] B. Saha, S. Chakraborty, G. Das, *J. Phys. Chem. C* **2010**, *114*, 9817.
- [17] W. Yantasee, R. D. Rutledge, W. Chouyyok, V. Sukwarotwat, G. Orr, C. L. Warner, M. G. Warner, G. E. Fryxell, R. J. Wiacek, Ch. Timchalk, R. Sh. Addleman, *ACS Appl. Mater. Interfaces* **2010**, *2*, 2749.
- [18] X. Ma, L. Li, L. Yang, C. Su, K. Wang, Sh. Yuan, J. Zhou, *J. Hazard. Mater.* **2012**, *209-210*, 467.
- [19] X. Man, L. Li, L. Yang, C. Su, K. Wang, K. Jiang, *J. Cryst. Growth* **2012**, *338*, 272.
- [20] Y. Ma, Ch. Lin, Y. Jiang, W. Lu, Ch. Si, Y. Liu, *J. Hazard. Mater.* **2009**, *172*, 1288.
- [21] G. B. Cai, G. X. Zhao, X. K. Wang, S. H. Yu, *J. Phys. Chem. C*, **2010**, *114*, 12948.

- [22] R. Tovar-Gómez, D. A. Rivera-Ramírez, V. Hernández-Montoya, A. Bonilla-Petriciolet, C. J. Durán-Valle, M. A. Montes-Morán, *J. Hazardous Mater.* **2012**, 199-200, 290.
- [23] Sh. Sugiyama, T. Ichii, M. Fujisawa, K. Kawashiro, T. Tomida, N. Shigemoto, H. Hayashi *J. Colloid Interface Sci.* **2003**, 259, 408.
- [24] X. Chen, J. V. Wright, J. L. Conca, L. M. Peurrung, *Environ. Sci. Technol.* **1997**, 31, 624.
- [25] B. C. Tappan, S. A. Steiner, E. P. Luther, *Angew. Chem. Int. Ed.* **2010**, 49, 4544.
- [26] X. Guo, G. Ta. Fei, H. Su, L. D. Zhang, *J. Phys. Chem. C* **2011**, 115, 1608.
- [27] M. J. Manos, V. G. Petkov, M. G. Kanatzidis, *Adv. Funct. Mater.* **2009**, 19, 1087.
- [28] A. López_Marzo, J. Pons, A. Merkoçi, *J. Mater. Chem.* **2012**, 22, 15326.
- [29] J. U. Kennedy Oubagaranadina, N. Sathyamurthy, Z.V.P. Murthy, *J. Hazardous Mater.* **2007**, 142, 165.
- [30] M. Khalfaoui, S. Knani, M. A. Hachicha, A. Ben Lamine. *J. Colloid Interface Sci.* **2003**, 263, 350.
- [31] K. S. W. Sing, D. H. Everett, R. A. W. Haul, L. Moscou, R. A. Pierotti, J. Rouquerol, T. Siemieniewska, *Pure Appl. Chem.* **1985**, 57, 603.

Supporting Information

Extremely fast and high Pb^{2+} adsorption capacity via use of a hybrid nanostructured vaterite

A. López_Marzo^{a,b}, Josefina Pons^b and Arben Merkoçi^{b,c,}*

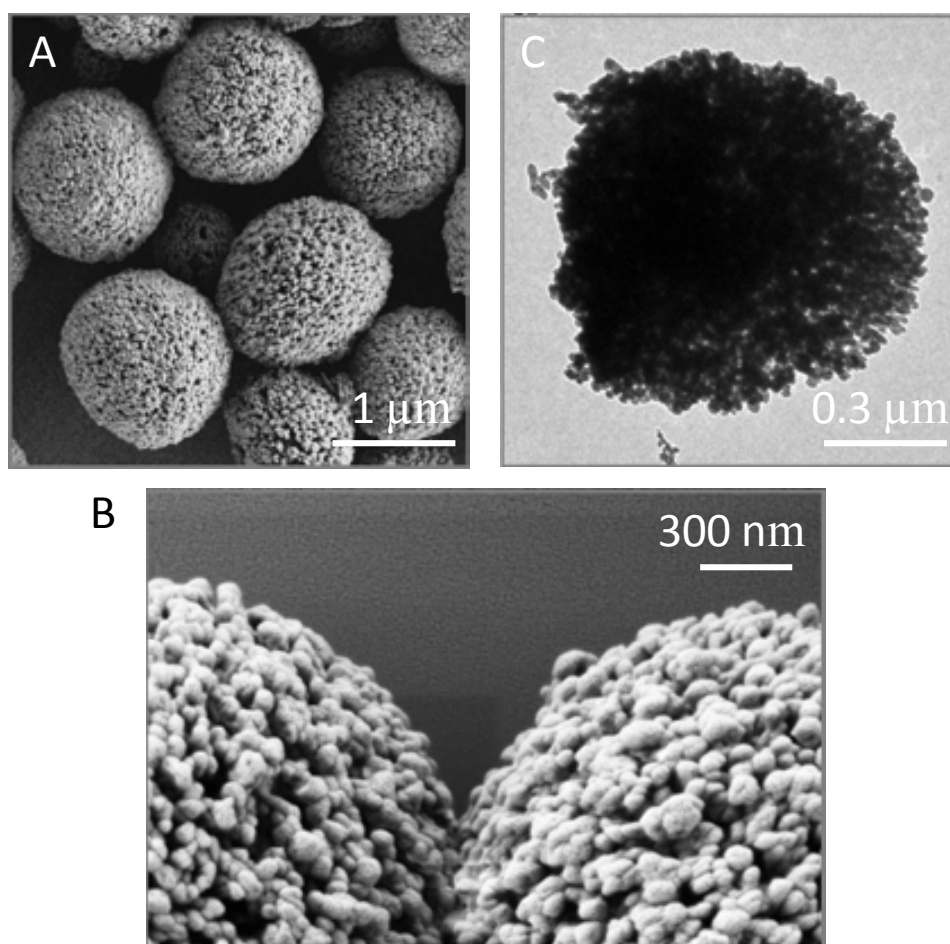
Nanobioelectronics and Biosensors Group, Catalan Institute of Nanotechnology,^a

Department of Chemistry, Universitat Autònoma de Barcelona,^b

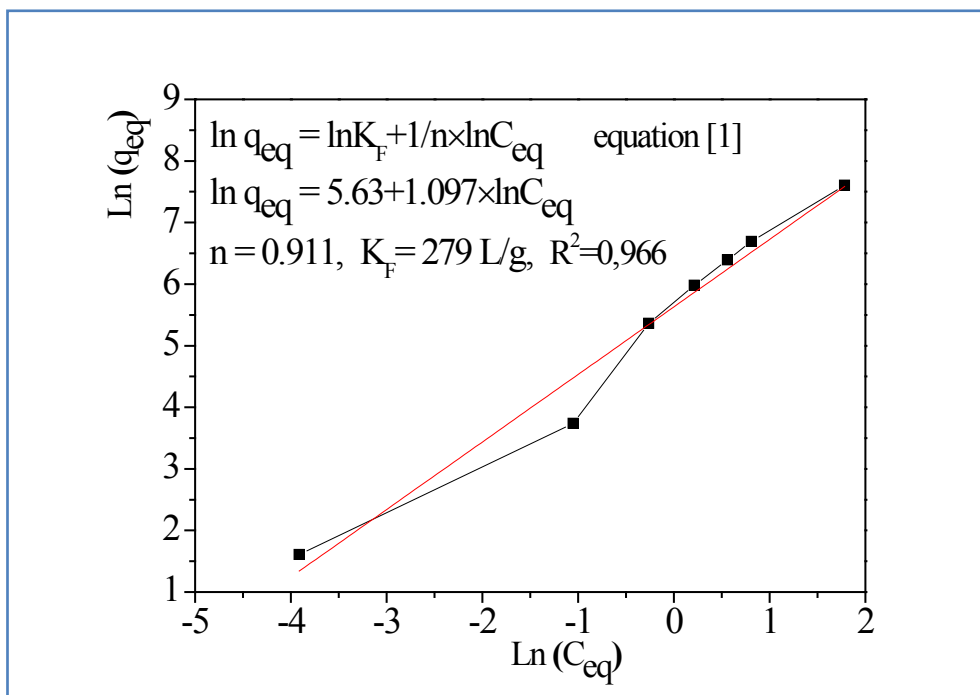
Campus de la UAB, 08193 Bellaterra, Barcelona, Spain

ICREA, Institució Catalana de Recerca i Estudis Avancats, 08010 Barcelona, Spain^c

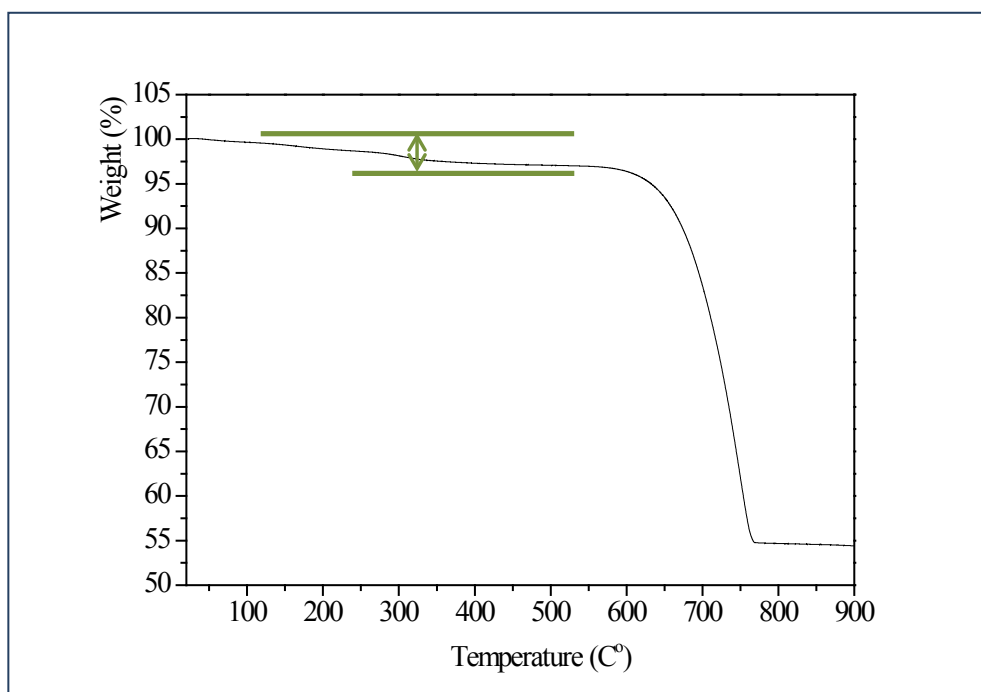
*E-mail: arben.merkoci@icn.cat



Figure_S1. Images of the synthesized NV-PEI microparticles. A and B SEM images and C TEM image. (B) Close up to the NV-PEI surface that displays the large macroporous caverns like structure that makes this material.

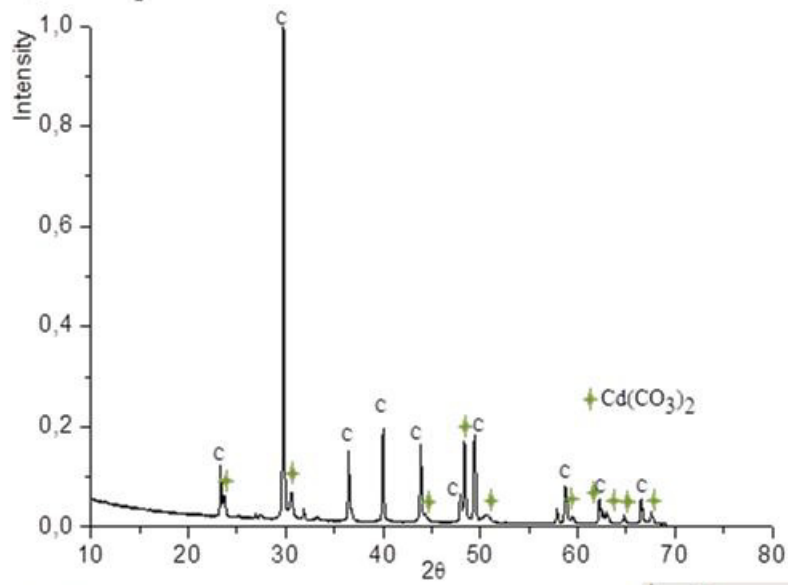


Figure_S2. Adjusting of the experimental points obtained during the Pb^{2+} adsorption onto NV-PEI surface at 25°C by the use of the Freundlich isotherm model. The equation 1 is the linear form of the Freundlich equation where K_F is the Freundlich constant (L/g) and $1/n$ the heterogeneity factor.

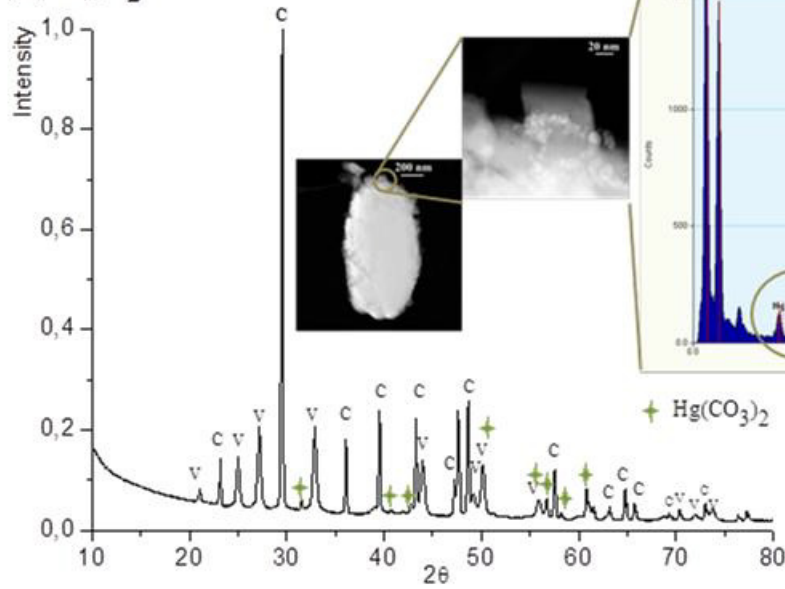


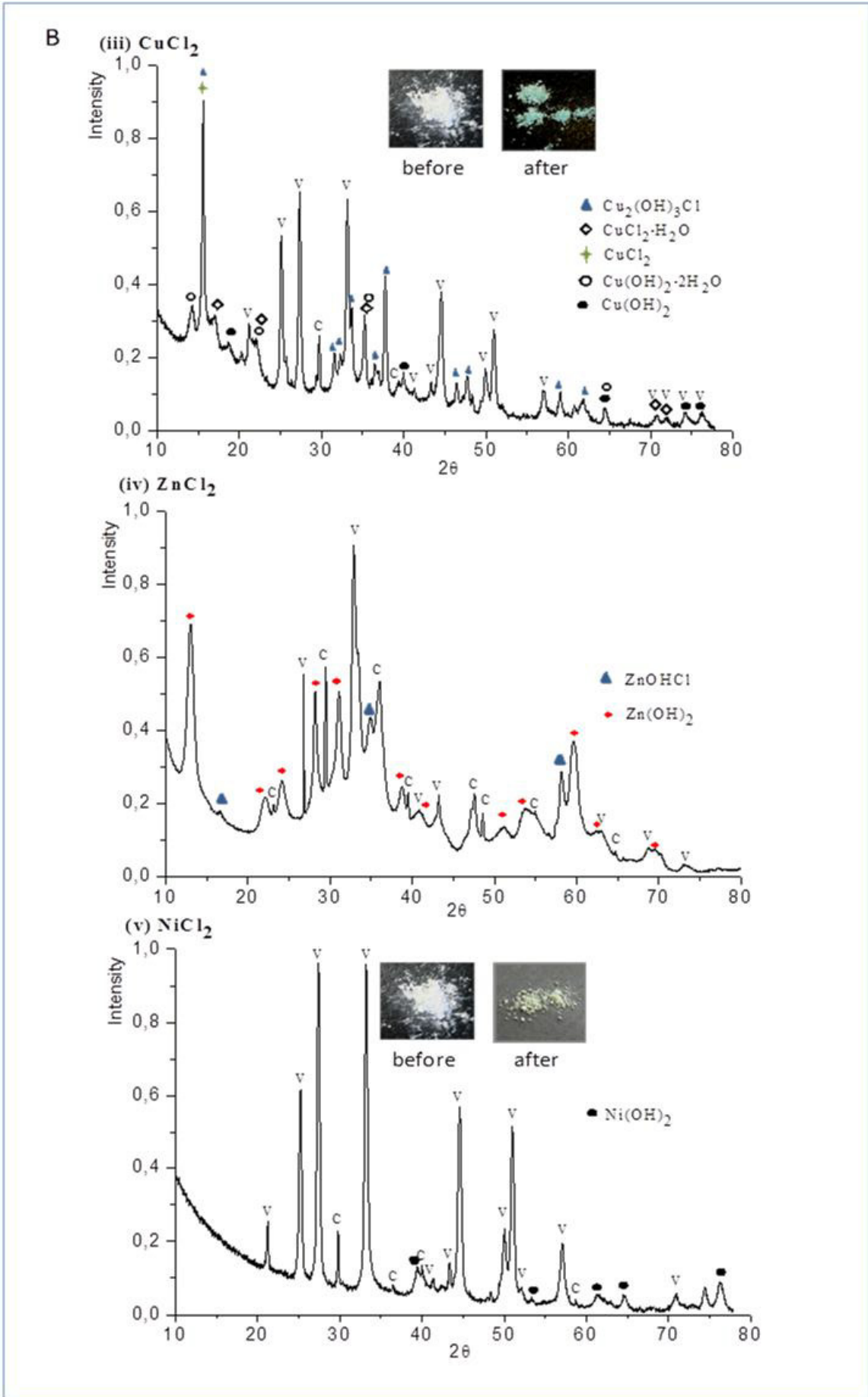
Figure_S3. TGA curve obtained for NV-PEI powder.

A (i) CdCl_2



(ii) HgCl_2





Figure_S4. XRD patterns of the solids obtained after 30 min of the treatment of the NV-PEI material with 400 ppm of initial metal dissolutions: (i) CdCl₂, (ii) HgCl₂, (iii) CuCl₂, (iv) ZnCl₂ and (v) NiCl₂ dissolutions. (A) Metal removing by ion exchange of Ca²⁺ in the CaCO₃ structure, and (B) metal removing by adsorption through interactions between the metallic species with the PEI's nitrogens. (A) The new peaks that arising in addition to corresponding CaCO₃ phases can be associated to the formation of Cd²⁺ (i) and Hg²⁺ (ii) carbonates. The inserts in A-ii correspond to scanning transmission electron microscope (STEM) images recorded to the power after the treatment and its energy dispersive X-ray (EDX). (B) The new peaks that arising in addition to those corresponding to CaCO₃ phases can be associated to the formation of Cu²⁺ chlorides, hydroxides and their hydrated species (iii), Zn²⁺ hydroxide and hydroxide chloride (iv), and Ni²⁺ hydroxide (v). The inserts in B-iii and B-v correspond to photos recorded before and after the treatment. Note: V means vaterite and C calcite.

Table_S1. Some of the properties of the studied heavy metal ions.

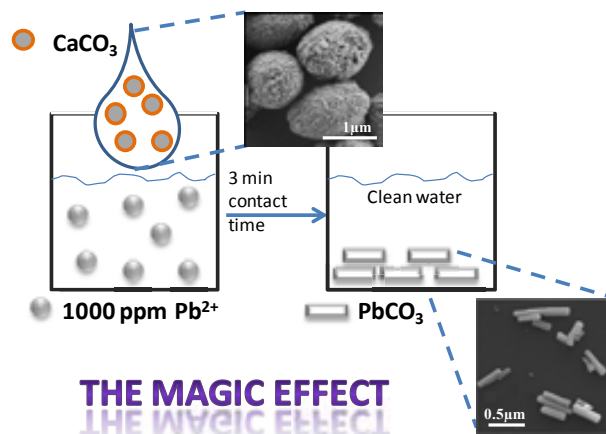
Metallic ions (M ²⁺)	Kps MCO ₃	Kps M(OH) ₂	Ionic Radius (Å)	Electronegativity (Pauling)
Pb ²⁺	7.30 x 10 ⁻¹⁴	1.43 x 10 ⁻¹⁵	1.19	2.33
Cu ²⁺	1.40 x 10 ⁻¹⁰	2.20 x 10 ⁻²⁰	0.73	1.90
Zn ²⁺	1.46 x 10 ⁻¹⁰	3.00 x 10 ⁻¹⁷	0.88	1.65
Hg ²⁺	3.60 x 10 ⁻¹⁷	2.00 x 10 ⁻²⁴	1.02	2.00
Cd ²⁺	1.00 x 10 ⁻¹²	7.20 x 10 ⁻¹⁵	0.99	1.69
Ni ²⁺	1.40 x 10 ⁻¹⁷	5.46 x 10 ⁻¹⁶	0.69	1.91
Ca ²⁺	3.40 x 10 ⁻⁹	5.50 x 10 ⁻⁶	1.10	1.00

Table_S2. Analysis of the properties that favour the removal mechanism by the recrystallization process mediated by ionic exchange. Note: +1 means that the property value favours this process, 0 means that property value is intermediate in relation to the other ones and don't determine an inclination, and -1 means that property value disfavour the ionic exchange process.

Metallic ions (M ²⁺)	Kps MCO ₃	Kps M(OH) ₂	Ionic Radius (Å)	Electronegativity (Pauling)	Total of favoured properties
Pb ²⁺	+1	+1	+1	+1	+4
Cu ²⁺	0	+1	-1	+1	+1
Zn ²⁺	0	+1	0	0	+1
Hg ²⁺	+1	+1	+1	+1	+4
Cd ²⁺	+1	+1	+1	0	+3
Ni ²⁺	+1	+1	-1	+1	+2
Ca ²⁺	reference of comparison				

TOC Figure

Extremely fast and high Pb^{2+} adsorption capacity via use of a hybrid nanostructured vaterite-PEI



Multifunctional system based on hybrid calcite-PEI nanostructured-rods formation, for Pb²⁺ ‘sensoremoval’ applications

By, A. López_Marzo, Josefina Pons, and Arben Merkoçi*

A. López_Marzo
Department of Chemistry,
Universitat Autònoma de Barcelona,
Nanobioelectronics and Biosensors Group,
Catalan Institute of Nanotechnology,
Campus de la UAB ,08193 Bellaterra, Barcelona, Spain

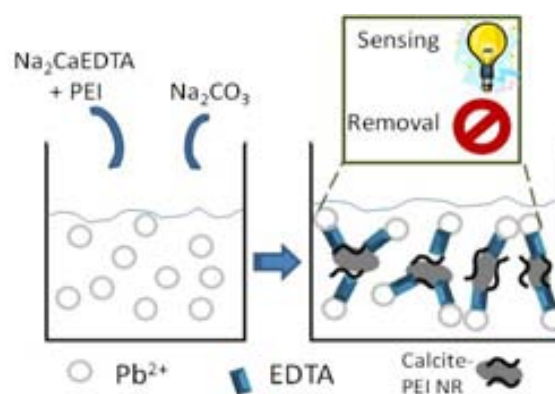
Prof. Dr. J. Pons
Department of Chemistry,
Universitat Autònoma de Barcelona,
08193 Bellaterra, Barcelona, Spain

[*] Prof. Dr. A. Merkoçi
ICREA Research Professor
Nanobioelectronics and Biosensors Group,
Catalan Institute of Nanotechnology.
E-mail: arben.merkoci@icn.cat
www.icn.cat, www.nanobiosensors.org

Keywords: nanostructured rods, calcite-PEI, lead, sensing, removing.

Abstract: A new and simple multifunctional system based on the formation of nanostructured rods (NRs) of hybrid calcite-PEI able to achieve the ‘sensoremoval’ (sensing and removing) of Pb²⁺ in waste waters is presented. When to a

Pb²⁺ contaminated water the solutions of CaNa₂EDTA and CO₃²⁻ are added the crystallization of calcite-PEI NRs, composed of self-assembly hexagonal plate-like shapes of around 450 nm, is obtained. The just formed calcite-PEI NRs in suspension permit the Pb²⁺ detection through a simple turbidimetric measurement, and at the same time act as heavy metal remover. This



sensing and removing system is able to detect up to 1 ppm Pb^{2+} (1-1000 ppm lineal range) and reaches an adsorption capacity of 240 mg Pb^{2+} /g NRs as evaluated using 342 ppm of initial Pb^{2+} concentration at pH 4 after 30 min incubation time. This maximum Pb^{2+} removal capacity reported here is higher than other ones reported before using materials that are not as cheap and biodegradable as calcite. The Pb^{2+} detection range found for this system is suitable to evaluate levels of metal contamination from industrial waste waters that use to be around 1-100 ppm. This system based on an advanced biomaterial constitutes a useful tool as proof-of-concept in the design of future multifunctional platforms for the development of integrated environmental technologies with sensing and remediation functions in a similar way as theranostic systems are doing in health field: combining diagnostic and therapy in the same material.

1. Introduction

Presence of heavy metals in industrial or municipal waste waters requires a previous monitoring and afterward an effective treatment strategy according to the contamination levels for the further use of these waters or their confinable delivery to rivers, lakes, etc, following the permissible limits of contamination statements by the regulatory agencies.^[1, 2]

Although colorimetric,^[3] fluorimetric^[4] and electrochemical^[5,6] techniques have been developed for heavy metal detection inductively coupled plasma (ICP)^[7] and atomic absorption spectroscopy (AAS)^[8] continue to be the main techniques used for metal determination, in spite of these methods are expensive and require a trained personnel.^[9, 10]

On the other hand, the most known methods used to remove heavy metal ions, are the chemical precipitation of metal hydroxides at high pH, ion-exchange with zeolites, adsorption, membrane filtration, and electro-chemical treatment technology. Especially adsorption is an effective and economic method for heavy metal wastewater treatment. Although activated carbon is the most used adsorbent, it is relatively expensive. Many researchers have tried to

find low-cost and easily available adsorbents to remove heavy metal ions, for examples, agricultural wastes composed mainly of cellulose fibers, plant wastes, zeolites, and clays.^[1, 2, 11, 12]

Advances in nanoscale science and engineering are providing new opportunities to develop more cost-effective and environmentally acceptable water purification processes through the use of nanomaterials. Nanomaterials have several physicochemical properties that make them particularly attractive for water purification such as higher surface area per unit volume and the ability to be functionalized with a number of surfactants to enhance their affinity toward target molecules. Many different nanoscale materials such as nanoscale zeolites, metal oxides, carbon nanotubes and fibers, enzymes, various noble metals (mainly as bimetallic nanoparticles) and titanium dioxide have been explored for water remediation. Nanomaterials from transition metal hydroxides or oxides, especially iron, are extensively studied for monitoring, remediation and water pollution prevention. In the last ten years biominerals as CaCO_3 have been added to the list of potential water treatment nanomaterials.^[13-17]

Calcium carbonate is one of the most important and cheapest biomineral in nature. Many organisms produce calcium carbonate with unique hierarchical structures and fascinating characters in their tissues for a variety of functions. Calcium carbonate has ideal biocompatibility and biodegradability properties. Several studies have demonstrated continuous interest to CaCO_3 crystallization.^[18-26] Although calcium carbonate has been studied for removal of heavy metal ions, the low efficiency and further treatment necessity, significantly limit the practical applications in water treatment. Considerable research has been focused on using hierarchical structures of hybrid CaCO_3 -organic materials as adsorbent for removal of heavy metal ions.^[11, 18, 27-30]

The development of materials, systems, devices or methods that integrate several process steps in one multifunctional step for clinical, environmental or industrial proposal constitutes a challenge for many ongoing researches. Multifunctional integrated materials and systems

permit to manage with more rapidity and efficiency the whole process saving resources and time in obtaining of the desired results. Advanced multifunctional materials and systems with medical interest have been matter of several works, but with respect to environmental applications these are more reduced.^[31-37]

Here an original and complete multifunctional system for sensing and removing (*'sensoremoval'*) of Pb^{2+} as proof-of-concept strategy with interest for environment is shown. This sensing and removing system is based on hybrid calcite-PEI NRs formation in Pb^{2+} contaminated waters followed by the subsequent detection and removal of the heavy metal contaminant thanks to the in situ NRs formation. Three components, Pb^{2+} ions or other contaminant metal ions to be removed, Na_2CaEDTA complex and carbonate ions are mixed and subsequently the metal-EDTA complexation and the CaCO_3 precipitation take place. A study of this CaCO_3 crystallization through changes in the reaction conditions such as the use or not of CGMs as PEI, glycerol and diethanolamine (DEA), the reagent order, the solvents reaction, the reagent volume, etc., is presented. Decreasing dramatically the reagents concentration for first time perfect hexagonal plates were found for calcite polymorph. A simple Pb^{2+} sensing based on the turbidity caused during the CaCO_3 precipitation, reaching 1 ppm of detection limit and a lineal response range between 1 and 1000 ppm is obtained when PEI is used as CGM. This detection range is suitable to evaluate levels of metals contamination in industrial waste waters that use to be around 1-100 ppm. Once CaCO_3 NRs are formed the heavy metal removal takes place by adsorption of the EDTA-metal onto their surface. The maximum adsorption capacity for an initial metal contamination of 342 ppm is 240 mg Pb/g NRs for 30 min of treatment time using CaCO_3 -PEI NRs at pH 4. This Pb^{2+} removal capacity reported here is higher than other ones reported before using materials which are not so cheap and environmental friendly as calcite.^[1,15,38,39] The introduced calcite NRs formation system can be easily applicated for fast control and remediation of heavy metals in case of accidents where urgent in-field measurements and remediation are necessary.

It represents a low cost alternative for heavy metals detection and removing. In addition the developed system, that constitutes a novel approach to integrate the detection and removal of chemical contaminants in one step process (*sensoremoval concept*), may open the way to several other simple and efficient systems, materials or methods for environment applications.

2. Results and Discussion

2.1 Multifunctional integrated sensoremoval system

The synthesis of CaCO_3 NRs using as reagents equal volumes and concentrations of an initial contaminated solution of Pb^{2+} , Na_2CaEDTA and Na_2CO_3 permitted to create a multifunctional system that integrates the formation of CaCO_3 NRs for its afterwards use in the detection and removal of the Pb^{2+} in the initial contaminated solution. The reaction of the CaCO_3 formation and a schematic representation of this system operation are displayed in **figure 1**. When into a Pb^{2+} dissolution are poured the Na_2CaEDTA and Na_2CO_3 dissolutions, the Pb^{2+} cations preferentially bind to EDTA ligand releasing Ca^{2+} cations able to react with CO_3^{2-} anions starting in this way the CaCO_3 precipitation. The possible collateral reaction in this system could be the formation of PbCO_3 precipitate, because the PbCO_3 K_{ps} (3.3×10^{-14}) is smaller than CaCO_3 K_{ps} (3.3×10^{-9}), but given that the Pb-EDTA complex formation constant (1×10^{18}) is higher than Ca-EDTA constant (5×10^{10}) all the Pb^{2+} ions form the complex with the EDTA, being the CaCO_3 the only precipitation product. The XRD patterns corresponding to all crystallization products obtained with different reaction conditions demonstrate that calcite is the unique precipitation product. Figure S_1A at SI shows an example of calcite XRD patterns that were obtained in all cases. While in figure S_1B the XRD pattern obtained from the aqueous medium of the reaction is presented. The peaks in this powder pattern corresponding with those indexed for $\text{Na}_2\text{PbEDTA} \cdot 2\text{H}_2\text{O}$ complex that has been reported in the CSD.⁴⁰

2.2. Characterization of the CaCO_3 crystallization product in the proposed system.

Morphologic analysis demonstrated that NRs-like structures form the crystallization product (**figure 2 A and B**). Although NRs-like shape has been synthesized before, ^[20, 21] it still represents an unusual morphology in the CaCO₃ crystallization product. Usually the calcite polymorph can crystallize in rhombohedral shape, while vaterite polymorph usually aggregate into spherical particles. Other polymorphic shapes use to be difficult to be obtained, offering few repeatability and high susceptibility to changes in the reaction conditions. However, these calcite NRs with sizes of around 2, 1 or 0.6 μm, depending on the type of reaction, were permanently synthesized changing the reagents order, using or not CGMs as PEI, DEA or glycerol, modifying the solvent used as reaction medium (ethanol, ethylacetate, etc), the use of Ca(NO₃)₂ instead of CaCl₂ or decreasing the reaction volumes. All these large variety of changes in the reaction conditions only affect the size or the surface texture of the NRs or as much the shape at the ends of the NRs, but the main rod shape continually persists in the crystallization product (figure_S2 at SI). The persistent formation of structures with rods-like shape in spite of the changes applied in the reaction conditions is ascribed to the fact that, Na₂CaEDTA in addition to be the reagent that supplies the Ca²⁺ cations is also the CGM that determines the crystallization process due to its high concentration in the system.

Nevertheless, a dramatic decreasing in the concentration of the reagents used in this reaction system produces large morphological changes with reduction of the size and variation of shape in the structures. A large decreasing in the reagents concentration guides to the small elemental structures that are making of the rods, which is related with the fact that at low concentrations there is not enough mass to favour their extensive growth. In this way, the formed precipitate can pass from rods-like structures, of around 2, 1 or 0.6 μm length and 350-450 nm width using 3.3x10⁻¹ M of reagents concentration, (figure 2, A-D) to perfect size and homogeneous calcite hexagonal nanoplates of around 450-550 nm length and 50-70 nm width (figure 2 E and G) or heterogeneous calcite nanoplates of around 150-250 nm length and 20-40 nm width (figure 2 F and H) using 3.3x10⁻⁴ M of reagents concentration. These

results suggest that the initial NRs synthesized using 3.3×10^{-1} M of reagents are obtained as consequence of a self assembly process of hexagonal or irregular plate-like nanoparticles.

More detailed information of the hexagonal plates is provided by figure 2 I-K with the SAED, TEM and HRTEM analysis. The figure 2I displays the SAED corresponding to the selected area taken from the single hexagonal plate that is shown in figure 2J. Reflections A, B, C, D and E correspond to Miller indices and measured d spacing of (1 -2 0), (2.54 Å^o), (-1 -1 0) (2.51 Å^o), (-2 1 0) (2.49 Å^o), (-1 2 0) (2.53 Å^o) and (0 -3 0) (1.45 Å^o) respectively; measured interplanar angles: A[^]B=60.0°, A[^]C=119.35°, A[^]D=179.35°. This ED pattern can be indexed as calcite single crystal (R-3c space group) viewed from the [001] zone axis. The corresponding HRTEM image (figure 2-K) is mainly composed of (1 1 0) plane of calcite with d spacing of about 0.25 nm indicating that the nanoparticles are formed along the (1 1 0) direction. The arrows in figure 2K show the formation of amorphous CaCO₃ nanoparticles indicating that our calcite hexagonal plates are in fact mesocrystal. These hexagonal plates-like structures have been reported before for vaterite polymorph [18, 22, 24, 25] but for first time perfect hexagonal plates are observed in calcite phase.

A possible explanation for the entire crystallization process that happens here is to consider that the proposed reactions constitute a self-reagent-delivery system, because while Ca²⁺ cations are being displaced by Pb²⁺ cations in the Na₂CaEDTA complex, the CO₃²⁻ anions are being added forming the first CaCO₃ nucleation centers. In the initial stages of crystallization when Ca²⁺ ions are being delivered by Pb²⁺ ions in the Na₂CaEDTA complex, a Ca-Na₂EDTA-Pb unstable intermediate complex, which keeps associated Ca²⁺ to Na₂PbEDTA as a first nucleation center for further addition of CO₃²⁻ anions, could appear (figure_S3-A). Once the Na₂PbEDTA complex is formed the Ca²⁺ can interact with the nucleophilic carboxylic acid groups of Na₂PbEDTA creating several local CaCO₃ nucleation centers by Ca²⁺ local supersaturation (figure_S3-B1). Several CaCO₃ nucleation clusters lead to the formation of the primary CaCO₃ nanoparticles. At this moment the primary plate-like crystals

start growing by aggregation of the nearly CaCO_3 nanoparticles in a preferential y -axis (figure_S3-C1). These primary plates-like crystals are temporally stabilized by metal-organic coating layer (Na_2PbEDTA). This stabilizer acts as building blocks in a spontaneous self-assembling process into preferential x -axis. Several plate-like crystals grow in a self-assembly process of multiple plates propitiated by the interaction with the carboxyl acid groups of Na_2PbEDTA that could be preferentially adsorbed onto the growing crystal surfaces parallel to y -axis and grow along x -axis crystallographic direction during the crystallographic process, resulting in a rod-like primary crystal (figure_S3-D1). The figure_S3-E1 shows a close up of the NRs surface obtained without PEI that suggests, that microrods are composed by assemble of thin nanostructures (20-40 nm) like-plate along the x axis.

J. Yu et *al.* explained microrods formation shape taking into account the rate of nucleation and growth through certain direction. They explained that when the rate of nucleation and growth if preferentially directed along the rod axes at the side-surfaces the rod-like shape is formed.^[20]

If PEI is added to initial Na_2CaEDTA reagent solution, the effect of formation of the local nucleation centers by Ca^{2+} supersaturation is increased. Under PEI presence when Ca^{2+} is delivered by Pb^{2+} from the Na_2CaEDTA complex, it is bound by the nucleophilic nitrogen (or cations captor nitrogen) of the amino group of PEI polymer, which creates additional nucleation centers of those created by Na_2PbEDTA (figure_S3-B2). Consequently, more CaCO_3 nanoparticles appear with the subsequence directional aggregation in primary hexagonal plate crystals (figure_S3-C2). Differently with the Na_2PbEDTA stabilizer, the PEI coating layer persists onto the surface of the primary hexagonal plate crystals, allowing better organization during the self-assemble of these small primary nanocrystals through a more oriented-attachment mechanism, in which the adjacent nanocrystals are self-assembled sharing a common crystallographic orientation process (figure_S3-D2). The final result is a more ordered structure with high porous surface than without PEI (figure-2 C). The

figure_S3-E2 shows a close up of the NRs surface obtained with PEI that suggests, that microrods are composed by assemble of thin nanostructures (50-70 nm) like- hexagonal plate along the x axis. The presence of PEI in the CaCO_3 structure was demonstrated in the thermogravimetric analysis plotted in figure_S4 at SI. The weight loss of about 3% that appears in the temperature range of 250-350 °C corresponds to PEI delivery from CaCO_3 structure and therefore that the CaCO_3 -PEI hybrid material has been synthesized.

In general, it seems that the use of Na_2CaEDTA and the delivering of Ca^{2+} ions through Pb^{2+} ions are determining the shape of the calcite product in the majority of the reactions. While few works have already reported the use of EDTA in the CaCO_3 crystallization process and in these cases the EDTA is used only as CGM,⁴¹ it is the first time that EDTA is also used as Ca^{2+} reagent-delivery through Pb^{2+} and Na_2CaEDTA solutions.

2.3. Pb^{2+} sensing by changes of turbidity during the calcite precipitation.

The Pb^{2+} concentration can be detected through the turbidity produced during calcite precipitation. In the described system Pb^{2+} cations present in the dissolution displace the Ca^{2+} cations from its Na_2CaEDTA complex and in consequence these Ca^{2+} cations remain free to bind with the CO_3^{2-} anions. A quantitative relation $1\text{Pb}^{2+}:1\text{Ca}^{2+}$, between each Ca^{2+} cation that form CaCO_3 precipitate and each Pb^{2+} cation that remains bound with EDTA, can be established. In this way the CaCO_3 turbidity can be related with the Pb^{2+} concentration when there is not other metal present in the system.

Between the assayed systems only adding PEI to the previous Na_2CaEDTA solution to obtain calcite NRs, a visible turbidity produced by calcite precipitation, is reached up to around 34 ppm of Pb^{2+} mixing 1.6×10^{-4} M of reagents concentration. While without or with the use of other CGMs a visible turbidity is reached until around 68 ppm of Pb^{2+} mixing 3.3×10^{-4} M of reagents concentration. It suggests that the use of PEI notably increases the CaCO_3 precipitation which gives more sensibility for Pb^{2+} detection. **Figure 3A** shows photos of the suspensions formed by CaCO_3 precipitation obtained for different Pb^{2+} concentrations using

PEI as modifier agent. An estimation of Pb^{2+} concentration even at naked eye can be made by turbidity observation until 34 ppm.

Photos of the turbidity produced by CaCO_3 precipitation, when the reagents concentration decreases, are shown in Figure_S5. The turbidity produced by decreasing the reagent concentration was evaluated making comparison tests with the traditional CaCO_3 precipitation reaction and the proposed CaCO_3 precipitation system with and without PEI use. The turbidity was observed by naked eye until 3.3×10^{-3} M of the reagents concentrations (that correspond to 684 ppm of Pb^{2+}) when simple CaCl_2 and NaCO_3 solutions are mixed (figure_S5-A). When PEI is present in the initial CaCl_2 solution the observed turbidity at 3.3×10^{-3} M is more significant than in the previous case (without PEI in the initial CaCl_2 solution) and can be observed by naked eye until around 342 ppm of Pb^{2+} (figure_S5-B). When the reaction to obtain CaCO_3 precipitate is the system based in the mixture of $\text{Pb}(\text{NO}_3)_2$, Na_2CaEDTA and Na_2CO_3 , then the visual CaCO_3 turbidity reaches 3.3×10^{-4} M in reagents concentration (that correspond to around 68 ppm of Pb^{2+}) (figure_S5-C). Using this same system when PEI is present in the Na_2CaEDTA solution the observed turbidity is more marked at 3.3×10^{-4} M than in the previous case, reaching visibility by naked eye until 1.6×10^{-4} M in reagents concentration (that corresponds to 34 ppm of Pb^{2+}) (figure_S5-D).

The CaCO_3 -PEI NRs formation in presence of Pb^{2+} concentration inferior to 34 ppm can be detected by use of a turbidimeter. In the figure 3B the calibration curve between the Pb^{2+} concentration and the CaCO_3 turbidity is presented. The lineal range from 1 to 1000 ppm is obtained, being 1 ppm the lowest Pb^{2+} concentration detected by CaCO_3 formation over the measured signal blank. A mixture of the Na_2CaEDTA and $\text{Pb}(\text{NO}_3)_2$ disolutions (1 ppm) whose turbidity response was similar to the Milli-Q water was used as blank. The lowest Pb^{2+} concentration detected by CaCO_3 turbidity formation depend on the characteristic turbidimeter and the concentrations of Ca^{2+} and CO_3^{2-} in the aqueous phase of the studied system. The insert in the figure 3B shows the graphic obtained during the accuracy assay

plotting the spiked vs. calculated concentrations. The slope and the intercept values of the fitting curve are not significantly different from theoretical values of 1 and 0, respectively. It means that the spiked and calculated concentrations are very close to each other and the recovery is almost 100% in the concentration interval from 2 to 150 ppm.

2.4 Pb²⁺ removal via CaCO₃-PEI NRs.

After the CaCO₃-PEI NRs formation, the initial Pb²⁺ cations in the contaminated solution remain as Na₂PbEDTA complex. This transformation of Pb²⁺ cations into Na₂PbEDTA complex, although becomes harmless the Pb²⁺ contaminant, makes difficult the Pb²⁺ removal due to the high stability constant between the Pb²⁺ and EDTA ligand, so that, the contaminant would have to be removed as Na₂PbEDTA complex. In this situation the type of CGM used in the crystallization process, which covers the NRs surface, plays an important role in the removal process. The adsorption rate experiments carried out demonstrate that the best Pb²⁺ removal capacity was obtained using CaCO₃-PEI NRs in comparison to those obtained under the same conditions but using NRs synthesized without CGM or using CGMs as glycerol or DEA (**figure 4A**). Figure 4A shows that the maximum adsorption capacity of an initial Na₂PbEDTA dissolution of 342 ppm at pH 4 for CaCO₃-PEI, CaCO₃-glycerol, CaCO₃-DEA and CaCO₃ NRs is respectively of 240, 126, 120 and 70 mg/g and that 30 min are enough to reach the maximum removal capacity in all the cases. The maximum adsorption capacity of 240 mg Pb/g CaCO₃-PEI NRs is higher than other ones previously reported.^[1, 15, 38, 39] The experiments demonstrate that when the removal process is carried out at pH 6, the adsorption capacity decreases in relation to that achieved at pH 4, as is shown in figure 4A with the curves labelled with the blue circle. Experiments (not shown here) demonstrated that initial concentrations of 2, 27, 54 and 137 ppm are almost declined to 0 in 30 min at pH 4 under the experimental condition used here. The Pb²⁺ removal process takes place just at superficial level due to the fact that the EDTA binds to Pb²⁺ keeping it trapped in a complex. The complex formation between Pb²⁺ and EDTA avoids substitutions of Ca²⁺ in the calcite

structure by Pb^{2+} cations in a new recrystallization process as occurs in other reported works where Pb^{2+} is directly removed using other CaCO_3 materials. [11,18] In figure _S6 images SEM recorded after 48 h of the Pb^{2+} removal process indicate that the morphology of calcite NRs remain stable. The close up shows a closer image of the NRs surface after the removal treatment.

The better removal of Na_2PbEDTA complex using calcite NRs modified with PEI with respect to the other NRs synthesized here is related with two factors. First, the NR surface obtained using PEI is more porous in relation to NR surface obtained without PEI presence (as seen in figure 2_C y D), which increases the contact surface for the adsorption/removal process. Second, PEI is a branched polymer that contains large numbers of amino groups that present basic nitrogens atoms that act as hydrogens captors which are expected to undertake interactions with the hydroxylic groups of the Na_2PbEDTA complex through hydrogen bonds formation. When the medium is more acidic these hydrogen bond interactions are intensified by the protonation of some PEI nitrogens or the carboxylic oxygens in the Na_2PbEDTA arising new hydrogen bonds. These new hydrogen bonds are produced by the interaction between the protonated carboxylic oxygen ($=\text{OH}^+$) with the nitrogen amino in PEI or by the interaction between the protonated nitrogen in amino PEI ($-\text{NH}_3^+$) with the carboxylic oxygens in Na_2PbEDTA (**figure 5**). This explains the better removal that occurs at pH 4 than pH 6, because at acid pH the hydrogen bond interactions between Na_2PbEDTA and PEI are increased. In figure 4B, the XRD pattern of the calcite powder after being used in the Pb^{2+} removal process can be seen. The raised peaks at 21.7, 25.0, 27.4 and 30.2° can be associated with peaks in the Na_2PbEDTA powder XRD pattern, which suggests that Na_2PbEDTA complex is adsorbed onto calcite-PEI NRs surface.

The multifunctional integrated system described here could be easily extended to other contaminated solutions with heavy metals (that have EDTA complex formation constant higher than Ca^{2+} such as Cd^{2+} , Hg^{2+} , Ni^{2+} , Zn^{2+} and Cu^{2+}) having only one metal contaminant,

by synthesizing new advanced CaCO₃ materials with more complex crystalline structure and their further use as sensoremoval platforms. As this sensoremoval system is not specific, in the case of a multi-metal contamination the turbidity by CaCO₃ precipitation could be correlated with the total metal concentration.

The sensing and removal capability of this novel nanostructured platform could lead to the next generation of environment 'sensoremoval' systems in the same way as in health applications, theranostic joins in the same platform diagnostic and therapy offering new opportunities in patient treatment. The introduction of this low cost and efficient alternative as 'sensoremoval' system may be useful for fast control and remediation of pollution where urgent in-field monitoring and immediate remediations are necessary.

3. Conclusions

A new and simple strategy based on calcite NRs formation for *sensoremoval* (sensing and removing) of Pb²⁺ from waste water is presented. We propose a novel multifunctional system that integrates three process, the *in situ* formation of the CaCO₃ NRs from Pb²⁺ contaminated initial solution, Na₂CaEDTA complex and CO₃²⁻ anions, followed by the utilization of the as-synthesized particles as sensing and adsorbing material of Pb²⁺. To the best of our knowledge, for the first time the detection and removing of chemical contaminant are integrated in the same material.

By decreasing the reagents concentration homogeneous and perfect hexagonal plates for calcite, never reported so far, were obtained for this polymorphic phase.

With the simple Pb²⁺ sensing strategy introduced here, via changes in turbidity during the CaCO₃ precipitation, until 34 ppm of Pb²⁺ can be estimated by naked eye and a concentration range from 1 to 1000 ppm can be quantified using a turbidimeter. This quantification range is suitable to evaluate levels of metals contamination in industrial waste waters that use to be around 1-100 ppm. On the other hand, in adsorption kinetic studies for calcite-PEI NRs, also without precedents, the maximum adsorption capacity reached in 30 min at pH 4 was 240 mg

Pb^{2+} /g of NRs obtained using PEI. The maximum removal capacity reported here for Pb^{2+} is higher than other reported before using materials which are not so cheap and environmental friendly as calcite.

It is important to highlight that the PEI used as CGM allowed to improve the Pb^{2+} LoD by increasing of the CaCO_3 precipitation and the turbidity produced during this precipitation, as well as, permitted to achieve better Na_2PbEDTA adsorption and removal through the obtaining of more porous NRs surface. In addition PEI enhances the removal process offering the appropriate chemical modification onto the NR surface to favour the interaction of this with the Na_2PbEDTA complex by via of hydrogen bond formation.

4. Experimental

4.1 Chemicals

All chemical reagents (analytical grade) were purchased from Sigma Aldrich and used as received. Poly(ethyleneimine) solution in H_2O (50% w/v) ($M_w=750\ 000$, $M_n=60\ 000$), diethanolamine (DEA, $\text{NH}(\text{CH}_2\text{CH}_2\text{OH})_2$) (98%), glycerol (99%) and anhydrous ethylenediaminetetraacetic acid (H_4EDTA) (99%) were used. Milli-Q water ($18.2\ \Omega\text{-cm}$ at 25°C) was obtained from Advantage Milli-Q apparatus (Millipore). All glass material were soaked with aqua regia for 3 h, rinsed with distilled water and dried before use.

4.2 Characterization techniques

The syntheses were carried out using an Ultrasons J. P. Selecta 45 ultrasonic bath. Scanning electron microscope (SEM) images were taken with ZEISS Merlin and Quanta 650FEG scanning electron microscopes. A water dispersion of samples ($150\ \mu\text{L}$) was deposited on glass support and dried at room temperature. Colloidal silver solution was deposited on the edges of the glass for the sample examination. High resolution SEM images were recorded depositing samples on silica support and gold sputtering during 1 min. High resolution transmission electron microscopy (HRTEM) images and the selected-area electron diffraction (SAED) patterns were obtained on TECNAI-F20 microscope with an accelerating voltage of

200 kV. Sample grids were prepared by sonicating powdered samples in milli-Q water for 20 s and evaporating one drop of the suspension onto a carbon-coated holey film supported on a copper grid for TEM measurements. For resolve the SAED patterns Gatan Digital Micrograph and CaRine crystallography programs were used.

X-ray diffraction (XRD) studies of CaCO_3 were recorded using a Siemens D-5000 X-ray diffractometer with $\text{Cu K}\alpha$ radiation, scanning rate of $0.02^\circ/\text{s}$ and 2θ range from 10 to 70° at 40 kV and 40 mA. The phase identification was done by comparing the XRD patterns of the crystals with the standard data available from Joint Committee on Powder Diffraction Standards (JCPDS) and Cambridge Structural Database (CSD). The CaCO_3 turbidity measurements were performed on 2100N turbidimeter. The concentration of Pb^{2+} ions in the aqueous solution was analyzed by using an inductively coupled plasma mass spectrometry (ICP-MS) Agilent 7500ce model system. The thermogravimetric analysis (TGA) was conducted by a TGA7 Perkin-Elmer with argon flow rate of 20 mL/min and a heating rate of $10^\circ\text{C}/\text{min}$.

4.3 Calcite formation and Pb^{2+} sensing

In a general procedure to obtain CaCO_3 NRs, 5 mL of CaNa_2EDTA (3.3×10^{-1} M) were quickly poured into equal volume of $\text{Pb}(\text{NO}_3)_2$ dissolution (3.3×10^{-1} M) under sonication, before to end this addition was added the Na_2CO_3 dissolution (3.3×10^{-1} M). The reaction vessel was capped and the reaction left for 15 min. The solid obtained was washed three times with milli-Q water through a centrifugation process, air dried and collected for further analysis. The supernatant after the first solid centrifugation was collected, dried, following washed quickly with cool water and dried again. This product that contains the Pb -EDTA synthesized complex was used for further XRD analysis. In other assays to obtain the CaCO_3 NRs, dissolutions of CaNa_2EDTA (3.3×10^{-1} M) prepared with PEI, glycerol or DEA (4 mg/mL) as CGM, were used. The CaNa_2EDTA was prepared by reaction of Na_3HEDTA (4×10^{-1} M) with CaCl_2 (3.3×10^{-1} M). The Na_3HEDTA was previously obtained mixing 1.3 M

NaOH with 0.4 M H₄EDTA anhydride. The identification of the Na₃HEDTA and CaNa₂EDTA complexes was realized comparing its XRD patterns obtained experimentally with those corresponding in the CSD.

For obtaining the calibration curve used for Pb²⁺ sensing by turbidity measurement, different suspensions of calcite precipitation were prepared for each point of the curve. Dissolutions of the three reagent components Pb(NO₃)₂, CaNa₂EDTA and Na₂CO₃ in a range of 1 to 1300 ppm) were mixed at the equal volume and concentration for each calcite precipitation suspension. To evaluate the accuracy of this Pb²⁺ sensing method a spike-and-recovery experiment was performed. A known amount of Pb²⁺ is added to the Pb(NO₃)₂ dissolution that is used to produce CaCO₃ turbidity as described before. The chosen spike concentration range was between 2 and 150 ppm (the low concentrations of the calibration curve). The recovery percent are determinate using the Pb²⁺ concentration obtained through the turbidity calibration curve (calculated) and the prepared known concentration (spike) by the equation:

$$\frac{\text{calculated concentration}}{\text{spike concentration}} \times 100\% = \text{recovery (\%)}$$

4.4 Pb²⁺ removal

Adsorption kinetic experiments were carried out to evaluate the Pb²⁺ removal. The CaCO₃ NRs (25 mg) obtained under different conditions were suspended in Na₂PbEDTA solutions (50 mL) with different concentrations (1, 27, 54, 137, 342 ppm) at pH 4 or 6 and stirred during 48 h. Aqueous samples (500 μL) were taken at several time intervals and the concentrations of Pb²⁺ ions were measured by ICP-MS. The amount of Pb²⁺ adsorption onto NRs surface at time interval t, q_t (mg/g), was calculated by:

$$q_t = \frac{(C_0 - C_t)}{W} V$$

where C₀ and C_t (mg/L) are the concentrations of Pb-EDTA in liquid phase at initial and any time interval t, respectively, V is the volume of the solution (L) and W is the mass of calcite used as adsorbent (g).

Acknowledgements

MICINN (Spain) for Spain-Japan International Bilateral PIB2010JP-00278 projects is acknowledged. Authors thank Belén Ballesteros and Marcos Rosado for the fruitful collaboration. A. Lopez-Marzo thanks to Generalitat of Catalunya for the FI-2010 scholarship given.

- [1] W. Yantasee, R. D. Rutledge, W. Chouyyok, V. Sukwarotwat, G. Orr, C. L. Warner, M. G. Warner, G. E. Fryxell, R. J. Wiacek, Ch. Timchalk, R. Sh. Addleman. *ACS Appl. Mater. Interfaces* **2010**, *2*, 2749.
- [2] A. Guijarro-Aldaco, V. Hernández-Montoya, A. Bonilla-Petriciolet, M. A. Montes-Morán, D. I. Mendoza-Castillo, *Ind. Eng. Chem. Res.* **2011**, *50*, 9354.
- [3] J. Du, Y. Sun, L. Jiang, X. Cao, D. Qi, S. Yin, J. Ma, C. F. Y Boey, X. Chen, *Small* **2011**, *7*, 1407.
- [4] Ch. Zong, K. Ai, G. Zhang, H. Li, L. Lu, *Anal. Chem.* **2011**, *83*, 3126.
- [5] G. Aragay, A. Puig-Font, M. Cadevall, A. Merkoçi, *J. Phys. Chem. C* **2010**, *114*, 9049.
- [6] G. Aragay, J. Pons, A. Merkoçi, *J. Mater. Chem.* **2011**, *21*, 4326.
- [7] T.-Y. Hoa, Ch.-T. Chiena, B.-N. Wanga, A. Siriraks, *Talanta* **2010**, *82*, 1478.
- [8] J. Gasparik, D. Vladarova, M. Capcarova, P. Smehyl, J. Slamecka, P. Garaj, R. Stawarz, P. Massanyi, *J. Environ. Sci. Health A* **2010**, *45*, 818.
- [9] G. Aragay, J. Pons, A. Merkoçi, *Chem. Rev.* **2011**, *111*, 3433.
- [10] G. Aragay, A. Merkoçi, *Electrochim. Acta* **2012**, *84*, 49.
- [11] K.-S. Hong, H. M. Lee, J. S. Bae, M. G. Ha, J. S. Jin, T. E. Hong, J. P. Kim, E. D. Jeong, *J. Anal. Sci. Technol.* **2011**, *2*, 75.
- [12] F. Mou, J. Guan, H. Ma, L. Xu, W. Shi, *ACS Appl. Mater. Interfaces*, **2012**, *4*, 3987.
- [13] B. Karn, T. Kuiken, M. Otto, *Environ. Health Perspectives* **2009**, *117*, 1823.
- [14] I. Ojea-Jiménez, X. López, J. Arbiol, V. Puentes. *ACS NANO*, **2012**, *6*, 2253.

- [15] B. Wang, H. Wu, L. Yu, R. Xu, T.-T. Lim, X. W. Lou, *Adv. Mater.* **2012**, *24*, 1111.
- [16] S.-W. Cao, Y.-J. Zhu, *J. Phys. Chem. C* **2008**, *112*, 6253.
- [17] Z. Wei, R. Xing, X. Zhang, S. Liu, H. Yu, P. Li, *ACS Appl. Mater. Interfaces* **2013**, *5*, 598.
- [18] X. Ma, L. Li, L. Yang, C. Su, K. Wang, Sh. Yuan, J. Zhou, *J. Hazard. Mater.* **2012**, *209–210*, 467.
- [19] Ch. Li, L. Qi, *Angew. Chem., Int. Ed.* **2008**, *47*, 2388.
- [20] J. Yu, X. Zhao, B. Cheng, Q. Zhang, *J. Solid State* **2005**, *178*, 861.
- [21] J. Yu, M. Lei, B. Cheng, X. Zhao, *J. Solid State* **2004**, *177*, 681.
- [22] A.-W. Xu, M. Antonietti, H. Cölfen, Y.-P. Fang, *Adv. Funct. Mater.* **2006**, *16*, 903.
- [23] A. López-Marzo, J. Pons, A. Merkoçi, *J. Mater Chem.* **2012**, *22*, 15326.
- [24] J. Xiao, Y. Zhu, Y. Liu, H. Liu, Y. Zeng, F. Xu, L. Wang, *Cryst. Growth Des.* **2008**, *8*, 2887.
- [25] J. Ahmed, M. A. Ganguli, K. Ganguli, *CrystEngComm*, **2009**, *11*, 927.
- [26] S. Kim, Ch. B. Park, *Adv. Funct. Mater.* **2013**, *23*, 10.
- [27] M. Lee, I. S. Paik, I. Kima, H. Kang, S. Lee, *J. Hazard. Mater.* **2007**, *144*, 2084.
- [28] Y. Ma, Ch. Lin, Y. Jiang, W. Lu, Ch. Si, Y. Liu, *J. Hazard. Mater.* **2009**, *172*, 1288.
- [29] X. Man, L. Li, L. Yang, C. Su, K. Wang, K. Jiang, *J. Cryst. Growth* **2012**, *338*, 272.
- [30] G. B. Cai, G.X. Zhao, X.K. Wang, S.H. Yu, *J. Phys. Chem. C*, **2010**, *114*, 12948.
- [31] O. Yavuz, R. Guzel, F. Aydin, I. Tegin, R. Ziyadanogullari, *Pol. J. Environ. Stud.* **2007**, *16*, 467.
- [32] J. Zhang, F. Laiwalla, J. A. Kim, H. Urabe, R. V. Wagenen, Y.-K. Song, B. W. Connors, F. Zhang, K. Deisseroth, A. V. Nurmikko, *J. Neural Eng.* **2009**, *6*, 055007.
- [33] A. Adami, C., C., S. Pedrotti, L. Lorenzelli, *Biosens. Bioelectron.* **2013**, *40*, 315.
- [34] M. Zhou, N. Zhou, F. Kuralay, J. R. Windmiller, S. Parkhomovsky, G. Valdés-Ramírez, E. Katz, J. Wang, *Angew. Chem., Int. Ed.* **2012**, *51*, 2686.

- [35] F. Khan, J. O. Smith, J. M. Kanczler, R. S. Tare, R. O. C. Oreffo, M Bradley, *Adv. Funct. Mater.* **2013**, DOI: 10.1002/adfm.201202710ark.
- [36] S. Wang, G. Kim, Y. E. K. Lee, H. J. Hah, M. Ethirajan, R. K. Pandey, R. Kopelman, *ACS NANO* **2012**, *6*, 6843.
- [37] S. Wang, G. Kim, Y. E. Lee, H. J. Hah, M. Ethirajan, R. K. Pandey, R. Kopelman, *Nanomedicine* **2012**, *6*, 941.
- [38] N. Li, L. Zhang, Y. Chen, Mi. Fang, J. Zhang, H. Wang, *Adv. Funct. Mater* **2012**, *22*, 835.
- [39] W. S. Choi, H. M. Yang, H. Y. Koo, H.-J. Lee, Y. B. Lee, T. S. Bae, Ch. Jeon, *Adv. Funct. Mater.* **2010**, *20*, 820.
- [40] a) Cambridge Structural Database version 5.33. Cambridge Crystal Data Centre, Cambridge UK, 2012. b) P. G. Harrison, A. T. Steel, *J. Organomet. Chem.* **1982**, *239*, 105.
- [41] E. Altay, T. Shahwan, M. Tanoğlu, *Powder Technol.* **2007**, *178*, 194.

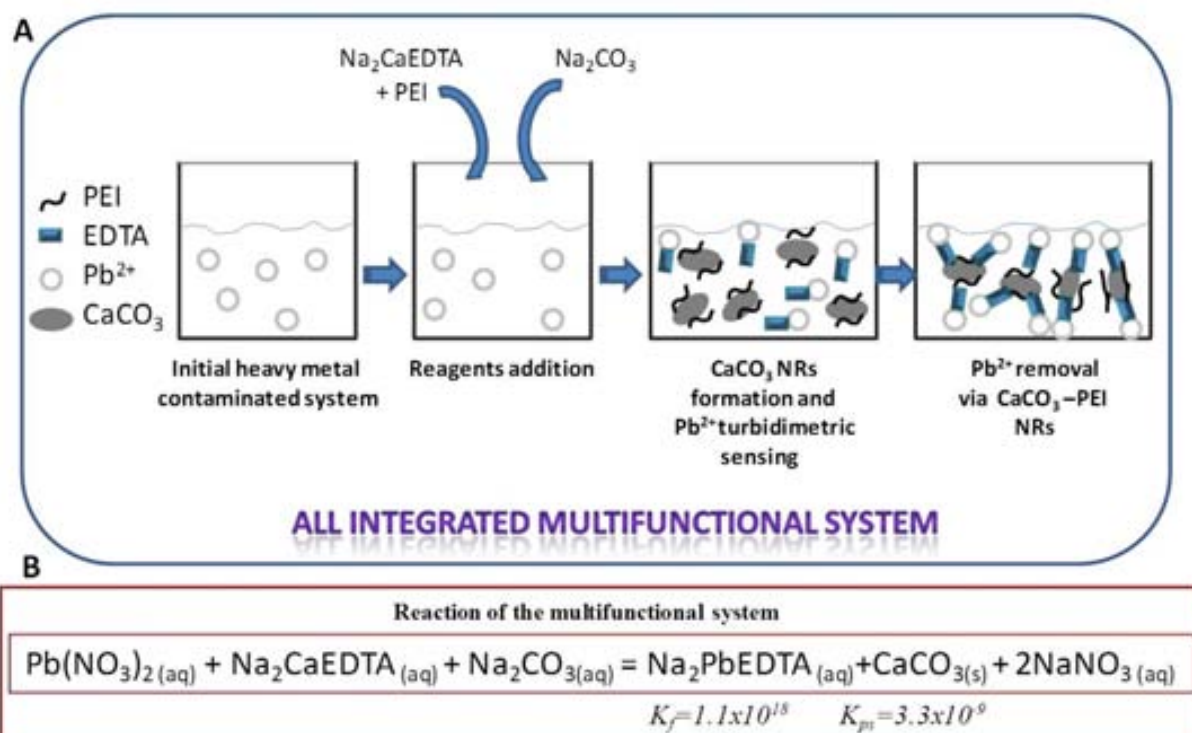


Figure 1. (A) Pb²⁺ sensor-removal (sensing and removing) principle based on the formation of the CaCO₃-PEI NRs absorbent material. (B) Reaction of the proposed CaCO₃ crystallization process.

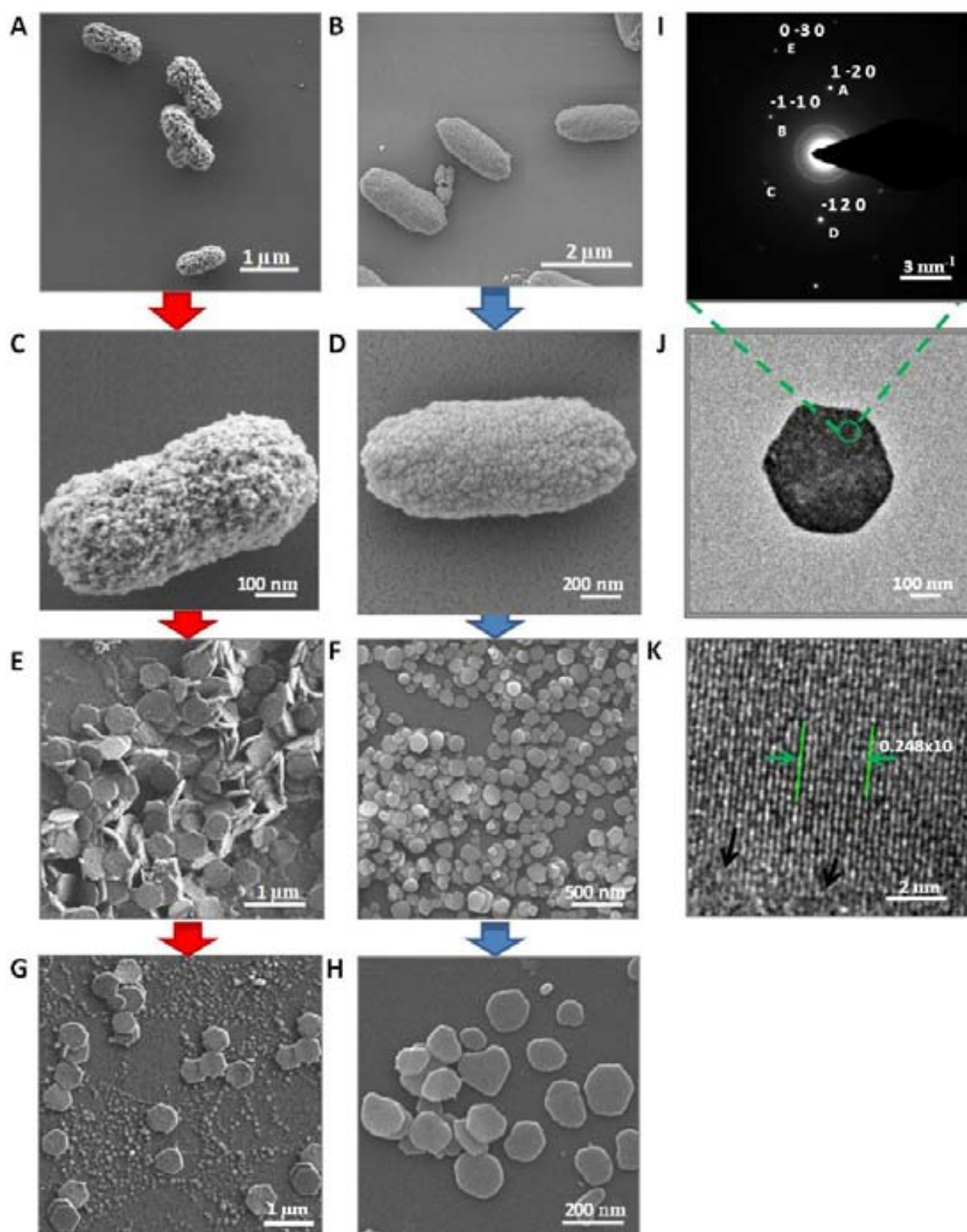


Figure 2. (A-H) SEM images of the CaCO₃ crystallization product synthesized under different reaction conditions. (A and B) Mixing 3.3×10^{-1} M of Pb(NO₃)₂, CaNa₂EDTA and NaNO₃ solutions with 4mg/mL PEI as CGM (A) and without the use of CGM (B). (C and D)

Close up each one of the structures obtained before. (E and F) Structures obtained mixing 3.3×10^{-4} M of $\text{Pb}(\text{NO}_3)_2$, CaNa_2EDTA and NaNO_3 solutions, (E) using 4mg/mL PEI as CGM homogeneous hexagonal plates like structures are obtained, (F) without the use of CGM heterogeneous plates are obtained. (G and H) Close up each one of the structures obtained before. (I-L) SAED, TEM and HRTEM images of the hexagonal plates obtained mixing 3.3×10^{-4} M of $\text{Pb}(\text{NO}_3)_2$, CaNa_2EDTA /4mg/mL PEI and NaNO_3 solutions. (I and K) ED data corresponding to the superposition of several single crystals and just single crystal, respectively. (J) TEM image of single hexagonal plate. (K) HRTEM image taken from a part of calcite hexagonal plate with resolved (1 1 0) planes ($d = 0.25$ nm).

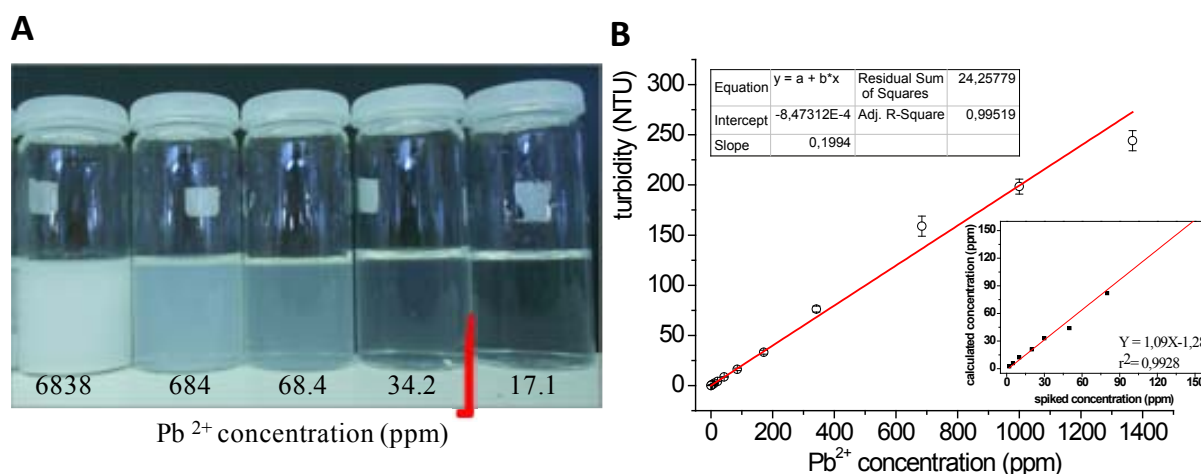


Figure 3. Pb^{2+} sensing by changes in the turbidity during calcite precipitation. (A) Pb^{2+} detection by naked eye through the turbidity produced in the CaCO_3 precipitation. (B) Correlation between the turbidity produced in the CaCO_3 precipitation and Pb^{2+} concentration. The insert graph corresponds to the plotting of the accuracy assay results.

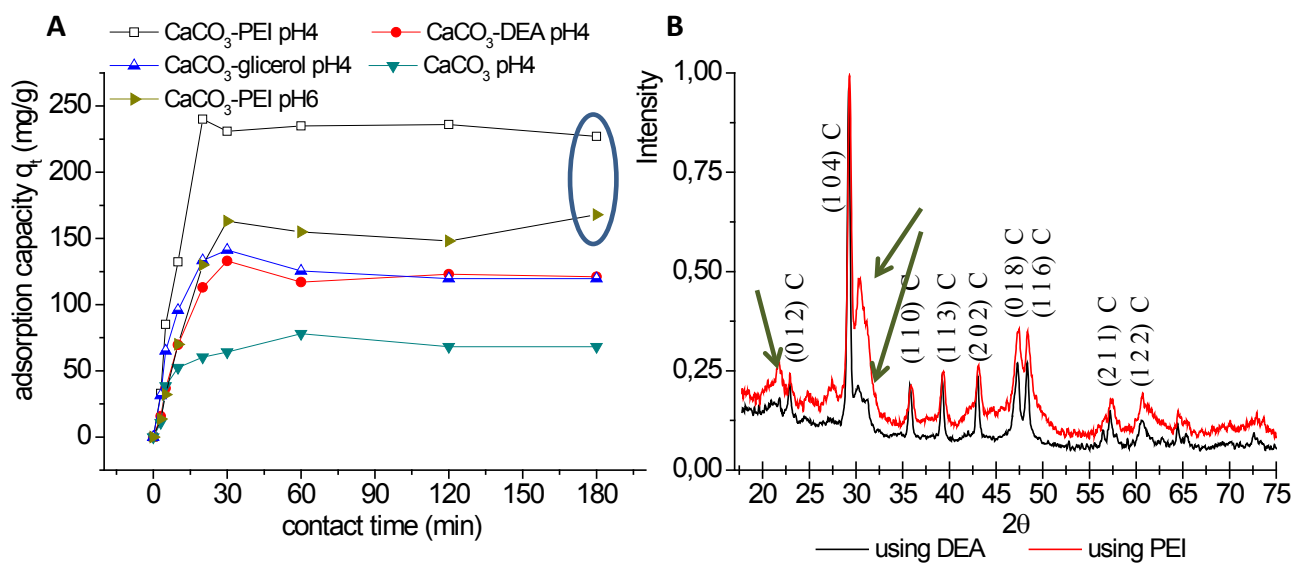


Figure 4. PbNa₂EDTA removal. (A) Adsorption kinetic curves for PbNa₂EDTA solutions (342 ppm) at pH 4 using the NRs obtained without or with different CGMs. The cases labelled with the circle correspond to the same experiment at different pH. (B) DRX patterns of the powder obtained after the removal process corresponding to 48 h of contact time (the C label denotes calcite phase and the green arrows denote the new phase corresponding to Pb²⁺ removal from dissolution as EDTA complex).

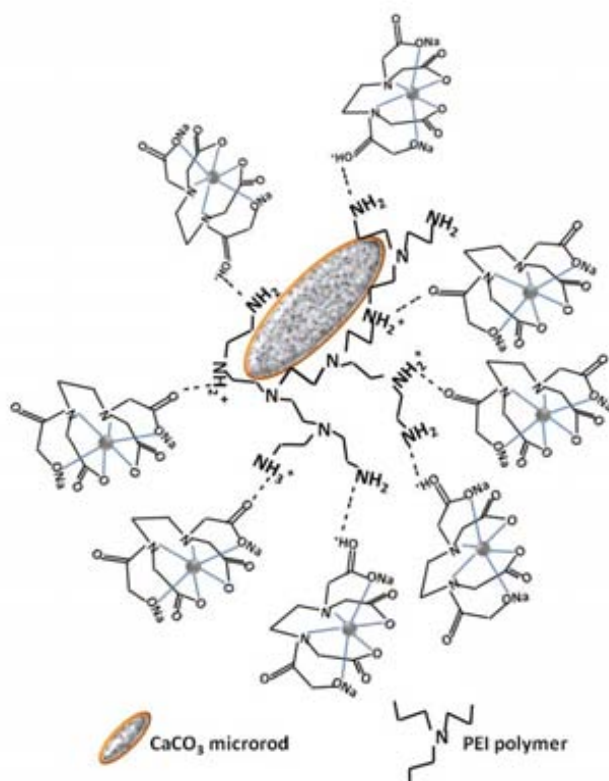


Figure 5. Schematic representation of the hydrogen bonds interactions between PbNa₂EDTA and PEI polymer onto NRs surface. The possibility of protonation of the amino and carboxylic groups increases at more acid pH which allows new hydrogen bond interactions, intensifying the adsorption of the Pb²⁺ complex onto NRs surface.

The table of contents

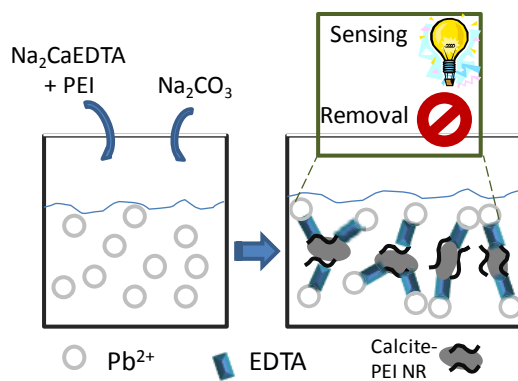
Multifunctional system based on hybrid calcite-PEI nanostructured rods (NRs) formation, that senses and removes Pb^{2+} (sensoremoval concept) for environmental applications.

Keyword: nanostructured rods, calcite-PEI, lead, sensing, removing.

A. López_Marzo, Josefina Pons, Arben Merkoçi*

Title: Multifunctional system based on hybrid calcite-PEI nanostructured-rods formation, for Pb^{2+} *sensoremoval* applications.

TOC figure



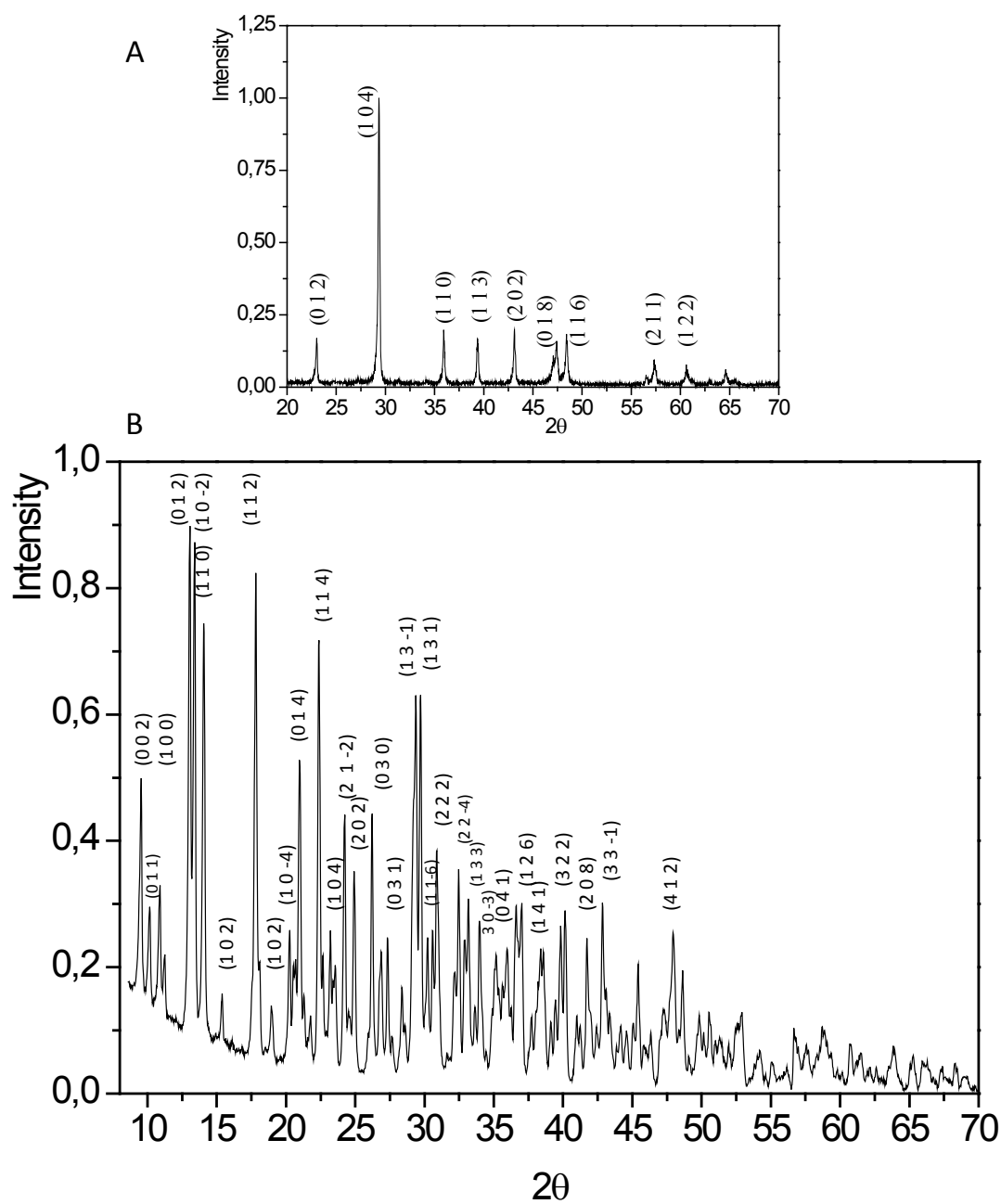
Supporting Information

Multifunctional system based on hybrid calcite-PEI nanostructured-rods formation, for Pb²⁺ ‘sensoremoval’ applications

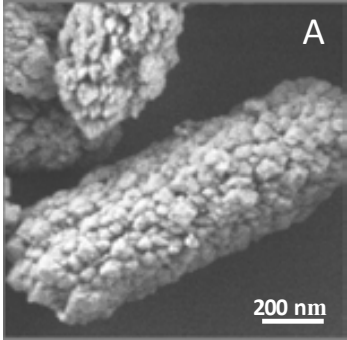
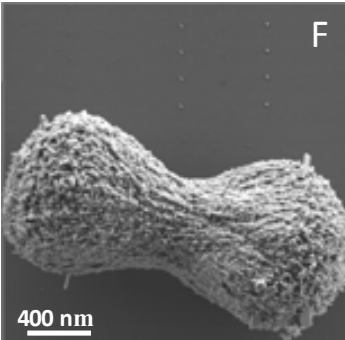
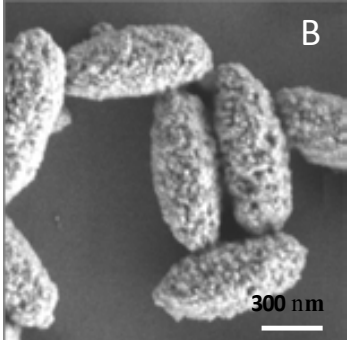
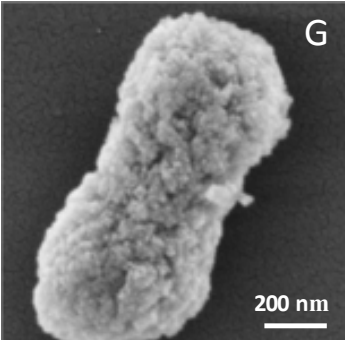
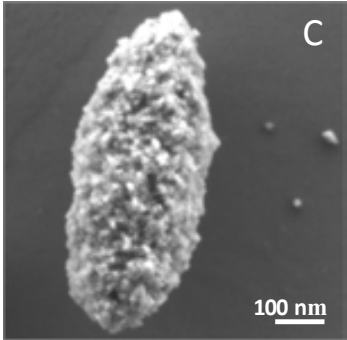
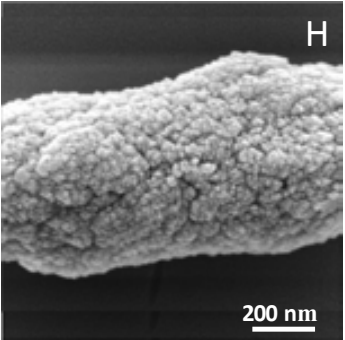
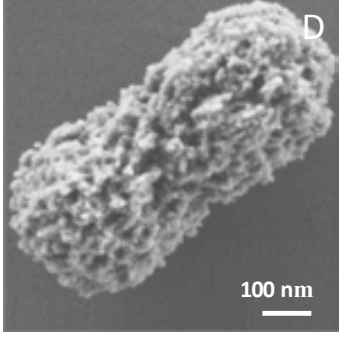
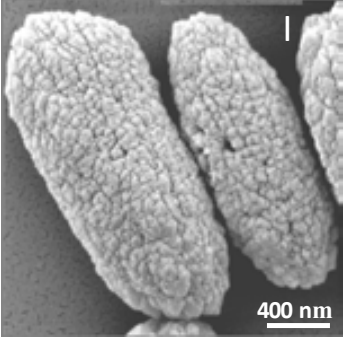
By, *A. López_Marzo, Josefina Pons, and A. Merkoçi**

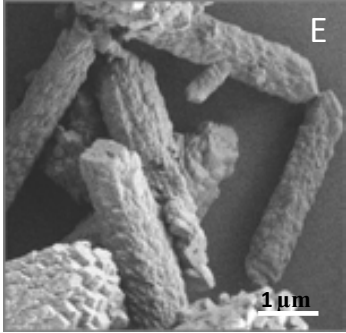
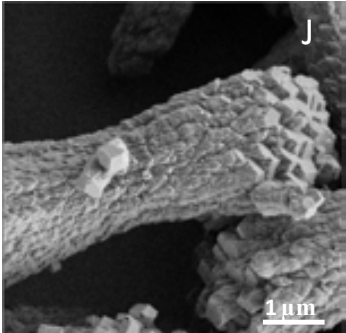
A. López_Marzo, Prof. Dr. A. Merkoçi*
Nanobioelectronics and Biosensors Group,
Catalan Institute of Nanotechnology,
Campus de la UAB, 08193 Bellaterra, Barcelona, Spain
*E-mail: arben.merkoci@icn.cat

A. López_Marzo, Prof. Dr. Josefina Pons
Department of Chemistry,
Universitat Autònoma de Barcelona,
Bellaterra 08193, Barcelona, Spain.



Figure_S1. (A) XRD patterns of calcite polymorph phase and the $\text{Na}_2\text{PbEDTA}\cdot 2\text{H}_2\text{O}$ complex. The XRD pattern related in (A) exhibits sharp reflections corresponding to the (0 1 2), (1 0 4), (1 1 0), (1 1 3), (2 0 2), (0 1 8), (1 1 6), (2 1 1) and (1 2 2) crystallographic planes of calcite, the most stable polymorph of CaCO_3 . (B) The XRD pattern related in (B) exhibits the most intensity peaks corresponding with $\text{Na}_2\text{PbEDTA}\cdot 2\text{H}_2\text{O}$ (P21/c) indexed in CSD.⁴⁰

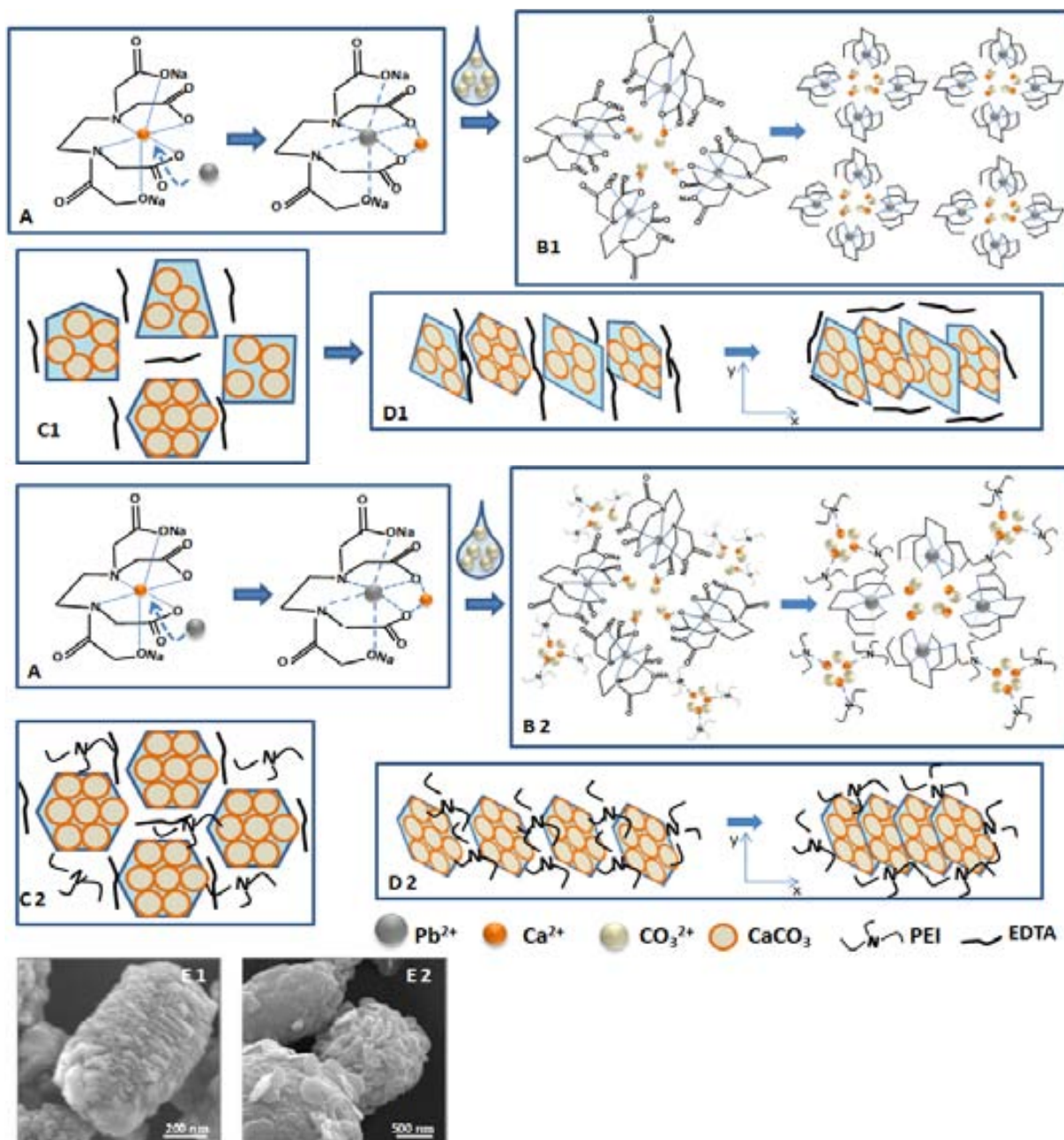
Reaction conditions and type of assay	SEM view and structure average size [μm]	Reaction conditions and type of assay	SEM view and structure average size [μm]
$\left[\frac{0.33\text{M CaCl}_2 + 0.4\text{M Na}_3\text{EDTA}}{5\text{mL H}_2\text{O}} \right]$ $+ \left[\frac{0.33\text{M Pb(NO}_3)_2}{5\text{mL H}_2\text{O}} \right]$ $+ \left[\frac{0.33\text{M Na}_2\text{CO}_3}{5\text{mL H}_2\text{O}} \right]$ <p>Assay 1-A</p>	 <p>1.16 \pm 0.41</p>	$\left[\frac{0.33\text{M CaCl}_2 + 0.4\text{M Na}_3\text{EDTA}}{2\text{mL H}_2\text{O}} \right]$ $+ \left[\frac{0.33\text{M Pb(NO}_3)_2}{2\text{mL H}_2\text{O}} \right]$ $+ \left[\frac{0.33\text{M Na}_2\text{CO}_3}{2\text{mL H}_2\text{O}} \right]$ <p>Assay 1-E</p>	 <p>1.19 \pm 0.42</p>
$\left[\frac{0.33\text{M CaCl}_2/\text{PEI} + 0.4\text{M Na}_3\text{EDTA}}{5\text{mL H}_2\text{O}} \right]$ $+ \left[\frac{0.33\text{M Pb(NO}_3)_2}{5\text{mL H}_2\text{O}} \right]$ $+ \left[\frac{0.33\text{M Na}_2\text{CO}_3}{5\text{mL H}_2\text{O}} \right]$ <p>Assay 1-B</p>	 <p>0.62 \pm 0.06</p>	$\left[\frac{0.3\text{M CaCl}_2/\text{PEI} + 0.4\text{M Na}_3\text{EDTA}}{2\text{mL H}_2\text{O}} \right]$ $+ \left[\frac{0.33\text{M Pb(NO}_3)_2}{2\text{mL H}_2\text{O}} \right]$ $+ \left[\frac{0.33\text{M Na}_2\text{CO}_3}{2\text{mL H}_2\text{O}} \right]$ <p>Assay 1-B-E</p>	 <p>1.11 \pm 0.25</p>
$\left[\frac{0.33\text{M CaCl}_2 + 0.4\text{M Na}_3\text{EDTA}}{5\text{mL H}_2\text{O} + 2\text{mL ethylacetate}} \right]$ $+ \left[\frac{0.33\text{M Pb(NO}_3)_2}{5\text{mL H}_2\text{O}} \right]$ $+ \left[\frac{0.33\text{M Na}_2\text{CO}_3}{5\text{mL H}_2\text{O}} \right]$ <p>Assay 1-C</p>	 <p>0.65 \pm 0.18</p>	$\left[\frac{0.33\text{M CaCl}_2 + 0.4\text{M Na}_3\text{EDTA}}{2.5\text{mL H}_2\text{O} + 2.5\text{mL ethanol}} \right]$ $+ \left[\frac{0.33\text{M Pb(NO}_3)_2}{5\text{mL H}_2\text{O}} \right]$ $+ \left[\frac{0.33\text{M Na}_2\text{CO}_3}{5\text{mL H}_2\text{O}} \right]$ <p>Assay 1-C</p>	 <p>1.02 \pm 0.31</p>
$\left[\frac{0.33\text{M CaCl}_2/\text{PEI} + 0.4\text{M Na}_3\text{EDTA}}{5\text{mL H}_2\text{O} + 2\text{mL ethylacetate}} \right]$ $+ \left[\frac{0.33\text{M Pb(NO}_3)_2}{5\text{mL H}_2\text{O}} \right]$ $+ \left[\frac{0.33\text{M Na}_2\text{CO}_3}{5\text{mL H}_2\text{O}} \right]$ <p>Assay 1-B-C</p>	 <p>0.63 \pm 0.11</p>	$\left[\frac{0.33\text{M Pb(NO}_3)_2}{5\text{mL H}_2\text{O}} \right] +$ $\left[\frac{0.3\text{M CaCl}_2/\text{gly} + 0.4\text{M Na}_3\text{EDTA}}{5\text{mL H}_2\text{O}} \right]$ $+ \left[\frac{0.33\text{M Na}_2\text{CO}_3}{5\text{mL H}_2\text{O}} \right]$ <p>Assay 2-B</p>	 <p>1.80 \pm 0.30</p>

Reaction conditions and type of assay	SEM view and structure average size [μm]	Reaction conditions and type of assay	SEM view and structure average size [μm]
$\left[\frac{0.33\text{M Ca(NO}_3)_2 + 0.4\text{M Na}_3\text{EDTA}}{5\text{mL H}_2\text{O}} \right]$ $+ \left[\frac{0.33\text{M Pb(NO}_3)_2}{5\text{mL H}_2\text{O}} \right]$ $+ \left[\frac{0.33\text{M Na}_2\text{CO}_3}{5\text{mL H}_2\text{O}} \right]$ Assay 1-D	 3.43 ± 0.51	$\left[\frac{0.33\text{M Ca(NO}_3)_2 + 0.4\text{M Na}_3\text{EDTA}}{2\text{mL H}_2\text{O}} \right]$ $+ \left[\frac{0.33\text{M Pb(NO}_3)_2}{2\text{mL H}_2\text{O}} \right]$ $+ \left[\frac{0.33\text{M Na}_2\text{CO}_3}{2\text{mL H}_2\text{O}} \right]$ Assay 1-D-E	 5.42 ± 0.52

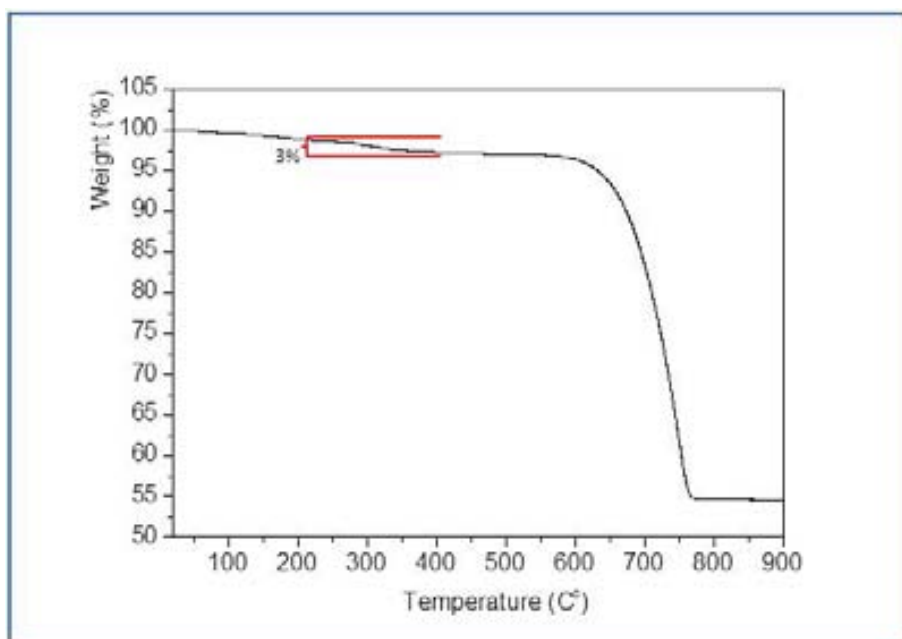
Figure_S2. Effect of different reaction conditions on the calcite morphology. [1], pouring Pb^{2+} and CO_3^{2-} solutions over CaNa_2EDTA solution; [2], pouring CaNa_2EDTA and CO_3^{2-} solutions over Pb^{2+} solution; [A], without use of CGM; [B], with the use of CGM; [C], using mixed solvents; [D], using $\text{Ca(NO}_3)_2$ as source of Ca^{2+} cations, [E], decreasing the reagents volume.

The analysis of the morphology of the product obtained under different changes in the reaction conditions guides to some regularity of behavior for the shape and the surface of the calcite product produced and the applied reaction condition. In first place, rod-like shapes are always obtained using 0.33 M of the basis mixture of CaNa_2EDTA , $\text{Pb(NO}_3)_2$ and NaNO_3 . In second place the reagents addition order ($\text{CaNa}_2\text{EDTA} + \text{Pb(NO}_3)_2 + \text{NaNO}_3$ or $\text{Pb(NO}_3)_2 + \text{CaNa}_2\text{EDTA} + \text{NaNO}_3$) don't affect the product as view in SEM images of the figure 2B and figure_S2-A or figure 2A and figure_S2-B. The addition of PEI in the original Ca^{2+} solution conduces to microrods with high porous surface and rounded to the ends as shown in figure_S2-B, D and G. While those obtained without CGM (figure_S2-A) or with other CGM as ethanol (figure_S2-H) or glycerol (figure_S2-I) don't present a high porous surface. In the same way the use of water/ethylacetate as mixed solvents produces high porous surface microrods but with sharp ends (figure_S2-C) and when PEI is introduced in this system the ends of this microrods became in rounded ends (figure_S2-D). The substitution of CaCl_2 by $\text{Ca(NO}_3)_2$ to produce CaNa_2EDTA leads to microrods compound of perfect nanocubes typical of calcite phase. Finally the diminution of the reaction volume from 15 to 7 mL produces the dumbbell-like shape structures (figure_S2-F, G and J). The dumbbell-like shape structure has been reported before by J. Yu et al. They explain the dumbbell shape in terms of nucleation and growth stimulated at the both ends of the rod-like primary crystals along electric field lines further than the nucleation and growth on the side-surfaces of rod-like primary crystals.

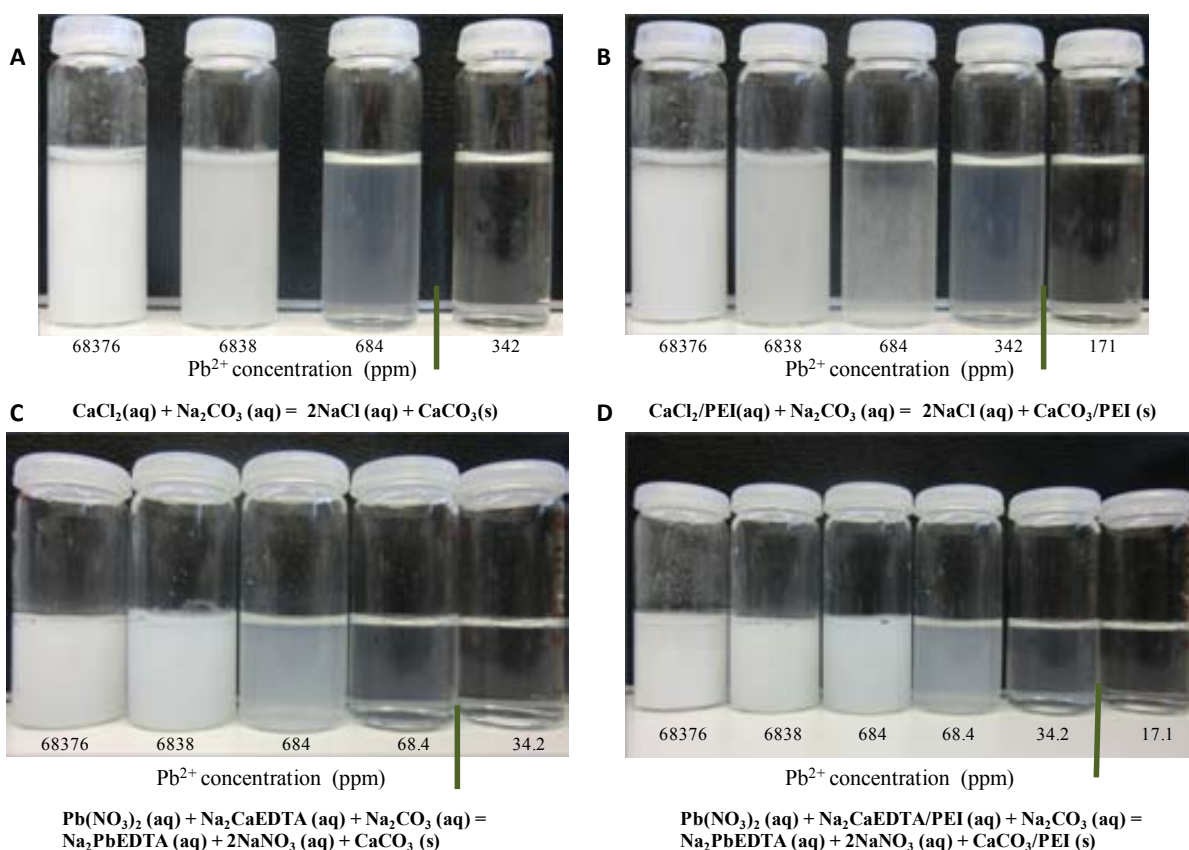
[20]



Figure_S3. Schematic representation of the NRs formation mechanism without use of CGM (1) and using PEI as CGM (2). (A) Formation of the possible intermediate complex $\text{Ca-Na}_2\text{EDTA-Pb}$ as Ca^{2+} self-reagent-delivery. (B1) Arising of the first local CaCO_3 nucleation centers by calcium supersaturation and nearly CaCO_3 nanoparticles stabilized by Na_2PbEDTA ; (B2) Formation of additional primary CaCO_3 nanoparticles by calcium supersaturation due to its interaction with nitrogen amino in PEI polymer. (C1) Growth of heterogeneous plate-like crystals by aggregation of the nearly CaCO_3 nanoparticles in preferential y -axis and its temporal Na_2PbEDTA stabilization. (C2) Growth of homogeneous hexagonal plate-like crystals by aggregation of the nearly CaCO_3 nanoparticles in preferential y -axis and its PEI stabilization by polymer retention onto particle surface. (D) Spontaneous self-assembly of the heterogeneous (D1) or hexagonal (D2) plate crystals mediated by organic stabilizer that acts as link of the plate building block into preferential x -axis. E1 and E2 SEM images that suggest the microrods composition by self assembly of heterogeneous and hexagonal nanoplates, respectively.

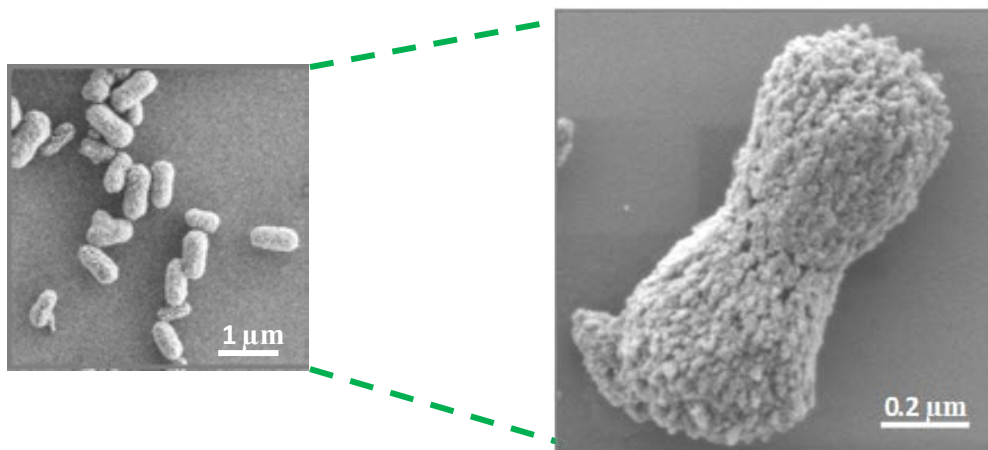


Figure_S4. TGA curve obtained for CaCO₃-PEI powder.



Figure_S5. Photos corresponding to the turbidity assays produced by CaCO₃ precipitation when decrease the reagents concentration. (A) Turbidity produced by CaCO₃ precipitation using CaCl₂ and Na₂CO₃ to synthesize the CaCO₃. (B) Turbidity produced by CaCO₃ precipitation using CaCl₂/PEI and Na₂CO₃ to synthesize the CaCO₃. (C) Turbidity produced by CaCO₃ precipitation using Pb(NO₃)₂, Na₂CaEDTA and Na₂CO₃ to synthesize

the CaCO_3 . (D) Turbidity produced by CaCO_3 precipitation using $\text{Pb}(\text{NO}_3)_2$, $\text{Na}_2\text{CaEDTA/PEI}$ and Na_2CO_3 to synthesize the CaCO_3 .



Figure_S6: SEM image taken to calcite powder after 48 h of removal treatment to initial Na_2PbEDTA solution (342 ppm) at pH 4.

**ANNEX III. ADITIONAL SUPPORT
MANUSCRIPTS/ARTICLES**

A simple phenol sensing and removing system using a nanostructured platform

Carmen C. Mayorga-Martinez,^{a,‡} Lenka Hlavata^{a,b,‡}, Sandrine Miserere^a, Adaris López-Marzo^{a,c}, Jan Labuda^b, Josefina Pons^c, Arben Merkoçi^{,a,d}*

^aNanobioelectronics & Biosensors Group, Catalan Institute of Nanotechnology, Campus UAB, Bellaterra (Barcelona) 08193 Spain

^bInstitute of Analytical Chemistry, Faculty of Chemical and Food Technology, Slovak University of Technology in Bratislava, Radlinského 9, Bratislava 81237 Slovakia

^cDepartament de Química, Universitat Autònoma de Barcelona, Bellaterra(Barcelona) 08193 Spain

^dICREA, Barcelona, Catalonia, Spain

*corresponding author: Prof. Arben Merkoçi, Phone number: +34935868014; Fax number: +34935868020, E-mail: arben.merkoci@icn.cat

‡ These authors have contributed equally to this work.

ABSTRACT. Phenol is a widely used chemical that for several reasons may be released into the environment and consequently its detection and subsequent destruction up to its trace levels released into the ground and surface water are of special importance. Inspired by theranostic devices with interest for human health where diagnostic and therapy are integrated in the same platform a new and simple strategy based on CaCO₃-poly(ethyleneimine) (PEI) nanostructured particles (NPs) for detection and removing of phenolic waste using hybrid polydimethylsiloxane (PDMS)/glass chrono-impedimetric microchip is developed. This fluidic system with an integrated biosensor can be easily fabricated and represents an inexpensive, disposable and amenable to mass production platform for phenol removing and detection. For the first time phenol detection is performed by using chrono-impedimetric measurements in a flow injection analytical (FIA) microsystem. The designed fluidic microsystem improves the detection limit (4.64 nM phenol) of the biosensor which is almost over 7 times lower than the level in batch measurements using the same system.

KEYWORDS. CaCO₃-PEI nanostructured particles; Chrono-impedance technique, phenol sensing and removing; microfluidic system

Phenolic compounds are widely found in petrochemical products, and in wood preservatives, textiles, plastics, dyes, paper, herbicides and pesticides.¹⁻³ As phenol is a major human carcinogen, the detection and destruction of phenol traces released into the ground and surface water is of special importance.¹⁻⁵ Many technologies for removing and degradation of phenolic compounds in wastewater have been investigated.⁶⁻⁸ Conventional treatment methods (chlorination, ozonation, solvent extraction, incineration, chemical oxidation, membrane process, coagulation, flocculation, adsorption, ion exchange, reverse osmosis, electrolysis beside other)⁹ of phenolic waste water are mostly based on physical and chemical processes but these processes led to secondary effluent problems due to formation of toxic compounds such as cyanates, chlorinated phenols, hydrocarbons, etc.

On the other hand, the development of analytical methodologies for phenol quantification in various samples as well as for evaluation of their total toxicity with respect to environmental and human health is also of great importance. The electrochemical tyrosinase-based biosensors constitute promising technology for the *in-situ* phenol monitoring because of the advantages, such as high selectivity, low production cost, promising response speed, potential for miniaturization, simple instrumentation and easy automation.^{1,2,9-11} However, the practical application of batch systems of tyrosinase-based biosensors is limited by short comings such as the high number of steps needed for the measurement procedure and stability problems for the continuous batch phenol measurement beside others. The combination of biosensors with advantages of the PDMS and screen-printing technologies in flow injection (FI) microsystems permits: automation, integration, control of the reagent addition steps, measurement of enzyme activity, and also simplifies the optimization of the reaction

conditions of phenol biosensing. Additionally, allows the production of reliable and low-cost microdevices at an industrial level.^{12,13}

A wide variety of nanomaterials, especially nanoparticles possess some unique chemical, physical and electronic properties caused by nanoscale effect (owing to their small size; normally in the range of 1 – 200 nm).^{14, 15, 16} For this reason this nanoparticles can be used to construct novel and improved sensing devices; in particular, electrochemical sensors and biosensors.^{5,15-19} Recently Lopez-Marzo *et al.* have reported a new nanostructured CaCO₃ (vaterite crystalline phase) composed of nanoparticles with diameters of 10-50 nm. In these new nanostructured materials (CaCO₃-PEI NPs) poly(ethyleneimine) (PEI) is introduced as a crystal growth modifier in the reaction system that increases the vaterite fraction in the final product and offers to it stability up to 8 months. This nanostructured CaCO₃-PEI presents high biofunctionalizing capacity with interest for biosensing due to hydrogen bond formation between the nitrogens of the amino groups in PEI and the hydrogens of the OH, NH or SH groups present in any type of biomolecule.²⁰

Chrono-impedance technique (CIT) has been reported for the real time glucose determination in a first and second generation glucose oxidase/carbon paste electrodes biosensors^{21, 22} and free-enzymatic glucose sensor.²³ This technique allows *on-line* and short time response measurements with less sensitivity toward electromagnetic interference in comparison to classical chronoamperometric method.²¹⁻²³

The use of nanomaterials in developing innovative sensing systems is getting an increase attention of the nowadays research and technologies applied to environmental monitoring of heavy metals,^{24, 25} pesticides²⁶ or other pollutants. In addition the development of smart systems able to achieve *in-situ* and *on-line* sensing and destroying

of pollutants (i.e. pesticides) can be considered an emerging area of research and development. In the current study, we propose for the first time an integrated sensing & removing phenol system that uses nanostructured CaCO₃-PEI platform. Such sensing & removing is *in-situ* achieved through a hybrid polydimethylsiloxane (PDMS) – glass fluidic platform with integrated screen-printed-electrodes (SPE) modified with CaCO₃-PEI NPs and Tyrosinase (Tyr) through cross-linking with glutaraldehyde. The chronoimpedimetric measurements have been performed for the first time in a FIA microsystem. On the other hand, the conditions for phenol removing by its adsorption onto CaCO₃-PEI NPs are optimized. This fluidic system including the integrated biosensor represents a low cost platform for detecting and removing of phenol in waters and may open the way to unprecedented applications including to several other pollutants with interest in environment, food, safety and security related technologies.

RESULTS AND DISCUSSION

The use of CaCO₃-PEI NPs represents an interesting platform for the immobilization of a large range of biomolecules, from enzymes, antibodies, nucleic acids such as aptamers and DNA.²⁰ Figures 1A show highly regular and uniform nanoparticles with a diameter of 50 nm of CaCO₃-PEI. Here CaCO₃-PEI NPs were immobilized onto the electrode surface and then modified with Tyrosinase and Glutaraldehyde and used for the electrochemical studies. Figure 1B shows a scanning electron microscopy (SEM) image indicating distribution of the CaCO₃-PEI nanostructured particles onto the working electrode surface of SPE. Figure C displays the effect of glutaraldehyde as a binding matrix, showing a good entrapment of the CaCO₃-PEI NPs and Tyrosinase within the mentioned matrix. Electrochemical impedance spectroscopy (EIS) is a well-known method used to study the surface features of modified electrodes.²⁷ The curve of EIS presented as Nyquist plot consists in two parts: one part is the semicircle section,

located at higher frequencies corresponding to the electron transfer limited process. The electron-transfer resistance (R_{ct}) can be obtained by measuring its diameter. The other part of Nyquist plot is the linear section, which brings the information related to the diffusion process held in solution and located at lower frequencies. The increase of electron transference through the CaCO_3 -PEI composite was observed with the decreasing of R_{ct} in the Nyquist plot (see Figure 1D). These improvements may be due to the fact that PEI might have enhanced the electronic conductivity as also observed in the single walled carbon nanotubes SWNT composite developed by Muñoz *et al.* and thoroughly discussed.²⁸ The adsorption of Tyr and glutaraldehyde onto the CaCO_3 -PEI (see R_{ct} increase at Figure 1D) indicate the effect of glutaraldehyde as a binding / good entrapment matrix achieving a successful immobilization of the enzyme (Fig. 1 D).

The CaCO_3 -PEI/Tyr biosensor operation for the phenol detection was evaluated by the electrochemical impedance spectroscopy (EIS) measurements. Figure 2A shows the Argand diagrams for the phosphate buffer solution (PBS) pH 6.5 with 0.1 M KCl in absence and the presence of different phenol concentrations. Tyrosinase (Tyr) has hydroxylase activity that ensures hydroxylation of phenol to catechol (see equation 1 in Figure 2B) and oxidase activity for oxidation of catechol to O-quinone (see equation 2 in Figure 2B). At moderately negative potential the o-quinone product of phenol oxidation may be electrochemically reduced to catechol (see equation 3 in Figure 2B). Oxidation by the enzyme followed by reduction at the electrode may result in cycling between the catechol and O-quinone.⁵ Changes of the electrode-electrolyte interface impedance (EEIZ), by increasing of the phenol concentration are evident at 100 mV alternating voltage superimposed on -200 mV DC. The variation of the impedance is due to the charge transfer which occurs during the electrochemical reaction (equation

3 in Fig. 2B) and which takes place between the electrode surface modified with CaCO₃-PEI/Tyr and the electrolyte.

As previously observed,²¹⁻²³ the bioelectrocatalysis of phenol oxidation is observed in the range of low frequency, where the Argand diagrams show the greatest separation for different concentrations. In order to verify this assertion, the real time determination of impedance module ($|Z|$), in PBS alone and with successive additions of 10 μ M phenol, was carried out by using two frequencies (0.4 Hz and 10 Hz) and a composed signal (-200 mV DC+ 100 mV AC). The response obtained at 0.4 Hz (Figure 3A) appreciably reflects $|Z|$ changes, while the response at 10 Hz (Figure 3B) is less appreciated. The frequency of 0.4 Hz was used for the chrono-impedimetric measurements.

Chrono-impedimetric response of the SPE/CaCO₃-PEI/Tyr biosensor to successive additions of 0.5 μ M phenol solution (Figure 3C and 3D) is further evaluated under optimized experimental conditions. The linear biosensor response within the range from 0.5 – 2.0 μ M phenol in PBS was observed with $r^2= 0.953$ and $r^2= 0.984$ for Module ($|Z|$) and Phase (θ) respectively. The electrode shows sensitive bioelectrocatalytic response, reaching about 95% of the steady-state impedance module within 140s after each addition of phenol. The typical calibration curves of the SPE/CaCO₃-PEI/Tyr for both $|Z|$ and θ toward 0.5 μ M phenol are showed (Inset Figures 3C and 3D). On the other hand, SPE/CaCO₃-PEI/Tyr biosensor shows LOD value of 32 nM for phenol that was calculated considering the linear response vs. concentration dependence. The inset calibration curves (Figure 3C and 3D) correspond to triplicates measured with different biosensors that showed signals with relative standard deviation (RSD) lower than 10%.

The high biocatalytic activity of the SPE/CaCO₃-PEI/Tyr biosensor can be related with several factors. The enzyme is immobilized by adsorption onto the CaCO₃-PEI porous nanostructure and remains entrapped via hydrogen bond between labile hydrogen in the

biomolecule and PEI's nitrogen²⁰ with a low mass transport barrier. In addition an increase in the amount of active enzyme available as a consequence of the enzyme activation by the presence of calcium might have occurred.²⁹⁻³² On the other hand a possible improvement of the electron transference through the CaCO₃-PEI NPs composite due to the fact that PEI enhances the electronic conductivity must be considered as well^{20,28} (see Fig. 1D). All these phenomena contribute to a high sensitivity and stability of this biosensor with interest overall for *in-situ* and *on-line* monitoring applications in comparison with other reported biosensors based in SPE.^{5, 17, 33, 34}

In order to achieve a good performance of the biosensor several parameters related to the FIA microsystem were optimized. In this way, measurements with and without phenol additions at different flow rates (50, 100 and 500 $\mu\text{L min}^{-1}$) were carried out. The highest changes of the impedance module by additions of phenol were found using the rate of 50 $\mu\text{L min}^{-1}$ for a frequency of 0.4 Hz, at higher flow rates the response time and the peak of the impedance module decreases. A need of the low flow rate is probably related to an efficiency of the diffusion process as the response time of the biosensor is slow at the used low frequency (0.4 Hz). The volume of injection was also optimized and a stable and repeatable response was obtained using 20 μL of injection volume. For smaller injection volumes the biosensor response was not reproducible and a decrease of the impedance related to the short exposure volume of the enzyme to the phenol substrate was observed. For high injection volume a saturation of the signal was observed. This behavior can be associated with chemical kinetics of the enzyme due to the fact that the response is better controlled by the enzymatic reaction at smaller volumes.

Chrono-impedimetric detection of phenol using the FIA microchip system was further studied (Figure 4). The biosensor exhibited good response as a function of phenol concentration. The inset calibration curves (Figure 4A and 4B) correspond to triplicates measured with different chips that showed signals with relative standard deviation (RSD) lower than 3%. The plot of the impedance module and phase versus the phenol concentration in the range of 0.01–10 μM phenol is characterized by a detection limit of 4.64 nM phenol which is almost over 7 times lower than the level in batch measurements using the same system. LOD was calculated from the calibration equation as 3 times the y-intercept standard deviation divided by the calibration slope. The stability and high electrobiocatalytic response of this biosensor is related to the good entrapment of the enzyme within the CaCO_3 -PEI NPs and glutaraldehyde matrix indicating that plasma cleaner procedure used to bond PDMS and glass does not alter the activity of the biomembrane. In-chip chrono-impedimetric measurements, well known for high sensitivity including high signal to noise related measurements were implemented for first time.

Considering the potential applications of the CaCO_3 -PEI NPs for removing phenol waste by adsorption using the hybrid PDMS/glass microchip (Figure 5), the operating conditions were optimized. Many parameters can influence the adsorption of phenol in flow. In this context different concentrations of phenol and CaCO_3 -PEI NPs were evaluated. The best proportion for the phenol removing was 5 mg of CaCO_3 -PEI for 2 μM of phenol. Phenol is adsorbed onto the surface of CaCO_3 -PEI NPs via hydrogen bond formation between acid hydrogen in the phenol molecule and PEI's nitrogen (see inset in Figure 5B).

Chrono-impedimetric measurements were carried out for evaluating of the phenol adsorption by the CaCO_3 -PEI NPs (see Figure 6). Measurements were performed under

different experimental conditions. The first (Figure 6A) and second (Figure 6B) FIA microsystems were carried out without CaCO₃-PEI NPs and cotton matrix in the phenol adsorption part injecting 20 μ L of PBS and phenol (2 μ M), respectively. The third microsystem (Figure 6C) corresponds to a tube containing only cotton, and the fourth setup (Figure 6D) uses a tube with CaCO₃-PEI NPs and cotton, both microsystems working with injections of 20 μ L of phenol (2 μ M). A decrease of $|Z|$ of around 136 Ω and 122 Ω can be observed for the 2^d and 3^d system respectively (See Figures 6B and 6C). While, the 4th microsystem (Figure 6D) does not show any response toward phenol injection. These experiments show the capacity of CaCO₃-PEI NPs to adsorb phenol.

In conclusion, we successfully implemented a new FIA microsystem that allows the *in-situ* and *on-line* phenol sensing and removal using nanostructure CaCO₃-PEI nanostructured platform. To the best of our knowledge, for the first time the chronopotentiometry technique is applied to sense phenol in a FIA microsystem (a versatile and efficient technique for quantitative automated analyses). This hybrid polydimethylsiloxane-glass (PDMS-G) microfluidic platform with the integrated CaCO₃-PEI /Tyr- based screen-printed-electrode (SPE) uses a very low DC potential, decreasing this way the effect of interferences and presents high repeatability, is easy to be fabricated, inexpensive, disposable and enable to mass production. This device shows good promises for further applications in automatic control systems with interest for the environment. The developed integrated pollutant sensing and removal system, thanks to the use of integrated enzyme modified CaCO₃-PEI nanostructured platforms, may open the way to several other applications with interest for environment, safety and security technologies. Its future miniaturization could lead to the next generation of environment 'nanotheranostic' microsystems in the same way as in health applications where diagnostics – sensing - and therapy - removal/destroying - are paving the way to

modern and efficient medical applications. These environment 'theranostic' microsystems may be useful for fast control and remediation of pollution in case of accidents where urgent in-field measures are necessary to be taken once the pollutants and their effective removal strategy are identified. The application of this system for real sample application would need further studies that include adsorption capacity and kinetics of removal between others and will be object of future research.

METHODS

Synthesis of CaCO₃-PEI NPs. Equal volumes of the PEI (4 mg/mL) containing dissolutions of CaCl₂ (0.33 M) in water/ethanol (1:1, v/v) and Na₂CO₃ (0.33 M) in water were quickly mixed under sonication and during 45 min. at room temperature to obtain the nanostructured vaterite CaCO₃-PEI hybrid material. CaCO₃-PEI precipitates were washed three times, air dried collected and saved under room temperature conditions while not in use.

Preparation of Screen Printed Electrode (SPE) and Modification with CaCO₃ NPs and Tyr. The fabrication of screen printed electrodes is based on the sequential deposition of a graphite ink, Ag/AgCl ink and insulating ink on a polyester substrate. After the deposition of each layer a drying process is followed by keeping the polyester substrate at 120°C for 45 min (graphite) and 30min (Ag/AgCl and insulating). ~~AL5~~ CaCO₃-PEI NPs at 1 mg/mL solution drop was deposited onto the working SPE electrode surface and allowed to dry at room temperature for 20min. 1 mg of tyrosinase enzyme (obtained from mushroom; ≥1000 unit/mg) was dissolved in 50 μL of 0.1 M phosphate buffer at pH 6.5. A 5 μL drop of Tyr solution was deposited onto the working SPE/CaCO₃ NPs electrode surface and allowed to be dried at room temperature for 3 h. Finally, 5 μL of glutaraldehyde (25%) solution at 1% were casted onto the SPE/Tyr electrode surface and let to be dried at 40°C for 30min. The prepared SPE/ CaCO₃-PEI /Tyr sensor was kept at 4°C while not in use.

Microdevice fabrication for phenol detection and removing. The microchannel based biosensor was based on a hybrid PDMS/glass microchip. The microchannel was fabricated in PDMS by soft lithography.^{35,36} PDMS was poured onto an aluminum micromachined mold and cured at 65 °C for 4 h. The channel was 5 mm wide by 100

μm depth and 5 cm long. Two reservoirs were punched at the inlet and the outlet of the channel. Finally, the PDMS and the glass layers were aligned and irreversibly bonded using a 30 s oxygen plasma treatment. The electrochemical detector consists of a set of three screen-printed electrodes. The working electrode was modified following the protocol described above. For phenol absorption a tube of 500 μm (ID) was filled with fibers cotton, 5mg of CaCO_3 NPs and again with cotton to avoid leaking of the NPs. This tube is connected between pump and PDMS channel. For the flow injection 2 syringe pumps were used, one for the buffer and the other one for phenol solution injection. A photograph and a schematic diagram of the integrated microfluidic device are presented in Figure 5A. The developed biosensors, given their low cost, are in principle previewed as disposable devices after being used in up to three calibrations within the same day.

Electrochemical Experiments. In order to assess the surface characterization and performance of the biosensor, electrochemical impedance spectroscopy (EIS) studies were performed using an Autolab302 potentiostat/galvanostat/ frequency-response analyzer PGST30, controlled by GPES/FRA Version 4.9. The AC frequency range was 0.1 Hz to 100 kHz, logarithmic scale with 10 points per decade. Nyquist (imaginary impedance versus real impedance) diagrams were recorded in 1 mM $[\text{Fe}(\text{CN})_6]^{3-/4-}$ (1:1) as a redox probe for surface characterization of biosensor using 240 mV of DC potential and 10 mV of AC potential. For biosensor performance evaluation the experiments were carried out at room temperature and in phosphate buffer solution at pH 6.5 with 0.1M KCl using -200 mV of DC potential and 100 mV of AC potential.

Conflict of Interest.

The authors declare no competing financial interest.

Acknowledgements.

This work was supported by grants from MICINN (Spain) for MAT2011-25870 and Spain-Japan International Bilateral PIB2010JP-00278 projects. A. López Marzo thanks the Generalitat of Catalunya for the FI2010 predoctoral scholarship given. L. H. and J. L. thank for support the Scientific Grant Agency VEGA of the Slovak Republic (Project 1/0182/11).

References

1. Shan, D.; Zhang, J.; Xue, H.-G.; Zhang, Y.-C.; Cosnier, S.; Ding, S.N.; Polycrystalline Bismuth Oxide Films for Development of Amperometric Biosensor for Phenolic Compounds. *Biosens. Bioelectron.* **2009**, *24*, 3671—3676.
2. Lu, L.; Zhang, L.; Zhang, X.; Huan, S.; Shen, G.; Yu, R.; A Novel Tyrosinase Biosensor Based on Hydroxyapatite–Chitosan Nanocomposite for the Detection of Phenolic Compounds. *Anal. Chim. Acta* **2010**, *665*, 146—151.
3. Dimoglo, A.; Akbulut, H. Y.; Cihan, F.; Karpuzcu, M. Petrochemical Wastewater Treatment by Means of Clean Electrochemical Technologies, *Clean Techn. Environ. Policy* **2004**, *6*, 288—295.
4. Apetrei, C.; Alessio, P.; Constantino, C. J. L.; de Saja, J. A.; Rodriguez-Mendez, M.; Pavinatto, F.; Giuliani Ramos Fernandes, E.; Zucolotto, V.; Oliveira Jr., O.N.; Biomimetic Biosensor Based on Lipidic Layers Containing Tyrosinase and Lutetium Bisphthalocyanine for the Detection of Antioxidants. *Biosens. Bioelectron.* **2011**, *26*, 2513—2519.
5. Mayorga-Martinez, C. C.; Cadevall, M.; Guix, M.; Ros, J.; Merkoçi; Bismuth Nanoparticles for Phenolic Compounds Biosensing Application A. *Biosens. Bioelectron.* **2013**, *40*, 57—62.
6. Hannafi, N. E.; Boumakhla, M.A.; Berrama, T.; Bendjama, Z. Elimination of Phenol by Adsorption on Activated Carbon Prepared from the Peach cCres: Modelling and Optimisation. *Desalination* **2008**, *223*, 264—268.
7. Sanchez, I.; Stüber, F.; Font, J.; Fortuny, A.; Fabregat, A.; Bengoa, C. Elimination of Phenol and Aromatic Compounds by Zero Valent Iron and EDTA at Low Temperature and Atmospheric Pressure. *Chemosphere* **2007**, *68*, 338—344.

8. Bandhyopadhyay, K.; Dasb, D.; Bhattacharyya, P.; Maiti, B.R. Reaction Engineering Studies on Biodegradation of Phenol by *Pseudomonas putida* MTCC 1194 Immobilized on Calcium Alginate. *Biochem. Eng. J.* **2001**, *8*, 179—186.
9. Popovtzer, R.; Neufeld, T.; Biran, D.; Ron, E. Z.; Rishpon, J.; Shacham-Diamand, Y. Novel Integrated Electrochemical Nano-Biochip for Toxicity Detection in Water. *Nano Lett.* **2005**, *5*, 1023—1027.
10. Lin, Y.; Timchalk, C. A.; Matson, D. W.; Wu, H.; Thrall, K. D. Integrated Microfluidics/Electrochemical Sensor System for Monitoring of Environmental Exposures to Lead and Chlorophenols. *Biomed. Microdevices.* **2001**, *3*, 331—338.
11. Star, A.; Han, T.-R.; Gabriel, J.-C. P.; Bradley, K.; Grüner, G. Electronic Detection of Specific Protein Binding Using Nanotube FET Devices. *Nano Lett.* **2003**, *3*, 459—463.
12. Medina-Sánchez, M.; Miserere, S.; Marín, S.; Aragay, G.; Merkoçi, A. On-chip Electrochemical Detection of CdS Quantum Dots Using Normal and Multiple Recycling Flow Through Modes. *Lab. Chip.* **2012**, *12*, 2000—2005.
13. Pumera, M.; Merkoçi, A.; Alegret, S. New Materials for electrochemical Sensing VII. Microfluidics chip platforms. *Trends Analyt. Chem.* **2006**, *25*(3), 219—235.
14. Taufik, S.; Yusof, N. A.T.; Tee, W.; Ramli, I. Bismuth Oxide Nanoparticles/Chitosan/Modified Electrode as Biosensor for DNA Hybridization. *Int. J. Electrochem.* **2011**, *6*, 1880—1891
15. Li, Y.-F.; Liu, Z.-M.; Liu, Y.-L.; Yang, Y.-H.; Shen, G.-L.; Yu, R.-Q. A Mediator-Free Phenol Biosensor Based on Immobilizing Tyrosinase to ZnO Nanoparticles. *Analytical biochemistry*, **2006**, *349*, 33—40.
16. Katz, E.; Willner, I. Integrated Nanoparticle–Biomolecule Hybrid Systems: Synthesis, Properties, and Applications. *Angew. Chem.* **2004**, *43*, 6042—6108.

17. Song, W.; Li, D.-W.; Li, Y.-T.; Li, Y.; Long, Y.-T. Disposable Biosensor Based on Graphene Oxide Conjugated with Tyrosinase Assembled Gold Nanoparticles. *Biosens. Bioelectron.*, **2011**, *26*, 3181—3186.
18. Lu, L.; Zhang, L.; Zhang, X.; Huan, S.; Shen, G.; Yu, R. A Novel Tyrosinase Biosensor Based on Hydroxyapatite-Chitosan Nanocomposite for the Detection of Phenolic Compounds. *Anal Chim Acta* **2010**, *665*, 146—151.
19. Shan, D.; Zhu, M.; Han, E.; Xue, H.; Cosnier, S. Calcium Carbonate Nanoparticles: a Host Matrix for the Construction of Highly Sensitive Amperometric Phenol Biosensor. *Biosens. Bioelectron.* **2007**, *23*, 648—654.
20. Lopez-Marzo, A.; Pons, J.; Merkoçi, A. Controlled Formation of Nanostructured CaCO₃–PEI Microparticles with High Biofunctionalizing Capacity. *J. Mater. Chem.* **2012**, *22*, 15326—15335.
21. Mayorga Martinez, C. C.; Treo, E. F.; Madrid, R. E.; Felice, C. J. Evaluation of Chrono-impedance Technique as Transduction Method for a Carbon Paste/Glucose Oxidase (CP/GOx) Based Glucose Biosensor. *Biosens. Bioelectron.* **2010**, *26*, 1239—1244.
22. Mayorga Martinez, C. C.; Treo, E. F.; Madrid, R. E.; Felice, C. J. Real-time Measurement of Glucose Using Chrono-Impedance Technique on a Second Generation Biosensor. *Biosens. Bioelectron.* **2011**, *29*, 200—203.
23. Mayorga-Martinez, C.C.; Guix, M.; Madrid, R.E.; Merkoçi, A. Bimetallic Nanowires as Electrocatalysts for Nonenzymatic Real-Time Impedancimetric Detection of Glucose. *Chem. Commun.* **2012**, *48*, 1686—1688.

24. Aragay, G.; Pons, J.; Merkoçi, A. Recent Trends in Macro-, Micro-, and Nanomaterial-Based Tools and Strategies for Heavy-Metal Detection. *Chem. Rev.* **2011**, 111, 3433—3458.
25. Willner, I.; Willner, B. Biomolecule-Based Nanomaterials and Nanostructures. *Nano Lett.* **2010**, 10, 3805—3815.
26. Aragay, G.; Pino, F.; Merkoçi, A. Nanomaterials for Sensing and Destroying Pesticides. *Chem. Rev.* **2012**, 112, 5317—5338.
27. Katz, E.; Willner, I. Probing Biomolecular Interactions at Conductive and Semiconductive Surfaces by Impedance Spectroscopy: Routes to Impedimetric Immunosensors, DNA-Sensors, and Enzyme Biosensors. *Electroanalysis* **2003**, 15, 913—947
28. Muñoz, E.; Suh, D.-S.; Collins, S.; Selvidge, M.; Dalton, A. B.; Kim, B. G.; Razal, J. M.; Ussery, G.; Rinzler, A. G.; Martinez, M.T.; Baughman R. H. Highly Conducting Carbon Nanotube/Polyethyleneimine Composite Fibers. *Adv. Mater.* **2005**, 17, 1064—1067
29. Sanchez-Paniagua López, M.; López-Cabarcos, E.; López-Ruiz, B. Influence of the Host Matrix of the Enzyme in the Performance of Amperometric Biosensors. *Sens. Actuators B: Chem.* **2012**, 171–172, 387—397.
30. Sánchez-Paniagua López, M.; Tamimi, F.; López-Cabarcos, E.; López-Ruiz, B. Highly Sensitive Amperometric Biosensor Based on a Biocompatible Calcium Phosphate Cement. *Biosens. Bioelectron.* **2009**, 24, 2574—2579.
31. Söderhäll, I.; Bergenstråhle, A.; Söderhäll, K. Purification and Some Properties of a *Daucus carota* Lectin which Enhances the Activation of Prophenoloxidase by CaCl_2 . *Plant Physiol.* **1990**, 93, 657—661.

32. Söderhäll, K.; Carlberg, I.; Eriksson, T. Isolation and Partial Purification of Prophenoloxidase from *Daucus carota* L. Cell Cultures. *Plant Physiol.* **1985**, *78*, 730—733.
33. Merkoçi, A.; Anik, U.; Çevik, S.; Çubukçu, M.; Guix, M. Bismuth Film Combined with Screen-Printed Electrode as Biosensing Platform for Phenol Detection. *Electroanalysis* **2010**, *22*, 1429—1436.
34. Alarcón, G., Guix, M., Ambrosi, a, Ramirez Silva, M.T., Palomar Pardave, M.E., Merkoçi, A. Stable and Sensitive Flow-through Monitoring of Phenol using a Carbon Nanotube Based Screen Printed biosensor. *Nanotechnology* **2010**, *21*, 245502.
35. Devaraju, N. S. G. K. ; Unger, M. A. Pressure Driven Digital Logic in PDMS Based Microfluidic Devices Fabricated by Multilayer Soft Lithography. *Lab. Chip.* **2012**, *12*, 4809—4815.
36. Lalo, H.; Ayela, C.; Dague, E.; Vieu, C.; Haupt, K. Nanopatterning Molecularly Imprinted Polymers by Soft Lithography: a Hierarchical Approach. *Lab. Chip.* **2010**, *10*, 1316—1318.

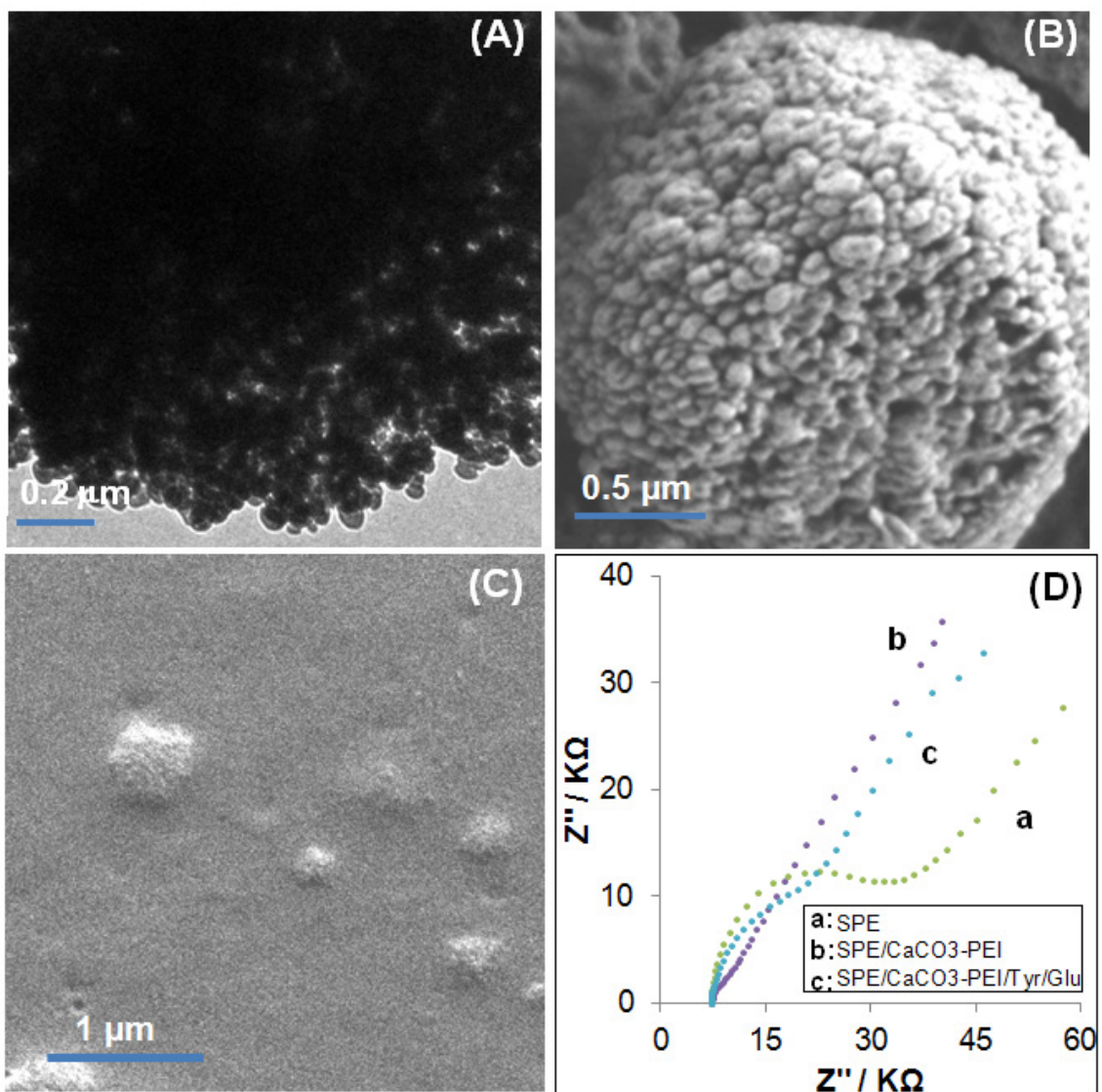


Figure 1. TEM images of a single CaCO_3 -PEI NPs (A). SEM micrographs of modified SPE with CaCO_3 -PEI NPs (B) and CaCO_3 -PEI /Tyr/glutaraldehyde(Glu) (C). Argand diagram of: bare SPE, SPE/ CaCO_3 -PEI and SPE/ CaCO_3 -PEI/Tyr/glutaraldehyde (Glu) modified electrodes in 1 mM $[\text{Fe}(\text{CN})_6]^{3+/4+}$ containing 0.1 M KCl.

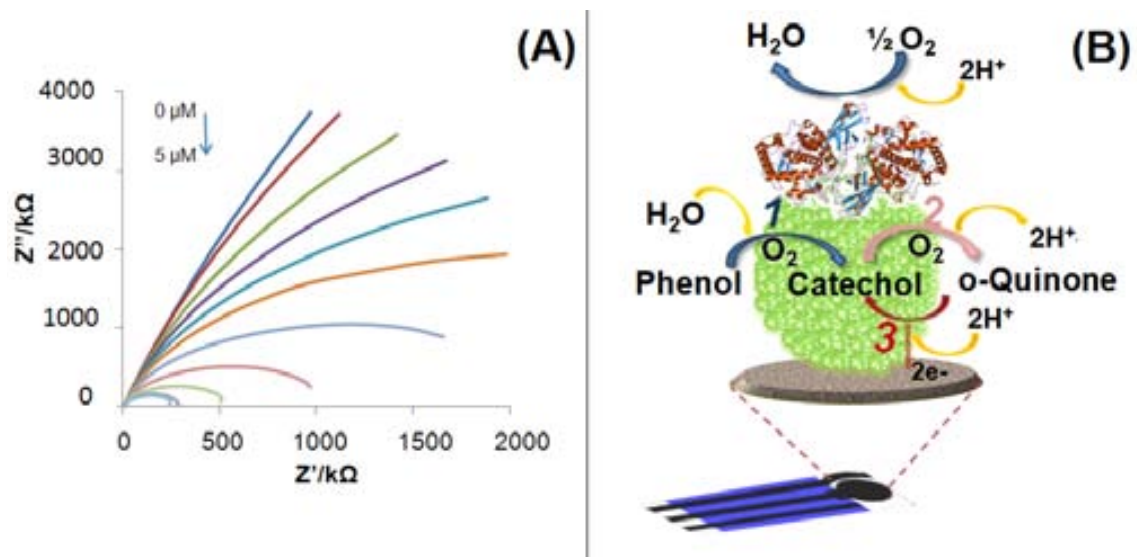


Figure 2. EIS Characterization of the biosensor SPE/ $\text{CaCO}_3\text{-PEI/Tyr}$: (A) Argand Diagram for 0, 0.5, 1.0, 1.5, 2.0, 2.5, 3.0, 3.5, 4.0, 4.5 and 5.0 μM phenol in PBS. (B) Proposed mechanism for the phenol electrocatalytic detection using $\text{CaCO}_3\text{-PEI NPs}$ based biosensor.

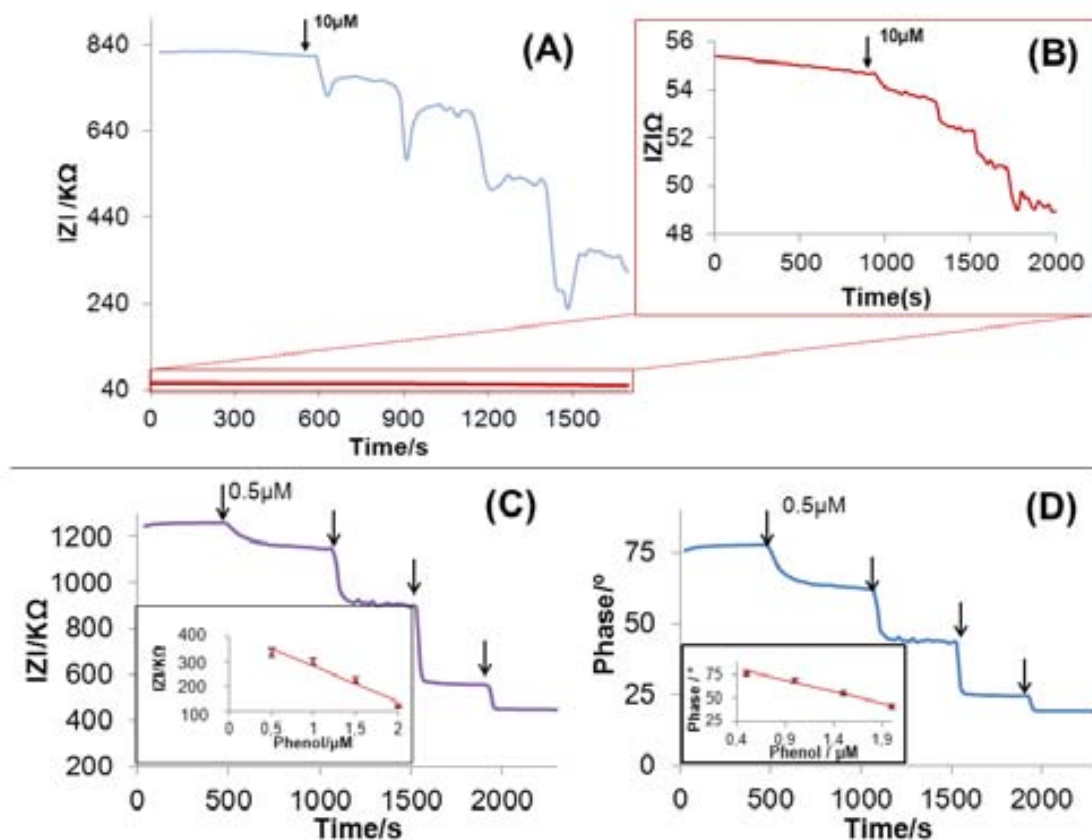


Figure 3. On-line impedimetric $CaCO_3$ -PEI/Tyr biosensor response to additions of phenol measured with the sinusoidal signal of 0.4 Hz (A) and 10 Hz (B). Biosensor calibrations at phenol concentration range of 0.5–2.0 μM as functions of the module (C) and phase (D) of impedance versus time.

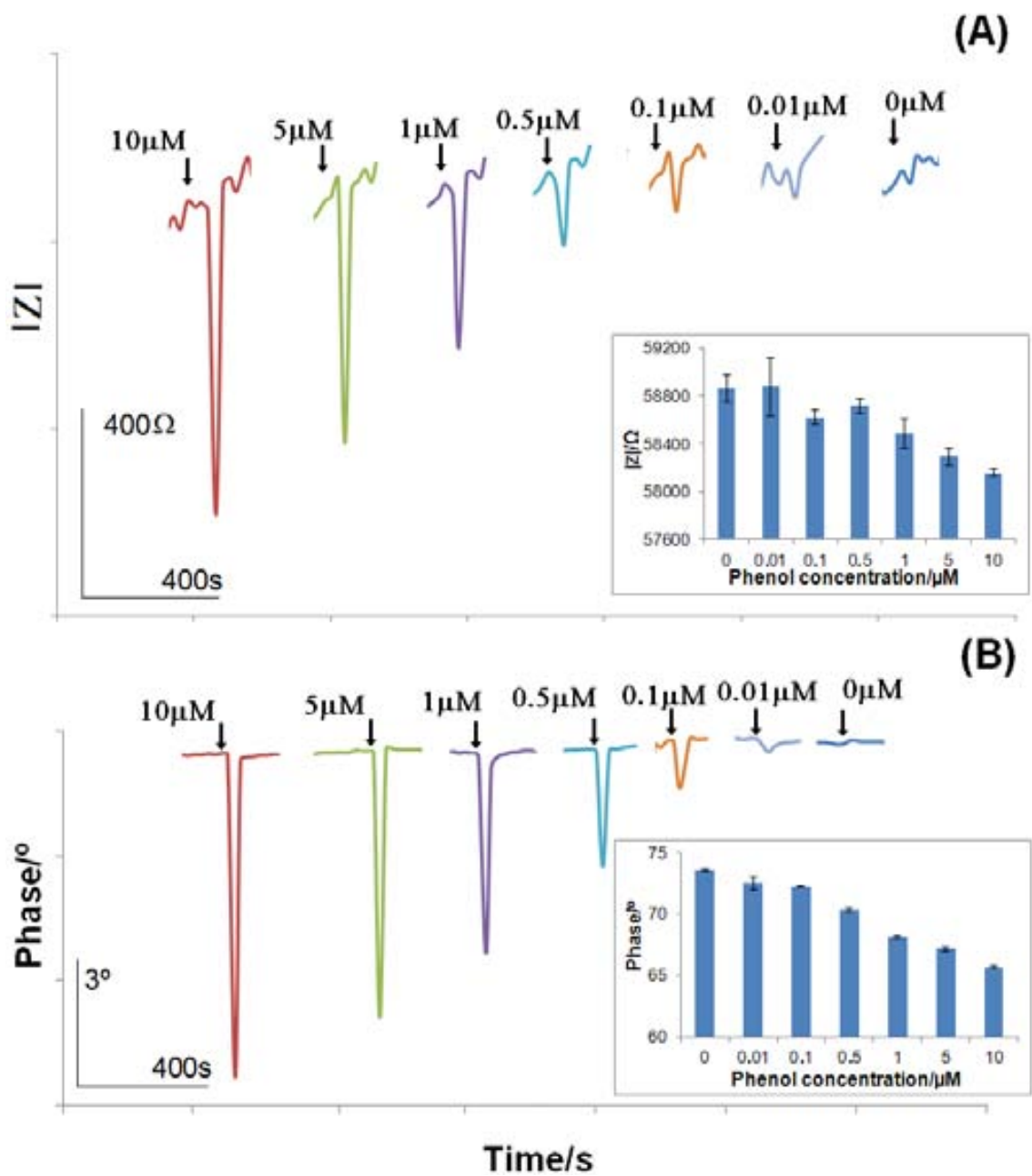


Figure 4. Chronoimpedimetric detection of different phenol concentrations using (FIA) microsystem. Insets: biosensor calibration curve given as impedance module and phase versus phenol concentration introduced in the PDMS/glass fluidic microsystem.

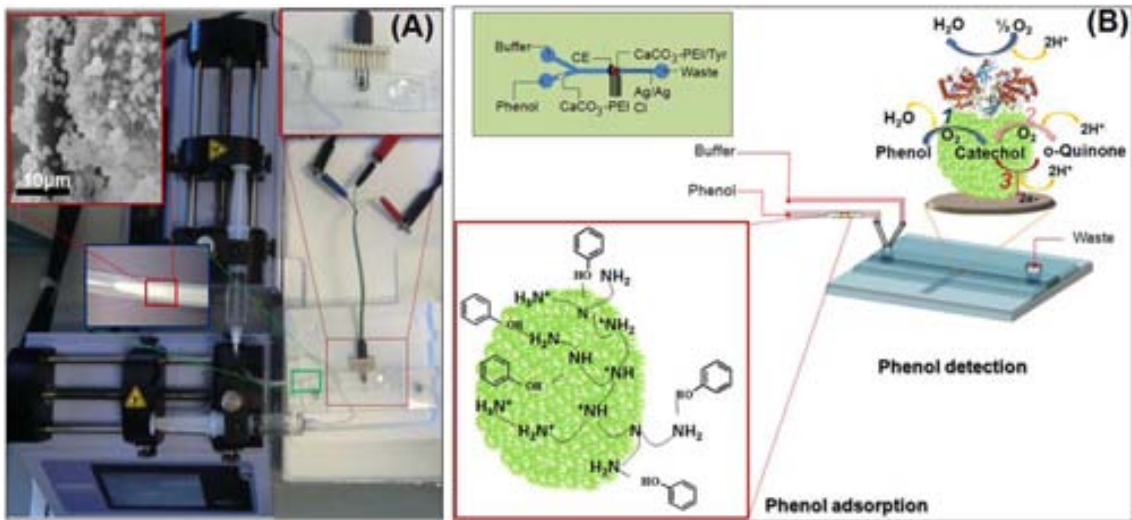


Figure 5. (A) Hybrid PDMS/glass microchip. (B) Schematic diagram of the integrated fluidic microsystem device and chemical mechanism of phenol detection and adsorption.

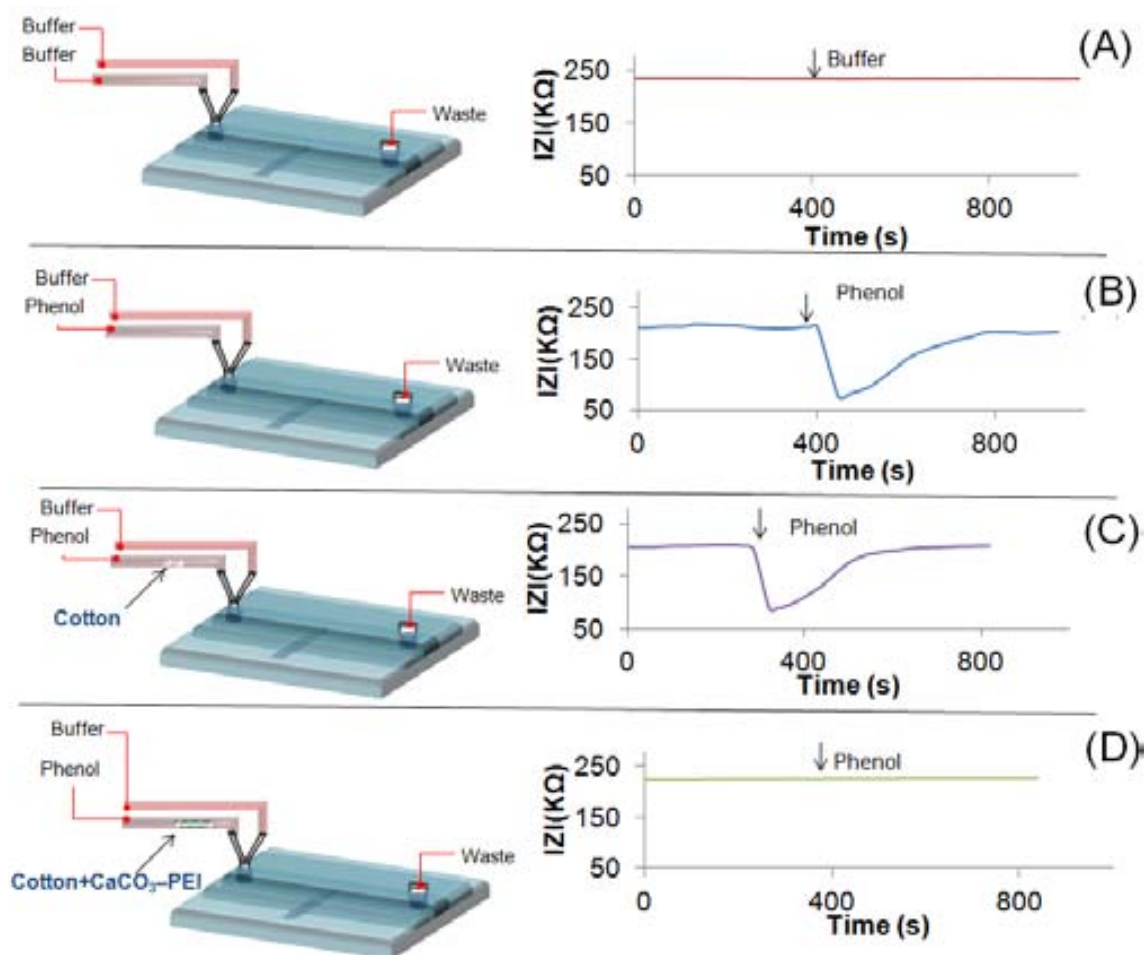


Figure 6. Experimental setup and chronoimpedimetric response of phenol adsorption. 1^d microsystem (A) and 2^d microsystem (B) without CaCO₃-PEI NPs and cotton matrix, and 3^d microsystem (C) with the tube containing only cotton matrix, and 4th microsystem (D) using the tube with cotton matrix and CaCO₃-PEI. Injection of 20 μ L PBS and phenol (2 μ M), respectively.

24-Apr-2013

Dear Dr. Merkoci,

I am pleased to inform you that your manuscript, "Nanostructured CaCO₃-PEI microparticles for phenol sensing in fluidic microsystem", is now acceptable for publication in ELECTROPHORESIS. With the acceptance of your manuscript the final uploaded version in MS-Central will be used for copy-editing and the subsequent production process, so please do not send a new text file.

Please find below a list of required material for production:

- Color and Page Charge Agreement.
- Electronic Copyright Transfer Agreement (eCTA).
- Cover Images.
- Permissions.

Please send this material to the Managing Editor at:

E-mail: elpho@wiley.com

Fax: +49-6201-606-525

After we have received this material, your paper will go into production and you will receive a galley proof by e-mail in due course. Once you have corrected the proof, the paper will then be published on-line via Wiley Online Library ahead of its appearance in the printed journal.

Thank you for supporting ELECTROPHORESIS. I look forward to seeing more of your work in the future.

Sincerely,

Prof. Ziad El Rassi
Editor-in-Chief, ELECTROPHORESIS

Nanostructured CaCO₃-PEI microparticles for phenol sensing in fluidic microsystem

Carmen C. Mayorga-Martinez¹, Lenka Hlavata^{1,2}, Sandrine Miserere¹, Adaris López-Marzo^{1,3}, Jan Labuda², Josefina Pons³ and Arben Merkoçi^{1,4}*

¹Nanobioelectronics & Biosensors Group, Catalan Institute of Nanotechnology, Campus UAB, 08193 Bellaterra, Barcelona, Catalonia, Spain

²Institute of Analytical Chemistry, Faculty of Chemical and Food Technology, Slovak University of Technology in Bratislava, Radlinského 9, 812 37 Bratislava, Slovakia

³Departament de Química, Universitat Autònoma de Barcelona, 08193 Bellaterra, Barcelona, Spain

⁴ICREA, Barcelona, Catalonia, Spain. E-mail: arben.merkoci@icn.cat

[*] Prof. Arben Merkoçi

ICREA, Institució Catalana de Recerca i Estudis Avançats and Nanobioelectronics & Biosensors Group, CIN2 (ICN-CSIC), Catalan Institute of Nanotechnology, Campus de la UAB Bellaterra (Barcelona)
08193 Spain

E-mail: arben.merkoci@icn.cat

Abbreviations: **PEI**, poly(ethyleneimine); **MPs**, microparticles; **PDMS**, polydimethylsiloxane; **Tyr**, tyrosinase; **FIA**, flow injection analysis; **SPE**, Screen Printed Electrode; **CV**, cyclic voltammograms; **DC**, direct current; **PB**, phosphate buffer; **SEM**, scanning electron microscopy; **LOD**, limit of detection.

Keywords: Nanostructured CaCO₃-PEI microparticles, fluidic microsystem, electrochemistry, phenolic compounds.

A new and simple strategy based on nanostructured CaCO_3 -PEI MPs for phenol sensing using PDMS/glass fluidic microchip is developed. This fluidic microsystem including integrated screen-printed-electrodes (SPE) modified with CaCO_3 -PEI MPs and tyrosinase (Tyr) through cross-linking with glutaraldehyde, represents a low cost platform for phenol detection. The designed fluidic microsystem improves the sensitivity of the biosensor allowing the detection of very low concentrations of phenol (up to 10 nM). This device shows high repeatability and low detection limit, is easy to be fabricated, inexpensive, disposable and amenable to mass production.

Introduction

Phenolic compounds are widely found in petrochemical products, and in wood preservatives, textiles, plastics, dyes, paper, herbicides and pesticides [1-3]. The development of analytical methodologies for phenol quantification in various samples as well as for evaluation of their total toxicity with respect to environmental and human health is of great importance [1-5]. The amperometric tyrosinase-based biosensors constitute promising technology for the *in-situ* phenol monitoring in discrete or batch systems because presents a number of advantages (high selectivity, low production cost, fast response, potential for miniaturization, simple instrumentation and easy automation) compared to classic procedures including instrumental methods (gas chromatography, liquid chromatography, etc.) [1,2,6-8].

The combination of nanomaterials and biotechnology open a promising field for the development of the phenol biosensor. Recently, Lopez-Marzo et al. have reported new nanostructured CaCO_3 -PEI (poly(ethyleneimine)) microparticles with high biofunctionalizing capacity and stability (up to 8 months) with interest for biosensing [9].

On the other hand the practical application of batch systems of tyrosinase-based biosensors is limited by the high number of steps needed for the measurement procedure. The biosensors used in these systems have short comings and stability problems for the continuous batch phenol measurement. Among automated systems, flow injection analysis (FIA) has become a very versatile and efficient technique for quantitative automated analyses since its introduction 20 years ago [10]. The combination of biosensors with flow injection (FI) techniques permits the automation and integration of phenol

biosensing. Additionally, this technique allows for the control of the reagent addition steps, the measurement of enzyme activity, and also simplifies the optimization of the conditions of the reaction.

In the current study, we propose the development of an amperometric CaCO_3 -PEI/tyrosinase-based biosensor integrated to a flow microsystem. This phenol biosensing is achieved through a PDMS/glass fluidic platform with integrated screen-printed-electrodes (SPE) modified with CaCO_3 -PEI MPs and tyrosinase (Tyr) through cross-linking with glutaraldehyde. The automated analytical biosystems proposed can be used for *on-line* monitoring of phenol that can be with interest for future sample screening prior to the use of sophisticated measurement systems. Combining the advantages of the PDMS and screen-printing technologies allows the production of reliable and low-cost microdevices. Screen-printing is a well-known technique to produce low cost electrodes at an industrial level [11, 12].

1. Materials and methods

1.1. Materials

All chemicals reagents were purchased from Sigma-Aldrich (Germany). The inks used for the fabrication of screen-printed electrode were purchased from Electroday (Twintec S.L, Badalona-Spain) and used as received. For the preparation of stock solution of 0.1 M PBS pH 6.5 and during the measurements the MilliQ water was used. The stock solution of 100 mM of phenol was prepared in 0.1 M PBS pH 6.5. 1 mg of tyrosinase enzyme from mushroom (≥ 1000 unit/mg) was dissolved in 50 μ L of 0.1 M phosphate buffer at pH 6.5. 1 % glutaraldehyde solution was prepared daily in MilliQ water.

1.2. Apparatus

Electrochemical measurements were performed with a model CH-Instrument potentiostat 660A electrochemical workstation from CH Instruments Inc. Austin, TX. Magnetic stirrer Lab-disc from IKA® Werke Staufen/Germany was used to provide the convective transport during the amperometric measurements. Two Syringe Pumps (standard infusion only pump 11 Elite) from Harvard apparatus were used for injected the phenol stock solution and buffer pH 6.5 solution respectively. Scanning electron microscope (SEM) analysis was performed by using a EVO (Carl Zeiss NTS GmbH. Germany).

1.3. Synthesis of CaCO₃-PEI MPs

Equal volumes of the PEI (4 mg/mL) containing dissolutions of CaCl₂ (0.33 M) in water/ethanol (1:1, v/v) and Na₂CO₃ (0.33 M) in water were quickly mixed under sonication and during 45 min. at room temperature to obtain the nanostructured vaterite CaCO₃-PEI hybrid material. CaCO₃ precipitates were

washed three times, air dried, collected and saved under room temperature conditions while not in use.

1.4. Preparation of SPE and modification with CaCO₃ and Tyr

Screen printing electrodes fabrication is based on the sequential deposition of a graphite ink, Ag/AgCl ink and insulating ink on a polyester substrate. After the deposition of each layer a drying process is followed by keeping the polyester substrate at 120°C for 45 min (graphite) and 30min (Ag/AgCl and insulating). A 5 µL CaCO₃-PEI MPS at 1 mg/mL solution drop was deposited onto the working SPE electrode surface and allowed to dry at room temperature for 20min. A 5 µL drop of Tyr solution was deposited onto the working SPE/CaCO₃ MPs electrode surface and allowed to be dried at room temperature for 3 h. Finally, 5 µL of glutaraldehyde (25%) solution at 1% were dropped onto the SPE/Tyr electrode surface and let to be dried at 40°C for 30min. The prepared SPE/CaCO₃-PEI/Tyr sensor was kept at 4°C while not in use.

1.5. Microdevice fabrication for phenol detection

The microchannel was based on a hybrid PDMS/glass microchip (see Fig. 1 A and B). The channel was fabricated in PDMS by soft lithography [13, 14]. PDMS was poured onto an aluminum micromachined mold and cured at 65 °C for 4 h. The channel was 5 mm wide by 100 µm depth and 5 cm long. Two reservoirs were punched at the inlet and the outlet of the channel. Finally, the PDMS and glass layers were aligned and irreversibly bonded using a 30 s oxygen plasma treatment. The electrochemical detector consists of a set of three screen-printed electrodes. The working electrode was modified following the protocol described above (see Fig. 1 C).

1.6. Electrochemical Experiments

In order to study the characteristics of the modified electrodes surface, CV measurements were carried out at the potential range of -0.55 to 0.8 V vs. Ag/AgCl with 50 mv/s scan rate in 1 mM $[\text{Fe}(\text{CN})_6]^{3-/4-}$ (1:1) as a redox indicator. Amperometric detection was performed applying -0.2 V DC potential vs. Ag/AgCl in 0.1 M phosphate buffer (PB) at pH 6.5 with 0.1 M KCl. All electrochemical experiments were carried out at room temperature.

2. Results and discussion

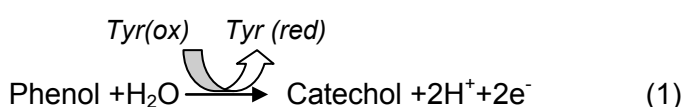
2.1. Characterization of the sensing surface

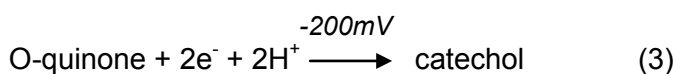
Fig. 2 shows SEM images and cyclic-voltammograms obtained from SPE (A), SPE/ CaCO_3 -PEI (B), SPE/ CaCO_3 -PEI/Tyr (C) and SPE/ CaCO_3 -PEI/Tyr/Glu (D) modified surfaces. The use of CaCO_3 -PEI MPs represents an interesting platform for the immobilization of a large range of biomolecules, because the PEI covering layer onto the MPs surface allows the hydrogen bond formation between the nitrogens of the amino groups in PEI and the hydrogens of the OH, NH or SH groups present in any type of biomolecules [9]. Homogeneous distribution of the CaCO_3 -PEI MPs onto the working electrode surface of SPE was observed (see Fig. 1B). The increase of the electron transfer through the CaCO_3 -PEI composite was observed with the increasing of cathodic and anodic peak currents and improvement of the reversibility in corresponding cyclic voltammograms. These improvements were due to the fact that PEI is a conductive polymer [9]. The adsorption of Tyr on the CaCO_3 -PEI, cause the cathodic and anodic peak currents decrease, indicating that Tyr has been successfully immobilized (Fig. 2 C). Finally, Fig. 2D displays the effect of

glutaraldehyde as a binding matrix, showing a good entrapment of the CaCO₃-PEI MPs and Tyr within the mentioned matrix. The cathodic and anodic peak currents decrease again when glutaraldehyde is adsorbed onto the modified SPE with CaCO₃-PEI and Tyr, which indicates that glutaraldehyde film was an obstacle making the electron transfer of interface more difficult. The result is consistent with that reported in literatures [15 - 16].

2.2. In batch evaluation of the sensing capability of the CaCO₃-PEI/Tyr Biosensor

The CaCO₃-PEI/Tyr biosensor for the phenol detection was evaluated by chronoamperometry measurement. Fig. 3B depicts the chrono-amperometric response for the CaCO₃-PEI/Tyr based biosensor, obtained in 0.1 M phosphate buffer (PBS) at pH 6.5 with 0.1M KCl upon successive additions of 0.5 μM phenol standard solution. Current change at an increase of the phenol concentration is evident at -0.2 V DC. The observed reduction current was attributed to the direct reduction of *o*-quinone liberated from the enzyme-catalyzed reaction on the electrode surface (see Fig. 3A). Tyr has hydroxylase activity, by which phenol can be hydroxylated to catechol using molecular oxygen (equation 1), and also oxidase activity that can catalyze the oxidation of catechol to *o*-quinone (equation 2). At moderately negative potential (-200 mV) the *o*-quinone product of phenol oxidation may be electrochemically reduced to catechol (equation 3). Oxidation by the enzyme followed by reduction at the electrode may result in cycling between the catechol and *o*-quinone [5].





The biosensors showed a rapid and sensitive bioelectrocatalytic response, reaching about 95% of the steady-state current within 40 s after each phenol addition step. Inset of Fig. 3B show the typical calibration curves of the SPE/CaCO₃-PEI/Tyr toward phenol. The obtained biosensing performance was as follows: linear response range from 0.5 -5 μM with $r^2 = 0.9767$, LOD of 25 nM. LOD was calculated as the concentration corresponding to three times the standard deviation of the estimate. The results of triplicate sets indicated by error bars reveal the repeatability (inset Fig. 3B) of the measurements with a relative standard deviation (RSD) lower than 13 %.

2.3. Implementation of the chrono-amperometric detection in FIA chip microsystem

The study of the analytical performance of the developed PDMS/glass microchip was performed in FIA conditions by following the cathodic current and using the optimal conditions obtained: applied -0.2 V DC potential; pH 6.5; flow rate 500 μL min⁻¹; injection volume 20 μL. The typical current–time peaks were obtained for different phenol concentration injections using the PDMS/glass fluidic platform with integrated SPE modified with CaCO₃-PEI MPs and Tyr (see Fig. 4). Well defined peaks were observed. The biosensor exhibited good response as a function of phenol concentration. In the phenol concentration range of 0.01–10 μM, phenol is characterized by a detection limit (LOD) of 5.1 nM which is almost over 5 times lower than the level in batch measurements

using the same system. LOD was calculated from the calibration equation as 3 times the y-intercept standard deviation divided by the calibration slope. A relative standard deviation (RSD) value for triplicate sets of 12.8 % was obtained (Fig. 4 B). The stability of this biosensor is related to the good entrapment of the enzyme within the CaCO₃-PEI and glutaraldehyde matrix indicating that plasma cleaner procedure used to bond PDMS and glass does not alter the activity of the biomembrane. On the other hand, the high biocatalytic activity of the SPE/CaCO₃-PEI/Tyr biosensor can be related with several factors. The enzyme is immobilized by adsorption onto the CaCO₃-PEI and remains entrapped onto the PEI surface via hydrogen bond between labile hydrogen in the biomolecule and PEI's nitrogen [9]. In addition an increase in the amount of active enzyme as a consequence of the enzyme activation by the presence of calcium probably have occurred [17-20]. On the other hand, an improvement of the electron transfer through the CaCO₃-PEI composite (increase of the z-potential and conductivity of the vaterite) due to the fact that PEI is a conductive polymer occurs as well [9]. All these phenomena contribute to the high sensitivity and stability of this biosensor with interest in overall for *in-situ* and *on-line* monitoring applications.

The analytical performances of the proposed amperometric CaCO₃-PEI/tyrosinase-based biosensor integrated to a flow microsystem were compared with other phenol biosensors integrated in microfluidic device reported in the literatures. The proposed FIA microsystem for phenol detection exhibited improved analytical performances in terms of a linear range and limit of detection in comparison with other microfluidic devices for phenol detection, such as phenol biosensor based on hydrogel microarrays entrapping tyrosinase

and quantum dots [21], microchip electrophoresis with amperometric detection for a novel determination of phenolic compounds in olive oil [22], analytic microdevices for the detection of phenol using polymer hydrogel particles containing enzyme–QD conjugates [23] and integrated microfluidics/electrochemical sensor system for monitoring of environmental exposures to lead and chlorophenols [24].

3. Conclusions

In this paper, a new system that allows the *in-situ* and *on-line* phenol sensing using CaCO₃-PEI microparticles in a PDMS/glass microchip was successfully implemented. This fluidic microsystem platform with the integrated CaCO₃-PEI /Tyr- based screen-printed-electrode (SPE) is easy to be fabricated, inexpensive, disposable and amenable to mass production. Very sensitive amperometric detection allowed phenol quantification at very low concentration (10 nM). The developed system uses a very low DC potential, decreasing this way the effect of interferences. On the other hand, the lower reagent consumption, inherent miniaturization and versatility represent the main advantages of the developed device which in the future could be used in automatic control systems with interest for environment monitoring between other applications.

This work was supported by grants from MICINN (Spain) for MAT2011-25870 and Spain-Japan International Bilateral PIB2010JP-00278 projects. A. López Marzo thanks the Generalitat of Catalunya for the FI2010 predoctoral scholarship given. L. H. and J. L. thank for support the Scientific Grant Agency VEGA of the Slovak Republic (Project 1/0182/11).

The authors have declared no conflict of interest.

References

- [1] Shan, D., Zhang, J., Xue, H.-G., Zhang, Y.-C., Cosnier, S., Ding, S.N. *Biosens. Bioelectron.* 2009, 24, 3671-3676.
- [2] Lu, L., Zhang, L., Zhang, X., Huan, S., Shen, G., Yu, R. *Anal. Chim. Acta* 2010, 665, 146-151.
- [3] Dimoglo, A., Akbulut, H. Y., Cihan, F., Karpuzcu, M. *Clean Techn. Environ. Policy* 2004, 6, 288-295.
- [4] Apetrei, C., Alessio, P., Constantino, C. J. L., de Saja, J. A., Rodriguez-Mendez, M. L., Pavinatto, F. J., Fernandes, E. G. R, Zucolotto, V., Oliveira, O.N. *Biosens. Bioelectron.* 2011, 26, 2513-2519.
- [5] Mayorga-Martinez, C. C., Cadevall, M., Guix, M., Ros, J., Merkoçi, A. *Biosens. Bioelectron.* 2012, 40, 57-62.
- [6] Popovtzer, R., Neufeld, T., Biran, D., Ron, E. Z., Rishpon, J., Shacham-Diamand, Y. *Nano Lett.* 2005, 5, 1023-1027.
- [7] Lin, Y., Timchalk, C. A., Matson, D. W., Wu, H., Thrall, K. D. *Biomed. Microdevices* 2001, 3, 331-338.
- [8] Star, A., Han, T.-R., Gabriel, J.-C. P., Bradley, K., Grüner, G. *Nano Lett.* 2003, 3, 459-463.
- [9] Lopez-Marzo, A., Pons, J., Merkoçi, A. *J. Mater. Chem.* 2012, 22, 15326-15335.
- [10] Solé, S., Merkoçi A., Alegret, S. *Anal. Chem.* 2003, 33, 127-143.
- [11] Medina-Sánchez, M., Miserere, S., Marín, S., Aragay, G., Merkoçi, A. *Lab. Chip.* 2012, 12, 2000-2005.
- [12] Pumera, M., Merkoçi, A., Alegret, S. *Trends Analyt. Chem.* 2006, 3, 219-235.

- [13] Devaraju, N. S. G. K., Unger, M. A. *Lab. Chip.* 2012, 12, 4809-4815.
- [14] Lalo, H. Ayela, C., Dague, E., Vieu, C., Haupt, K. *Lab. Chip.* 2010, 10, 1316-1318.
- [15] Mayorga-Martinez, C.C., Guix, M., Madrid, R.E., Merkoçi, A. *Chem. Commun.* 2012, 48, 1686-1688.
- [16] Alarcón, G., Guix, M., Ambrosi, A., Ramirez Silva, M.T., Palomar Pardave, M.E., Merkoçi, A. *Nanotechnology* 2010. 21, 245502 (9pp).
- [17] Sanchez-Paniagua López, M., López-Cabarcos, E., López-Ruiz, B. *Sens. Actuators B: Chem.* 2012, 171– 172, 387-397.
- [18] Sánchez-Paniagua López, M., Tamimi, F., López-Cabarcos, E., López-Ruiz, B. *Biosens. Bioelectron.* 2009, 24, 2574-2579.
- [19] Söderhäll, I., Bergenstråhle, A., Söderhäll, K. *Plant Physiol.* 1990, 93, 657-661.
- [20] Söderhäll, K., Carlberg, I., Eriksson, T. *Plant Physiol.* 1985, 78, 730-733.
- [21] Jang, E., Son, K. J., Kim, B., Koh W.-G., *Analyst* 2010, 135, 2871–2878.
- [22] Godoy-Caballero, M., Acedo-Valenzuela, M. I., Galeano-Díaz, T., Costa-García, A., Fernández-Abedul, M. T. *Analyst* 2012, 137, 5153–5160.
- [23] Park, S.-A. Jang, E., Koh, W.-G., Kim, B. *Talanta* 2011, 84, 1000–1003.
- [24] Lin, Y., Timchalk, C. A., Matson, D. W., Wu, H., Thrall, K. D. *Biomed. Microdevices* 2001, 3, 331-338.

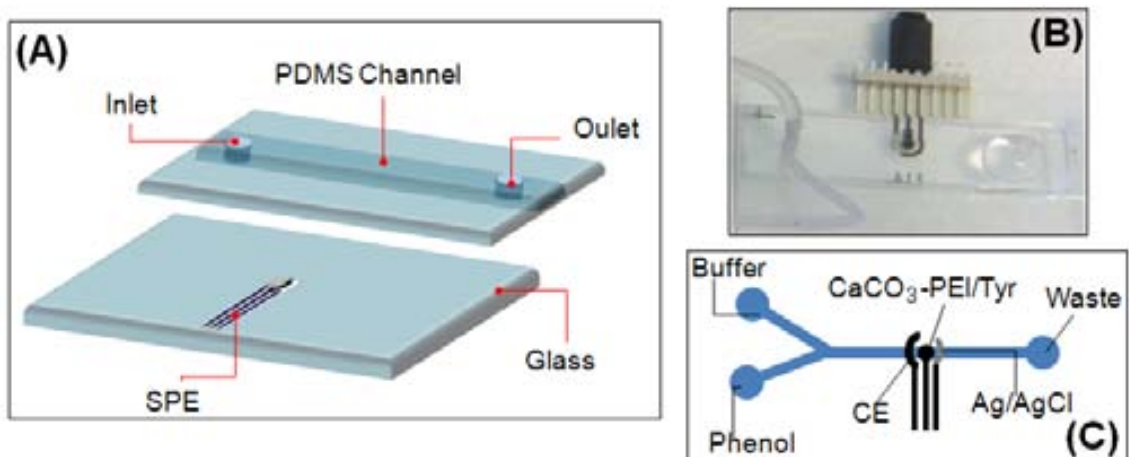


Figure 1. (A) Schematic representation of the PDMS/glass microchip device components. (B) Photograph of the PDMS/glass fluidic microsystem setup. (C) Schematic representation of the microchip design with the channel and SPE modified with CaCO_3 -PEI MPs and tyrosinase.

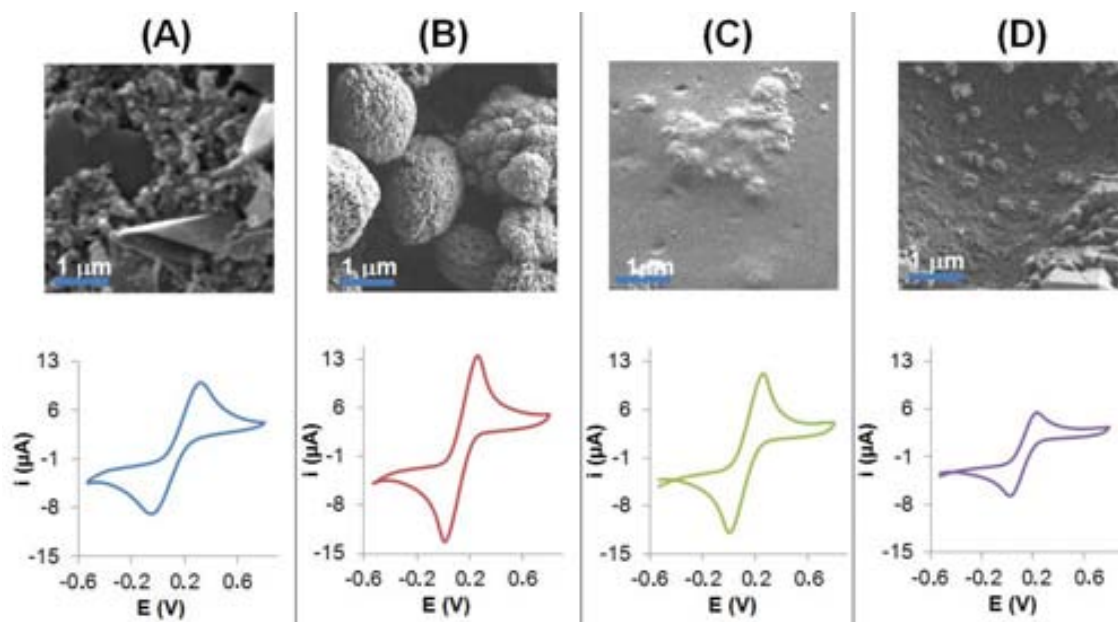


Figure 2. SEM micrographs and cyclic voltammograms of bare SPE (A) and SPE modified with: CaCO₃-PEI MPs (B) and CaCO₃-PEI/Tyr (C); effect of glutaraldehyde as a binding matrix for CaCO₃-PEI MPs and tyrosinase entrapment (D). Cyclic voltammograms curves recorded at 0.05 V/s in 1 mM [Fe(CN)₆]^{3-/4-}.

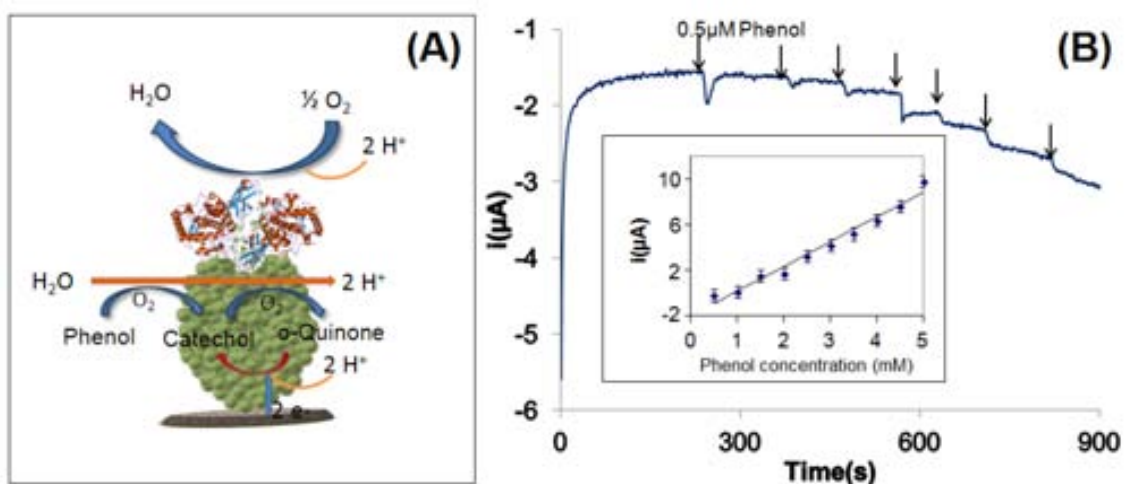


Figure 3. Mechanism for the phenol bioelectrocatalytic detection using CaCO₃-PEI MPs (A). Current-time response curves for the successive additions of 0.5 μM phenol standard solution (B), inset: Biosensor calibration given as cathodic current versus phenol concentration. Working potential is -0.2 V. Other conditions as given in the experiment description part.

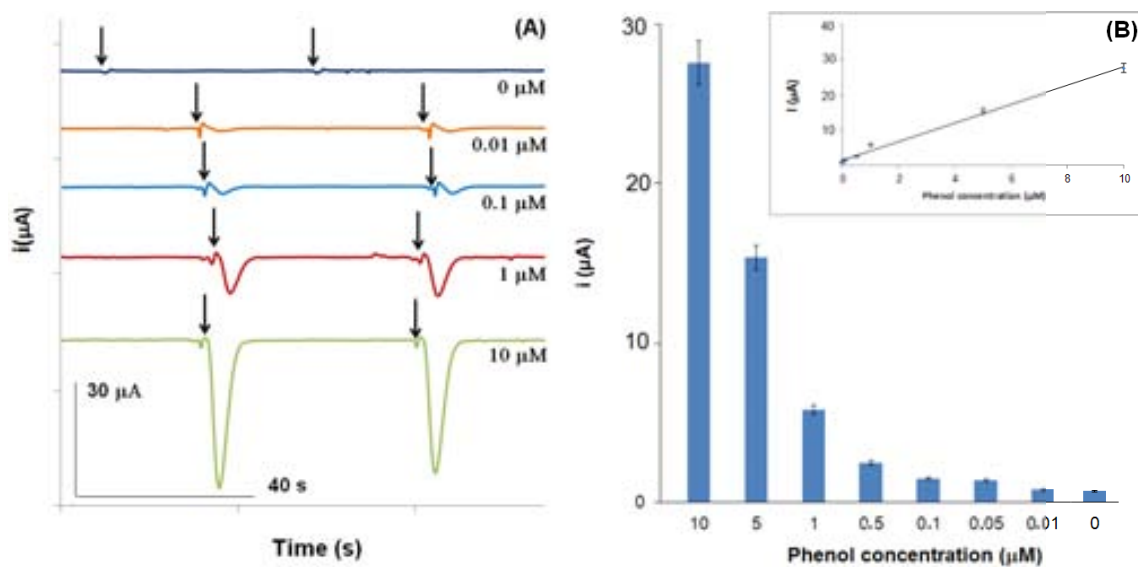


Figure 4. Current-time responses for different phenol concentrations using fluidic microsystem (A). Biosensor calibration curve given as cathodic current versus phenol concentration introduced in the PDMS/glass fluidic microsystem (B).

